OPEN ACCESS

EMPOrIA 2026

Proceedings of the third International Joint Conference on Enhanced Material and Part Optimization and Process Intensification

Uwe Reisgen,
Dietmar Drummer (eds.)

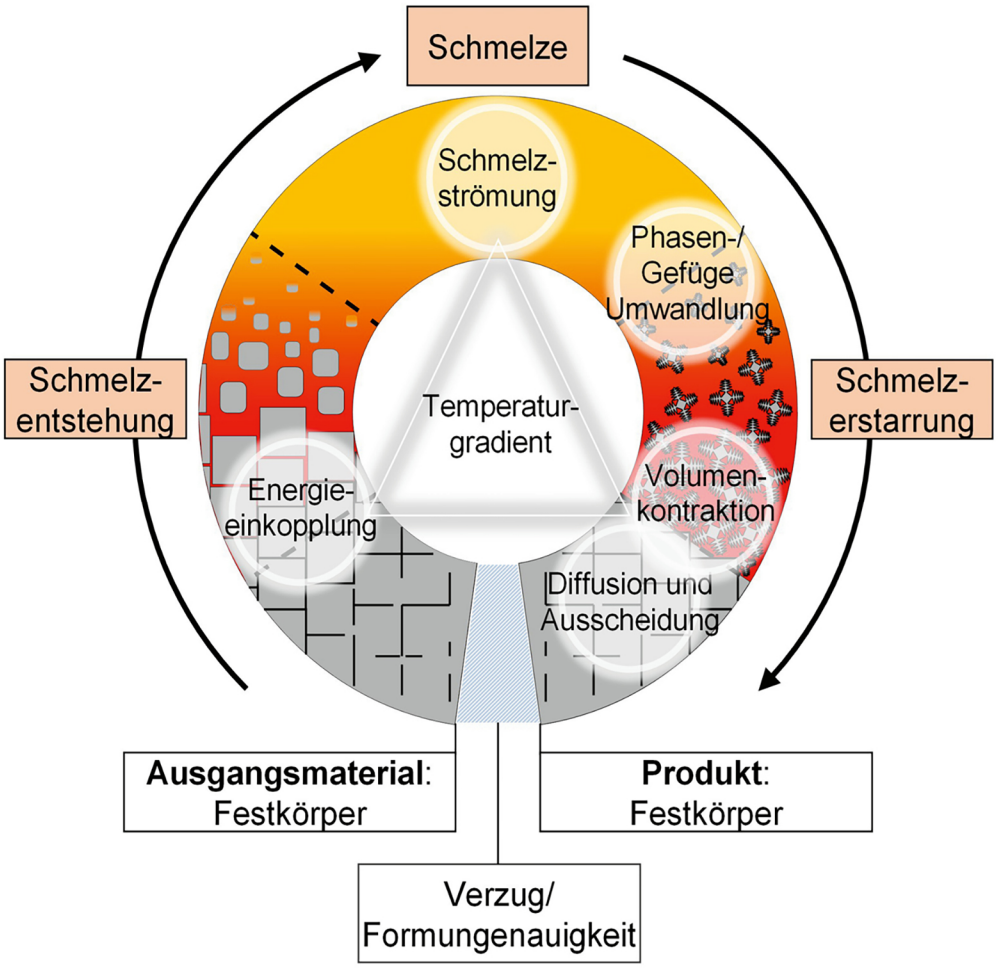

Uwe Reisgen • Dietmar Drummer

Enhanced Material and Part Optimization and Process Intensification

Proceedings of the third International Joint Conference on
Enhanced Material and Part Optimization and Process Intensification EMPOrIA 2026
02nd and 03rd of June 2026, Aachen, Germany

Editors

Uwe Reisgen
RWTH Aachen University
Welding and Joining Institute
Germany

Dietmar Drummer
Friedrich-Alexander-Universität Erlangen-Nürnberg
Institute of Polymer Technology
Germany

Uwe Reisgen, Dietmar Drummer (eds.)

EMPOrIA 2026

Proceedings of the third International Joint Conference
on Enhanced Material and Part Optimization and
Process Intensification

Shaker Verlag
Düren 2026

Bibliographic information published by the Deutsche Nationalbibliothek
The Deutsche Nationalbibliothek lists this publication in the Deutsche Nationalbibliografie; detailed bibliographic data are available in the Internet at http://dnb.d-nb.de.

Shaker Verlag 2026

Print-ISBN 978-3-8191-0730-6
PDF-ISBN 978-3-8191-0670-5
https://doi.org/10.2370/9783819106705

Shaker Verlag GmbH • Am Langen Graben 15a • 52353 Düren
Phone: 0049/2421/99011-0 • Telefax: 0049/2421/99011-9
Internet: www.shaker.de • e-mail: info@shaker.de

Preface

This conference proceedings volume contains papers from the international joint conference “Enhanced Material and Part Optimization and Process Intensification” (EMPOrIA 2026, 2–3 June 2026 in Aachen). The conference was organized by SFB 1120 Aachen (Precision Melt Engineering) and SFB 814 Erlangen (Additive Manufacturing).

Many of the results published in this volume were funded by the Deutsche Forschungsgemeinschaft e.V. (DFG, German Research Foundation). We would like to take this opportunity to express our gratitude for this support.

Highest precision in the manufacturing process in preferably simple process chains with a low number of process steps – that’s one of the main demands made by manufacturing companies that seek to maintain and expand stable and sustainable production in high-wage countries such as Germany at competitive costs. The Collaborative Research Center 1120 (SFB 1120) addresses these research topics with the aim to give a comprehensive description of melt-based manufacturing technologies such as casting, injection molding, welding, cutting, additive manufacturing and melt based coating. For these processes, in which the material is at least temporarily in a liquid phase, a multi-scale description of the involved physical and material-based processes will be developed, so as to increase part precision by at least one order of magnitude.

Wherever innovations and personalized products are desired: With almost unlimited freedom of design, additive manufacturing technologies open up new perspectives to achieve constructive solutions. These types of manufacturing techniques barely set any limits to the spirit of innovation. Additive manufacturing techniques follow the trend towards individual customized products and will allow for serial production in the future. To take advantage of the potentials included in additive manufacturing techniques the Collaborative Research Centre 814 (SFB814) does fundamental research on this technology, so it can be used for the production of multifunctional components. The most important thing is to analyze the process chain from beginning to end. This not only includes design and process simulation, but also especially characteristics, creation and modification of suitable materials and their reactions in the fabrication process, up to the final component.

The EMPOrIA 2026 is a perfect platform for efficient knowledge transfer in the field of materials processing and their applications. The EMPOrIA 2026 is devoted to scientific presentations on the latest research results.

The EMPOrIA 2026 focuses on the latest developments as well as future trends in the field of materials processing. The conference topics address anyone who is interested in the potential of manufacturing in theory and application. It is the aim of the

EMPOrIA 2026 to bring together international experts from research and industry to match scientific advances and economic needs for mutual benefit.

Thank you very much for EMPOrIA 2026 Team. Their involvement and hard work were crucial to the success of the EMPOrIA 2026 conference.

April 2026

Uwe Reisgen
Dietmar Drummer

Contents

Date: 25.03.2026

Thermo-optical-rheological interactions in variothermal powder bed fusion of carbon fiber modified PEEK

Author: S. Schlicht

Authors: S. Schlicht[1,2*], D. Drummer[1,2]

[1] Institute of Polymer Technology, Friedrich-Alexander-Universität Erlangen-Nürnberg (FAU), Am Weichselgarten 10, 91058 Erlangen, Germany

[2] Collaborative Research Center 814, Friedrich-Alexander-Universität Erlangen-Nürnberg (FAU), Am Weichselgarten 10, 91058 Erlangen, Germany

*Corresponding author: E-mail: samuel.schlicht@fau.de, ORCID: 0000-0002-4304-1027

Abstract

Non-linear fractal exposure strategies enable the cold, support-free laser powder bed fusion (PBF) of semicrystalline thermoplastics by transiently decoupling crystallization-induced shrinkage from the macroscopic geometry at powder bed temperatures significantly below the crystallization onset. This paper addresses the interaction between optical characteristics, quasi-simultaneous exposure conditions, and rheological melt properties in the processing of carbon fiber (CF) modified polyetheretherketone (PEEK) at a powder bed temperature of 50 °C. Extended instantaneous dwell times under identical accumulated energy densities are interlinked with pronounced charring, implying that degradation is governed by the intensity-time product, corresponding to the area energy density per exposure pass, rather than the isolated focal intensity. Increased exposure velocities under correspondingly reduced cycle times allow for mesoscopic coalescence while limiting transient thermal peaks. Complementarily, increased CF fractions constrain the inter-layer fusion through elevated melt stiffness, corroborating the coupled significance of optical properties, exposure-induced temperature fields, and melt rheology in cold PBF.

Keywords

Powder Bed Fusion; PEEK; Carbon Fiber; Quasi-simultaneous; Degradation; Variothermal

1 Introduction

The additive manufacturing of high-melting thermoplastics, in particular of polyaryletherketones (PAEK), has received increasing academic and industrial attention in recent years [1]. As one industrially significant manufacturing process, the laser-based powder bed fusion (PBF) of PAEKs has been studied with special emphasis on the influence of applied exposure parameters on structural and mechanical properties [2]. In this regard, Chen et al. (2022) described the energy density as a significant influence on the degradation of PEEK in quasi-isothermal powder bed fusion [3]. In particular, elevated energy densities were observed to be associated with rapid carbonization alongside a significant decline in mechanical part properties. Niino et al. (2015)

confirmed the association of reduced powder bed temperatures and exposure-induced in-process degradation, leading to pronounced degradation under elevated focal intensities [4]. In addition, Kigure et al. (2022) described the feasibility of PBF of PEEK through adapted, repeated meander scanning using comparably low hatch distances of d = 50 µm and defocused beam diameters of up to 1685 µm at a powder bed temperature of 170 °C [5], yielding de facto multi-pass strategies based on the relation between the hatch distance and the laser focus diameter. While using an underlying rigid support structure, the authors reported a positive correlation of the layer height and the degree of degradation, likely associated with the locally impaired dissipation of heat [5]. Complementing different multi-scanning approaches, which were described by Kigure et al. [5,6] for limiting transient thermal peaks and thus yielding satisfactory morphological and mechanical properties of manufactured parts, Yang et al. (2025) described the use of multi-scan regimes for optimizing the coalescence of PEEK/CF composites [7]. In particular, Yang et al. derived a limit for the fraction of carbon fiber for satisfactory coalescence, the interlinked *in situ* impregnation, and the formation of dense composites under laser irradiation, with a gravimetric fraction of 25% CF leading to the formation of voids alongside incomplete coalescence despite the application of multi-exposure regimes. In contrast to predominantly applied quasi-isothermal processing regimes, which are associated with thermally induced changes to the chemical composition and rheological material properties [8], variothermal processing has been shown to allow for the control of residual stresses that intrinsically form under reduced ambient temperatures [9], which are characterized by the inter-layer crystallization and solidification while avoiding support structures. In previous work, the suitability of both locally quasi-simultaneous [10,11] and fractal, discretized strategies [12,13] for the *cold* processing of semicrystalline polymers was demonstrated: These exposure strategies have been shown to allow for the intermediate solidification while they, due to the spatio-temporal separation of the formation of nearby melt pools, intrinsically limit the formation of directed residual stresses and hence allow for the minimization of process-limiting deflections, usually referred to as *warping*. While these previous studies have established the fundamental feasibility of quasi-simultaneous, locally segmented strategies, the interaction of the underlying optical, thermal, and rheological material-related influences under the constraint of comparably short timespans above the crystallization onset temperature remains poorly understood. In particular, the modalities of the interaction of the laser irradiation with optically dense materials and the emerging structure formation upon repeated exposure remain unclear. Based on these open challenges, the present study explores the decoupled interaction of focal intensity and incident exposure time in the quasi-simultaneous, fractal processing of optically dense composites under cold conditions.

2 Processing and materials

Based on fractal, superposed exposure strategies, the present study aims to decouple the influence of the focal intensity and the incident exposure time on the process-induced degradation of PEEK/CF composites under variothermal conditions. PEEK powder of type VESTAKEEP FP 2000 (Evonik Industries AG, Essen, Germany) was modified with milled carbon fiber (R&G Faserverbundwerkstoffe GmbH, Waldenbuch, Germany) in fractions of 5 wt.-% and 10 wt.-% through blending in a laboratory mixer at a rotational speed of $n = 5000\ min^{-1}$ for 10 minutes.

Applied exposure strategies were based on the quasi-simultaneous, repeated exposure of fractal Gosper curves. Based on a hatch distance of 1.6 mm, two phase-shifted Gosper curves were exposed applying varying numbers of consecutive cycles (Table 1), following protocols described earlier by Schlicht et al. (2022, 2025) for the locally quasi-simultaneous exposure during variothermal PBF [10,11] and the phase-shifted, superposed application of fractal curves [12,13]. Square cross-sections ($A = 10 \times 10$ mm²) were exposed two-fold in each layer while varying the applied laser power in discrete steps (Table 1). A commercially available laser sintering machine of type Sinterit Lisa X (Sinterit GmbH, Krakow, Poland), equipped with a NIR laser ($\lambda = 976$ nm, $d_{Focus}(I = I_0\, e^{-2}) = 650$ µm), was employed using a custom scanner control for generating superposed, quasi-simultaneous exposure strategies. To minimize coating-induced shear stresses on consolidated parts, we employed a counter-rotating roller, using a coating speed of $v = 50$ mm s^{-1}. A layer height of 150 µm and a powder bed temperature of 50 °C were kept constant throughout all process variations.

Table 1: Overview of the full-factorial parameter variation applied in the variothermal processing.

Laser power / W	Quasi-simultaneous exposure conditions	Focal intensity * instantaneous exposure time / W m^{-2} s	Cumulative averaged volumetric energy density / J mm^{-3}
15	$v = 0.5$ m s^{-1}, $n_{Repetitions} = 13$	58765	6.50
15	$v = 0.5$ m s^{-1}, $n_{Repetitions} = 15$	58765	7.50
15	$v = 0.5$ m s^{-1}, $n_{Repetitions} = 17$	58765	8.50
15	$v = 1$ m s^{-1}, $n_{Repetitions} = 25$	29382	6.25
15	$v = 1$ m s^{-1}, $n_{Repetitions} = 30$	29382	7.50
15	$v = 1$ m s^{-1}, $n_{Repetitions} = 35$	29382	8.75
15	$v = 2$ m s^{-1}, $n_{Repetitions} = 50$	14691	6.25
15	$v = 2$ m s^{-1}, $n_{Repetitions} = 60$	14691	7.50
15	$v = 2$ m s^{-1}, $n_{Repetitions} = 70$	14691	8.75
20	$v = 0.5$ m s^{-1}, $n_{Repetitions} = 13$	78353	8.67
20	$v = 0.5$ m s^{-1}, $n_{Repetitions} = 15$	78353	10.00
20	$v = 0.5$ m s^{-1}, $n_{Repetitions} = 17$	78353	11.33
20	$v = 1$ m s^{-1}, $n_{Repetitions} = 25$	39177	8.33
20	$v = 1$ m s^{-1}, $n_{Repetitions} = 30$	39177	10.00
20	$v = 1$ m s^{-1}, $n_{Repetitions} = 35$	39177	11.67
20	$v = 2$ m s^{-1}, $n_{Repetitions} = 50$	19588	8.33
20	$v = 2$ m s^{-1}, $n_{Repetitions} = 60$	19588	10.00
20	$v = 2$ m s^{-1}, $n_{Repetitions} = 70$	19588	11.67
25	$v = 0.5$ m s^{-1}, $n_{Repetitions} = 13$	97942	10.83
25	$v = 0.5$ m s^{-1}, $n_{Repetitions} = 15$	97942	12.50
25	$v = 0.5$ m s^{-1}, $n_{Repetitions} = 17$	97942	14.17
25	$v = 1$ m s^{-1}, $n_{Repetitions} = 25$	48971	10.42
25	$v = 1$ m s^{-1}, $n_{Repetitions} = 30$	48971	12.50
25	$v = 1$ m s^{-1}, $n_{Repetitions} = 35$	48971	14.58
25	$v = 2$ m s^{-1}, $n_{Repetitions} = 50$	24485	10.42
25	$v = 2$ m s^{-1}, $n_{Repetitions} = 60$	24485	12.50
25	$v = 2$ m s^{-1}, $n_{Repetitions} = 70$	24485	14.58

Single layers were manufactured applying aforementioned scan velocities for both material compositions to assess the velocity-dependent degradation behavior. Complementarily, multi-layer cuboid specimens with a nominal height of 10 mm were manufactured at a scan velocity of 2 m s^{-1} to evaluate the inter-layer coalescence. The characterization was performed using both bright field

and dark field incident light microscopy (AxioImager M2, Carl Zeiss Microscopy GmbH, Oberkochen, Germany) as well as scanning electron microscopy (SEM) for the assessment of the parameter-dependent surface formation of single layers. Degradation-associated metrics were obtained based on ATR-FTIR and DRIFT spectroscopy (Nicolet FTIR spectroscope, Thermo Fisher Scientific), complemented by rheological characterizations through rotational viscometry (HR 20, TA Instruments, New Castle, DE, USA) and thermogravimetric characterizations.

3 Results and Discussion

3.1 Temporal influences on degradation mechanisms in optically dense systems

The variation of scan velocity at constant focal intensity is associated with a pronounced, non-linear influence of the instantaneous exposure time on the degree of thermal degradation. Considering an exposure velocity of v = 2 m s^{-1}, no microscopically detectable degradation is observed for either PEEK/CF5 or PEEK/CF10 in light microscopy. In contrast, an exposure velocity of 0.5 m s^{-1} is correlated with macroscopically visible, pronounced charring alongside pronounced variations in the fingerprint region in ATR-FTIR measurements (Fig. 1) [14].

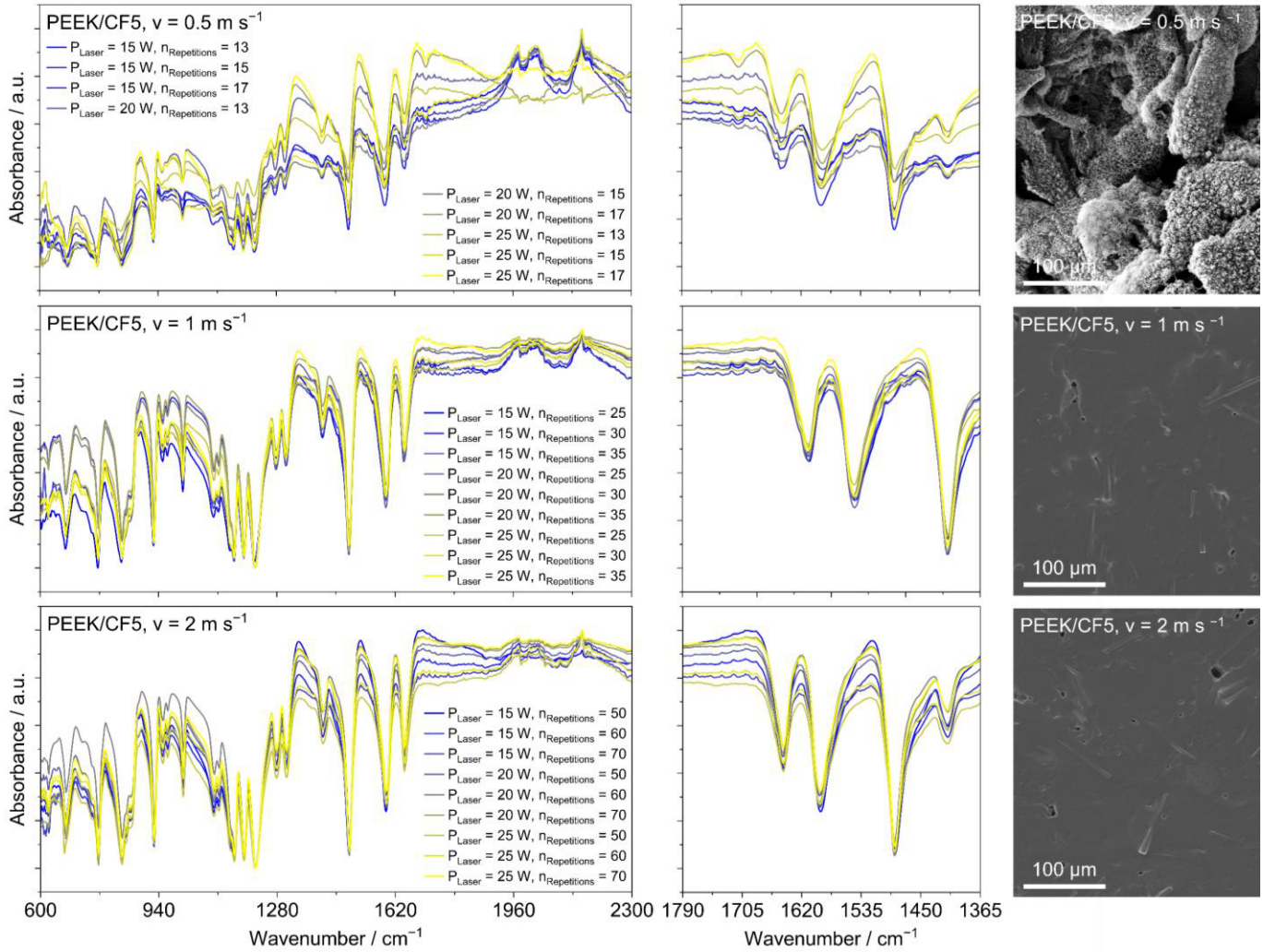

Figure 1: ATR-FTIR spectra and corresponding parameter-dependent scanning electron micrographs of PEEK/CF5 single layers, shown scanning electron micrographs were manufactured using P_{Laser} = 25 W and $n_{Repetitions}$ = 17 (v = 0.5 m s^{-1}), $n_{Repetitions}$ = 35 (v = 1 m s^{-1}), and $n_{Repetitions}$ = 70 (v = 2 m s^{-1}).

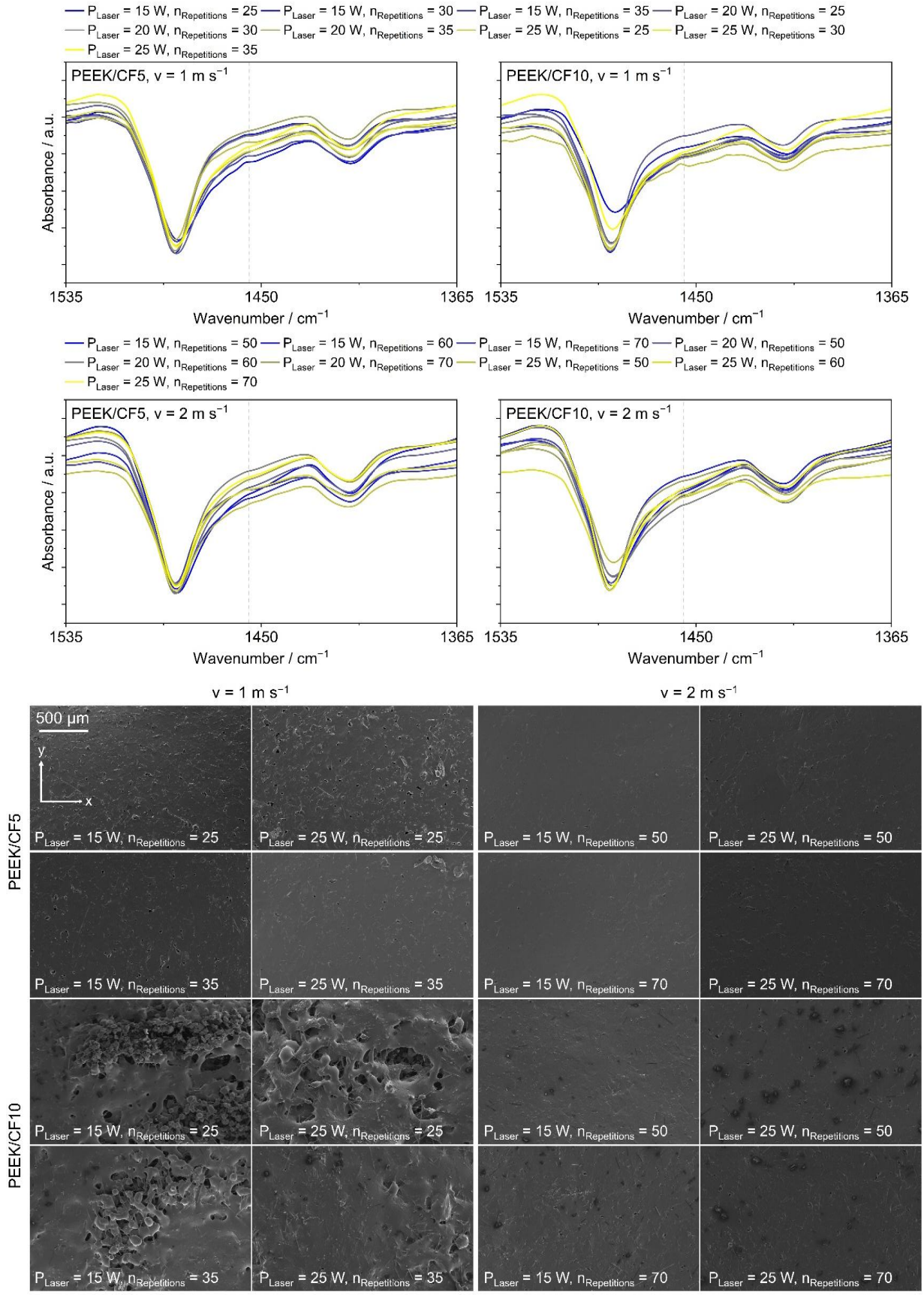

Figure 2: Material-dependent FTIR spectra and corresponding scanning electron micrographs in dependence of the fraction of carbon fibers under varied process parameters.

Corresponding scanning electron micrographs display significant process-induced variations in the emerging surface topography. At both v = 1 m s^{-1} and v = 2 m s^{-1}, coalesced, dense layers with protruding, partially embedded carbon fibers without signs of topographically represented degradation phenomena are observed, displayed in Fig. 1. In contrast, a relatively reduced exposure velocity of v = 0.5 m s^{-1} is associated with the pronounced formation of an intumescent, porous residue, associated with extensive matrix pyrolysis in proximity to the embedded fibers. While a pronounced degradation can be observed regardless of the underlying material at an exposure velocity of v = 0.5 m s^{-1}, a more nuanced interaction between the fraction of CF and the applied exposure parameters on both degradation-associated metrics and the inter-particle fusion can be observed (Fig. 2). In particular, while the inter-particle coalescence is significantly impaired in the processing of elevated CF fractions under a reduced number of repetitions, no correlation between the ATR-FTIR-derived degradation and the intra- and inter-layer fusion, discussed in section 3.2, can be observed. Displayed in Fig. 3 (a), neither the fraction of CF, despite differences in the optical properties (Fig. 3 (b)), nor the distinction between exposure velocities of v = 1 m s^{-1} and v = 2 m s^{-1} is associated with a significant increase in the extent of thermo-oxidative degradation.

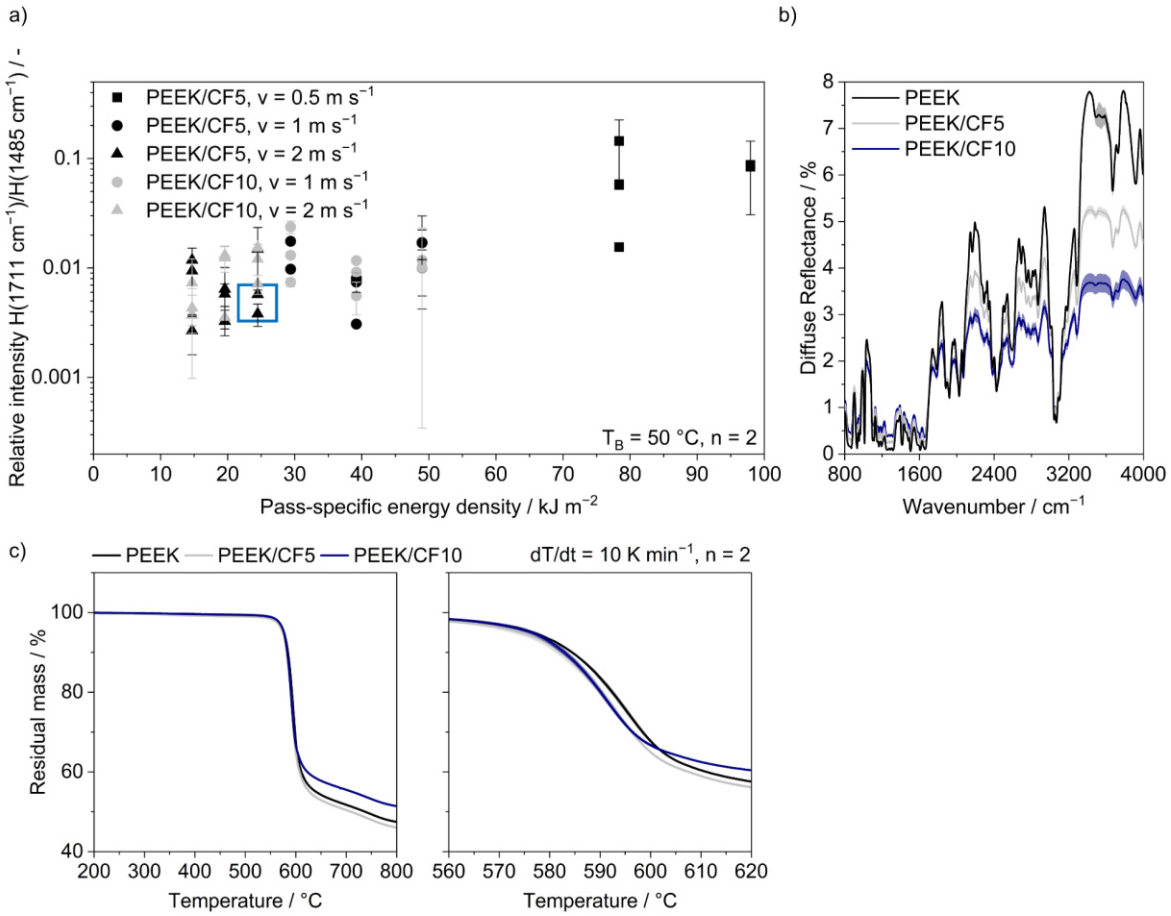

Figure 3: Scatter plot of the (a) relation of the pass-specific energy density and the corresponding relative FTIR-derived degradation alongside the (b) optical and (c) thermogravimetric properties of applied materials relative to the non-modified matrix; the region of stable multi-layer fusion is indicated by a blue frame; PEEK/CF5 | v = 0.5 m s^{-1} | P_{Laser} = 15 W and PEEK/CF10 | v = 0.5 m s^{-1} not displayed due to insufficient reference signal quality arising from pronounced degradation.

This is in contrast to significantly elevated degradation markers observed for samples manufactured with a velocity of v = 0.5 m s^{-1}, which are equivalent to elevated pass-specific energy densities. In particular, given the significant influence of the exposure velocity, these observations imply that the isolated consideration of the focal intensity is insufficient for describing the occurrence of degradation processes in optically dense polymer systems. Notably, thermographic investigations in variothermal processes indicate the presence of rapid cooling following the initial heating, while the extent of superheating beyond the material melting point displays a positive correlation with the focal intensity [15]. Based on corresponding thermogravimetric measurements, the significantly increased degradation under the applied process conditions indicates that transient peak temperatures beyond 600 °C may be reached during processing, considerably exceeding the matrix melting temperatures. Spectroscopic data indicate a dwell time-dominated degradation mechanism that exhibits a non-linear dependency on the exposure velocity, which is consistent across both filler fractions. The negligible presence of significant FTIR degradation markers at v = 2 m s^{-1} alongside the significantly elevated carbonyl signal at v = 0.5 m s^{-1} are furthermore in accordance with the previously discussed microscopic observations. Hence, our observations indicate an intrinsic stability of sufficiently time-segmented quasi-simultaneous exposure strategies against local overheating for optically dense systems.

3.2 Rheological correlates in multi-layer structure formation

Since previous observations, discussed in section 3.1 and reflected in Fig. 3, indicate the predominant absence of degradation effects at elevated exposure velocities, the characterization of multi-layer cuboid samples was limited to samples manufactured at a scan velocity of 2 m s^{-1}.

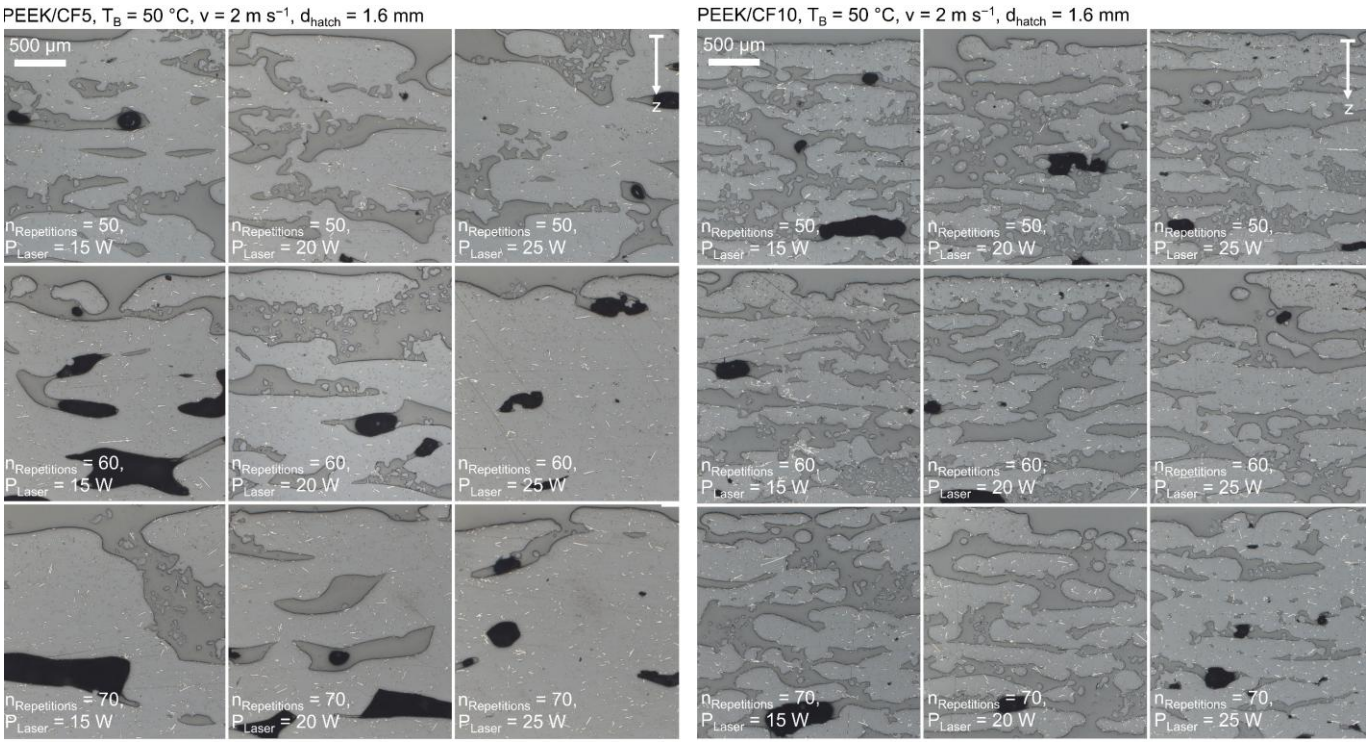

Figure 4: Process-dependent microstructural characteristics of manufactured specimens generated from PEEK/CF5 (l.) and PEEK/CF10 (r.), dark regions associated with cavities that were not infiltrated during microscopic preparation.

Manufactured specimens exhibit a significant dependence of the qualitatively assessed extent of inter-layer fusion on the fraction of CF. PEEK/CF5 displays a dense inter-layer fusion under the influence of both elevated laser powers and increased numbers of quasi-simultaneous repetitions. In contrast to the predominantly dense structures and satisfactory inter-layer fusion achievable with PEEK/CF5 under elevated laser power, the processing of PEEK/CF10 is associated with predominantly dense individual layers, which, however, display pronounced gaps between consecutive layers (Fig. 4, r.), which distinguishes the PBF of PEEK from the previously reported processing of low-melting thermoplastics [12]. Under bright field microscopy, a predominantly homogeneous distribution of carbon fibers can be observed, indicating that the observed mechanisms may be attributed to the macroscopic rheological characteristics of the formed melt instead of the local presence of carbon fiber agglomerates. In particular, the increased viscosity of PEEK/CF10 (Fig. 5) appears to restrict the inter-layer fusion within the available timespan above the melting temperature, while the lower viscosity of PEEK/CF5 allows for a sufficient deformation of the partially molten structure, which is associated with an improved, dense inter-layer bonding.

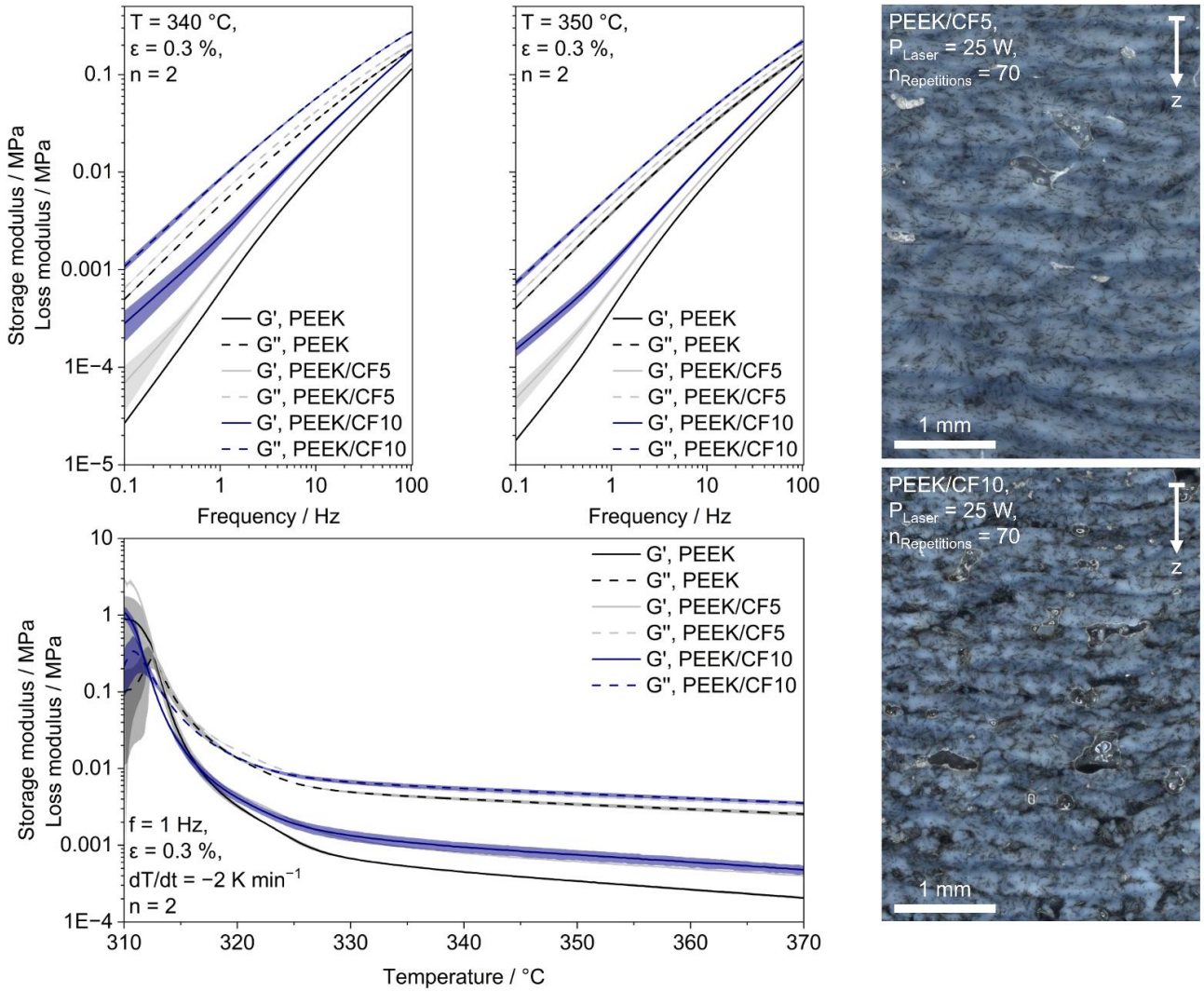

Figure 5: Frequency- and temperature-dependent rheological characteristics of applied CF-filled PEEK systems and corresponding incident light macrographs of the rheology-dependent multi-layer formation.

Given the temporal segmentation of subsequently exposed, phase-shifted cycles, the observed phenomenon can thus be interpreted as a stabilization of the melt stiffness at increased CF fractions, which impairs the bonding of consecutive layers under the sole influence of gravitational forces. These interpretations are in accordance with the rheological characteristics of the underlying materials (Fig. 5 (l.)). At low shear rates, which are representative of gravity-driven flow in PBF, the relative viscosity difference between PEEK/CF5 and PEEK/CF10 is particularly pronounced, indicating that the coalescence of transiently formed, discrete melt pools is substantially impaired at elevated CF fractions, which is furthermore in accordance with the discrepancies between satisfactory intra-layer fusion and partially insufficient inter-layer fusion. The fraction of absorbing fillers in variothermal PBF thus requires consideration with regard to its thermal, optical, and rheological effects, with the latter introducing a mesoscopic constraint on the multi-layer density. In particular, the relation of viscous and elastic properties of the melt is governed by the timespan available for inter-layer fusion, which is proportional to the number of repetitions.

4 Summary and Outlook

In the present study, we demonstrated the degradation-minimized laser powder bed fusion of PEEK/CF composites under cold ambient temperatures (T_B = 50 °C) under the influence of varying rheological and optical material properties. By varying the scan velocity while maintaining constant focal intensities and cumulative energy densities through correspondingly adapted numbers of quasi-simultaneous exposure cycles, the transient focal intensity-time product, in contrast to the isolated consideration of the focal intensity, was identified to govern the onset and extent of thermal and thermo-oxidative degradation. Based on infrared spectroscopic results, a progressively increasing degradation with increasing area energy densities per scan pass could be derived, while specimens processed at elevated exposure velocities and a correspondingly reduced energy density per scan pass display negligible indications of carbonyl-associated degradation. In addition to the influence of temporal process characteristics, formed multi-layer morphologies indicate the presence of rheological constraints on the inter-layer fusion. Elevated filler fractions are interlinked with significant increases in the storage modulus of the CF-modified melt under comparably short-term laser exposure, which leads to an impaired inter-layer fusion. In contrast, pronounced intra-layer fusion and the interlinked coalescence of discrete PEEK particles are observed to occur for significantly lower energy densities compared to those required for inter-layer fusion. These observations thus allow for deriving a coupled thermo-optical-rheological processing window for the cold PBF of optically dense, CF-modified PEEK composites and furthermore indicate a transferability to a broad range of high-melting, filler-modified material systems.

Acknowledgements

The authors acknowledge financial support by the Central Innovation Programme for small and medium-sized enterprises (SMEs) under the project “Cold Sintering of High Performance Thermoplastics for High Technology Applications – ColdHT”, funding reference number KK6010201KX5. The authors thank Prof. Dr.-Ing. Karl Kuhmann, Evonik Industries AG, and Philipp Kilian, Evonik Operations GmbH, for providing materials.

Conflict of Interest

The authors declare no conflict of interest.

Data Availability Statement

Underlying data are available from the corresponding author upon reasonable request.

References

[1] T. Yap, N. Heathman, T. Phillips, J. Beaman, M. Tehrani, Additive Manufacturing of Polyaryletherketone (PAEK) polymers and their composites, Compos. Part B Eng. 266 (2023) 111019.

[2] P. Chen, H. Wang, J. Su, Y. Tian, S. Wen, B. Su, C. Yang, B. Chen, K. Zhou, C. Yan, Recent advances on high-performance polyaryletherketone materials for additive manufacturing, Adv. Mater. 34 (2022) 2200750.

[3] P. Chen, J. Su, H. Wang, L. Yang, H. Cai, M. Li, Z. Li, J. Liu, S. Wen, Y. Zhou, C. Yan, Y. Shi, Mechanical properties and microstructure characteristics of lattice-surfaced PEEK cage fabricated by high-temperature laser powder bed fusion, J. Mater. Sci. Technol. 125 (2022) 105–117. 10.1016/j.jmst.2022.03.009.

[4] T. Niino, T. Uehara, Low temperature selective laser melting of high temperature plastic powder, in: 2015 Int. Solid Free. Fabr. Symp. (2015) 866–877.

[5] T. Kigure, Y. Yamauchi, T. Niino, Investigation into effect of beam defocusing in low temperature laser sintering of PEEK, Int. Solid Free. Fabr. Symp. (2022) 1118–1129.

[6] T. Kigure, Y. Yamauchi, T. Niino, Investigation into laser sintering of PEEK using commercially available low powder bed temperature machine, Int. Solid Free. Fabr. Symp., University of Texas at Austin (2021) 546–559.

[7] Y. Yang, H. Tang, J. Gao, S. Zhang, T. Liu, Understanding the multi-scan strategies in L-PBFed CF/PEEK composites: micro–macro tests and multi-scale modelling, Virtual Phys. Prototyp. (2025) e2565475. 10.1080/17452759.2025.2565475.

[8] A. Patel, V. Venoor, F. Yang, X. Chen, M.J. Sobkowicz, Evaluating poly (ether ether ketone) powder recyclability for selective laser sintering applications, Polym. Degrad. Stab. 185 (2021) 109502.

[9] S. Greiner, S. Schlicht, D. Drummer, New Process Strategies for Laser Powder Bed Fusion of Polymers - Progress in Powder Based Additive Manufacturing, in: D. Drummer, M. Schmidt (Eds.), Springer Nature Switzerland, Cham, 2025: pp. 83–106.

[10] S. Schlicht, C. Gabriel, D. Drummer, Low temperature powder bed fusion of polyamide 6: transient process characteristics and process-dependent part properties, Prog. Addit. Manuf. 10(5) (2025) 3529–3543. 10.1007/s40964-024-00812-9.

[11] S. Schlicht, S. Greiner, D. Drummer, Low Temperature Powder Bed Fusion of Polymers by Means of Fractal Quasi-Simultaneous Exposure Strategies, Polymers (Basel). 14 (2022).

[12] S. Schlicht, D. Drummer, Layer-dependent temperature evolution and cooling kinetics in non-isothermal Powder Bed Fusion of polypropylene, Procedia CIRP 124 (2024) 261–264.

[13] S. Schlicht, D. Drummer, Geometry-induced process and part characteristics in support-free powder bed fusion of polypropylene at room temperature, Prog. Addit. Manuf. 9 (2024) 575–584. 10.1007/s40964-024-00656-3.

[14] D. Gaitanelis, C. Worrall, M. Kazilas, Detecting, characterising and assessing PEEK's and CF-PEEK's thermal degradation in rapid high-temperature processing, Polym. Degrad. Stab. 204 (2022) 110096. 10.1016/j.polymdegradstab.2022.110096.

[15] S. Schlicht, D. Drummer, Accelerated Non-Isothermal Powder Bed Fusion of Polypropylene Using Superposed Fractal Exposure Strategies, in: I. Drstvensek, S. Pal, N. Ihan Hren (Eds.), Addit. Manuf. Multidiscip. Coop. Prod., Springer International Publishing, Cham (2024) 3–14. 10.1007/978-3-031-37671-9_1.

Date: 31.03.2026

Control of laser micro welding by influencing the melt pool dynamics via spatially and temporally adjusted energy input

Author: Christoph Spurk

Authors: C. Spurk[1], M. Hummel[1,2], A. Häusler[2], A. Gillner[1], A. Olowinsky[2], J. Brüggenjürgen[1,2], F. Beckmann[3], J. Moosmann[3], C. Häfner[1,2], R. Poprawe[1,2]

[1]RWTH Aachen University, Chair for Laser Technology LLT, Steinbachstr. 15, 52074, AACHEN, GERMANY
[2]Fraunhofer Institute for Laser Technology ILT, Steinbachstr. 15, 52074, AACHEN, GERMANY
[3]Institute of Materials Physics, Helmholtz-Zentrum Hereon, Max-Planck-Str. 1, 21502, Geesthacht, Germany

*Corresponding author: E-mail: christoph.spurk@llt.rwth-aachen.de, ORCID: 0000-0002-5190-4187

Abstract

Precise control in laser micro welding is essential to mitigate process instabilities arising from highly dynamic vapor capillary and melt pool behavior. Achieving stable keyhole formation, consistent weld depth, and low defect rates requires a fundamental understanding of energy deposition and melt dynamics. To meet industrial demands for high precision joining of sensitive and dissimilar materials, advanced control strategies that manipulate both spatial and temporal energy input are increasingly necessary.

This paper presents a three-phase methodology for enhancing welding precision through adaptive energy deposition. Phase 1 establishes the precision-determining time constants and boundary conditions using high-resolution diagnostics. Phase 2 expands this analysis with in situ synchrotron imaging, visible-wavelength beam sources, and spatial and temporal power modulation to control weld geometry and melt pool dynamics. Phase 3 unifies these approaches by combining multi-beam, multi-wavelength, and highly dynamic modulation strategies to enable robust compensation of process fluctuations and achieve significantly improved weld quality.

Keywords

Laser welding, energy deposition, power modulation, high-resolution diagnostics, process control

1 Introduction

Laser beam micro welding has become a key enabling technology for high-precision joining in fields such as microelectronics, medical devices, and battery manufacturing [1]. The demand for reliable joining of increasingly small, sensitive, and dissimilar material combinations places stringent requirements on process stability, reproducibility, and dimensional accuracy. In particular, the achievable weld quality is strongly influenced by the complex interaction between the vapor capillary and the surrounding molten material. The molten phase plays a decisive role in determining weld precision through its interaction with keyhole stability. This influence manifests across multiple scales, including geometric characteristics such as weld depth and width, metallurgical aspects such as the formation of intermetallic phases, and functional properties such as mechanical strengths and surface properties. However, these characteristics are governed by highly dynamic and coupled thermos-fluid phenomena, including energy absorption, phase transitions, and heat and mass transport within the melt pool while interacting with the gaseous and solid phases [2].

Prior to the investigations of subproject A01 of the Collaborative Research Center SFB 1120, the state of the art in laser micro welding was largely characterized by empirical parameter optimization and limited access to high-resolution in situ diagnostics. While fundamental mechanisms such as keyhole formation and melt pool dynamics were qualitatively understood, there was no systematic methodology to suppress or compensate process instabilities arising from the dynamic behavior of the molten phase. In particular, the lack of quantitative knowledge regarding precision-determining time constants, process boundary conditions, and the spatial and temporal distribution of energy input limited the ability to achieve consistent weld quality under industrially relevant conditions. At the same time, increasing industrial demands required not only high process stability but also exceptional precision, including weld depth constancy, depth control within a few micrometers, and defined surface quality. These challenges highlighted the need for advanced process control strategies that go beyond static parameter optimization. In this context, spatially and temporally modulated energy deposition has emerged as a promising approach, as it enables direct influence on melt pool size, heat transport mechanisms, and keyhole stability.

2 Aim of the Investigation

The aim of this paper is to provide a comprehensive overview and workflow of the methodological and technological advancements in laser beam micro welding achieved within the three phases of subproject A01 “Control of geometry and metallurgy in laser beam micro welding by influencing the melt pool dynamics via locally and temporally adjusted energy input” of the Collaborative Research Center over the last twelve years. To address the identified limitations in process understanding and control, a structured research approach was followed, consisting of three consecutive phases: analysis, understanding, and compensation (**Figure 1**).

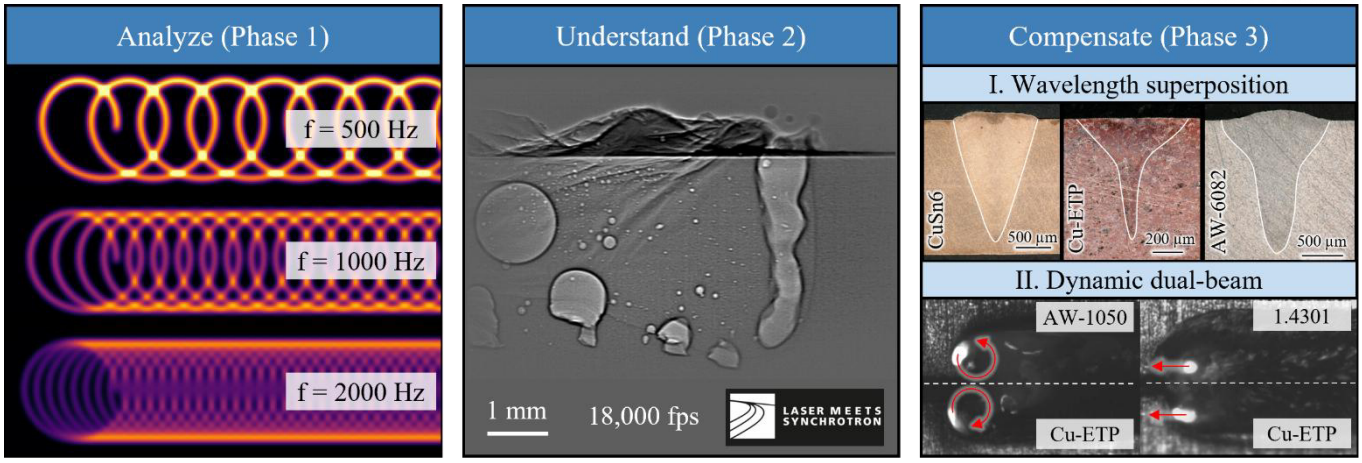

Figure 1: Analyzing, understanding and compensating: The phases of the subproject A01 workflow with a preview of the highlights from each phase: (1) A detailed description of laser power modulation; (2) High-resolution in situ synchrotron analysis of the process; (3) Multibeam approaches for tailored energy deposition in complex systems.

The objective of Phase 1 is the identification of precision-determining time constants and process boundary conditions using high-resolution diagnostic techniques, combined with model-based evaluations of influencing factors. Phase 2 aimed at establishing a deeper understanding of the underlying process mechanisms through advanced in situ diagnostics, including synchrotron-based imaging and wavelength-dependent investigations. Building upon these insights, Phase 3 focuses on the development and implementation of strategies for active process control through spatially and temporally modulated energy input, including multi-beam and multi-wavelength approaches. By consolidating the results of all three phases, this work seeks to demonstrate how systematic progression from analysis to understanding and ultimately to compensation enables precise control of melt pool dynamics. The overarching objective is to establish a workflow method and a framework for adaptive energy deposition strategies that significantly improve weld quality, enhance process robustness, and enable reliable joining of demanding material systems.

3 Materials and Experimental Details

The investigations focus on laser beam welding of metallic materials with high industrial relevance in the energy sector, particularly copper, steel and aluminum alloys. These materials, especially copper materials, are characterized by high thermal conductivity [3], wavelength-dependent absorptivity, and a pronounced susceptibility to process instabilities. To investigate and influence energy coupling and melt pool dynamics, laser beam sources with different wavelengths and emission characteristics were employed. Near-infrared fiber lasers were used to analyze fundamental process behavior and establish relationships between energy input, keyhole stability, and weld formation [4-6]. To investigate wavelength-dependent effects, additional laser sources in the green ($\lambda = 515$ nm) and blue ($\lambda = 450$ nm) spectral range were applied, enabling improved energy coupling and modified melt pool behavior in highly reflective materials such as copper [7-9]. Based on these approaches, multi-wavelength and multi-beam configurations were

implemented, allowing simultaneous or superimposed energy deposition with tailored spatial and temporal characteristics [10-14]. All experiments were conducted mainly using scanner-based beam guidance systems enabling flexible spatial modulation of the laser power distribution.

A combination of complementary diagnostic and characterization techniques was applied to capture relevant process phenomena across different spatial and temporal scales. Metallographic analyses were performed to evaluate weld seam geometry, including weld depth, seam width, and pore formation [4,5,15,16]. Surface-resolved process dynamics were investigated by high-speed imaging, allowing observation of melt flow, spatter formation, and transient instabilities [4-6]. Subsurface process behavior, including vapor capillary formation and melt pool dynamics, was analyzed using synchrotron-based imaging at PETRA III at the German Electron Synchrotron DESY, enabling direct analysis of keyhole geometry, oscillation, and pore formation mechanisms [7,11,13,16-18]. In addition, process emissions were measured using optical sensors and Ulbricht sphere setups to determine reflected and transmitted radiation, providing insight into absorption behavior and energy coupling efficiency [4,6,19,20].

Spatial and temporal modulation of the laser energy input was implemented using galvanometric scanner systems and dynamic power control. Spatial power modulation was achieved by superimposed beam oscillation, enabling controlled energy distribution and adjustment of melt-pool dimensions [4-6]. Temporal power modulation was applied to influence transient process behavior, particularly keyhole oscillations and melt pool stabilities [19]. To further influence energy coupling and the effect of different spot diameters, laser beam sources with different wavelengths were combined. The superposition of blue and near-infrared radiation enables simultaneous control of surface-near absorption and deeper energy penetration, allowing targeted manipulation of melt pool geometry and keyhole characteristics [8,9,13-15].

4 Results and Discussion

The following section presents three key subject areas illustrating the progression from analysis to active process control. Further details can be found in the corresponding publications of the first authors of this paper.

4.1 Influence of Spatial Energy Deposition on Melt Pool Dynamics and Energy Coupling

Spatial and temporal modulation of the laser energy input provides a direct lever to influence melt pool and vapor capillary dynamics in deep penetration welding. By superimposing an oscillatory beam movement onto the linear welding motion, the local interaction time and energy distribution within the process zone can be systematically adjusted. This results in distinct regimes of melt pool behavior depending on the applied modulation parameters. Figure 2 illustrates three characteristic process regimes arising from spatial power modulation. In the stationary regime (Fig. 2a), corresponding to conventional welding without modulation, the melt pool remains fixed relative to the welding direction and the oscillation movement of the capillary. This leads to a highly localized energy input and promotes unstable process behavior, including irregular melt flow and spatter

formation. With increasing modulation amplitude A_S, a pendeling regime is established (Fig. 2b), characterized by a periodic displacement of the melt pool. In this regime, the interaction zone is spatially redistributed, resulting in a more homogeneous energy deposition. The periodic motion of the melt pool reduces local overheating and stabilizes the vapor capillary, leading to improved process stability. At high modulation amplitudes, an oscillating regime is reached (Fig. 2c), in which the melt pool follows the beam oscillation trajectory. The interaction zone is significantly extended, and the energy input is distributed over a larger area. While this regime enables strong modification of melt pool geometry, excessive oscillation alters weld seam characteristics [4].

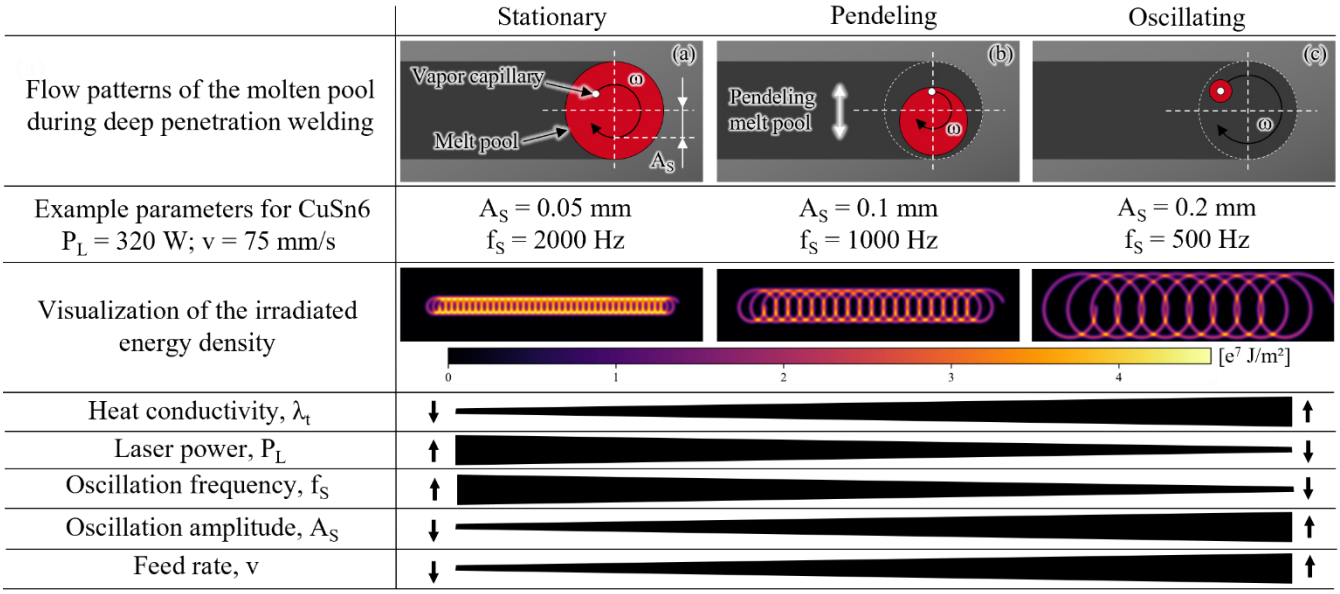

Figure 2: Spatial power modulation and resulting process regimes in laser beam micro welding depending on process parameters. (a) Stationary regime characterized by a fixed melt pool position; (b) Pendeling regime characterized by a periodic displacement of the melt pool; (c) Oscillating regime characterized by a pronounced melt pool movement following the oscillation trajectory. (based on [4])

The transition between these regimes demonstrates that spatial energy deposition acts as a key control parameter for melt pool behavior. By adjusting modulation amplitude and frequency, the energy distribution can be tailored to influence melt flow, vapor capillary stability, and ultimately weld seam formation. In particular, the redistribution of energy becomes increasingly relevant at higher feed rates, where reduced interaction times and enhanced heat conduction effects require a more homogeneous energy deposition to maintain process stability.

4.2 Synchrotron-based analysis of melt pool and process dynamics

In situ synchrotron X-ray imaging was employed to analyze subsurface process dynamics during laser-based material processing. All investigations were conducted at beamline P07 of PETRA III (DESY), enabling high temporal and spatial resolution of vapor capillary and melt pool behavior. Figure 3a shows laser beam welding of aluminum alloy AW-5083 recorded at 18,000 frames per second. Vapor capillary formation, oscillation and collapse can be directly observed. Strong

fluctuations lead to unstable melt flow and bubble formation, resulting in pore generation during solidification [21,22]. Although representing an unstable process regime, these results demonstrate the capability of the developed synchrotron diagnostics to resolve transient phenomena governing weld quality. Figure 3b presents wavelength-superpositioned dual-beam welding of CuSn6, combining blue (445 nm, 1750 W) and near-infrared radiation (1070 nm, 750 W) at a feed rate of 100 mm/s. The additional blue radiation promotes opening and stabilization of the vapor capillary, leading to reduced fluctuations and improved process stability [13]. Automated detection of capillary geometry and pore formation was performed using a YOLO-based segmentation approach.

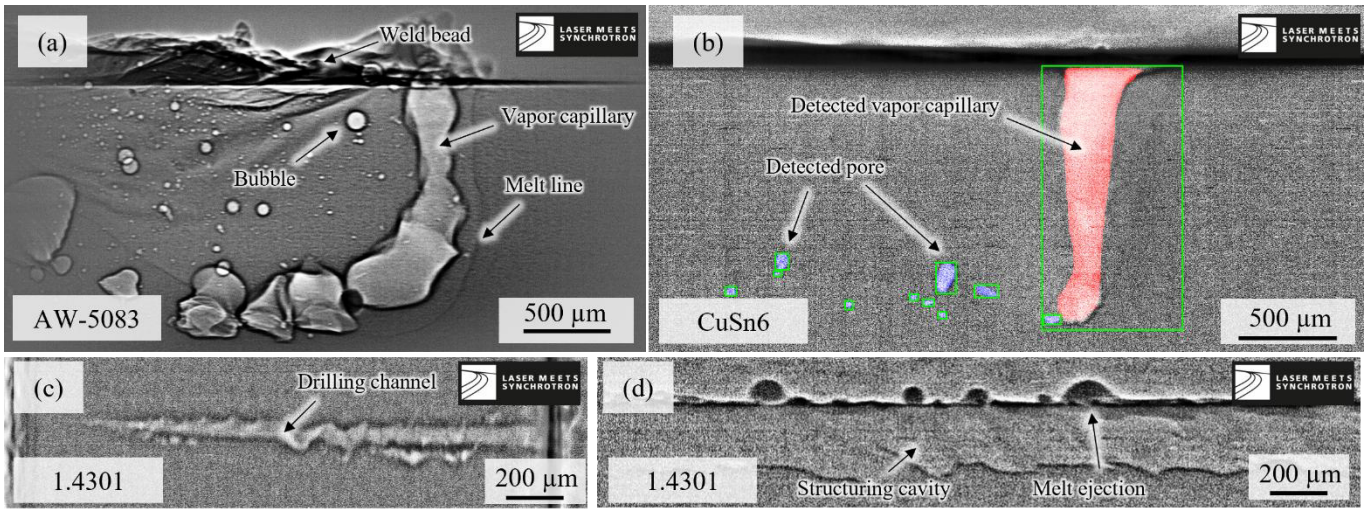

Figure 3: In situ synchrotron X-ray imaging of process dynamics during laser-based material processing, (a) Laser beam welding of aluminum (AW-5083), illustrating keyhole formation, melt pool geometry, and pore dynamics. (b) Wavelength-superpositioned dual-beam laser welding of CuSn6 and AI-driven data acquisition. (c) USP laser drilling, showing the formation and evolution of a drilling channel. (d) Laser surface structuring, revealing melt ejection and cavity formation.

Figure 3c and 3d illustrate the transferability of synchrotron-based diagnostics to other laser-based processes such as drilling (3c), structuring (3d), cutting or soldering. These results highlight that access to subsurface process mechanisms is a key enabler for understanding the interaction between energy deposition, capillary dynamics, and defect formation.

4.3 Active Control via Spatially and Temporally Modulated Energy Input

Building upon the understanding of melt pool and vapor capillary dynamics, active process control can be achieved by tailored energy deposition using multi-wavelength and multi-beam strategies. Figure 4 summarizes two complementary approaches enabling targeted manipulation of weld seam geometry and process stability. The first approach is based on wavelength-superpositioned dual-beam welding (Fig. 4a,c), combining near-infrared and blue laser radiation.

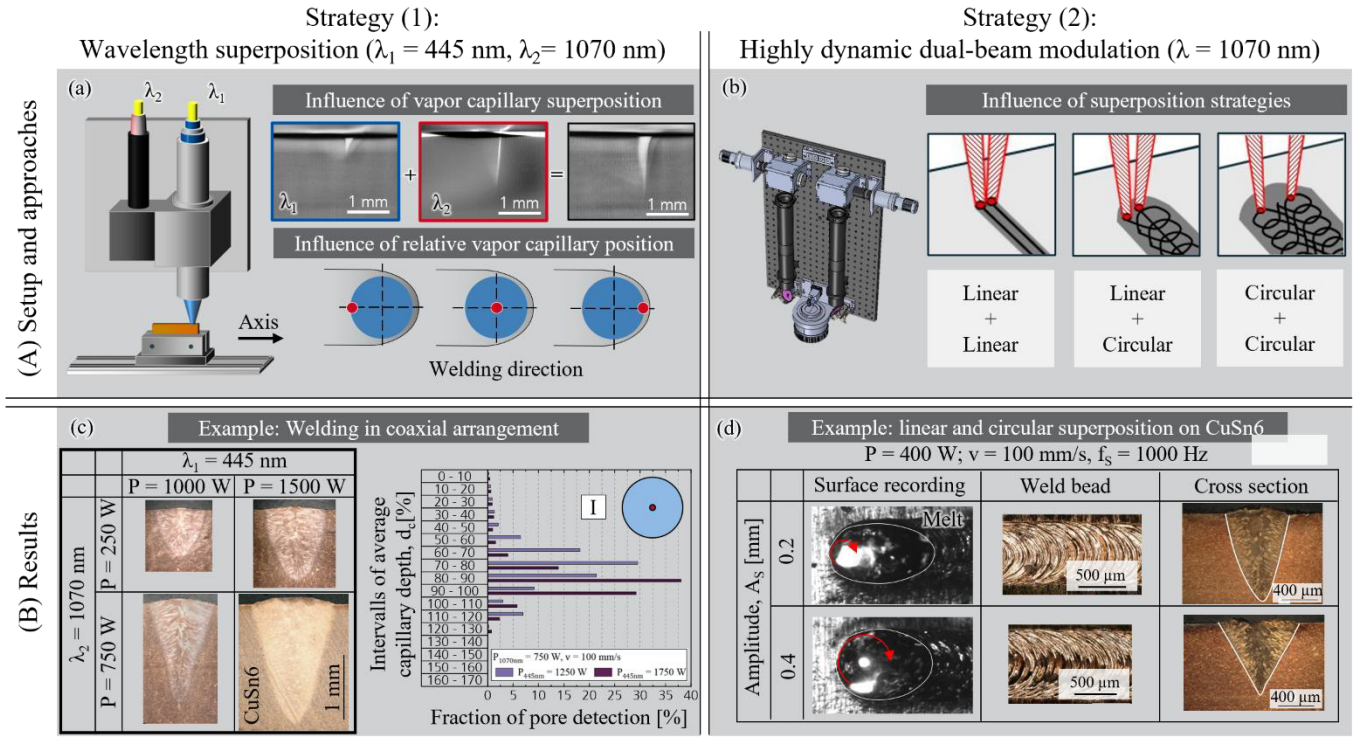

Figure 4: Control of weld seam formation by tailored energy deposition using multi-wavelength and beam superposition strategies (based on [11,12]). (a) Schematic illustration of wavelength-superpositioned dual-beam welding and the resulting interaction of individual capillaries, including the influence of their relative spatial position. (b) Superposition strategies regarding the combination of linear and oscillatory trajectories. (c) Results of wavelength superposition on the weld seam cross section and pore distribution. (d) Example of linear and circular beam superposition during welding of CuSn6, illustrating the influence of modulation amplitude on melt pool behavior, weld seam morphology and cross-section geometry.

Synchrotron investigations (Fig. 3b) reveal that the additional blue radiation promotes the opening and stabilization of the vapor capillary, resulting in reduced fluctuations and improved process stability [13]. Beyond this effect, the relative spatial positioning of the beams provides an additional degree of freedom for process control. Due to the significantly different beam diameters (34 µm for near-infrared and 609 µm for blue radiation), the overlap conditions determine the local energy distribution within the interaction zone. Experimental investigations show that variations in the relative beam position directly influence weld penetration depth, seam width, and surface roughness. In particular, a controlled offset between both beams enables independent adjustment of keyhole stability and melt pool geometry [14].

A second approach is realized by highly dynamic dual-beam modulation strategies (Fig. 4b,d), where different beam trajectories are superimposed. By combining linear and oscillatory beam movements, the spatial and temporal distribution of the energy input can be tailored to homogenize the melt pool and control transient process behavior. The superposition of individual beam strategies enables targeted modification of melt flow and heat distribution, resulting in improved weld seam homogeneity and reduced defect formation. As shown in Fig. 4d, increasing the modulation amplitude A_S leads to a broader and more uniform energy input, which directly influences melt pool size and weld seam geometry. At the same time, appropriate selection of

modulation parameters allows suppression of instabilities such as melt ejection and irregular solidification.

The presented approaches demonstrate that combining wavelength-dependent absorption with dynamic beam shaping provides a powerful framework for active process control. By decoupling and superimposing different energy deposition mechanisms, key process characteristics such as penetration depth, seam geometry, and defect formation can be adjusted. This enables the transition from process understanding to robust control of laser beam micro welding.

5 Summary

This work presents a systematic approach to controlling laser beam micro welding by tailoring spatial and temporal energy deposition. By combining high-resolution diagnostics, wavelength-dependent process analysis, and advanced multi-beam strategies, a transition from empirical parameter optimization to process control is achieved. Spatial power modulation enables the definition of distinct process regimes and provides a first level of control over melt pool dynamics. In situ synchrotron diagnostics further reveal the relationship between energy deposition, vapor capillary behavior, and defect formation, providing direct access to subsurface process mechanisms. Building on this, multi-wavelength and multi-beam approaches enable active process control. Compared to the initial state of the art, the following key advancements may be mentioned:

- **Enhanced process efficiency:** Utilization of otherwise dissipating heat flows in dual-beam welding increases the molten cross-sectional area by up to 48%, depending on beam spacing (value determined by joining two parallel lines)
- **Tailored weld geometry:** Superposition enables targeted adjustment of weld seam geometry (depth vs. width) by controlling the relative position of interacting vapor capillaries
- **Defect control:** Synchrotron investigations show that the interaction of multiple capillaries directly influences pore formation, enabling targeted control of defect distribution

Overall, the presented methodology establishes a framework for adaptive energy deposition, enabling robust and high-precision laser micro welding of challenging material systems.

Acknowledgements

The presented investigations were carried out at RWTH Aachen University within the framework of the Collaborative Research Centre SFB1120-236616214 “Bauteilpräzision durch Beherrschung von Schmelze und Erstarrung in Produktionsprozessen” and funded by the Deutsche Forschungsgemeinschaft e.V. (DFG, German Research Foundation). The sponsorship and support are gratefully acknowledged. The presented synchrotron investigations were carried out within the cooperation “Laser Meets Synchrotron” (www.laser-meets-synchrotron.de). We acknowledge Hereon (Geesthacht, Germany) and DESY (Hamburg, Germany), members of the Helmholtz

Association HGF, for the provision of experimental facilities. The experiments were carried out at Beamline P07 of PETRA III as part of proposal BAG-20211050, and we would like to thank F. Beckmann, J. Moosmann and all people involved for their support. Many thanks to our numerous industry partners, who have actively supported us over the past years by providing advice and equipment.

Conflict of Interest

The author declares no conflict of interest.

Data Availability Statement

The data that supports the findings in this study are available upon reasonable request. Selected data are available after authorization in Coscine with the persistent identifier (PID) http://hdl.handle.net/21.11102/7b891c8f-9bca-4f90-942c-b27141388857 (last accessed on March 24, 2026). The pool of all published “Laser Meets Synchrotron” publications is linked under: https://laser-meets-synchrotron.de/en/publications/. For further information, please contact the corresponding author.

References

[1] S. Katayama. Handbook of Laser Welding Technologies. Woodhead Publishing, **2013**. ISBN: 978-0-85709-264-9

[2] K. Schricker, L. Schmidt, H. Friedmann, C. Diegel, M. Seibold, P. Hellwig, F. Fröhlich, J. P. Bergmann, F. Nagel, P. Kallage, A. Rack, H. Requardt, Y. Chen. Characterization of keyhole dynamics in laser welding of copper by means of high-speed synchrotron X-ray imaging. Procedia CIRP, 111, 501-506, **2022**.

[3] Deutsches Kupferinstitut. Datenblatt CuSn6, **2005** (https://kupfer.de/wp-content/uploads/2019/11/CuSn6-1.pdf; last accessed: 31.03.2026)

[4] A. Häusler. Präzisionserhöhung beim Laserstrahl-Mikroschweißen durch angepasstes Energiemanagement. Dissertation RWTH Aachen University, Apprimus Verlag, **2021**.

[5] A. Häusler, B. Mehlmann, A. Olowinsky, A. Gillner and R. Poprawe. Efficient Copper Micro Welding with Fiber Lasers Using Spatial Power Modulation. Proceedings of the 38th International MATADOR Conference, Springer, **2022**. DOI: https://doi.org/10.1007/978-3-319-64943-6_15.

[6] A. Häusler, A. Schürmann, C. Schöler, A. Olowinsky, A. Gillner, R. Poprawe. Quality improvement of copper welds by laser microwelding with the usage of spatial power modulation. Journal of Laser Applications, 29, 022422, **2017**. DOI: https://doi.org/10.2351/1.4983505.

[7] M. Hummel. Synchrotron-basierte in situ Analyse wellenlängenabhängiger Prozessphänomene beim Laserstrahlschweißen von Kupfer. Dissertation, RWTH Aachen University, Apprimus Verlag, **2025**. ISBN: 978-3-98555-269-6.

[8] M. Hummel, A. Häusler, A. Olowinsky, A. Gillner and R. Poprawe. Comparing 1070 nm and 515 nm Wavelength Laser Beam Sources in Terms of Efficiency for Laser Microwelding Copper. Lasers in Engineering, 46.1-4, 187-202, **2020**.

[9] M. Hummel, C. Schöler, A. Häusler, A. Gillner and R. Poprawe. New approaches on laser micro welding of copper by using a laser beam source with a wavelength of 450 nm. Journal of Advanced Joining Processes, 1, 100012, **2020**. DOI: https://doi.org/10.1016/j.jajp.2020.100012.

[10] A. Olowinsky, C. Spurk, J. Helm and A. Gillner. Laser-Based Joining of Electrode Stacks for Automated Large-Scale Production of Li-Ion Battery Cells. Energy Technology, 11: 2200770, **2023**. DOI: https://doi.org/10.1002/ente.202200770

[11] C. Spurk, F. Dietrich, M. Hummel, A. Gillner, F. Beckmann, J. Moosmann and C. Häfner. In situ Synchrotron Investigations of Beam Diameter Influence on Vapor Capillary Formation during Laser Beam Welding of Copper Alloy with a Blue Laser Beam Source. Journal of Manufacturing and Materials Processing, 8(2), 47, **2024**.
DOI: https://doi.org/10.3390/jmmp8020047

[12] C. Spurk, S. Hollatz, W. Lipnicki, M. Hummel, A. Gillner and C. Häfner. Controlling the weld penetration depth of laser beam micro welding by using an iterative learning approach. Materialwissenschaft und Werkstofftechnik, 55, 533, **2024**.
DOI: https://doi.org/10.1002/mawe.202300154

[13] C. Spurk, F. Dietrich, J. Brüggenjürgen, M. Hummel, A. Häusler, A. Olowinsky, A. Gillner, F. Beckmann and J. Moosmann. Analysis of laser beam welding with superimposed 445 nm and 1070 nm wavelength lasers on copper by in situ synchrotron diagnostics. Journal of Laser Applications, 36, 4, **2024**. DOI: https://doi.org/10.2351/7.0001598

[14] C. Spurk, D. Nettelbeck, A. Häusler, A. Olowinsky and Arnold Gillner. Influencing Precision-Determining Weld Seam Properties in Laser Welding of Copper and Aluminum by Spatial Superposition of 445 nm and 1070 nm Wavelength Lasers. Journal of Laser Micro/Nanoengineering, 21, 1, **2026**. DOI: 10.2961/jlmn.2026.01.2012.

[15] M. Hummel, C. Schöler and A. Gillner. Metallographic Comparison for Laser Welding of Cu-ETP and CuSn6 with Laser Beam Sources of 515 nm and 1030 nm Wavelength. Enhanced Material, Parts Optimization and Process Intensification (EMPOrIA), 14-28, **2021**.

[16] M. Hummel, C. Hagenlocher, A. Haeusler, S. Hollatz, J. Lind, A. Olowinsky, A. Gillner, F. Beckmann, J. Moosmann, R. Weber, T. Graf and C. Häfner. Analysis on the influence of vapor capillary aspect ratio on pore formation in laser beam welding of aluminum. Journal of Materials Processing Technology, 312, 117862, **2023**.
DOI: https://doi.org/10.1016/j.jmatprotec.2023.117862

[17] M. Hummel, M. Külkens, C. Schöler, W. Schulz and A. Gillner. In situ X-ray tomography investigations on laser welding of copper with 515 and 1030 nm laser beam sources. Journal of Manufacturing Processes, 67, 170-176, **2021**. DOI: https://doi.org/10.1016/j.jmapro.2021.04.063.

[18] M. Hummel, C. Meier, A. Olowinsky, A. Gillner, F. Beckmann, J. Moosmann and C. Häfner. In situ synchrotron observation of the vapor capillary geometry in laser welding of copper with 1030 nm and 515 nm laser beam sources. SPIE LASE, Proceedings Volume 12414, High-Power Laser Materials Processing: Applications, Diagnostics, and Systems XII, 124140A, **2023**. DOI: https://doi.org/10.1117/12.2648946

[19] M. Hummel, A. Häusler and A. Gillner. High-Precision Adjustment of Welding Depth during Laser Micro Welding of Copper Using Superpositioned Spatial and Temporal Power Modulation. Journal of Manufacturing and Materials Processing, 5(4), 127, **2021**.
DOI: https://doi.org/10.3390/jmmp5040127

[20] J. Brüggenjürgen, C. Spurk, M. Hummel, C. Franz, A. Häusler, A. Olowinsky, F. Beckmann and J. Moosmann. Analyzing multispectral emission and synchrotron data to evaluate the quality of laser welds on copper. Journal of Laser Applications, 36, 3, **2024**. DOI: https://doi.org/10.2351/7.0001600

[21] J. Xu, Y. Rong, Y. Huang, P. Wang, C. Wang. Keyhole-induced porosity formation during laser welding. Journal of Materials Processing Technology, 252, 720.727, **2018**.

[22] R. D. Seidgazov, F. Kh. Mirzade. Keyhole-induced Porosity in Laser Manufacturing Processes: Formation Mechanisms and Dependence on Scan Speed. Chinese Journal of Mechanical Engineering: Additive Manufacturing Frontiers, 1, 100044, **2022**.

Date: 14.02.2026

Development of an End-to-End Simulation Chain for Atmospheric Plasma Spraying

Author: K. Bobzin[1], M. Erck[1], K. Jasutyn[1], F. Alberding[1]*

[1]RWTH Aachen University, Surface Engineering Institute, Kackertstraße 15, 52072 Aachen, Germany

*Corresponding author: E-mail: alberding@iot.rwth-aachen.de, ORCID: 0009-0004-1909-0656

Abstract

This work presents the development of an end-to-end simulation chain for atmospheric plasma spraying to predict effective coating properties and design compensation strategies against short- and long-term disturbances. A coupled CFD framework was established, integrating models for the plasma generator, plasma free jet, particle kinetics, and coating build-up. By incorporating realistic particle morphologies, binary-gas mixtures, and high-resolution smoothed-particle-hydrodynamics impact models, the framework achieves high predictive precision. The unique value of this tool lies in its ability to directly link process parameters to coating performance, as validated in industrial applications such as functional coatings for plastic injection molding and aluminum die casting.

Keywords

APS, SPH, Coating, Multiphase Flows, Process Precision

1. Introduction

Atmospheric plasma spraying (APS) is a versatile coating technology used to apply high-melting materials, such as oxide ceramics, onto substrates for thermal insulation, wear resistance, and corrosion protection. The functional quality of these coatings, characterized by porosity and effective thermal conductivity, is governed by the coating, which is formed by the thermal and kinetic history of the feedstock particles in the plasma jet. Accordingly, the coating microstructure is controlled by a set of interdependent process parameters.

Prior to the establishment of the Collaborative Research Centre (SFB) 1120, modeling of APS processes exhibited a clear imbalance in the scientific understanding of plasma generator technologies. Whereas the general foundations of plasma spraying technology had been comprehensively reviewed [1], and the stochastic behavior and arc fluctuations of conventional single-arc plasma generators had been extensively investigated numerically [2], multi-arc plasma spraying, employing multi-cathode configurations in combination with cascaded anode designs, received little attention. Despite the potential of these generators to enhance process stability through spatially distributed arc roots, comprehensive numerical models capturing their characteristic flow behavior were largely absent.

Furthermore, existing simulations commonly relied on simplified representations of the feedstock material. Particles were typically modeled as dense, spherical bodies, neglecting the complex morphology of agglomerated and sintered powders used in industrial applications [3]. In addition, the influence of external disturbances on coating accuracy, such as injector wall roughness and carrier gas fluctuations, was neither systematically analyzed nor quantitatively captured in numerical models.

2. Aim of the Investigation

The primary objective of this project was the development of a holistic numerical simulation framework encompassing the entire APS process, from the plasma generation and free jet flow to particle impact and coating build-up. The scientific objectives evolved across the three funding phases to address progressively higher levels of complexity and to incorporate real-world disturbances.

2.1. Phase I: Establishment of the Coupled Simulation Chain

In the initial phase, the aim was to couple previously isolated sub-process models by establishing continuous data transfer between the plasma generator, free jet, and coating build-up simulations. Particular emphasis was placed on multi-arc systems, whose enhanced stability relative to single-arc generators enabled the formulation of robust steady-state models [4]. The aim was to directly correlate fundamental process parameters with coating properties such as porosity and thickness.

2.2. Phase II: Integration of Disturbances and Realistic Morphologies

Building upon the simulation chain, the second phase aimed to close the gap between idealized simulations and real process conditions by integrating stochastic disturbances such as injector-related effects. The specific objectives were:

- **Realistic Particle Modeling:** To replace the assumption of dense spheres with discrete models of realistic, complex particle morphologies to accurately predict heat and momentum transfer [5].
- **Injector Influence:** To identify and model the influence of injector geometry and surface roughness as critical disturbance variables affecting particle injection stability [6].
- **Process Stability:** To quantify and model the impact of plasma jet fluctuations and electrode wear on the particle in-flight properties [5], as well as to capture the statistical influence of these fluctuations on particle trajectories [7].

2.3. Phase III: Precision, Binary Gases, and Compensation Strategies

In phase III, the focus was on maximizing simulation prediction accuracy and on developing active compensation strategies to enhance process stability. The specific objectives included:

- **Binary Gas Mixtures:** Extension of the models to incorporate industrially relevant binary gas mixtures, Ar/H_2 and Ar/N_2, thereby covering the full operational process window [8].
- **Advanced Impact Modeling:** Implementation of smoothed-particle-hydrodynamics (SPH) for particle impact simulations. Compared to previous volume-of-fluid (VOF) approaches, SPH provides higher fidelity resolution of pore formation and substrate roughness [9].
- **Disturbance Compensation:** Development and validation of compensation strategies for identified disturbances. These included mitigation of free-jet turbulence using shroud gas systems to damp velocity fluctuations and shield the jet from ambient perturbations. Additional strategies comprised optimization of injector geometries to reduce shear gradients and pressure oscillations, and targeted adjustment of gas composition to stabilize particle trajectories under varying operating conditions [10].

3. Materials and Experimental Details

3.1. Numerical Framework

The numerical simulation of the APS process was realized through a modular, multi-scale simulation chain to efficiently map the widely varying temporal and spatial scales. This framework subdivides the total process into coupled sub-models: plasma generator, plasma free jet, and coating build-up. The overall methodology relies on the sequential coupling of these sub-models, as illustrated in **Figure 1**.

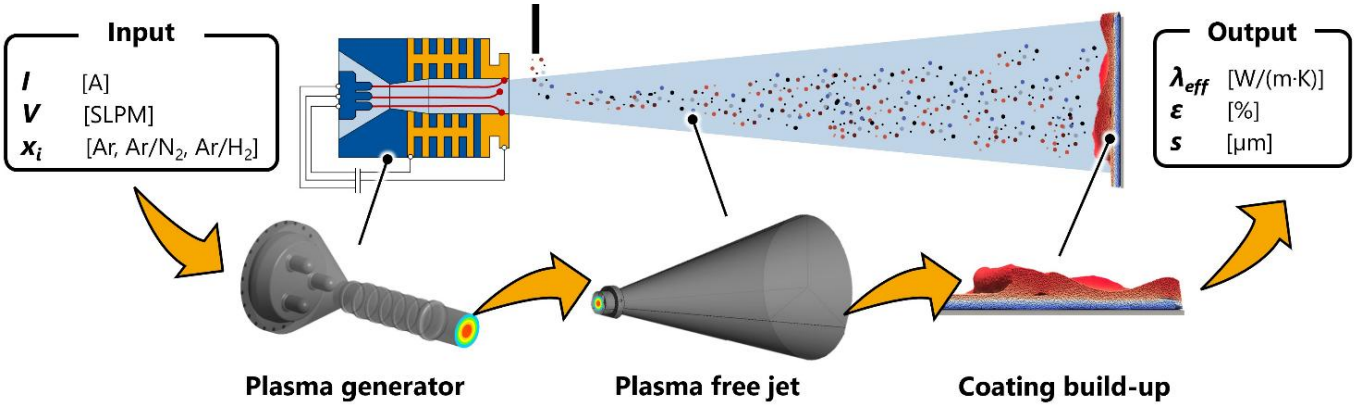

Figure 1: Schematic representation of the APS simulation chain.

The output of the plasma generator simulation – specifically the spatial profiles of temperature, velocity, turbulence kinetic energy, and turbulence eddy dissipation at the nozzle outlet – serves as the boundary condition for the free jet simulation, which in turn determines the thermal and kinetic history of the particles necessary for the impact and coating build-up models [11].

The modeling of the plasma generator was based on the magnetohydrodynamics equations under the assumption of a local thermodynamic equilibrium [4]. To account for turbulence inside the plasma generator and in the free jet, the shear-stress-transport (SST) model was utilized in later phases, as it depicts flow separation and shear layers more precisely than standard κ-ε models. For

the simulation of process gases, such as Ar, Ar/H_2, and Ar/N_2, temperature- and pressure-dependent thermodynamic properties from Murphy et al. were implemented [8].

Particle transport in the free jet was calculated using an Euler-Lagrange approach with two-way coupling to account for the momentum and heat exchange between the plasma and the particles. For ceramic particles, the simplifying Lumped-Capacitance method, which assumes a uniform temperature distribution throughout the particle, was replaced by a spatially discretized heat conduction model. This modification was necessary because ceramic feedstock materials exhibit low thermal conductivity, leading to Biot numbers greater than $B_i > 0.02$. The Biot number, defined as the ratio of internal thermal resistance to external heat transfer resistance, indicates that for $B_i > 0.02$, significant temperature gradients exist within the particle. The internal temperature distribution must be modeled accurately [12] to predict the melting degree of the ceramic powder particles [13].

Furthermore, a macroscopic modeling approach was developed to derive effective drag and Nusselt coefficients for complex, non-spherical particle morphologies to correct the standard correlations used for spherical particles [5]. To bridge the free jet and the impact models, the calculated particle state variables – namely impact coordinates, velocity, temperature, diameter, and melting degree – were extracted and applied as initial boundary conditions for the coating build-up simulation. While early phases utilized VOF-methods [14], the third phase introduced SPH to resolve droplet impact, spreading, and solidification with higher resolution and to account for substrate roughness and pore formation [9].

3.2. Plasma Generators and Operating Conditions

The experimental and numerical investigations focused on the TriplexPro-210^{TM}, Oerlikon Metco, Switzerland, a three-cathode plasma generator. This torch features a cascaded anode design and is operated with a nozzle diameter of 9 mm. The three-cathode configuration provides a temporally stable plasma jet with reduced arc fluctuations compared to conventional single-cathode systems, which justified steady-state assumptions in the early simulation phases [4]. The process gases investigated included pure Ar, Ar/H_2, and Ar/N_2.

3.3. Feedstock Materials and Injection Systems

For experimental validation, the commercial Al_2O_3 powder Amdry 6062 (-45 +22 µm) was used. Numerically, however, idealized spherical assumptions were expanded to include agglomerated and sintered morphologies, as shown in Section 4.2. Represented as primary particle clusters, their unique surface-to-volume ratios significantly alter gas penetration and heat conduction. Utilizing these complex models to derive shape-tailored effective drag coefficients was essential for the precise simulation of real in-flight particle kinematics.

3.4. Experimental Validation Techniques

To validate the numerical models, advanced diagnostic methods were employed:

- **Plasma Jet Diagnostics:** The temperature fields of the plasma free jet were measured using Optical Emission Spectroscopy Computed Tomography (OES-CT). The diagnostic system was developed by and operated in collaboration with the Institute of Plasma Technology and Mathematics, University of the Federal Armed Forces Munich.
- **Particle Diagnostics:** In-flight particle properties, such as velocity, temperature, and diameter, were measured using DPV-2000, Tecnar Automation Ltd., St-Bruno, QC, Canada. Additionally, Laser Doppler Anemometry (LDA) was used for imagining the particle plume and determining particle velocities via a time-of-flight technique [11].
- **Process Stability:** To quantify plasma jet fluctuations and arc stability, high-speed video analysis was performed using a Fastcam SA-Z, Photron, Tokyo, Japan, with frame rates up to 210,000 fps. This allowed for the time-resolved analysis of the plasma jet core and the calculation of fluctuation coefficients [15].
- **Coating Characterization:** The effective thermal conductivity of the sprayed coatings was determined using Flashline™ 4010, Anter Corporation, PA, USA. The microstructure was analyzed using scanning electron microscopy (SEM), PhenomX, Thermo Fisher Scientific, and X-ray diffraction, XRD 3000, Seifert, Ahrensburg, Germany [16].

4. Results and Discussion

4.1. Development of the Simulation Chain and Plasma Generator Modeling

In the initial phase, a robust numerical model for the three-cathode plasma generator was established. The spatial configuration of the system – including the obstruction caused by the powder injector and the definition of the simulation and measurement domains – is schematically illustrated in **Figure 2a**.

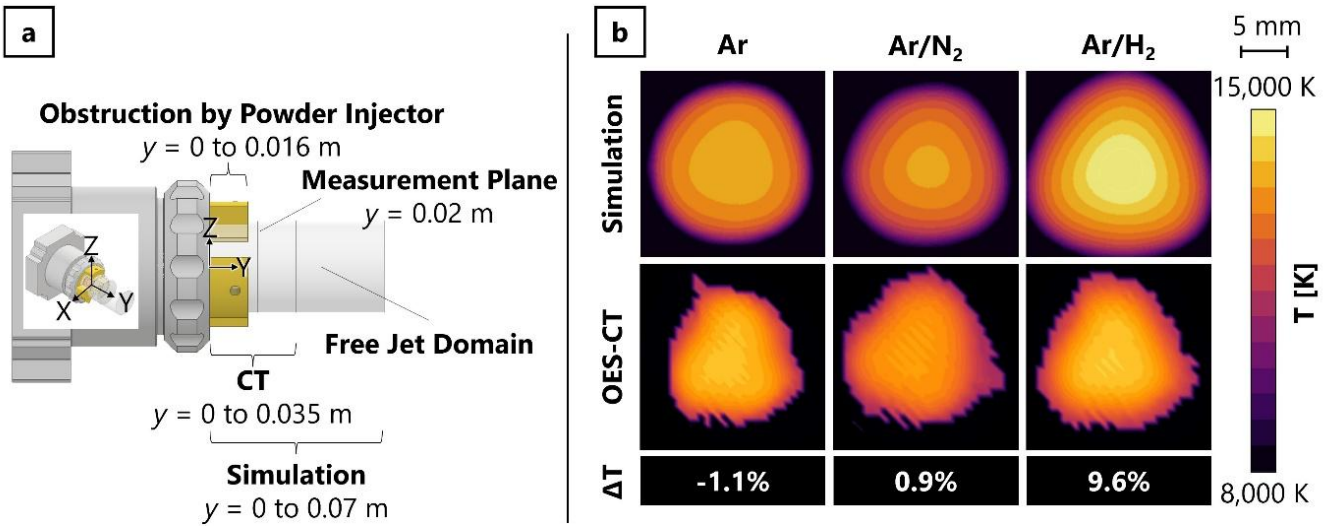

Figure 2: a) Schematic of the experimental setup **b)** comparison between numerical predictions and OES-CT measured temperature fields for pure Ar as well as Ar/N_2 and Ar/H_2 at the measurement plane y = 0.02 m [17].

A significant advancement in Phase III was the successful integration of binary gas mixtures into the simulation chain. The numerical results demonstrated that the addition of H_2 or N_2 significantly alters the specific enthalpy and thermal conductivity of plasma. This results in a more constricted plasma core and increases kinetic energy [8]. Validation of these findings was performed via OES-CT. As shown in the cross-sectional temperature fields in **Figure 2b**, the numerically predicted distributions for pure Ar as well as Ar/H_2 and Ar/N_2 mixtures show high quantitative and qualitative agreement with the experimental measurements. Specifically, the numerical model predicts the maximum plasma temperatures with a high accuracy, exhibiting relative deviations of less than 10% compared to the OES-CT measurements.

4.2. Impact of Particle Morphology and Injection

A critical advancement in enhancing predictive precision was the transition from modeling idealized dense spheres to realistic particle morphologies. As shown in the morphological comparison in **Figure 3a**, these models consist of primary particle clusters that accurately mirror the complex structure of agglomerated and sintered powders observed in SEM imagery. To capture their unique aerodynamic behavior, a novel macroscopic modeling approach was developed. By performing detailed 3D flow simulations around these specific particle shapes – using a defined computational domain as schematically illustrated in **Figure 3b** – effective drag coefficients were directly calculated from the resulting forces [5]. The significance of this morphological effect is clearly evidenced in **Figure 3c**, which demonstrates that the drag coefficient of the agglomerate systematically diverges from that of an idealized sphere across the relevant Reynolds number range. By integrating these shape-tailored coefficients into the coupled free jet model, the prediction accuracy for particle trajectories, dwell times, and heating behaviors were significantly improved [18].

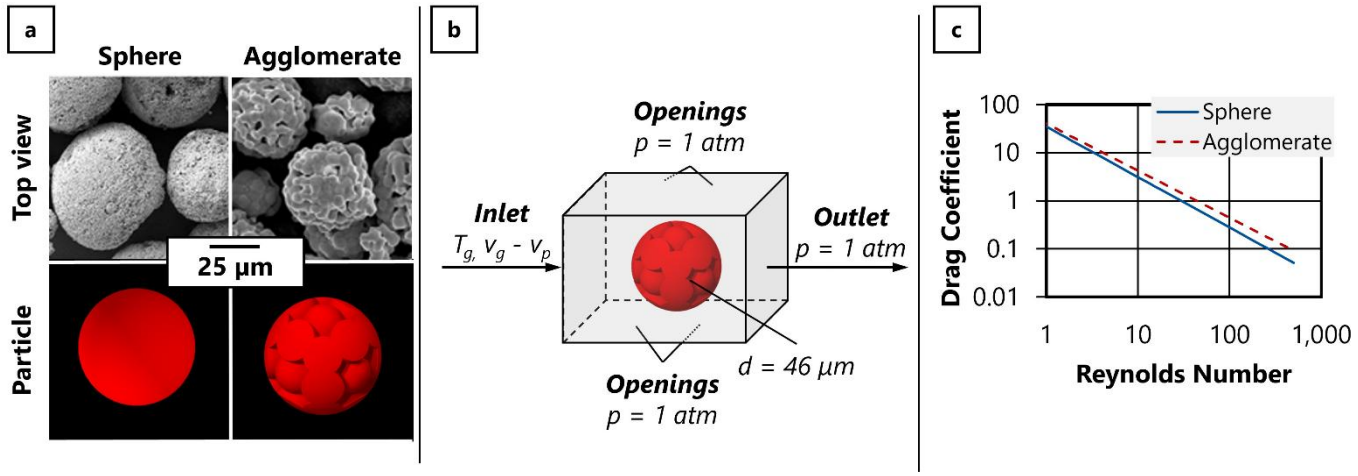

Figure 3: a) geometry of spherical and agglomerated particles [5] **b)** schematic illustration of external particle model [5]; **c)** comparison of the effective drag coefficients [18].

4.3. Process Stability and Disturbance Compensation

To enhance process precision, the project quantified plasma jet fluctuations through the application of high-speed video analysis combined with inverse Abel transformation. A new parameter was introduced for the purpose of quantifying the impact of jet instability within the frequency range that is relevant to particle heating. The investigations demonstrated that multi-arc generators with a fluctuation coefficient of 0.02 as well as cascaded single-arc generators exhibit significantly higher stability than conventional non-cascaded torches, which possess a fluctuation coefficient of 0.19. Despite this increased stability, residual fluctuations continue to affect particle trajectories [15].

During the final phase, various strategies were simulated with the specific objective of reducing turbulence within the plasma jet. The primary research focus involved geometric modifications, especially the implementation of shroud gas systems, which serve to minimize air entrainment and thereby decrease the turbulent kinetic energy (TKE).

Simulations demonstrate that specific shroud gas configurations stabilize the jet's shear layer, significantly reducing peak TKE. Compared to the unshielded reference, this stabilization mitigates TKE while maintaining the average gas temperature (T_{avg}), as illustrated in **Figure 4**. Consequently, the resulting uniform particle trajectories and heating are anticipated to enhance the reproducibility and microstructural homogeneity of deposited Al_2O_3 coatings.

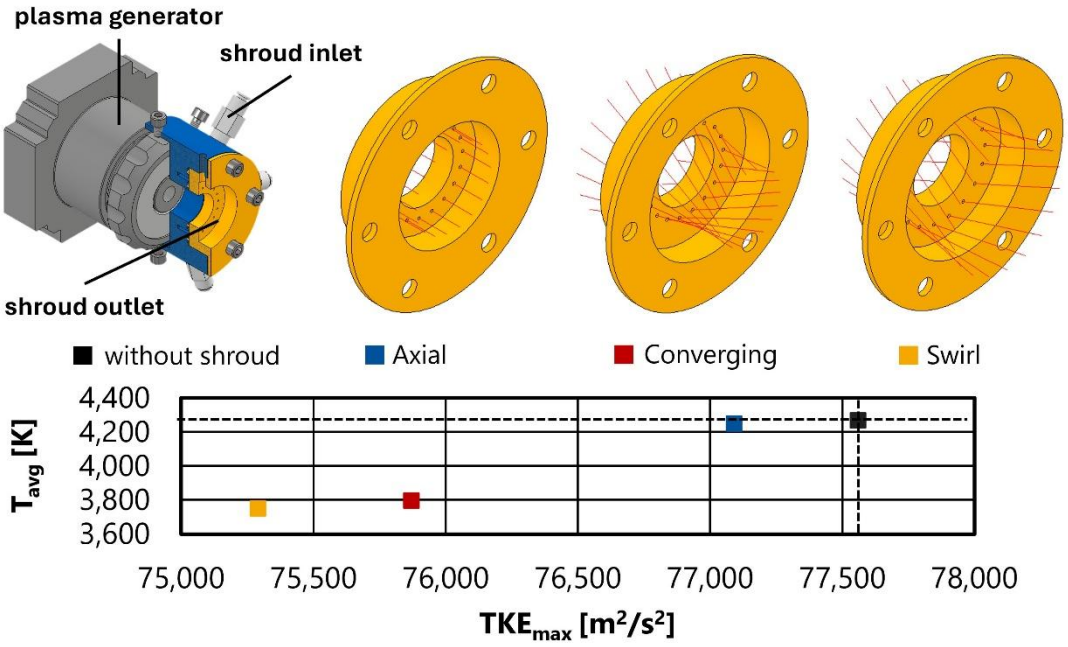

Figure 4: Influence of different shroud gas configurations on the maximum of turbulent kinetic energy and average gas temperature within the plasma jet for electric current of 450 A and gas volume rate 69 SLPM.

4.4. Coating Formation and Effective Properties

The final link in the simulation chain was the prediction of coating properties. Early models using VOF methods were employed to simulate the impact of multiple particles and the formation of

splats [14]. However, these methods proved to be computationally expensive. The introduction of SPH in Phase III allowed for a more efficient simulation of particle impact, solidification, and heat transfer.

As visualized in **Figure 5a**, the SPH approach provides a detailed resolution of the particle impact and splashing morphology. **Figure 5b** shows that the SPH method achieves a fourfold reduction in computational time compared to the VOF benchmark [9]. Subsequent investigations further examined droplet impact with varying surface preparation conditions [19].

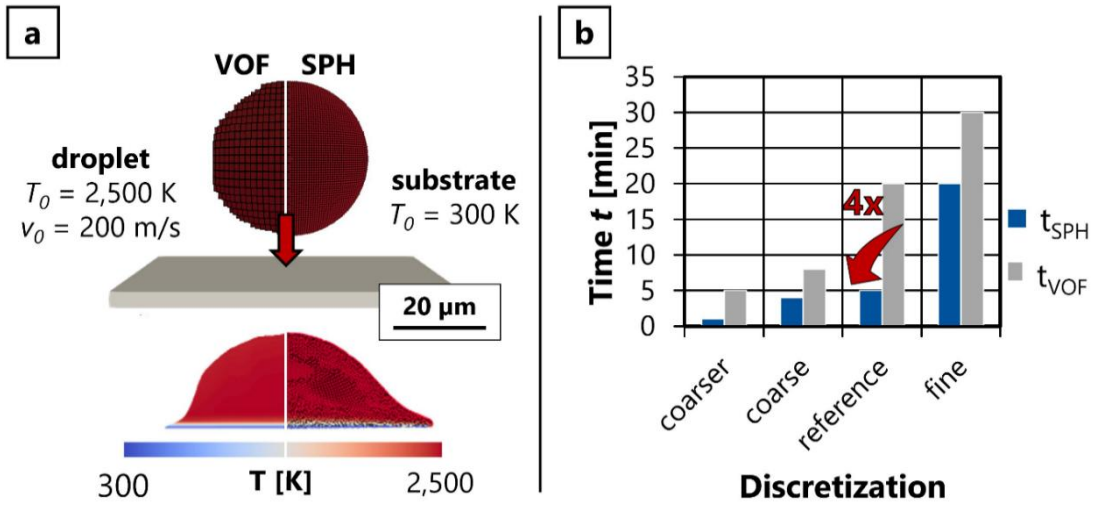

Figure 5: SPH and VOF comparison of particle impact: **a)** morphology of splashing; **b)** simulation time.

During Phase III, the droplet impact on substrates with various surface preparations was investigated to analyze the influence of preheating and topography on the coating formation. The numerical model incorporated preheated surfaces as well as grit-blasted topographies to simulate realistic mechanical interlocking between the ceramic Al_2O_3 and the metallic substrate. Analysis reveals that an increased substrate temperature of 900 K results in a reduced cooling rate compared to room temperature. For an initial droplet diameter of 45 µm, this delayed solidification promotes larger spreading diameters of approximately 98 µm, which corresponds to a spread factor of 2.18, and leads to more extensive splashing. Furthermore, the implementation of a semi-implicit enthalpy-porosity method enabled the precise tracking of the solidification front within the mushy zone. Finally, the simulation of a coating build-up involving 20 droplets demonstrated the capability of the SPH approach to qualitatively predict microstructural defects such as voids, thereby providing a basis for assessing the resulting coating properties [19].

To bridge the scale to macroscopic coating properties, a methodology within the VOF framework was developed to simulate effective thermal conductivity. Splat boundaries were explicitly modeled as thermal barriers by introducing a gap function that locally reduces thermal conductivity [16]. Through the application of this model, the simulation predicted effective thermal conductivities for porous Al_2O_3 coatings in the range of 5.8 to 11.4 W/(m·K).

5. Summary

Over 12 years, the project successfully bridged the gap between process parameters and coating properties in plasma spraying. Starting from isolated models, a coupled simulation chain was developed. Quantitatively, the project achieved significant milestones in predictive precision:

- **Advanced Impact Modeling:** The implementation of SPH enabled the high-fidelity resolution of fine-scale microstructural features and substrate roughness, which facilitated a fourfold reduction in computational time compared to traditional grid-based methods.
- **Stability Quantification:** The project quantified the stability advantage of cascaded systems, showing a reduction in relevant fluctuation coefficients by a factor of 10 compared to conventional plasma generators.
- **Binary Gas Modeling:** The extended generator models predicted temperature fields for binary gas mixtures with deviations below 10% compared to experimental measurements.

Acknowledgements

The presented investigations were carried out at RWTH Aachen University within the framework of the SFB 1120 “Precision Melt Engineering” under Project ID 236616214. The sponsorship and support are gratefully acknowledged. Simulations were performed with computing resources granted by RWTH Aachen University under project rwth0570.

Data Availability Statement

The data supporting the findings of this study are available at http://hdl.handle.net/21.11102/eca0461c-649f-40f5-8fee-302145af3165.

References

1. Trelles JP, Chazelas C, Vardelle A, Heberlein JVR (2009) Arc Plasma Torch Modeling. J Therm Spray Tech 18(5-6):728–752. doi:10.1007/s11666-009-9342-1
2. Fauchais P (2004) Understanding plasma spraying. J. Phys. D: Appl. Phys. 37(9):R86-R108. doi:10.1088/0022-3727/37/9/R02
3. Mostaghimi J, Chandra S, Ghafouri-Azar R, Dolatabadi A (2003) Modeling thermal spray coating processes: a powerful tool in design and optimization. Surface and Coatings Technology 163-164:1–11. doi:10.1016/S0257-8972(02)00686-2
4. Bobzin K, Öte M (2016) Modeling Multi-Arc Spraying Systems. J Therm Spray Tech 25(5):920–932. doi:10.1007/s11666-016-0407-7
5. Bobzin K, Öte M, Knoch MA, Alkhasli I (2020) Macroscopic Modeling of an Agglomerated and Sintered Particle in Air Plasma Spraying. J Therm Spray Tech 29(1-2):13–24. doi:10.1007/s11666-019-00964-z
6. Bobzin K, Öte M, Knoch MA, Heinemann H (2020) Influence of the Injector Head Geometry on the Particle Injection in Plasma Spraying. J Therm Spray Tech 29(4):534–545. doi:10.1007/s11666-020-01009-6
7. Bobzin K, Heinemann H, O'Brien A (2022) Capturing the Influence of Jet Fluctuations on Particles in Plasma Spraying. J Therm Spray Tech 31(1-2):59–69. doi:10.1007/s11666-021-01307-7
8. Bobzin K, Heinemann H, Erck M, Warkentin S, Mokrov O, Sharma R, Reisgen U, Jasutyn K (2025) Modeling of arcs with binary gas mixtures in a multi‐arc plasma generator. Materialwissenschaft Werkst 56(1):77‐87. doi:10.1002/mawe.202300134

9. Jeske SR, Bender J, Bobzin K, Heinemann H, Jasutyn K, Simon M, Mokrov O, Sharma R, Reisgen U (2022) Application and benchmark of SPH for modeling the impact in thermal spraying. Comp. Part. Mech. 9(6):1137–1152. doi:10.1007/s40571-022-00459-9
10. Bobzin K, Heinemann H, Erck M, Jasutyn K (2024) Understanding the Impact of Binary Plasma Gas Mixtures in Plasma Spraying Thermal Spray 2024: Proceedings from the International Thermal Spray Conference. ASM International, S 689–695
11. Bobzin K, Öte M, Schein J, Zimmermann S (2017) Numerical Study on Plasma Jet and Particle Behavior in Multi-arc Plasma Spraying. J Therm Spray Tech 26(5):811–830. doi:10.1007/s11666-017-0564-3
12. Bobzin K, Öte M, Knoch MA, Alkhasli I, Reisgen U, Mokrov O, Lisnyi O (2016) Modelling of the Temperature Distribution Inside a Sprayed Particle in Air Plasma Spraying, München, 3 Jul 2016 - 7 Jul 2016, München (Germany), S 25
13. Bobzin K, Öte M, Knoch MA, Alkhasli I Numerical investigation of the melting degree of ceramic powder particles during air plasma spraying:291–292
14. Bobzin K, Öte M, Knoch MA, Alkhasli I, Dokhanchi SR (2019) Modelling of particle impact using modified momentum source method in thermal spraying. IOP Conf. Ser.: Mater. Sci. Eng. 480:12003. doi:10.1088/1757-899X/480/1/012003
15. Bobzin K, Öte M, Knoch MA, Alkhasli I, Heinemann H (2021) High-Speed Video Analysis of the Process Stability in Plasma Spraying. J Therm Spray Tech 30(4):987–1000. doi:10.1007/s11666-021-01159-1
16. Bobzin K, Wietheger W, Heinemann H, Wolf F (2021) Simulation of thermally sprayed coating properties considering the splat boundaries. IOP Conf. Ser.: Mater. Sci. Eng. 1147(1):12026. doi:10.1088/1757-899X/1147/1/012026
17. Bobzin K, Heinemann H, Erck M, Jasutyn K, Nassar G, Alberding F (2026) Numerical Modeling of Binary-Gas Plasma Jets in Multi-Arc Plasma Spraying and Validation of Temperature Profiles. J Therm Spray Tech. doi:10.1007/s11666-026-02197-3
18. Bobzin K, Wietheger W, Heinemann H, Alkhasli I (2021) Particle tailored effective particle-gas interaction coefficients during plasma spraying. Thermal spray bulletin 14(1):40–45
19. Bobzin K, Heinemann H, Jasutyn K, Jeske SR, Bender J, Warkentin S, Mokrov O, Sharma R, Reisgen U (2023) Modeling the Droplet Impact on the Substrate with Surface Preparation in Thermal Spraying with SPH. J Therm Spray Tech 32(2-3):599–608. doi:10.1007/s11666-023-01534-0

Date: 25.03.2026

Reusability of an Intumescent Flame Retardant System for Polyamide 12 in PBF-LB/P

Author: Paul Roumeliotis

Authors: Paul Roumeliotis[1,*], Dietmar Drummer[1]

[1]Friedrich-Alexander-Universität Erlangen-Nürnberg, Institute of Polymer Technology (LKT), Am Weichselgarten 10, 91058 Erlangen, Germany

*Corresponding author: E-mail: Paul.Roumeliotis@fau.de, ORCID: 0009-0004-3337-4137

Abstract

The current lack of reusability of flame-retardant powders in laser-based powder bed fusion of polymers (PBF-LB/P) is one of the key challenges for industrial adaptation of PBF-LB/P for safety critical applications. In this study we investigate the reusability for 50:50 (aged:virgin powder) refreshing rates for a flame-retardant system based on Ammonium polyphosphate, pentaerythritol and manganese oxide over three cycles in PBF-LB/P. The impact of manufacturing was investigated employing four different energy densities. The resulting samples were evaluated for their mechanical and flame-retardant properties. The results of the samples with MnO indicate that powder aging does not negatively affect the mechanical properties of the samples. Furthermore, the flame-retardant properties in UL-94 testing indicate improved fire resistance due to increased viscosity and thus reduced dripping of the samples from aged powder. Lastly, cone calorimeter testing indicates the influence of powder aging resulting in higher total heat release and peak heat release rate.

Keywords

Powder aging, selective laser sintering, intumescent flame retardant, Polyamide 12

1 Introduction

The increasing stringency of safety standards and regulatory requirements has elevated the importance of flame-retardant components, particularly for lightweight applications within the aerospace, automotive, and rail industries. [1,2] PBF-LB/P represents an ideal manufacturing methodology for these sectors, offering unparalleled geometrical freedom and the capacity for significant weight reduction in final parts. However, these industries require flame retardant part properties, due to strict safety regulations. [3] Despite the existence of several commercially available and literature-documented flame-retardant systems, their industrial adoption remains limited. A primary barrier to integration is the high material cost associated with these systems. In

a typical PBF-LB/P process, only 10–20% of the powder volume is melted to form the part, while the remaining material is subjected to elevated temperatures that induce powder aging. [4–6] To date, neither commercial nor experimental powders have demonstrated sufficient recyclability. Typically, refreshed powders exhibit a significant degradation in both mechanical performance and flame-retardant efficiency after thermal exposure.

Powder aging in PBF-LB/P is a well-documented phenomenon, particularly for neat PA12, and can be categorized into physical and chemical aging processes. [7] Physical degradation, considered a secondary effect, typically involves particle agglomeration alongside increases in both the degree of crystallinity and lamellae thickness. In contrast, chemical aging represents the dominant and irreversible degradation mechanism. [8,9] This is primarily driven by thermal oxidation resulting from residual oxygen within the inert process atmosphere, hydrolysis, solid-state post-condensation, and the Brill transition-related peak merging. These mechanisms induce significant shifts in molecular weight and thermal characteristics, which ultimately diminish the mechanical performance of the manufactured parts. [6] To mitigate this decline in material properties, a standard industrial practice involves refreshing aged powder with virgin material. Typically, a mixture of 50 wt.% aged powder and 50 wt.% virgin powder is utilized for subsequent PBF-LB/P cycles [10,11], a strategy that has been shown to maintain consistent mechanical properties in the resulting components. [12]

For flame retardant PA12-based powders, Yu et al. [13] previously analysed the mechanical and fire-retardant properties of regenerated powders where the additives were introduced after the aging process. Their results demonstrated favourable flame retardancy, achieving a V0 rating in UL-94 tests for 3 mm specimens. However, the synergistic impact of aging on a pre-mixed system of flame-retardant additives and PA12 remained unexplored. In a subsequent study, our group [14] investigated the aging behaviour of a flame-retardant system based on ammonium polyphosphate (APP) and pentaerythritol (PER) within a PA12 matrix for PBF-LB/P. This research focused on the reuse of 100% aged powder to characterize the resulting mechanical and flame-retardant performance. While the mechanical properties exhibited a significant decline, the flame-retardant efficiency remained robust, consistently achieving a V0 rating for 3 mm thick samples.

2 Aim of the Investigation

In this study, we investigate the reusability of a flame-retardant system based on APP and PER, both with and without the addition of Manganese oxide (MnO), utilizing a standard industrial refreshing strategy of 50 wt.% virgin and 50 wt.% aged powder within the PBF-LB/P process. To evaluate this, the aged powder collected from an initial build job consisting entirely of virgin material was blended with 50 wt.% virgin powder and subsequently processed. This cycle was repeated for a total of three successive generations, using the aged powder from each preceding build. The resulting specimens were characterized with respect to their mechanical performance and flame-retardant properties to determine whether these functionalized powders can be effectively recirculated in accordance with common industrial practices.

3 Materials and Experimental Details

A PA12 powder type PA2200 by EOS was used as a matrix material. The flame retardant additive APP (Ammonium Polyphosphate, Exolit AP 422, Clariant) was used as received. As a charring agent, PER (Pentaerythritol, P4755 Sigma-Aldrich, purity >98%) was used. Manganese(II)-oxide (377201 Sigma-Aldrich, purity >99%) was used as a catalyst for the flame retardant system. [15] As a flow agent, Aerosil R202 (Evonik) was employed in a fraction of 0.2%. The additives APP (16.6 wt.%) and PER (8.3 wt.%) were mixed together according in a batch-based mixer (Thermomix, Vorwerk) with 0.2 wt% Aerosil R202 for 20 min in rotation mode 4. For the samples with MnO, it was also added to the APP and PER mixture. Afterwards, the prepared additives were mixed with PA12 powder in a bulk mixer at a frequency of 200 min^{-1} in bulk masses of 8 kg. PBF-LB/P manufacturing was conducted employing an EOS P110 at a building chamber temperature of 169°C and an extraction chamber temperature of 130°C. Samples were manufactured with the energy densities 0.25, 0.30, 0.35 and 0.40 J mm^{-3}, varying only the laser power with 15, 18, 21 and 24 W while scanning speed and hatch distance was kept constant with 2000 mm s^{-1} and 0.3 mm.

In a first step only virgin powder was manufactured with said parameters. The remaining powder is sieved three times to get rid of agglomerated. The powder for the first aging cycle are manufactured from 50 wt.% of the thus aged powder and 50 wt.% of virgin powder. The remaining powder was sieved again three times and used for the second aging cycle. For this circle 50 wt.% of the aged powder after the first cycle was mixed with 50 wt.% virgin powder. For the third cycle once again the three times sieved powder from the building job from circle two is used with 50 wt.% and mixed with 50 wt.% virgin powder. Samples manufactured from the combination of 16.6 wt.% APP and 8.3 wt.% PER are named PA12_FR, samples containing 2 wt.% MnO are named PA12_FR_2MnO. Additionally, the sample names include VP for virgin powder or C1, C2 or C3 for the aging cycles one to three.

Thin sections of 10 µm thickness of samples manufactured with an energy density of 0.3 J mm^{-3} were prepared using a Leica Polycut E microtome. The resulting sections were then examined with a Zeiss Axioplan microscope to capture images in both bright-field and dark-field illumination modes. Rotational viscometry was conducted to evaluate and compare the complex viscosity of the samples. Therefore, samples manufactured at an energy density of 0.30 J mm^{-3} were tested in a plate-plate rheometer of the type Discovery HR-2, performing a frequency sweep with 0.2 strain at 190°C. For the characterization of mechanical properties, tensile test specimens were fabricated according to ISO 3167, type 1A, with a scaling factor of 0.5. Prior to testing, samples were dried in a vacuum cabinet. Tensile testing was conducted on an Instron 5948 universal testing machine in accordance with DIN EN ISO 527. Young's modulus was determined at a crosshead speed of 0.5 mm min^{-1}, while tensile strength and elongation at break were measured at a speed of 25 mm min^{-1}.

The samples were furthermore tested towards their burning properties using UL-94 and Cone calorimetry. UL-94 vertical burning tests were performed using a prototype of the Netzsch UL-94

device, in accordance with DIN EN 60695-11-10. Ten specimens measuring 10x80 mm² with thicknesses of 2.5 or 2 mm were tested. Prior to testing, the specimens were conditioned for at least 48 hours at 23±2 °C and 50±10 % relative humidity. Each specimen was ignited twice by applying a 50 W flame to the bottom edge for 10 seconds, after which the flame was removed and the time to self-extinguishing was recorded. The rating of each specimen was based on the burning time and behaviour during both ignitions. The final material rating was determined from the worse result of two sets of five samples each, with negative factors such as dripping or combustion to the sample holder potentially lowering the rating. Ratings are classified as V-0, V-1, V-2, or no rating, from best to worst. Cone calorimeter measurements were conducted using a prototype of the Netzsch-Gerätebau GmbH TCC 918 device, following ISO 5660-1. Specimens with dimensions of 100x100x4 mm³ were prepared and tested. A heat flux of 50, 65 and 80 kW m² was applied. The samples were wrapped in aluminium foil, leaving the top surface exposed, and placed horizontally in an insulated metallic holder. Ignition was achieved with an electrical igniter. During combustion, the heat release rate (HRR), total heat evolved (THE), and peak heat release rate (pHRR) were quantified. The measurements were performed in triplicate, and the reported values represent the average. An infrared camera was used to monitor residue formation throughout the tests.

4 Results and Discussion

To demonstrate the success of the manufacturing process, the microscopy images of the samples manufactured from virgin and refreshed powder are shown in Figure 1.

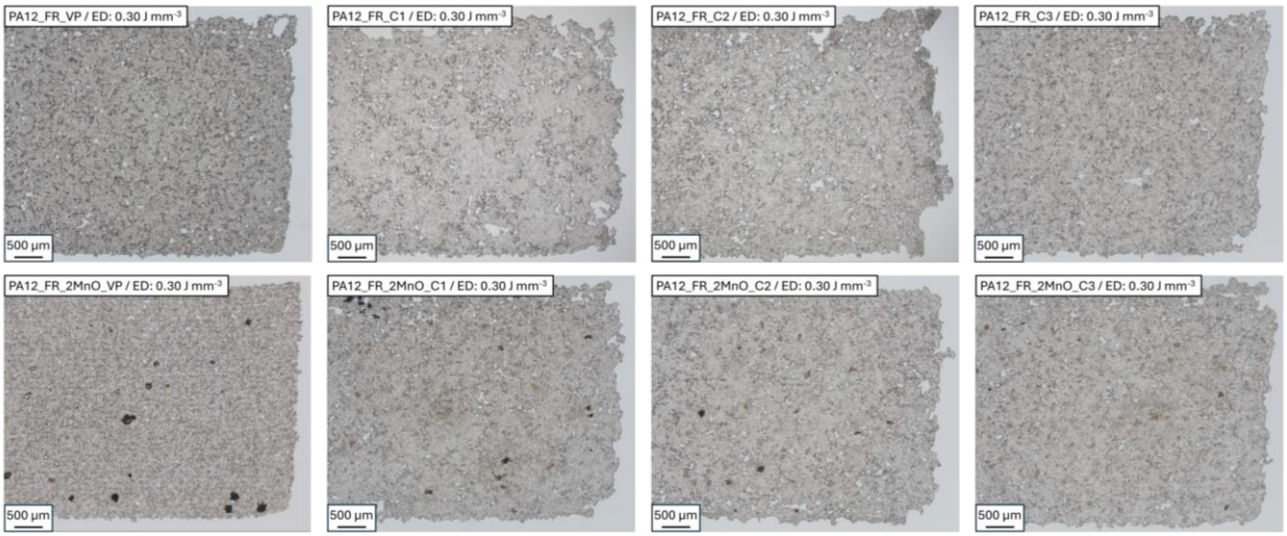

Figure 1: Microscopy images in bright field of thin sections of samples manufactured from PA12_FR (upper row) and PA12_FR_2MnO (lower row).

Across all examined specimens, the manufacturing process was successful, resulting in a well-sintered microstructure characterized by the absence of pronounced layer-wise formations. However, specimen preparation was notably complicated by the brittle nature of the material, particularly in samples synthesized from aged powder. Microstructural observations revealed that these aged powder samples exhibited a slightly higher degree of porosity and less defined

peripheral regions compared to those produced from virgin powder. Furthermore, several pores in the aged samples were significantly larger in scale. These morphological deviations are likely a consequence of the reduced flowability inherent in aged powders, which may have induced specific defects during the coating phase of the process.

To assess the important aspects of mechanical properties for the flame retardant samples manufactured from aged powder, mechanical testing was performed. The results are shown in Figure 2.

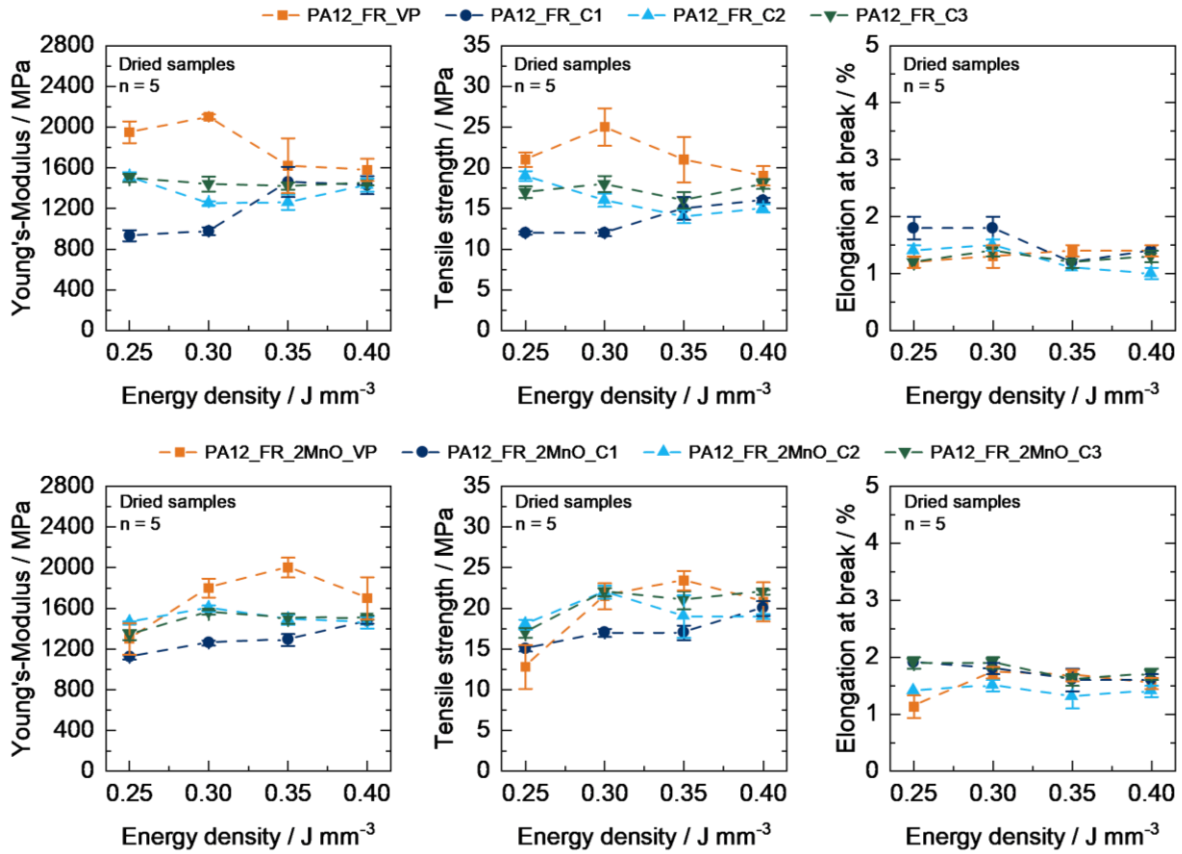

Figure 2: Results of mechanical testing for dried samples for different energy densities for the materials PA12_FR (upper row) and PA12_FR_2MnO (lower row).

Regarding the mechanical characterization of PA12_FR, the Young's modulus at energy densities of 0.25 and 0.30 J mm^{-3} exhibited a reduction of 29%, accompanied by a 24% decrease in tensile strength. While the elongation at break remained unchanged, the specimens demonstrated highly brittle behavior even when using virgin powder. In contrast, the PA12_FR_2MnO material showed a more moderate reduction in Young's modulus of only 20%. Specifically, the modulus for samples produced from refreshed PA12_FR_2MnO powder was approximately 1600 MPa, surpassing the values observed for the refreshed PA12_FR baseline. Furthermore, the tensile strength of the PA12_FR_2MnO samples remained stable within the standard deviation when comparing refreshed to virgin powder; refreshed PA12_FR_2MnO specimens achieved 22 MPa, whereas PA12_FR reached only 19 MPa. Although both materials exhibited a similar brittle fracture mechanism regarding elongation at break, these results represent a significant improvement over

samples manufactured from purely aged powder, as previously reported by Roumeliotis et al. [14] This degradation in mechanical properties is attributed to the combined aging effects of the flame retardant additives and the PA12 matrix. However, the data suggests that for refreshed powders, the negative impact of the aging process is effectively neutralized by the inclusion of virgin powder, which facilitates superior coalescence properties.

Table 1: Results for UL-94 testing for 2 mm thick samples.

2 mm thickness	**PA12_FR**				**PA12_FR_2MnO**			
Energy density / J mm^{-3}	**VP**	**C1**	**C2**	**C3**	**VP**	**C1**	**C2**	**C3**
0.25	V2	V2	**V0**	V1	V2	V2	V2	**V0**
0.30	V2	V2	V2	V2	V2	V2	V2	V2
0.35	V2	V2	V2	V2	V1	**V0**	**V0**	V2
0.40	V2	V2	**V0**	**V0**	V2	**V0**	**V0**	**V0**

Table 2: Results for UL-94 testing for 2.5 mm thick samples.

2.5 mm thickness	**PA12_FR**				**PA12_FR_2MnO**			
Energy density / J mm^{-3}	**VP**	**C1**	**C2**	**C3**	**VP**	**C1**	**C2**	**C3**
0.25	V2	V2	**V0**	V1	V1	**V0**	**V0**	**V0**
0.30	V2	**V0**	V1	V2	V1	V2	**V0**	**V0**
0.35	V2	**V0**	**V0**	V2	**V0**	**V0**	**V0**	**V0**
0.40	V2	**V0**	**V0**	**V0**	V1	**V0**	**V0**	**V0**

Ignition tests and subsequent flame testing demonstrated a clear positive influence of powder aging on the overall fire properties of the material. Specifically, specimens produced from aged powder exhibited an increasing frequency of V0 ratings compared to those made from virgin powder. This improvement was particularly remarkable in the 2 mm thick samples, which failed to achieve a V0 rating when processed from virgin powder. This enhanced performance in UL-94 testing is primarily attributed to a significant reduction in dripping behavior during combustion.

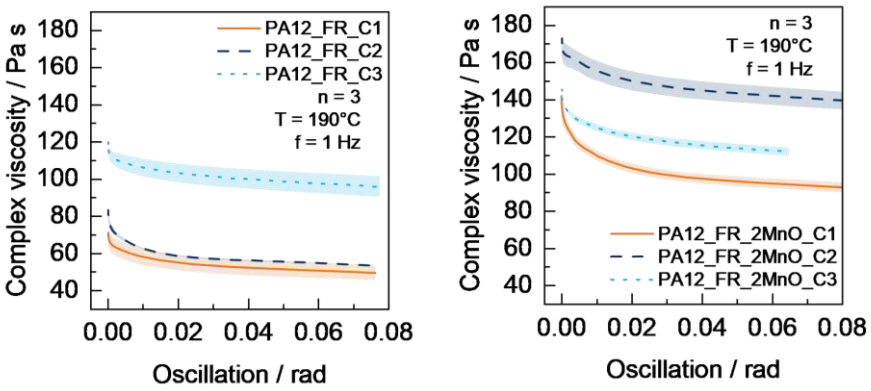

Figure 3: Measurements of complex viscosity of the samples employing an oscillation sweep.

Complex viscosity measurements (Figure 3) further support these observations, revealing that viscosity increases progressively with aging cycles. Such an increase typically correlates with reduced dripping in UL-94 tests, as a stable melt prevents the disruption of barrier formation, thereby ensuring a more efficient flame-retardant mechanism. These findings align with established research on PA12, where aging is known to increase viscosity, as well as prior studies by our group regarding the aging of flame-retardant powders. In earlier investigations, this phenomenon was explained by a pre-reaction between the PER and APP additives when subjected to the elevated building chamber temperatures of 180°C. [14]

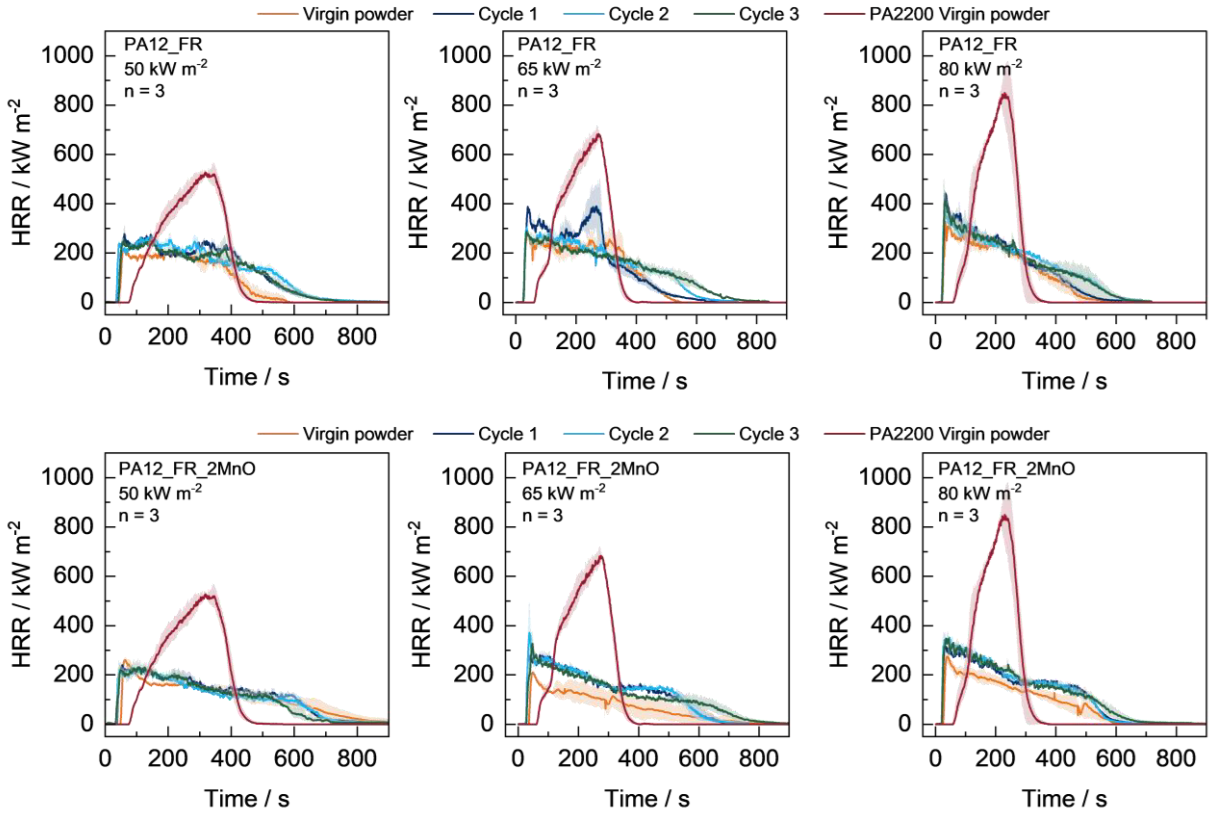

Figure 4: HRR curves of the samples manufactured from PA12_FR (upper row) and PA12_FR_2MnO (lower row) with an energy density of 0.30 J mm^{-3} measured with the heat fluxes 50, 65 and 80 kW m^{-2} in a cone calorimeter.

All samples containing flame retardant additivs demonstrate enhanced flame retardancy compared to pristine PA12 (PA2200). The HRR curves for PA12_FR revealed no significant alterations in burning behavior across the different aging cycles. All curves were characterized by a sharp increase immediately following ignition, followed by a continuous decline in HRR. This profile is typical for intumescent flame retardant systems and suggests that the efficiency of the additives remains intact and undamaged by the aging process. In contrast, the PA12_FR_2MnO specimens exhibited an increase in HRR at higher heat fluxes of 65 and 80 kW m^{-2}, indicating a somewhat diminished response to more intense, realistic fire scenarios. Despite this increase, the pHRR for PA12_FR_2MnO remained lower than that of the standard PA12_FR samples. Ultimately, for both material systems, the overall burning behavior remained stable and did not undergo significant changes as a function of the powder aging cycle.

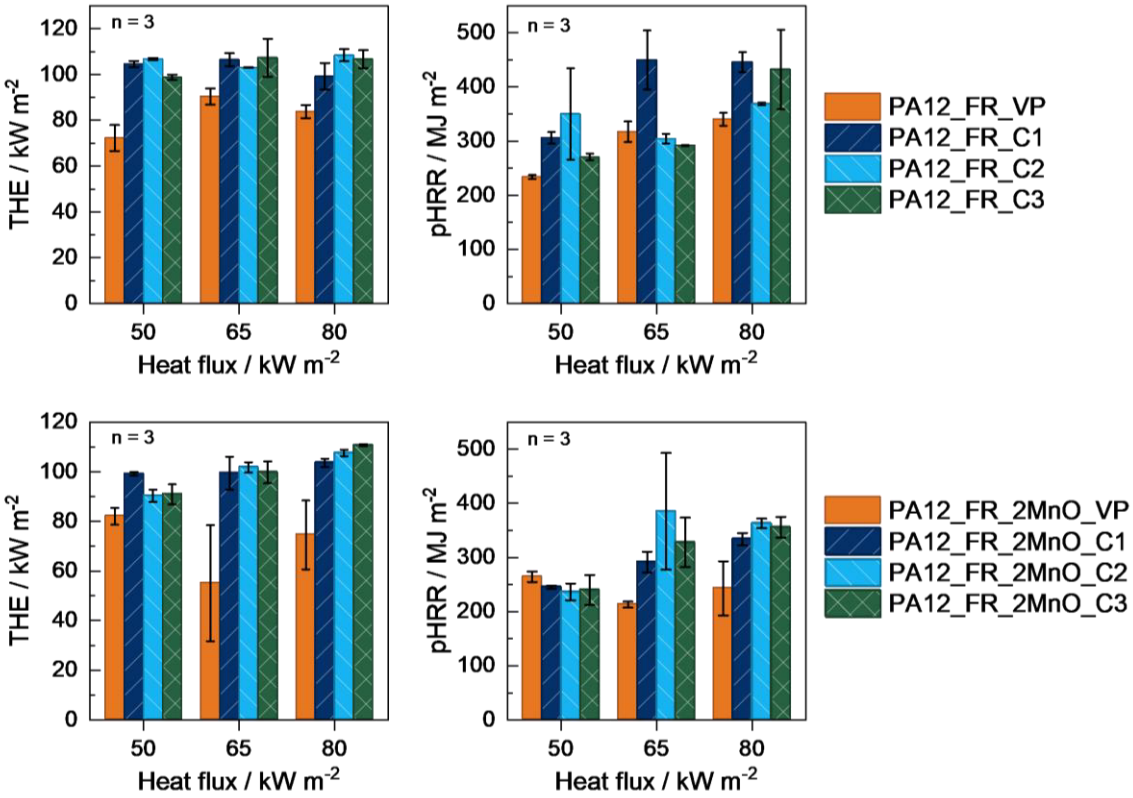

Figure 5: Results for THE and pHRR of the samples manufactured from PA12_FR (upper row) and PA12_FR_2MnO (lower row) with an energy density of 0.30 J mm^{-3} measured with the heat fluxes 50, 65 and 80 kW m^{-2} in a cone calorimeter.

Analysis of the THE for PA12_FR_VP specimens shows approximately 10% lower values compared to those processed with refreshed powder. At a heat flux of 50 kW m^{-2}, the peak heat release rate pHRR is similarly reduced by roughly 10%, though this discrepancy diminishes as the heat flux increases. A comparable trend is observed for the PA12_FR_2MnO material, where virgin powder samples consistently exhibit lower THE and pHRR than their recycled counterparts. While THE increases across all samples with rising heat flux, the response of the virgin powder to higher thermal loads is notably less pronounced than that of the recycled powder. Furthermore, when comparing the two material systems, PA12_FR_2MnO demonstrates a more stable pHRR response to increasing heat flux than PA12_FR. In accordance with previous aging studies, the observed

increase in THE can be traced back to the degradation of the PA12 matrix. The aging process generates degradation products with higher combustion enthalpies, directly contributing to the elevated THE and pHRR values seen in the recycled and refreshed powder specimens. [14]

5 Summary

The present study demonstrates the reusability of a flame-retardant system containing APP, PER and MnO over three cycles with unchanged mechanical and flame-retardant properties for the first time. The resulting samples show good mechanical properties, close to the level of samples from virgin powder. Hereby the samples PA12_FR show a stronger decline from the virgin powder level compared to samples containing MnO. The UL-94 test demonstrates the positive influence of aging on the dripping behavior of the samples, resulting in an increasing number of V0 ratings with ongoing reuse of the powder over multiple aging cycles. The aging of the powder increases the complex viscosity of the samples due to PA12 aging and thus prevents dripping, which in turn promotes barrier formation due to no deformation of the sample. Cone calorimeter testing demonstrates a slight increase in THR and pHRR, however the samples still show outstanding burning behavior in realistic flame testing. Notably the response to increasing heat fluxes for samples containing MnO is not as pronounced as for samples without MnO, highlighting the positive effect of MnO on the burning behavior, even for samples from aged powder. The constant level of the recycled powder over multiple cycles indicates a highly stable flame-retardant powder, which enhances the ecological and economical application of flame-retardant powders in PBF-LB/P.

Acknowledgements

The authors would like to express their gratitude to EOS GmbH for the provision of the PA2200 powder and to Clariant AG for supplying the Exolit® AP422 utilized in this study.

Conflict of Interest

The author declares no conflict of interest.

Data Availability Statement

Data will be made available on reasonable request.

References

[1] B. van Hooreweder, F. de Coninck, D. Moens, R. Boonen, P. Sas, Microstructural characterization of SLS-PA12 specimens under dynamic tension/compression excitation, Polymer Testing 29 (2010) 319–326. https://doi.org/10.1016/j.polymertesting.2009.12.006.

[2] M. Kohutiar, L. Kakošová, M. Krbata, R. Janík, J.J. Fekiač, A. Breznická, M. Eckert, P. Mikuš, Ľ. Timárová, Comprehensive Review: Technological Approaches, Properties, and Applications of Pure and Reinforced Polyamide 6 (PA6) and Polyamide 12 (PA12) Composite Materials, Polymers (Basel) 17 (2025). https://doi.org/10.3390/polym17040442.

[3] Y.F. Lv, W. Thomas, R. Chalk, S. Singamneni, Flame retardant polymeric materials for additive manufacturing, Materials Today: Proceedings 33 (2020) 5720–5724. https://doi.org/10.1016/j.matpr.2020.05.081.

[4] K. Wudy, D. Drummer, Aging effects of polyamide 12 in selective laser sintering: Molecular weight distribution and thermal properties, Additive Manufacturing 25 (2019) 1–9. https://doi.org/10.1016/j.addma.2018.11.007.

[5] A. Kubeczek, M. Olejarczyk, P. Gruber, A.J. Antończak, Continuous reuse of polyamide 12 in powder bed fusion, Sci. Rep. 15 (2025) 27249. https://doi.org/10.1038/s41598-025-12573-8.

[6] P.C. Gomes, O.G. Piñeiro, A.C. Alves, O.S. Carneiro, On the Reuse of SLS Polyamide 12 Powder, Materials (Basel) 15 (2022). https://doi.org/10.3390/ma15165486.

[7] F. Yang, N. Zobeiry, R. Mamidala, X. Chen, A review of aging, degradation, and reusability of PA12 powders in selective laser sintering additive manufacturing, Materials Today Communications 34 (2023) 105279. https://doi.org/10.1016/j.mtcomm.2022.105279.

[8] S. Dadbakhsh, L. Verbelen, O. Verkinderen, D. Strobbe, P. van Puyvelde, J.-P. Kruth, Effect of PA12 powder reuse on coalescence behaviour and microstructure of SLS parts, European Polymer Journal 92 (2017) 250–262. https://doi.org/10.1016/j.eurpolymj.2017.05.014.

[9] F. Yang, X. Chen, A combined theoretical and experimental approach to model polyamide 12 degradation in selective laser sintering additive manufacturing, Journal of Manufacturing Processes 70 (2021) 271–289. https://doi.org/10.1016/j.jmapro.2021.08.051.

[10] M.N. Baba, Flatwise to Upright Build Orientations under Three-Point Bending Test of Nylon 12 (PA12) Additively Manufactured by SLS, Polymers (Basel) 14 (2022). https://doi.org/10.3390/polym14051026.

[11] K. Wudy, D. Drummer, F. Kühnlein, M. Drexler, Influence of degradation behavior of polyamide 12 powders in laser sintering process on produced parts, Nuremberg, Germany, American Institute of Physics, 2014, pp. 691–695.

[12] Gornet, Timothy & Davis, K.R. & Starr, Characterization of selective laser sintering materials to determine process stability, Solid Freeform Fabrication Symposium (2002) 546–553.

[13] S. Yu, A. Tan, W.M. Tan, X. Deng, C.L. Tan, J. Wei, Additive manufacturing of flame retardant polyamide 12 with high mechanical properties from regenerated powder, RPJ 29 (2023) 1409–1419. https://doi.org/10.1108/RPJ-05-2022-0146.

[14] P. Roumeliotis, S. Schlicht, R. Detsch, Q. Nawaz, A.R. Boccaccini, D. Drummer, Powder Aging Effects on Mechanical and Fire Properties of a Flame Retardant PA12 in Laser Powder Bed Fusion, Polymer Testing 153 (2025) 109048. https://doi.org/10.1016/j.polymertesting.2025.109048.

[15] P. Roumeliotis, S. Schlicht, D. Drummer, Intumescent, catalyzed flame retardant systems for polyamide‐based powder bed fusion, Vinyl Additive Technology 31 (2025) 853‐868. https://doi.org/10.1002/vnl.22212.

Date: 30.03.2026

Part warpage compensation through optimization and automation of thermal injection mold design

Authors: D. Fritsche*, C. Hopmann

[1]RWTH Aachen University, Chair for Plastics Processing, Seffenter Weg 201, 52074, AACHEN, GERMANY

*Corresponding author: E-mail: publications@ikv.rwth-aachen.de, ORCID: 0000-0001-9225-1285

Abstract

The cooling channel layout shows significant impact on shrinkage and warpage in injection molding and thus the precision of molded parts. In this work an automated method to design such a channel layouts from inverse thermal mold design was experimentally validated against a professional conventional manual layout on a warpage-sensitive casing-type demonstrator. Under a factorial variation of processing conditions, parts were injection molded and assessed via optical 3D metrology against the cavity geometry. The automated routing produced manufacturable layouts. Despite globally similar paths imposed by identical inlets/outlets and obstacles, the automatic design introduced non-orthogonal segments and targeted corner cooling near regions of elevated thermal mass. Meanwhile the design was created by this methodology by ca 3 days of computing time and no manual construction was necessary. Measurements indicate equal or lower warpage of up to the factor of 78 than the manual layout, including order-of-magnitude reductions at corner features and more symmetric deformation of opposing walls. A slender central feature remained highly process-sensitive, indicating that parameter settings can rival layout effects. These findings support automated straight-channel derivation as a drill-ready complement to inverse design that improves feature-level dimensional stability while still requiring coordinated process optimization.

Keywords

Injection molding, thermal mold design, cooling channel, automation, warpage

1 Introduction

A central lever for quality and cycle time of injection molded parts is the design of the mold's cooling system, which governs the heat transfer from the molten polymer into the mold steel and the circulating coolant. The cooling phase can account for up to 70% of the overall cycle time, so that any improvement in thermal management directly affects productivity and energy efficiency. Insufficiently balanced cooling often manifests during initial sampling as inadequate dimensional accuracy or visible defects, making parts unsuitable for their intended use and triggering costly iterations on mold and process settings [HopMMM18, Sch23].

In industrial practice with support from simulation, cooling systems were and still often are designed largely manually. Designers rely on empirical rules, corporate guidelines and personal experience to position straight drilled channels under geometric and manufacturing constraints. While modern simulation tools allow the evaluation of candidate layouts, the resulting design process is typically iterative, time-consuming and strongly dependent on individual expertise. Local cooling requirements are rarely captured comprehensively, and the final layout often represents a compromise that does not fully exploit the potential for warpage reduction or cycle time optimization [Hoh21].

Over roughly the last two decades, research on automatic and optimal cooling system design has advanced significantly. *Feng et al.* classify existing approaches into experimental design strategies, methods based on conformal cooling line patterns, expert-algorithm-driven optimization, modular or parametric conformal channel design, and topology-optimization-based solid modelling of cooling structures. [FKP21]

Within these categories, a broad range of techniques has been proposed, including rule-based expert systems, evolutionary algorithms, surrogate-based optimization and topology optimization workflows, often applied to conformal channels manufactured additively in mold inserts. Nevertheless, most available approaches were subject to substantial limitations: many required a pre-specified channel layout or parameterization, restricted the solution space by strong geometric assumptions or optimized only a small subset of the factors governing warpage, such as surface temperature uniformity. As a result, an objectively optimal solution could not be guaranteed, and the user's initial assumptions dominates the outcome. However, the emergence of conformal cooling and its high freedom of design underlines the demand for the automated design routine for these complex channel layouts.

Within this context, a project of the Collaborative Research Centre 1120 (CRC1120) "Precision Melt Engineering" aims to develop a holistic methodology for thermal mold design that goes beyond local design rules and isolated optimization of individual components. The project established and refined an inverse thermal mold design framework that formulates the cooling system layout as the solution of an inverse problem based on the work of *Agazzi et al*. Instead of designing a cooling system and then analyzing its effect, an optimal thermal state of the mold–part system is defined (Sec. 1.1) and the required thermal measures are derived from this target state (Sec. 1.2) [AgaSL+10, Hoh21, Nik18]. This concept builds on earlier inverse design approaches for injection molds and combines them with advanced material modelling, numerical optimization and automated derivation of cooling channels and also explores additional topics like surface coatings [HFK+24, HZF+24].

In recent years, commercial software vendors have begun to integrate approaches for automatic and optimal cooling design of industrial molds. Autodesk Inc., USA for example, offers a feature for automated generation and optimization of conformal cooling channel layouts based on voxelized meshes and signed distance fields for obstacle avoidance [KA25]. Using a boundary-

element-method solver, the system adaptively positions channels closer to thick, hot sections and further from thin regions, while maintaining minimum distances to parting planes, inserts, ejectors and existing channels [KA25]. Users can specify parameters such as the number of channels, their proximity to the part, mold half assignment, and inlet/outlet locations, and the software searches for layouts that balance part quality and cycle time [KA25].

Maya HTT, Canada has implemented an optimization feature inspired by the inverse thermal mold design approach of *Agazzi et al.* and the CRC1120 project, utilizing the periodic thermal steady state and temperature history of the mold [AgaSL+10]. By leveraging GPU-based meshing and solving, typical molds can be optimized within approximately 15 minutes, making inverse design concepts more accessible in industrial environments [Bla25].

These commercial solutions illustrate the transfer of academic research on automatic and inverse cooling design into practice and highlight the growing acceptance of algorithmic layout generation in industrial mold design. At the same time, they typically expose only a subset of the underlying optimization parameters to the user and primarily address thermal criteria such as temperature uniformity and cycle time, with limited explicit coupling to detailed warpage or morphology models. Furthermore, the results are only rough recommendations for positioning channels or sketches for cooling channel layouts.

2 Inverse thermal mold design

With the CRC1120 we developed a holistic, inverse workflow for temperature-control design in injection molding that first optimizes the desired thermal state at the mold–part interface and then derives manufacturable cooling channels from that optimum [Hoh21]. The pipeline comprises the preparation step (step 2, Figure 1) with the creation of an adaptive offset (computation space) around the part and a filling/cooling injection molding simulation to supply realistic periodic steady-state initial temperature and pressure histories [HFHN22]. Next is the optimization (step 3) with a gradient-based solver adjusting the local temperature boundary on the offset surface to achieve the target heat-flux field. Last, the channel derivation (step 4) approximates channels along iso-surfaces of the optimized heat exchange into either conformal or straight (drillable) channel layouts. Compared with conventional forward design, the inverse approach reduces designer bias and directly targets part quality like warpage through physics-based objectives and material models.

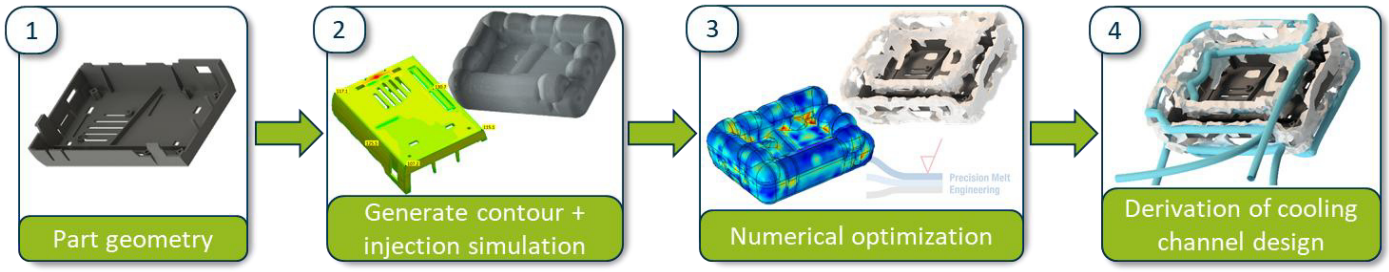

Figure 1: Procedure for inverse thermal cooling channel design methodology.

2.1 Objective functions

The initial objective from *Agazzi et al.* was extended to include density homogeneity by adressing pressure-dependent shrinkage [AgaSL+10, Nik18]. A later refinement introduced normalization of the evaluated state variables and mesh-area weighting so neither dense meshes nor a single term dominate [HFH22]. Because time integrals are awkward in large, time-dependent gradient problems, CRC1120 ultimately targeted cooling-rate uniformity and freeze time as surrogates for microstructure and shrinkage uniformity. Practical validation on a casing demonstrator showed warpage reduction of the factor 1.33 by optimized conformal cooling channels versus a professional conventional layout [Hoh21]. The newer method (cooling-rate/transition-time) achieved an extra 40–110 µm improvement over the earlier formulation (temperature/density). However, gains vary by feature. Some geometries show limited benefit depending on the dominant warpage mechanism. However, one important advantage of the CRC1120's methodology is the independence of the result from the knowledge and capacity of the design engineer.

2.2 Automatic derivation of cooling channels

After the thermal optimization yields iso-surfaces that encode where the mold should exchange heat with the part, CRC1120 replaces manual drafting with an automatic, path-planning-based derivation of conformal channels [HH21]. The algorithm first generates candidate channel segments near the iso-surfaces by solving a local geometric minimization problem, so that each segment follows the target heat-exchange geometry as closely as manufacturability allows. It then connects these segments into complete flow paths using a routing strategy that finds the shortest path, while ensuring collision-free placement relative to the cavity, parting plane and other channels and preventing self-intersections. This removes user-dependent variability present in manual translation from iso-surface to channel, thereby stabilizing the design outcome against individual choices. In validations on multiple parts, the automatically derived conformal layouts achieved thermal performance and computation times comparable to careful manual designs, with substantially less user effort and a more reproducible result, supporting the method's suitability for routine engineering use [HFH22, HH21].

Because conformal channels can be limited by mold material choices, maintenance, and cost, industrial practice still leans heavily on conventional drilled channels. To match the inverse-design intent into this reality, CRC1120 developed an automatic straight-channel derivation that starts from the same iso-surfaces and simplifies them to extract robust anchor and intersection points [FHSS25]. Using these anchors, the method assembles straight, drillable segments that approximate the iso-surface locally while forming a continuous, hydraulically sensible network. During this optimization, the algorithm respects manufacturing and mold constraints including parting plane, ejector pins, hot runners and the special rule of drill accessibility for every segment. Once the start and end points are set, the routine proceeds fully automatically, removing operator dependence. In simulation, straight-channel layouts produced by this method deliver temperature fields, transient development, and warpage that are very similar to expert-designed conventional

layouts. Deviations fall within the envelope of numerical fluctuations and model simplifications [FHSS25]. Similarity between the compared layouts is partly attributed to matching diameters and the constraints that limit the solution space and drive convergent designs.

3 Aim of the Investigation

While simulations indicate that automatically derived straight, drillable channels can reproduce the thermal fields and warpage levels of expert conventional designs, decisive evidence ultimately depends on controlled experiments under realistic manufacturing conditions [FHSS25]. The simplifications made in the simulative investigation like neglecting the influence of flow behavior or warming of the cooling fluid along the channels should be considered in a next step. Moreover, prior observations suggest that process parameters may rival or exceed layout effects, underscoring the need for coordinated assessment [FHSS25]. The following chapters therefore present a practical investigation of the automated straight-channel derivation.

4 Materials and Experimental Details

4.1 Part Geometry and Cooling Channel Design

Experiments employed a casing geometry, selected for its warpage sensitivity due to a free-standing rib, large planar walls, right-angle corners, fillets, and a through-hole that together produce significant deviations under realistic process variations. The nominal wall thickness is 2 mm and the geometry is displayed in Figure 2.

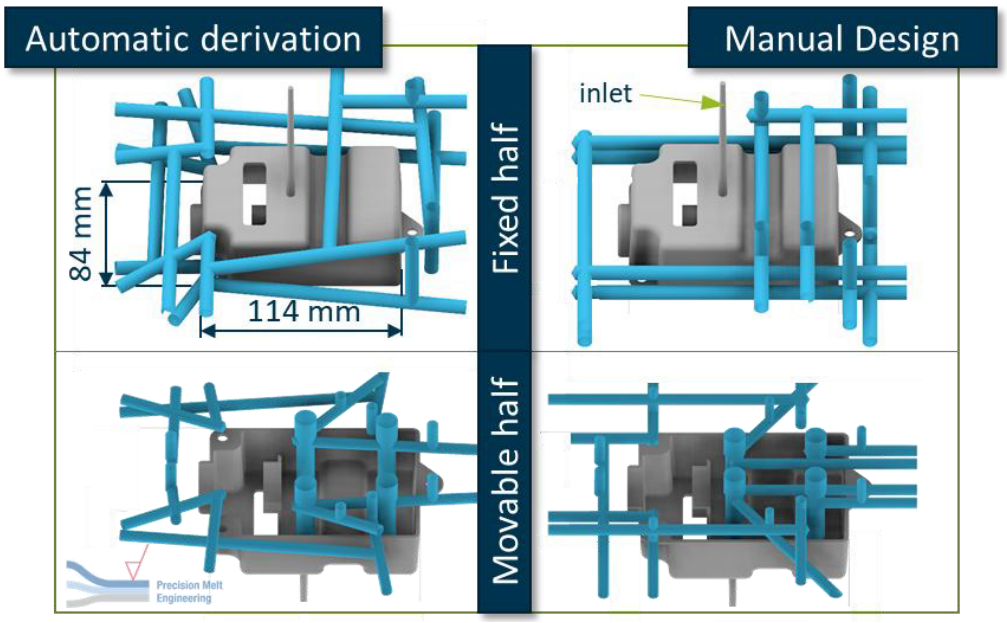

Figure 2: Part geometry with manually designed cooling channel layout (right) and automatically derived layout (left)

A pre-existing base mold was adapted via new cavity inserts for the fixed and movable half of the mold. The fixed inlet/outlet positions for the cooling circuits thus constrain feasible routing. Two layout variants were realized. A cooling channel layout manually designed by a professional mold

maker with predominantly parallel/orthogonal routing and an automatically derived straight-channel layout. It was generated algorithmically from iso-surfaces of the inverse design thermal mold design routine. The used objective function homogenized the surface temperature, cooling rate and freeze time of the part in the optimization step. The computing time which was necessary instead of manual test and channel design was ca. 3 days without parallelization of the different circuits.

The insert pair was manufactured in 1.2312 steel for each layout. Channel diameters were kept identical across both variants for fair comparison: 8 mm on the fixed side and only 6 mm on the movable side as there a more obstacles like the ejector pins. Core-cooling fingers were placed at comparable positions to the conventional layout and set to a uniform depth of 34 mm as the algorithm does not place mold core cooling automatically yet. However, the position depends on the automatically generated cooling layout.

The automated derivation enforced drill accessibility and collision avoidance with the cavity, parting plane, gating system, sensors, ejectors, insert boundaries, mold–insert interfaces, and existing bores. Minimum clearance was 1x channel diameter (1D), minimum segment length 3D, and segment angles 45–150 °. The wider angle range extends placement options beyond the 45 °/90 °patterns common in manual layouts. Symmetries on the movable side were exploited by generating one half and mirroring it to reduce computational cost. The channel layout of the fixed half is generated in one run without symmetry as a boundary condition. The automatically derived channel circuits are displayed in Figure 2.

4.2 Injection Molding and Warpage Measurement

Unfilled polybutylene terephthalate Pocan B1305, Envalior GmbH, Germany, was processed on an ENGEL e-motion 160, Engel Austria GmbH, Austria, all-electric press to emphasize crystallization-related shrinkage and warpage signatures. For the experiments, the dosing volume was 55 cm³, holding pressure 330 bar, switch-over volume 12.5 cm³. A full-factorial design of experiments varied mold temperature (T_{Mold}), cylinder temperature ($T_{Cylinder}$), and volume rate ($\dot{V}$) at two levels each, yielding 8 process points per channel layout (Table 1). An integrated robot removed parts, recorded part mass, and placed them on a conveyor to standardize early cooling. After 2 h cooling at room temperature the parts are stored in boxes without stacking for 24 h.

Table 1: Process parameters for design of experiments.

Parameter	Mold temperature [°C]	Cylinder temperature [°C]	Volume rate [cm³/s]
+	100	250	25
-	80	260	35

4.3 Dimensional Metrology

Warpage was quantified using an optical 3D coordinate-measurement system (GOM ATOS Q MV 270, Carl Zeiss GOM Metrology, Germany) after 24 h of storage. The system measured the parts by structured-light projection with triangulation and compared it to the cavity CAD as the nominal reference. Consequently, a global best fit alignment between a part geometry without shrinkage compensation and the scan is created. Five wall angles as geometrically sensitive features were measured on ten parts for each channel layout and process parameter combination (Figure 3). These metrics are known to be highly sensitive to thermally induced warpage, enabling robust comparison between the two cooling strategies under the factorial settings.

5 Results and Discussion

The generated cooling channels are functional and can be manufactured. The general routing is similar to the manual layout because inlets/outlets and obstacles are identical. However, the range of allowed angles between channels results in a high variation of channel orientation. An additional difference between the layout is short channels leading to and from a corner of the part which also contains the biggest mass accumulation of ca. 4 mm thickness. Thus, the heat transfer is increased locally in this area to achieve a more homogeneous temperature and cooling rate.

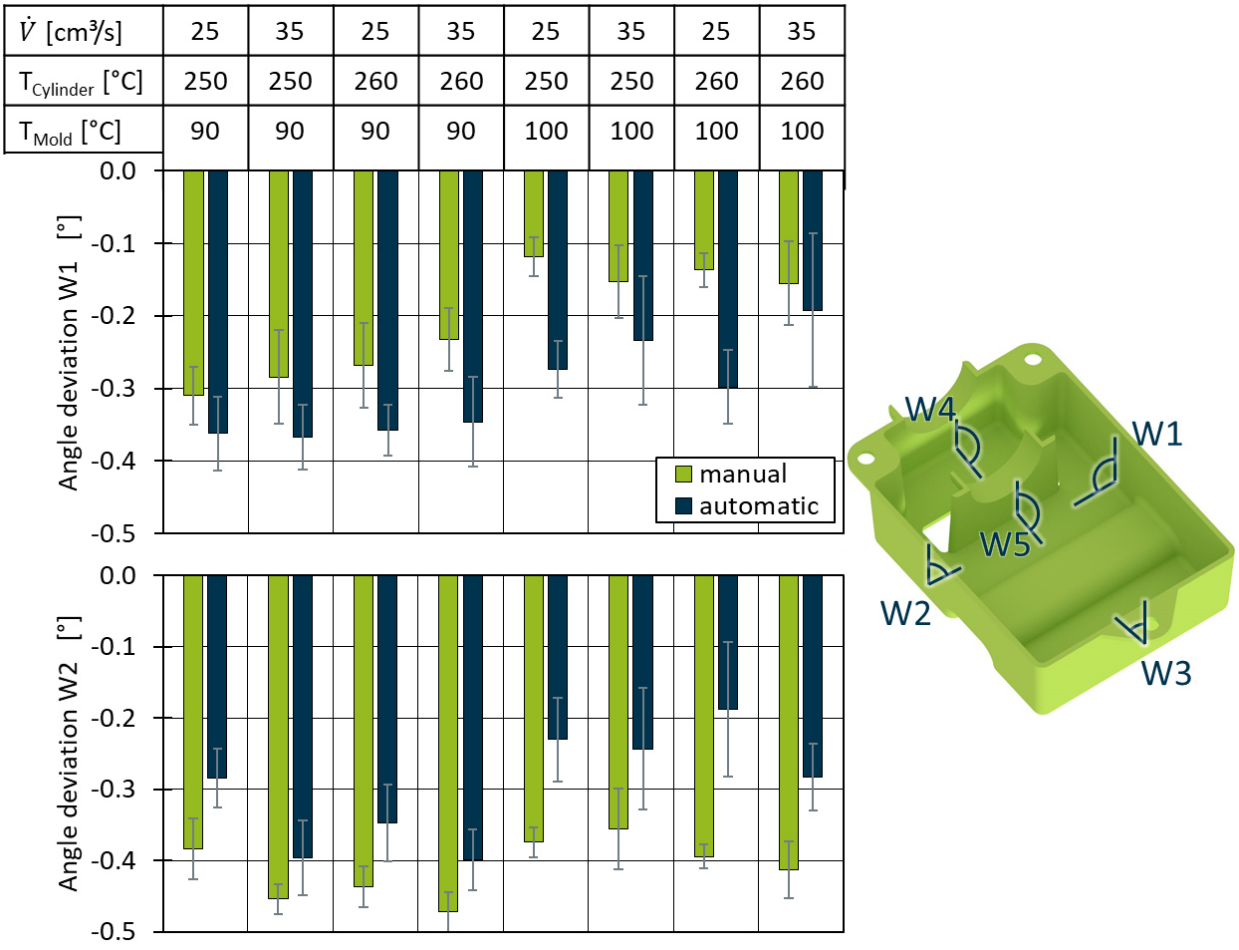

Figure 3: Position of measured angles and angle deviation of W1 and W2 parts produced by both cooling layouts.

The resulting warpage as angle deviations is displayed in Figure 3 and Figure 4. The angles of the two long walls W1 and W2 warp inwards for both cases. For all process parameters combinations, the automatic layout produces parts with more warpage for W1 but less warpage for W2. In case of the automatic design the different tendency can result from the asymmetric channel layout, which can lead to different cooling and therefore, different warpage. However, the average warpage of W1 with -0.30 is similar to the average warpage of W2 with -0.29°, whereas the manual design results in part with a significantly higher average warpage of W2 with -0.40° than W1 with -0.21°. Consequently, the automatic design produces a more symmetric part. The different local shrinkage and resulting varying wall collapse in the manual design can result from different cooling fluid temperature and pressure at the two walls, as the respective channel segments are in the same circuit.

Angle W4 shows the highest relative differences between the two layouts over all investigated angles. The automatic design produces parts with on average 0.004°, whereas the manual design results in an average warpage of 0.31° which is an improvement of the factor 78. As the most significant difference between the two layout is the cooling of the corner close to the angle W4 its influence on the part warpage in this scale is the most probable cause.

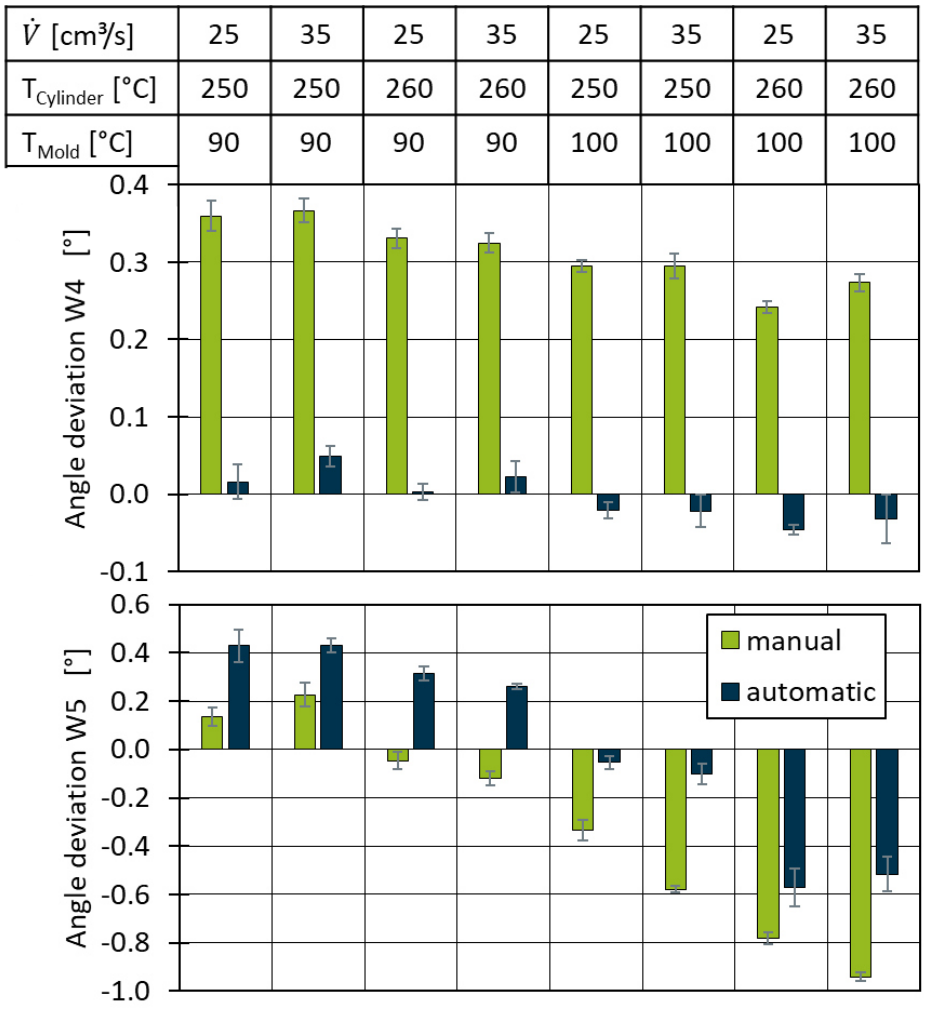

Figure 4: Measured angle deviation of W4 and W5 parts produced by both cooling layouts.

The free-standing wall in the middle has low structural stiffness, which means that its warpage is highly dependent on the process parameters. This can be seen at angle W5 (Figure 4). The warpage direction changes from a positive deflection with low mold temperature to a negative deviation with high mold temperatures. This results in a higher warpage for low mold temperatures with the automatic layout. When the mold temperature is increased the deviation of the manual design is higher as the effect of the mold temperature on the warpage is similar for the manual (0.71°) and automatic (0.67°) layout. This underlines the importance of regarding the process parameters during the optimization step in the inverse thermal mold design.

Angle W3 shows low warpage under 0.1° for both layout and all process parameters. The warpage tendency is similar to W5 and it depends on the process parameter which cooling system results in the lowest warpage. For these two reasons the results are not displayed.

Compared to the simulative investigation of the automatic straight cooling channel derivation the warpage is higher due to the different investigated part and thermoplastic used [FHSS25]. Additionally, only the practical validation shows a major improvement of one feature (W4), whereas the warpage in the simulative study is very similar for both layouts. However, this work shows as well that the methodology produces competitive channel layouts automatically and other influencing factors like the process parameters are more significant the difference between the effects of the compared channel layouts.

6 Conclusion and Outlook

In CRC1120 a holistic and objective methodology for the thermal injection mold design was researched which creates applicable cooling channel layouts. The new algorithm for the derivation of conventional cooling channels closes the gap between the calculated optimal heat flux distribution and final cooling layout. The presented application of the algorithm and measured part warpage validates its usability. The warpage of parts produced with the automatically generated design is either in the similar range as the manual layout or much lower like for the angle W4 with a factor of 78.

In future, the influence of the cooling fluid warming up along the circuit must be taken into account in the algorithm as the asymmetric channel layout has shown benefits for a symmetric part and results in a more symmetric warpage than the comparison layout.

Acknowledgements

The depicted research has been funded by the Deutsche Forschungsgemeinschaft (DFG) as part of the Collaborative Research Centres CRC 1120. We would like to extend our thanks to the DFG.

Conflict of Interest

The author declares no conflict of interest.

Data Availability Statement

The data and materials for this publication are available on request at the following link: http://hdl.handle.net/21.11102/d7ddcd70-0280-4a77-80c1-e8be878af9fb

References

[AgaSL+10] AGAZZI, A.; SOBOTKA, V.; LE GOFF, R.; GARCIA, D.; JARNY, Y. *A Methodology for the Design of Effective Cooling System in Injection Moulding. International Journal of Material Forming* 3 (2010) S1, S. 13–16.

[Bla25] BLAKE, C. *Fast Cooling Simulation for the Generative Design of Injection Mold Cooling Layouts that Reduce Cycle-Time and Improve Part Quality.* Philadelphia, 06.03.2025

[FHSS25] Fritsche, D.C. et al. Hrsg.*Automatic derivation of conventional cooling channels for digital thermal mold design.* Society of Plastics Engineers, 2025

[FKP21] FENG, S.; KAMAT, A. M.; PEI, Y. *Design and fabrication of conformal cooling channels in molds: Review and progress updates,* International Journal of Heat and Mass Transfer 171 (2021)

[HFH22] HOHLWECK, T.; FRITSCHE, D.; HOPMANN, C. *Validation of an extended objective function for the thermal optimisation of injection moulds. International Journal of Heat and Mass Transfer* 198 (2022), S. 123365.

[HFHN22] HOPMANN, C.; FRITSCHE, D. C.; HOHLWECK, T.; NEHRING-WIRXEL, J. *Variable Offset Computation Space for Automatic Cooling Dimensioning. Polymers* 14 (2022) 4.

[HFK+24] HOPMANN, C.; FRITSCHE, D. C.; KAHVE, C. E.; BOBZIN, K.; HEINEMANN, H.; ERCK, M.; VOGELS, C. *Methodology of a thermal injection mold design with locally applied heating coatings on the cavity wall. Materialwissenschaft und Werkstofftechnik* 55 (2024) 4, S. 518–532.

[HH21] Hohlweck, T.; Hopmann, C. Hrsg.*Path-Planning Algorithm For The Automatic Generation Of A Cooling Channel Layout In Injection Moulds.* Danbury, USA. SPE, 2021

[Hoh21] HOHLWECK, T. *Inverse thermische Optimierung zur wissensbasierten thermischen Spritzgießwerkzeugauslegung.* RWTH Aachen, Disseration, 2021. - Betreuer: C. Hopmann

[HopMMM18] HOPMANN, C.; MENGES, G.; MICHAELI, W.; MOHREN, P. *Spritzgießwerkzeuge.* Auslegung, Bau, Anwendung. München. Hanser, 2018 - ISBN: 9783446451926.

[HZF+24] HOPMANN, C.; ZIMMERMANN, C.; FRITSCHE, D. C.; BOBZIN, K.; HEINEMANN, H.; ERCK, M.; LOHREY, N. *Design of an injection mold with local placement of heating coatings for warpage compensation.* Universidad de los Andes, 2024

[KA25] Kietzmann, C.; Astbury, D. Hrsg.*Automatic cooling channel layout generation for injection molding,* 2025

[Nik18] NIKOLEIZIG, P. *Inverse thermische Spritzgießwerkzeugauslegung auf Basis des lokalen Kühlbedarfs.* RWTH Aachen, Dissertation, 2018. - Betreuer: C. Hopmann

[Sch23] SCHÖTZ, A. *Abmusterung von Spritzgießwerkzeugen.* Strukturierte und analytische Vorgehensweise. München. Carl Hanser, 2023 - ISBN: 9783446477223.

Date: 30.03.2026

Influence of transient temperature on liquid metal embrittlement (LME) of Laser-DED brazed CuSn12Ni2 on 42CrMo4 investigated via 2D-quotient thermography

M. Troise[1*], K. Murthy[1], S. Olschok[1], U. Reisgen[1]

[1]RWTH Aachen University, Welding and Joining Institute - ISF, Pontstr. 49, 52062, AACHEN, GERMANY

*Corresponding author: E-mail: marcel.troise@isf.rwth-aachen.de, ORCID: 0009-0002-6836-7979

Abstract

The favorable tribological properties of bronze alloys such as CuSn12Ni2 allow for its use as brazing alloy for coating of tempered steel, mainly for components in tribological contact, including gears, pistons and bearings. Brazing via Laser-DED is an advanced coating method that allows for precise control of heat input and good mechanical properties. Liquid metal embrittlement (LME), a common defect in such joints, is strongly linked to transient temperature, which is difficult to measure due to the high temperature gradients and cooling rates. In this study, the thermal influence of the brazing process on liquid metal embrittlement is investigated using a specially developed 2D-quotient thermography setup. Considering influence of substrate temperature, process temperatures, and sample geometry, transient temperature is then correlated with LME crack length and frequency. The results demonstrate the viability of 2D-quotient thermography to investigate such processes and show a clear link between transient temperature and LME.

Keywords

Laser brazing, Laser material processing, Liquid Metal Embrittlement (LME)

1 Introduction

The application of bronze materials via brazing is a well-established industrial practice aimed at improving the tribological performance of steel components. It is widely utilized in sectors such as automotive engineering, aviation, and shipbuilding, particularly for components operating under tribological contact, including bearings, gears, pistons, and shafts. [1–8] Due to their favorable tribological and mechanical characteristics, tin bronzes such as CuSn12Ni2-c (CC484K) [9] and comparable alloys are especially suitable for these applications [1–3, 10–12]. Directed Energy Deposition (DED) via laser-powder or in this case, laser-wire deposition represents an effective brazing technique for joining dissimilar materials across a broad range of substrate materials. This process enables precise thermal control, facilitates the coating of complex geometries, and produces dense coatings with strong adhesion to the substrate [13–16], while also offering improved sustainability compared to conventional casting methods. Liquid metal embrittlement (LME), meaning the loss of ductility on a liquid-solid metal interface, has been recognized for decades in the context of brazing tin bronzes onto tempered steels . [17–20]. Liquid metal penetration (LMP) refers more specifically to the infiltration of the embrittling metal into the resulting cracks. In this work, LME is used as a collective term encompassing the observed cracking phenomena. The occurrence of LME leads to a deterioration of mechanical properties, particularly a reduction in the ductility of the base material [20]. Several mechanisms have been proposed to explain this type of metal-physical degradation. [20–25]. The likelihood of LME depends on various factors, including the specific material pairing of substrate and penetrant [20, 22]. In particular, copper and bronze alloys are known to induce LME in high-strength martensitic steels, thereby reducing their ductility [21]. Additional influencing factors include adequate interfacial contact, i.e., proper wetting of the substrate by the filler metal [22], the transient thermal conditions [23], and both residual and externally applied stresses within the substrate. These stresses may originate from prior manufacturing steps such as welding or from localized heat input during brazing. Furthermore, the initial microstructure of the substrate can also affect the susceptibility to LME [25]. To date, precise control of process parameters, including temperature gradients and strain distributions, has proven effective in mitigating LME [26]. It is well established that higher heat input increases the tendency for LME [19].

2 Aim of the Investigation

In this study, a comprehensive thermographic investigation of CuSn12Ni2-c onto 42CrMo4 using laser wire deposition has been conducted. The objective is to determine temperature distributions and cooling rates of the process by means of 2D quotient pyrometry. This method enables the characterization of the highly dynamic and otherwise difficult-to-measure process zone during laser brazing. These findings will be substantiated via analysis of the substrate temperature via classical thermography. The present study focuses on correlating transient temperature profiles with crack frequency and crack length. The goal is to identify and evaluate these parameters as additional factors influencing LME in this specific material system.

3 Materials and Experimental Details.

A schematic depiction of the laser-wire brazing setup is shown in Figure 1. The brazing setup uses a Trumpf Tru Disk 16002, with a 400 µm fibre diameter and optics with 200 mm collimation and 400 mm focal length. The focal position is set to 80 mm over the sample surface to archive a spot size of 7 mm. The CuSn12Ni2-c wire is fed into the center of the laser spot with a drag angle of 45°. The process is shielded using 15 l/min argon 4.6 gas. The deposition strategy involves brazing of a spiral shape, initiated from the center of the specimen and progressing outward with a layer overlap of 50% and a layer width of 8 mm. This is followed by the completion of an additional circle, ensuring coverage of the specimen. The spiral is created by rotating the workpiece while moving the laser brazing head outwards. The relative brazing speed remains constant during the deposition process.

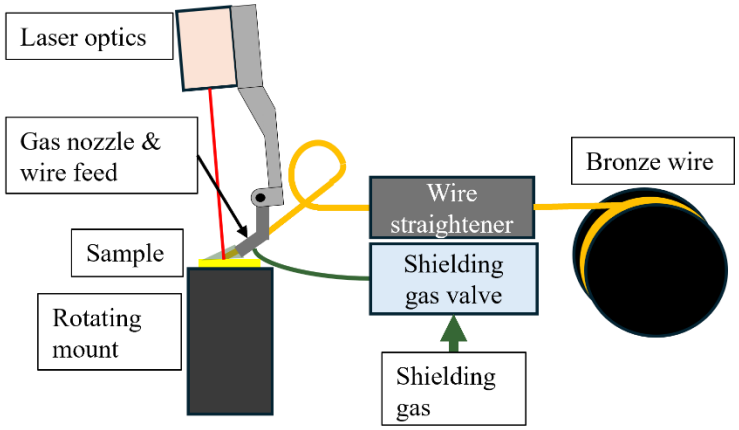

Figure 1: Schematic depiction of the laser-wire brazing setup

Two parameter sets were selected for brazing, shown in **Table 1**. A lower deposition rate parameter, which tends to cause more cracks, and a high deposition rate parameter, which causes fewer cracks, as preliminary investigations have shown. All other parameters remained constant and are described below.

Table 1: Laser brazing parameters

Parameter	Unit	Sample 1	Sample 2
Laser power	W	3500	3600
Brazing speed	mm/s	16	16
Energy per unit length	J/mm	220	225
Wire feed	mm/s	87	75
Deposition rate	g/min	45	41

The 42CrMo4 samples were machined to Ø 114 x 18 mm discs. Brazing filler metal was CuSn12Ni2, diameter d = 1 mm. Material composition of the materials used are listed in Table 2. Samples are degreased and coated in Castolin Flux 18 before deposition.

Table 2: OES analysis of base materials and filler wire composition according to [27] in m%

Material	C [m%]	Si [m%]	Mn [m%]	P [m%]	S [m%]	Cr [m%]	Mo [m%]
42CrMo4	0.387	0.281	0.822	0.0078	0.0161	1.06	0.184
Material	Ni [m%]	Sn [m%]	Zn [m%]	Pb [m%]	Fe [m%]	Mn [m%]	P [m%]
CuSn12Ni2	1.5-2.4	11.3-13.0	≤0.3	≤0.2	≤0.15	≤0.1	≤0.05

An Optris Xi410 LT ETH thermal camera was used to determine substrate temperature i.e. sample temperature. The measurement data was referenced using data from thermocouple measurements to correct for the emission coefficient, which changes with temperature. A specially built 2D-quotient thermography camera, designed by University of Stuttgart, Institut für Strahlwerkzeuge – ISFW, was used to analyze process temperatures, as detailed in the literature [28].

4 Results and Discussion

The as-deposited, laser-brazed samples are presented in Figure 2 a) and b). The darker appearance of sample B indicates elevated deposition temperatures, as evidenced by the more pronounced surface oxidation. While deposition rate and laser power vary between the two samples, shielding gas flow was maintained.

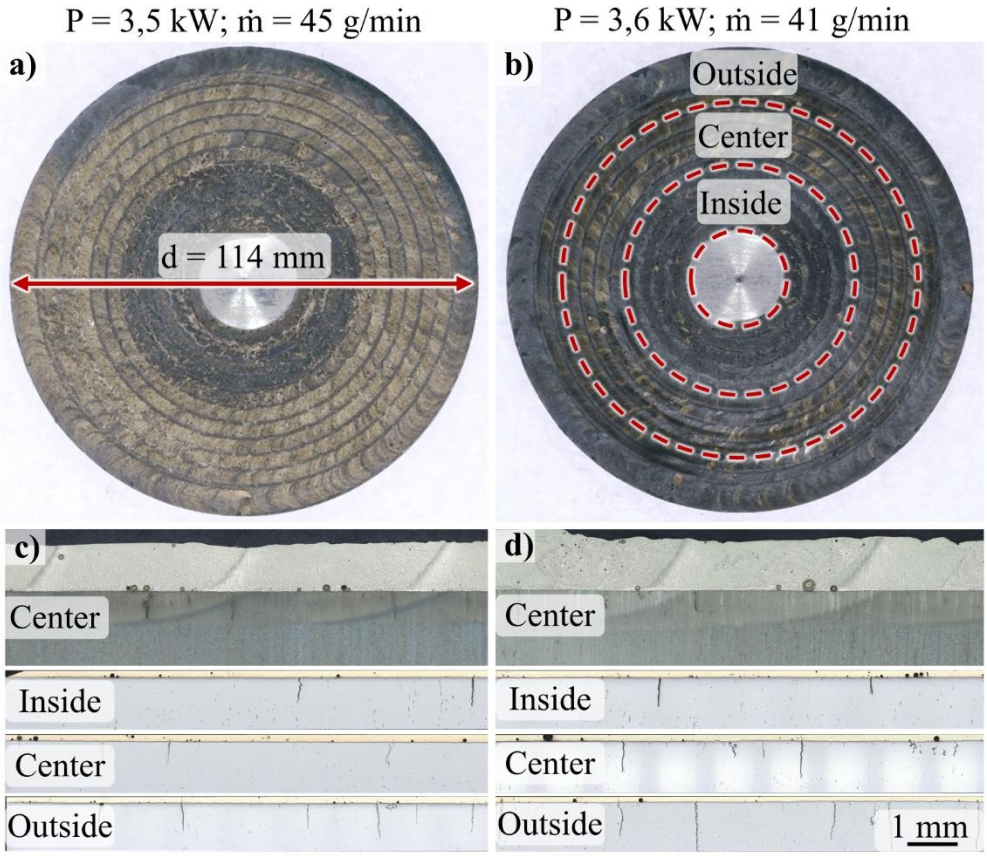

Figure 2: Images of the laser brazed samples and cross sections of the analyzed sample sections

The deposition strategy is discernible in the images. Upon completion of the spiral path, an additional rotation was performed without translational movement of the laser head, ensuring full coverage of the sample geometry, while the center of the samples remains uncoated. For cross-

sectional analysis as well as characterization of LME cracks size and distribution, the samples were subdivided into the regions “inside,” “center,” and “outside,”. Figure 2 c) and d) shows exemplary cross sections of the sectioned sample, as indicated in Figure 2 b). As deposition rate varies only slightly between the two parameter sets the layer thickness is similar. The top images in Figure 2 show an overview of the deposited coatings. The width of the individual layers is discernible. The structure is dense but shows some porosity. Porosity in such coatings is seen in the literature and can be optimized by means of optimizing deposition rate, laser power and gas shielding [2, 3]. Below the coating, the substrate HAZ can be seen. Hardness is H = 400 HV0,5 right below the coating interface and linearly decreases to H = 250 HV0,5, which is the base material hardness, at around 1,5 mm distance from the interface. The three cross sections below show polished sections that were used to measure the crack length and distribution. Crack quantification was performed based on ten cross-sections per sample position, as indicated in Figure 2 b). As the standard relevant to laser brazing (ISO 18279) does not specify a minimum crack size, crack evaluation was conducted in accordance with DIN EN ISO 13919-1. Accordingly, features requiring magnification greater than 500× for unambiguous identification were excluded from the analysis, resulting in a minimum detectable crack length of approximately 20 µm.

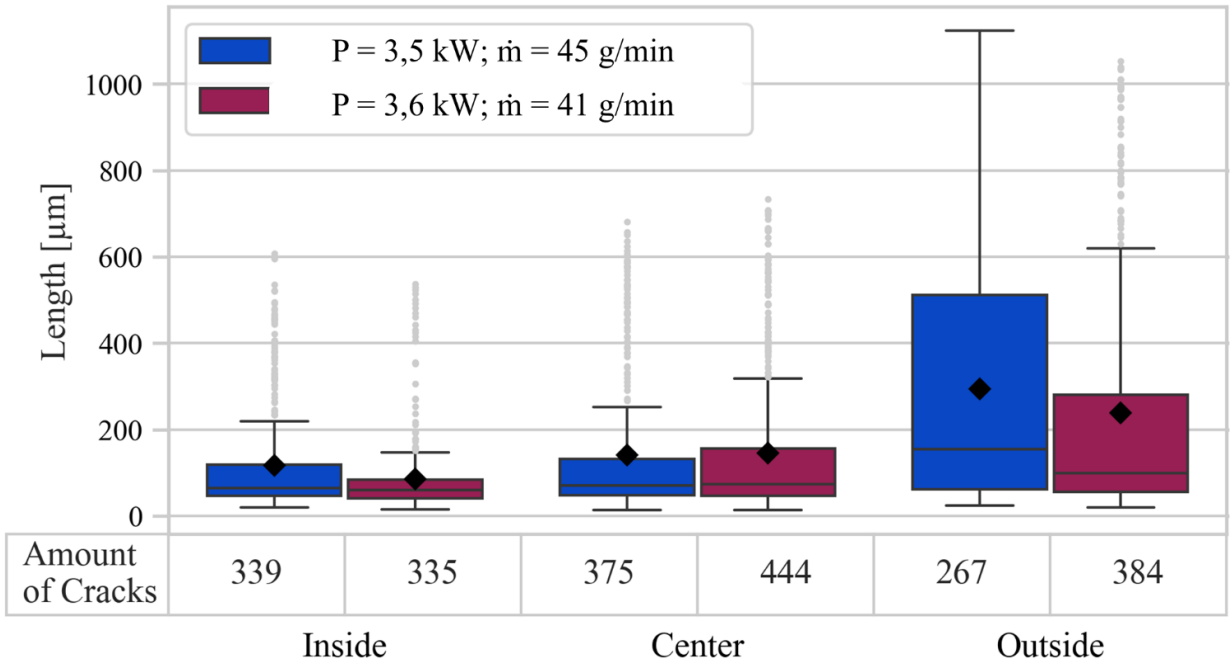

Figure 3: Boxplots of crack length and distribution

Figure 3 shows the crack length distributions for both samples across the inner, center, and outer regions. In the inner region, the median crack lengths differ only slightly (~5 µm), with values of approximately 64 µm for the lower energy input and 59.4 µm for the higher energy input. Furthermore, the interquartile ranges are comparatively small for both cases and the total amount of cracks is roughly the same. In the center region, the median values remain similar, differing by only ~3 µm, with slightly higher crack lengths overall. However, the interquartile ranges increase, particularly for the P = 3,6 kW sample, which also exhibits a greater number of cracks across most size ranges. In the outer region, more pronounced differences are observed. The median crack

length for the lower energy input (≈154 µm) is significantly higher than that of the higher energy input (≈99.5 µm). Additionally, the interquartile range is substantially larger. While the higher energy input results in more cracks at smaller sizes (<200 µm), the lower energy input shows a higher frequency of cracks in the intermediate range (~200–700 µm). Overall, the higher energy input tends to produce more small cracks, and therefore more cracks in total. Whereas both conditions exhibit comparable maximum crack lengths and similar distribution characteristics at the extremes.

Strain-, stress-, and temperature-induced LME effects are altered in the outer regions of the samples, as can be seen by the greatly increased crack sizes, but a decrease in number of cracks. This may result from increased substrate temperature due to preceding laser process [19], as well as altered strain and stress conditions near the sample edge [29–31]. Since both samples share identical geometry, the higher median crack amount across center and outside indicates a predominantly thermal origin. Overall, a clear trend is observed toward higher crack density and longer crack growth as process time progresses and temperature increases. Heat accumulation may delay the solidification of the molten metal, thereby extending liquid metal exposure time. These hypotheses are explored in the following sections.

Figure 4 shows the substrate temperatures of both samples, measured at 12 equidistant points. The measurement range of the camera was calibrated against thermocouple data to correct for the temperature-dependent variation in the emissivity coefficient. Table 3 shows a moving average with a window size of 40 data points, corresponding to a time interval of 0.5 seconds. This temperature can be considered representative of the substrate temperature right before the corresponding brazing layer is applied.

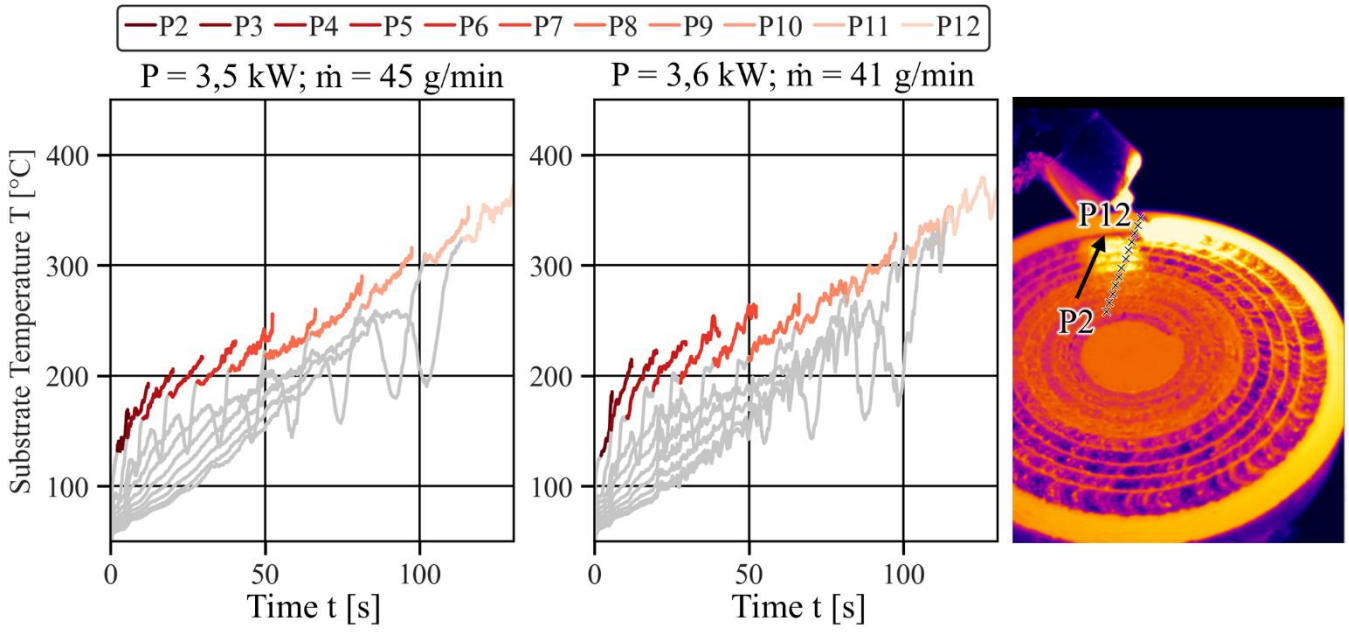

Figure 4: Substrate temperatures over time based on 12 measurement points

The minima observed prior to the selected measurement intervals result from process shadowing caused by the wire, enabling precise temporal identification of the relevant regions. In the process with lower energy input, the substrate temperature increases on average by 9.04% between successive layers, while for the higher energy input spiral, the increase is 8.26%. In general, the difference in preheating temperature between the two spirals decreases with increasing number of layers, i.e. in the progressing brazing process. Starting from around 9% and decreasing to less than 1% in the outside layers.

Table 3: Calculated substrate temperatures at selected points

Point	Section	P = 3,5 kW	P = 3,6 kW	Difference in %
Layer 2	Inside	145,2	157,8	8,68 %
Layer 4	Inside	183,5	192,4	4,85 %
Layer 6	Center	208,1	219,1	5,29 %
Layer 8	Center	228,9	233,7	2,1 %
Layer 10	Outside	284,9	285,8	0,32 %
Layer 12	Outside	343,2	345,4	0,64 %

In the inside regions, cracking behaves very much the same between the two samples. The 5-10% difference in substrate temperature in the inner layers does not amount to a difference in cracking behavior. In the later stages, temperature differences equalize and diminish completely in the outside regions. Nonetheless, here the number of cracks differs between hotter and colder process, suggesting little influence of the substrate temperature itself on LME phenomena in this case. Sample temperature is T = 280 °C or higher in both samples in the outside regions. Since both Samples exhibit less, but much longer cracks in those areas, having reached this temperature might be one of the conditions necessary for this behavior.

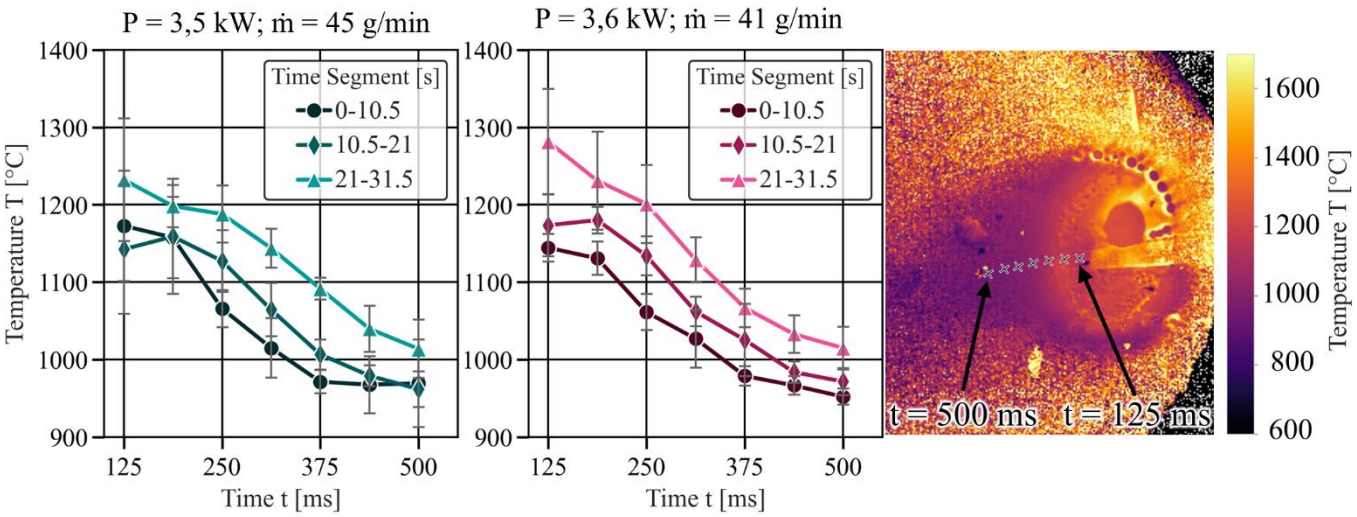

Figure 5: Quotient pyrography measurement of the process temperatures.

Figure 5 shows the process temperatures over time in selected time segments. Peak temperature at around 2 mm distance from the center of the laser spot is around T = 1150 °C in the early time segment in both processes. The cooling rate is at around 550 °C/s, meaning that T_{solid} = 830 °C is

reached from peak temperature after about 0.62 s. In later stages of the process, the peak temperature rises as the substrate warms up. Yet the cooling rate remains similar. Cooling down to solidus therefore takes longer since peak temperature has increased, causing a longer liquid-solid contact time and more time for cracks to develop and grow, explaining the higher number of cracks in the center regions. Especially in the later segments, temperatures of the P = 3,6 kW sample increase more. On average that process is slightly hotter on most points of measurement, resulting in increased crack amount in the hotter samples in those regions. In the outside region, the number of cracks reduces again, instead many cracks become much larger, as shown in Figure 3. Since the peak temperatures of the higher energy process are reached by the lower energy process only in later stages, a critical temperature for the development of fewer but lager cracks cannot be determined, inferring that the spatial location on the sample outside, where strain can develop more easily due to less support of surrounding material may likely be the reason for this behavior, rather than transient temperature alone. Furthermore, differences in crack morphology between segments may be attributed to variations in local stress states. Lower compressive stresses in the outer regions may facilitate grain boundary opening, thereby promoting the formation of longer LME cracks. Previous studies have demonstrated the significant influence of the stress field on LME behavior, indicating that a more detailed characterization of the stress and strain states during processing is necessary to establish accurate correlations between crack formation and spatial location [29–31].

5 Summary

Two-dimensional quotient thermography has proven to be a suitable method for measuring and characterizing the complex thermal conditions present during laser brazing. In combination with conventional thermography, it enables a nearly comprehensive thermal analysis of the process. Transient temperature has a pronounced effect on crack formation. Increased occurrence of LME cracks and lager crack sizes correlate with increased substrate as well as process temperatures, indicating that controlled cooling phases may represent an effective strategy for mitigating LME cracking. Although reduced heat dissipation in an already preheated workpiece should affect crack formation, it does not account for the difference in crack formation between the lower energy and higher energy sample, suggesting increased process temperatures to be the main influence. The observed increase in crack length toward the outer regions is not attributable to extended diffusion times resulting from prolonged dwell times above the solidus temperature, as the hotter process reaches higher temperatures much earlier in the process, yet behaves similarly with regards to the spatial locations of the longer cracks, suggesting that local stress fields and strain distribution in the outside regions of the sample to be the main influence.

Acknowledgements

The presented investigations were carried out at RWTH Aachen University within the framework of the Collaborative Research Centre SFB1120 236616214 “Bauteilpräzision durch Beherrschung von Schmelze und Erstarrung in Produktionsprozessen” and funded by the Deutsche

Forschungsgemeinschaft e.V. (DFG, German Research Foundation). The sponsorship and support is gratefully acknowledged.

Conflict of Interest

The author declares no conflict of interest.

Data Availability Statement

The data that supports the findings of this study are available at http://hdl.handle.net/21.11102/01338aea-287e-4ac3-a88f-19d7d45403db upon request.

References

[1] P. K. Hu *et al., Influence of Ni content on electrochemical corrosion and tribological behavior of Cu-10Sn coatings by laser cladding*, Materials Today Communications, **2024**

[2] S. Raghavendra *et al., Process enhancements and wear evaluation of directed energy deposited bronze: Implications for reducing bronze in worm gear manufacturing*, Journal of Materials Research and Technology, **2025.**

[3] S. Raghavendra, *et al, Development of DED Process Parameters for Deposition of Bronze and Evaluation of Its Wear Properties under Dry Sliding Conditions,* Procedia Structural Integrity, **2024.**

[4] M.V.S. *Babu et al. Review of Journal Bearing Materials and Current Trends*, American Journal of Materials Science and Technology, **2015**.

[5] V. Fontanari *et al., Tribological behavior of the bronze–steel pair for worm gearing,* Wear, **2013.**

[6] V. Mastan *et al.*, *study of Friction and Wear on Journal Bearings,* International Refereed Journal of Engineering and Science (IRJES), **2012**.

[7] Biryukov, V. P. *et al*., *Laser Cladding of Copper Alloys on Steel* Phys. Atom. Nuclei **2019.**

[8] Le Wan, *et al., Annular laser cladding of CuPb10Sn10 copper alloy for high-quality anti-friction coating on 42CrMo steel surface*, Optics & Laser Technology, **2023**.

[9] DIN EN 1982, *Kupfer und Kupferlegierungen –Blockmetalle und Gussstücke*; Deutsche Fassung EN 1982:2024

[10] F. Rippa*, et al., Bronze-on-steel deposition with blue light high-speed Laser Cladding and IR Laser Cladding properties and differences*, Procedia CIRP 124 **2024.**

[11] Jie Chen, *et al., Influence mechanism of process parameters on the interfacial characterization of selective laser melting 316L/CuSn10*, Materials Science and Engineering: A **2020**.

[12] S. Raghavendra *et al., Wear and material characterization of CuSn10 additively manufactured using directed energy deposition,* Additive Manufacturing Letters 2023

[13] V. P. Biryukov *et al, Laser Cladding of Copper Alloys on Steel*, Phys. Atom. Nuclei, **2019.**

[14] H. Hügel und T. Graf, *Laser in der Fertigung: Strahlquellen, Systeme, Fertigungsverfahren,* 2. Aufl. Wiesbaden: Vieweg + Teubner, **2009**.

[15] L. Zhu *et al., Recent research and development status of laser cladding: A review*, Optics & Laser Technology, **2021**.

[16] A. S. Bolokang *et al., Laser cladding—a modern joining technique*, Advanced Welding and Deforming **2021**.

[17] M. H. Razmpoosh *et al., Atomic-scale Investigation of Liquid-Metal-Embrittlement Crack-path: Revealing Mechanism and Role of Grain Boundary Chemistry,* Acta Materialia, **2021**.

[18] M. H. Razmpoosh *et al., Pathway to understand liquid metal embrittlement (LME) in Fe-Zn couple: From fundamentals toward application,* Progress in Materials Science, **2021**.

[19] J. E. Norkett *et al., A Review of Liquid Metal Embrittlement: Cracking Open the Disparate Mechanisms,* Metall Mater Trans **2021**.

[20] M. G. Nicholas and C. F. Old, *Liquid metal embrittlement*, J Mater Sci,**1979**.

[21] S. P. Lynch, *Failures of structures and components by metal-induced embrittlement*, Stress Corrosion Cracking Theory and Practice **2011**.

[22] P. J. Fernandes and D. R. Jones, *Specificity in liquid metal induced embrittlement: Specificity in liquid metal induced embrittlement*, Engineering Failure Analysis, **1996**.

[23] C. F. Old, *Liquid metal embrittlement of nuclear materials,* Journal of Nuclear Materials,**1980**

[25] W. F. Savage, *et al., Intergranular attack of steel by molten copper,* Welding Research Supplement, **1978**.

[26] S. Chen, *et al., Interfacial ferrite band formation to suppress intergranular liquid copper penetration of solid steel,* Journal of Alloys and Compounds, **2019**.

[28] U. Reisgen, et al., *Temporally and spatially controlled temperature fields during material processing with the electron beam*, DVS Verl, RWTH **2021.**

[29] M. I. Chaevskii, et al., *Role of stresses in accelerating the penetration of liquid into solid metals*, Mater Sci, **1972**.

[30] C. DiGiovanni *et al, Liquid metal embrittlement transport mechanism in the Fe/Zn system: Stress-assisted diffusion,* Materialia, **2021**.

[31] K. Yang, *et al, The Identification of a New Liquid Metal Embrittlement (LME) Type in Resistance Spot Welding of Advanced High-Strength Steels on Reduced Flange Widths*, metals **2023**.

Date: 03.02.2026

Determining the grid spacing for spot melting in electron beam powder bed fusion

Author: Tobias Kupfer

Authors: T. Kupfer*, M. Markl

Chair of Materials Science and Engineering for Metals, Friedrich-Alexander-Universität Erlangen-Nürnberg, Martensstr. 5, 91058 Erlangen, Germany

*Corresponding author: E-mail: tobias.kupfer@fau.de, ORCID: 0000-0001-5228-6555

Abstract

Spot Melting is becoming increasingly popular in electron beam powder bed fusion. The melted volume, which largely depends on process parameters like beam profile, power or preheating temperature, of neighboring spots on the spot grid must fully overlap to achieve a fully dense part. Thus, determining the grid spacing is essential for a defect-free process. Numerical simulations offer the ability to rapidly test parameter sets in only a fracture of time needed for experimental studies. Therefore, this study presents an approach to determine the grid spacing from the simulated melt pool width of individual spots from a three-dimensional finite difference method. The approach is applied on reasonable parameter sets.

Keywords

Additive manufacturing, Electron beam powder bed fusion, Spot melting, Simulation

1 Introduction

Spot Melting in electron beam powder bed fusion (PBF-EB) is gaining popularity over traditional line melting. A key advantage of spot melting is the high level of control over energy input. While maintaining a constant return time in line melting requires considerable effort for complex geometries, spot melting can achieve this more easily by employing an overarching group structure [1, 2]. Whether the scan strategy in spot melting is based on random [3, 4, 5], pattern [1, 6, 7] or tailored [2] spot selection, the energy is distributed more evenly across the layer than in line melting. This allows melted spots more time to cool down, leading to a reduced exploitation of preheating effects from previously melted spots. Consequently, spot melting generally requires more energy to reach the same melting depth as line melting.

For a part to become dense, the melted volume of neighboring spots must fully overlap. Which primarily depends on the grid type used (usually square or hexagonal) and the associated grid spacing. To minimize melting time or utilized energy as well as simplify the spot sequence determination, only as many spots as necessary to achieve the desired melting depth across the layer should be melted. Thus, determining the appropriate grid spacing is crucial. This requires an accurate understanding of the extent of the melted volume, which is influenced by various process parameters such as the preheating temperature, beam power, and beam profile.

2 Aim of the Investigation

Simulations using parallelized approaches provide the capability to explore large parameter spaces, which wouldn't be feasible through experimental means [8]. This study presents an approach for calculating the optimal grid spacing to achieve dense layers for the two most common grid types based on simulated expanse of the melt pool. The proposed method determines suitable grid spacings from thermal simulations for a process parameter set from Kupfer et al. [2] and for reasonable variations from this set.

3 Materials and Experimental Details

3.1 Numerical Model

The simulations are based on single spots using the finite difference method, the detailed implementation of which is described by Breuning et al. [8]. The domain size is 5 mm x 5 mm x 1.25 mm. The cell size is 12.5 µm. The time step is 1 µs. Only heat conduction is considered; convection, evaporation, or radiation losses are neglected. The acceleration voltage for the electron beam is considered to be 150 kV. Because of the high acceleration voltage, the penetration depth is higher [9] compared to the traditionally used 60 kV. To consider for the higher penetration depth the energy from the Gaussian beam profile in the simulation is equally coupled into the first five layers, the first 60 µm. A Neumann no flux boundary condition is applied to the top layer. A constant initial temperature is assumed, which is also set at all boundary surfaces of the domain except the top boundary surface. As the material Ti-6Al-4V compact material is assumed with a thermal diffusivity of 9e-6 m^2/s, a density of 4122 kg/m^3, a specific heat capacity of 670 J/kgK and an absorption coefficient of 0.85. The melting temperature is 1929 K.

3.2 Evaluated Parameters

Due to the lower bulk density of the powder, double the nominal layer thickness is usually raked, resulting in an effective layer thickness. During melting, the powder layer is compacted to the nominal layer thickness. If the melting depth in the simulation over the entire layer corresponds to twice the nominal layer thickness, it is assumed that the melted layer is fully compacted. So, the grid spacing is determined from single-spot simulations from the lateral expansion x_{2ds} of the melt

pool at a depth corresponding to twice the layer thickness $2d_s$ as shown in Figure 1. The iso-surface of the melting temperature corresponds to the maximum expansion of the melt pool.

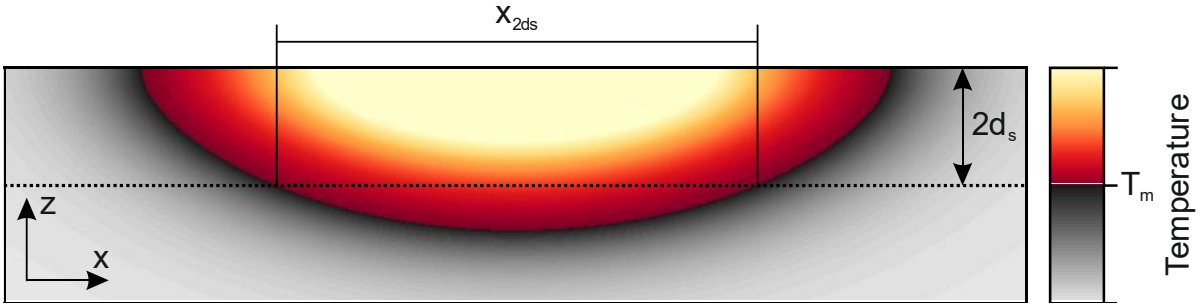

Figure 1: Lateral expansion of the melt pool x_{2ds} at a depth corresponding to twice the nominal layer thickness $2d_s$.

A parameter set from previous studies by Kupfer et al. [2] with a 333 µs dwell time, 50 µm nominal layer thickness, 1000 K preheating temperature, a Gaussian beam with a beam diameter of 4σ = 505 µm, beam power of 825 W, and all spots positioned on a square grid with a grid spacing of 400 µm is evaluated regarding the maximum possible grid spacing *g* for square and hexagonal grids according the proposed criterium. Subsequently, the influence of variations in power over 500 W to 1500 W, in beam diameter 4σ from 250 µm to 1000 µm, and in preheating temperature from 900 K to 1300 K on *g* is illustrated.

4 Results and Discussion

4.1 Evaluation of Existing Parameters

To cover a square grid with a using circles of the same size centered around the intersections of the grid, the radius of the circles must be greater than: grid spacing / $\sqrt{2}$. On the other hand, to cover a hexagonal grid, the radius must be greater than: grid spacing / $\sqrt{3}$. The temperature simulation results in $x_{2ds}/2$ = 298 µm. Thus, the chosen grid spacing of 400 µm is fully covered as shown in Figure 2a. The maximum possible grid spacing with the simulated melt pool extension using a square grid is 423 µm, as displayed in Figure 2d.

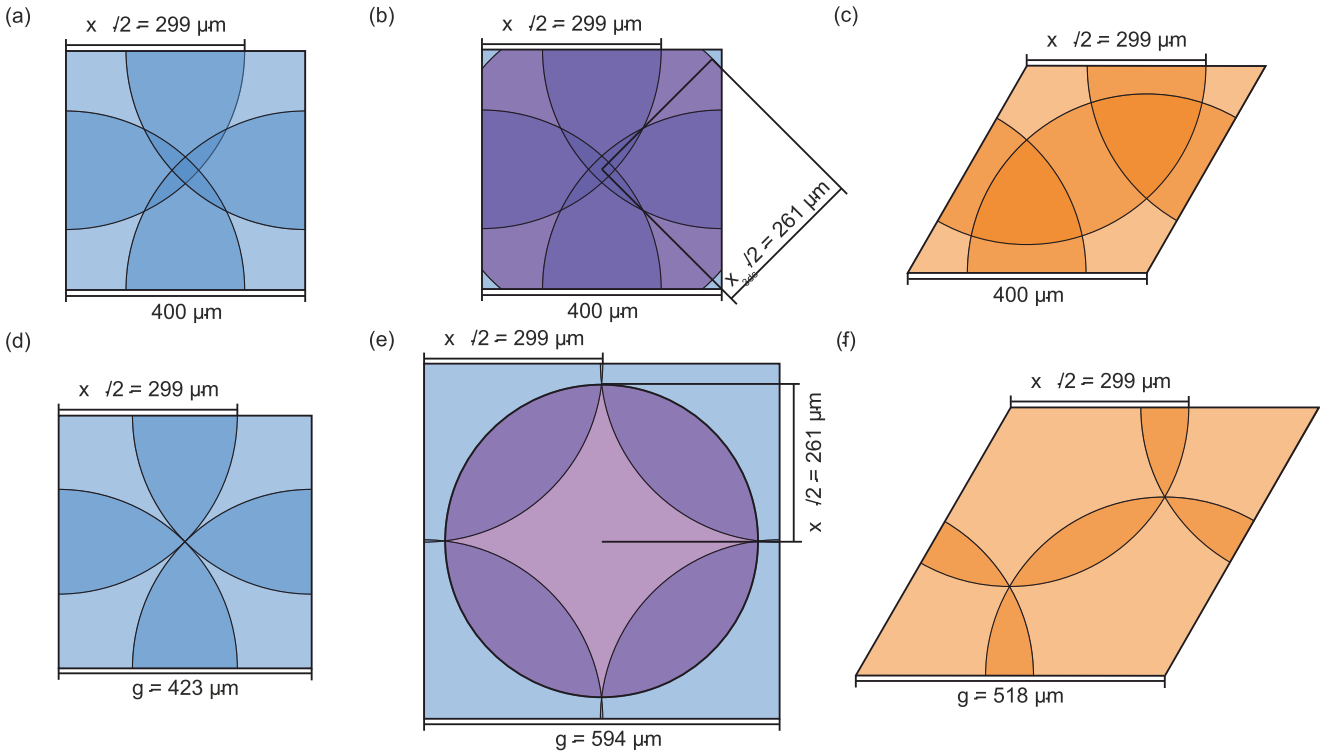

Figure 2: Coverage for various grids. (a-c) grid spacing = 400 µm for (a) square grid (b) square grid with AB-stacking (c) hexagonal grid. (d-f) maximum possible grid spacing *g* for (d) square grid (e) square grid with AB-stacking (f) hexagonal grid.

Consequently, the hexagonal grid with a grid spacing of 400 µm is also fully covered, as shown in Figure 2c. It should be noted that the energy density for the hexagonal grid with the same grid spacing is higher than in a square grid. If the same energy density is desired for the hexagonal grid the grid spacing should be increased to 430 µm, which would also be covered by melt pools with $x_{2ds}/2 = 298$ µm. The maximum grid spacing for a hexagonal grid and the present melt pools would be 518 µm, as shown in Figure 2f.

Apart from switching to a more closely packed grid, there is also the option to use stacking to improve coverage. Stacking means that grids of consecutive layers are shifted with respect to each other, for example by half the grid spacing in x- and y-direction to create AB-stacking for square grids. Since the melt pool depth is greater than three times the layer thickness, missing coverage in one layer can theoretically be compensated by the following layer. To achieve this, the lateral expansion of the melt pool x_{3ds} at a depth corresponding to three times the nominal layer thickness $3d_s$ must be large enough. The simulated melt pool achieves a $x_{3ds}/2$ of 261 µm. Together with $x_{2ds}/2 = 298$ µm this is enough to cover a square grid with a grid spacing of 400 µm, as shown in Figure 2b. The maximum possible grid spacing for an AB-stacked square grid can be determined geometrically by determining the point, which fulfills (1)

$$x^2 + y^2 = \left(\frac{x_{2ds}}{2}\right)^2 \quad (1)$$

with

$$x = \frac{g}{2} \quad (2)$$

and

$$y = \frac{g}{2} - \left(\frac{x_{3ds}}{2}\right). \quad (3)$$

(2) and (3) in (1) yield

$$g = \frac{x_{3ds}}{2} \pm \sqrt{2\left(\frac{x_{2ds}}{2}\right)^2 - \left(\frac{x_{3ds}}{2}\right)^2} \quad (4)$$

So, for the given $x_{2ds}/2$ and $x_{3ds}/2$, this results in g = 594 µm.

4.2 Parameter Variations

Figure 3 shows the maximum possible grid spacing for the square, square-stacked and the hexagonal grid, depending on (a) powder, (b) preheating temperature, and (c) beam diameter. The remaining parameters are equal to the ones in Chapter 4.1.

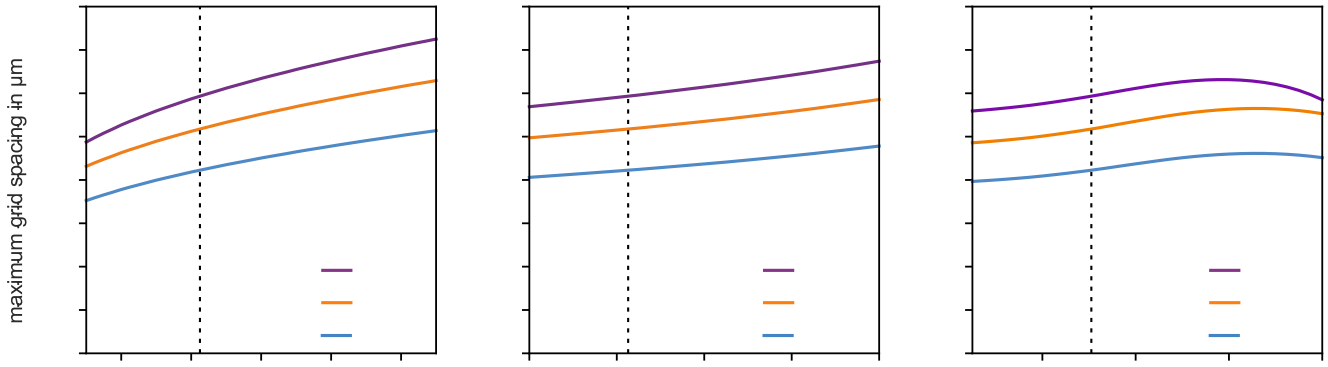

Figure 3: Calculated maximum possible grid spacing for square (blue), square-stacked (purple) and hexagonal (orange) grids with variations in (a) power, (b) preheating temperature, and (c) beam diameter. The parameters from Chapter 4.1 are indicated by a dashed black line.

The calculated maximum grid spacing for the square grid is shown in blue, for the square and stacked grid in purple, and for the hexagonal grid in orange. The only difference between square and hexagonal is the pre-factor ($1/\sqrt{3}$ for hexagonal versus $1/\sqrt{2}$ for square). The utilized parameters from Chapter 4.1 are marked with a dashed black line.

In Figure 3a the maximum grid spacing shows an increase from 350 µm at 500 W to 516 µm at 1500 W for the square grid. Its stacking variant increases from 486 µm to 725 µm over the same power range. An increase in preheating temperature also leads to an increase in the maximum

grid spacing, starting from 419 µm at 900 K to 509 µm at 1300 K for the square grid and from 592 µm at 900 K to 717 µm at 1300 K for its stacked counterpart. An increase in beam diameter from 4σ = 250 µm to 4σ = 1000 µm leads to a maximum grid spacing of 457 µm at 4σ = 850 µm for the square grid. For the square-stacked grid the maximum is located at 4σ = 780 µm with a grid spacing of 634 µm. To achieve a large maximum grid spacing the width of the melt pool at a depth two times the layer thickness is decisive. A smaller beam diameter generally creates a deeper melt pool with a smaller lateral extension. A big diameter can create a big melt pool surface area, but may create a melt pool that is too shallow and thus leads to a smaller x_{2ds}.

5 Summary

Determining an appropriate grid and its grid spacing is essential for an efficient process yielding defect-free parts. This study proposes a scheme towards fitting process parameters, based on simulating the melt pool width at two times the layer thickness. The resulting width should be enough to fully cover the present spot grid. To reduce unnecessarily large overlap, there are the options to switch to a hexagonal lattice or to extend the square grid via stacking. Both options allow for a larger grid spacing utilizing the same melt spots. Many parameters influence the maximum grid spacing. Both higher power and preheating temperature lead to a higher possible grid spacing, whereas variations of the beam diameter show a maximum at certain beam diameters. The approach is thought to be used to calculate maximum grid spacings, which hint towards fitting process parameters, thereby reducing the number of experimental iterations. It relies on single-spot simulations (which neglects heating effects from neighboring spots) and on strong simplifications regarding in the melting step. In future studies high fidelity models could be used or preheating effects could be taken into account, if the beam return time is known.

Acknowledgements

The authors gratefully acknowledge funding by the Deutsche Forschungsgemeinschaft (DFG, German Research Foundation) – Project ID 61375930 – SFB 814 – “Additive Fertigung” TP T07.

Conflict of Interest

The authors declare no conflict of interest.

Data Availability Statement

Data will be made available upon reasonable request.

References

[1] Kirka, M. M., Lee, Y., Greeley, D. A., Okello, A., Goin, M. J., Pearce, M. T., & Dehoff, R. R. (2017). Strategy for texture management in metals additive manufacturing. Jom, 69(3), 523-531.

[2] Kupfer, T., Leimbach, S., Spano, L., Pohl, S., Körner, C., & Markl, M. (2025). Spot melting sequences for complex geometries in electron beam powder bed fusion. Progress in Additive Manufacturing, 1-15.

[3] Westrich, Y., Kammermeier, E., Wahlmann, B., & Körner, C. (2025). Three-dimensional spot melting patterns in electron beam powder bed fusion: high efficiency and tailored texture. Progress in Additive Manufacturing, 1-14.

[4] Rittinghaus, S. K., Shokri, H., Shkodich, N., Bruder, E., Farle, M., & Gökce, B. (2023). Comparative insights into microstructure and magnetism of Ni-Mn-Sn Heusler alloys manufactured by electron beam and laser beam powder bed fusion. Additive Manufacturing Letters, 7, 100159.

[5] Sjöström, W., Roos, S., Zhu, L., Botero, C., Jimenez-Pique, E., Balachandramurthi, A., & Rännar, L. E. (2025). PBF-EB process development of chemically reduced tungsten via a dual-gradient parameter approach utilizing the backscatter signal. Progress in Additive Manufacturing, 10(12), 10515-10532.

[6] Raghavan, N., Simunovic, S., Dehoff, R., Plotkowski, A., Turner, J., Kirka, M., & Babu, S. (2017). Localized melt-scan strategy for site specific control of grain size and primary dendrite arm spacing in electron beam additive manufacturing. Acta Materialia, 140, 375-387.

[7] Balachandramurthi, A. R., Olsson, J., Ålgårdh, J., Snis, A., Moverare, J., & Pederson, R. (2019). Microstructure tailoring in Electron Beam Powder Bed Fusion additive manufacturing and its potential consequences. Results in Materials, 1, 100017.

[8] Breuning, C., Böhm, J., Markl, M., & Körner, C. (2023). High-throughput numerical investigation of process parameter-melt pool relationships in electron beam powder bed fusion. Modelling, 4(3), 336-350.

[9] Klassen, A., Bauereiß, A., & Körner, C. (2014). Modelling of electron beam absorption in complex geometries. Journal of Physics D: Applied Physics, 47(6), 065307.

Date: 31.03.2026

Title: Enhanced thermal control in casting processes using thermally sprayed resistive heating coatings

Author: Benedikt Schmidt*

Authors: K. Bobzin, M. Erck, K. Jasutyn

RWTH Aachen University, Surface Engineering Institute, Kackertstr. 15, 52072, AACHEN, GERMANY

*Corresponding author: E-mail: schmidt@iot.rwth-aachen.de, ORCID: 0009-0004-1937-7905

Abstract

Thermally sprayed resistive heating coatings based on semiconducting TiO_x offer a promising solution to compensate for uneven cooling and premature solidification in casting processes. A deep understanding of how spray parameters influence coating properties is essential. Statistical analysis of input variables enables the design of tailored heating coatings for both simple and complex geometries, tested in casting processes. Spray parameters fundamentally shape the phase composition of TiO_x and resulting temperature homogeneity. Optimized coatings withstand 20.000 heating cycles at a power density of p = 40 W/cm^2 and achieve a heating rate up to $\dot{T}$ = 28 K/s. The system transfers effectively from simple to free-form geometries and model tools, reducing cycle times to t = 16 s and reducing part warpage by a factor of four in injection molding. TiO_x enables a novel heating and sensor system with direct melt contact, enhancing precision in casting processes.

Keywords

Thermal compensation, thermal spray, heating coatings, casting, injection molding

1 Introduction

In casting processes, precise thermal control is essential for achieving high part quality. Non-uniform cooling rates can lead to e.g. warpage. Although elevated mould temperatures may be beneficial for part quality, they also increase cooling times and thus reduce throughput, making it economically unfeasible for processes such as injection moulding. As part of the research program SFB 1120, this project investigates the use of thermally sprayed heating coatings to dynamically control mould temperatures and compensate detrimental effects based on inhomogeneous temperature fields.

With thermal spraying (TS), resistive heating elements based on metallic or ceramic conductive layers in between ceramic insolating layers can be applied directly onto tool surfaces (Fig. 1). The use of thermally sprayed heating elements in casting processes was introduced by Deckert for injection moulding in 2012 for a NiCr20 based metallic heating coating [Dec12]. Ceramic based, sub-stoichiometric titanium oxides (TiO_x) on the other hand have gained attention as heating coating materials due to their low thermal expansion coefficient, which matches that of insulating ceramics such as Al_2O_3 [FFK+10]. To improve the stability of the semiconducting system, Cr_2O_3 is commonly added to the TiO_x powder at concentrations of 20 wt. % [TBT+11].

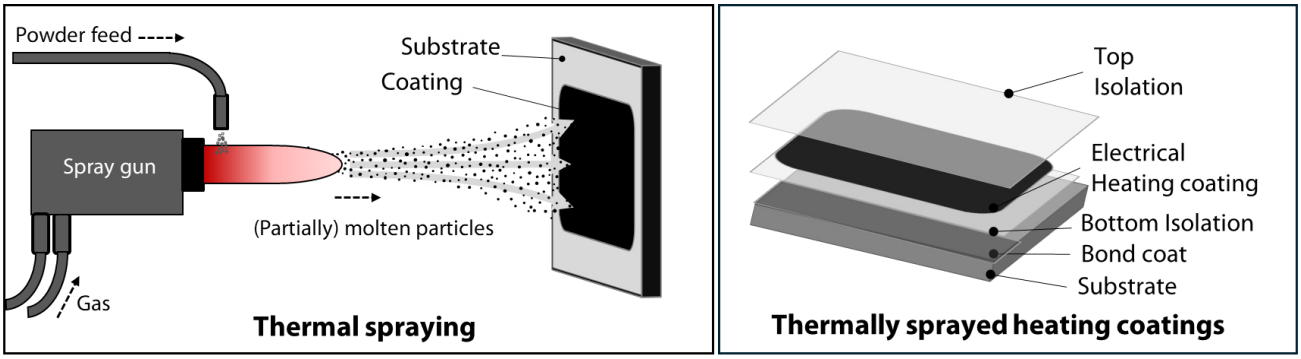

a) b)

Figure 1: a) Schematics of the thermal spraying process b) explosion drawing of thermally sprayed heating coatings

Owing to its significantly higher electrical resistance compared to metal conductors, which typically need to be structured in meander geometries, $TiO_x/20Cr_2O_3$ allows full-area deposition of the heating coating [BWK+20], thereby easing the fabrication of heating elements. Furthermore, the temperature-dependent resistance of the material exhibits negative temperature coefficient (NTC) behaviour and can be approximated with an Arrhenius-type equation [BWK+20]. This property may also enable the use of the actuator coating in sensing applications.

2 Aim of the Investigation

Aim of this work is the advancement of thermally sprayed ceramic heating coating systems based on $TiO_x/20Cr_2O_3$ in casting systems for advanced thermal control (Fig. 2). During the two phases as part of the SFB 1120, the following research areas are adressed:

- Determining the influence of spray parameters on electrical properties (Phase II, III)
- Increasing the durability of the coatings (Phase II)
- Transferring the multilayer system onto freeform geometries (Phase III)
- Evaluate temperature control based on the electrical resistance of the coatings (Phase III)
- Applying the heating coatings in casting processes (Phase II/III)

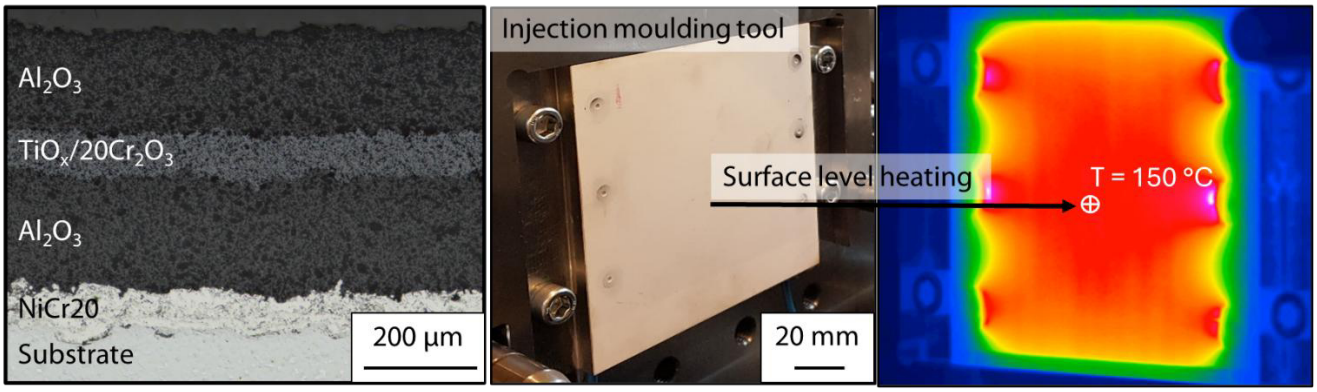

Figure 2: a) cross section of TS-heating coatings based on TiOx/20Cr_2O_3 b) Injection moulding tool with heating coatings. Electrical connection is obtained by isolated screws from the backside of the tool geometry.

3 Materials and Experimental Details

Atmospheric plasma spraying (APS) is conducted using a TriplexPro™-210 plasma generator (Oerlikon Metco, Wohlen, Switzerland) for the NiCr20 bond coat, the Al_2O_3 insulation layer and the $TiO_x/20Cr_2O_3$ heating coating. Spray powders are obtained from commercially available suppliers: NiCr20 (GTV Verschleißschutz GmbH, Luckenbach, Germany), $TiO_x/20Cr_2O_3$ (Ceram GmbH, Albbruck-Birndorf, Germany) and Al_2O_3 (Oerlikon Metco). Coatings are applied using a KR16 robot handling system (KUKA, Augsburg, Germany), with the spray gun moved over the surface in a meander pattern. The substrate materials, unalloyed carbon tool- (C45U) and structural steels (S235JR), are cleaned and sandblasted before coating. The spray parameters are listed in Table 1.

Table 1: Parameter set for the heating coating systems

Parameter	**APS**		
Function	Bondcoat	Insulation	Heating coating
Material	NiCr20	Al_2O_3	TiO_x/Cr_2O_3
Particle size distribution / µm	-53 +25	-45 +22	-25 +5
Injector diameter / mm	2	2	2
Primary gas Ar / SLPM	70	60	60
Secondary gas H_2 / SLPM	0	6	6
Current / A	400	450	450
Stand-off distance / mm	120	120	120
Meander width / mm	5	5	5
Robot velocity / mm·s^{-1}	800	1,000	1,000
Carrier gas Ar / SLPM	4.5	5.5	7.5
Feeding rate / g·min^{-1}	31	21	24

Heating experiments are conducted using a custom-built electrical test bench (RST Rostock System Technik GmbH, Rostok, Germany) equipped with a LabView-based PID-controller to regulate the power supply. The temperature levels are selected according to the intended application of the

coatings. Electrical resistance is measured using a four-point probe method with a TM-508A device (Isothermal Technology, Southport, United Kingdom). Sample cross-sections are polished and examined by scanning electron microscopy (Phenom XL, Thermo Fisher Scientific Inc., MA USA) and optical light microscopy (Carl Zeiss AG, Oberkochen, Germany). Phase composition was determined by X-ray diffraction (XRD) using a XRD 3000 (GE Energy Germany GmbH, Ratingen, Germany)

4 Results and Discussion

Influence of spray parameters on the conductivity of $TiO_X/20Cr_2O_3$

To determine a stable process window with homogenous and robust coating properties, a design of experiments (DoE) is chosen around the current and gas flow for the APS process, using C45U as the substrate material. The influence of these parameters on the electrical resistivity is evaluated using the response surface method (RSM) with a second order correlation model combining linear and non-linear terms. A statistically significant influence on the resistivity ($p = 0.05$) is identified for the investigated parameters (Fig. 3) [BWH+21a].

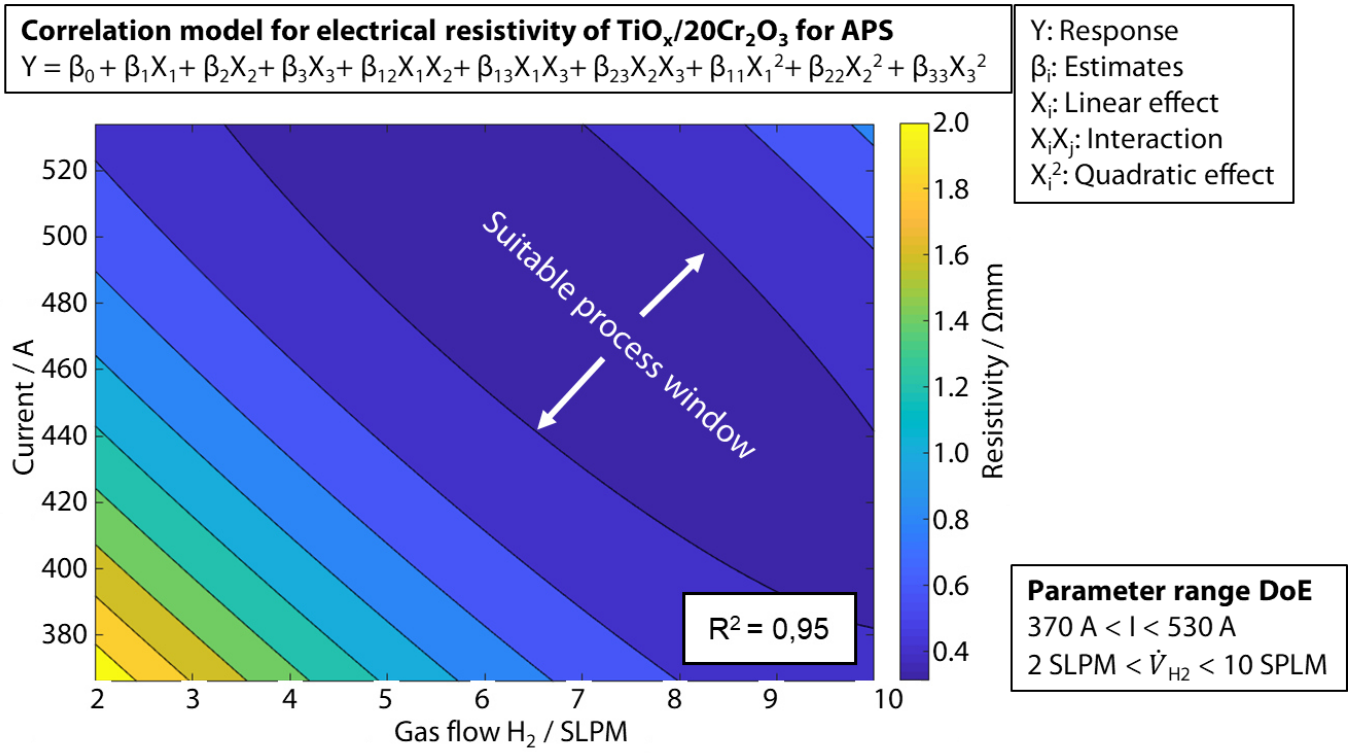

Figure 3: Correlation between plasma current, H_2 gas flow and resistivity for $TiO_x/20Cr_2O_3$. Values for the correlation coefficients can be found in [BWH+21a]. Modified after [BWH+21a].

As shown in Fig. 3, high currents and increased H_2-flow rates result in a wide window with homogenous properties, which corresponds to the lowest measured resistance of $R \sim 0.5$ Ωmm. Measurements of particle temperatures using SprayWatch 4S (Oseir Ltd., Tampere, Finland) indicate that this process window is associated with relatively homogeneous particle temperatures above T = 2,500 °C. Lower current values and reduced H_2 flow lead to lower particle temperatures

below T = 2,500 °C and increased scatter in the measured resistance. This behavior may be attributed to a higher fraction of unmelted particles, which is also associated with increased coating porosity in the coatings [Sch24].

Measurable variations between powder batches prior to coating have little influence on the phase composition of the final coating [BWH+21a]. This might be explained by the oxidative effects of the atmosphere during spraying, which are countered by the reductive properties of H_2 secondary gas. The resulting equilibrium likely governs the formation of the sub-stoichiometric phases, which do not significantly vary in between different coatings [BWH+21a].

Durability of the heating coatings

Heating coatings must withstand thousands of heating cycles for economic viability. It was found, that the electrical connection to the heating coating represents a significant point of failure [BWH+21b]. A substantial increase in the number of heating cycles can be achieved through an improved contact design based on isolated contact screws, which is also better suited for in-mold applications [Sch24]. Using the improved electrical connection and the parameter set derived from the correlation model (Table 1), cyclic heating tests are conducted (Fig. 4).

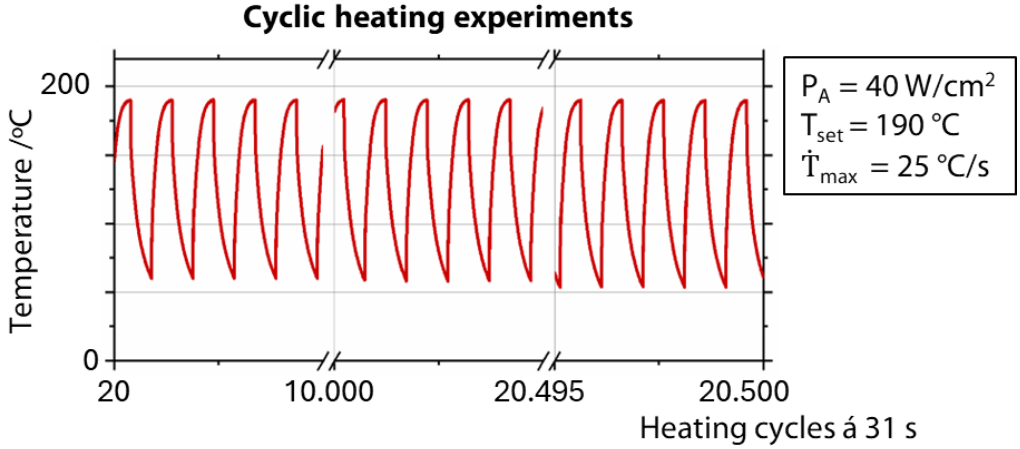

Figure 4: Cyclic heating experiments with optimized heating coatings for flat sample geometries. Modified from [Sch24].

Ceramic $TiO_x/20Cr_2O_3$ heating coatings can withstand more than 20.000+ heating cycles in the range of T = 50 °C to T = 190 °C, with a cycle time of t = 31 s. The cycle number was limited by experimental time rather than sample failure. At a power density of P_A = 40 W/cm², a maximum heating rate of $\dot{T}_{max}$ = 25 °C/s can be achieved. These findings underline the suitability of the $TiO_x/20Cr_2O_3$ heating coatings for applications with rapidly changing temperature levels, such as variothermal injection moulding.

Complex geometries

In cooperation with the project partners of the plastic processing institute (IKV), geometries with pronounced warpage are identified. Simulation data obtained using GOM-Inspect indicate that in box geometries, corners are in danger of warpage, as the outermost and innermost corners

experience different cooling rates. While the outer corner have already solidified, the inner corners may remain molten, resulting in steep gradients in specific volume [HBK+23]. To homogenize temperature distributions in corners, triangular and strip-like heating coating designs were investigated. The simulation results show, that strip-like heating coatings are superior for warpage compensation, achieving up to an eightfold reduction in warpage [HBK+23] (Fig.5a). The application of multilayer heating coating systems on freeform geometries, such as parts with radii, is challenging because the spray angle can deviate from the ideal 90° angle. To investigate these effects, the spray angle is gradually reduced by an angle α, down to α = 45° and the electrical properties of the coatings were measured (Fig 5b). At a deviation of α = 45°, the resistance of the $TiO_x/20Cr_2O_3$ heating coating increased significantly. This can be partially attributed by the reduced coating thickness resulting from decreased deposition efficiency, as well as increased porosity. Furthermore, the increase in resistance may also be caused by prolonged particle in-flight oxidation, as the particles traverse longer paths at higher spray angle deviations geometrically [BHE+24].

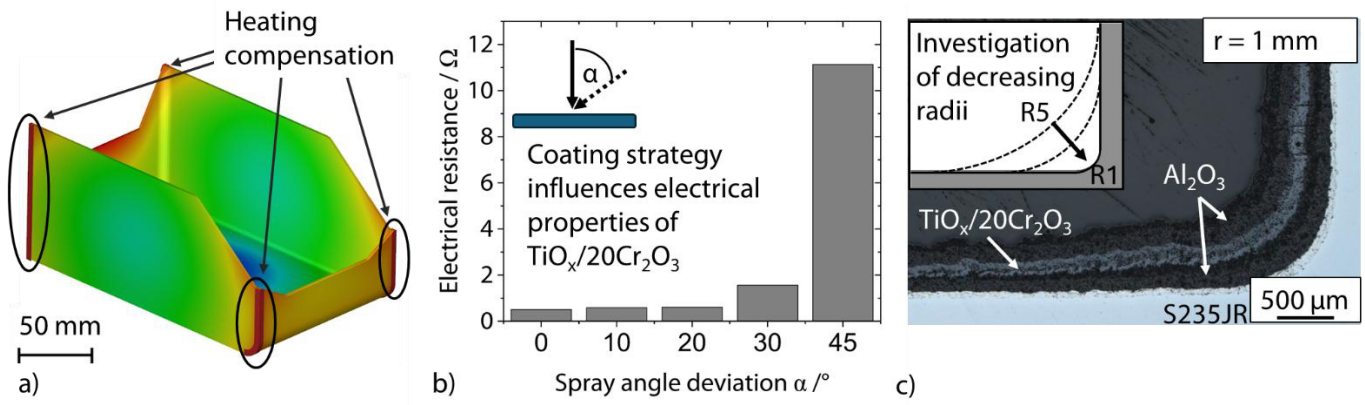

Figure 5: a) Simulative data on the requirements of heating compensation in box shaped geometries [HBK+23] b) Electrical resistance in dependence to the spray angle. Modified from [BHE+24] c) Cross section of sample with a radii of r = 1 mm

Based on these findings, coating strategies are developed for the coating of radii (Fig 5c). With a vertical coating strategy, the radii are coated in one continuous step, while with the orthogonal strategy, each side is coated in a 90° angle. This affects the temperature distribution during heating: the orthogonal approach results in higher temperatures at the vertex of the coating, while the vertical approach produces higher temperatures adjacent to the vertex [BHE+25a]. Using these strategies, radii up to r = 1 mm can be coated and withstand over 3.000+ heating cycles in the temperature range of T = 70 °C to T = 220 °C (Fig. 6a) [BEJ+26].

Cooling represents a major limitation on achievable cycle times. When applied to a model tool with internal cooling channels (Fig.6b), active cooling of the geometry enabled cycle times as low as t = 16 s within the temperature range of T = 70 °C to T = 150 °C [BEJ+26]. These results demonstrate, that the developed heating coatings can meet the requirements predicted by simulation data [HBK+23] for warpage compensation in box-shaped geometries.

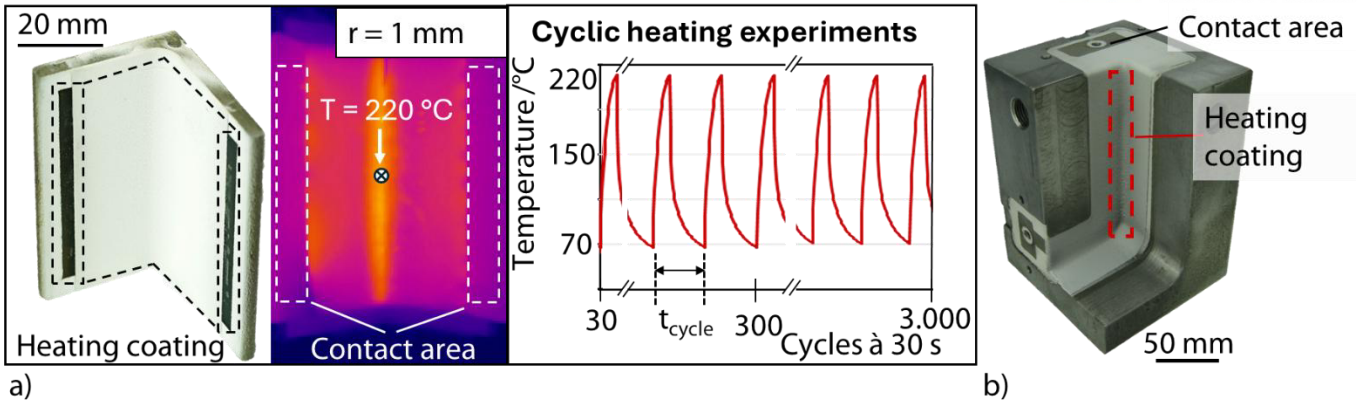

Figure 6: a) Cyclic heating experiments for a sample prepared by the orthogonal coating strategy b) Model of tool geometry.

Temperature control

As a semiconductor, thermally sprayed $TiO_x/20Cr_2O_3$ coatings exhibit negative temperature coefficient (NTC) behavior which means that the electrical resistance of the coating decreases with increasing temperature. In this case its relation is in a non-linear manner, which can be described by an Arrhenius-equation (Fig. 7b) [BWK+20].

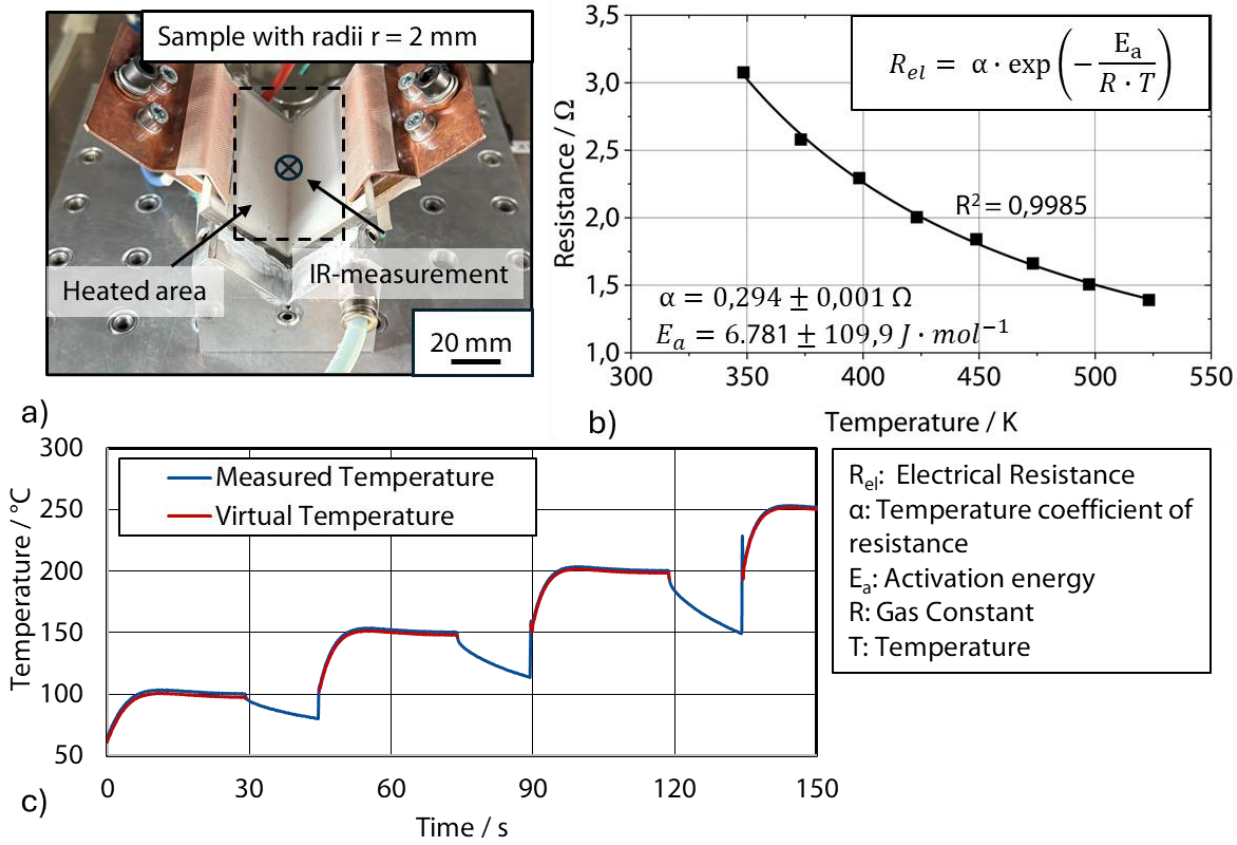

Figure 7: a) Experimental setup inside the test bench b) Temperature dependent resistance for the $TiO_x/20Cr_2O_3$ heating coating on the L-shaped sample c) Thermal control using the temperature dependent resistance

By determining the parameters of this Arrhenius-Equation, sensor applications of the coating become feasible [BWK+21]. Furthermore, temperature control of the heating coating through its temperature dependent resistance can be achieved, as demonstrated for plate

geometries [BHE+25b]. This property is particularly relevant for applications in mold geometries, where space for external sensors is often limited. To investigate this, the application on free form geometries is tested using samples with a radius of r = 2 mm (Fig 7a). The activation energy E_a of the charge carriers was determined as E_a = -6.781 J/mol in good agreement with previous reports of E_a = - 7.072 J/mol [BHE+25b]. However, the temperature coefficient α differs between free form and flat geometries by a factor of two. This difference may arise from variations in overall resistance or from microstructural differences. This warrants further investigation, as it may allow for thermal control without the need for prior calibration. Good agreement was observed between temperatures measured with external IR-sensors and the virtual temperature derived from the sensor properties (Fig 7c), demonstrating the viability of this approach for tool geometries.

Application in injection molding

To verify the performance of the thermally sprayed heating coatings in casting processes, coated tool inserts were integrated into an industrial injection mould. (Fig .8a) [FHK+21]. The investigated part geometry exhibits warpage due to structural ribs on the backside of the sample, which locally increases part mass and reduces the cooling rate.

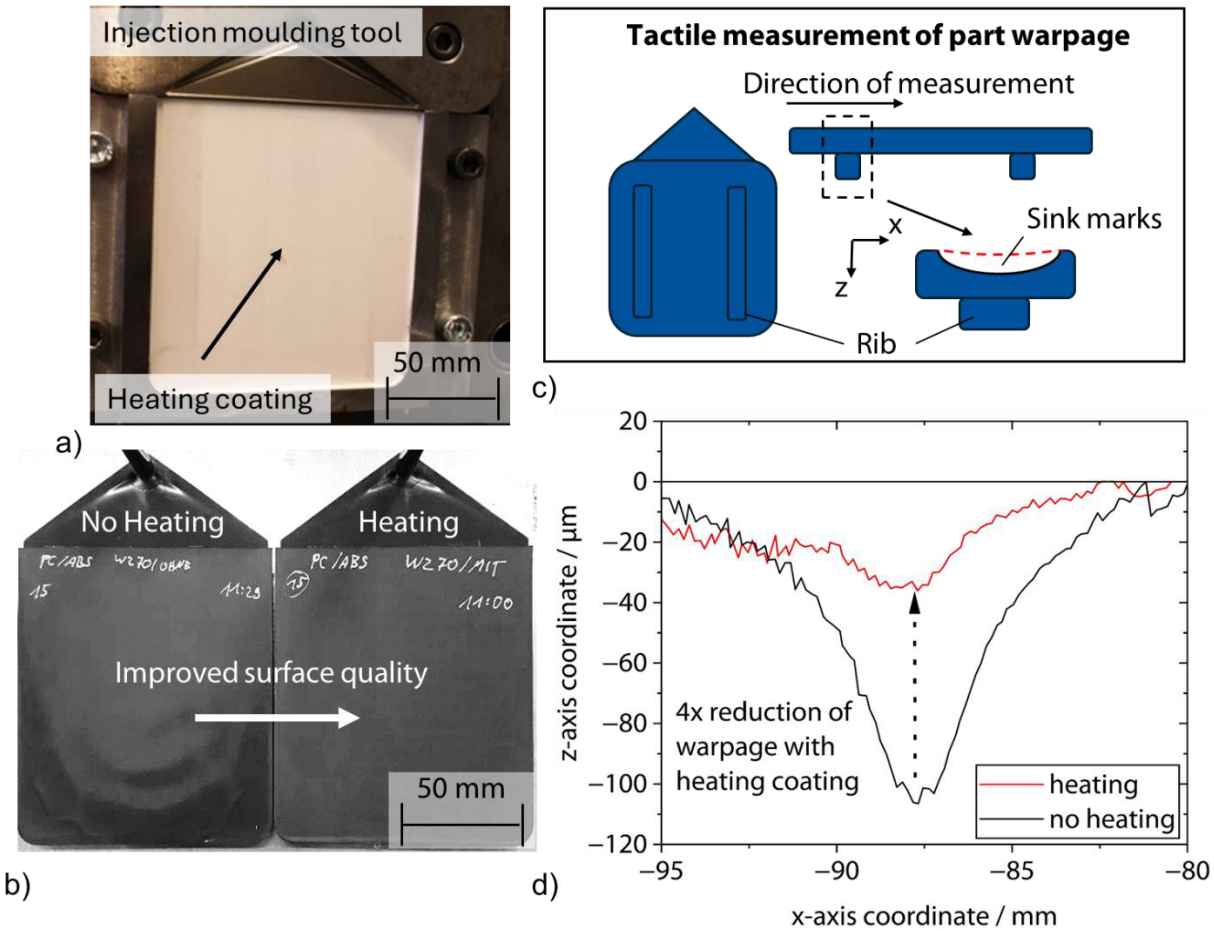

Figure 8: a) Injection moulding tool with integrated heating coating. Taken from [Sch24]. b) Improved surface quality in parts produced with active heating coatings c) Schematics of part geometry and tactile measurement d) Tactile measurements of parts fabricated with heating coatings. Data from [FHK+21]

The use of the heating coating results in an overall improved surface quality for the tested samples (Fig. 8b). For polypropylene (PP), pronounced sink marks are observed, caused by the uneven cooling between the tool sides, resulting in reduced part accuracy (Fig 8c) [FHK+21]. To compensate for this, active heating with thermally sprayed coatings is applied up to T = 120 °C. Warpage is reduced by a factor of four compared to samples without active heating. More than 400 parts can be produced using the active heating coatings without significant changes in heating behaviour [FHK+21].

In the next steps, the obtained knowledge on the coating of free-form geometries is applied on the box-shaped demonstrator shown in Fig. 5a. Using four coated segments (Fig. 6b), the warpage compensation is tested for more advanced tool geometries to advance the application field of the coatings.

5 Summary

Thermally sprayed heating coatings based on TiOx/20Cr_2O_3 enable rapid surface heating, making them suitable for applications where thermal compensation is needed. The properties of the coatings are influenced by the process parameters in the plasma spraying process. Ceramic coatings exhibit high durability, withstanding multiple thousands of rapid heating cycles. Multilayered coatings can be applied to freeform geometries, such as box-shaped parts with radii. TiO_x/20Cr_2O_3 provides thermal control through its temperature-dependent resistance. By using active heating coatings in injection moulds, warpage can be reduced significantly.

Acknowledgements

The presented investigations were carried out at RWTH Aachen University within the framework of the Collaborative Research Centre SFB 1120-236616214 “Bauteilpräzision durch Beherrschung von Schmelze und Erstarrung in Produktionsprozessen” and funded by the Deutsche Forschungsgemeinschaft e.V. (DFG, German Research Foundation). The sponsorship and support are gratefully acknowledged.

Conflict of Interest

The author declares no conflict of interest.

Data Availability Statement

The data that support the findings of this study are available from the corresponding author upon reasonable request on http://hdl.handle.net/ using the persistent identifier (PID): 21.11102/63d2e243-6847-4ce5-961b-c9b0d78605ee

References

[BEJ+26] Bobzin, K., Erck, M., Jasutyn, K., Schmidt, B., Multilayered thermally sprayed heating coating systems on model tools for injection molding, in: ITSC 2026, 18.03.2026 - 20.03.2026, Bangkok, Thailand, ASM International, 2026

[BHE+24] Bobzin, K., Heinemann, H., Erck, M., Schacht, A., Hopmann, C., Fritsche, D., Kahve, C., Vogels, C., Influence of the spray angle on thermally sprayed heating coatings, Materialwissenschaft und Werkstofftechnik, 55 (2024), 1074–1081, DOI: 10.1002/mawe.202300163

[BHE+25a] Bobzin, K., Heinemann, H., Erck, M., Körner, J., Use of Thermally Sprayed Heating Elements on Free-Form Geometries for Use in Plastic Injection Moulds, in: , ITSC 2025, 05.05.2025 - 08.05.2025, Vancouver, Canada, ASM International, 2025, 322–328, DOI: 10.31399/asm.cp.itsc2025p0322

[BHE+25b] Bobzin, K., Heinemann, H., Erck, M., Lohrey, N., Oberflächentemperaturregelung beim Kunsstoffspritzgießen, Jahrbuch der Oberflächentechnik, 80 (2025), 184–191

[BWH+21a] Bobzin, K., Wietheger, W., Heinemann, H., Schacht, A., Parameter study on the electrical resistivity of plasma sprayed TiO x /Cr 2 O 3 coatings, IOP Conference Series: Materials Science and Engineering, 1147 (2021), 12027, DOI: 10.1088/1757-899X/1147/1/012027

[BWH+21b] Bobzin, K., Wietheger, W., Heinemann, H., Schacht, A., TiOx/Cr2O3 Heating Coatings for Injection Molding of Polyamide, in: EMPOrIA 2020, May 19-20, 2020, Aachen, Germany, Cham, Springer, 2021, 81–90, DOI: 10.1007/978-3-030-70332-5_8

[BWK+20] Bobzin, K., Wietheger, W., Knoch, M. A., Schacht, A., Heating behaviour of plasma sprayed TiOx/Cr2O3 coatings for injection moulding, Surface and Coatings Technology, 399 (2020), 126199, DOI: 10.1016/j.surfcoat.2020.126199

[BWK+21] Bobzin, K., Wietheger, W., Knoch, M. A., Heinemann, H., Schacht, A., Gillner, A., Hummel, M., Thermally sprayed sensor coatings for spatially resolved temperature detection, Journal of Materials Processing Technology, 291 (2021), 117043, DOI: 10.1016/j.jmatprotec.2021.117043

[Dec12] Deckert, M. H., Beitrag zur Entwicklung eines hochdynamischen variothermen Temperiersystems für Spritzgießwerkzeuge. Zugl.: Chemnitz, Techn. Univ., Diss., 2012, Chemnitz: Universitätsverlag Chemnitz, 2012, ISBN: 9783941003644

[FFK+10] Floristán, M., Fontarnau, R., Killinger, A., Gadow, R., Development of electrically conductive plasma sprayed coatings on glass ceramic substrates, Surface and Coatings Technology, 205 (2010), 1021–1028, DOI: 10.1016/j.surfcoat.2010.05.033

[FHK+21] Fritsche, D., Hopmann, C., Kahve, C. E., Hohlweck, T., Bobzin, K., Heinemann, H., Schacht, A., Einsatz und Einflussnahme von thermisch gespritzten Heizschichten im variothermen Spritzgießprozess, in: Gehde, Michael; Wagenknecht, U.; Bloß, P., Chemnitz, , 2021, ISBN: 9783939382157

[HBK+23] Hopmann, C., Bobzin, K., Kahve, C. E., Erck, M., Fritsche, D. C., Kassel, T., Heinemann, H., Vogels, C., Identification and compensation of part warpage in injection molding using on-cavity thermally sprayed heating coatings, 2023

[Sch24] Schacht, A., Thermisch gespritzte Heizschichten für das Kunststoffspritzgießen, Surface Engineering Institute IOT, RWTH Aachen University. Dissertation, Bobzin, K., 2024

[TBT+11] Trache, R., Berger, L.-M., Toma, F.-L., Stahr, S., Lima, R. S., Marple, B. R., Electrical Resistivity of Thermally Sprayed Cr2O3-TiO2 Coatings, in: ITSC 2011, 9/27/2011 - 9/29/2011, Hamburg, Germany, DVS Media GmbH, 2011, 1008–1013, DOI: 10.31399/asm.cp.itsc2011p1008

Date: 30.03.2026

Predictive Modelling of Weld Seam Formation for Industrial GMAW Joints Using a Hybrid Simulation Approach

Author:

O. Mokrov[1], S. Warkentin[1], L. Kesselburg[1], L. Westhofen[2], J. Bender[2], R. Sharma[1], U. Reisgen[1]

[1]RWTH Aachen University, Welding and Joining Institute, Pontstr. 49, 52062, AACHEN, GERMANY

[2] RWTH Aachen University, Visual Computing Institute (VCI), AACHEN, GERMANY

*Corresponding author: E-mail: warkentin@isf.rwth-aachen.de, ORCID: 0009-0004-4514-8962

Abstract

We present a simulation framework that unifies the major physical scales of Gas Metal Arc Welding (GMAW) to predict weld seam formation with high fidelity. Over more than a decade, research focused on the development and coupling of models dedicated to electrical circuit behaviour, plasma and arc physics, droplet transfer, weld-pool flow, and solidification. Mesh-based magneto-hydrodynamics (MHD) calculations incorporating the EDACC model resolve the characteristic asymmetric arc attachment in the cathode region, while particle-based SPH methods capture transient droplet detachment, short-arc behaviour, melt-pool dynamics and enthalpy-porosity–based solidification. The hybrid approach quantifies how local evaporation, current density distribution, and metal flows govern weld-pool evolution and weld seam formation. The applicability to industrial welding configurations is demonstrated.

Keywords

GMAW, simulation, arc attachment, SPH, hybrid modelling, weld pool dynamics

1 Introduction

Gas metal arc welding (GMAW) is one of the most widely used joining technologies in industrial manufacturing due to its high productivity, flexibility, and applicability to a broad range of materials and joint configurations. Despite its industrial relevance, the predictive simulation of weld seam formation remains a major scientific challenge. The process involves strongly coupled physical phenomena, including arc plasma behaviour, heat and mass transfer, droplet detachment, weld pool flow, and phase transformations during solidification, Figure 1. These phenomena span multiple spatial and temporal scales, ranging from fast electromagnetic processes in the arc to slower thermofluid dynamics in the molten metal. A central difficulty in GMAW simulation lies in the interaction between the arc plasma and the weld pool surface. The local temperature of the

molten metal governs evaporation, which modifies plasma composition, electrical conductivity, and ultimately the distribution of current density and heat flux at the cathode. This feedback mechanism controls weld pool evolution and, consequently, the resulting weld seam geometry. However, many modelling approaches still treat the arc as a prescribed heat source and therefore neglect the self-consistent plasma-metal interaction.

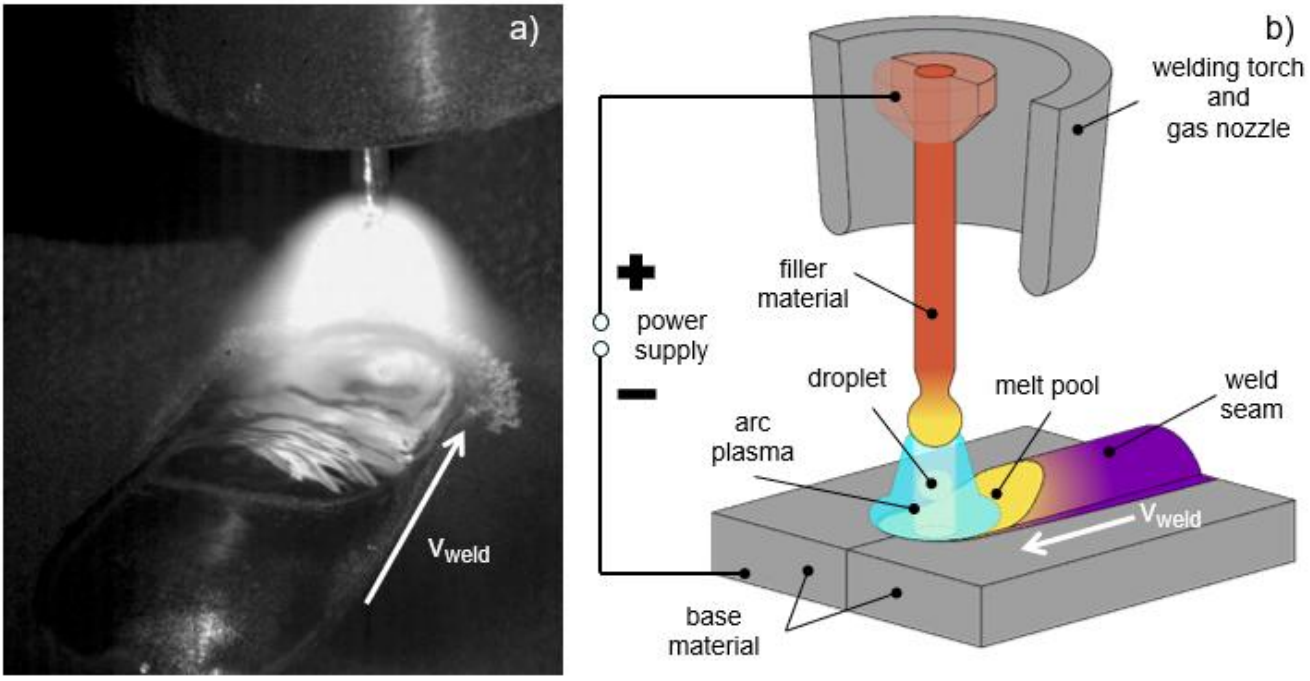

Figure 1: left: High-speed footage of the GMAW process clearly shows the rippling of the molten pool and the concentration of the arc intensity in the front portion of the molten pool, right: Schematic diagram of GMAW highlighting key areas and components.

Over the past decades, different modelling strategies have been developed to describe individual aspects of the GMAW process. Early approaches relied on simplified analytical or empirical heat source descriptions [1–4], whereas more advanced models incorporated fluid flow and phase transformation in the weld pool [5,6]. More comprehensive approaches include magnetohydrodynamic (MHD) descriptions of the arc plasma [7–9], while dedicated studies emphasized the importance of metal vapour in determining arc behaviour [10,11]. In parallel, detailed investigations of near-electrode plasma sheath regions provided an important physical basis for describing anode and cathode interactions [12–14]. Despite these advances, a consistent and computationally efficient framework that combines arc physics, droplet transfer, and transient weld pool evolution is still missing. Within the Collaborative Research Centre (CRC 1120), subproject A04 addressed this gap by developing physics-based models for the key subprocesses of GMAW. In particular, the interaction between evaporation and cathodic heat input was systematically investigated, leading to the formulation and validation of the Evaporation Determined Arc–Cathode Coupling (EDACC) model [15–19]. These studies showed that arc attachment and heat input are strongly governed by local evaporation effects and become inherently asymmetric under realistic welding conditions. A further step in the project was the transition from

stationary or weakly coupled descriptions towards transient process modelling. In this context, alternative numerical strategies for time-resolved multiphase flow simulation were evaluated [20]. At the same time, Smoothed Particle Hydrodynamics (SPH) was introduced as a promising Lagrangian framework for welding-related free-surface problems. Its applicability was first demonstrated for wire metal transfer in GMAW process variants [21], quantitatively assessed for welding-like thermal flow problems [22], and further supported by related SPH developments for particle impact and free-surface deformation [23,24]. These works established the methodological basis for using SPH to resolve droplet detachment, weld pool dynamics, and evolving free surfaces without remeshing. Based on these developments, a hybrid simulation strategy was established in which Eulerian finite-element approaches are used to resolve arc plasma behaviour, while Lagrangian SPH methods are applied to transient melt flow and weld seam formation. The coupling of both domains through physically based surrogate models enables a predictive simulation framework that combines high physical fidelity with improved computational efficiency.

2 Aim of the Investigation

The aim of this work is to develop a predictive simulation framework for weld seam formation in GMAW that consistently captures the key interacting physical phenomena, including arc plasma behaviour, droplet transfer, and weld pool dynamics. To this end, modelling approaches developed over more than a decade within subproject A04 of the CRC 1120 are integrated into a unified hybrid framework. A particular focus is placed on the EDACC model and its influence on heat input distribution, melt pool evolution, and resulting weld geometry. Furthermore, the suitability of a hybrid modelling strategy combining Eulerian finite element methods for arc simulation with Lagrangian Smoothed Particle Hydrodynamics (SPH) for transient free-surface flows is investigated. The developed approach is finally applied to industrially relevant welding configurations to assess its predictive capability.

3 Evolution of the Modelling Approach and Key Physical Contributions

3.1 Evaporation determined arc–cathode coupling (EDACC)

In gas metal arc welding (GMAW), heat input is governed by the interaction between the arc plasma and the metal surfaces of the consumable electrode (anode) and the workpiece (cathode). The main conversion of electrical energy into heat occurs in the near-electrode regions, whereas the arc column primarily serves as a current-carrying medium, Figure 1. This description applies to arc lengths exceeding approximately one to two wire diameters, where anode and cathode regions remain spatially separated and can be treated as distinct. The anode is typically formed by the molten droplet at the wire tip. Its arc attachment is mainly controlled by plasma processes within the arc column, resulting in a compact and nearly axisymmetric current density distribution. Heat transfer is dominated by ion recombination, supplying energy for melting and droplet formation. Although metal evaporation increases with temperature and alters plasma properties, the anode attachment remains stable and adjusts gradually in size. In contrast, the cathode region (weld pool

surface) is characterized by strong plasma-surface interaction under a pronounced potential gradient. Here, heat input and current density distribution are governed by the EDACC mechanism. According to this concept, metal evaporation from the cathode surface determines local plasma properties and thereby controls current distribution. The feedback mechanism can be summarized as follows: local heating enhances evaporation; metal vapour reduces plasma ionization and electrical conductivity; consequently, current is redistributed toward regions with more favourable conditions. Additionally, ionized metal species are accelerated back to the surface, intensifying the plasma-surface interaction. This leads to a highly non-linear and spatially sensitive system. As a result, the cathode coupling is inherently asymmetric, strongly dependent on the local temperature distribution, and dynamically influenced by process parameters such as welding current. Since current density directly correlates with heat flux, this non-uniform energy input governs melt pool flow through thermal and electromagnetic forces. Therefore, the cathode region becomes the dominant factor controlling weld pool shape, stability, and overall process behaviour. Figure 2 illustrates these effects. For a lower welding current (100 A), the current density distribution remains approximately Gaussian and centred near the wire projection. At higher current (400 A), however, the maxima shift towards the weld pool edge, and a symmetric distribution is no longer observed. This demonstrates the transition to evaporation-driven, asymmetric arc attachment as predicted by the EDACC model.

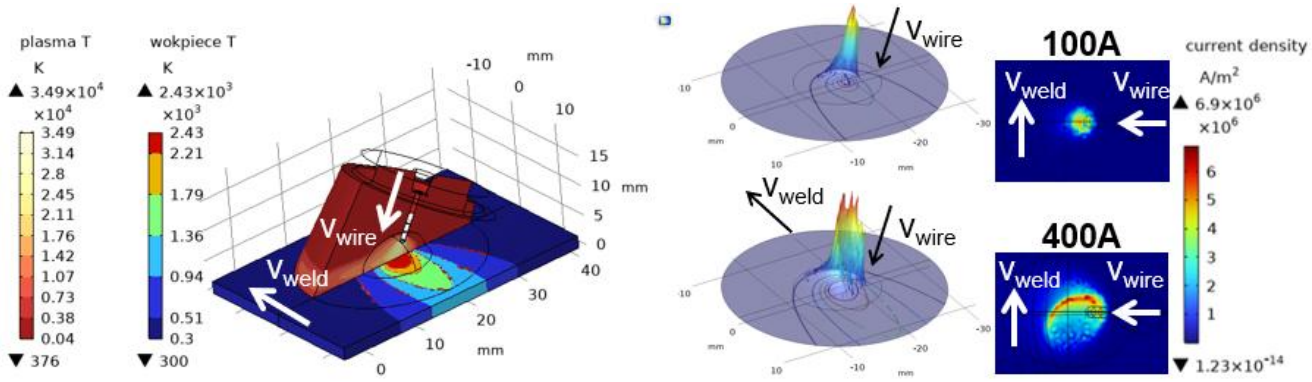

Figure 2: Asymmetric current density and heat flux distribution at the cathode predicted by the EDACC model.

3.2 Transition to transient modelling and SPH

The coupled multiphysics models demonstrate that key GMAW phenomena - arc dynamics, droplet formation, and rapid solidification - can only be captured consistently in a transient formulation. This requires a numerical approach capable of handling strong topological changes such as droplet detachment, breakup, and coalescence without remeshing. Smoothed Particle Hydrodynamics (SPH), a fully Lagrangian method, fulfills these requirements by representing the continuum with particles carrying mass, momentum, and thermal state. This enables a natural description of free-surface evolution and makes SPH particularly suitable for modelling droplet transfer and weld pool dynamics, Figure 3.

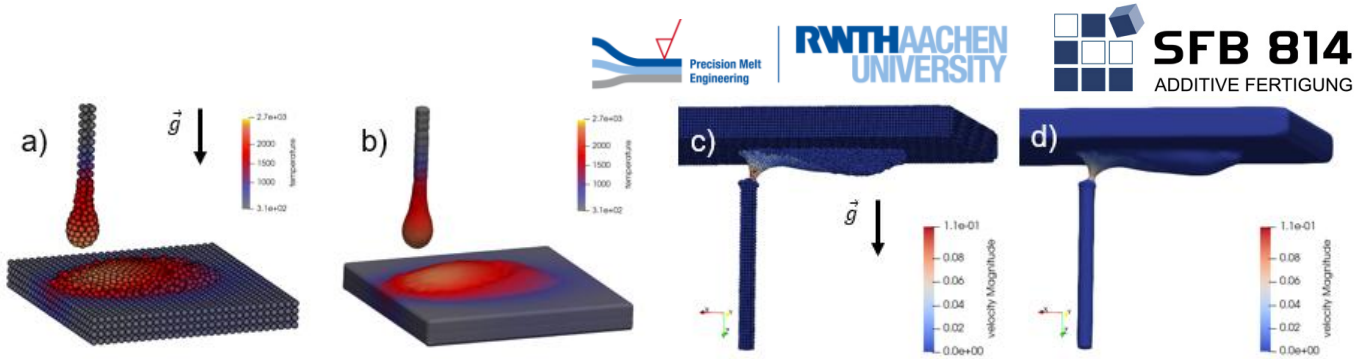

Figure 3: SPH simulation of droplet transfer and weld pool dynamics showing strong topological changes and SPH capability for capturing the physics. a) Snapshot of the droplet detachment with the according temperature field, particle representation, b) reconstructed surface representation of a).

The transient welding process is simulated using the open-source framework SPlisHSPlasH [25], which has been extended for welding-specific applications. It allows the import of arbitrary CAD geometries and process data, including current and wire feed rate, enabling time-resolved simulations under realistic conditions. The capability of the framework to capture heat and mass transfer in GMAW is illustrated in Figure 3. Surface reconstruction and interpolation of field quantities are performed using splashsurf [26], providing a continuous representation of particle-based results, Figure 3, b).

3.3 Weld seam formation and Solidification

The arc heat source is represented as a surface heat flux distribution acting on the metal surface exposed to the arc. In the numerical implementation, this surface-based energy input is converted into an additional thermal contribution assigned to the SPH particles located at the arc–metal interface. The heat input is applied exclusively to surface particles, ensuring a physically consistent representation of energy transfer from the arc while preserving the particle-based formulation. Surface tension is modelled using two approaches: a curvature-based formulation and a cohesion-based method derived from an effective Lennard–Jones potential. The cohesion-based approach has proven particularly suitable for SPH, as surface tension emerges implicitly from inter-particle forces. This enables a stable and consistent description of interface dynamics, including droplet formation, melt pool deformation, and weld pool shape evolution. Solidification is described using an enthalpy-based formulation with a mushy zone, in which liquid and solid phases coexist. As the solid fraction increases, fluid motion is progressively damped by introducing a momentum sink term in the Navier–Stokes equations. This term represents the Darcy-type resistance of the semi-solid dendritic structure and depends on temperature via the local liquid fraction. The permeability of the mushy zone is evaluated using a Carman–Kozeny relation, linking microstructural evolution to macroscopic flow resistance. This approach allows a consistent description of the transition from liquid flow to solid structure and enables the prediction of weld seam formation within the particle-based framework.

3.4 Simulation area decomposition and development of the hybrid framework

The GMAW process involves vastly different time and length scales: electromagnetic and plasma phenomena settle in microseconds and sub-millimetre regions, while heat conduction, fluid flow,

droplet detachment, and solidification evolve over milliseconds to seconds across centimetre-scale domains. By exploiting the quasistationary nature of the electromagnetic (EM) and plasma fields, they can be represented with an efficient Eulerian heat-source model that provides steady Lorentz forces and heat fluxes, Figure 4 right). The slower thermofluidic and solidification processes require a Lagrangian description capable of handling large deformations and topological changes. Consequently, a hybrid framework is built in which surrogate SPH models are driven by the Eulerian solutions, using the latter's results to define reduced-order inputs for the particle-based calculations, Figure 4 left).

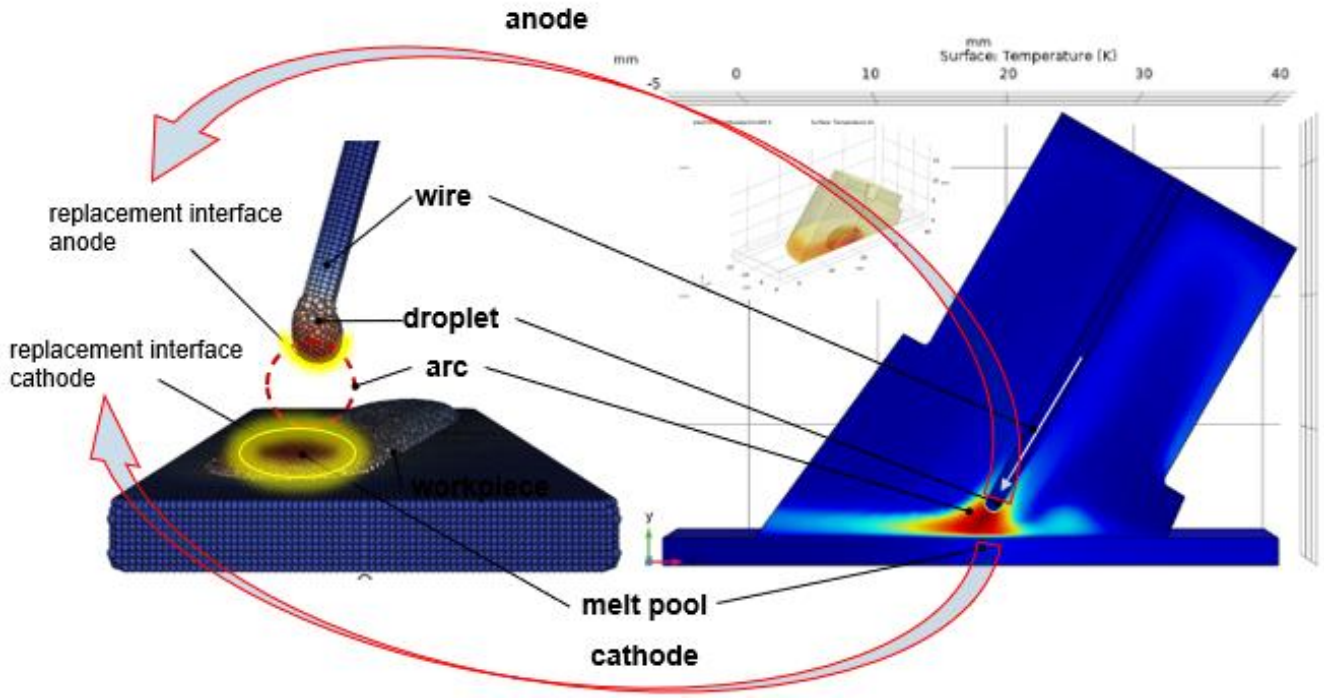

Figure 4: Hybrid modelling concept combining right) Eulerian arc simulation and left) Lagrangian SPH weld pool simulation.

4. Results for Industrial Welding Configurations

Industrial welding demands a modelling tool that can reproduce the full range of GMAW process variants used in production-controlled short-circuit (SC) welding, pulsed spray-arc (impulse) processes, and conventional continuous arcs - by simply varying the input parameters (current and wire feed waveform, travel speed, shielding-gas flow, etc.). In addition, the model must be capable of representing the actual workpiece geometries, joint configurations, and seam-preparation conditions (e.g., gap size, edge bevel, root opening) that are encountered in practice. To answer engineering questions such as productivity, bead geometry, and defect susceptibility, the model must therefore resolve the key physical phenomena that differentiate these modes: rapid arc-plasma dynamics and associated Lorentz forces, intermittent droplet detachment and metal-vapor generation, and the resulting transient heat-transfer and solidification behaviour. Moreover, the framework ought to accommodate a wide spectrum of material properties - and, ideally, material mixtures as well - because these dictate the mechanical-technological performance of the final construction; however, the current implementation is limited to homogeneous base materials and

does not yet support dissimilar-material welds. By meeting these requirements, the hybrid framework offers a predictive, parameter-driven virtual laboratory for the optimisation of real-world welding processes. With the presented simulation framework, a wide range of possibilities is enabled, since many of the physical effects necessary for simulating the gas metal arc welding process are considered. Figure 5 illustrates the simulation results for industry-relevant welding tasks. The models are capable not only of reproducing safe, validated process variants but also of depicting process limits, such as a through-weld shown in Figure 5 a). Additionally, both the torch, represented by the wire in Figure 5 a), b), d) and e), and the workpieces, shown in Figure 5 c), can be moved in the simulation. For GMAW-based additive manufacturing processes, in particular Wire and Arc Additive Manufacturing (WAAM), the new aspect is the focus on the deposition of many layers and on massive constructions.

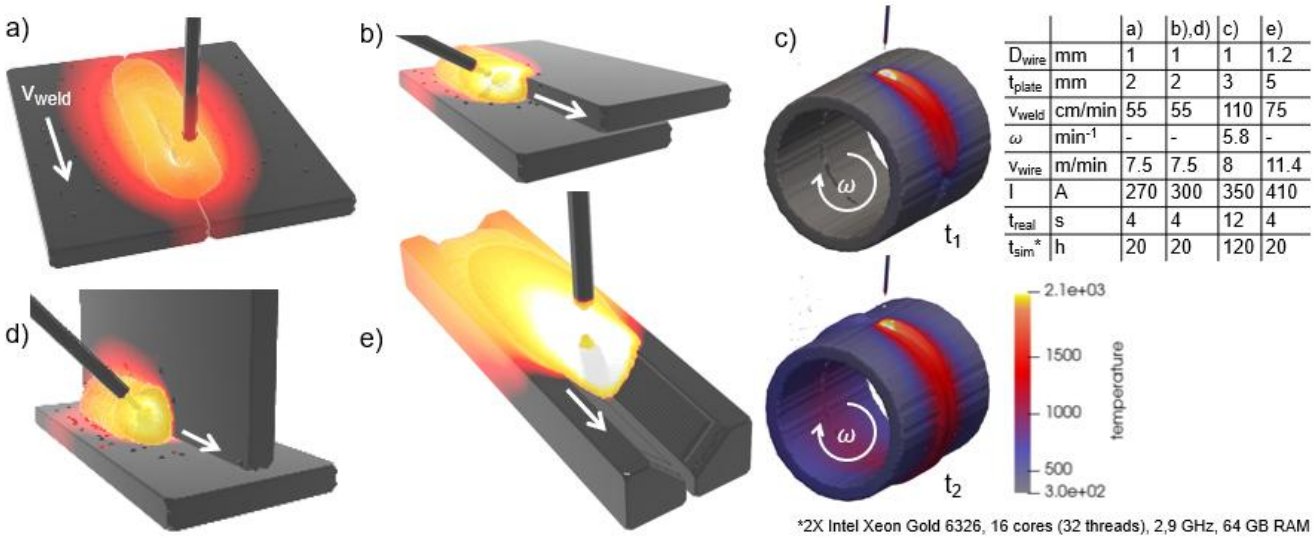

		a)	b),d)	c)	e)
D_{wire}	mm	1	1	1	1.2
t_{plate}	mm	2	2	3	5
v_{weld}	cm/min	55	55	110	75
ω	min^{-1}	-	-	5.8	-
v_{wire}	m/min	7.5	7.5	8	11.4
I	A	270	300	350	410
t_{real}	s	4	4	12	4
t_{sim}*	h	20	20	120	20

Figure 5: Application of the hybrid model to industrial welding configurations: a) butt joint, cooling phase, end of the solidification process, b) lap joint, wire inclination 60 °, snapshot of the weld seam formation process, c) pipe weld, snapshot of the weld seam formation with moving workpiece, d) T-joint, wire inclination 45 °, e) butt joint, Y-groove configuration, elevated material thickness and filler material deposition.

The actual challenge of this process is the path planning and the influence of the path on the energy input and resulting mechanical and technological properties. Therefore, there is a great need for a transient prediction of the component geometry and temperature. A new concept was developed to tackle this task: the focus on the workpiece and the deposited weld seam structure rather than on the droplet formation and detachment process. The concept concentrates the computing power on the heat and mass transfer in the workpiece or in the structure built up by numerous layers. The approach envisages that the phenomena in the anode up to the time of free flight of the droplet are captured by substitute models. Furthermore, the approach includes the assumption that an SPH particle assumes the size of a droplet. This eliminates the need to represent the anode for the simulation of the WAAM process. The droplets or particles are inserted according to the wire feed speed and heated by the heat input model of the arc effect. An explicit resolution of the wire and droplet detachment process is not necessary for the questions regarding material deposition.

5 Discussion

Several physical and modelling aspects remain open and define promising directions for future work. From a material science perspective, the temperature dependence of surface tension in the high-temperature range is still insufficiently known. Since surface tension and its gradients govern capillary and Marangoni-driven flow, improved data and models are essential for a more reliable prediction of weld pool dynamics and final seam geometry. On the arc side, the role of anode evaporation and the resulting vapour fraction in the plasma has not yet been fully resolved. A more detailed description of anode vapour transport and its interaction with the plasma could refine the prediction of arc attachment patterns and local heat input. In addition, the effect of droplet impingement on the molten pool deserves further attention: the strong local cooling induced by the droplet is expected to promote a more concentrated arc attachment in the pool centre and thereby induce additional acceleration of the liquid metal. From a numerical standpoint, dynamic discretization in SPH (e.g. adaptive refinement and coarsening of particles) would allow a better resolution of local phenomena at comparable computational cost. Incorporating volumetric contraction and an extended material model covering the liquid-solid transition would further enable the prediction of solidification defects such as shrinkage cavities or porosity. The current hybrid Eulerian–SPH framework is structured in a modular way, so that these additional physical and numerical features can be integrated stepwise in future developments.

6 Summary

This paper presents the concept development, implementation and application results of a hybrid Eulerian-Lagrangian simulation platform for GMAW over a period of more than ten years. At the outset of CRC 1120, no fully coupled numerical description of GMAW was available. During the first funding period, we therefore developed an in-house Fortran code for transient, fully coupled magnetohydrodynamic (MHD) simulation of the arc–melt pool system including free-surface deformation. For a simplified joint configuration (blind seam in a symmetric butt joint in PA position), 1 s of process time required about 48 h of computation, which severely constrained parametric studies and practical applications. In the second funding period, the focus shifted from demonstrating full coupling towards understanding and modelling the dominant driving mechanisms of melt-pool flow and surface energy input. Within this analysis the cathode layer was identified as the key link in the physical chain between plasma and the liquid metal. A dedicated model was formulated to couple the arc action to the MHD behaviour of the weld pool. In the same context, the foundation for including metal evaporation in the arc attachment region was laid and ultimately led to the EDACC model. Based on the insights and experience gained, a phenomenological splitting strategy was established. Short-time-scale phenomena (plasma, electromagnetics, layer processes) are now computed with mesh-based finite-element methods, whereas large-scale and slow processes such as heat transfer, droplet detachment, and weld-pool dynamics are resolved with a particle-based (SPH) approach. This separation of time scales avoids solving all processes within a single monolithic model and instead allows pre-computing plasma and electromagnetic fields as input for the transient SPH simulations. Furthermore, the

evaporation-controlled attachment has proven to be so dominant that parameterized representations of its effects can be formulated for the surrogate model and used in the SPH simulations. As a result, the plasma itself does not need to be resolved in the transient calculation. As a result, stationary 3D simulations including the EDACC model can today be carried out with commercial solvers within a few hours. In parallel, the advanced SPH framework enables particle-based simulations of arbitrarily complex, industrially relevant joint topologies, with typical runtimes of about 4 h per 1 s of process time. Consequently, subproject A04 has significantly broadened both the range of accessible physical phenomena and the spectrum of practically relevant welding configurations, while achieving an overall speed-up of approximately one order of magnitude compared to the initial in-house Fortran solution. The combination of physically based arc modelling using the EDACC concept and transient SPH simulation of weld pool dynamics enables a realistic prediction of weld seam formation. The results highlight the importance of asymmetric arc attachment and evaporation effects for heat input distribution. The developed approach provides a robust basis for future applications in process optimization and digital twins of welding processes.

Acknowledgements

All presented investigations were conducted in the context of the Collaborative Research Centre SFB 1120 "Precision Melt Engineering" (Grant No. 236616214) at RWTH Aachen University and funded by the German Research Foundation (DFG). For the sponsorship and the support we wish to express our sincere gratitude. Computations were performed with computing resources granted by RWTH Aachen University under project rwth0398.

The authors thank Marek Simon for his effort on developing the EDACC model and enabling a transferable base for algorithms.

Conflict of Interest

The author declares no conflict of interest.

Data Availability Statement

The data supporting the findings of this study are available on reasonable request at http://hdl.handle.net/21.11102/c894c7f3-e06b-4ea9-914c-8defc7a97340.

References

[1] Loose, T., Mokrov, O., and Reisgen, U., *"SimWeld" and "DynaWeld" - Software tools to set up simulation models for the analysis of welded structures with "LS-Dyna",* Welding and cutting: technical journal for welding and allied processes, edited by DVS-Verl. : Düsseldorf, pp. 168–172.

[2] Loose, T., Mokrov, O., Scharff, A., and Reisgen, U., *Prediction of weld quality with expanded welding process analysis by SimWeld and WeldWare for GMA welding,* Mathematical modelling of weld phenomena 11, edited by Christof Sommitsch, Norbert Enzinger, Peter Mayr, Verlag der Techn. Univ. Graz, **2016**, pp. 205–212.

[3] Mokrov, O., Lysnyi, O., Simon, M., Reisgen, U., Laschet, G., and Apel, M., *Numerical investigation of droplet impact on the welding pool in gas metal arc welding,* Materialwissenschaft und Werkstofftechnik, Vol. 48, No. 12, **2017**, pp. 1206–1212.
doi: 10.1002/mawe.201700147

[4] Mokrov, O., Simon, M., Schiebahn, A., and Reisgen, U., *A fine modification of the double ellipsoid heat source,* Mathematical Modelling of Weld Phenomena 12, edited by C. Sommitsch, N. Enzinger and P. Mayr, Verlag der Technischen Universität Graz, Graz, **2019**, pp. 39–51.

[5] Reisgen, U., Mokrov, O., and Lisnyi, O., *Mathematical model of an arc welding weld seam formation on the basis of three dimensional CFD simulations,* Mathematical modelling of weld phenomena 11, edited by Christof Sommitsch, Norbert Enzinger, Peter Mayr, Verlag der Techn. Univ. Graz, **2016**, pp. 753–772.

[6] Mokrov, O., Lisnyi, O., Simon, M. S., Schiebahn, A., and Reisgen, U., *A study of coupled influence of evaporation and fluid flow inside a weld pool on welded seam formation in GMAW,* Mathematical Modelling of Weld Phenomena 12, edited by C. Sommitsch, N. Enzinger and P. Mayr, Verlag der Technischen Universität Graz, Graz, **2019**, pp. 81–90.

[7] Bobzin, K., Heinemann, H., Erck, M., Warkentin, S., Mokrov, O., Sharma, R., Reisgen, U., and Jasutyn, K., *Modeling of arcs with binary gas mixtures in a multi‐arc plasma generator,* Materialwissenschaft und Werkstofftechnik, Vol. 56, No. 1, **2025**, pp. 77–87.
doi: 10.1002/mawe.202300134

[8] Krivtsun, I. V., Momot, A. I., Denysenko, I. B., Mokrov, O., Sharma, R., and Reisgen, U., *Transport properties and kinetic coefficients of copper thermal plasmas,* Physics of Plasmas, Vol. 31, No. 8, **2024.**
doi: 10.1063/5.0216753

[9] Cadiou, S., Courtois, M., Carin, M., Berckmans, W., and Le masson, P., *3D heat transfer, fluid flow and electromagnetic model for cold metal transfer wire arc additive manufacturing (Cmt-Waam),* Additive Manufacturing, Vol. 36, **2020**, p. 101541.
doi: 10.1016/j.addma.2020.101541

[10] Murphy, A. B., Tanaka, M., Yamamoto, K., Tashiro, S., Lowke, J. J., and Ostrikov, K., *Modelling of arc welding: The importance of including the arc plasma in the computational domain,* Vacuum, Vol. 85, No. 5, **2010**, pp. 579–584.
doi: 10.1016/j.vacuum.2010.08.015

[11] Schnick, M., Fuessel, U., Hertel, M., Spille-Kohoff, A., and Murphy, A. B., *Numerical investigations of arc behaviour in gas metal arc welding using ANSYS CFX,* Frontiers of Materials Science, Vol. 5, No. 2, **2011**, pp. 98–108.
doi: 10.1007/s11706-011-0134-4

[12] Almeida, N. A., Benilov, M. S., Hechtfischer, U., and Naidis, G. V., *Investigating near-anode plasma layers of very high-pressure arc discharges,* Journal of Physics D: Applied Physics, Vol. 42, No. 4, **2009**, p. 45210.
doi: 10.1088/0022-3727/42/4/045210

[13] Semenov, I. L., Krivtsun, I. V., and Reisgen, U., *Numerical study of the anode boundary layer in atmospheric pressure arc discharges,* Journal of Physics D: Applied Physics, Vol. 49, No. 10, **2016**, p. 105204.
doi: 10.1088/0022-3727/49/10/105204

[14] Almeida, N. A., Benilov, M. S., and Naidis, G. V., *Unified modelling of near-cathode plasma layers in high-pressure arc discharges,* Journal of Physics D: Applied Physics, Vol. 41, No. 24, **2008**, p. 245201.
doi: 10.1088/0022-3727/41/24/245201

[15] Mokrov, O., Simon, M., Sharma, R., and Reisgen, U., *Arc-cathode attachment in GMA welding,* Journal of Physics D: Applied Physics, Vol. 52, No. 36, **2019**, p. 364003.
doi: 10.1088/1361-6463/ab2bd9

[16] Mokrov, O., Simon, M., Schiebahn, A., and Reisgen, U., *Evaporation-determined model for arc heat input in the cathode area by GMA welding,* Mathematical Modelling of Weld Phenomena 12, edited by C. Sommitsch, N. Enzinger and P. Mayr, Verlag der Technischen Universität Graz, Graz, **2019**, pp. 953–964.

[17] Simon, M., Mokrov, O., Sharma, R., Reisgen, U., Zhang, G., Gött, G., and Uhrlandt, D., *Validation of evaporation-determined model of arc-cathode coupling in the peak current phase in pulsed GMA welding,* Journal of Physics D: Applied Physics, Vol. 55, No. 10, **2022**, p. 105204.
doi: 10.1088/1361-6463/ac3daa

[18] Mokrov, O., Simon, M., Shvartc, I., Sharma, R., and Reisgen, U., *Validation of the EDACC Model for GMAW Process Simulation by Weld Pool Dimension Comparison,* Enhanced material, parts optimization and process intensification. Proceedings of the First International Joint Conference on Enhanced Material and Part Optimization and Process Intensification, EMPOrIA 2020, May 19-20, 2020, Aachen, Germany, edited by U. Reisgen, D. Drummer and H. Marschall, Springer, Cham, **2021**, pp. 51–59.

[19] Mokrov, O., Simon, M., Schiebahn, A., and Reisgen, U., *Concept for the calculation of the distribution of heat input in the cathode area by GMA welding,* Welding in the World, Vol. 64, No. 9, **2020**, pp. 1605–1614.
doi: 10.1007/s40194-020-00929-9

[20] Karyofylli, V., Kamaldinova, L., Simon, M., Mokrov, O., Reisgen, U., and Behr, M., *Axisymmetric two‐phase flow simulations on space‐time meshes,* PAMM, Vol. 19, No. 1, **2019.**
doi: 10.1002/pamm.201900409

[21] Mokrov, O., Warkentin, S., Westhofen, L., Jeske, S., Bender, J., Sharma, R., and Reisgen, U., *Simulation of wire metal transfer in the cold metal transfer (CMT) variant of gas metal arc welding using the smoothed particle hydrodynamics (SPH) approach,* Materialwissenschaft und Werkstofftechnik, Vol. 55, No. 1, **2024**, pp. 62–71.
doi: 10.1002/mawe.202300166

[22] Jeske, S. R., Simon, M. S., Semenov, O., Kruska, J., Mokrov, O., Sharma, R., Reisgen, U., and Bender, J., *Quantitative evaluation of SPH in TIG spot welding,* Computational Particle Mechanics, Vol. 10, No. 1, **2023**, pp. 1–18. doi: 10.1007/s40571-022-00465-x

[23] Jeske, S. R., Bender, J., Bobzin, K., Heinemann, H., Jasutyn, K., Simon, M., Mokrov, O., Sharma, R., and Reisgen, U., *Application and benchmark of SPH for modeling the impact in thermal spraying,* Computational Particle Mechanics, Vol. 9, No. 6, **2022**, pp. 1137–1152. doi: 10.1007/s40571-022-00459-9

[24] Bobzin, K., Heinemann, H., Jasutyn, K., Jeske, S. R., Bender, J., Warkentin, S., Mokrov, O., Sharma, R., and Reisgen, U., *Modeling the Droplet Impact on the Substrate with Surface Preparation in Thermal Spraying with SPH,* Journal of Thermal Spray Technology, Vol. 32, 2-3, **2023**, pp. 599–608. doi: 10.1007/s11666-023-01534-0

[25] Bender, J. a. o., SPlisHSPlasH Library, URL: https://github.com/InteractiveComputerGraphics/SPlisHSPlasH.

[26] Löschner, F., Böttcher, T., Rhys Jeske, S., and Bender, J., *Weighted Laplacian Smoothing for Surface Reconstruction of Particle-based Fluids,* Vision, Modeling, and Visualization, **2023.** **doi:** 10.2312/vmv.20231245

Date: 31.03.2026

Hardening of PBF-LB/M low alloyed steel by in-situ alloying compared to subsequent case hardening

Author: Maximilian Marschall[1,2,5,6*]

Authors: Florian Kostrewa[3], Matthias Pitz[4], Dominic Bartels[1,5], Michael Schmidt[1,2,6]
[1]Institute of Photonic Technologies (LPT), Friedrich-Alexander-Universität Erlangen-Nürnberg (FAU), Konrad-Zuse-Straße 3/5, 91052 Erlangen, Germany
[2]Erlangen Graduate School in Advanced Optical Technologies (SAOT), Konrad-Zuse-Straße 3-5, 91052 Erlangen, Germany
[3]H-O-T Härte- und Oberflächentechnik GmbH & Co. KG, Kleinreuther Weg 118, 90425 Nürnberg, Germany
[4]Schaeffler Technologies AG & Co. KG, Industriestraße 1-3, 91074 Herzogenaurach, Germany
[5]Bayerisches Laserzentrum GmbH (blz), Konrad-Zuse-Straße 2-6, 91052 Erlangen, Germany
[6]Collaborative Research Center (CRC) 814 "Additive Manufacturing", 91058 Erlangen, Germany
*Corresponding author: E-mail: Maximilian.Marschall@lpt.uni-erlangen.de, ORCID: 0009-0009-7782-0414

Abstract

In laser-based powder bed fusion of metals (PBF-LB/M) low alloyed steel parts can be produced and if needed case hardened after the process. With in-situ alloying hardness could already be tailored in the printing process. Case hardening is a very specific material and purpose tailored process to modify the microstructure hardness, also dependent of the incoming microstructure of the component. Here, the microstructure gained from case hardening of a low alloy PBF-LB/M steel will be compared to an as-built part hardened by in-situ alloying during the process with premixed powder. The PBF-LB/M process creates complex microstructures caused by the recurring remelting of small melt pool volumes and passive heat accumulation, paired with the carbon in-situ alloying. Hardness testing, optical microscopy and SEM EBSD images will be elaborated. This contribution aims to showcase the differences, pros and cons of in-situ alloying hardening with additional carbon, on low alloyed steel Bainidur AM, compared to conventional case hardening.

Keywords

PBF-LB/M, in-situ alloying, low alloyed steel, in-situ hardening, case hardening

1 Introduction

Laser-based powder bed fusion of metals (PBF-LB/M) enables the fabrication of metallic components with complex geometries by selectively consolidating successive powder layers using a scanned laser beam. Originating from rapid prototyping and initially positioned as a route to shorten development cycles and supply chains through enhanced design freedom, the technology has matured into a platform predominantly serving high-value, performance-critical applications - for example in aerospace, motorsport, and biomedical implants - where functionality outweighs

part cost. But slowly merging into the market, more machine components are also emphasized to be built by additive manufacturing. The material wise focus in PBF-LB/M currently show allrounder alloys like 316L or AlSi10Mg and then rapidly going to highly specialized and expensive materials. For bearing or gear applications, conventional, rather inexpensive materials are often the choice, such as (16-20)MnCr5 for bainitic low alloy steels, which can already be processed by PBF-LB/M [1]. But processing these conventional materials in PBF-LB/M can results in different microstructure and mechanical properties than accustomed in classic construction requirements, sometimes even after heat treatment [2]. Therefore, sometimes alloys have to be tailored for PBF-LB/M to obtain comparable material properties. One result of this approach is the Bainidur© AM low alloy steel [3] to result in as-built bainitic microstructure. Especially bearing applications require a high-impact toughness and equally sufficient hardness and wear resistance. On the microstructural side, the part needs to offer a ductile core and a hardened shell by heat treatment or case hardening [4]. In steels ductility is mostly represented by Austenite while the Martensite phase shows the highest hardness [5]. But as both is required in one part, the Bainite metastable phase, consisting of Ferrite and Fe3C carbides (Cementite), is the favoured microstructure to have sufficient toughness, hardness and ductility. This is a challenging demand for the underlying microstructure and additionally for PBF-LB/M parts with its high cooling rates and on the other hand recurring melting events in the layer-based process. Post process heat treatment is often required for PBF-LB/M parts to secure a certain microstructure.

Currently additive manufacturing aims for low effort in post-processing steps. Every step or additional process reduces the advantage of additive manufacturing regarding lead time in production compared to conventional forming processes. Case hardening, more specific carburizing, is a process that requires additional time to the printing process itself, introducing carbon to surface, the case of the part. Depending on temperature, pressure and the elements of Chromium, Nickel and Molybdenum, the carbon diffuses into the material to a certain depth. With carburizing additional carbon is introduced that is needed for the hardening effect during rapid cooling [6,7]. Low alloy steels have a low carbon content, which makes them unable to harden by heat treatment only. During the heating phase of the case hardening, the microstructure changes to austenite to enforce better carbon diffusion into the steel. This step requires high temperature, typically between 850-950 °C, to form the austenite. Ferrite with body centred cubic (bcc) crystal structure hinders the diffusion. Austenite is characterized by a face centred cubic (fcc) crystal. After the diffusion of carbon into the austenite of the peripheral areas, the part is rapidly cooled by quenching in water or oil. After the rapid cooling, to reduce internal stresses and brittleness of the case, the part is tempered by reheating to a low temperature of 125-200 °C without losing its significantly increased hardness. The internal core consists of bainite while the peripheral surface near volume consists of martensite due to the rapid cooling of carbon enriched austenite. The ductility of bainite is typically higher compared to martensite, while martensite has higher hardness and wear resistance.

With in-situ alloying in PBF-LB/M it is possible to bring in additional alloying elements, here carbon, during the manufacturing process. While operating a process that is based on powder particles which are remolten by a laser beam, homogenous alloy synthesis must be achieved within the transient lifespan of the melt pool with cooling rates in the range of 103 to 105 K/s. The question arises, whether an alloy formed under these conditions is comparable to a case hardened or heat-treated counterpart. Can in-situ alloying with carbon lead to a hardening effect that makes a case hardening step skippable?

The Bainidur© AM steel is a PBF-LB/M tailored case hardening steel alloy, capable of forming a bainitic microstructure in the as-built state despite the high cooling rates in the process [8]. Conventional process chains for use cases where bainitic microstructure is needed, often rely on 16-20MnCr5 alloys whose chemical composition is close to Bainidur© AM. Yet no studies show the microstructure comparison between those different manufacturing routes of conventional material + case hardening, PBF-LB/M part + case hardening and in-situ alloying hardening.

Adding more carbon to the PBF-LB/M powder could result in the same microstructure compared to case hardening of a conventional counterpart material. During the transient lifespan of the melt pool Bainidur© AM base material is alloyed with the additional carbon. The high cooling rates in the process substitute the quenching after the austenitization during the case hardening heat cycle.

2 Aim of the Investigation

This contribution investigates the microstructure formation during in-situ alloying of the low alloyed PBF steel Bainidur© AM with carbon nano particles compared to conventional case hardening of the same PBF-LB/M processes base material and a conventional comparable 16MnCr5 steel. Surface near microstructure is compared between the manufacturing routes.

3 Materials and Experimental Details

The conventional reference material was 1.7131/16MnCr5 steel. The cylindric specimen (height: 10 mm, diameter: 20 mm) were provided and hardened by H-O-T Härte- und Oberflächentechnik GmbH & Co. KG, Germany.

The low alloyed steel powder Bainidur® AM was used; produced by Deutsche Edelstahlwerke (DEW specialty steel) / Swiss Steel Group with a particle size distribution (PSD) between 20 - 63 µm and spherical particle morphology [3]. The development base for this alloy were the conventional 1.7980 and 1.7979 steels. It achieves an as-built hardness of 44 HRC with bainitic microstructure despite the high cooling rates in PBF-LB/M [8].

For the in-situ alloying with C, carbon black N550 nanoparticles from Harold Schold & Co. GmbH were used. The Bainidur powder was blended to 0.8 wt.% total carbon using glass pearl blending aids (diameter 1.25-1.65 mm) and a tumble mixer for two hours. The glass pearls are removed afterwards by sieving with 500 µm meh size.

The blend material was processed on an AconityMINI (Aconity3D GmbH, Herzogenrath, Germany). It operates an infrared 1 kW single mode fiber laser with a wavelength of 1070 nm. A 3D-scanner with F-Theta optic is used. The laser beam focus diameter w0 = 71.9 µm with Rayleigh length ZR = 2.34 mm. Substrate plates of 1.7147 / 20MnCr5 steel with 6.3 mm height and 100 mm diameter were used and screwed to the heated building plate. Argon 5.0 was used as protective gas to secure oxygen values below 100 ppm.

The process parameters are selected according to previous studies [9] and adapted to the high carbon content. Powder layer height was set to 60 µm. The laser output power was 300 W with a scanning velocity of 900 mm/s and a hatch distance of 100 µm with hatch roation angel 67°. The beam was defocused 3.5 mm below the interaction surface to a spot diameter of 129.4 µm. This diameter reduces the welding depth and widens the melt pool to reduce cracking behaviour. Additionally the substrate was heated to 400 °C to reduce cold cracking susceptibility while preventing a complete martensitic transformation due to the fast cooling rates in PBF-LB/M. The martensite start temperature for continious cooling calculations with JMatPro is 144 °C for the Bainidur with 0.8 wt.% carbon. These also show an enlarged bainite nose at around 400 °C. A rigid modification of the stainless steel support, gerated by Autodesk Netfabb, was used. The samples geometry was a standing 10x10x12 mm cuboid.

The Bainidur samples were built on a modified SLM 280 (Nikon SLM Solutions AG, Germany) PBF-LB/M machine with integrated nLight AFX-1000 laser [10] and the gaussian like beam index with spot diameter of 87 µm. The samples geometry was a standing 10x10x20 mm cuboid, built without support on to the substrate plate of 1.7147 / 20MnCr5 steel. The scanning speed was 750 mm/s with a laser powder of 300 W operating in focus position and a layer height of 60 µm. The hatch distance was 100 µm with 67° rotation. The samples relative density was in both process routes above 99.9 % analysed by cross section picture analyses.

Table 1: Chemical alloy composition in wt.% for 1.7131 according to [11], for Bainidur© AM according to [3] and modified version with carbon black.

Source / Element	C	Si	Mn	Mo	Cr	Fe
Bainidur© AM	0.22	0.8	1.4	1.0	1.0	bal.
Bainidur 0.8 wt.% C	0.8	0.8	1.4	1.0	1.0	bal.
1.7131 / 16MnCr5	0.14-0.19	0.4 max.	1.0-1.3	0.15-0.3	0.8-1.1	bal.

Some Bainidur samples were heat treated (HT), in annealing foil to prevent oxidation, with austenitization at 930 °C, quenching in oil and tempering at 200 °C for 60 min. The case hardening with carburization of the Bainidur samples and the reference cylinder 16MnCr5 was done by H-O-T according to their case hardening profile for 16MnCr5 parts for industry applications. The simplified temperature profile can be seen in Figure 1. The 16MnCr5 and Bainidur samples are case hardened and tempered, one Bainidur sample was not tempered. The modified Bainidur with 0.8 wt.% carbon was not heat treated.

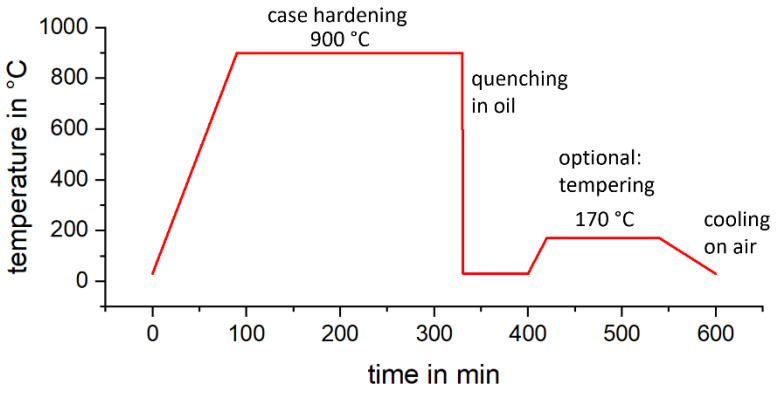

Figure 1: Simplified case hardening with carburization process temperature profile according to H-O-T.

The samples were cut along building direction. The cross sections were hot mounted with QATM QPREP DUROPLAST BLACK for metallographic analysis. After grinding and polishing, the samples prepared for electron backscatter diffraction microscopy (EBSD) were treated with oxide polishing suspension (OPS). For EBSD measurement, a step size of 0.04 µm was taken within a resolution of 1250x938 pixels on an image width of 50 µm. The samples for optical microscopy were etched with a 3% Nital solution at room temperature. Scanning electron microscopy (SEM) was conducted with a ZEISS MERLIN GEMINI II (Carl Zeiss Microscopy GmbH, Germany) equipped with additional EBSD. Hardness measurement was conducted with a KB30S (Hegewald & Peschke, Germany) for Vickers hardness HV1 on polished samples.

4 Results and Discussion

When using different forming routes, microstructure of those differently produces samples tend to differ. Especially when a conventional forming route of semi-finished products from a cold-pressed or extruded 16MnCr5 rods are compared to a PBF-LB/M tailored material with microstructure formation under rapid cooling and recurring melting. Different microstructures are expected. Undergoing heat treatment like case hardening, comparable materials of different forming routes should express similar properties afterwards. Taking a closer look on the density for all samples in Figure 2. While hardening, regardless of the hardening process, creates different microstructures on the surface compared to the core of the sample, the analysis has to be split in those two sections. For the hardness in the sample core, it is shown in Figure 2, that Bainidur shows comparable hardness in the PBF-LB/M as-built state to the 16MnCr5 core after its heat case hardening process. The data is presented with error bars exclusively for the modified Bainidur for better readability. When Bainidur is heat treated with or without case hardening, it exhibits a distinct comparable hardness around 525 HV in the core. Those states of Bainidur, as well as the as-built state show a strong linear behaviour in the core regarding hardness, making the reachable hardness well scalable and trustworthy. The reference 16MnCr5 hardness decreases slightly to the middle of the sample, but is still considered very stable. Bainidur as-built and 16MnCr5 share partially equal hardness values and deviate around the 450 HV mark, which is close to the benchmark as-built hardness for Bainidur according to the datasheet with 44 HRC correlating to roughly 440 HV [3]. Now going

the hardness ladder upwards to the modified Bainidur with 0.8 wt.% C, it shows a wider spread hardness in the core in which a microstructure switch can already be foreseen deeper in the sample. Until 6 mm depth from the surface, the hardness seems still to be stable, then the deviation rises and the mean hardness is getting lower.

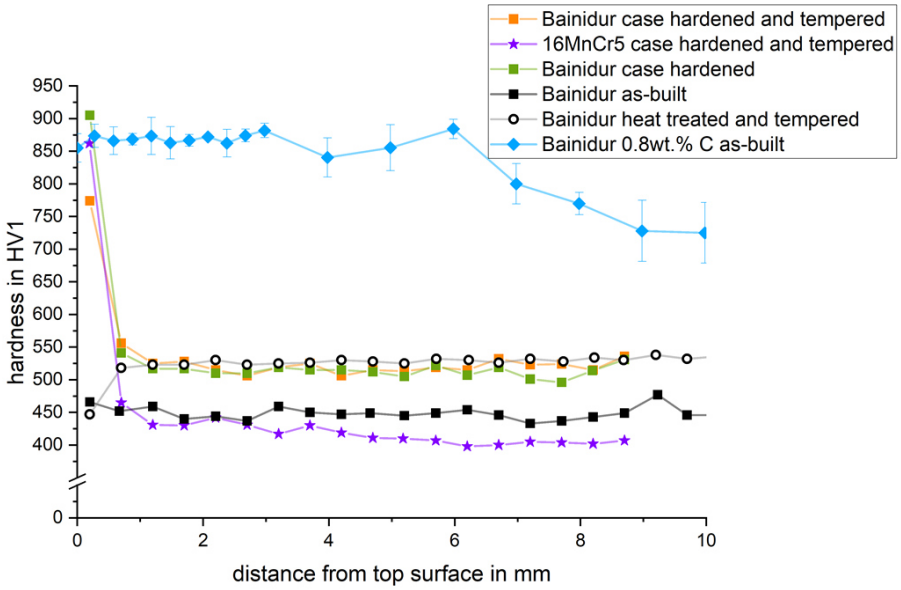

Figure 2: hardness in dependency of the cuboid top surface distance measured with HV1 for all samples.

This hardness is reflected by the corresponding microstructure development. From only looking on the hardness values, all sample cored, besides the modified Bainidur, should reveal some kind of bainitic microstructure. Keeping in mind, that 16MnCr5 is a case hardening steel used for bearing applications, the hardening process should end with a core microstructure of lower bainite. Lower bainite is favoured over upper bainite because of its hardness, wear resistance, ductility and thermal stability. For deeper classification about bainite microstructure refer to Bartels et al. [8] for PBF-LB/M or Bhadeshia and Honeycombe [5]. For now, it has to be sufficient to divide between those upper and lower bainite and martensitic microstructure, which appears as microstructure with sharp needles. Martensite possesses the excellent hardness, while being less ductile, more brittle. Followed by the lower bainite with balanced ductility and good hardness. The upper bainite is the least favoured possible microstructures, with carbides between the bainite plates, making it less ductile but also it shows a lower hardness compared to lower bainite [5].

According to the description of the microstructure and the hardness of the as-built Bainidur, it can be concluded, that an upper bainite dominated microstructure is present. It was already shown, martensite is not present in Bainidur in a material property defining amount [8]. Here the as-built hardness shows to be around 450 HV. When the Bainidur is case hardened with the same parameters like 16MnCr5, a comparable bainitic microstructure should evolve, aside the different base hardness due to deviations in the carbon content. Form this it can be deducted, that the heat treated and the case hardened Bainidur samples core consists of lower bainite due to the higher hardness without having a martensitic microstructure. The lower bainite in Bainidur composition will therefore possess a hardness of 525 HV deducted from this explanation. The as-built Bainidur

will therefore be mostly upper bainite with its 400 HV [8]- 450 HV. Like discussed on the base of hardness, this is also shown on the microstructure in Figure 4 for the sample core and in Figure 3 for the case. Bainidur heat treated and case hardened are pictured by comparable microstructure with comparable feature size and colour of after etching. Same goes for the case hardened 16MnCr5, which seems to have a slightly coarser microstructure, mostly in the core. The as-built Bainidur shows homogenous microstructure from core to case with brown to grey etched heat affected zones between the characteristic layers of the PBF-LB/M process. This brown to grey indicates upper bainite, which goes hand in hand to the effects pictured with the hardness difference between upper and lower bainite.

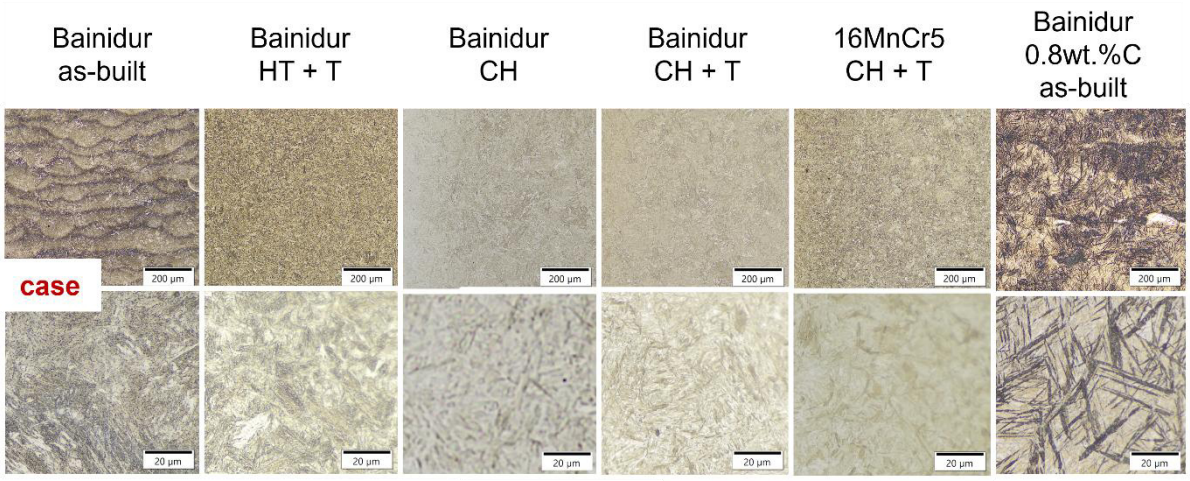

Figure 3: Optical microscopy images of nital etched microstructure of sample case - heat treated (HT), tempered (T), case hardened (CH).

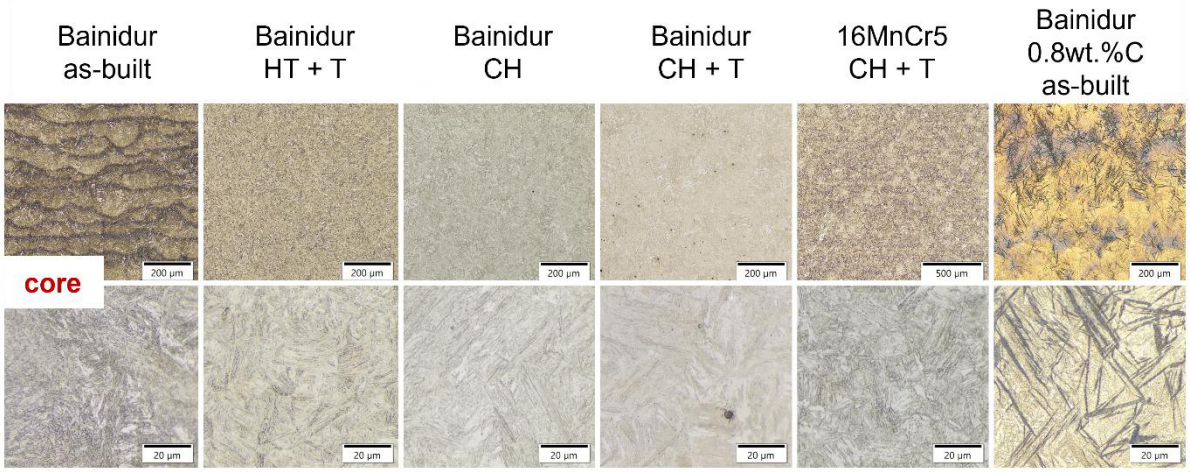

Figure 4: Optical microscopy images of nital etched microstructure of sample core - heat treated (HT), tempered (T), case hardened (CH).

The modified Bainidur with 0.8 wt.% C shows outstanding microstructure from the row of samples. Case and core show similar microstructure, whereby the core pictures are taken on a 5 mm distance from the top surface. Both case and core possess comparable hardness to the case of the case hardened and tempered 16MnCr5 and of the only case hardened Bainidur. But the microstructure shows to be different. The modified Bainidur is dominated by the dark spike or lath like features. First impression, also supported by the hardness, would be a martensitic microstructure which is

pictured in literature as chaotic orientated spikes. But when taking a closer look on the needles, they are interrupted and partially shed. Additionally, not all of them are not random orientated, like martensite is. Keeping in mind that the PBF-LB/M process is a recurring melting process that changes the scanning direction in each layer, also the solidification and microstructure development has changing directions. Within this chaotic appearing, the needles have sub bundles and shared orientations. This is pictured on some examples in red circles in Figure 5. As bainite formation is a diffusion dependant process [12] and martensite formation not, this regularity hints towards the presence of bainite, while smaller or more random orientated needles will be martensite. From calculations with JMatPro, the martensite hardness in a conventional continuous rapid cooling model for the modified Bainidur is around 800 HV. However, this PBF-LB/M produced microstructure of the modified Bainidur surpasses this calculated expectation with 860 ± 25 HV. This should point out a martensite dominated microstructure is present, because the hardness could not be reached by lower bainite. But still the partially orientated lath packages are an unexpected occurrence.

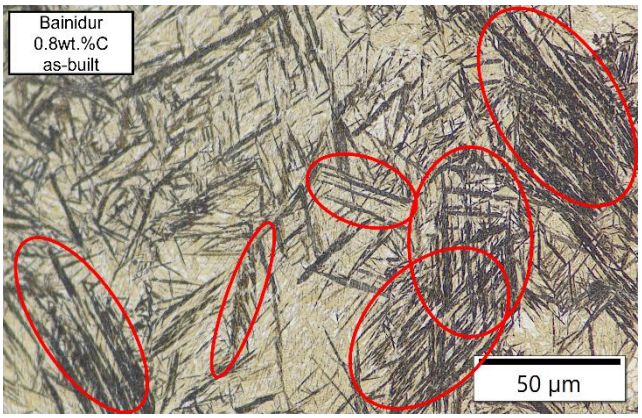

Figure 5: Bainidur 0.8 wt.% C as-built microstructure with lath bundles.

With EBSD the grain morphology and phase composition are analysed. Bainidur develops a very fine microstructure, which is correlated to lots of zero solutions in EBSD measurement due to the fine distributed Fe3C carbides within the common bainite. Fine grains and within distributed carbides are leading to resolution problems for the indication of unambiguous Kikuchi pattern in the EBSD analyses. Carbides, but even more martensite leads to stress inside of the laths. Martensite distorts the bcc crystallographic structure of ferrite tetragonally and creates internal stresses. Stress deforms the Kikuchi pattern of the EBSD measurement. This stress can approximately be pictured with the Kernel Average Misorientation (KAM), where blue is lower and green is higher misorientation from the detected to the perfect matching Kikuchi pattern. Depending on the position and its surrounding identified phases, high KAM points towards fine carbides especially at grain boundaries or martensite. In Figure 6 the phases, grain orientation, band contrast and KAM are shown for the case microstructure of the case hardened and tempered Bainidur and 16MnCr5, as well the as-built Bainidur with 0.8 wt.% C. Having the information about the locally resolved presence of carbides and the KAM, will reveal where martensite is present. Case hardening is known to produce a martensitic case. The conventional 16MnCr5 therefore serves as reference for a martensite dominated microstructure. It can be clearly seen, that there are no carbides in the laths of ferrite, which are rather fine and randomly orientated with no

grain orientation preference. This is a good indicator for martensite. The case hardened Bainidur shows comparable results in EBSD, proving its hardenability. The modified Bainidur makes it even easier. There are not a lot of carbides visible. There are only very small islands of retained austenite. While not showing significant shares of carbides, the KAM is very high all over the picture, especially in the fine grain upper half of the KAM when compared to its band contrast image. That reveals that even with preheating the substrate plate to 400 °C within the built job martensite formation can take place when parts are printed on support structures. As in Figure 2, a hardness drop for the modified Bainidur can be seen, preheating prevents only the formation of martensite in the substrate plate near regions, while the melt pool and upper part segments are dominated by the cooling against the building chamber and shielding gas flow.

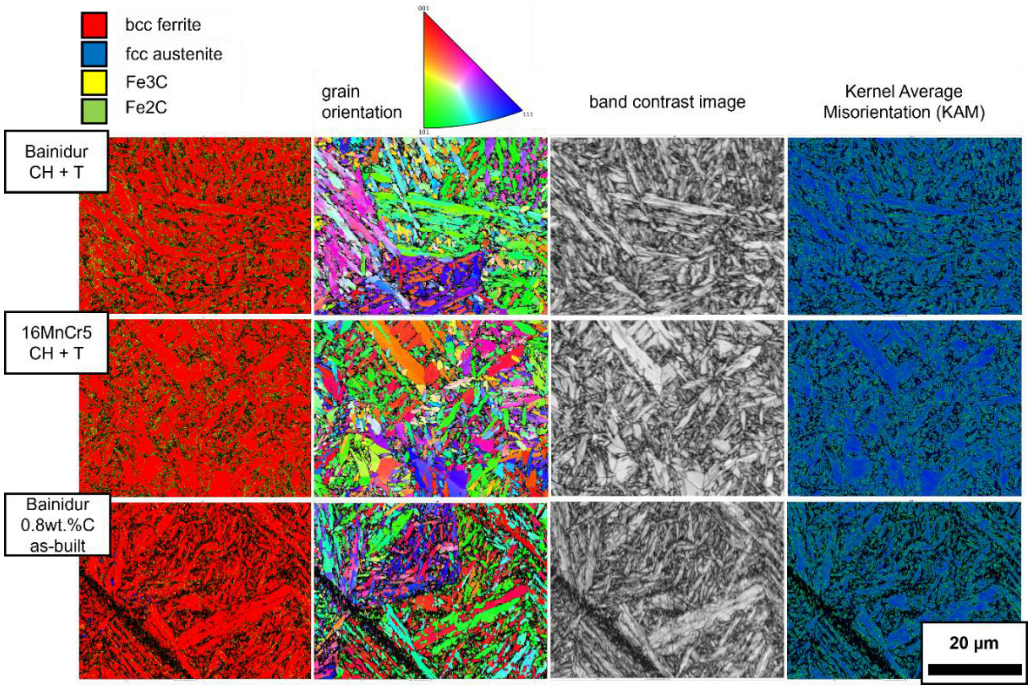

Figure 6: EBSD image analyses for case hardened Bainidur, 16MnCr5 and Bainidur with 0.8 wt.% C - including phase distribution, grain oriantation map parallel to the building direction, band contrast imaging and Kernel Average Misorientation.

5 Summary

Conventional case hardening was compared to in-situ alloying hardening by adding nano particles of carbon to a low alloyed PBF-LB/M steel. Microstructure of case hardened conventional fabricated 16MnCr5 and case hardened PBF-LB/M Bainidur was comparable, even though a 22MnCr5 would be the best comparison to achieve similar hardness in the lower bainite. The in-situ hardened Bainidur with 0.8 wt.% C results in the same hardness like the case hardness of the 16MnCr5. The microstructure, even though both are foreseen to be martensitic, differs in the characteristics of the manifestation of its martensite. The modified Bainidur reveals uncommonly long spikes compared to the 16MnCr5 throughout an underlying even finer grained microstructure from the PBF-LB/M process.

Following research will focus on the local resolved hardness dependant on the process conditions of substrate heating and support structures. Additionally, Microstructure of pre-alloyed and in-situ

alloyed steels should be compared regarding their stability of maintaining their elemental composition and the resulting microstructure. The forming mechanisms of bainite and martensite and its tempering during the PBF-LB/M process should be investigated towards involved metastable carbides like Fe2C.

Acknowledgements

The authors gratefully acknowledge funding of the Collaborative Research Center 814 (CRC 814), sub-project T5, by the German Research Foundation (DFG)-Project No. 61375930 and of the Erlangen Graduate School in Advanced Optical Technologies (SAOT) by the Bavarian State Ministry for Science and Art.

Conflict of Interest

The author declares no conflict of interest.

Data Availability Statement

Data is available upon request.

CRediT authorship contribution statement

Conceptualization MM,DB; methodology MM; formal analysis MM; Investigation MM; Resources MM,MS,FK,MP; data curation MM; supervision DB,MS; writing-original draft MM; writing-review and editing MM,DB,MS,MP; funding acquisition MS.

References

[1] Brummer M, Raddatz KJ, Schmitt MM, Schlick G, Tobie T, Daub R, et al. Static load-carrying behavior and material properties of additively manufactured gears (PBF-LB/M, 16MnCr5). Rapid Prototyp J 2023;29:117–30. https://doi.org/10.1108/RPJ-02-2023-0035.
[2] Bartels D, Klaffki J, Pitz I, Merklein C, Kostrewa F, Schmidt M. Investigation on the Case-Hardening Behavior of Additively Manufactured 16MnCr5. Metals 2020;10:536. https://doi.org/10.3390/met10040536.
[3] Bainidur AM - dew-powder.com n.d. https://www.dew-powder.com/additive-fertigung/bainidur-am (accessed February 20, 2024).
[4] Ilschner B, Singer RF. Werkstoffwissenschaften und Fertigungstechnik. Berlin, Heidelberg: Springer; 2016. https://doi.org/10.1007/978-3-642-53891-9.
[5] Bhadeshia H, Honeycombe R. Steels: Structure and Properties, Fourth Edition. 4th ed. Elsevier Ltd.; 2017.
[6] Bleck W, Moeller E. Handbuch Stahl. München: Carl Hanser Verlag GmbH & Co. KG; 2018.
[7] Laepple V. Wärmebehandlung des Stahls Grundlagen, Verfahren und Werkstoffe. n.d.
[8] Bartels D, Novotny T, Mohr A, van Soest F, Hentschel O, Merklein C, et al. PBF-LB/M of Low-Alloyed Steels: Bainite-like Microstructures despite High Cooling Rates. Materials 2022;15:6171. https://doi.org/10.3390/ma15176171.
[9] Marschall M, Bartels D, Tangermann-Gerk K, Roth S, Schmidt M. In-situ modification of material hardness for low-alloyed steels processed via PBF-LB/M – a view on process related microstructure 2025. https://doi.org/10.58134/FH-AACHEN-RTE_2025_005.
[10] nLight Additive. nLIGHT 2023. https://www.nlight.net/additive.
[11] Werkzeugstahl - 1.7131 (16MnCr5) - Datenblatt - Stahl Online-Shop! n.d. https://www.stauberstahl.com/werkstoffe/17131-werkstoff-datenblatt/ (accessed January 23, 2026).
[12] Bhadeshia HKDH. The lower bainite transformation and the significance of carbide precipitation. Acta Metall 1980;28:1103–14. https://doi.org/10.1016/0001-6160(80)90093-0.

Date: 31.03.2026

Development of a compensation strategy for casting distortion in aluminum gravity die casting

Author: Nino Wolff[1]

Authors: B. Pustal[1], A. Bührig-Polaczek[1]

[1]RWTH Aachen University, Foundry Institute, Intzestraße 5, 52072 AACHEN, GERMANY

*Corresponding author: E-mail: n.wolff@gi.rwth-aachen.de, ORCID: 0000-0002-4838-4926

Abstract

An initial study of previous research on distortion formation in gravity casting revealed a lack of holistic descriptions, particularly regarding heat transfer between mold and casting. This work aims to better understand the various influencing factors and their mechanisms affecting distortion in aluminum gravity die casting through targeted experiments. The causal chain of heat balance, mold constraint, solidification, cooling, stresses, and component distortion was examined both individually and contextually. An experimental methodology was developed to investigate these variables. Findings indicate that thermal interaction primarily affects process stability while distortion can be largely compensated by adjusting demolding temperature. These Insights can be used to derive a strategy for compensating distortion in aluminum die casting. An initial review of this strategy in a numerical simulation concludes the work.

Keywords

Aluminum, die casting, distortion, compensation

1 Introduction

Aluminum is one of the most important engineering materials and is widely used in the foundry industry, particularly in transportation applications where lightweight design plays a key role in improving energy efficiency. With increasing demands for functional integration and structural performance, the complexity of cast components has risen significantly. As a result, requirements regarding dimensional accuracy and casting quality have become more stringent. A central challenge in this context is distortion, which originates from thermally induced shrinkage during solidification and subsequent cooling. If shrinkage occurs non-uniformly due to geometric asymmetries, local temperature gradients, or constraints from a mold, internal stresses lead to shape deviations that may exceed allowable tolerances. Although permanent mold casting offers high

dimensional accuracy, shrinkage-related distortion remains a challenge due to the high thermal conductivity and mechanical rigidity of the metal mold, which lead to stress formation.

In research, this topic is mainly addressed in numerical studies on the prediction of distortion in high pressure die casting (HPDC) [1-3]. These works often point out that there are deficiencies in the understanding of the fundamental mechanisms and their analytical description. Such knowledge about the respective influences of component geometry, material, and process on component distortion is essential for the development of precise numerical models, particularly in coupled thermo-mechanical approaches [4]. One of the studies using a “triple U-shape” geometry and AlSi7,5Mg0,4 in HPDC concluded that the final geometry and distortion of the casting depend strongly on the demolding temperature, internal stresses at the time of demolding, and the thermal conditions in the mold and during cooling after demolding [2]. Related studies compared numerical simulations with experiments on component distortion and residual stresses using two special test geometries, a thick stress grid and a thin V-shaped shell [1, 5, 6]. In experimental series varied oil-cooling, holding time (and by this demolding temperature), and in some cases water quenching were investigated. The results for the grid indicated that distortion is influenced by the cast material with the mold acting as the limiting factor for heat dissipation [5]. The results of the V-shape showed stronger dependence on mold temperature control and holding time due to low high-temperature strength and resulting plastic deformation [6]. The studies also highlighted that simulation accuracy strongly depends on precise material models and correct thermal-mechanical contact descriptions. Another study investigated distortion compensation in automotive structural castings. Distortion was mitigated via geometric tool adaptations (pre-compensation) and simulated using global and local compensation factors. Results showed that applying tailored local or global compensation factors effectively reduced deviations, with trade-offs depending on undercut areas and manufacturability constraints [7].

Overall, the previous studies indicate that in permanent mold casting, distortion is primarily influenced by the thermal management and holding time – and therefore demolding temperature. Practiced compensation is mostly achieved through costly tool adaptations, while the underlying mechanisms of distortion formation remain insufficiently understood. Furthermore, almost all previous studies focus on HPDC, and investigations for gravity die casting – a process with minimal disturbances such as high pressure and high flow rates – are nearly nonexistent.

2 Aim of the Investigation

The overarching objective is to establish a comprehensive empirical understanding of distortion formation in permanent mold casting and derive a compensation strategy from the findings. Specifically, this work aims to analyze the mechanisms leading to distortion in aluminum gravity die casting and to quantify the influence of relevant process parameters. For this purpose, the causal chain consisting of heat balance, mold constraint, solidification, cooling, stress development, and resulting component distortion is investigated both individually and in terms of their interactions. A systematic experimental methodology is developed to isolate and evaluate these influencing

factors. This approach enables the identification of cause-effect relationships between thermal conditions, mechanical constraints, and resulting deformation behavior. Based on the experimental findings, a strategy for distortion compensation is derived. This strategy is intended to enable targeted and efficient reduction of distortion by addressing the relevant mechanisms at different stages of the casting process. Finally, the applicability of the proposed approach is evaluated through an initial validation using numerical simulation.

3 Materials and Experimental Details

To investigate these influencing factors on distortion an experimental methodology was developed and corresponding test series and individual experiments were conducted. As the geometry of the test component, a U-shaped design was selected due to its simplicity and ease of measurement [8]. The distortion can thus be quantified as a two-dimensional value based on the opening width. By extending the "U" geometry to an F-shape, a freely shrinking reference element was added. The wall thickness of the test component in the initial configuration is 10 mm, and the opening width of the "U" is 130 mm with a component height of 120 mm. This results in a casting weight of 2,4 kg in aluminum. To determine and describe the relationships, the distortion value (D) is defined as the deviation of the opening width of the "U" from the nominal value. The deviation of the inner length (Δl_i) – the connection between the two legs of the "U" – from the nominal value is used as a measure to evaluate the hindrance of shrinkage, which leads to internal stresses. The difference between the opening width (ΔO) and the inner length is considered a measure of the shape-change contribution to the distortion induced by the release of these internal stresses during demolding. The designations of the areas, variables, and measurement points are shown in *Figure 1* (left). The expected thermomechanical behavior of the test component is illustrated and explained in *Figure 1* (right). From the demolding, which corresponds to the demolding temperature, a uniform shrinkage of the entire casting is assumed until it reaches ambient temperature.

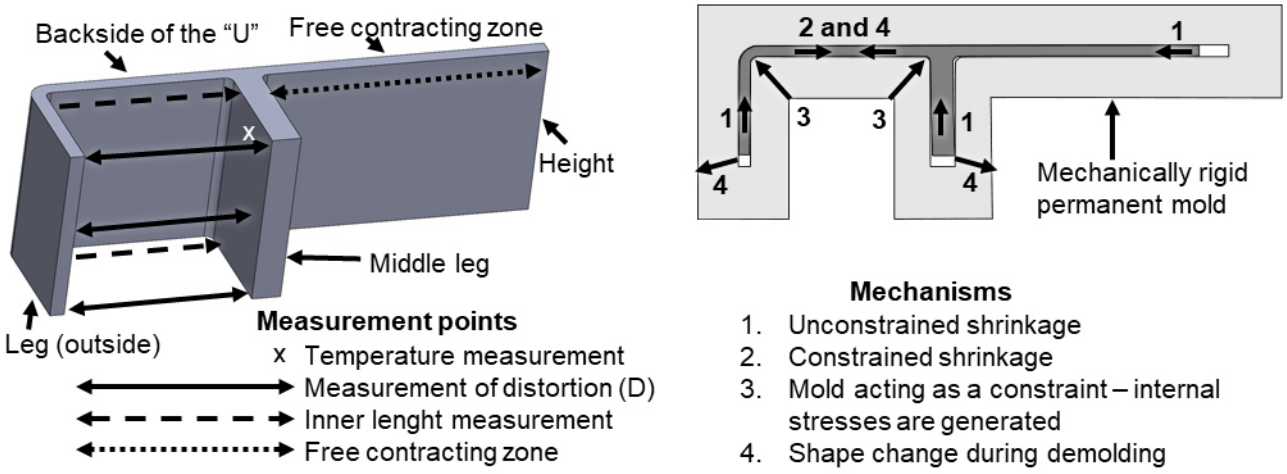

Figure 1: Test geometry with measurement points (left) and schematic representation of the governing distortion mechanisms (right). The distortion results from the interaction of unconstrained and constrained shrinkage, stress formation due to mold constraint, and subsequent shape change when the mold constraint is lifted.

The casting is enclosed by steel die modules arranged along the circumference of the "F", incorporating cooling channels equidistant from its surface. The influence of geometry, such as global and local wall thickness variations, inherent shrinkage restraint of the component, or geometric pre-compensation, can be investigated through modifications of the die. For most variations, this can be achieved by replacing a die module located between the two legs of the “U”, which is referred to in the following as the core [8]. This module, which in the base configuration is a conventionally manufactured tool steel insert, can also be replaced by an additive manufactured steel insert or by a sand core. The preheating temperature of the die can be adjusted via cooling circuits. For locally differentiated temperature control, the region of the core module can be regulated independently from the rest of the die. For detailed process analysis, an in-situ measurement system consisting of multiple temperature and displacement sensors is implemented. The casting alloy used in all experiments is the industry-standard AlSi7Mg0,3, with a pouring temperature of 720 °C. Unless otherwise specified, castings are demolded after cooling to ambient temperature, and each series of castings consists of 5 to 8 samples. The experimental program is structured into three main areas:

- Variation of thermal conditions: Global and local different die preheating was investigated (30 to 150 °C). To verify whether the hypothesis established in the SFB1120 for plastic injection molding – that a more uniformly solidifying component develops less distortion [9, 10] – can be transferred to metal casting, the methodology developed there for heat-balance-optimized cooling channels was applied to an additively manufactured core module.
- Variation of mold constraint: One variation of the mold constraint effect was realized by variation of the demolding temperature. As an additional variation, the influence of mold constraint was examined by using a sand core instead of the steel core module.
- Variation of component geometry: To investigate the influence of component volume through a global reduction of wall thickness, corresponding experimental series were carried out. Additional individual experiments were conducted to study the influence of local wall thickness variations, achieved by thickening the middle leg. To investigate the influence of geometric pre-compensation experimental series were carried out using a core module with a geometry adapted according to an empirically determined compensation value.

Apart from distortion, the evaluation includes solidification and cooling, metallographic analysis and a process stability assessment. The latter is quantified using the relative scatter of distortion, defined as the normalized standard deviation within a test series.

Based on the insights gained from these individual series of experiments regarding the formation of distortion, a compensation strategy is subsequently derived. This strategy is intended to enable the targeted and localized compensation of distortion in a cast component by applying interventions at different stages in the chain – namely, component design, process design, and process-inherent factors. To verify this strategy, a complex cast component, modeled after an automotive structural casting part, is simulated in MAGMASOFT®, which had already been used during the design of

the experimental setup. In *Figure 2*, the corresponding cast component is shown on the left as a CAD model with the inlet on top, and on the right as a sketch for visualization of the associated dimensions. Flatness of the circumferential annular flange is used here as a measure of distortion. As a means of process-inherent control, the different regions of the steel mold surrounding the component can be temperature-controlled locally and temporally along the circumference.

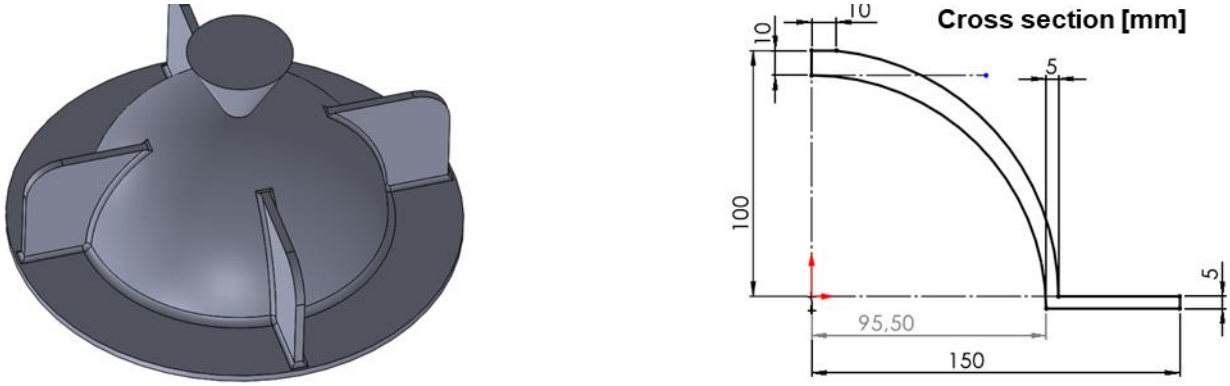

Figure 2: The complex cast component to verify the compensation strategy.

4 Results and Discussion

The results of individual influencing factors and their mechanisms of action are partly presented in separate earlier publications in more detail and are incorporated below as required for the development of the compensation strategy.

The variation of die temperature shows no direct correlation with the absolute magnitude of distortion [8]. However, an effect on process stability is observed. Using the conventional core lower die temperatures lead to increased scatter in distortion, indicating more heterogeneous solidification and stress development. The use of optimized cooling channels results in more homogeneous solidification conditions. This leads to an increase in mean distortion, which can be attributed to the formation of a continuous load-bearing dendritic network over a larger temperature range. At the same time, the relative scatter decreases, indicating improved process stability due to more uniform stress evolution [11]. *Figure 3* shows the distortion results for different mold temperature control configurations: on the left for conventional cooling, and on the right for the optimized cooling channels.

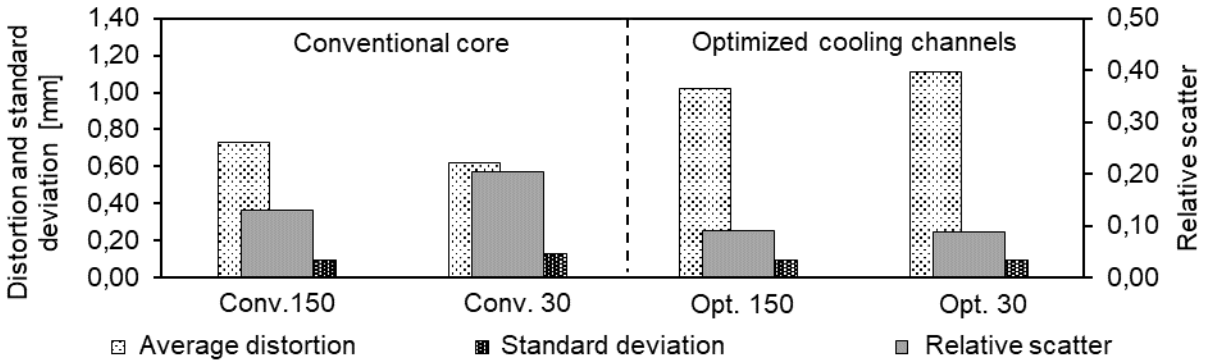

Figure 3: Mean distortion, its standard deviation, and the resulting relative scatter for the influence of temperature control (30 and 150 °C) and optimized cooling channels.

A particularly strong influence is observed for the demolding temperature [12]. The results show an almost linear relationship between demolding temperature and distortion. With increasing demolding temperature, the deformation behavior transitions from opening to closing of the U-geometry. At a specific temperature (285 °C), nearly distortion-free conditions can be achieved, see *Figure 4*. The deviation of the inner length also shows an almost linear behavior, but without a sign change. Its magnitude, compared with the shrinkage of the free end, indicates that significant shrinkage constraint occurs within the mold. This behavior suggests that distortion is governed by a combination of elastic and plastic deformation mechanisms, with stress relaxation occurring predominantly during the constrained state in the mold. The influence of mold material is investigated by the comparison between steel and sand cores. Sand cores exhibit significantly lower shrinkage restraint, resulting in reduced distortion but increased relative scatter [13]. In the experiments with sand cores, higher preheating temperatures lead to smaller distortion magnitudes. This behavior highlights the importance of thermomechanical material properties and their temperature dependence.

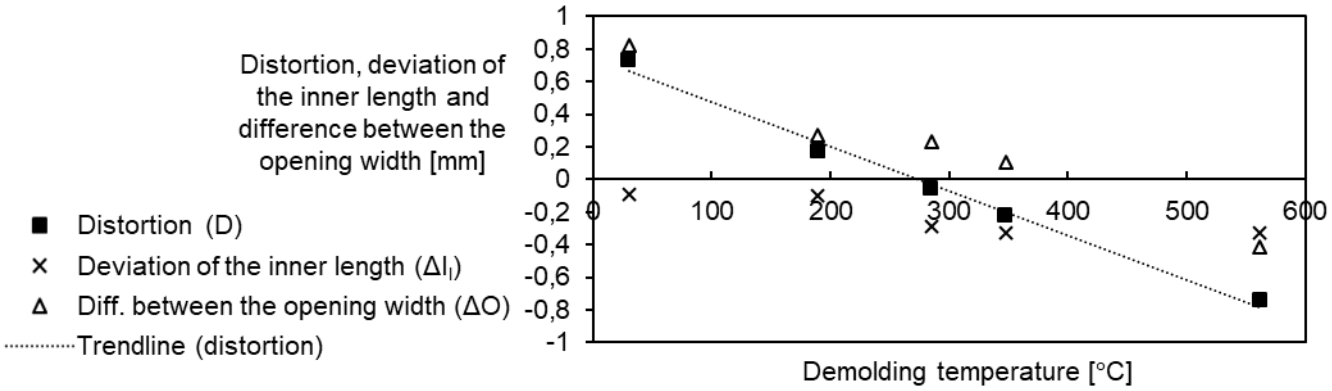

Figure 4: Measured values plotted against the temperature at which the mold constraint is released (demolding).

Geometric variations further illustrate the sensitivity of distortion to component design [13]. Reduced wall thickness shows with the initial nominal core no influence on distortion, while local mass accumulations increase distortion due to delayed solidification and localized stress formation. Geometric pre-compensation proves to be an effective measure for distortion reduction, although its efficiency depends on the specific geometry and boundary conditions, see *Figure 5*.

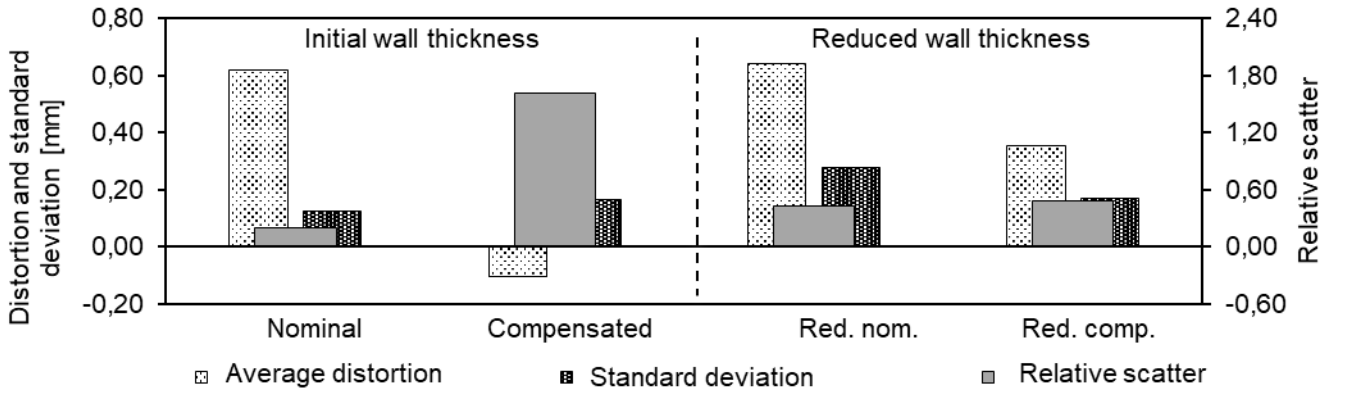

Figure 5: On the left, the results for the experiments with the original wall thickness, each shown for the core with the nominal geometry and for the variant with geometric pre-compensation. On the right, the corresponding values for the globally reduced wall thickness.

Comparative Evaluation

The results show that thermal interactions mainly influence process stability, while mechanical interactions (e. g. mold constraint and demolding temperature) primarily affect the magnitude of distortion. Distortion can therefore be largely compensated through a combination of controlled demolding temperature and geometric pre-compensation, after separating the phenomenon into linear shrinkage and shape change components. For the development of a targeted compensation strategy, it is also essential to identify when each influencing factor acts: during component design, casting process design, or the ongoing casting process.

Derivation of a Compensation Strategy

Based on the findings a path toward complete distortion compensation can be derived by compensating both linear shrinkage and shape change. The means for distortion compensation are divided by the stage of their appearance, see *Figure 6*. In practice, component geometry, including wall thicknesses, mass centers, and inherent shrinkage restraints, is treated as a fixed input parameter. Distortion compensation can be achieved through a combination of geometric pre-compensation during design and control of the demolding temperature during the process. The predictive geometric pre-compensation is applied so that relevant casting dimensions are in a way that in the process the final compensation is possible with time and place differentiated cooling and thereby demolding temperatures. This enables localized adjustment and compensation of dimensional deviations within complex castings. At the same time, thermal control can be used to create a more homogeneous temperature field at the end of solidification, thereby reducing the scatter of distortion and improving process stability.

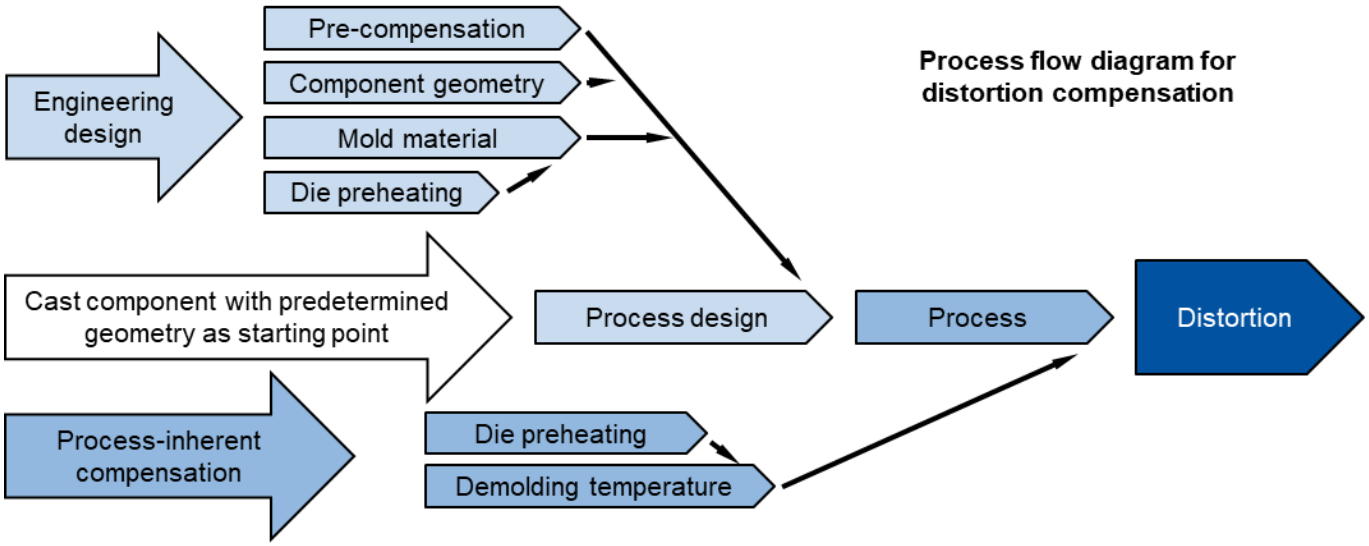

Figure 6: Distortion is influenced by design-related factors such as component geometry, mold material, and geometric pre-compensation, as well as by process-inherent parameters, including die preheating and demolding temperature.

Applying the compensation strategy outlined above to a complex cast component demonstrates in simulations that local distortion can be reduced through process-immanent adjustment of the local demolding temperature. The top of *Figure 7* shows the temperature fields at the moment when the mold constraint is released. On the left, a nearly homogeneous

temperature distribution along the circumference is depicted, whereas on the right locally differentiated temperatures are applied, distinguishing between the regions of the outer ribs and the intermediate sections. The resulting distortion is illustrated in the center with a 25-fold magnification, where the flange remains visibly flatter. A flatness analysis indicates that the deviation of the flange from an ideal plane is reduced from 0,34 mm to 0,12 mm (bottom).

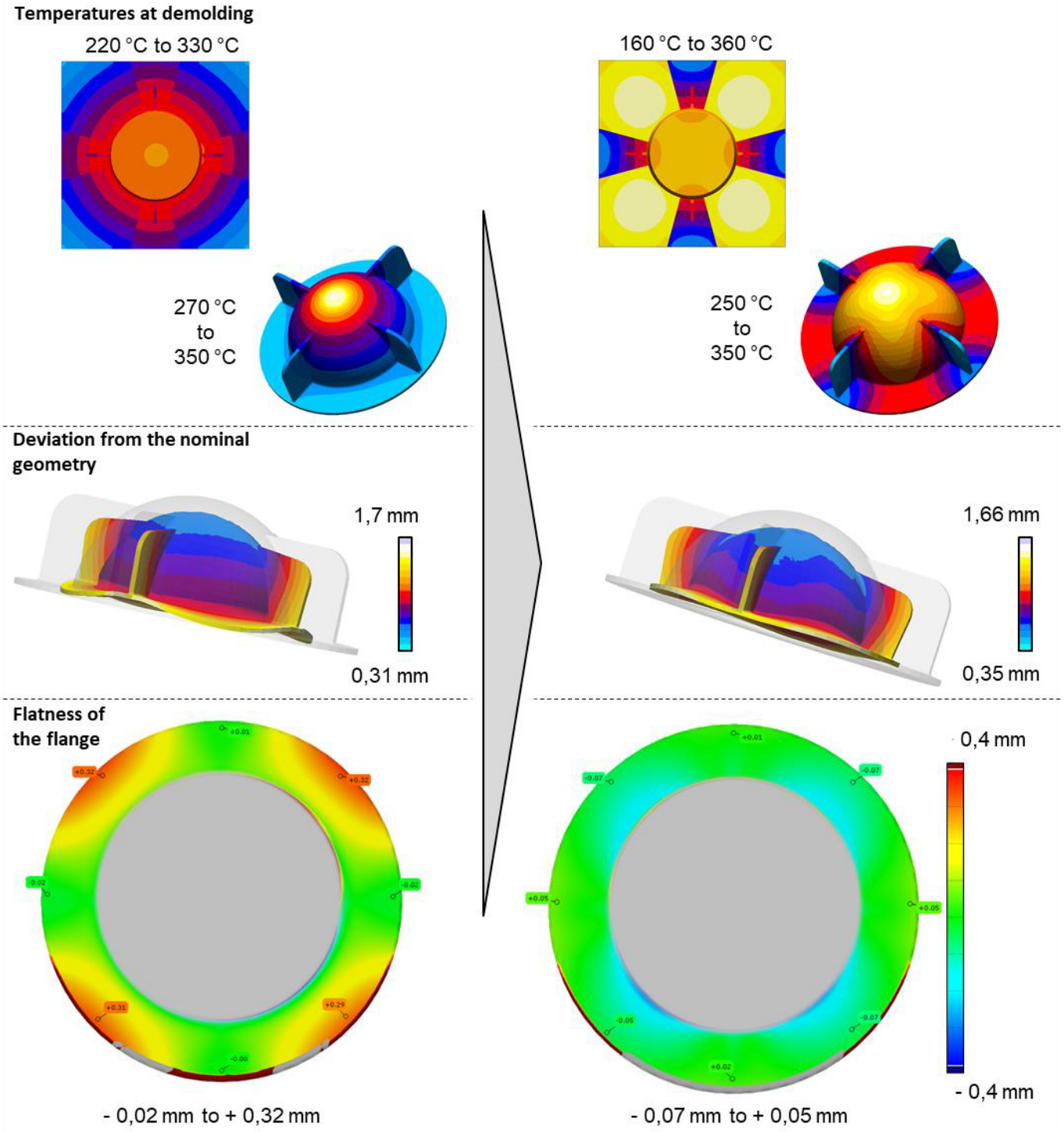

Figure 7: Compensation of the distortion of the complex cast component through locally differentiated demolding temperatures. The left side shows the initial condition, and the right side the compensated variation.

5 Summary

By systematically analyzing the causal chain of thermal and mechanical effects, a deeper understanding of the underlying mechanisms is achieved. The results show that demolding temperature and mold constraint are the dominant factors influencing distortion, while thermal conditions mainly affect process stability. This approach provides a deeper understanding of distortion formation in aluminum die casting by linking linear shrinkage, its hindrance, and shape change, thereby yielding insights beyond the current state of knowledge. Based on these findings, a novel combined compensation strategy was developed, integrating geometric pre-compensation and locally controlled demolding conditions. Initial validation through numerical simulation demonstrates that locally adjusted thermal boundary conditions can improve dimensional accuracy in complex cast components. The presented methodology provides a foundation for the development of predictive thermo-mechanical models and offers a pathway toward near distortion-free casting processes. The consistent experimental methodology enabled the first quantitative comparison of various influencing factors and their contributions to distortion, while the introduced relative scatter allows assessment of process stability. Analysis of mechanisms and interactions facilitates the attribution of factors to either part design or the casting process, providing a foundation for effective distortion compensation strategies. The developed compensation strategy was identified in a study as being goal-oriented.

Looking forward, the modular mold setup supports further investigation of input variations. Ultimately, a multi-step approach combining predictive design and locally adjustable demolding temperatures can achieve near-complete distortion-free castings, with thermal management further reducing variability through a more homogeneous solidification temperature field.

Acknowledgements

The presented investigations were carried out at RWTH Aachen University within the frame-work of the Collaborative Research Centre SFB1120-236616214 “Bauteilpräzision durch Beherrschung von Schmelze und Erstarrung in Produktionsprozessen” and funded by the Deutsche Forschungsgemeinschaft e.V. (DFG, German Research Foundation). The sponsorship and support is gratefully acknowledged.

Conflict of Interest

The author declares no conflict of interest.

Data Availability Statement

The underlying data are available upon request at: http://hdl.handle.net/21.11102/bcea071e-b41a-4c1f-82d0-7a3e7bd94e18

References

[1] P. Hofer, E. Kaschnitz, P. Schumacher. Distortion and Residual Stress in High-Pressure Die Castings: Simulation and Measurements. *JOM*. **2014**, 66.

[2] A. Garza-Delgado. *Study of Casting Distortion and Residual Stresses in Die Casting*. [Hrsg.] Ohio State University. Columbus : s.n., **2007**.

[3] R. Miller. *A Prediction of Part Distortion in Die Casting*. [Hrsg.] University of North Texas Libraries. Columbus : s.n., **2005**.

[4] N. Wolff, U. Vroomen, A. Bührig-Polaczek. Über die Beschreibung des Bauteilverzugs im Aluminium-Kokillenguss als Folge behinderter Schwindung. *Niedersächsisches Symposium Materialtechnik Tagungsband*. **2023**, Bd. 5.

[5] P. Hofer, E. Kaschnitz, P. Schumacher. Simulation of distortion and residual stress in high pressure die casting – modelling and experiments. *Materials Science and Engineering*. **2012**, 33.

[6] P. Hofer, E. Kaschnitz, P. Schumacher. Messung und Simulation von Verzug und Eigenspannungen in Druckgussteilen. *Giesserei.* **2012**, 98, S. 30 - 41.

[7] Ch. Thoma, W. Volk, G. Branner, H. Eibisch. Simulationsgestützte Optimierung der Maßhaltigkeit Simulationsgestützte Optimierung der Maßhaltigkeit in der Prozesskette Aluminium-Druckguss. *GIESSEREI RUNDSCHAU*. **2013**, 60, S. 282 - 286.

[8] N. Wolff, T. Hohlweck, U. Vroomen, A. Bührig-Polaczek, Ch. Hopmann. Entwicklung einer Versuchskokille zur Untersuchung und thermischen Beeinflussung des Bauteilverzugs beim Schwerkraftkokillengießen. *Gießerei Special*, Bd. 1, S. 14-23, **2020**.

[9] Ch. Hopmann, P. Nikoleizig. Inverse thermal mold design for injection molds. I*nternational Journal of Material Forming*. **2018**, Bd. 11, S. 113 - 124.

[10] Ch. Hopmann, P. Nikoleizig, H. Dornebusch, T. Schneppe. Minimization of Warpage for Injection Molded Parts by Inverse Thermal Mold Design. *International Polymer Processing.* **2018**, Bd. 1, 33, S. 110 - 116.

[11] N. Wolff, T. Hohlweck, U. Vroomen, A. Bührig-Polaczek, Ch. Hopmann. Development of an Experimental Setup to Investigate Influences on Component Distortion in Gravity Die Casting and a First Variation of Temperature Control Strategy. *Metals*. **2021**. 11(12), 2028. https://doi.org/10.3390/met11122028

[12] N. Wolff, S. Gor, U. Vroomen, A. Bührig-Polaczek. Description of component distortion in aluminum gravity die casting as a result of hindered shrinkage and evaluation of numerical predictions. *Materialwiss. Werkstoff-tech.* **2024**, 55, 33. https://doi.org/10.1002/mawe.202300133

[13] N. Wolff, *Eine Untersuchung der verzugsbestimmenden Faktoren im Aluminium-Kokillenguss*; Dissertation, RWTH-Aachen, **2025**, Doi:10.18154/RWTH-2025-08578

Date: 14.03.2026

Use of optimised process control for highly segmented heating elements to reduce warpage in injection-moulded parts

Author: Sebastian Schwan

Authors: S. Schwan[1*], Ch. Hopmann[1]

[1]RWTH Aachen University, Institute for Plastics Processing (IKV) in Industry and Craft, Seffenter Weg 201, 52074, AACHEN, GERMANY

*Corresponding author: E-mail: publications@ikv.rwth-aachen.de, ORCID: 0009-0009-3242-2623

Abstract

In injection moulding, the specific volume and thus the shrinkage and warpage are influenced by the process variables of pressure and temperature. By homogenising the specific volume a uniform shrinkage and thus minimised warpage can be achieved. The specific volume can be homogenised by locally manipulating the mould temperature. For that a model-based predictive control system was developed for a highly segmented mould heating system, which is validated using a plate geometry. Subsequently, the transfer to a complex geometry is examined. To this end, a methodology is developed to reduce the number of sensors required for temperature control. The mould temperature is measured based on the resistance of the heating elements and adjusted using a PID controller. The controller was initially configured using simulation. This results in a calculated reduction of warpage by a factor of six compared to a version without heating elements.

Keywords

Injection moulding, pvT-behaviour, model-predictive control, simulation

1 Introduction

In injection moulding, non-uniform cooling conditions lead to local variations in shrinkage, which in turn cause internal stresses and warpage [HMM+18]. Warpage can shift the dimensions of injection moulded parts beyond allowed tolerances and should therefore be prevented. Various strategies with different approaches can be utilised for this purpose. The use of conformal cooling of the mould cavity creates more uniform cooling conditions compared to traditional cooling channel layouts and therefore reduces the thermal gradients that generate warpage [HFH22]. Another approach involves the use of ceramic coatings within the cavity, which could be used to control the local heat transfer coefficient [BHÖ+17] Furthermore, warpage can be factored in

during the production of the injection mould, and a warpage compensation can be incorporated. This does not prevent warping, but instead utilises the warping that occurs during cooling to achieve the desired target dimensions [Kah24, TSF+24].

Whilst the systems described can effectively reduce warpage in injection-moulded parts, they are static systems and do not allow for dynamic adjustment of the injection moulding process. The aim of this study is therefore to create a dynamic method for local warpage control. To this end, a self-optimising strategy is being developed for highly segmented heating elements in moulds. The aim is to homogenise the specific volume of the cooling plastic melt, as shrinkage and warpage depend on the pvT behaviour of the plastic [HMM+18]. Whilst the local pressure cannot be influenced, the temperature during cooling can be controlled using heating elements in the mould, thereby reducing warpage by homogenising the shrinkage.

2 Development of a controlled raster tempering system for simple moulded parts

To evaluate the use of highly segmented heating elements to reduce warpage an injection mould was developed. To this end, a simple plate geometry was initially selected as the test specimen. Following an assessment of effective temperature control concepts, a mould with 18 temperature control zones, nine in each half of the mould, was constructed [HST+17]. Each temperature control zone is equipped with a ceramic heating element, a CO2 cooling chamber. These heating elements offer high power density, suitable thermal response characteristics and the ability to be controlled directly [HFN+16, HS17]. Infrared temperature sensors are used to measure the temperature in each zone. Compared to conventional temperature sensors, these offer a shorter response time and provide a more accurate measurement of the melt temperature. Three of the sensors used are also equipped with a pressure sensor to measure the pressure of the melt along the flow path. This enables the measurement of the pressure drop along the flow path, allowing the zone temperatures to be adjusted accordingly [HSD18].

The structure of a single zone is shown in Figure 1. The cooling chamber and the ceramic heating element are mounted behind the mould surface. The distance between the cavity surface and the heating element stems from the trade-off between the need for a rigid mould, which must withstand the high mechanical stresses generated during injection moulding, and the requirement for dynamic temperature control. This means that a large thermal mass must be heated or cooled, resulting in a slow temperature response. A controller for the temperature control zones must therefore be designed accordingly to compensate for the resulting delay in temperature control. For the tests aimed at developing and optimising the controller, an unmodified polypropylene (PP) (type: PP 505 P, Saudi Basic Industries Corporation, Riyadh, Saudi Arabia) is used.

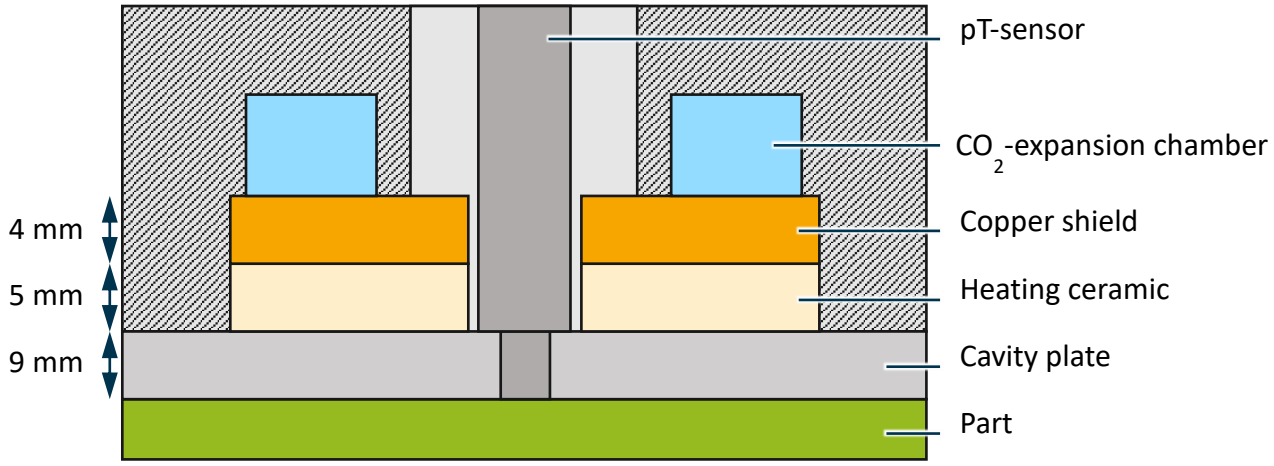

Figure 1: Setup of a temperature control zone used in the demonstrator mould [HKS20]

To compensate for the dead time resulting from slow thermal diffusion processes, a model predictive control (MPC) approach was chosen to regulate the zone temperatures [HS18]. In this approach, the system state is predicted using a system model, enabling the heating or cooling output to be adjusted in advance. To this end, a prediction model was developed based on a one-dimensional heat conduction equation derived from Fourier's law (cf. Equation 1). This describes heat conduction through a cylindrical wall of thickness r based on the effective thermal diffusivity a_{eff}. Using this model, the temperature of the plastic, the mould steel, the heating elements, the cooling chambers and the base tempering of the mould can be calculated in discrete time and location. Based on the model, temperature curves resulting from various scenarios (e.g. different power settings of the heating elements) are used. Together with pressure curves recorded during the injection moulding process, these can be used to determine how the temperature must be controlled during the process in order to achieve the best possible homogenisation of the specific volume [HS18].

$$\frac{\delta T}{\delta t} = a_{eff}\left(\frac{1}{r}\frac{\delta T}{\delta r} + \frac{\delta^2 T}{\delta r^2}\right) \tag{1}$$

3 Development of a needs-based, system-wide control concept for process management using raster tempering system

The aim of the second project phase is to further develop the control system for the mould produced previously. To this end, the control strategy is to be expanded in order to achieve more precise control and better self-optimisation. To validate the performance of the developed MPC, the controller is being compared with a PID controller. To this end, a target curve is specified for the specific volume and approximated by adjusting the controllers. To determine the quality of the controllers, the warpage achieved by using the controllers is compared to the warpage of the moulded parts produced using the target curve. The MPC achieves a significantly better approximation of the pvT-curve than the PID controller [HKS20]. The use of MPC results in a

deviation of the specific volume from the target curve that is 4.5 times smaller than that of the PID controller. This ensures that the deviation in warpage when using MPC is 8.3 times smaller than when using the PID controller (see Figure 2) [HKS+21]. Furthermore, when controlling the specific volume, the PID controller results in a higher standard deviation of the deviation relative to the reference value and the MPC. Process stability is therefore reduced by the PID controller used.

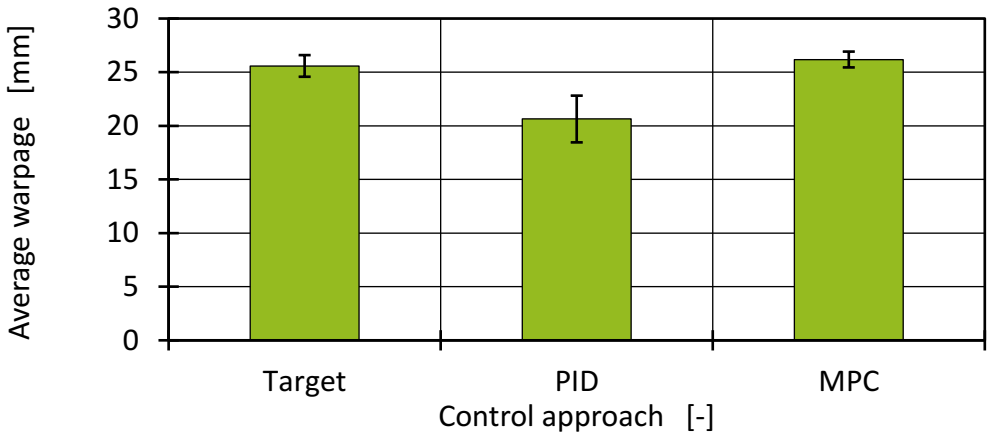

Figure 2: Comparision of the averaged warpage using the PID and MPC approach to the target warpage [Kah24]

To control the heating elements and cooling chambers, adjustments must be possible within a maximum of 100 ms. To enable a sufficiently rapid adjustment, simplifications were therefore employed in the MPC approach in the first project phase, such as calculating the heat flux using a one-dimensional heat conduction equation via the finite difference method (FDM). In doing so, constant, non-temperature-dependent material data for thermal conductivity and heat capacity were assumed. This results in deviations between the calculated behaviour and reality. To achieve higher control quality, the material data and heat transfer coefficients used were optimized to depict heat transfer effects more realistically using simulation. For this purpose, simulations were carried out using the Moldex3D (CoreTech System Co., Ltd., Taiwan). Through iterative calibration of the parameters, the accuracy of the FDM temperature prediction could be enhanced.

As the accuracy of specific volume predictions has a significant impact on control precision, the description of the pvT behaviour was also investigated. Since the cooling rate, in addition to pressure and temperature, also influences the specific volume, a new cooling-rate-dependent pvT model was developed [WHK+20, WHR+20, WHS+19]. In addition, the empirical models used were further adapted to reduce discontinuities in the description of the transition region from the molten to the solid state by adjusting the equations of state. By implementing the developed pvT models into the MPC, it was possible to achieve more accurate prediction and, consequently, more precise control of the melt. Furthermore, the MPC approach was extended to predict the temperature profile after ejection and, consequently, the density at ambient conditions. In doing so, two approaches were compared: the assumption of dynamic and constant cooling rates. The prediction can be significantly influenced by the cooling rate used, with material behaviour being

better represented using a constant cooling rate than a dynamic cooling rate [HXK+21]. This allows for a more precise control of the warpage with a lower standard deviation between different cycles.

In addition to the adjustments based on the material models used, modifications must also be made to the MPC approach due to the tooling technology employed. Because of their proximity, the various heating zones heat each other up [HKX21]. By extending the MPC approach to include coupling of the heating zones, precision can be further improved. Furthermore, the approach is extended to include a self-optimisation function. This optimisation analyses the measurement and prediction data and iteratively adapts the local target value across cycles to achieve a globally homogeneous pattern in the specific volume [Kah24].

Injection moulding tests are carried out to validate the adapted MPC. These compare the results for the system using MPC and deactivated heating elements. The results show that, when temperature control is activated, the temperature difference between the two mould halves decreases and the variance per zone over several cycles is 60% lower than in the reference testings carried out [HKF+24a, Kah24]. When examining the warpage of the plates, it is noticeable that the mean and maximum warpage are only slightly reduced compared to the reference, at 7.4% and 8.4% respectively, but that process consistency also increases significantly here. Thus, the standard deviation of the mean warpage can be reduced by 62.0% over the five measured cycles [HKF+24a, Kah24]. It is likely that the coathanger distributor of the plate has a significant influence on the warping behaviour. The mould wall opposite the hot runner cannot be dynamically temperature-controlled. As the manifold has not been removed, the internal stresses generated within it are transferred to the rest of the moulded part, causing the plate to warp. Overall, the self-optimising control system achieves a reduction in plate warpage by a maximum factor of 1.1 compared to a traditional cooling system.

4 Mastering moulding precision for complex geometries and different materials

Based on the results obtained so far, the approach is to be applied to a complex geometry. In doing so, the required sensor and temperature control technology is also to be reduced in order to test a more industry-ready implementation of the technology. A ceramic heating layer, developed at the Surface Engineering Institute at the RWTH Aachen University and sprayed onto the cavity surface, is to be used to control the mould temperature [HFK+24]. This enables the temperature of the mould surface to be adjusted much more quickly, as heat conduction takes place over a significantly shorter distance. Furthermore, compared to the heating elements used previously, a much lower thermal mass is heated, thereby enabling more dynamic temperature control.

In order to reduce the number of sensors required to control the heating layers, a simulation-based design of the heating layers and the controllers used is being carried out. This is intended to enable simulation-based temperature control. To this end, process simulation software such as Moldex3D

and Moldflow (Autodesk, Inc., San Francisco, United States) is being used. Subsequently, the transferability of the simulation results to a demonstrator mould will be tested.

To evaluate the reduction in warpage of complex moulded parts using dynamically temperature-controlled heating layers, a simplified stacking box, as shown in Figure 3, is examined. As the chosen geometry was revised several times over the course of the project to improve the manufacturability of both the injection mould and the heating layers, different versions of the box are shown. The selected geometry is particularly suitable for the investigation as it exhibits a high potential for warpage due to thermal inhomogeneities in the edge areas of the box. In the first step, various heating layer layouts are validated for the geometry. Strip-shaped heating layers across the edges of the box and triangular corner heating layers were investigated. The positioning of the heating layers is based on the plastic's plastic core, i.e. the areas in which the plastic melt solidifies most slowly [HKF+24b].

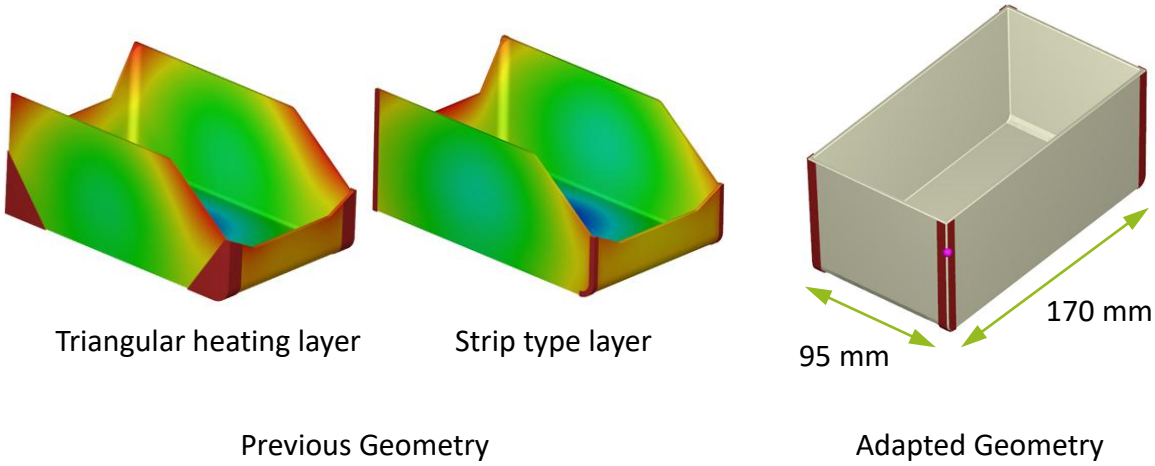

Figure 3: Stack box geometry and heating layer layout: initial version (left) and updated version (right)

For the heating layers, the effects on the warping of the stacking box are simulated at various constant heating powers of 100 W, 200 W and 500 W, which are derived from the power of the heating elements previously used. For both layouts, the lowest warpage occurs at 200 W. Analysis of the different heating layer configurations shows that the strip-shaped heating layers along the edges consistently achieve better results than the triangular corner heating layer. They result in lower average, maximum and minimum warpage. In addition, by using the strip-shaped heating elements, the average warpage on the measured walls of the box can be reduced from 0.55 mm to 0.09 mm compared to reference simulations without the use of heating layers, which corresponds to an improvement by a factor of six. Strip-shaped heating layers are therefore used for the adapted versions of the stacking box.

For the modified geometry (see Figure 3), strip-shaped heating layers are again being investigated. These are divided into four sections. The heating layers are divided in the middle of the edges, perpendicular to the flow path, and at the edge between the short and long sides of the box. This

division was implemented to enable temperature control along the flow path and to enable the production of the coatings. In Moldflow, permanently activated heating layers are initially investigated, as before. The investigations are based on two material types: a polybutylene terephthalate (PBT) (type: Ultradur B 4520, BASF SE, Ludwigshafen, Germany) and, a polycarbonate (PC) (type: Makrolon 6585, Covestro AG, Leverkusen, Germany). The results for PBT are shown in Figure 4.

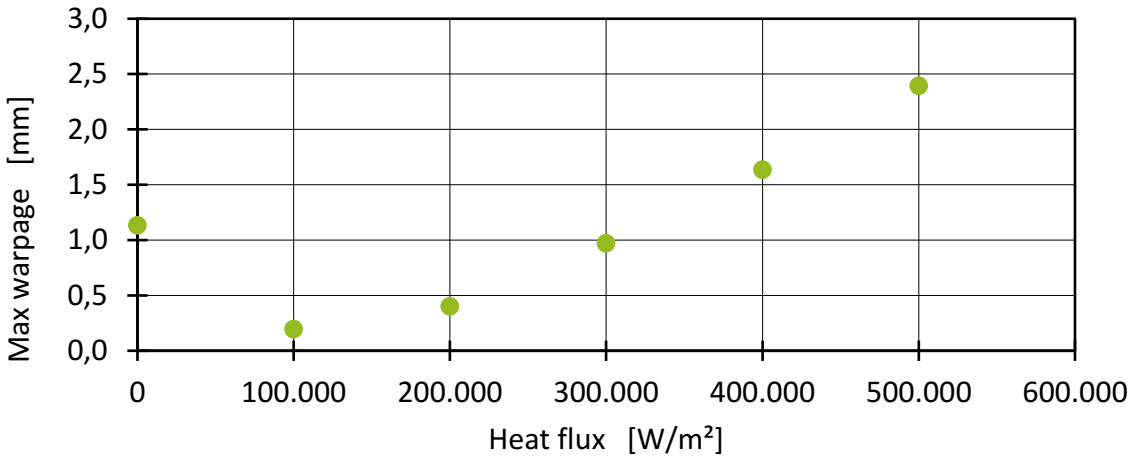

Figure 4: Simulation-based calculation of the effect of different heat inputs on maximum warpage when using PBT

For PBT, simulations at a heating power of 100,000 W/m² show a reduction in the maximum warpage along the long sides of the stacking box by a factor of 6. At higher heating powers, the warpage is overcompensated. This causes the walls of the box to bend outwards, resulting in increased warpage. Whilst the reduction in maximum warpage for PC is smaller, at a factor of 3 compared to a conventional process, warpage also increases here at higher heating rates. For the PBT examined, a further reduction in warpage was achieved by adjusting the heating powers on each side of the stacking box. To this end, various adjusted heating outputs were examined based on the measured warpage on both sides of the box. With a heating power of 50,000 W/m² on the short side and 125,000 W/m² on the long side of the mould, a total reduction in maximum warpage by a factor of 6.5 was achieved. Compared to the previous results, the adjustment of the heating power led to a 15% reduction in the energy consumption of the heating layers.

After the initial proof of the new design of the stack box a controller for the heating layers power was tested in Moldex3D. To this end, a PID control system was parameterised using serial tuning. This system offers a number of advantages. Firstly, it is possible to simulate the controller's performance using process simulation software. Furthermore, the newly developed heating layers eliminate the long response time associated with the heating elements previously used, and temperature adjustments can be made much more dynamically. Consequently, the aim is to achieve the fastest possible adjustment of the output. Unlike previous approaches, the PID controller does not regulate based on specific volume, but rather uses simulation-based temperature curves. This

allows for a control system with minimal sensor requirements, in order to simulate a realistic application scenario. As the temperature rises particularly rapidly during injection and then cools more slowly, a two-stage control concept was chosen, comprising a dynamic controller for the first two seconds of the process, in which the temperature rises rapidly, and an inertial controller for the remaining holding and cooling time. In the simulations, in which the warpage for the previously investigated PBT is determined once again, the temperature of the heating layers is adjusted based on the temperature on the opposite wall sides in order to achieve temperature homogenisation across the wall thickness during cooling and thus reduce residual stresses and the potential for warpage.

When parameterising the controller, it becomes apparent that the use of a D-term leads to poorer control performance and increased noise; consequently, a combination of two PI controllers is used for both phases. Once the controller has been parameterised, the effect of adjusting the temperature profile on moulded part warpage is investigated. The simulations show that raising the temperature of the heating layers relative to the temperature on the opposite mould wall results in reduced warpage. Thus, with suitable temperature settings, warpage caused by heating can be completely compensated for in specific areas.

5 Conclusion and Outlook

The investigations carried out demonstrate significant potential for the use of controlled heating elements to reduce warpage. This is particularly evident in modern, highly dynamic heating methods. Warpage was successfully reduced in a plate geometry, although residual warpage persists due to internal stresses in uncontrolled areas of the moulded part. For complex moulded parts, simulations indicate a significantly increased potential for warpage reduction, even when simple heating layer layouts and control concepts are used. This forms a fundamental basis for the potential industrial transfer of the results. For the geometry under consideration, a reduction in maximum warpage by a factor of 6.5 can already be achieved with permanently active heating. When a control system is used, warpage can even be completely avoided in certain areas. An injection moulding mould for validating the approach for complex moulded parts is currently being produced, so that the results can be validated during the project period. In addition, injection moulding tests are being carried out to transfer the results from the MPC to other materials.

Acknowledgements

The depicted research has been funded by the Deutsche Forschungsgemeinschaft (DFG) as part of the Collaborative Research Centres CRC1120-260065981. We would like to extend our thanks to the DFG.

Conflict of Interest

The author declares no conflict of interest.

Data Availability Statement

The data and materials for this publication are available on request at the following link:

http://hdl.handle.net/21.11102/fd1af693-aed1-480d-84e7-ef09b749fa98

References

BHÖ+17 BOBZIN, K.; HOPMANN, C.; ÖTE, M.; KNOCH, M. A.; ALKHASLI, I.; DORNEBUSCH, H.; SCHMITZ, M.: Tailoring the heat transfer on the injection moulding cavity by plasma sprayed ceramic coatings. *IOP Conference Series: Materials Science and Engineering* 181 (2017), S. 12013

HFH22 HOHLWECK, T.; FRITSCHE, D.; HOPMANN, C.: Validation of an extended objective function for the thermal optimisation of injection moulds. *International Journal of Heat and Mass Transfer* 198 (2022), S. 123365

HFK+24 HOPMANN, C.; FRITSCHE, D. C.; KAHVE, C. E.; BOBZIN, K.; HEINEMANN, H.; ERCK, M.; VOGELS, C.: Methodology of a thermal injection mold design with locally applied heating coatings on the cavity wall. *Materialwissenschaft und Werkstofftechnik* 55 (2024)Nr. *4,* S. 518–532

HFN+16 HOPMANN, C.; FILZ, P.; NIKOLEIZIG, P.; SCHMITZ, M.: Präzision aus Schmelze - Beherrschung der Erstarrung im Spritzgießen, In: : Integrative Kunststofftechnik 2016 : 28. Internationales Kolloquium Kunststofftechnik, 2016

HKF+24a HOPMANN, C.; KAHVE, C. E.; FRITSCHE, D. C.; FELLERHOFF, J.: Evaluation of a self‐optimizing local mold temperature control for inline warpage reduction of injection molded parts. *Materialwissenschaft und Werkstofftechnik* 55 (2024)Nr. *1,* S. 21–32

HKF+24b HOPMANN, C.; KAHVE, C. E.; FRITSCHE, D. C.; KASSEL, T.; BOBZIN, K.; HEINEMANN, H.; ERCK, M.; VOGELS, C.: Identification and compensation of part warpage in injection molding using on-cavity thermally sprayed heating coatings, In: : SPE ANTEC 2023, Red Hook, NY: Curran Associates Inc, 2024

HKS+21 HOPMANN, C.; KAHVE, C. E.; SCHMITZ, M.; RÖBIG, M.: A comparison of predictive control strategies for a highly segmented injection mold tempering. *Polymer* 218 (2021), S. 123494

HKS20 HOPMANN, C.; KAHVE, C.; SCHMITZ, M.: Development of a novel control strategy for a highly segmented injection mold tempering for inline part warpage control. *Polymer Engineering & Science* 60 (2020)Nr. *10,* S. 2428–2438

HKX21 HOPMANN, C.; KAHVE, C.; XIAO, C.-L.: Analysis of Radial Heat Transfer in an Injection Mold with Highly Dynamic Segmented Mold Tempering, In: Uwe Reisgen, Dietmar Drummer, Holger Marschall (Hrsg.): Enhanced material, parts optimization and process intensification, Cham: Springer, 2021

HMM+18 HOPMANN, C.; MENGES, G.; MICHAELI, W.; MOHREN, P.: Maßänderungen, Schwindung und Verzug, In: Christian Hopmann, Georg Menges, Walter Michaeli, Paul Mohren (Hrsg.): Spritzgießwerkzeuge, München: Hanser, 2018

HS17 HOPMANN, C.; SCHMITZ, M.: Gezielte Erstarrung durch eine selbstoptimierende, hochsegmentierte Werkzeugtemperierung im Spritzgießen. *GAK: Gummi, Fasern, Kunststoffe* 70 (2017)Nr. *6,* S. 377–383

HS18 HOPMANN, C.; SCHMITZ, M.: Controlling the local part properties using a segmented temperature control in injection molding. *Annual Technical Conference - ANTEC, Conference Proceedings* 2018 (2018)

HSD18 HOPMANN, C.; SCHMITZ, M.; DORNEBUSCH, H.: Development of a Segmented Temperature Control for Targeted Solidification in Injection Molding. *International Polymer Processing* 33 (2018)Nr. *2,* S. 206–216

HST+17 HOPMANN, C.; SCHMITZ, M.; THEUNISSEN, M.; NIKOLEIZIG, P.: Development of a highly segmented temperature control in injection moulding for reduced warpage and increased process stability, In: Abderrahim Maazouz (Hrsg.): Proceedings of PPS-32, Melville, New York: AIP Publishing, 2017

HXK+21 HOPMANN, C.; XIAO, C.; KAHVE, C. E.; FELLERHOFF, J.: Prediction and validation of the specific volume for inline warpage control in injection molding. *Polymer Testing* 104 (2021), S. 107393

Kah24 KAHVE, C. E.: *Herstellung form- und maßgenauer Spritzgießbauteile durch eine simulationsbasierte Auslegung der Kavitätsgeometrie und einer dynamischen Inline Werkzeugtemperierung,* RWTH Aachen University, 2024 - Betreuer: Hopmann, Christian; Behr, Marek

TSF+24 TILLMANN, S.; SCHWAN, S.; FRITSCHE, D. C.; KAHVE, C. E.; ELGETI, S.; HOPMANN, C.: Using the reverse geometry method for warpage compensation on changing meshes with interpolation methods. *PAMM* 24 (2024)Nr. *4*

WHK+20 WANG, J.; HOPMANN, C.; KAHVE, C.; HOHLWECK, T.; ALMS, J.: Measurement of specific volume of polymers under simulated injection molding processes. *Materials & Design* 196 (2020), S. 109136

WHR+20 WANG, J.; HOPMANN, C.; RÖBIG, M.; HOHLWECK, T.; KAHVE, C.; ALMS, J.: Continuous Two-Domain Equations of State for the Description of the Pressure-Specific Volume-Temperature Behavior of Polymers. *Polymers* 12 (2020)Nr. *2*

WHS+19 WANG, J.; HOPMANN, C.; SCHMITZ, M.; HOHLWECK, T.; WIPPERFÜRTH, J.: Modeling of pvT behavior of semi-crystalline polymer based on the two-domain Tait equation of state for injection molding (2019)

Date: 31.03.2026

Advances in Geometric Warpage Compensation for Injection Molding

Authors: Steffen Tillmann[1,*], Stefanie Elgeti[1,2]

[1]RWTH Aachen University, Chair for Computational Analysis of Technical Systems, Schinkelstraße 2, Aachen, 52062, Germany

[2] TU Wien, Institute of Lightweight Design and Structural Biomechanics, Gumpendorfer Straße 7, Vienna, A-1060, Austria

*Corresponding author: E-mail: tillmann@cats.rwth-aachen.de , ORCID: 0009-0006-5895-0406

Abstract

In injection molding, shrinkage and warpage lead to deviations between the produced part and the target geometry. Shrinkage is primarily driven by density changes during solidification, while warpage results from nonuniform cooling and the associated residual stress development. A promising way to reduce these deviations is geometric compensation, where the cavity is pre-deformed so that the final cooled part approaches the desired shape. Although such compensation is often experience-based in industrial practice, simulation-supported numerical design methods provide a systematic and reproducible alternative.

This paper presents three robustness modifications to the interpolation-based reverse geometry method for warpage compensation on changing meshes: a surface correction step that prevents remeshing-induced contour distortions, a closest-point ideal-geometry correction that eliminates interpolation-error accumulation in curved regions, and an iterative update of the injection point. These modifications are formalized mathematically and integrated into an automated compensation workflow using the commercial simulation software Moldflow. The method is demonstrated on two industry-relevant geometries simulated with polyoxymethylene (POM). In both cases, the adapted reverse geometry method reduces the root mean square warpage error by more than two orders of magnitude within a few iterations and remains stable over extended iterative runs. These results confirm the practical applicability of the method for industry-relevant warpage-compensation scenarios. The paper also summarizes the broader development trajectory of geometric warpage compensation within the Collaborative Research Centre SFB 1120, tracing the progression from inverse thermoelastic design formulations to the present reverse geometry workflow.

Keywords

Injection molding; warpage compensation; reverse geometry method; warpage simulation

1 Introduction

Injection molding is among the most widely used manufacturing processes for polymer components. Improving both process efficiency and part quality therefore remains a central research objective. A persistent quality issue is limited geometric accuracy caused by shrinkage and warpage. Shrinkage is primarily driven by temperature- and pressure-dependent density changes in the polymer melt, whereas warpage originates from nonuniform shrinkage due to mold constraints and inhomogeneous temperature fields during and after solidification [1]. Warpage remains a persistent manufacturing challenge and highlights the need for robust prediction and compensation strategies across industrial applications [2].

The magnitude of shrinkage and warpage depends on a broad set of interacting factors, including material behavior, part design, process settings (for example melt temperature, injection time, injection pressure, holding pressure, and cooling time), and cavity design [3]. Each of these factors offers potential for improvement. For instance, materials with lower thermal expansion tend to reduce warpage, and wall-thickness design is especially influential, since large thin-walled components are particularly susceptible to distortion [4], [5]. Where functional requirements permit, optimized wall-thickness distributions can significantly decrease warpage [6]. Process-parameter optimization has been addressed with a range of methods, including genetic algorithms [7], [8], response-surface approaches [9], [10], [11], Bayesian optimization [12], [13], and particle swarm optimization [3], [14], [15]. In addition, locally adapted cooling strategies have shown strong potential for warpage reduction [16], [17].

This paper focuses on geometry-compensation methods, in which the mold cavity is intentionally modified to counteract expected deformation. In this concept, the molded part still deforms, but ideally relaxes toward the target geometry after cooling [18]. Although such compensation can be implemented experimentally through iterative measurement and manual cavity correction, this approach is typically costly and time-intensive [19], [20]. As an alternative, simulation-based numerical methods have been proposed to compute compensated cavity geometries in a systematic and efficient manner. These include the normal vector method, where the cavity surface is displaced along mesh-node normal vectors by the deviation from the ideal geometry [21], and a combined approach of process-parameter optimization and cavity-contour optimization [22].

The present work extends the interpolation-based reverse geometry method introduced in [23] with three robustness modifications for complex geometries with automatic remeshing. The specific contributions of this paper are: (1) a surface correction step that projects remeshing-induced surface outliers back onto the previous-iteration geometry; (2) a closest-point ideal-geometry correction that prevents interpolation-error accumulation in curved regions; (3) an iterative update of the injection point; and (4) a demonstration of the complete compensation workflow on two industry-relevant geometries using the commercial simulation software Moldflow Insight.

The remainder of this paper is organized as follows. Section 2 reviews recent methodological developments in geometric warpage compensation within the Collaborative Research Centre SFB 1120. The following section describes the adapted reverse geometry method and formalizes the three new modification. Section 4 presents numerical results for both benchmark geometries and discusses the convergence behavior, followed by a conclusion and an outlook on future work.

2 Recent Advancements in Warpage Compensation

The initial approach within the SFB 1120 was to develop an inverse design formulation for injection molding based on nonlinear thermoelastic material models [24], [25], [26], [27]. This stage introduced the key idea that warpage compensation should be treated as an inverse problem driven by physically based simulations rather than as a trial-and-error correction. With this method, the cavity geometry can be computed directly; however, the temperature field in the cavity must be prescribed a priori [28]. The advantage of the inverse method is that no iterative process is required. The main disadvantages are the complex implementation and the fact that the method cannot be used with commercial simulation software.

To gain more flexibility, the compensation problem was subsequently formulated as a simulation-based cavity-shape optimization problem [29]. This method combines a finite-element warpage model with spline-based free-form deformation and Bayesian optimization, where Gaussian process regression serves as a surrogate to reduce the number of expensive forward simulations. An adaptive search-space strategy improves optimization efficiency and robustness during the iterative design loop. The reported numerical example demonstrates a clear warpage reduction and shows that Bayesian optimization can provide an effective route to compensated cavity geometries. A practical limitation is the high dimensionality of the parameterization, which increases the number of required iterations.

To evaluate and compare the available methods, a systematic benchmark was performed in [30]. Shape optimization was compared with the normal vector method [21], the reverse geometry method, and the inverse method across five different geometries. The reverse geometry method and the normal vector method performed best overall. However, the normal vector method has difficulties with small geometric features and requires hyperparameter tuning. The reverse geometry method is straightforward to implement and follows a simple iterative principle: it computes the remaining warpage as the nodal deviation from the ideal geometry and updates the cavity shape accordingly. Its main limitation is the requirement of node-wise correspondence between meshes, which is not guaranteed when commercial simulation tools enforce remeshing between iterations. The inverse method also shows good compensation performance but is intrusive, requires modifying the simulation-model source code, and cannot be applied with commercial tools. Shape optimization is functional but computationally more expensive and, in this benchmark, yielded lower compensation quality.

To overcome the mesh-correspondence limitation, an interpolation-based extension of the reverse geometry method was introduced in [23]. In this approach, deformation information is interpolated between changing meshes using radial basis function (RBF) interpolation, so that the cavity update remains possible even when remeshing occurs between iterations. This preserves the core iterative compensation concept while making the method compatible with commercial simulation workflows.

The reverse geometry method has also been transferred to metal casting [31]. In that work, the simulation-based compensation loop includes models of both the mold and the part, which must both be updated iteratively. The study demonstrated efficient warpage reduction on a test geometry, showing that the core idea of geometric pre-compensation is not process-specific but can be generalized to other melt-based manufacturing routes.

3 Methods

The warpage-compensation algorithm is based on the interpolation-extended reverse geometry method proposed in [23]. In that work, the interpolation scheme used to transfer ideal-geometry information to newly generated mesh nodes is described in detail. For the present study, three additional modifications were introduced to improve robustness for complex geometries with automatic remeshing.

The first modification addresses remeshing-induced surface distortions. In some iterations, remeshing slightly altered the outer contour of the part. To reduce these deviations, a remeshing-correction step was introduced. Surface nodes whose distance from the previous compensated geometry exceeds a prescribed threshold are identified, local surface normals are computed, and the affected nodes are shifted along these normals by the corresponding implicit-distance value d_i. The same correction is then applied to the corresponding nodes of the warped mesh. In this way, remeshing artifacts are reduced before the interpolation and compensation steps are carried out. The second modification addresses the accumulation of interpolation errors over multiple iterations. This effect is particularly pronounced in regions of high curvature, where tetrahedral meshes represent the geometry only approximately. Therefore, in each iteration, the interpolated ideal geometry on the current mesh is corrected using the true ideal surface. For every node of the interpolated ideal geometry, the closest point on the true ideal surface is determined, and the resulting correction vector v_i is added to the node coordinates. This prevents interpolation errors from accumulating over successive remeshing steps. The third modification is the iterative update of the injection point. After each iteration, the injection point is interpolated from the ideal geometry to the current compensated geometry and projected onto the current surface, ensuring a consistent injection-point location throughout the iterative loop.

The adapted reverse geometry method is summarized in Algorithm 1. In the notation used below, subscripts denote the compensation state, whereas superscripts denote the mesh on which the geometry is represented. Since the mesh is regenerated in each iteration, both indices increase

during the iterative process. Consequently, the ideal geometry stored on the previous mesh must be interpolated onto the current mesh before the compensation update is applied.

Algorithm 1: Summary of the adapted reverse geometry method. Subscripts denote the compensation state, and superscripts denote the mesh index.

Run an initial warpage simulation on the ideal geometry $x_0^0 = x_{ideal}^0$ to obtain the corresponding warped geometry $\tilde{x}_0^0$.
for $k = 0, \ldots, K-1$ do
1. Compute the compensated geometry for the next iteration: $x_{k+1}^k = x_{ideal}^k - (\tilde{x}_k^k - x_k^k)$.
2. Remesh the compensated geometry to obtain x_{k+1}^{k+1}.
3. Run the warpage simulation for the remeshed compensated geometry to obtain the warped geometry $\tilde{x}_{k+1}^{k+1}$.
4. Compute the implicit distance d_i from each node of x_{k+1}^{k+1} to the previous mesh representation x_{k+1}^k.
5. If $|d_i| > \varepsilon = 10^{-6}$ shift the corresponding node of x_{k+1}^{k+1} along its surface normal by the distance d_i.
6. Apply the same correction to the corresponding node of $\tilde{x}_{k+1}^{k+1}$.
7. Interpolate the ideal geometry onto the new mesh: $x_{ideal}^{k+1} = interpolate(x_{k+1}^k, x_{ideal}^k, x_{k+1}^{k+1})$ using a combination of sampling and radial basis function interpolation.
8. For each node of x_{ideal}^{k+1}, compute the closest point on the surface of x_{ideal}^0.
9. Add the resulting correction vector v_i to the node coordinates of x_{ideal}^{k+1}.
10. Update the injection point by interpolating it to the current compensated geometry and projecting it onto the surface.
end for

All correction steps were implemented using the Python library PyVista [32]. With these extensions, the adapted reverse geometry method can be applied reliably to complex parts, even when remeshing is enforced in every iteration. In each iteration, warpage is evaluated by the root mean square error (RMSE) between the nodal coordinates of the deformed geometry $\tilde{\boldsymbol{x}}_k^k$ and those of the corrected interpolated ideal geometry $\boldsymbol{x}_{ideal}^k$. For a mesh with N nodes, the RMSE in iteration k is defined as:

$$RMSE_k = \sqrt{\frac{1}{N}\sum_{i=1}^{N}\left\|\tilde{\boldsymbol{x}}_{k,i}^k - \boldsymbol{x}_{ideal,i}^k\right\|_2^2} \quad (1)$$

4 Numerical Example and Discussion

For the warpage simulation we use the commercial simulation software Moldflow Insight 2023 from Autodesk, Inc, San Francisco, California, United States. The polyoxymethylene (POM) used in the simulation is Hostaform C 9021 from Celanese Corporation, Irving, Texas, USA. The melt temperature is set at 210°C. Two benchmark geometries were examined, namely a stacking box and a housing case (Figures 1 and 2). The adapted reverse geometry method was applied for 9 iterations to the stacking box and for 80 iterations to the housing case. In the cases studied, convergence was typically achieved within 2 to 10 iterations. The longer run for the housing case was performed to assess long-term stability and to confirm the absence of divergence at larger iteration counts.

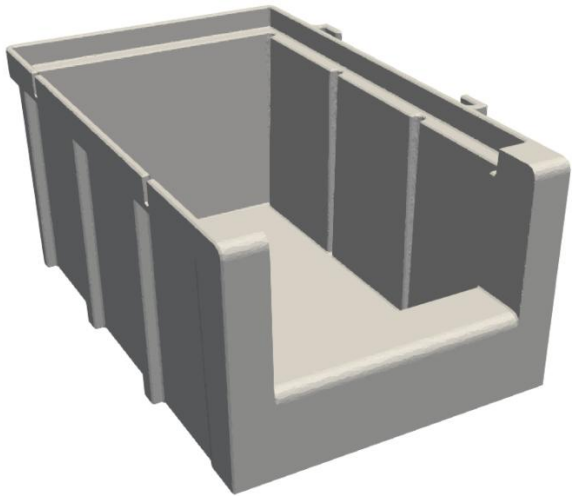

Figure 1: 3D view of the stacking box geometry. The size of the box is 100 mm in width, 160 mm in depth, and 75 mm in height. The injection point is placed in the middle of the bottom of the box.

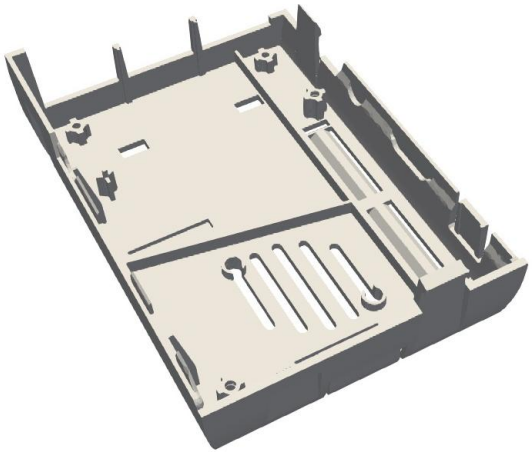

Figure 2: 3D view of the housing case geometry. The size of the case is 65 mm in width, 90 mm in depth, and 20 mm in height. The injection point is placed in the middle of the bottom of the case.

For the stacking box, the RMSE of the nodal warpage decreases from 1.25 mm in the initial configuration to 0.0035 mm after the second iteration (Figure 3), which corresponds to a reduction factor of approximately 357. Beyond this rapid initial decrease, only minor oscillations remain, indicating that the method converges after about two iterations. Figure 4 shows the residual nodal warpage field with a display range of 0.02 mm. Most regions of the component exhibit residual warpage close to zero, whereas larger residuals are concentrated in highly curved regions. These localized deviations are primarily caused by geometric approximation errors of the tetrahedral mesh in curved areas and can be reduced by further mesh refinement. Smaller residuals in other regions result from remeshing-related interpolation errors; however, these are corrected in subsequent iterations and therefore do not accumulate.

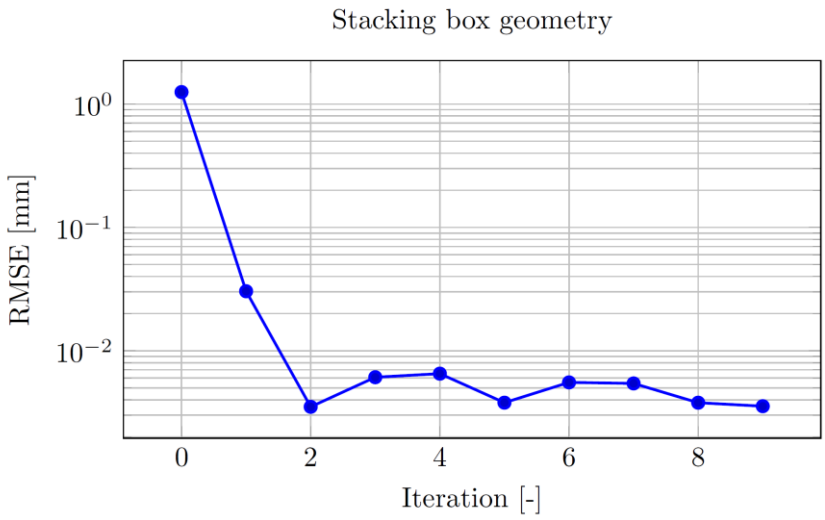

Figure 3: RMSE of the warpage for each iteration using the adapted reverse geometry algorithm for the stacking box geometry.

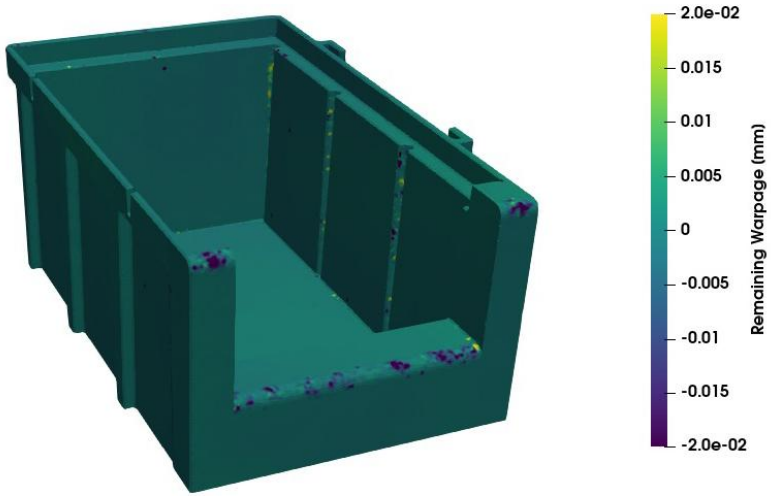

Figure 4: Remaining warpage for each mesh node for the stacking box geometry. Positive values indicate warpage in the direction of the local surface normal pointing outwards, while negative values indicate warpage in the opposite direction.

For the housing case, a similar convergence behavior is observed (Figure 5). The RMSE decreases from 0.58 mm in the initial configuration to 0.0027 mm after 10 iterations, corresponding to a reduction factor of approximately 214. Beyond the tenth iteration, the solution remains in a low-amplitude oscillatory regime, indicating stable convergence. A slight increase around iteration 60 is followed by a renewed decrease, which further supports the numerical robustness of the method. Figure 6 shows the residual nodal warpage field with a display range of 0.01 mm. Most regions remain below 0.006 mm, whereas larger residuals are again concentrated in locally curved features.

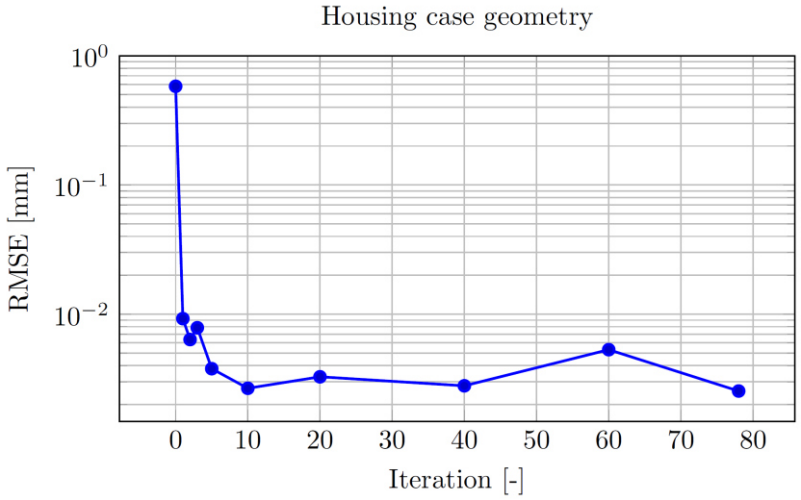

Figure 5: RMSE of the warpage for each iteration using the adapted reverse geometry algorithm for the housing case geometry.

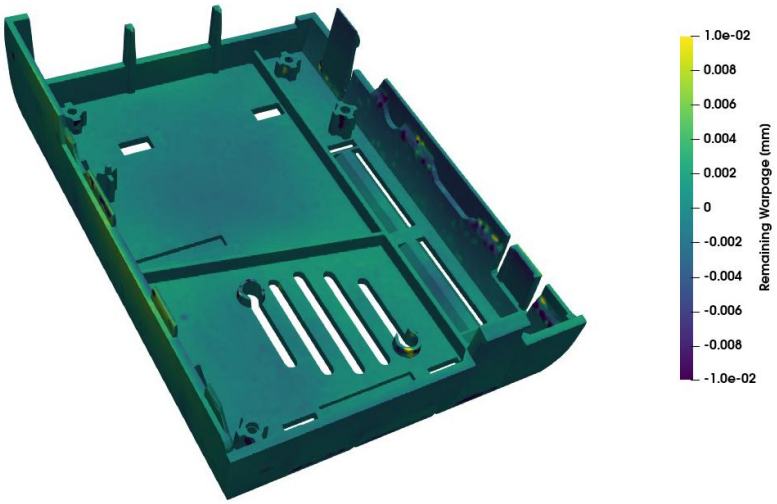

Figure 6: Remaining warpage for each mesh node for the housing case geometry. Positive values indicate warpage in the direction of the local surface normal pointing outwards, while negative values indicate warpage in the opposite direction.

Overall, the two case studies demonstrate that the adapted reverse geometry method provides rapid and robust warpage reduction. In both examples, the error decreases substantially within the first few iterations, while stable behavior is maintained even over extended iterative runs. The computational cost of the compensation procedure itself is negligible compared with the cost of the warpage simulation. Therefore, only the number of iterations is reported, whereas wall-clock times are not considered separately.

5 Summary and Outlook

The main conclusion of this study is that geometric warpage compensation is most effective when formulated as an iterative, simulation-coupled design problem. Within the development path of SFB 1120, the progression from inverse thermoelastic design to optimization-based and reverse

geometry approaches highlights two key requirements for practical application: robust handling of remeshing and low algorithmic complexity.

In the Moldflow-based case studies, the adapted reverse geometry method reduced warpage by more than two orders of magnitude within only a few iterations and remained stable over extended iterative runs. The method thus combines rapid initial error reduction with reliable long-term behavior. The remaining local deviations are concentrated in strongly curved regions and are mainly associated with mesh discretization, indicating that geometric representation quality becomes the dominant limitation once the compensation loop has stabilized. Together with previous findings, these results suggest that the adapted reverse geometry method is a transferable and practically relevant workflow for industrial warpage-compensation problems. At the same time, the present conclusions are based on simulated benchmark geometries and materials; broader validation through experiments on additional industrial components is therefore an important next step.

Future work should combine geometric compensation with complementary warpage-reduction strategies, in particular process-parameter optimization and cooling-layout optimization. In addition, uncertainty-aware compensation methods should be developed to account for variability in material data and process conditions. Finally, manufacturability constraints, especially demoldability and tooling feasibility, should be incorporated directly into the compensation loop.

Acknowledgements

The presented investigations were carried out at RWTH Aachen University within the framework of the Collaborative Research “Centre SFB1120-236616214 Bauteilpräzision durch Beherrschung von Schmelze und Erstarrung in Produktionsprozessen” and funded by the Deutsche Forschungsgemeinschaft e.V. (DFG, German Research Foundation). The sponsorship and support are gratefully acknowledged.

This work was also partly supported by the IRTG Modern Inverse Problems which is funded by the Deutsche Forschungsgemeinschaft (DFG, German Research Foundation) – 333849990/GRK2379.

Conflict of Interest

The authors declare no conflict of interest.

Data Availability Statement

The data and materials for this publication are available on request at the following link: https://coscine.rwth-aachen.de/pid/?pid=21.11102%2fa76bd864-f0a7-4a9e-93f3-9f420334fc5e

References

[1] J. Fischer, *Handbook of molded part shrinkage and warpage*. William Andrew, 2012.

[2] M. Coca-Gonzalez and M. Jimenez-Martinez, "Warpage: Causes, manufacturing processes and future challenges: A review," *Proceedings of the Institution of Mechanical Engineers, Part L: Journal of Materials: Design and Applications*, vol. 239, no. 6, pp. 1201–1217, Jun. 2025, doi: 10.1177/14644207241285399.

[3] N. Zhao, J. Lian, P. Wang, and Z. Xu, "Recent progress in minimizing the warpage and shrinkage deformations by the optimization of process parameters in plastic injection molding: A review," *The International Journal of Advanced Manufacturing Technology*, vol. 120, no. 1–2, pp. 85–101, 2022.

[4] R. Azad and H. Shahrajabian, "Experimental study of warpage and shrinkage in injection molding of HDPE/rPET/wood composites with multiobjective optimization," *Materials and Manufacturing Processes*, vol. 34, no. 3, pp. 274–282, 2019.

[5] Y. Chen and J. Zhu, "Warpage analysis and optimization of thin-walled injection molding parts based on numerical simulation and orthogonal experiment," in *IOP Conference Series: Materials Science and Engineering*, 2019, p. 33027.

[6] B. H. Lee and B. H. Kim, "Variation of part wall thicknesses to reduce warpage of injection-molded part: robust design against process variability," *Polym. Plast. Technol. Eng.*, vol. 36, no. 5, pp. 791–807, 1997.

[7] J. Zhao, G. Cheng, S. Ruan, and Z. Li, "Multi-objective optimization design of injection molding process parameters based on the improved efficient global optimization algorithm and non-dominated sorting-based genetic algorithm," *The International Journal of Advanced Manufacturing Technology*, vol. 78, pp. 1813–1826, 2015.

[8] K. Li, S. Yan, Y. Zhong, W. Pan, and G. Zhao, "Multi-objective optimization of the fiber-reinforced composite injection molding process using Taguchi method, RSM, and NSGA-II," *Simul. Model. Pract. Theory*, vol. 91, pp. 69–82, 2019.

[9] B. S. Heidari *et al.*, "Simulation of mechanical behavior and optimization of simulated injection molding process for PLA based antibacterial composite and nanocomposite bone screws using central composite design," *J. Mech. Behav. Biomed. Mater.*, vol. 65, pp. 160–176, 2017.

[10] M. U. Rosli, S. N. A. A. Termizi, C. Y. Khor, M. A. M. Nawi, A. A. Omar, and M. I. Ishak, "Simulation Based Optimization of Thin Wall Injection Molding Parameter Using Response Surface Methodology," in *IOP Conference Series: Materials Science and Engineering*, 2020, p. 12193.

[11] S. J. A. Rizvi, A. K. Singh, and G. R. Bhadu, "Optimization of tensile properties of injection molded α-nucleated polypropylene using response surface methodology," *Polym. Test.*, vol. 60, pp. 198–210, 2017.

[12] X. Wang, J. Gu, C. Shen, and X. Wang, "Warpage optimization with dynamic injection molding technology and sequential optimization method," *The International Journal of Advanced Manufacturing Technology*, vol. 78, pp. 177–187, 2015.

[13] H. Li, K. Liu, D. Zhao, M. Wang, Q. Li, and J. Hou, "Multi-objective optimizations for microinjection molding process parameters of biodegradable polymer stent," *Materials*, vol. 11, no. 11, p. 2322, 2018.

[14] Y. Xu, Q. Zhang, W. Zhang, and P. Zhang, "Optimization of injection molding process parameters to improve the mechanical performance of polymer product against impact," *The International Journal of Advanced Manufacturing Technology*, vol. 76, pp. 2199–2208, 2015.

[15] J. Zhang, J. Wang, J. Lin, Q. Guo, K. Chen, and L. Ma, "Multiobjective optimization of injection molding process parameters based on Opt LHD, EBFNN, and MOPSO," *The International Journal of Advanced Manufacturing Technology*, vol. 85, pp. 2857–2872, 2016.

[16] S. Kitayama, Y. Yamazaki, M. Takano, and S. Aiba, "Numerical and experimental investigation of process parameters optimization in plastic injection molding using multi-criteria decision making," *Simul. Model. Pract. Theory*, vol. 85, pp. 95–105, 2018.

[17] C. Hopmann and P. Nikoleizig, "Inverse thermal mold design for injection molds: Adressing the local cooling demand as quality function for an inverse heat transfer problem," *International Journal of Material Forming*, vol. 11, pp. 113–124, 2018.

[18] M. Keuerleber and P. Eyerer, "6 Gestalten, Fügen, Berechnungsansätze und Simulation EDV-unterstützter Konstruktionen und Auslegung von Kunststoffbauteilen," *Polymer Engineering*, pp. 466–485, 2008.

[19] R. Schlutter, *Einstieg in die Spritzgießsimulation*. Munich: Carl Hanser Verlag GmbH Co KG, 2023.

[20] H. Zhai *et al.*, “A research method to improve the quality of box-type thin-walled parts by combining parameter optimization and inverse-deformation design,” 2022, doi: https://doi.org/10.21203/rs.3.rs-1733087/v1.
[21] T. Kastelic, B. Starman, G. Cafuta, M. Halilovic, and N. Mole, “Correction of mould cavity geometry for warpage compensation,” *The International Journal of Advanced Manufacturing Technology*, vol. 123, no. 5–6, pp. 1957–1971, 2022.
[22] D. Godec, F. Panđa, M. Tujmer, and K. Monkova, “Molded Part Warpage Optimization Using Inverse Contouring Method,” *Polymers (Basel).*, vol. 17, no. 17, p. 2278, Aug. 2025, doi: 10.3390/polym17172278.
[23] S. Tillmann, S. Schwan, D. C. Fritsche, C. E. Kahve, S. Elgeti, and C. Hopmann, “Using the reverse geometry method for warpage compensation on changing meshes with interpolation methods,” *PAMM*, vol. 24, no. 4, p. e202400010, 2024.
[24] F. Zwicke and S. Elgeti, “Inverse design based on nonlinear thermoelastic material models applied to injection molding,” *Finite Elements in Analysis and Design*, vol. 165, pp. 65–76, 2019.
[25] F. Zwicke, M. Behr, and S. Elgeti, “Predicting shrinkage and warpage in injection molding: Towards automatized mold design,” in *AIP Conference Proceedings*, 2017, p. 100001.
[26] F. Zwicke, T. Hohlweck, C. Hopmann, and S. Elgeti, “Inverse design based on nonlinear thermoelastic material models,” *PAMM*, vol. 20.1, p. e202000130, 2021.
[27] F. Zwicke, T. Schneppe, C. Hopmann, and S. Elgeti, “Numerical Design for Primary Shaping Manufacturing Processes,” *PAMM*, vol. 18, no. 1, Dec. 2018, doi: 10.1002/pamm.201800218.
[28] F. Zwicke, M. Behr, and K. Veroy, “Inverse Shape Design in Injection Molding Based on the Finite Element Method,” 2020.
[29] S. Tillmann, M. Behr, and S. Elgeti, “Using Bayesian optimization for warpage compensation in injection molding,” *Materwiss. Werksttech.*, vol. 55, no. 1, pp. 13–20, 2024, doi: https://doi.org/10.1002/mawe.202300157.
[30] S. Tillmann, S. Basermann, and S. Elgeti, “Comparison of Numerical Methods for Geometric Warpage Compensation,” *Int. J. Numer. Methods Fluids*, vol. 97, no. 9, pp. 1280–1288, Sep. 2025, doi: 10.1002/fld.5404.
[31] S. Tillmann, S. Gor, S. Elgeti, A. Bührig-Polaczek, and B. Pustal, “Iterative Mold Adaptation for Pre-Compensation of Warpage in Aluminum Casting,” *PAMM*, vol. 26, no. 1, Mar. 2026, doi: 10.1002/pamm.70057.
[32] C. Sullivan and A. Kaszynski, “PyVista: 3D plotting and mesh analysis through a streamlined interface for the Visualization Toolkit (VTK),” *J. Open Source Softw.*, vol. 4, no. 37, p. 1450, May 2019, doi: 10.21105/joss.01450.

Date: 30.03.2026

Advancing Casting Quality with Predictive Thermomechanical Simulation and Targeted Compensation Strategies

Author: G. Nassar

Authors: G. Nassar, B. Pustal, A. Bührig-Polaczek, S. Tillmann, S. Elgeti

[1]Foundry Institute, RWTH Aachen University, Intzestrasse 5, 52072, AACHEN, GERMANY

[2]Chair for Computational Analysis of Technical Systems, RWTH Aachen University, 52062, AACHEN, GERMANY

*Corresponding author: E-mail: g.nassar@gi.rwth-aachen.de

Abstract

Solidification in metal casting is accompanied by distortion, hotspot formation, and crack initiation, all of which degrade final part quality. This study presents an ABAQUS-based coupled thermomechanical simulation framework that integrates a novel temperature- and gap-width-dependent heat transfer coefficient (HTC) model with microstructure-informed material data to capture the thermal–mechanical response during cooling of aluminum alloy A356 in gravity die casting. The HTC model distinguishes four interface contact states—liquid–solid contact, pressureless solid contact, contact-pressure-dominated, and air-gap-dominated regimes—and is validated against experimental measurements of temperature, air gap width, and contact pressure. Building on these predictions, the influences of oil tempering temperature and demolding temperature on solidification behavior and final distortion are systematically investigated. Two complementary compensation strategies are then developed: thermally sprayed heating conductor coatings applied as localized heat sources to redirect solidification towards the feeder, and an iterative geometric compensation method that adjusts the mold cavity geometry to offset predicted deformation. Both compensation approaches perform as intended: coatings promote more uniform solidification, while the reverse geometry method reduces warpage by two orders of magnitude. Together, these innovations enhance simulation-driven control of casting quality.

Keywords

thermomechanical simulation, heat transfer coefficient, distortion, warpage compensation, heating conductor, gravity die casting, A356

1 Introduction

Permanent mold casting of aluminum alloys is a widely used manufacturing process valued for its combination of favorable mechanical properties and good dimensional accuracy. However, the solidification of a metallic melt inside a rigid mold cavity is inevitably accompanied by a range of thermomechanical phenomena—including volumetric shrinkage, thermal contraction, air gap formation, contact pressure buildup, residual stress development, and distortion—that can compromise the quality and dimensional integrity of the finished part [1, 2]. Addressing these issues post-production through machining or straightening entails substantial cost and process complexity. Consequently, the ability to predict and compensate for such defects prior to or during the casting process is of significant industrial and scientific interest.

The accuracy of any thermomechanical casting simulation depends critically on the description of heat transfer at the casting–mold interface. The heat transfer coefficient (HTC) at this interface varies locally and temporally as a function of the evolving contact conditions, transitioning from an initial liquid–solid contact to either an air-gap-dominated or contact-pressure-dominated regime as solidification progresses [3, 4]. A physically motivated HTC model that accounts for these transitions is therefore essential for reliable prediction of temperature fields, solidification sequences, and ultimately the resulting distortion.

Beyond accurate simulation, reducing distortion requires active compensation strategies. Two fundamentally different approaches can be distinguished: thermal compensation, which modifies the local heat balance to influence the solidification sequence, and geometric compensation, which pre-adjusts the mold cavity shape so that the predicted warpage transforms the part into the desired final geometry. Thermal compensation can be realized through thermally sprayed heating conductor coatings that provide localized, near-surface heat input at the casting–mold interface [7, 10]. Geometric compensation can be achieved through iterative methods such as the reverse geometry approach or shape optimization algorithms [8].

This paper consolidates the research outcomes of DFG-funded Collaborative Research Centre SFB1120 at RWTH Aachen University, presenting the development and validation of a coupled thermomechanical simulation framework, the systematic investigation of process parameter influences on solidification and distortion, and the development of both thermal and geometric compensation strategies for gravity die casting of aluminum alloy A356 (AlSi7Mg0.3).

2 Aim of the Investigation

The overarching objective of this work is to develop and validate a simulation-driven framework for predicting and mitigating solidification-induced defects in gravity die casting. Specifically, the investigation pursues three interrelated goals. First, the development and experimental validation of a coupled thermomechanical simulation framework in ABAQUS, with particular attention to the accurate modeling of the HTC at the casting–mold interface under conditions of local air gap formation and contact pressure. Second, the systematic investigation of how process parameters—

specifically oil tempering temperature and demolding temperature—influence solidification characteristics and final part distortion. Third, the development and evaluation of two distinct compensation strategies: the application of thermally sprayed heating conductor coatings as localized heat sources for influencing the solidification sequence and mitigating hotspots, and the use of iterative geometric compensation methods for reducing warpage through pre-compensated mold cavity design.

3 Materials and Experimental Details

3.1 Experimental Setups

Two complementary experimental setups were developed for this research program. The first setup, used for investigating heat transfer and solidification, features a rotationally symmetric "bowl" geometry cast on an inner steel core (Figure 1). Aluminum alloy A356 is gravity cast into a central feeder at 720°C, with a filling time of approximately 5 seconds. The outer casting cavity wall consists of copper inserts fitted into a steel die and temperature-controlled via oil-filled cooling channels, ensuring quasi-one-dimensional radial heat flow. Temperature development is measured via Type-K thermocouples at multiple positions, local material movement via quartz rods connected to LVDTs for air gap determination and contact pressure on the inner core surface via a load cell arrangement [3, 5].

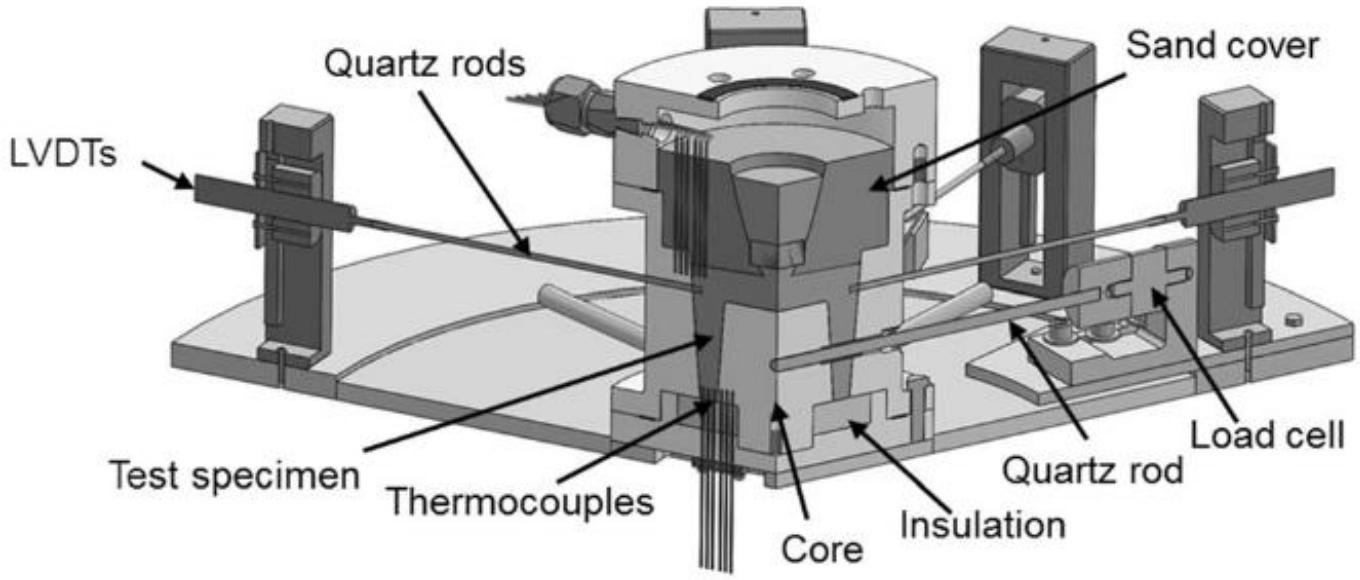

Figure 1: (a) Schematic of the rotationally symmetric "bowl" experimental setup with measurement instrumentation. (b) Thermocouple positions in the die and casting [3].

The second setup, developed for investigating distortion behavior, employs an "F"-shaped casting geometry with a central feeder that also serves as sprue (Figure 2). A modular steel die with four independent oil cooling circuits surrounds the casting cavity. The base consists of a ceramic insulation sheet, while the upper mold cover is made of sand. This configuration directs the primary heat dissipation through the steel die walls. Distortion is quantified as the change in distance

between the two flanges of the “U”-shaped region of the casting, measured on both inner and outer sides [6, 7].

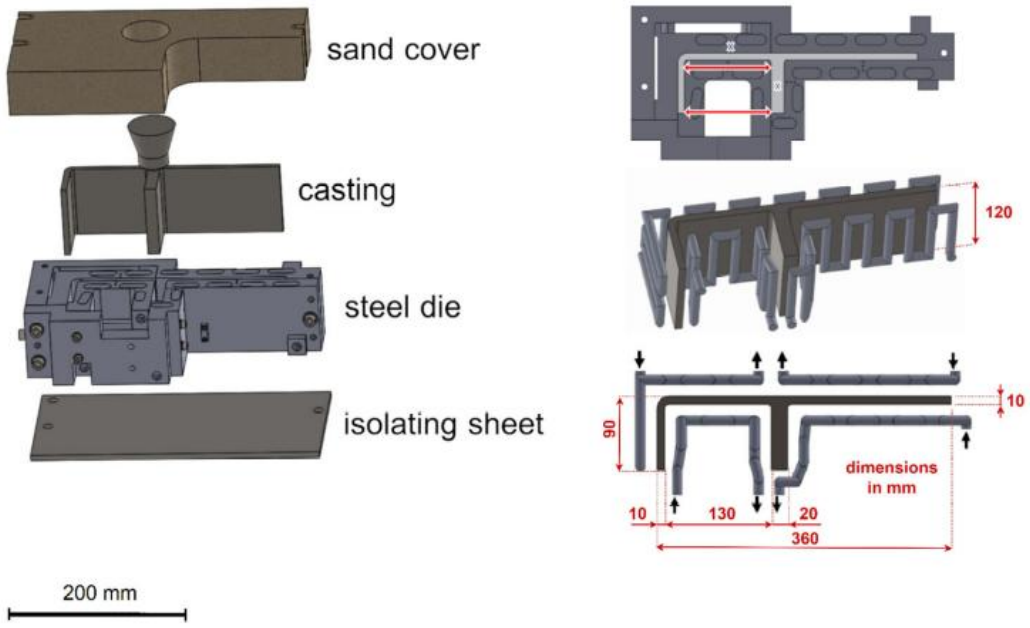

Figure 2: (a) Schematic of the “F”-shaped casting setup with modular die and cooling channels. (b) Dimensions and distortion measurement positions [6].

3.2 Simulation Framework

All simulations are performed as coupled thermomechanical analyses using the commercial finite element software ABAQUS. The framework applies the principle of virtual work for the displacement field and the heat equation for the temperature field in a fully coupled formulation, solving the system simultaneously to account for the interdependence of stress and temperature fields [6, 8]. The liquid–solid phase change is modeled through a user-defined algorithm for latent heat release, implemented via the ABAQUS HETVAL subroutine. The temperature-dependent fraction solid curve (Figure 3a) is derived from a three-dimensional, thermodynamically coupled phase field simulation of the A356 microstructure using the Micress software, capturing heterogeneous nucleation followed by primary and eutectic solidification [3, 4]. The liquid melt is modeled as a viscous solid with strain-rate-independent behavior. Temperature-dependent material properties—including density, specific heat, elastic modulus, thermal conductivity, and thermal expansion coefficient—are incorporated, with plastic behavior data sourced from the literature [6, 13].

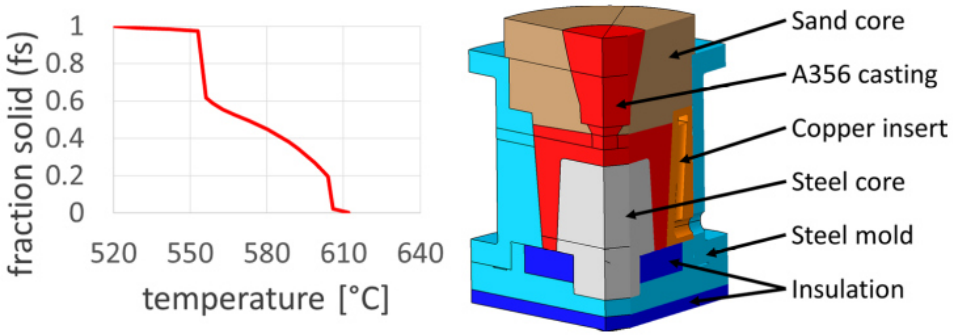

Figure 3: (a) Fraction solid development for A356 as a function of temperature, obtained via coupled phase field simulations with Micress. (b) Representative ABAQUS simulation model and mesh [3].

For the "F"-shaped casting simulations, the initial temperature distribution after mold filling is obtained from a separate filling simulation performed using MAGMAsoft, as the Lagrangian mesh formulation of the FEM solver precludes direct simulation of the pouring process [6].

3.3 HTC Modeling Approach

The HTC model distinguishes four contact states based on experimental observations [3, 4, 9]. In state A, a liquid–solid contact exists before coherence of the solidifying alloy is reached (approximately 565°C for A356), with an HTC value of 2000 W/(m²·K). Once a load-bearing solid shell has formed, the contact transitions to a pressureless solid–solid contact (state B) with an HTC of 1000 W/(m²·K). Subsequently, depending on local geometry, either contact pressure builds up as the casting shrinks onto internal features such as a core (state C), or an air gap forms as the casting contracts away from the outer mold wall (state D). For the contact-pressure condition, the HTC increases exponentially to a maximum of approximately 4000 W/(m²·K). For the air-gap condition, the HTC is governed by Fourier's law of heat conduction through the gap, decreasing rapidly with increasing gap width to an asymptotic value of approximately 100 W/(m²·K) for large gaps (Figure 4). These models are implemented via the ABAQUS GAPCON user subroutine [3].

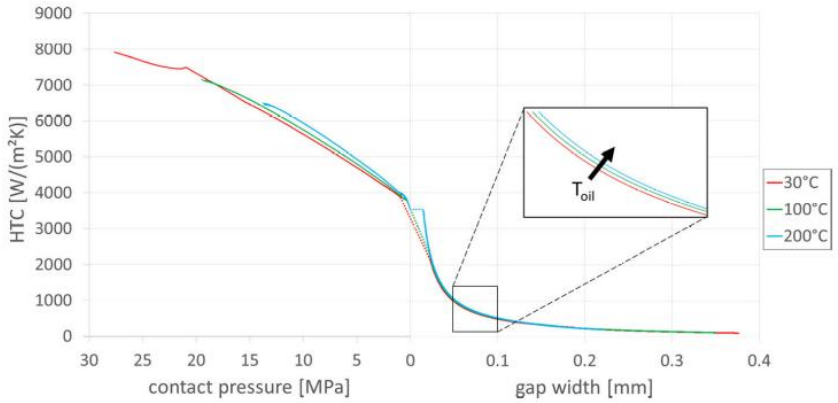

Figure 4: Experimentally determined HTC as a function of contact pressure (left) and gap width (right) for different oil tempering temperatures [3].

4 Results and Discussion

4.1 Simulation Validation

The simulation results were validated against experimental measurements at multiple levels. As shown in Figure 5, the predicted cooling curves show good qualitative agreement with experimental data, particularly during the critical phase change regime. The simulated gap width development exhibits the same increasing trend as the experimental data, with a systematic overestimation of approximately 15–20% in the final gap size and a time delay in the onset of gap formation. This discrepancy may be attributed to the finite element mesh resolution, which is insufficient to resolve the formation of a very thin load-bearing solid chill at the interface, a phenomenon that enables immediate gap formation in the experiment but requires complete local solidification in the simulation. The simulated contact pressure development agrees well with the experimental measurements up to approximately 60 seconds, after which experimental measurement artifacts temporarily disturb the recorded values [3].

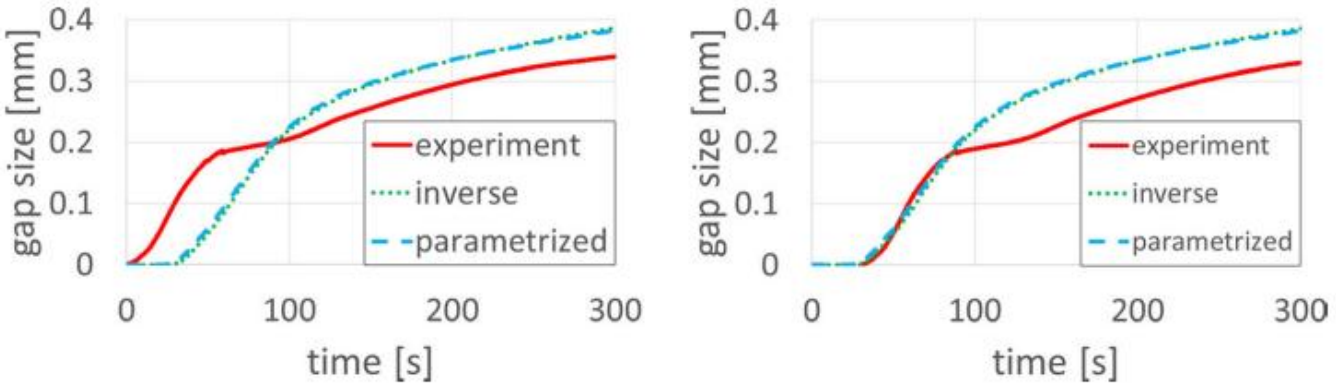

Figure 5: Comparison of experimental and simulated cooling curves, gap width development, and contact pressure development for the 30°C oil tempering case [3].

4.2 Process Parameter Influences

A systematic investigation of oil tempering temperature influence was conducted using the bowl setup with tempering levels of 30, 100, 200, and 300°C [5]. The thermal analysis reveals that in the upper region with its large melt reservoir, the onset of primary solidification is nearly independent of the oil tempering setting, owing to aluminum's high thermal conductivity. In the lower, thinner-walled region, however, the tempering level exerts a clear influence, with undercooling differences of up to 5°C between settings. The total solidification time scales nonlinearly with die tempering: an increase from 30°C to 300°C nearly doubles the solidification time, with the percentage increase per degree growing at higher base temperatures. Regarding the mechanical response, lower tempering temperatures lead to larger and faster-developing air gaps, while contact pressure on the inner core reaches higher maxima (approximately 25 MPa at 30°C vs. 14 MPa at 200°C). However, the von Mises stress as a function of casting–metal interface temperature shows no significant dependency on die tempering—all curves are nearly identical. The die tempering thus primarily

affects the temporal development of thermomechanical quantities rather than their fundamental relationship to local temperature [5].

The influence of demolding temperature on final distortion was investigated numerically using the "F"-shaped casting with demolding temperatures of 562, 347, 285, 190, and 30°C [6]. Two key mechanisms governing final distortion were identified. The first is the release of accumulated elastic strain at the moment of demolding: as shown in Figure 6, at low demolding temperatures the material's higher yield point allows substantial elastic strain to accumulate, producing a discontinuous jump in distortion upon mold removal. At high demolding temperatures, most deformation during in-mold cooling is plastic, leaving negligible elastic strain to release. The second mechanism is post-demolding thermal strain accumulation, which closely aligns with cumulative thermal contraction as the casting cools to room temperature [6].

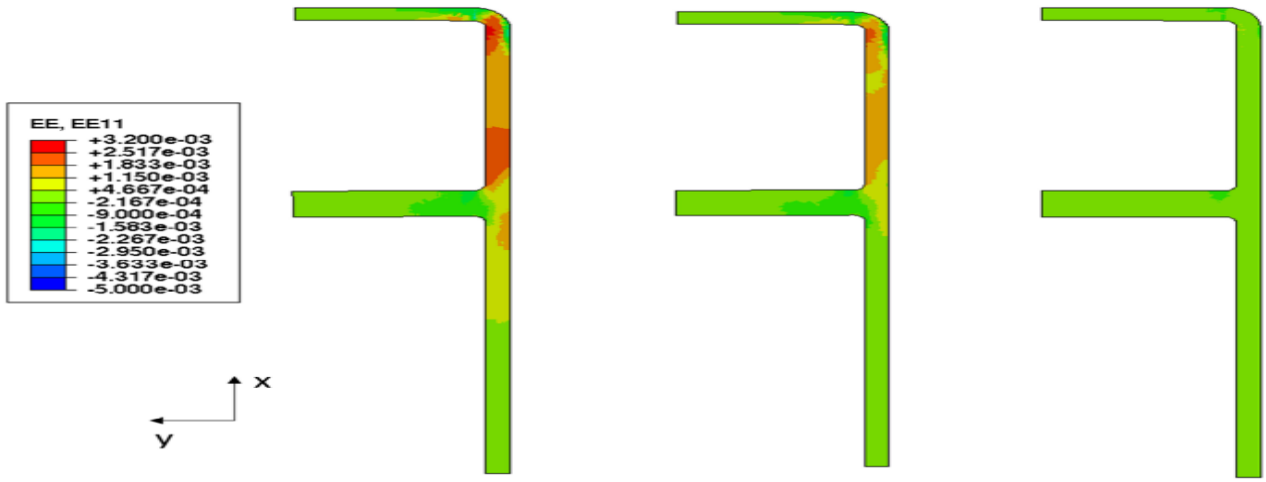

Figure 6: Elastic strain (x-component) immediately before demolding at 30°C, 190°C, and 562°C, illustrating the accumulation of elastic strain at lower demolding temperatures [6].

Comparison with experiments (Figure 7) reveals qualitatively similar trends: both simulation and experiment show converging inner and outer distortion trendlines with increasing demolding temperature. However, a quantitative offset exists that increases linearly with demolding temperature (0.06 mm per 100°C for outer distortion, 0.13 mm per 100°C for inner distortion), attributed primarily to the Lagrangian mesh formulation's inability to account for feeding dynamics during solidification [6].

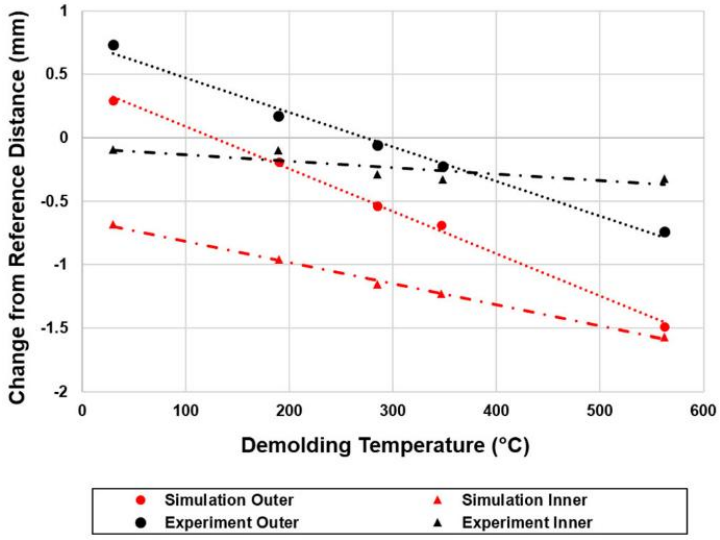

Figure 7: Comparison of outer and inner final distortion at different demolding temperatures for experimental and simulation data, with linear trendlines [6].

4.3 Thermal Compensation via Heating Conductor Coatings

The first compensation strategy targets modification of the local heat balance through heating conductor layers integrated into plasma-sprayed mold coatings [7, 10]. For the "F"-shaped casting, the four junctions connecting the base section to the flanks of the "U"-shaped region were identified as critical areas with hindered thermal shrinkage, and heating conductor layers were applied at these locations (Figure 8). Six simulation cases combining two oil temperatures (30 and 300°C) with two surface power densities (10 and 30 W/cm²) plus two reference cases were computed. The simulation proceeded through a 30-minute preheating phase, a 5-minute solidification/cooldown phase with activated conductors, and a 2-hour free-cooling phase after demolding [7].

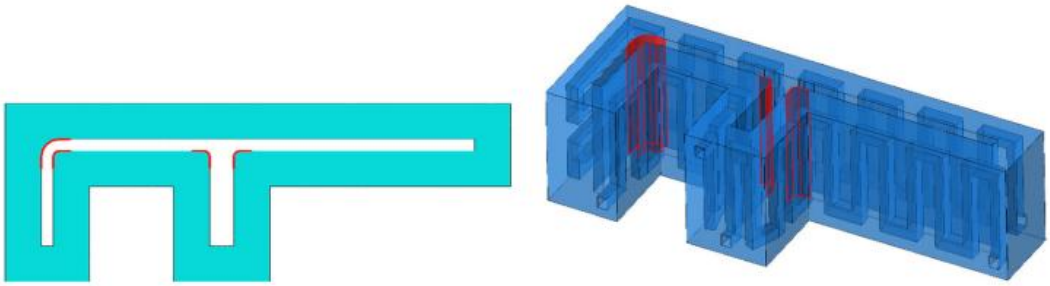

Figure 8: Position of the four junctions fitted with heating conductor layers on the "F"-shaped casting [7].

The heating conductor layers produced measurable changes in both the temperature field and distortion behavior. At evaluation positions, the conductor layers slowed local cooling and raised final temperatures—for instance, casting temperature at 300 seconds increased from 40.4°C to 125.6°C (30°C oil, 30 W/cm²) and from 293.9°C to 388.1°C (300°C oil, 30 W/cm²). The influence on distortion is complex: during the in-mold stage, additional heat opposes extraction, resulting in lower displacements; however, after demolding, higher residual temperatures lead to greater thermal contraction. For the outer flank, final distortion increased by 10–60% depending on power density, while for the inner flank, distortion was reduced by approximately 10% at 30 W/cm². A

key finding is that thermally influencing only the four junctions—rather than the entire mold surface—is a valid approach for significantly affecting the distortion pattern, providing fast, localized, near-interface heat input that cannot be achieved with conventional cooling channels [7].

4.4 Iterative Geometric Compensation for Warpage Reduction

The second compensation strategy addresses distortion through pre-compensation of the mold cavity geometry [8]. Two methods were adapted from injection molding and applied to aluminum casting. The reverse geometry method iteratively updates the mold cavity shape by subtracting the predicted warpage from the ideal geometry: each iteration runs a forward simulation, computes the resulting deformation, and applies the inverse to the cavity shape. Both cast and mold meshes must be simultaneously updated; the mold mesh is adapted using radial basis function (RBF) interpolation-based mesh morphing to maintain mesh quality. The shape optimization method formulates the problem as a derivative-free optimization task using the COBYQA algorithm, minimizing the root mean square distance between the deformed surface and the ideal shape through free-form deformation with quadratic B-spline parametrization [8].

Both methods were applied to an L-shaped test geometry with an initial temperature of 720°C for the cast and 300°C for the mold. As shown in Figure 9, the reverse geometry method achieves rapid convergence, reducing the average RMS warpage from 1.95×10^{-2} mm to approximately 1×10^{-3} mm within the first iteration, ultimately achieving a two-orders-of-magnitude reduction after approximately 20 iterations. The shape optimization approach requires about 1000 iterations to halve the initial warpage, with the first 180 iterations consumed by initialization. While computationally more expensive, shape optimization offers greater generality for incorporating additional objectives such as avoiding hot cracking. For pure warpage reduction, the reverse geometry method is strongly recommended for its superior convergence [8].

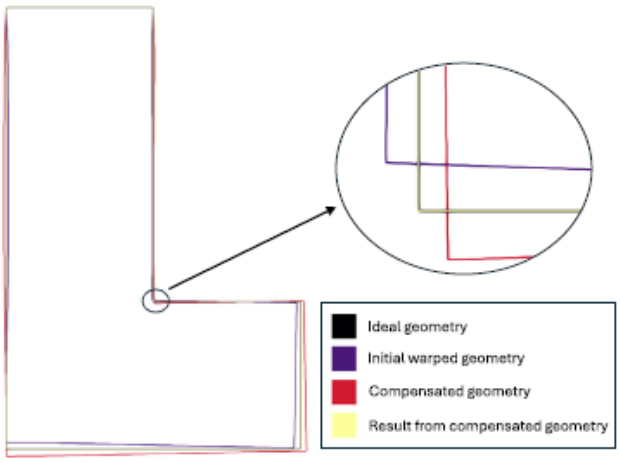

Figure 9: 2D slice comparison of the L-shape geometry showing ideal, initial warpage, compensated, and resulting geometries [8].

5 Summary

This work demonstrates the development of a comprehensive, simulation-driven approach to casting quality control. The coupled thermomechanical simulation framework in ABAQUS, incorporating an HTC model that distinguishes between four contact states (liquid–solid, pressureless solid, contact-pressure-dominated, and air-gap-dominated), provides a robust predictive tool validated against experimental measurements of temperature fields, gap widths, and contact pressures. Key remaining challenges include accurate prediction of initial gap formation onset and the description of feeding dynamics within the Lagrangian framework.

The systematic investigation of process parameters yielded important insights for process optimization. Solidification time scales nonlinearly with die tempering, with each incremental temperature increase having a progressively larger effect—a finding with direct implications for cycle time planning. The identification of two distinct mechanisms governing distortion at demolding—elastic strain release and post-demolding thermal strain accumulation—provides clear guidance for selecting optimal demolding conditions.

Both compensation strategies address the distortion problem from complementary angles. The heating conductor concept provides fast, localized heat input directly at the casting–mold interface, enabling thermal balance modifications unachievable with conventional cooling channels. Its effectiveness in influencing in-mold distortion through targeted application at critical junctions makes it a promising technology for industrial use. The reverse geometry method achieves a reduction in warpage by two orders of magnitude through systematic mold cavity pre-compensation, demonstrating powerful potential even on a simplified test geometry. Their combined application—first optimizing thermal conditions for favorable solidification, then pre-compensating residual warpage through mold cavity design—offers a systematic pathway toward high-precision casting.

Acknowledgements

The presented investigations were carried out at RWTH Aachen University within the framework of the Collaborative Research Centre SFB1120-236616214 “Bauteilpräzision durch Beherrschung von Schmelze und Erstarrung in Produktionsprozessen” and funded by the Deutsche Forschungsgemeinschaft e.V. (DFG, German Research Foundation). The sponsorship and support is gratefully acknowledged. Simulations were performed with computing resources granted by RWTH Aachen University under projects rwth1259 and p0020502.

Conflict of Interest

The authors declare no conflict of interest.

Data Availability Statement

The data that support the findings of this study are available upon reasonable request under

http://hdl.handle.net/21.11102/b74248f6-6d2e-4a25-86ef-b6f2aa27c885

References

[1] J. Campbell, Complete Casting Handbook: Metal Casting Processes, Metallurgy, Techniques and Design, Butterworth-Heinemann, 2015.

[2] A. Bührig-Polaczek, W. Michaeli, G. Spur, Handbuch Urformen, Carl Hanser Verlag, München, 2014.

[3] T. Vossel, N. Wolff, B. Pustal, A. Bührig-Polaczek, M. Ahmadein, Heat transfer coefficient determination in a gravity die casting process with local air gap formation and contact pressure using experimental evaluation and numerical simulation, Int. J. Metalcast. 16 (2022) 595–612.

[4] G. Laschet, J. Jakumeit, S. Benke, Thermo-mechanical analysis of cast/mould interaction in casting processes, Int. J. Mater. Res. 95 (2004) 1087–1096.

[5] T. Vossel, N. Wolff, B. Pustal, A. Bührig-Polaczek, Influence of die temperature control on solidification and the casting process, Int. J. Metalcast. 14 (2020) 907–925.

[6] S. Gor, N. Wolff, B. Pustal, A. Bührig-Polaczek, Numerical analysis of the influence of demolding temperature on final distortion in gravity die casting process, Int. J. Metalcast. 19 (2025) 1507–1515.

[7] T. Vossel, S. Gor, B. Pustal, A. Bührig-Polaczek, Evaluating the application of heating conductor surfaces inside plasma sprayed coatings in permanent mold metal casting processes for local, near-surface heat release, Int. J. Metalcast. 16 (2022) 585–594.

[8] S. Tillmann, S. Gor, S. Elgeti, A. Bührig-Polaczek, B. Pustal, Iterative mold adaptation for pre-compensation of warpage in aluminum casting, PAMM 26 (2026) e70057.

[9] G. Laschet, T. Vossel, N. Wolff, M. Apel, A. Bührig-Polaczek, Multiscale solidification simulation of an axisymmetric A356 component in die casting, Proc. 6th Decenn. Int. Conf. Solidif. Process. (SP17), Old Windsor, UK, 2017, pp. 576–580.

[10] K. Bobzin, M. Öte, M.A. Knoch, I. Alkhasli, Temperature distribution on thermally sprayed heating conductor, IOP Conf. Series: Materials Science and Engineering 480 (2019).

[11] N. Wolff, T. Hohlweck, U. Vroomen, A. Bührig-Polaczek, C. Hopmann, Development of an experimental setup to investigate influences on component distortion in gravity die casting, Metals 11 (2021) 2028.

[12] N. Wolff, S. Gor, U. Vroomen, A. Bührig-Polaczek, Description of component distortion in aluminum gravity die casting as a result of hindered shrinkage, Materialwiss. Werkstofftech. 55 (2024) 33–39.

[13] M.J. Roy, D.M. Maijer, L. Dancoine, Constitutive behavior of as-cast A356, Mater. Sci. Eng. A 548 (2012) 195–205.

[14] B.B. Mikic, Thermal contact conductance; theoretical considerations, Int. J. Heat Mass Transfer 17 (1974) 205–214.

Date: 31.03.2026

Dynamic Laser Beam Welding of Steel & Aluminum Components using Coherent Beam Combining

Author: S. Brechelt[1,*], R. Assa, N. Armon, Z. Sanders

[1]Civan Lasers Europe GmbH, Hollerithallee 16, 30419, HANOVER, GERMANY

*Corresponding author: E-mail: sascha.brechelt@civanlasers.com

Abstract

The quality of the weld seam and process efficiency are two crucial aspects of laser beam welding. Coherent Beam Combining (CBC) contributes to the highest weld seam quality by precisely shaping the temporal and spatial intensity of the laser beam. The Dynamic Beam Laser (DBL) from Civan Lasers enables alignment of the laser spot via beam shaping and can deliver up to 120 kW of laser power. Through dynamic beam shaping and frequency modulation, diverse intensity distributions can be used and varied within microseconds. This enables direct control of heat distribution, manipulation of the melt pool flow, and stabilization of the keyhole. This article focuses on controlling the keyhole during welding steel and aluminum components. It demonstrates how CBC can overcome material-specific challenges to enhance weld seam quality and process efficiency. Additionally, dynamic sequences are employed to actively adjust the laser intensity distribution to match the characteristics of each individual material.

Keywords

Laser Beam Welding, Coherent Beam Combining, Dynamic Sequences, Keyhole Stabilization

1 Introduction

Laser beam welding offers high processing speeds and high joint quality due to its high energy density. This results in high penetration capability combined with a thin heat-affected zone and a limited heat distortion of the base material. [1] Although laser beam welding is used for a wide range of different materials, challenges remain for conventional laser beam sources.

Aluminum die-cast alloys are frequently used in the automotive and electrical industries. Die-cast structural components and housings offer various benefits, such as low production costs in high-volume segments, a lightweight design and corrosion resistance. Current applications commonly use joining techniques such as structural bonding and mechanical processes such as friction stir welding. [2] In comparison, laser beam welding offers the advantage of joining more complex geometries with various weld joint types like butt joint, lap joint or corner joint. The high concentration of bound hydrogen in aluminum die casting is an obstacle, because it leads to high

porosity and an increased risk of cracks and other imperfections when welding. [3] This makes it difficult to manufacture components with higher strength and leak tightness requirements.

Due to the increasing demand for enhanced productivity, single-pass laser beam welding of thick-section steel has great potential. In the butt weld configuration, laser beam welding does not require a complex weld seam preparation, and the capability for single-sided processing reduces the workload significantly. Challenges occur when high processing speeds are required. Fluctuations in the key hole can result in reduced joint quality [4] and the rapid cooling of the material can increase the hardness of the heat-affected zone [5].

The limitations of conventional laser beam sources have led to the development of new technological applications for overcoming challenges when welding aluminum die-castings and thick-section structural steels. Linear oscillation of the laser beam can reduce the porosity content and improve the weld quality. However, this oscillation is limited to a range of several hundred Hertz and uses an amplitude of up to 7 mm. [6] By using a galvo scanner, a combined linear and circular oscillation of the laser beam is possible, [7] but the options for stabilizing the keyhole remain limited. A precise stabilization of the keyhole requires a spatial and temporal control of the laser energy distribution and the resulting local heat input. A coaxial core-ring laser beam with an independent variation of the laser power between the core and the ring shows promising results in terms of controlling the keyhole during welding. [8] Diffractive optical elements offer a spatial control of the laser energy distribution. This approach, a static beam shape, results in an adaptability of the heat input for different materials in the laser welding industry. [9] For a universal adaptability of the laser intensity for different scenarios, a combined spatial and temporal control of the laser intensity is essential. DBL's use several individual fibers to allow spatial and temporal control of the laser intensity within microseconds. This technological approach results in dynamic beam shaping based on CBC. Shifting the laser intensity profile with a frequence of hundred Kilohertz allows a precise alignment of the local heat input and the stabilization of the keyhole. [10]

2 Aim of the Investigation

This paper demonstrates how the DBL from Civan Lasers can contribute to high-quality joints and fast processing speeds when welding aluminum die castings and thick-section structural steel. CBC is used to shift the laser intensity within the focal plane to create a specific energy distribution. By the temporal and spatial shifting, the resulting dynamic beam shape can be used for precisely adapting the heat input to the specific material properties. The combination of different beam shapes offers the possibility of defining sequences, which allow a nearly unlimited control of the heat input in the material.

The first part focuses on welding die-cast aluminum tubes with a wall thickness of 5 mm. The objectives are divided into several steps: 1. A penetration depth of at least 4 mm at a feed rate of 200 mm/s; 2. Ensuring tightness against gaseous media; 3. Reducing porosity to increase the maximum load capacity in burst tests. The second part describes the single-sided and single pass

welding of thick-sectioned steel components with a plate thickness of 6 mm and a weld length of 400 mm. The aim is to demonstrate how different beam shapes affect the quality of the weld. In particular, the quality of the weld top and root faces is examined along the length of the weld.

3 Materials and Experimental Details

The materials used in the investigations are AlSi10Mg (3.2381) and S355J2+N (1.0577). The die-cast aluminum alloy is used in the shape of a tube and cover element (⌀ 150 mm / t = 5 mm), and the steel in the shape of sheets (400 x 80 mm / t = 6 mm). All specimens used are welded in butt weld configuration, see Figure 1.

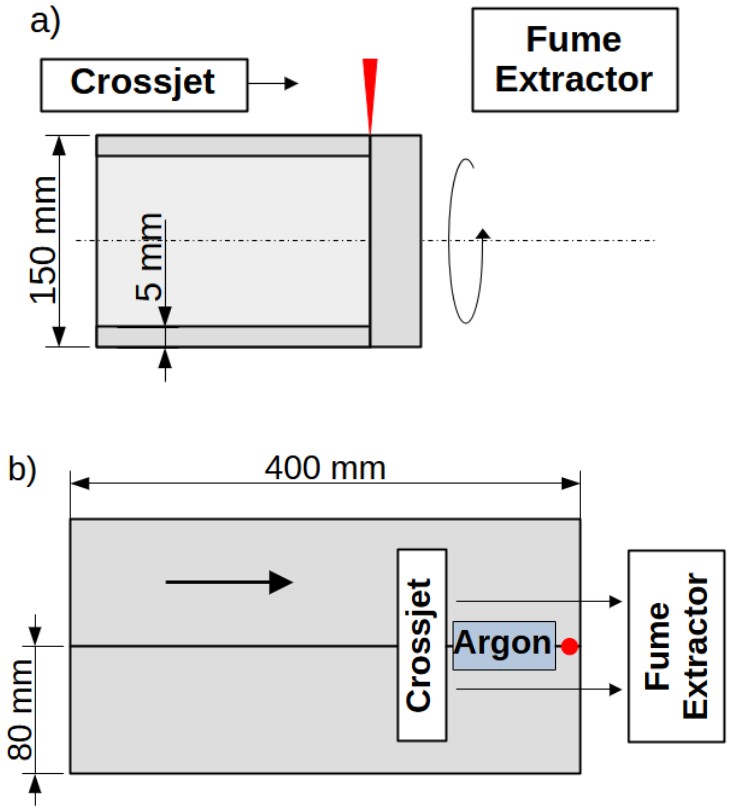

Figure 1: Weld Configuration – a) AlSi10Mg Tube / 5 mm & b) S355J2+N Plate / 6 mm.

A DBL from Civan Lasers with 14 kW of laser power and 1.5 m focal length is used. The laser focus, crossjet, and fume extractor are fixed in position. The components are moved using an XY table or a rotary axis. All surfaces are cleaned with isopropanol prior to welding. No additional shielding gas is used for the die-cast aluminum alloy. Argon is used as shielding gas for the S355JS+N sheets (nozzle: ⌀ 12.7 mm; distance: 10 mm; flow rate: 15 l/min).

By using CBC, different laser intensity distributions are defined for the welding experiments. Individual solid-state fibers are controlled to emit coherent wave fronts, see Figure 2.

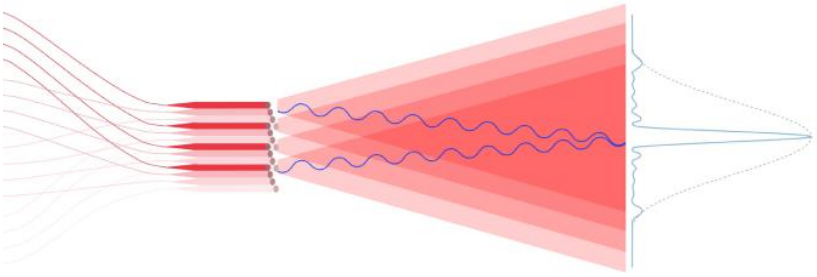

Figure 2: Coherent Beam Combining of individual fibers

Within the focus plane constructive and destructive interferences form a specific energy distribution pattern. This pattern can be shifted within the MHz domain to create specific beam shapes to precisely control the heat input in the focal plane. The combination of different beam shapes to sequences allows a nearly unlimited control of the laser intensity distribution, see Table 1.

Table 1: Beam Shape Sequences.

Beam Shape Sequence	Laser Intensity Pattern			
RasterPattern	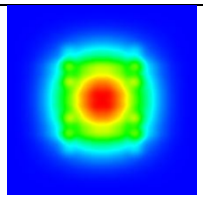			
	Shape Frequency: 434 kHz Shape Duration: 1 ms			
InwardsU+OnePoint	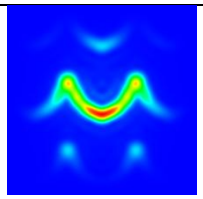		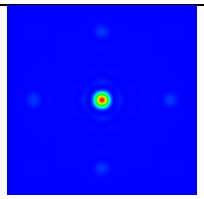	
	Shape Frequency: 5 kHz Shape Duration: 5 ms		Shape Frequency: 5 kHz Shape Duration: 5 ms	
Spiral+Infinity	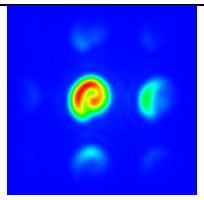	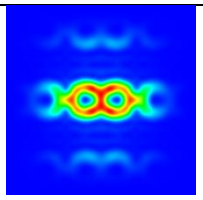	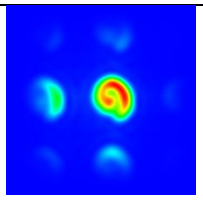	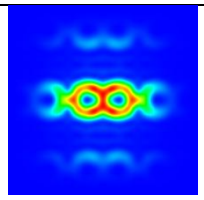
	20 kHz / 2 ms	20 kHz / 0.25 ms	20 kHz / 2 ms	20 kHz / 0.25 ms

For welding thick-walled steel, the sequences `Raster Pattern´ and `InwardsU+OnePoint´ are examined. The varying intensities directly affect the weld along its entire 400 mm length. The focus is on assessing potential material loss and weld sagging. For the examinations on the aluminum

die-cast tubes, the sequence `Spiral+Infinity´ is used. The alternating rotations of the beam shapes are intended to stabilize the keyhole during welding. Furthermore, they are supposed to control the flow of the melt pool and help reduce porosity by degassing. The weld seam is analyzed along with its circumference for weld penetration depth and porosity content. The weld seam is examined in detail using metallographic cross sections. The following laser process parameters are used for the experiments, see Table 2.

Table 2: Laser Process Parameters.

Value	Steel	Aluminum	Unit
Laser power	6.5	7.5	kW
Feed rate	20	200	mm/s
Argon flow	15	-	l/min

4 Results and Discussion

Welding of the aluminum specimens with the beam shape `Spiral+Infinity´ shows an average penetration depth of 4.1 mm and a standard deviation of 0.21 mm. The maximum weld width is 2.8 mm. The geometry of the weld was measured at four points around the circumference. No external imperfections are visible on the outer weld surface. The examinations show that a noticeable increase in porosity occurs when the penetration depth exceeds 3 mm., see Figure 3.

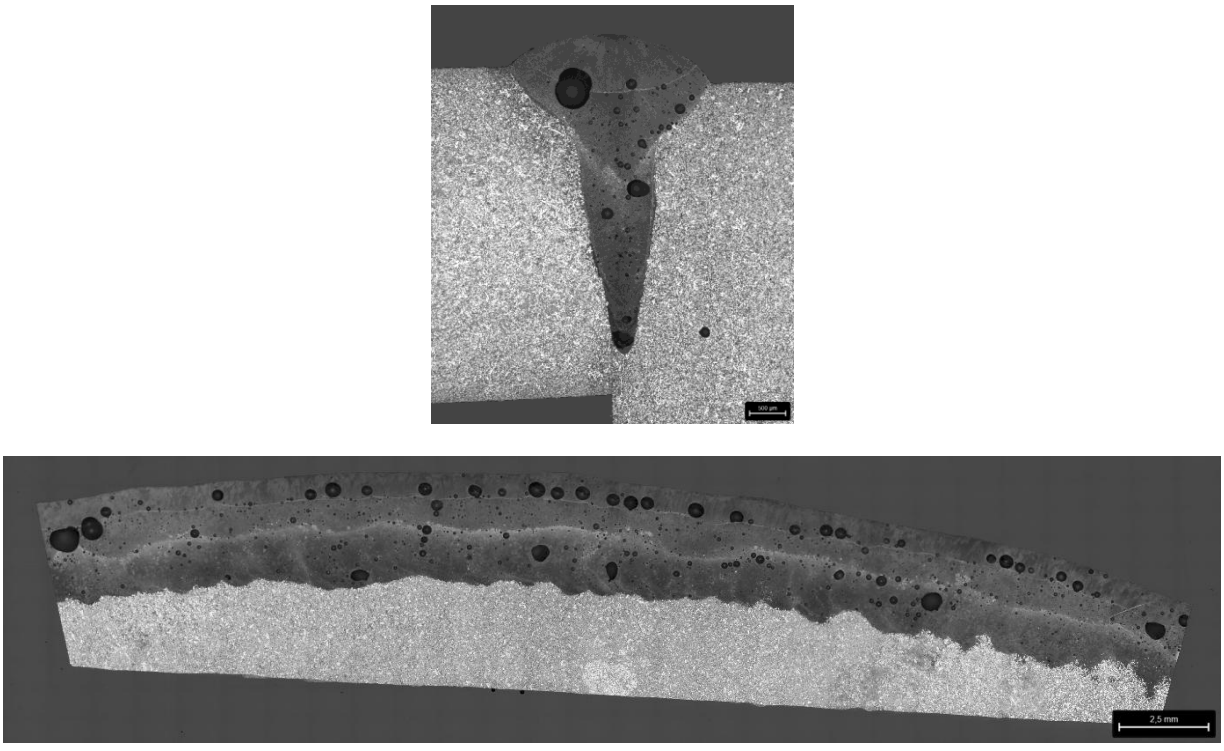

Figure 3: Transversal and longitudinal cross section (NaOH etched) of a AlSi10Mg specimen

The majority of gas inclusions occur in the upper third of the weld seam. A distinction must be made between the distribution of smaller and larger gas pores. The smaller pores are finely distributed and do not form areas of increased concentration. The larger pores occur more frequently at greater penetration depths. For this reason, the selected beam shape does not allow for complete degassing of the weld at a feed rate of 200 mm/s.

To improve the surface quality, a subsequent polishing weld is performed using a higher beam shape frequency of 500 kHz and lower laser power of 4 kW. The feed rate remains unchanged at 200 mm/s. This step results in the remelting of the top 1.6 mm of the weld seam. The goal is to further reduce porosity in the upper area of the weld seam and improve surface quality. The distinction between the initial penetration weld and the subsequent polishing weld is visible in the cross sections. However, the polishing weld only slightly reduces porosity. It can be assumed that sufficient degassing of the weld seam at a penetration depth of 4 mm requires a reduction in feed rate. Therefore, a reduction in feed rate and laser power offers the possibility of achieving penetration depths of 4 mm with significantly lower porosity in future studies.

The welding experiments on the steel specimens vary significantly in regard to laser intensity depending on the selected beam shape. Although the same linear energy density is required for joining, differences in the geometry of the weld bead are evident (Figures 4 and 5).

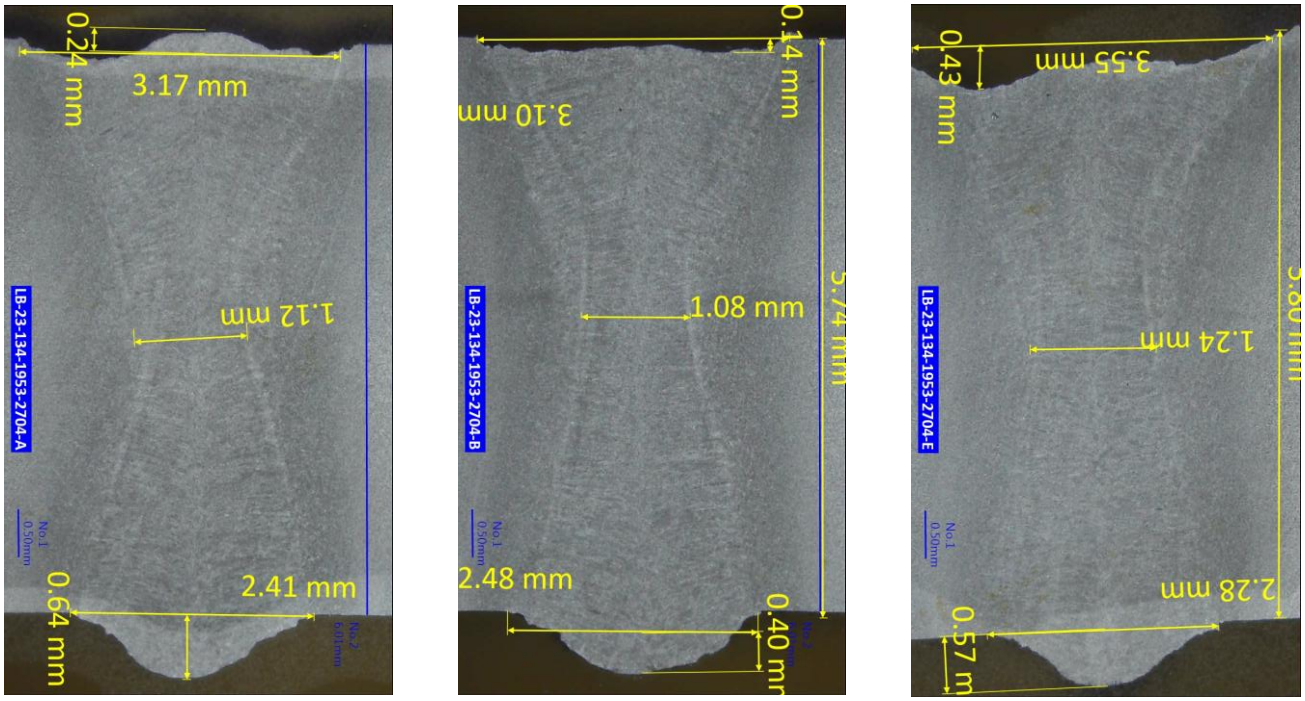

Figure 4: Transversal cross section (Nital etched) – S355J2+N with Beam Shape `RasterPattern´

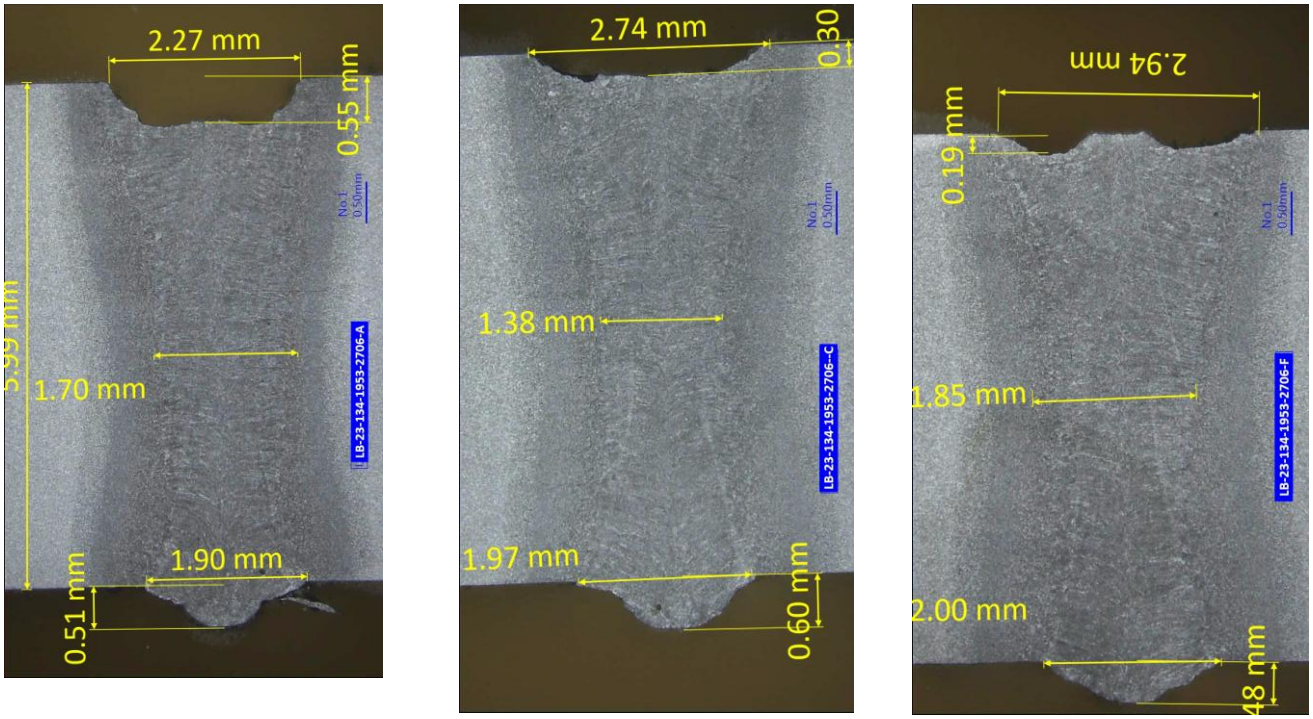

Figure 5: Transversal cross section (Nital etched) – S355J2+N with the Beam Shape `InwardsU+OnePoint´

Metallographic cross-sections are prepared at three positions along the 400-mm weld. The samples are taken along the weld at 30 mm (Figure 4/5, left), 200 mm (Figure 4/5, middle), and 370 mm (Figure 4/5, right).

The beam shape `Raster Pattern´ has a low laser intensity. This is evident in a significantly wider weld seam of approximately 3.3 mm in the upper region and 2.4 mm in the lower region of the cross-section. The center of the weld seam is significantly narrower at 1.2 mm. Due to the high laser intensity of the `OnePoint´, the sequence `InwardsU+OnePoint´ has a slightly narrower weld seam of 2.6 mm in the upper section, 1.6 mm in the middle section, and 2.0 mm in the lower section. Overall, the weld seam of the sequence `InwardsU+OnePoint´ exhibits significantly less variation in its geometry. However, it can be seen that `RasterPattern´ tends to cause an excessive penetration of ~ 0.54 mm, while `InwardsU+OnePoint´ tends to cause an incompletely filled groove of ~ 0.35 mm. Both criteria regarding the excessive penetration and incompletely filled groove fulfill the requirements of ISO 13919-1.

5 Summary

The use of DBL's enables processing of die-cast aluminum materials and thick-walled steel materials with high quality and feed rates. It has been demonstrated that die-cast aluminum (AlSi10Mg) can be processed at a high feed rate of 200 mm/s with a penetration depth of up to 4 mm. Stabilizing the keyhole can help reduce porosity in the lower region of the weld. However, complete degassing of the weld requires additional processing steps or a minor reduction in feed rate.

Steels with a sheet thickness of 6 mm can be welded single-sided using the investigated beam shapes in a single operation. The evaluated criteria comply with the general requirements of ISO 13919-1. In the future, the investigation of the influence of the beam shapes used will extend beyond geometric properties to include the mechanical properties of the weld.

Conflict of Interest

The author declares no conflict of interest.

Data Availability Statement

All data generated or analyzed during this study are available from the corresponding author upon request, without restriction.

References

[1] D. Li, C. Slater, H. Cai, X. Hou, Y. Li, und Q. Wang, „Joining Technologies for Aluminium Castings—A Review“, *Coatings*, Bd. 13, Nr. 5, S. 958, Mai 2023, doi: 10.3390/coatings13050958.

[2] S. Völkers, S. Böhm, und V. Somonov, „Porosity reduction in the laser beam welding of aluminium die cast alloys through the overlapping of mechanically induced sound waves“, *J. Phys. Conf. Ser.*, Bd. 1109, S. 012019, Nov. 2018, doi: 10.1088/1742-6596/1109/1/012019.

[3] R. D. Ardika, T. Triyono, N. Muhayat, und Triyono, „A review porosity in aluminum welding“, *Procedia Struct. Integr.*, Bd. 33, S. 171–180, 2021, doi: 10.1016/j.prostr.2021.10.021.

[4] X. Meng, S. N. Putra, M. Bachmann, und M. Rethmeier, „A statistical assessment of the laser energy absorption and keyhole stability in high-power laser welding“, *J. Manuf. Process.*, Bd. 141, S. 885–896, Mai 2025, doi: 10.1016/j.jmapro.2025.03.053.

[5] I. Bunaziv *u. a.*, „Root formation and metallurgical challenges in laser beam and laser-arc hybrid welding of thick structural steel“, *Int. J. Adv. Manuf. Technol.*, Bd. 116, Nr. 1–2, S. 561–578, Sep. 2021, doi: 10.1007/s00170-021-07453-0.

[6] H. Xu *u. a.*, „Investigation of the Microstructure and Mechanical Properties of Heat-Treatment-Free Die-Casting Aluminum Alloys Through the Control of Laser Oscillation Amplitude“, *Materials*, Bd. 18, Nr. 6, S. 1194, März 2025, doi: 10.3390/ma18061194.

[7] T. Girerd, A. Gameros, M. Simonelli, A. Norton, und A. T. Clare, „Modulation of melt pool behaviour using novel laser beam oscillation methods“, *J. Mater. Process. Technol.*, Bd. 325, S. 118300, Apr. 2024, doi: 10.1016/j.jmatprotec.2024.118300.

[8] F. Zaiß *u. a.*, „The influence of different core-ring intensity distributions on the capillary shape and resulting weld in laser welding of steel“, *Opt. Laser Technol.*, Bd. 194, S. 114495, Feb. 2026, doi: 10.1016/j.optlastec.2025.114495.

[9] S. P. Murzin, „Diffractive Optics in Laser Processing: Digital Approaches to Design and Application“, *Opt. Mem. Neural Netw.*, Bd. 34, Nr. S2, S. S357–S368, Dez. 2025, doi: 10.3103/S1060992X25602647.

[10] R. Bernhard, R. Assa, N. Armon, und E. Shekel, „Tailored beamshape sequences for welding using a Dynamic Beam Laser“, *Procedia CIRP*, Bd. 124, S. 730–732, 2024, doi: 10.1016/j.procir.2024.08.212.

Date: 03.06.2026

Predicting Warpage and Residual Stresses in Isotactic Polypropylene using Microstructure-Based Multiscale Simulations

Author: Nicolas Rozo Lopez

Authors: N. Rozo Lopez[1*], K. Willkomm[1], J. Alms[1], R. Dahlmann[1], Ch. Hopmann[1]

[1]Institute and Chair for Plastic Processing (IKV) at the RWTH Aachen University, Seffenter Weg 201, 52074, AACHEN, GERMANY

*Corresponding author: E-mail: nicolas.rozolopez@ikv.rwth-aachen.de, ORCID: 0000-0001-6085-628X

Abstract

In injection-molded of semi-crystalline polymers, warpage cannot be predicted reliably by macroscopic pvT-based shrinkage modelling alone. The reason is that the local thermal and pressure histories during processing generate pronounced gradients in crystallization degree, microstructure, effective properties, and residual stresses, which collectively determine the final part distortion. This study presents an integrated multiscale framework for isotactic polypropylene that couples non-isothermal filling, packing, and cooling simulation with DSC/Flash-DSC-based crystallization modelling, hierarchical lamella-spherulite homogenization, and thermo-mechanical warpage analysis of a stepped-plate benchmark. The simulations a more thermally expansive skin layers and a stiffer core, in agreement with the measured through-thickness property. Incorporating local crystallization-dependent properties improves the warpage prediction from 50.94 to 32.82 µm, compared with an experimental value of 35.4 µm, reducing the prediction error from 15.54 to 2.58 µm, corresponding to an improvement factor of approximately six. Residual packing pressure has little effect on global shrinkage, but substantially alters local residual stress distributions.

Keywords

Injection molding; isotactic polypropylene; multiscale simulation; warpage; residual stresses

1 Introduction

The increasing geometrical complexity of injection molded thermoplastic parts, together with ever tighter dimensional tolerances, has intensified the need to predict and control shrinkage and warpage. For semi-crystalline thermoplastics in particular, these distortion phenomena arise from strongly inhomogeneous thermal and solidification history within the material [HT01]. A principal cause is the development of non-uniform shrinkage across the part thickness, which originates from

cooling-rate gradients. This is especially pronounced in thick-walled geometries [SKR21]. The resulting non-uniform contraction generates residual stresses that ultimately drive part distortion. In addition, the overall magnitude of shrinkage is affected by process parameters such as packing pressure and packing time, while the local volumetric evolution during solidification is commonly described by pressure-volume-temperature (pvT) behavior [AKL+24, LAH+26].

In thick-walled polypropylene (PP) components, the local cooling rate may differ by several orders of magnitude between the rapidly solidifying skin layers adjacent at the mold wall and the more slowly cooling core region [ACH23]. These local thermal histories govern not only the attainable crystallization degree, but also the formation of the underlying spherulitic microstructure. Since the thermo-mechanical behavior of the material is determined by locally evolving microstructure, the deformation of the final part cannot be described adequately by homogeneous material data or by simplified pvT-based shrinkage modelling alone (Figure 1A). This limitation becomes even more relevant when the pressure state is idealized as dropping instantaneously to ambient after packing, although residual cavity pressure can persist well into the cooling phase and influence the development of residual stresses [LAH+25]. Figure 1B illustrates this idealized representation.

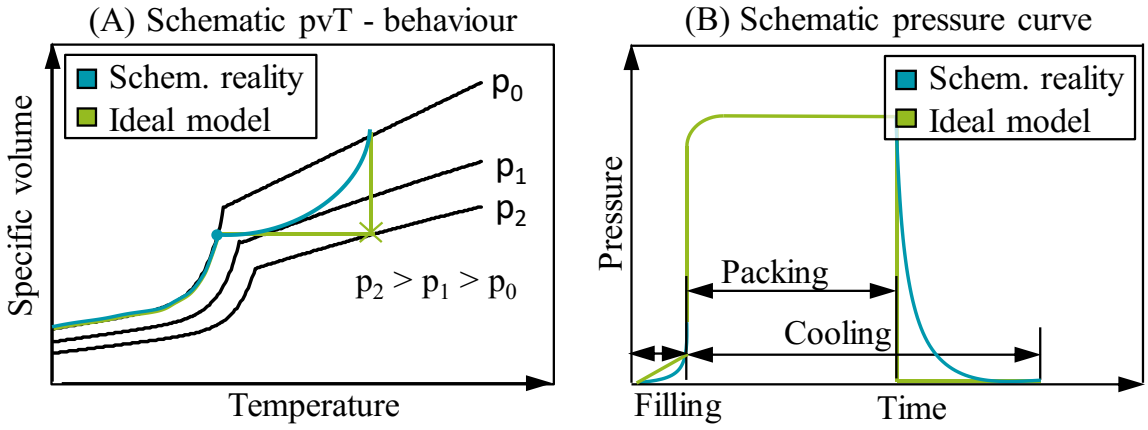

Figure 1: Schematic comparison of simplified and real pvT behavior (A) and cavity pressure (B)

Consequently, warpage prediction requires more than a purely macroscopic pvT-based description of shrinkage. Rather, it requires a physically consistent process-structure-property framework that relates local thermal and pressure histories to crystallization kinetics, microstructure formation, effective material behavior, and the resulting residual stress and distortion state [ACH23, AKL+24, LAH+26, AWH26].

This study presents an integrated multiscale simulation framework for predicting shrinkage and warpage in injection-molded semi-crystalline isotactic polypropylene (iPP). The approach combines injection molding process simulation of filling, packing, and cooling with microstructure evolution modeling and a hierarchical homogenization strategy to derive local crystallization- and microstructure-dependent thermoelastic and thermal properties across the part thickness. On this basis, the macroscopic shrinkage related deformation of a staggered iPP plate is analyzed and validated against warpage measurements. Particular emphasis is placed on demonstrating that local crystallization-dependent property gradients are essential for recovering the correct warpage

behavior, while the inclusion of residual packing pressure is a necessary refinement for representing evolving residual stresses with greater physical fidelity.

2 Integrative Multiscale Simulation Framework

To capture the coupling between process conditions, microstructure formation, local material behavior, and final part distortion, an integrative multiscale simulation framework is developed (Figure 2). Its central objective is to resolve the local inhomogeneous mechanical properties formed during solidification in the filling simulation and to transfer their effects consistently to the warpage prediction of the final part. The framework, therefore, links processing conditions to microstructure development and microstructure related mechanical properties to macroscopic part behavior to predict part warpage.

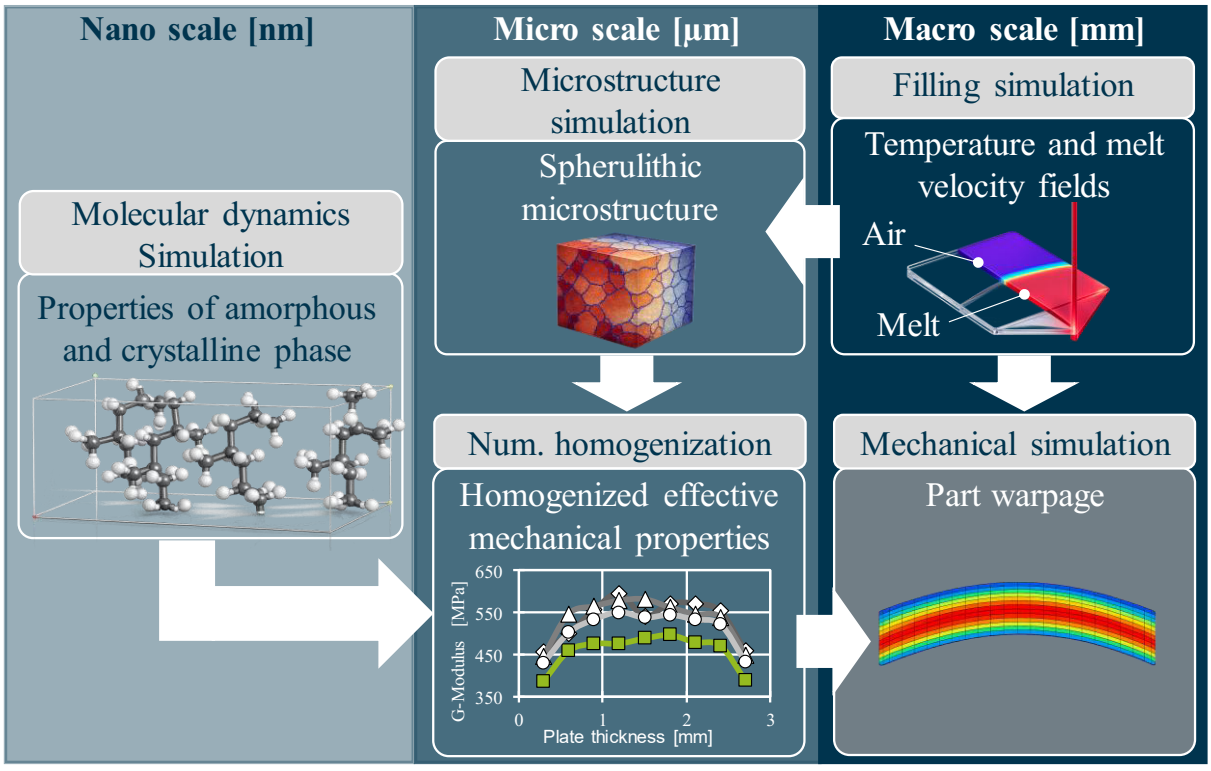

Figure 2: Integrative multiscale simulation framework for predicting of shrinkage and warpage in injection-molded parts

First, the injection-molding process is simulated in COMSOL Multiphysics in order to obtain the local temperature, melt-velocity, and pressure histories during filling, packing, and cooling [AKL+24, AWH26]. The filling stage assumes non-isothermal melt flow. In the post-packing state, residual packing pressure is allowed to relax during cooling, capturing a more realistic temperature and pressure evolution in the cavity. The local temperature and pressure histories control crystallization and volumetric shrinkage and thus define the boundary conditions for all lower-scale analyses.

The second stage describes the evolution of the semi-crystalline microstructure. For this purpose, the time-dependent temperature and velocity fields obtained from the injection-molding simulation are transferred to a microscale crystallization model. Based on these local process histories,

spherulitic microstructures are predicted in representative volume elements (RVEs) distributed across the component thickness. A cellular automaton model combining Ziabicki athermal nucleation with Hoffman-Lauritzen-Davis growth is implemented in the SphaeroSim software [AKL+24, LAH+26]. In parallel, the local crystallization degree assigned to these RVEs is derived from differential scanning calorimetry (DSC) and Flash-DSC measurements as a function of cooling rate [LAM+25]. Because these spherulitic microstructures are composed of crystalline-amorphous lamellar substructures, they define the microstructural basis for the subsequent hierarchical homogenization.

In the third stage, the predicted crystallization degree and spherulitic morphology are converted into local effective material properties by hierarchical homogenization. First, the lamella RVE is homogenized at the nanoscale to determine the effective lamella properties. These properties are then transferred to the predicted spherulitic RVEs and homogenized at the microscale using a radial spherulite model. The resulting local thermo-elastic and thermal properties across the thickness provide the material input for the macroscale warpage simulation [LAM+25, LAH+26]. These local effective properties are then mapped, together with the temperature and pressure fields from the injection-molding simulation, to a 2D thermomechanical plane-strain model [LAH+26, AWH26]. The analysis includes both in-mold and post-demolding cooling. By accounting for residual packing pressure during cooling, the model represents the delayed onset of shrinkage more consistently than a purely thermal approach. This enables direct analysis of the interaction among local shrinkage, stiffness gradients, and residual stresses in the final warpage of the component [LAH+26, AWH26].

A staggered plate serves as benchmark geometry for this investigation (Figure 3). Its defined thickness variation from 4 mm to 1 mm generates strong local differences in cooling rate, solidification, and pressure loss.

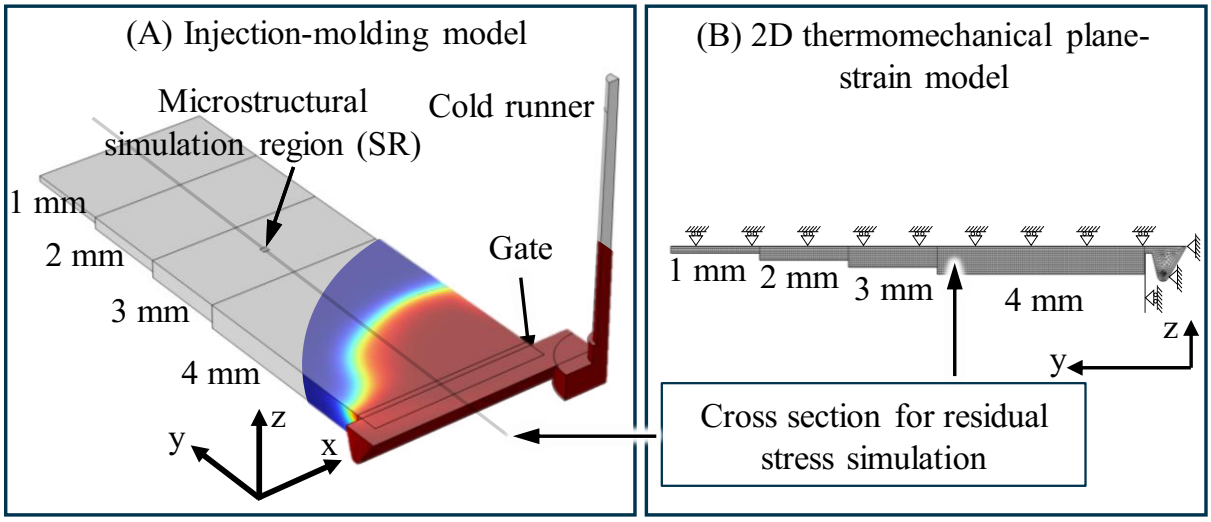

Figure 3: Staggered plate model for injection-molding process simulation (A) and thermomechanical plane-strain analysis (B)

These differences promote pronounced gradients in crystallization degree, spherulitic morphology, local effective properties, and residual stresses, while the geometry remains simple enough for

systematic analysis and experimental validation. The present investigation uses the middle region of the 3 mm thick segment as the simulation region (SR) to analyze the full multiscale chain (Figure 3A), and the cross-section of the staggered plate for the thermomechanical analysis (Figure 3B). The benchmark material is isotactic polypropylene PP505P from Sabic, selected for its industrial relevance, low cost, and well-defined spherulitic α-iPP morphology. Because iPP responds strongly to locally non-uniform cooling, it is particularly suitable for studying the process-induced microstructural inhomogeneities and resulting warpage addressed here. Together, the selected geometry, material, and processing conditions define the basis of the present investigation.

3 Prediction of Effective Thermo-Elastic and Thermal Properties

The injection-molding process of the stepped plate is simulated using the pvT-model parameters, process parameters, and boundary conditions reported in [WHS+19, LAH+26, AWH26]. In SR, the simulation predicts cooling rates from about 2.6 °C/s in the core to about 700 °C/s at the mold wall, while the temperature difference between the upper and lower surfaces remains below 2.0 °C during packing and cooling [LAH+26]. Although the applied packing pressure is reduced from 600 bar to 1 bar after 15 s, residual cavity pressures of up to 46 MPa are still present. Ambient pressure is reached only after about 24 s. After demolding, the plate cools further by natural convection and reaches nearly room temperature after about 135 s [LAH+26, AWH26].

The resulting temperature and melt-velocity fields are transferred to the microstructure analysis in SR. Across the 3 mm thickness, 30 cubic spherulitic RVEs with an edge length of 100 µm are defined. For each spherulitic RVE, the local cooling rate at solidification is evaluated and converted into a local crystallization degree by means of the empirical DSC/Flash-DSC cooling-rate relation [LAM+25]. This local crystallization degree defines the corresponding crystalline-amorphous lamella RVE and, after nanoscale homogenization, the associated effective lamella properties. These local lamella properties are subsequently assigned to the predicted spherulitic RVEs, whose solidified microstructures are transferred to HOMAT for thermoelastic and thermal homogenization [NN20]. The resulting predictions provide the local effective Poisson's ratios, elastic moduli, coefficients of thermal expansion, and thermal conductivities.

To assess the effect of the local crystallization gradient on the predicted effective properties, the properties predicted with the local crystallization model are compared with those obtained under the assumption of constant crystallization degree properties [LAM+25, LAH+26]. Figure 4 shows the effective Poisson's ratios and elastic moduli across the plate thickness in SR. The comparison shows that the use of local crystallization properties mainly affects the skin regions, whereas the constant-crytallization-degree model remains almost uniform across the thickness. For the effective Poisson's ratios, both approaches predict similar values in the central part of the plate, but the local model yields a pronounced increase near both surfaces. The effect on the elastic modulus is even more pronounced. While the constant model predicts an almost uniform stiffness across the thickness, the local-crystallization-degree model shows an increase from the surface toward the

core. This trend is confirmed by experiments, which show similar behavior across the thickness. Further details on the experimental validation are provided in [LAH+26].

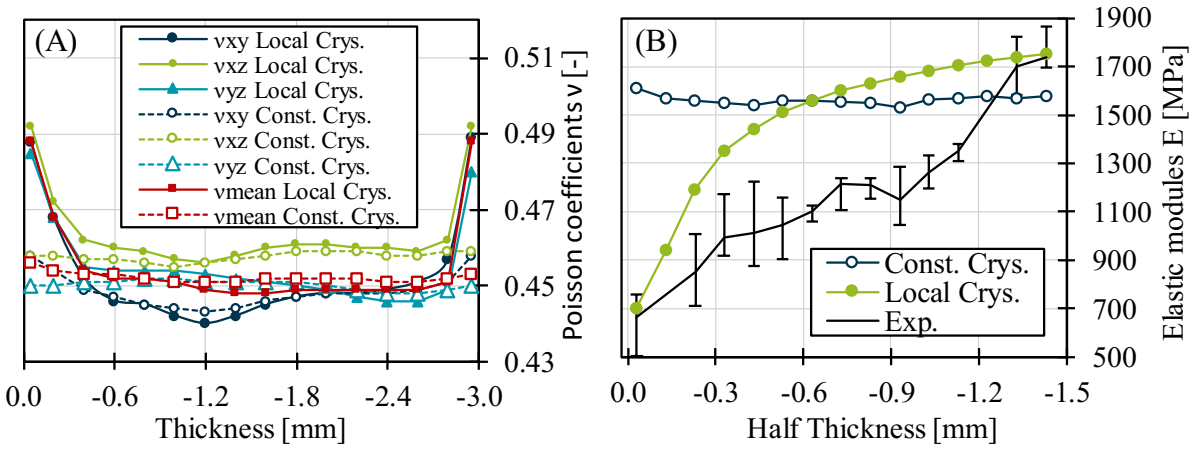

Figure 4: Variation over the plate thickness of the effective Poisson coefficients (A) and elastic modules (B) predicted with constant and variable effective properties and comparison to experiments.

Figure 5 shows the results of the predicted thermal response across the plate thickness in SR. Both models predict a pronounced orthotropy of the effective thermal expansion coefficients, with the general tendency $\alpha_z > \alpha_x > \alpha_y$ throughout the plate thickness. The differences between the two approaches appear near the plate surfaces, close to the mold walls. While the constant crystallization model predicts nearly uniform properties, the local model predicts an increase in all thermal expansion coefficients in the layers near the plate surfaces. A similar observation is obtained for the effective thermal conductivity. Whereas the constant model predicts an almost uniform conductivity across the thickness, the local model yields a clear reduction near the surfaces.

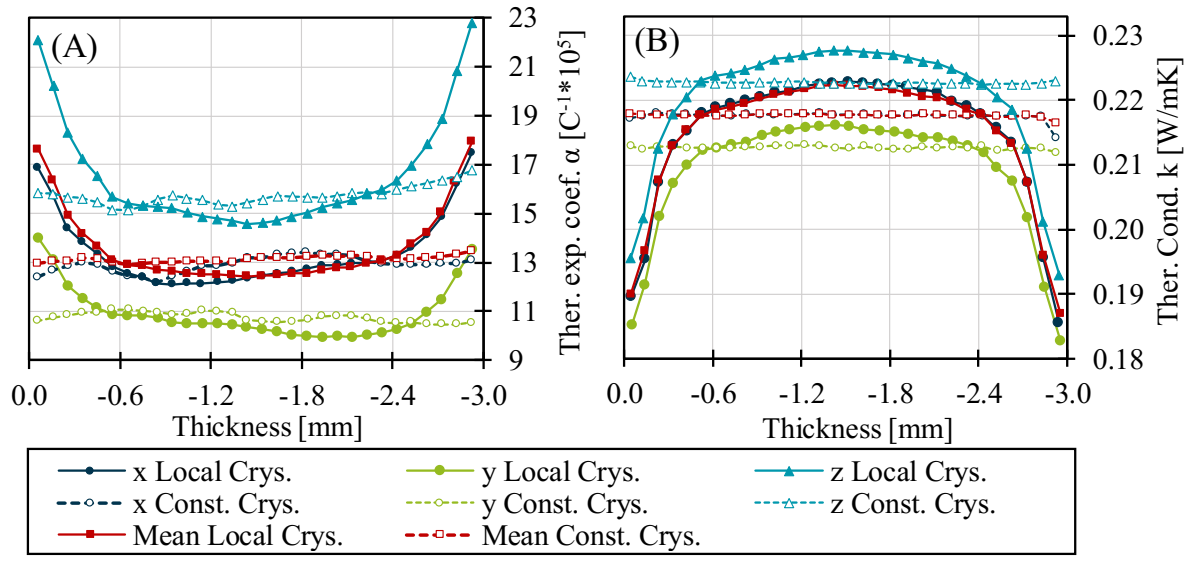

Figure 5: Variation over the plate thickness of the effective thermal expansion coefficients (A) and thermal conductivity (B) predicted with constant and variable effective properties.

These results show that the local crystallization history mainly changes the effective properties in the near-surface regions. Near the plate surfaces, where the crystallization degree is lowest, higher Poisson's ratios, higher thermal expansion coefficients, and lower thermal conductivities are

predicted, while the elastic moduli decrease. Towards the highly crystallized core, the material becomes stiffer and thermally less expansive. Further details regarding the degree of crystallization can be found in [AKL+24]. This demonstrates that local crystallization must be considered to predict realistic effective-property distributions. Its effect on the prediction of shrinkage and warpage in the molded part is analyzed in the next section.

4 Distortion and Warpage Prediction

The local effective thermoelastic and thermal properties derived in the previous section are subsequently transferred to the thermomechanical plane-strain model to evaluate their effect on the macroscopic distortion behavior of the 3 mm plate section. Further details on the plane-strain model are provided in [LAH+26]. To quantify the influence of the local crystallization gradient, the predictions obtained with crystallization-dependent local properties are compared with those based on constant effective properties across the plate thickness [LAH+26, AWH26]. Figure 6 shows the evolution of the predicted shrinkage after mold opening. In both the width and thickness directions, the model with local properties predicts greater shrinkage than the constant-property model. This difference is caused by the weakly crystallized skin layers, which contract more during cooling.

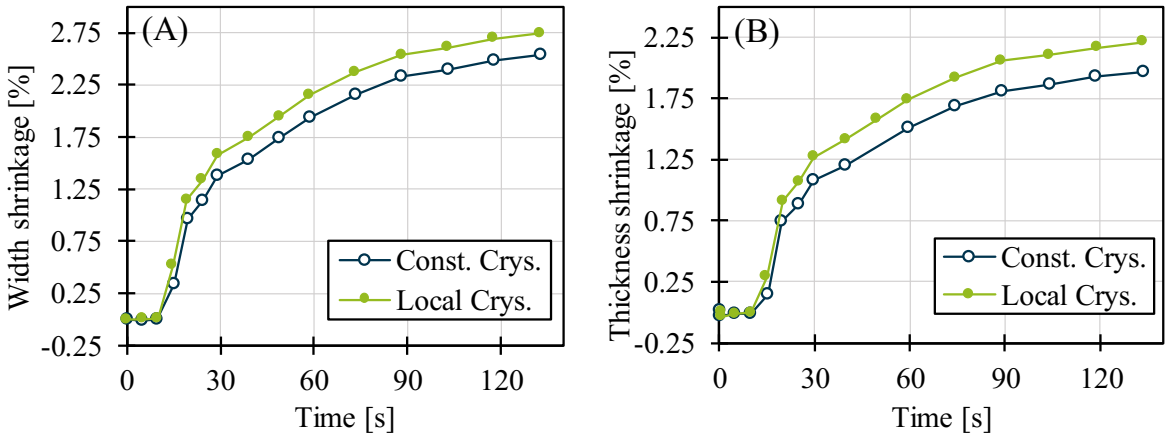

Figure 6: Evolution of the width shrinkage (A) and thickness shrinkage (B) predicted by the two model variants.

The effect on warpage after mold opening is shown in Figure 7. In the present analysis, warpage is defined as the vertical displacement Uy of the bottom node at the right-hand side of the 3 mm plate section. For validation, the final warpage was measured on five iPP plates by optical 3D scanning using a GOM ATOS system. The measured mean value was used for comparison with the simulation. Further details on the experimental warpage measurement are provided in [LAH+26]. Although the local-property model predicts greater shrinkage, it leads to smaller final warpage. The simulation with constant properties yields a predicted warpage of 50.94 µm, whereas accounting for local crystallization-dependent properties reduces the predicted warpage to 32.82 µm. The experimental reference value is 35.4 µm. As a result, the prediction error decreases from 15.54 µm to 2.58 µm, corresponding to an improvement factor of 6 in predictive accuracy.

Overall, the distortion analysis confirms the central role of local crystallization in predicting the final part geometry. A constant-property description is not sufficient to represent the actual

shrinkage and warpage behavior. Instead, local crystallization-dependent effective properties must be considered to predict realistic distortion in injection-molded semi-crystalline iPP components.

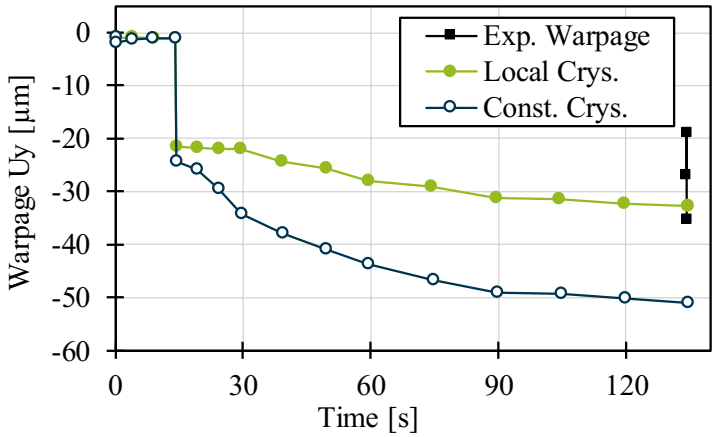

Figure 7: Warpage evolution after mold opening predicted with constant and variable effective properties

5 Process Refinement Through Residual Packing Pressure and Residual Stresses

A further refinement concerns the transfer of the pressure state from packing to cooling. In conventional shrinkage analyses, the cavity pressure is often assumed to drop instantaneously to ambient pressure once the applied packing pressure is released. For the present iPP stepped plate, however, the process simulation shows that this assumption is not valid. Although the applied packing pressure is reduced from 600 bar to 1 bar after 15 s, residual cavity pressures of up to 46 MPa are still present at 15.05 s, and ambient pressure is reached in section SR only after about 24 s. The cooling phase can therefore not be treated as purely thermal from the end of packing onward. Instead, volumetric shrinkage can fully develop only after the local residual pressure has relaxed sufficiently.

This process refinement has only a minor effect on the overall shrinkage prediction. When residual in-mold pressure is taken into account, the effective time at ambient pressure during cooling is reduced to about 6 s instead of about 15 s. Nevertheless, the difference in shrinkage along the longest part axis remains small, with a maximum deviation of only 3.5 µm, which is within the measurement uncertainty of the optical 3D scanning system. From the viewpoint of global shrinkage, the residual packing pressure may, therefore, be neglected.

In terms of the development of process-induced residual stresses (Figure 8), the simulations show that the local stress distribution at the end of cooling changes when residual packing pressure is considered. The strongest differences occur in the early-solidifying 1 mm and 2 mm sections and in the gate region, where local stresses are frozen in before the pressure can relax completely. This should not be interpreted as a sustained pressure effect. The absolute stress levels must therefore be assessed with caution, since viscoelastic relaxation is not yet fully represented in the present framework. This result is of direct relevance for warpage prediction, since the final distortion results not only from the shrinkage magnitude, but also from the interaction between shrinkage and the residual stress state present at demolding. The refinement introduced here, therefore, shows that

accurate future warpage predictions must combine local crystallization-dependent material properties with a realistic process-induced initial stress state [AWH26].

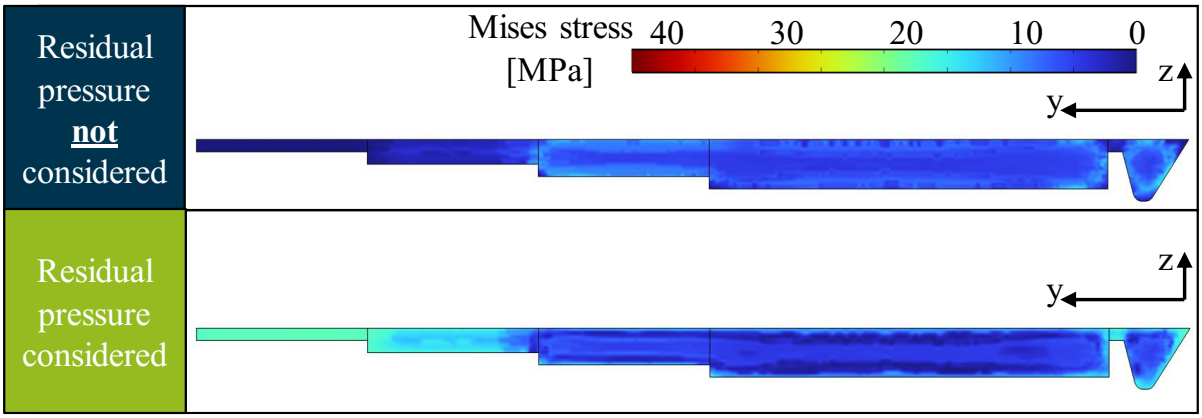

Figure 8: Comparison of the residual stresses with and without consideration of residual packing pressure

6 Summary and Conclusions

This study shows that accurate warpage prediction for injection-molded semi-crystalline isotactic polypropylene requires an integrated process-structure-property framework. At the component level, the developed multiscale simulation chain captures how local cooling conditions determine crystallization degree, microstructure, effective thermos-elastic properties, and ultimately part distortion.

The comparison between the two modeling approaches demonstrates the importance of local crystallization-dependent properties. The simulation with constant material properties predicts a warpage of 50.94 µm, whereas the model with local crystallization-dependent properties predicts 32.82 µm, compared with an experimental value of 35.4 µm. Accordingly, the prediction error decreases from 15.54 µm to 2.58 µm, corresponding to an approximate **improvement factor of 6** in predictive accuracy. These results confirm that a constant-property description is not sufficient to reproduce the actual shrinkage and warpage behavior of the molded part.

The results further show that residual packing pressure has only a minor effect on global shrinkage, but a pronounced effect on the local residual stresses. This is especially relevant in the early-solidifying 1 mm and 2 mm sections and in the gate region, where stresses can be frozen in before pressure relaxation is complete. Future refinement of the framework should, therefore, focus on expanding it to include other polymers, polymers with polycrystalline microstructures, or filled/anisotropic materials.

Acknowledgements

The presented investigations were carried out at Institute for Plastic Processing (IKV) at the RWTH Aachen University within the framework of the Collaborative Research centre SFB1120–236616214 "*Bauteilpräzision durch Beherrschung von Schmelze und Erstarrung in*

Produktionsprozessen" and funded by the Deutsche Forschungsgemeinschaft e.V. (DFG, German Research Foundation). The sponsorship and support are gratefully acknowledged.

Conflict of Interest

The authors declare no conflicts of interest.

Data Availability Statement

The data supporting the findings of this study are available at:
http://hdl.handle.net/21.11102/7ab0387c-f490-4863-baaf-4668a867da7a

References

[ACH23] Alms, J.; Çelik, H.; Hopmann, Ch.: Direct measurement of the thermal conductivity depending on the thermal crystallisation conditions of injection moulding processes using flash-DSC. *Proceedings of the ANTEC 2023*, Denver, USA, 2023

[AKL+24] Alms, J; Kahve, C.; Laschet, G.; Çelik, H.; Mentges, N.; Hopmann, Ch.: Validation of A Multi-Scale Simulation for Precise Warpage Prediction of Injection Molded Semi-Crystalline Parts. *AIP Conference Proceedings* 3158 (2024), S. 110009

[AWH26] Alms, J; Willkomm, K.; Hopmann, Ch.: The effect of residual packing pressure on the simulative prediction of shrinkage in injection-moulded components. *33rd International Colloquium Plastics Technology 2026* (2026)

[HT01] Huang, M.C.; Tai, C.C.: The effective factors in the warpage problem of an injection-molded part with a thin shell feature. *Journal of Materials Processing Technology* 110 (2001) 1, S. 1–9

[LAH+26] Laschet, G.; Alms, J.; Heym, M.K.; Gamerdinger, M.; Apel, M.; Hopmann, Ch.: Effective Local, Crystallization Degree and Microstructure Dependent Thermo-Elastic Properties of an Injection Molded i-PP Component via a Multiscale Approach and Their Impact on Warpage Simulations. *Journal of Applied Polymer Science* 143 (2026) S. e70187

[LAM+25] Laschet G.; Alms, J.; Müller, M.; Apel, M.; Hopmann, Ch.: Crystallization degree dependent effective thermo-elastic and thermal properties of an injection molded polypropylene component. Part 1: Multiscale simulation scheme and effective lamella properties. *Polymer* 320 (2025), S. 128051

[NN20] N.N. *HOMAT, Online Documentation of Version 6.0*, ACCESS e.V., Aachen, 2020, URL-https://docs. micre ss.de/homat/

[SKR21] Sreejith, P.; Kannan, K.; Rajagopal, K.R.: A thermodynamic framework for additive manufacturing, using amorphous polymers, capable of predicting residual stress, warpage and shrinkage. *Intern. Jour. of Engineering Science* 159 (2021) 1, S. 103412

[WHS+19] Wang, J.; Hopmann, Ch.; Schmitz, M.; Hohlweck, T.; Wipperfürth, J.: Modeling of PVT Behavior of Semi-Crystalline Polymer Based on the Two-Domain Tait Equation of State for Injection Molding. *Materials & Design* 183 (2019), S. 108149

Date: 31.03.2026

From Observation to Control —Local residual stress build-up during solidification of technical alloys during welding

Author: K. Mäde, J. Kellerwessel, R. Sharma, U. Reisgen

RWTH Aachen University, Welding and Joining Institute,
Pontstr. 49, 52062, AACHEN, GERMANY
E-mail: maede@isf.rwth-aachen.de
ORCID: *0000-0001-8287-3128
0009-0008-9433-8876
0000-0002-6976-4530

Abstract

This work presents the findings of SFB1120 subproject TPA2, which over twelve years pursued the goal of understanding and controlling residual stress formation in technical alloys during welding. Initiated from the standpoint that transient strain fields during solidification had only minutely been directly observed, the project developed a succession of in-situ measurement techniques — from electronic speckle pattern interferometry (ESPI) through digital image correlation (DIC) to synchrotron energy-dispersive X-ray diffraction (EDXRD) — each replacing or complementing the previous when its limits were reached. The starting assumptions with which the project started turned out to be in need of adjusting: first, commercial simulations do not accurately capture the transient thermomechanical state (measured peak strains exceeded predictions by two orders of magnitude), and second, global clamping actually does not govern the local strain state near the weld pool (local thermal gradients dominate instead). Building on these findings, two residual stress control strategies were pursued: thermal management via active cooling and compositional control via in-situ alloying with cold wire. Both proved effective within their domains — aerosol cooling halved interpass times, while low-transformation-temperature (LTT) alloys generated compressive residual stresses yet both depended on the same enabling condition: a spatially homogeneous temperature field set by the deposition path. This convergence identified weld order and path planning in welds as the critical integration variable. The most recent experimental program validates the developed a-priori convolution-based geometry predictions through DED-Arc welding trials combined with ex situ analysis and in situ transient recording coupled with machine learning. This enables correction, closing the loop from diagnosis through modelling to welding and compensation.

Keywords

Residual stress, in-situ diffraction, wire arc additive manufacturing, low-transformation-temperature alloys, path planning, cold wire

1 Introduction

Residual stresses are among the most consequential yet least accessible quantities in welded structures. Their influence on fatigue life, dimensional stability, and susceptibility to cracking has been recognized for decades [1]. Yet the engineering understanding of residual stress formation has historically been confined to the final state: measuring what remains after the workpiece has cooled, without knowledge of the transient thermomechanical path that produced it. The available post-process characterization methods — hole-drilling, laboratory X-ray diffraction, and the contour method — can answer the question of what the stress state is, but not how it came to be [2].

Commercial finite element simulation tools based on the double-ellipsoid heat source model introduced by Goldak et al. [3] have long been capable of predicting post-weld residual stresses with reasonable accuracy. The constitutive models feeding these simulations rely on material data obtained from ex-situ dilatometry at constant cooling rates, which was assumed to be representative of real welding thermal cycles [4]. Process optimization followed empirical rules — reduce heat input to reduce residual stress or use low-transformation-temperature filler materials to introduce compressive stress — but no quantitative chain linked process parameters through the transient regime to the final stress state [1, 5,23].

The current work was initiated to address this gap. The central premise was that direct observation of strain evolution during solidification would reveal the mechanisms that govern residual stress formation and thereby enable rational control strategies. What began as a measurement challenge evolved into a comprehensive investigation spanning in-situ diagnostics, material characterization, alloy design, thermal management, and ultimately path planning for additive manufacturing. This paper traces the chain that connected these domains, from the original assumptions through the pivotal experimental findings to the current integration framework.

2 Aim of the Investigation

The objective was to develop in-situ measurement techniques capable of capturing the transient buildup of strain and stress during welding, to use these measurements to validate and correct thermomechanical simulation models, and to translate the resulting understanding into strategies for residual stress control in welding and additive manufacturing processes. Six initial assumptions framed the research program:

(A1) In-situ neutron and synchrotron diffraction can provide spatially resolved strain measurements during active welding.
(A2) High-temperature material behavior follows a three-regime model and flow curve data adequately describes these transitions.
(A3) Phase transformation kinetics obtained by ex-situ dilatometry at constant cooling rates can be representative of real welding conditions.

(A4) Residual stress can be altered independently by certain parameters only which ones is unknown.
(A5) Global restraint conditions govern the local strain state near the weld pool.
(A6) ESPI can be suitable for surface strain measurement during welding.
The investigation was structured to test each assumption experimentally and, where assumptions failed, to develop alternative approaches.

3 Materials and Experimental Details

The experimental approach spanned multiple material systems selected to isolate specific physical mechanisms: Al99.5 and AlSi7Mg0.3 aluminium alloys served as model materials for purely thermomechanical strain analysis due to their high thermal conductivity and absence of solid-state phase transformations [6, 7]. Alloy 625 nickel-base alloy was used to probe the transient regime under extreme gradient conditions [6]. X5CrNi18-10 austenitic stainless steel, was chosen to isolate thermomechanical strain during synchrotron measurements [8]. S235JR+N structural steel, which undergoes austenite-to-ferrite transformation during cooling, was used to study the coupling of phase transformation and strain [9]. High-strength low-alloy steel weld metals with varying transformation temperatures were employed for correlating phase transformation onset with mechanical properties [10]. Duplex stainless steel was investigated for the influence of cooling on high-temperature phase balance [11], and G3Si1 and Mn4Ni2CrMo weld metals were used for WAAM and graded material studies [12, 13].

Welding processes included submerged arc welding with and without cold wire (SAW-CW) [14, 15], gas tungsten arc welding [6,16, 17], gas metal arc welding with single and dual cold wire [18], plasma multiwire welding [12], and laser welding and laser metal deposition [8, 9,19]. Cold wire feed rates ranged from 0% to 200% of the primary wire [18, 20].

Measurement techniques evolved over the project: 3D-ESPI was applied for initial surface strain measurements [15] before being replaced by DIC, later extended to the semi-solid regime using blue LED illumination at 470 nm with bandpass and polarization filters. In-situ neutron diffraction was performed at STRESS-SPEC (FRM II, Garching) with 3×3×2 mm³ gauge volumes and 300-second exposures [14, 17]. Synchrotron EDXRD was conducted at DESY PETRA III beamline P61A with white-beam energy range 30–200 keV, slit-defined gauge volumes achieving 0.1 mm² cross-section — approximately 300 times finer spatial resolution than neutron diffraction — and 1-second temporal resolution [8, 9]. Complementary thermal measurements included infrared thermography, thermocouples, single-sensor differential thermal analysis [21], and the Debye-Waller method for extracting gauge volume temperature directly from diffraction peak intensity [6].

4 Results and Discussion

Evolution of in-situ measurement capability

The measurement methodology followed a trajectory of progressive refinement. The first milestone was the demonstration of in-situ neutron diffraction during submerged arc welding [14], representing the first direct observation of lattice strain evolution during an industrial welding process. This experiment revealed that cold wire addition fundamentally altered the strain state behind the weld pool: conventional SAW produced tensile longitudinal strain, while SAW with cold wire produced compressive strain. However, the 2–3 mm³ gauge volume could not resolve the steep thermal gradient zone near the fusion line where gradients exceed 100 K/mm, partially invalidating assumption A1. A definitive neutron feasibility study during TIG welding [17] confirmed that the measured strain distribution — compressive ahead, tensile behind the weld pool — experimentally validates the classical thermomechanical model for the first time during active welding, but spatial limitations remained.

The pivot to synchrotron EDXRD at DESY PETRA III resolved this limitation. On austenitic X5CrNi18-10 steel, the first EDXRD strain maps during laser welding achieved 1-second temporal resolution [8]. Maximum strains of 2.92% longitudinal and 2.25% transverse were measured approximately 20 mm behind the laser. (Figure 1)

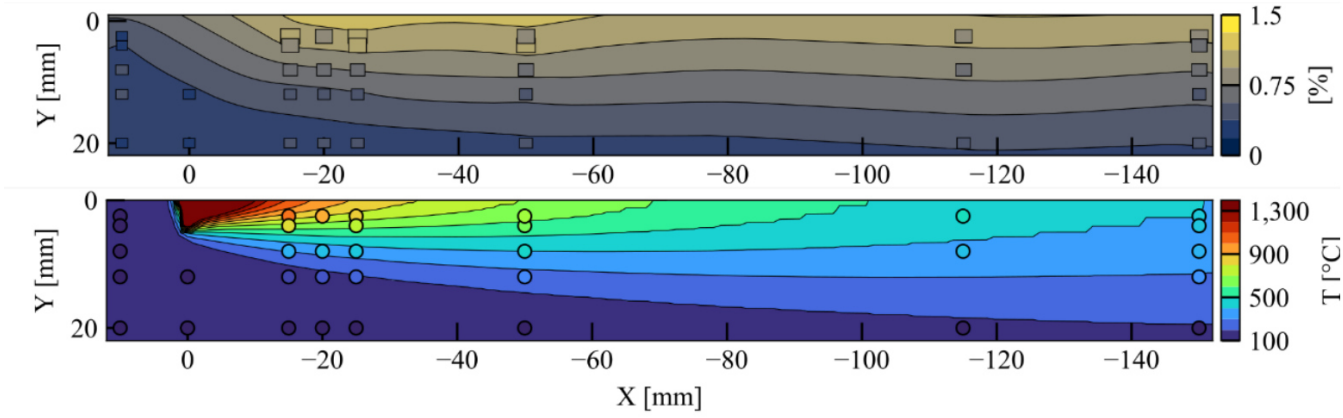

Figure 1: Top: Planar von Mises equivalent strain distribution; Bottom: Temperature distribution within the sample centre cross section by means of calibrated thermal simulation

When phase transformation complexity was added using S235 structural steel [9], distinct strain maxima at 700–800°C coinciding with the austenite-to-ferrite transformation were observed, followed by partial relaxation and then a residual strain plateau — a simultaneous tracking of austenite and ferrite diffraction peaks during transformation in a real welding process. (Figure 2)

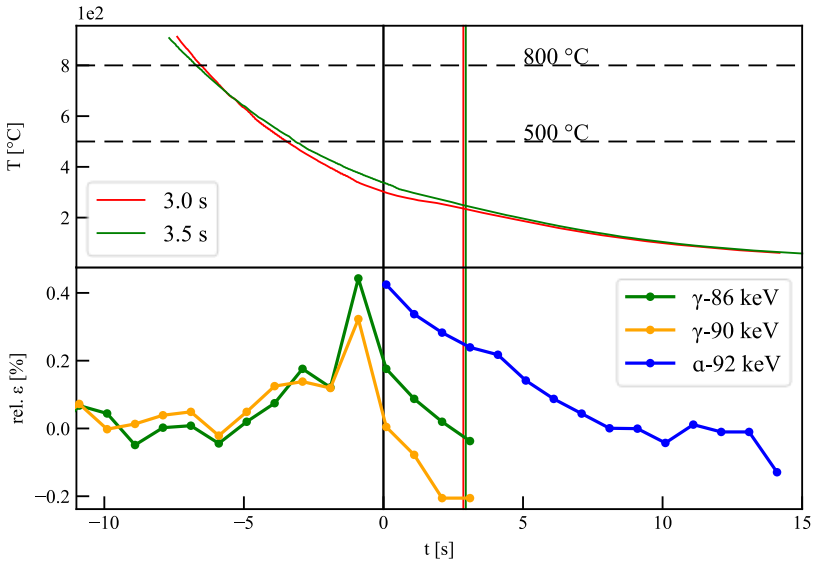

Figure 2: Superposition of Dilatometer and Diffraction aligned using the phase transformation time

A critical methodological advance was the separation of thermal from mechanical strain. For non-transforming materials, [6] demonstrated the Debye-Waller method, extracting temperature from the temperature-dependent decline in diffraction peak intensity. For transforming steels, [26] developed dilatometry synchronization: systematic dilatometry on S235JR+N calibrated transformation duration versus cooling rate, allowing the EDXRD-measured transformation duration to map to a specific thermal history. This yielded the first experimentally self-consistent time-temperature-strain correlation during laser welding of a transforming steel without numerical thermal simulation. The cross-validation study by [6], comparing five independent techniques on the same TIG configurations, established that DIC and diffraction are complementary — DIC measures total surface strain, diffraction measures elastic lattice strain in the bulk.

4.2 Overturning of foundational assumptions

The in-situ measurements overturned two foundational assumptions. Regarding A2: [6] measured peak elastic strains of 1.6% in Alloy 625 near the melt pool, while commercial simulation tools predicted transient strains approximately two orders of magnitude smaller — yet the same simulations predicted post-weld residual stresses with reasonable accuracy. (Figure 3)

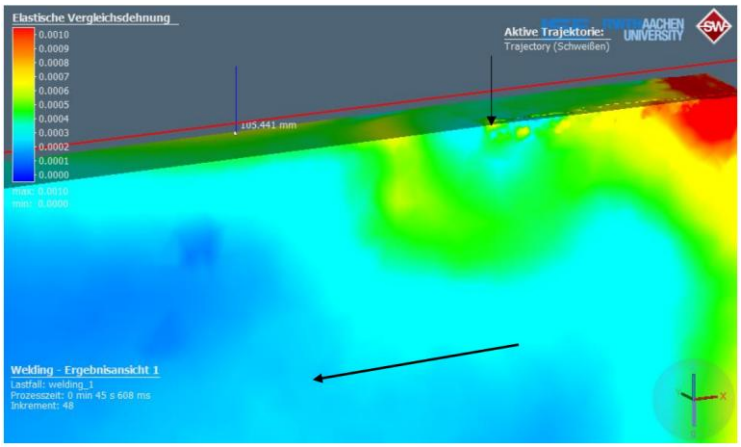

Figure 3: Thermomechanical simulation of the elastic strain, Al99.5; the vertical arrow indicates the position of the moving heat source; maximum elastic strain predicted ~0.05 %

This means the high-temperature constitutive models are fundamentally inadequate for the transient regime, even though their errors compensate in the final cooled state. Regarding A5: clamping conditions had no significant influence on near-pool lattice spacing. The local strain state is dominated by thermal gradients rather than global restraint, implying that local thermomechanical models matter more than global finite element boundary conditions.

Thermal management strategies

Active cooling was investigated for DED-Arc. Aerosol cooling reduced the cooling time t8/5 from 21.3 s to 12.2 s while cutting interpass idle time by 91%, and multi-wire feeding increased deposition rate by 82% at constant line energy [22]. Water bath cooling achieved the best thermal performance (t8/5 = 7.1 s) but was geometry constrained [27]. WAAM steel met structural requirements (>500 MPa tensile, yield exceeding S355, ~24% elongation, adequate Charpy toughness to -70°C) but surface roughness and residual stress remained challenges [13]. The central learning: cooling modifies the temporal cycle but cannot control where heat accumulates spatially — and it is the spatial gradient distribution that governs the local strain state.

Compositional control through in-situ alloying

Cold wire was initially a thermal modifier in SAW, reducing penetration depth from 5.1 mm to 3.3 mm [15]. Its compositional significance emerged when high-alloy cold wires shifted weld pool chemistry on the Schaeffler diagram. Plasma multiwire WAAM demonstrated functionally graded materials with dynamically varying wire feed speed [12]. The dual-cold-wire GMA process [18] targeted the martensitic region for LTT alloy generation, achieving 3–13% Cr and 1.5–9.5% Ni with martensite start temperatures of 81–180°C. The systematic exploration with eight cold-wire combinations found that K5 (7.2% Cr, 6.4% Ni, $M_s \approx 239$°C) produced compressive residual stresses up to -643 MPa. (Figure 4)

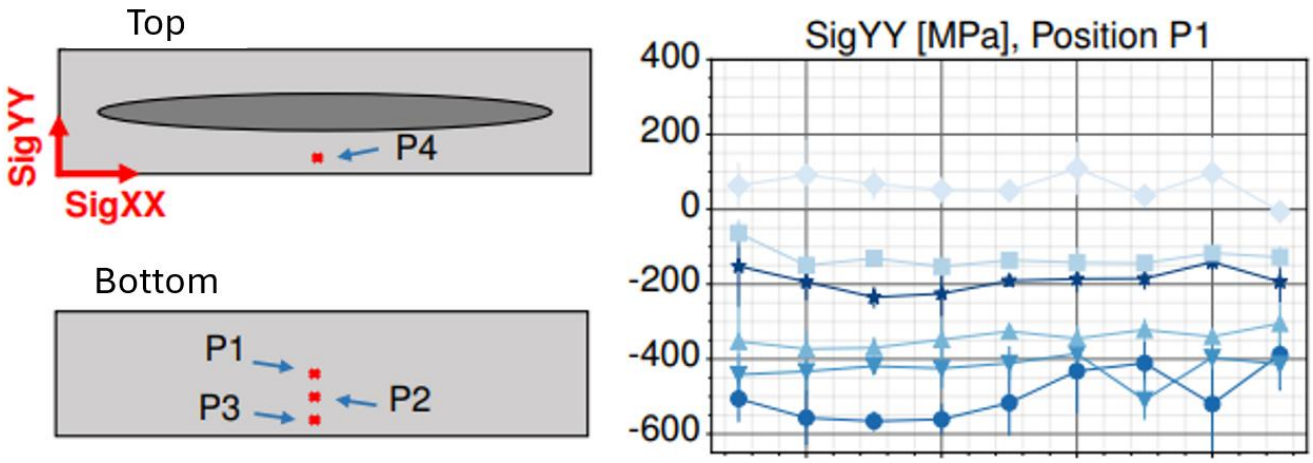

Figure 4: Left: Measurement points for residual stress measurements; Right: plot of residual stress measurement results for point P1, Reduction of residual stress by 643 MPa

However, the same alloy with a unidirectional deposition path caused increased distortion: steep gradients caused premature, asynchronous martensite transformation, self-cancelling the LTT volume expansion. Homogeneous paths achieved 50–65% distortion reduction; unidirectional deposition produced negative compensation. [24]

Cold wire delivery encountered hard capacity limits for GMAW at 200% process wire feed rate, and wire availability constrained the accessible alloy space. These limitations motivated powder-cored wire development for arcwelding, where the powder fill determines composition directly, eliminating concentration gradients and multi-wire stability constraints.

Convergence on path planning

Both thermal management and compositional control depended on the spatial temperature field distribution set by the deposition path. This overturned assumption A4 — not because the individual levers were weak, but because they are coupled through the temperature field. Direct evidence came from LMD trials [19]: spiral inward reached 820°C peak substrate temperature, spiral outward 600–650°C, and meander produced gradual linear increase — same energy input, radically different thermal fields. (Figure 5)

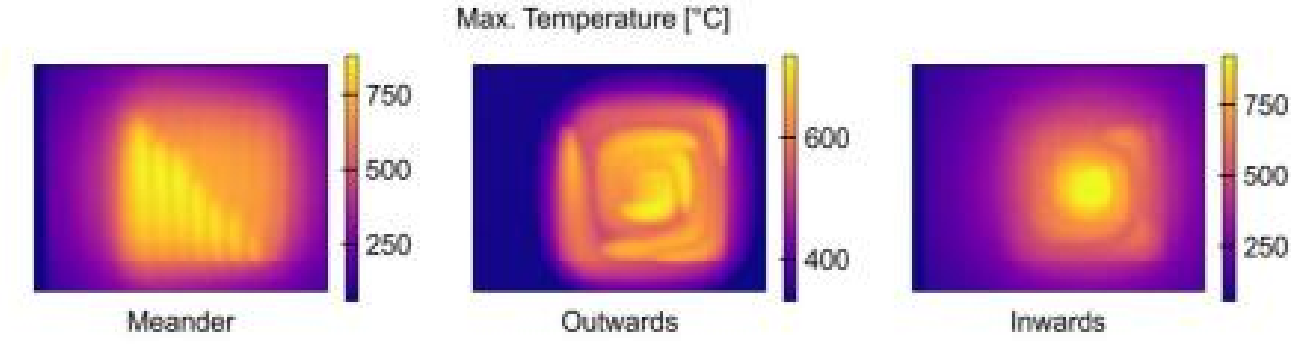

Figure 5: Superposition of multiple thermographic measurements for different path geometries until end of welding

An a-priori convolution-based geometry prediction [25] was developed, approximating single-bead cross-section as a parabolic kernel convolved with the path matrix to predict layer height before welding.

5 Summary

The twelve-years of collaborative research yielded several insights reshaping the understanding of residual stress. First, the transient thermomechanical state differs fundamentally from the final state: peak elastic strains exceed simulation predictions by two orders of magnitude, revealing inadequate high-temperature constitutive models. Second, local strain is governed by thermal gradients rather than global clamping. Third, both thermal management and compositional control depend on the spatial temperature field set by the deposition path, identifying path planning as the central integration variable.

Ongoing experimental efforts aim to lessen the remaining gap: DED-Arc welding with systematically varied paths and power inputs produces geometries measured by laser scanning, with machine learning correlating measurements against a-priori convolution predictions to learn the deviation between idealized model and real deposition height. Open challenges include high-temperature flow curves at welding-relevant rates, sub-0.01 s measurement resolution for closed-loop control, industrial scaling of powder-cored wire, and generalization of ML-corrected path planning across materials and processes.

Acknowledgements

The presented investigations were carried out at RWTH Aachen University within the framework of the Collaborative Research Centre SFB1120-236616214 “Bauteilpräzision durch Beherrschung von Schmelze und Erstarrung in Produktionsprozessen” and funded by the Deutsche Forschungsgemeinschaft e.V. (DFG, German Research Foundation). This work is based upon experiments performed at the STRESS-SPEC instrument operated by Hereon at the Heinz Maier-Leibnitz Zentrum (MLZ), Garching, Germany. We would like to thank DESY (Hamburg, Germany), a member of the Helmholtz Association (HGF), for providing the experimental facilities. Parts of this research were carried out at PETRA III, and we would like to thank all staff for their support in using beamline P61A. The beamtime was allocated under grant I-20210328.

Conflict of Interest

The authors declare no conflict of interest.

Data Availability Statement

The original images and the data of this publication are available on request at the following address hdl.handle.net/21.11102/8e38f9e5-cd1d-4252-8557-560e1eb92113

References

[1] K. Masubuchi, Analysis of Welded Structures, Pergamon Press, 1980. [2] P.J. Withers, H.K.D.H. Bhadeshia, Residual stress. Part 1 — Measurement techniques, Mater. Sci. Technol. 17 (2001) 355–365. [1] K. Masubuchi, Analysis of Welded Structures, Pergamon Press, 1980.

[2] P.J. Withers, H.K.D.H. Bhadeshia, Residual stress. Part 1 — Measurement techniques, Mater. Sci. Technol. 17 (2001) 355–365.

[3] J.A. Goldak, A. Chakravarti, M. Bibby, A new finite element model for welding heat sources, Metall. Trans. B 15 (1984) 299–305.

[4] L.-E. Lindgren, Numerical modelling of welding, Comput. Methods Appl. Mech. Eng. 195 (2006) 6710–6736.

[5] A. Kromm, J. Dixneit, T. Kannengiesser, Residual stress engineering by low transformation temperature alloys, Weld. World 58 (2014) 729–741.

[6] R. Sharma, Strain Field Determination in the Vicinity of the Molten Pool During Arc Welding, Ph.D. thesis, RWTH Aachen, 2022.

[7] U. Reisgen, R. Sharma, W. Wietheger, M.A. Knoch, A. Schacht, K. Bobzin, L. Oster, Comparison of Residual Stress Measurements Conducted by X-Ray Stress Analysis and Incremental Hole Drilling Method, Materialwiss. Werkstofftech. 48 (2017) 1270–1275.

[8] K. Mäde, R. Sharma, U. Reisgen, In-Situ Dehnungsbestimmung mittels EDXRD während des Laserschweißens, DVS Proc. (2023).

[9] K. Mäde, R. Sharma, U. Reisgen, Synchrotron EDXRD Strain-Temperature Measurement During Laser Welding, submitted (2024).

[10] R. Sharma, U. Reisgen, Assessment of Mechanical Properties in High-Strength Steel Weld Metals by Means of Phase Transformation Temperature, Weld. World 62 (2018) 1227–1236.

[11] U. Reisgen, R. Sharma, L. Oster, M. Christ, Einfluss von aktiven Kühlmethoden auf die Metallurgie von Duplexstählen bei WAAM, DVS Congress 2020.

[12] U. Reisgen, R. Sharma, L. Oster, Plasma Multiwire Technology with Alternating Wire Feed for Tailor-Made Material Properties in WAAM, Metals 9 (2019) 745.

[13] U. Reisgen, R. Sharma, L. Oster, 3D Printing in Steel Construction with the Automated Wire Arc Additive Manufacturing, Proc. Nordic Steel 2019, Copenhagen.

[14] R. Sharma, U. Reisgen, Comparison of Submerged Arc Welding Process Modification Influence on Thermal Strain by In-Situ Neutron Diffraction, Proc. ICRS-10, Mater. Res. Proc. 2 (2016) 533–538.

[15] R. Sharma, U. Reisgen, In-Situ Strain Measurement of Submerged Arc Welding Process Through Application of ESPI, J. Weld. Join. (2017).

[16] R. Sharma, U. Reisgen, Influence of Mill Scale on Weld Bead Geometry and Thermal Cycle During GTA Welding of High-Strength Steels, Weld. World 64 (2020) 1175–1183.

[17] R. Sharma, M. Hofmann, U. Reisgen, Investigation on the Feasibility of Strain Measurement by In Situ Neutron Diffraction During Welding, Forces Mech. 9 (2022) 100139.

[18] U. Reisgen, R. Sharma, L. Oster, In-Situ Alloying in Gas Metal Arc Welding for WAAM, Springer, 2021, pp. 168–177.

[19] K. Mäde, R. Sharma, U. Reisgen, Measurement Routine for Analysing the Thermal Impact of AM Processes on Deformation, Conf. Proc. (2023).

[20] K. Mäde, U. Reisgen, Cold Wire Alloying in GMAW and Related Arc Processes, IIW Doc. II-2381-2025, Genoa, 2025.

[21] R. Sharma, U. Reisgen, Comparative Study of Phase Transformation Temperatures in High Strength Steel Weld Metals, Mater. Test. 59 (2017) 344–347.

[22] U. Reisgen, R. Sharma, L. Oster, S. Mann, Effizienzsteigerung von WAAM durch Aerosolkühlung und Mehrdrahttechnologie, Conf. Proc. (2019).

[23] U. Reisgen, V. Dilthey, I. Aretov, SAW Cold Wire Technology, in: Hot Cracking Phenomena in Welds II, Springer, 2008, pp. 215–237.

[24] L. Oster, Fabrication of LTT Alloys by In Situ Alloying with Arc Welding, Ph.D. thesis, RWTH Aachen, 2023.

[25] K. Mäde, P.J. Kellerwessel, R. Sharma, U. Reisgen, A-Priori Layer Height Determination for WAAM Based on Weld Geometry, Materialwiss. Werkstofftech. 55 (2024) 995–1004.

[26] K. Mäde, R. Sharma, U. Reisgen, EDXRD-Dilatometry Synchronization for Time-Temperature-Strain Correlation During Laser Welding, Proc. ECRS-11, Prague, 2024.

[27] U. Reisgen, R. Sharma, S. Mann, L. Oster, Increasing the Manufacturing Efficiency of WAAM by Advanced Cooling Strategies, Weld. World 64 (2020) 1409–1416.

Date: 31.03.2026

Modelling the influence of thermal fields on residual stress evolution incorporating LTT effect in low and high alloy steels

Author: Karthik Ravi Krishna Murthy[1]

Authors: Maximilian Gamerdinger[1], Marcel Troise[1], Simon Olschok[1], Uwe Reisgen[1]

[1]RWTH Aachen University, Welding and Joining Institute, Pontstr. 49, 52062, AACHEN, GERMANY

Corresponding author: E-mail: karthik.krishnamurthy@isf.rwth-aachen.de, ORCID: 0000-0003-1978-7002

Abstract

This study presents a numerical analysis of the influence of thermal fields on the development of residual stress in both low and high alloy steels, specifically addressing low-transformation-temperature (LTT) effects during electron beam welding. A coupled thermo-metallurgical-mechanical finite element model is created to simulate the interplay between transient heat transfer, phase changes, and stress development during cooling. The LTT phenomenon is integrated using a UEXPAN user defined subroutine by considering the transformation-induced plasticity and strain linked to martensitic transformation at lower temperatures. This combinational effect allows to depict the stress relaxation and distortion behavior. Comparative analyses of low and high alloy steels highlight the influence of localized thermal input and LTT characteristics on the determination of final stress states. The findings show the importance of accurately modeling both the position of the applied thermal field and the transformation kinetics when evaluating deformation and structural integrity in thermally processed components.

Keywords

Laser beam welding, electron beam welding, low transformation temperature (LTT) effect, numerical simulation, residual stress, distortion

1 Introduction

In Beam welding, distortion and residual stress are inevitable problems that are primarily brought on by sudden change in temperature and uneven cooling. These effects can have a detrimental impact on the performance of welded components and frequently result in dimensional errors, particularly in applications where extreme precision is needed. It has become evident in recent years that metallurgical transformations have a significant impact on residual stress formation in addition to thermal effects. In particular, the martensitic transformation during cooling plays an important role in how stress develop in the weld [1,2]. Based on this understanding, low–

transformation–temperature (LTT) alloys have been introduced as a promising approach to reduce welding-induced stress.

The key idea behind LTT materials is that the martensitic transformation occurs at relatively low temperatures. This delayed transformation leads to a volume expansion that can counteract the shrinkage during cooling. As a result, tensile residual stress can be significantly reduced or even converted into compressive stress [3,4]. In addition, studies have shown that the effectiveness of this mechanism depends strongly on the chemical composition, as it directly influences the transformation temperature and the resulting strain potential [5]. Further work by Kannengiesser, Kromm, and Hübner has shown that LTT welding consumables can actively be used to tailor residual stress. Their results indicate that compressive stress can be introduced during cooling, with reductions in the range of several hundred MPa depending on weld geometry [6]. They also demonstrated that this approach could improve fatigue performance by reducing critical tensile stress in welded components [7].

To better understand these interactions, numerical simulations have been increasingly used. These models combine thermal, metallurgical, and mechanical effects and allow the prediction of residual stress with good spatial and temporal resolution [8]. It has also been observed that even small changes in chemical composition can influence melt pool behavior and transformation kinetics, which in turn affects the final stress state [9]. More recent developments focus on using this knowledge for process control. By adjusting the alloy composition locally, for example through controlled filler material deposition, it becomes possible to influence residual stress in a targeted way. This opens new possibilities for reducing distortion in complex welded structures [10–12].

2 Aim of the Investigation

The primary aim of this study is to mitigate welding-induced deformation by comprehending and regulating the formation of residual stress in fusion welding. The emphasis is on the utilization of chemical composition and phase transformations, especially in low-transformation-temperature (LTT) materials, to affect the stress state during cooling. A primary objective is to establish explicit correlations among chemical composition, temperature gradients, phase change behavior, and the resultant residual stress. Furthermore, the study aims to describe and predict these interactions by numerical simulations that integrate thermal, metallurgical, and mechanical influences. Based on this understanding, the final objective is to develop practical process strategies such as controlled adjustment of alloy composition during welding to enable targeted control of residual stress and minimize distortion in complex components.

3 Materials and Experimental Details

The materials used in this study were low-alloy carbon–manganese steel S235JR and austenitic stainless steel EN 1.4301. Both were made into plates measuring 100 × 50 × 5 mm. These steels were chosen to represent two very different metallurgical structures: the low-alloy steel had a ferritic–pearlitic structure, while the high-alloy steel had a fully austenitic structure. This enables a

comparative investigation of the low–transformation–temperature (LTT) effect under contrasting phase stability and thermal conditions. To ensure consistent weld geometry and controlled filler material deposition, all samples were prepared with a central groove measuring 1 × 1 mm in both width and depth. Two filler wire types supplied by ESAB (Sweden) were used: a high-alloy wire G19 9 (EN ISO 14343-A G 19 9 L Si / AWS A5.9: ER308LSi) and a low-alloy wire G3Si1 (EN ISO 14341-A G 38 3 C13Si1 / AWS A5.18: ER70S-6), both with a diameter of 1 mm. The LTT effect was introduced using an in-situ alloying approach by varying the combination of base and filler materials. For the low-alloy steel S235, the LTT condition was achieved by alloying with the high-alloy filler wire G19 9, while the reference weld was produced using G3Si1. In contrast, for the austenitic stainless steel EN 1.4301, the reference weld was produced using the high-alloy filler wire G19 9, whereas the LTT condition was obtained by dilution with the low-alloy filler wire G3Si1. This approach allowed controlled modification of the weld metal composition and transformation behavior in both material systems. The chemical compositions of the base materials and filler wires were determined using optical emission spectroscopy, **Table 1**.

Table 1: Chemical compositions for base material and filler wire in wt%

		Fe	C	Si	Mn	Cr	Ni	Mo
Base	S235JR	98.2	0.08	0.056	1.01	0.413	0.041	0.014
Material	EN1.4301	70.7	0.02	0.42	1.68	18.2	8.24	0.036
Filler	G 19 9	67.4	0.026	0.75	1.84	19.84	10.14	0.026
wire	G3Si1	97.3	0.07	0.86	1.44	0.045	0.019	0.008

The welding experiments were carried out using both an electron and laser beam welding system equipped with a clamping fixture and a filler wire feeding unit **Figure 1**. Welding parameters were optimized through preliminary trials and finalized in accordance with ISO EN 13919-1:1996, ensuring that all welds met quality group B requirements.

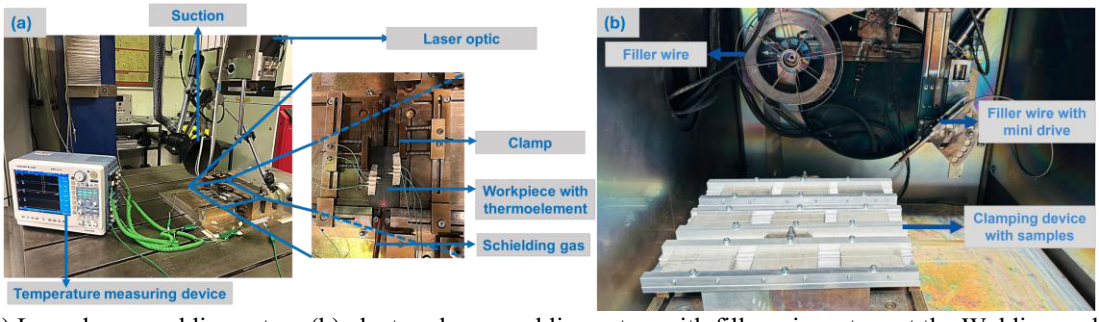

Figure 1: (a) Laser beam welding setup, (b) electron beam welding setup with filler wire set up at the Welding and Joining Institute (ISF)

Residual stress is measured using a near-surface method. A drill with a diameter of 0.8 mm was used, and measurements were taken at a depth of 0.5 mm, where the highest tensile residual stress is typically expected in beam welded joints. The longitudinal residual stress component, parallel to

the welding direction, was recorded at intervals of 3 mm in the transverse direction up to a distance of 9 mm from the weld centerline. Angular distortion was evaluated using a laser line-scan technique by comparing the geometry of the specimens before and after welding.

To further investigate phase transformation behavior, dilatometry experiments were conducted. For this purpose, samples with controlled chemical compositions were first prepared by melting predefined amounts of base and filler material in an electric arc furnace. Optical emission spectroscopy was used to confirm the chemical makeup, specifically to verify the intended chromium and nickel concentrations. Subsequently, the material underwent machining to produce hollow cylindrical specimens. These specimens measured 10 mm in length, had an outer diameter of 4 mm, and possessed a wall thickness of 1 mm, as specified by ASTM A1033-18.

Dilatometry experiments were conducted utilizing a quenching and deformation dilatometer. Temperature data were acquired via a K-type thermocouple, and dimensional alterations were assessed using a linear variable displacement transducer. The specimens underwent heating to an austenitization temperature of roughly 930 °C, maintained for a duration of 5 minutes, subsequent to which they were quenched at a rate of 100 °C/s within a helium environment. The resulting dilation curves were used to analyze phase transformation behavior.

Since the primary transformation occurs during the cooling stage, the phase fractions were determined from the cooling segments of the dilation curves. The martensitic transformation was evaluated using both a graphical approach based on the lever rule and an empirical method based on lattice parameters. Due to the high cooling rate, the transformation from austenite to martensite occurred directly without intermediate phases. The martensite fraction was found to depend mainly on the martensite start temperature and the associated volume expansion, with the transformation temperature determined from the dilatometry data as well as empirical relationships based on chemical composition.

The numerical simulations were carried out to describe the coupled thermo-metallurgical-mechanical behavior during welding and to predict the resulting residual stress, **Figure 2**. A multi-physics modeling approach was adopted, in which heat transfer, phase transformation, and mechanical response were solved in a sequentially coupled manner. Initially, the thermal field was determined through the simulation of the welding heat source and its consequent heat input into the material. This involved accounting for temperature-dependent material characteristics and relevant boundary conditions, such as heat dissipation via conduction, convection, and radiation for laser beam welding and just radiation in case of electron beam welding. The dynamic heat source was specified in accordance with the welding process parameters, thereby facilitating the computation of transient temperature profiles and cooling rates.

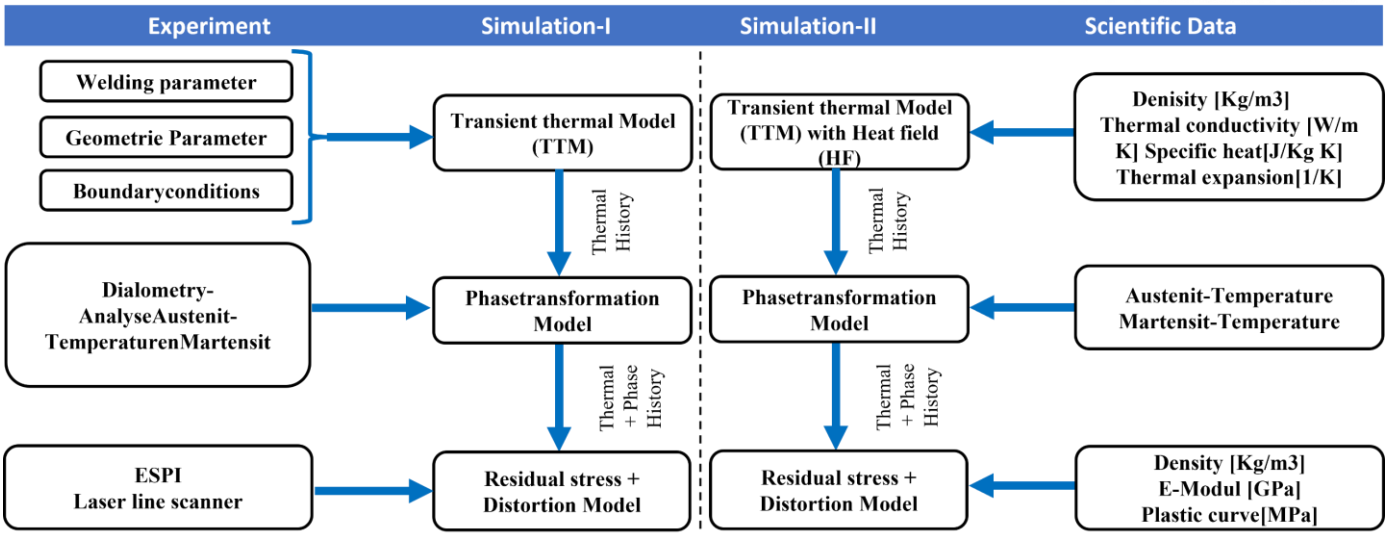

Figure 2: Simulation methodology

Based on the computed temperature field, the metallurgical model was applied to describe phase transformations during the cooling cycle. In particular, the martensitic transformation was modeled as a function of temperature and chemical composition, allowing the determination of transformation start temperature and phase fractions. The transformation-induced strain associated with the formation of martensite was included in the model to capture its influence on stress development. The mechanical analysis was then performed, using the calculated temperature history and phase fractions as input. Thermal strains, transformation-induced strains, and elastic-plastic material behavior were considered to determine the evolution of residual stress. The interaction between these effects enabled a realistic prediction of distribution of stress in the weld region. In addition, the simulation model was extended to include the effect of an external heat field applied during or after welding. This allowed the investigation of how modified thermal conditions influence cooling behavior, phase transformation timing, and residual stress formation. The model was validated by comparing the simulation results with experimental measurements of temperature, phase fraction, and residual stress. Simulation methods provide a comprehensive way to analyze and predict how process parameters and material properties affect the development of residual stress during welding.

4 Results and Discussion

In Phase 1, the study focused on the influence of chemical composition on residual stress formation and on confirming the LTT effect, using low-alloy steel as the base material and electron beam welding as the process. The results clearly show that residual stress formation is not governed solely by thermal effects but is strongly influenced by the interaction between chemical composition and phase transformation behavior. In conventional materials, cooling primarily results in tensile residual stress due to thermal contraction under constraint. With the introduction of LTT materials, a clear reduction in residual stress was observed. The delayed martensitic transformation at lower temperatures caused volume expansion during the final stages of cooling, which counteracted thermal shrinkage. As a result, the weld area, especially near the center, showed a shift from tensile

to compressive residual stress. Furthermore, a strong influence of chemical composition was identified, confirming that alloy design plays a key role in controlling residual stress development and validating the effectiveness of the LTT approach, **Figure 3**.

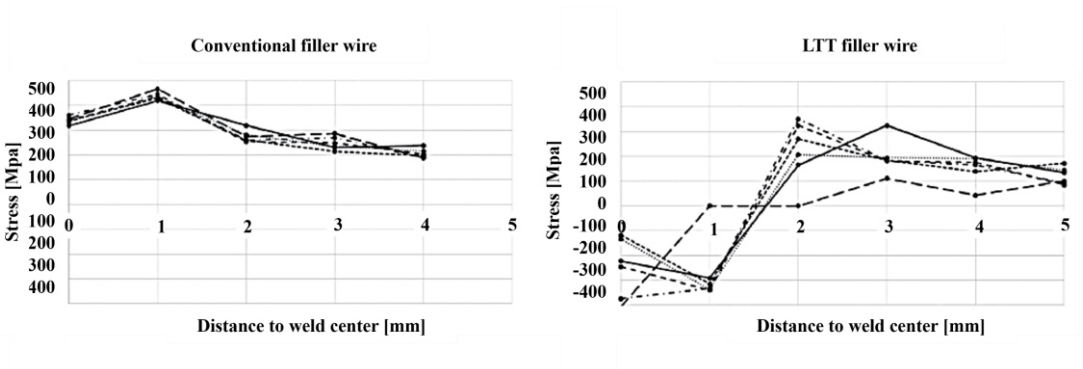

Figure 3: Comparison of residual stress measurements for conventional and LTT wires

In Phase 2, the focus was on temperature gradients and phase transformation behavior using numerical simulations, supported by in-situ experimental validation.

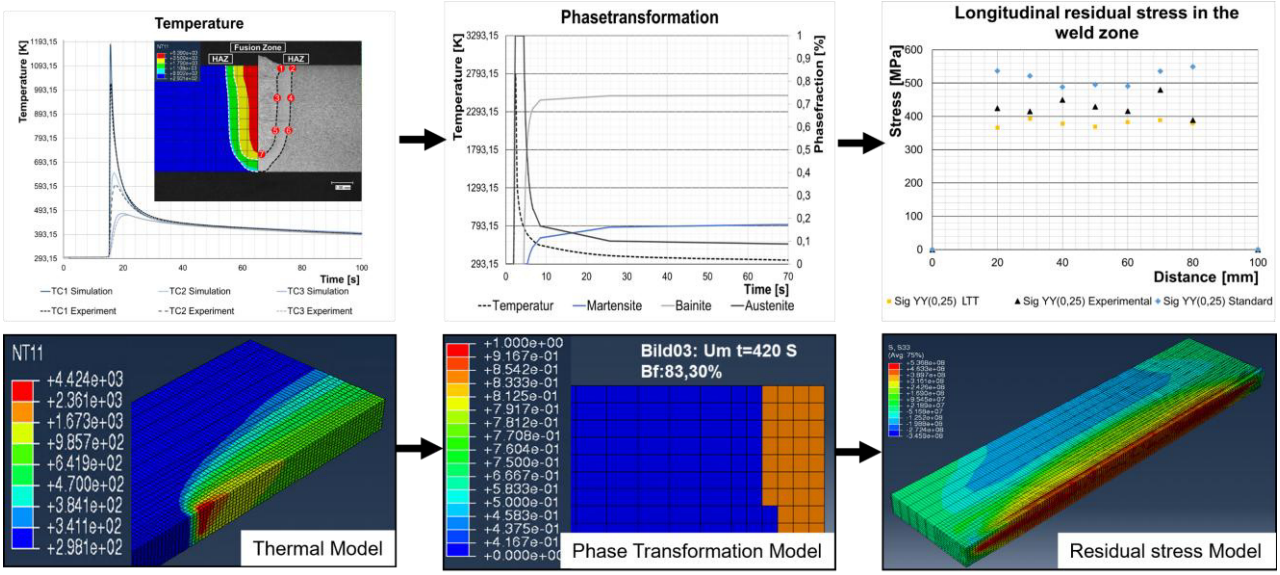

Figure 4: Comparison of residual stress measurements for conventional LTT wires

The results show a clear difference in residual stress distribution and temperature fields when phase transformation is included in the simulations compared to when it is neglected. Incorporating phase transformation leads to a more accurate prediction of residual stress, highlighting its significant influence. In addition, in-situ EDXRD measurements during laser beam welding confirmed the transformation behavior of LTT materials. The results show that the delayed martensitic transformation occurs during the cooling stage and is closely linked to local thermal conditions. This provides direct experimental evidence that transformation-induced strains interact with thermally induced stress during welding. The results demonstrate that residual stress development is governed by a strong coupling between thermal, metallurgical, and mechanical effects, emphasizing the importance of a thermo-metallurgical approach for accurate prediction and understanding of the LTT effect, **Figure 4**.

In Phase 3, the focus shifted from understanding the LTT effect to its application for active residual stress and distortion control. The results show that alloy composition and process conditions can be combined in a targeted manner to improve the final stress state of the weld.

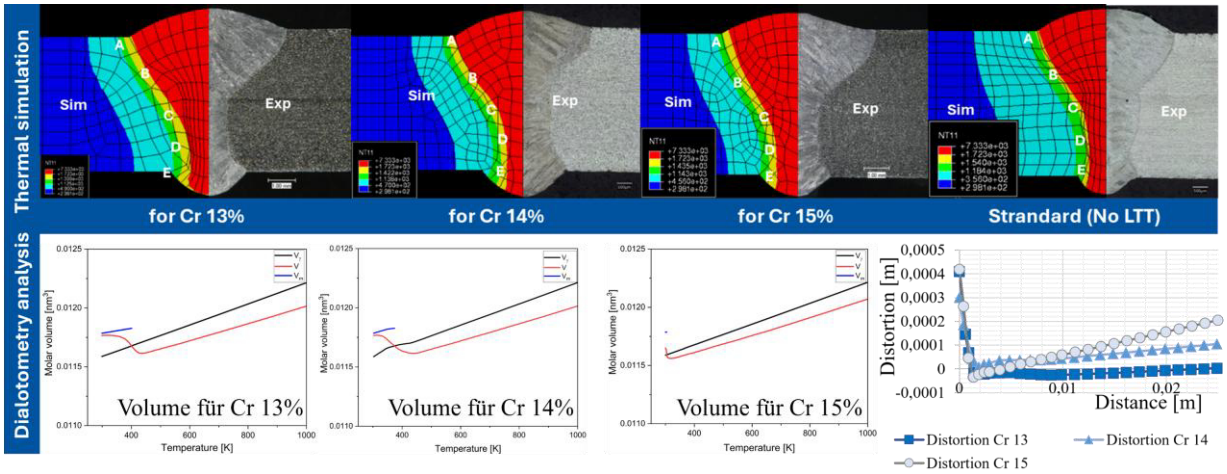

Figure 5: Calibrated equivalent thermal models for different Cr% along with dilatometry and distortion analysis.

The impact of chromium content on the LTT effect was examined across weld metal compositions containing 13%, 14%, and 15% Cr, **Figure 5**. The findings reveal a significant correlation between phase transformation characteristics, residual stress profiles, and the specific composition. In the instance of 13% Cr, the martensitic transformation initiates around 160.7 °C and concludes at 50.99 °C, yielding a substantial martensite fraction of approximately 72%. Consequently, this engenders considerable volume expansion during the cooling process, thereby generating compressive residual stress within the weld seam, which is indicative of a pronounced LTT effect. In contrast, at 14% Cr, the martensite start temperature decreases to around 70.5 °C and the martensite fraction drops to ~33%. The transformation is less pronounced and extends below room temperature, resulting in reduced transformation-induced strain and therefore weaker stress compensation. With a chromium content of 15%, the martensite start temperature drops to about 34 °C, and the amount of martensite formed decreases significantly (by about 16%). As a result, the martensitic transformation is largely suppressed, which reduces the LTT effect and increases the residual tensile stress. The findings suggest that a chromium concentration of approximately 13% yields the most favorable LTT characteristics, as it facilitates adequate martensite development at a critical point in the cooling process, thereby inducing compressive stress. Elevated chromium levels diminish the efficacy of the LTT effect, a consequence of transformation being delayed or inhibited, which underscores the significance of precise alloy design in managing residual stress and distortion.

Further the numerical model was extended to include coupled thermo-metallurgical-mechanical behavior along with the influence of an additional heat field, allowing both metallurgical and thermal contributions to residual stress development to be evaluated.

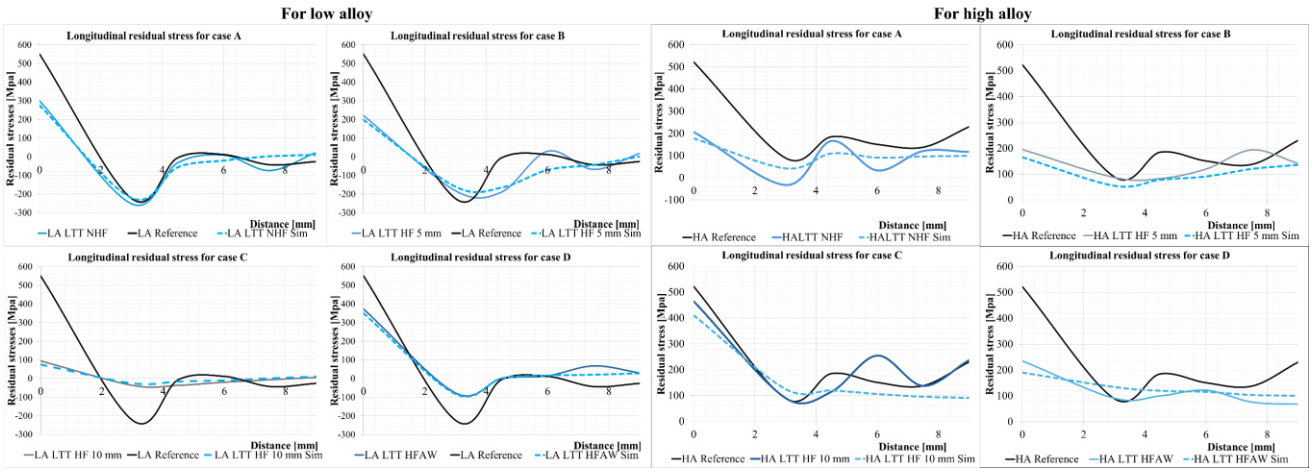

Figure 6: Residual stress comparison with and without LTT effect for both high and low alloy considering the heat fields where HA refers to high alloy and LA refers to low alloy.

The results in **Figure 6** confirm that the LTT effect plays a key role in generating compressive stress in the weld seam through delayed martensitic transformation. At the same time, the applied heat field influences thermal strains and further improves the residual stress profile. For low-alloy steel, the optimal condition was achieved when the heat field was applied 10 mm behind the melt pool. The delayed martensitic transformation, occurring later in the cooling process and nearer to ambient temperature, effectively diminished the thermal contraction range. Consequently, stress compensation was enhanced, which in turn reduced peak weld stress by roughly 100 MPa and achieved an overall stress reduction of approximately 82% relative to the baseline scenario. Furthermore, the elimination of compressive stress within the heat-affected zone facilitated a more uniform stress distribution. For the high-alloy steel, the most effective strategy was to apply the heat field after completion of the welding process. This allowed the weld to cool naturally, enabling the LTT transformation to occur without interference. The subsequent heat input primarily contributed to relaxation of existing thermal stress rather than altering transformation behavior. As a result, the stress at the weld center decreased to about 220 MPa, and the stress distribution within the heat-affected zone became much more uniform. Consequently, the overall residual stress was reduced by roughly 58% compared to the initial weld. These observations highlight the substantial impact of the base material on the heat field's implementation. In low-alloy steel, the increased thermal conductivity promotes rapid cooling, thus making the transformation characteristics especially susceptible to additional heat. Conversely, high-alloy steel, distinguished by its lower thermal conductivity and metastable austenitic phase, demonstrates greater sensitivity to thermal variations, demanding precise control over the heat field's application. Therefore, the combined findings suggest that the most efficient reduction of residual stress is achieved through a combined approach, where metallurgical control, enabled by the LTT effect, is integrated with a carefully designed thermal strategy.

5 Summary

The present investigation establishes that a combined thermos-metallurgical strategy, particularly the application of low-transformation-temperature (LTT) materials, can be employed to manage residual stress and distortion in fusion welding. Throughout the three phases of the study, the development of residual stress was found to be controlled not only by thermal phenomena but also, and to a considerable extent, by phase transformation dynamics; these, in turn, are modifiable via alloy composition and processing parameters.

Phase 1 results confirmed that using LTT filler materials significantly reduced tensile residual stress. In some cases, this also led to compressive stress in the weld area. This effect is mainly due to a delayed martensitic transformation, which helps to counteract thermal shrinkage during cooling.

In Phase 2, numerical simulations combined with in-situ experimental validation demonstrated that accurate prediction of residual stress requires consideration of coupled thermal, metallurgical, and mechanical effects. The results highlighted the strong influence of chemical composition on temperature gradients, melt pool behavior, and phase transformation kinetics.

In Phase 3, the management of residual stress was successfully accomplished through a combined strategy that integrated alloy design and process techniques, notably the use of a heat field. The introduction of an auxiliary heat field, alongside an optimized alloy composition, resulted in significant stress reductions, specifically approximately 82% in low-alloy steel and 58% in high-alloy steel.

Furthermore, the impact of Cr–Ni composition was distinctly observed; a chromium content of approximately 13% exhibited the most favorable LTT behavior, attributable to adequate martensite formation and transformation-induced strain.

Higher chromium contents (14–15%) resulted in reduced martensite fractions and diminished stress compensation. The results also emphasized that the timing and placement of the heat field are crucial for maximizing the effectiveness of the LTT effect.

Overall, the study confirms that optimal residual stress reduction is achieved through an integrated approach, where metallurgical control via tailored alloy composition is combined with controlled thermal management, providing a reliable pathway for minimizing residual stress and distortion in welded components.

Acknowledgements

The presented investigations were carried out at RWTH Aachen University within the framework of the Collaborative Research Centre SFB1120-236616214 “Bauteilpräzision durch Beherrschung von Schmelze und Erstarrung in Produktionsprozessen” and funded by the Deutsche Forschungsgemeinschaft e.V. (DFG, German Research Foundation) and simulations were

performed with computing resources granted by RWTH Aachen University under project rwth1256. The sponsorship and support is gratefully acknowledged.

Conflict of Interest

The author declares no conflict of interest.

Data Availability Statement

The data that support the findings of this study are available at http://hdl.handle.net/21.11102/e66b83c7-a6b2-4134-9c73-cfb528332dec upon request.

References

[1] S. Gach, A. Schwedt, S. Olschok, U. Reisgen, J. Mayer, Confirmation of tensile residual stress reduction in electron beam welding using low transformation temperature materials (LTT) as localized metallurgical injection – Part 1: Metallographic analysis, Materials Testing 59 (2017) 148–154.

[2] U. Reisgen, S. Olschok, S. Gach, Nutzung von Low‐Transformation‐Temperature‐Werkstoffen (LTT) zur Eigenspannungsreduzierung im Elektronenstrahlschweißprozess, Materialwissenschaft Werkst 47 (2016) 589‐599.

[3] S. Gach, S. Olschok, D. Arntz, U. Reisgen, Erratum: “Residual stress reduction of laser beam welds by use of low-transformation temperature (LTT) filler materials in carbon manganese steels— In situ diagnostic: Image correlation” [J. Laser Appl. 30, 032416 (2018)], Journal of Laser Applications 32 (2020).

[4] S. Gach, S. Olschok, D. Arntz, U. Reisgen, Residual stress reduction of laser beam welds by use of low-transformation-temperature (LTT) filler materials in carbon manganese steels— In situ diagnostic: Image correlation, Journal of Laser Applications 30 (2018).

[5] U. Reisgen, S. Olschok, R. Sharma, S. Gach, Influence on martensite‐start‐temperature and volume expansion of low‐transformation‐temperature materials used for residual stress relief in beam welding, Materialwissenschaft Werkst 48 (2017) 1276‐1282.

[6] M. Hübner, F. Dittmann, A. Kromm, I. Varfolomeev, T. Kannengießer, Residual stress reduction using a low transformation temperature welding consumable with focus on the weld geometry, Weld World 69 (2025) 3129–3139.

[7] M. Huebner, F. Dittmann, A. Kromm, I. Varfolomeev, T. Kannengiesser, Enhancement of the fatigue strength by application of a low transformation temperature (LTT) welding consumable, Weld World (2026).

[8] F. Akyel, S. Olschok, U. Reisgen, Dissimilar material combination in laser beam welding: reduction of distortion and residual stress, in: High-Power Laser Materials Processing: Applications, Diagnostics, and Systems IX, San Francisco, United States, 2020 - 2020, p. 11.

[9] M. Gamerdinger, F. Akyel, S. Olschok, C. Kahve, D.C. Fritsche, U. Elliesen et al., Use of a low transformation temperature effect for the targeted reduction of welding distortion in stainless chromium‐nickel steel for an application in rail vehicle construction, Materialwissenschaft Werkst 55 (2024) 1005–1017.

[10] K.R. Krishna Murthy, F. Akyel, U. Reisgen, S. Olschok, Simulation of transient heat transfer and phase transformation in laser beam welding for low alloy steel and studying its influences on the welding residual stresses, Journal of Advanced Joining Processes 5 (2022) 100080.

[11] M. Gamerdinger, F. Akyel, S. Olschok, U. Reisgen, Investigating mechanical properties of laser beam weld seams with LTT-effect in 1.4307 and S235JR by tensile test and DIC, Procedia CIRP 111 (2022) 420–424.

[12] F. Akyel, M. Gamerdinger, S. Olschok, U. Reisgen, A. Schwedt, J. Mayer, Residual Stress Reduction with the LTT Effect in Low Carbon Manganese-Steel through Chemical Composition Manipulation Using Dissimilar Filler Material in Laser Beam Welding, Metals 12 (2022) 911.

Date: 31.03.2026

Adaptive Grids in Time for Efficient Simulations for Injection Molding Applications

Authors: B. Ferrer Fabón*[1], M. Behr[1]

[1]RWTH Aachen University, Chair for Computational Analysis of Technical Systems, Schinkelstr. 2, 52062, AACHEN, GERMANY

*Corresponding author: E-mail: ferrer@cats.rwth-aachen.de, ORCID: 0000-0002-8817-4659

Abstract

This paper summarizes the advances in numerical simulations of polymer injection molding through the use of space-time finite elements, combined with localized adaptive time refinement. We reference various publications generated by our research group over the past years that explore this topic and demonstrate how this methodology enhances both the accuracy and efficiency of cavity filling simulations. Additionally, we showcase the latest results regarding the precision of our approach, demonstrating strong alignment with experimental data. Our findings contribute to optimizing injection molding processes and advancing the field of computer-assisted manufacturing.

Keywords

Injection Molding, Finite Elements, Two-Phase Flow, Adaptive Refinement, Space-Time

1 Introduction

Injection molding is a widely utilized manufacturing process for producing plastic components. This method enables rapid manufacturing and scalable design, accommodating processes that range from quick prototyping to high-volume production at low costs. The technique involves injecting molten polymer into a cooled mold, where it solidifies to form the desired shape. Accurate numerical simulations are essential for optimizing this process, as they play a crucial role in predicting material behavior and ensuring product quality.

The numerical simulation of injection molding presents inherent complexities due to factors such as moving melt boundaries, complex rheological behavior of molten polymers, and solidification dynamics during filling. These challenges contribute to inaccuracies and computational demands associated with existing simulation methods.

Around the beginning of this project in 2014—and continuing today—most commercial software employed for injection molding simulations has relied on simplified numerical models (2.5D) and

basic material assumptions (e.g., non-Newtonian flow and isothermal conditions). While these approaches do offer insights, they often fall short when precise predictions are required. Conversely, more sophisticated models tend to be computationally prohibitive for industrial applications. Therefore, there remains the need for numerical methods that can effectively address these complexities while enhancing overall simulation efficiency.

This paper summarizes the research conducted by our group within the framework of the German Government-Funded Research Project SFB 1120: *Component Precision through Control of Melting and Solidification in Production Processes*. Specifically, we focus on the subproject dedicated to *Adaptive Grids in Space and Time for Efficient Simulation of Moving Phase Boundaries*. Over the past years, we have achieved significant advancements in the numerical simulation of polymer injection molding applications. Specifically, this concerns the cavity filling stage of the process, when the molten polymer fills the solid cooled mold. We highlight the developments made during the project period from 2014 to the present, including our latest three-dimensional simulation results that align closely with experimental data.

2 Aim of the Investigation

This project aims to improve the computer-assisted predictions for injection molding processes, specifically for the cavity filling stage. A first objective is to improve the accuracy of numerical simulations by developing a robust solver that accounts for the complexities of the process while minimizing simplifications. Simultaneously, we aim to achieve feasible computational times by employing efficient numerical methods tailored for these simulations. In summary, our goal is to achieve accurate and efficient cavity filling simulations for injection molding applications.

3 Materials and Numerical Methods

3.1. Numerical methods

To model the cavity filling process, we use a two-phase flow formulation, describing both the molten polymer and the air inside the static domain contained in the mold. The governing equations for both fluids are the Stokes equations coupled with the heat equation. Additionally, to distinguish between the polymer and air phase, the level-set equation is employed [1]. The strong form that describes our problem is described in [2].

The solver used for the numerical simulations presented in this work is a finite-element in-house solver at the Chair for Computational Analysis of Technical Systems, named XNS. With this solver, the governing equations are discretized using equal-order continuous finite elements. The Galerkin/Least-Squares method is used for the stabilization [3]. The system is strongly coupled, i.e., all equations are solved together (iteratively) at each time step, until convergence is reached.

We solve the system equations within a space-time framework, i.e., using finite-element discretization for both space and time [4]. In general, the discontinuous prismatic space-time [5] is used. For the examples with time refinement in localized areas of interest, the discontinuous

simplex space-time needs to be used [6], since it gives the flexibility to add extra nodes in the time direction.

3.2. Materials

For the injection molding simulations and the experiment presented in this work, the polymer used is isotactic polypropylene PP505P by Saudi Basic Industries Corporation, Riyadh, Saudi-Arabia. The material properties used for the polymer have been experimentally determined and can be found in [2]. For simplicity, the air properties are considered constant and can be also be found in [2]. For the polymer modeling, we consider the shear-thinning behavior and temperature dependency with the Cross-Williams-Landel-Ferry (Cross-WLF) model for viscosity [7]. In the temperature equation, the heat viscous dissipation is included, and any crystallization effect is neglected. These considerations are based on the results in [8] and discussed in [2].

3.3. Experimental setup

For the new results presented in this paper, the experimental data presented in [2] are used. These data are obtained from practical injection molding trials conducted by the Institute for Plastics Processing at the RWTH Aachen University. For the geometry depicted in Figure 1, nine infrared sensors are mounted on each side of the mold in a regular grid pattern to measure the local temperature. More details on the experimental setup are specified in [2].

4 Results and Discussion

4.1. High-fidelity injection molding simulation

To ensure accurate macroscale injection molding simulations using our finite element space-time framework, several studies have been performed. A first study about the relevant material models during the cavity filling simulation was performed in [8]. The most relevant models proved to be the shear-thinning viscosity and the temperature field. The formulations studied and the methodology used are described in the aforementioned publication.

To validate our model and methodology, an experiment was performed to provide data for comparison with numerical simulations, as described in [2]. The experimental data includes temperature measurements taken at nine sensor positions throughout the filling process (see Figure 1). However, there are several limitations to consider regarding this data:

1. The measurements are taken with a time interval of 0.1 seconds.
2. The sensor averages in an area of 2mm radius.
3. The depth (z direction in Figure 1) at which the sensor measures is uncertain.
4. The sensor only measures opaque material, i.e., the measurements on the air phase are not accurate.

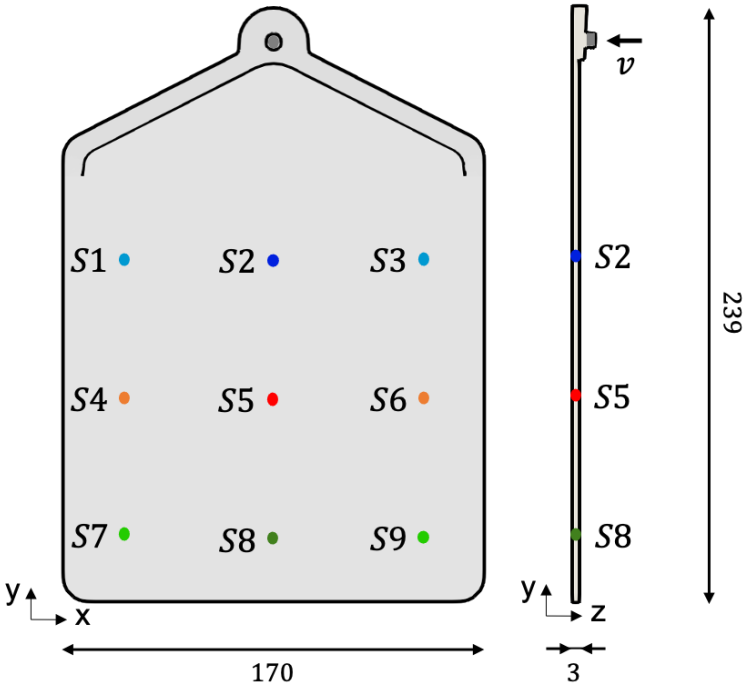

Figure 1: Testing geometry. Measures in mm. Sensors are located symmetrically at locations 28.33, 85, and 141.67 mm in x and y directions from the low-left corner of the geometry.

An initial comparison between the 2D simulation and the experimental data is presented in [2]. Good agreement was found in terms of temperature cooling and filling pace. However, the 2D simulation presented limitations for a full validation. For this purpose, a 3D simulation is compared here. To reduce computational time, we utilized only half of the geometry with symmetry boundary conditions. The results are shown in Figure 2.

In the 3D simulation, we can address limitation number 2 by averaging temperatures within the sensor's area of a 2 mm radius. Both the temperature range and mean temperature within this area are plotted in the results. To account for limitation number 3, following the approach outlined in [2], the measuring depth z has been estimated to be at ~0.53mm from the wall; thus, simulation results are extracted from this z-plane. Due to limitation number 4, two different simulations were conducted. In the first one, in Figure 2(a), the experiment conditions are replicated. Here, we expect matching the cooling of the polymer in time and the filling pace. However, because the sensor does not measure the air temperature correctly, we expect some errors in the data before the polymer completely crosses the sensor. To verify the crossing of the polymer through the sensor, an adapted simulation has been performed, where the air temperature has been set to 353K, approximately the temperature that the sensors detect, and not 303K, which is the real data during the experiment.

The results are shown in Figure 2(b). Results are qualitatively similar during the polymer crossing the sensor. The main differences arise from the wide sampling interval chosen to align with the experimental data. When more time solutions are considered, Figure 2(c), we observe that the temperature gradient when the polymer crosses the sensor is steeper. In contrast, the experimental

data reflect a more gradual temperature change, as seen in Figure 2(a) and Figure 2(b). This discrepancy could suggest that a steeper change is not captured by experiments due to limited data sampling.

It is also evident from the experimental results that as the polymer approaches the sensor, there is a gradual rise in temperature, a phenomenon not observed in our simulation results. This could be attributed to limitation number 4, i.e., the air phase data does not accurately represent reality, or alternatively, that our simplified model for air in the numerical simulation is insufficient. The latter would imply that, in reality, air near the flow front is warmer than indicated by simulation results.

Another discrepancy between experiments and simulations is observed in the cooling curve in sensor 1. After the polymer crosses this sensor and begins to cool down, the melt heats up again. A similar behavior can be mildly noted at sensor 2. This might indicate a boundary condition setting problem at the symmetry axis.

Despite these discrepancies, we find that our simulation captures filling pace very effectively, as the time at which the polymer crosses the sensor aligns closely with the data obtained by experiments. Additionally, cooling curves for sensors located outside of the symmetry plane (sensors 1, 4, and 7) match well with experimental results.

The cavity filling simulations have been further verified by comparing them with commercial software solutions. Particularly, we compared our predictions with the ones provided by Comsol Multiphysics. The methodology and results obtained are described in [9]. There, we observed very similar predictions between solvers, which were highly dependent on the wall boundary conditions applied. Our solver proved to be more flexible in this regard and was more efficient regarding the computational times.

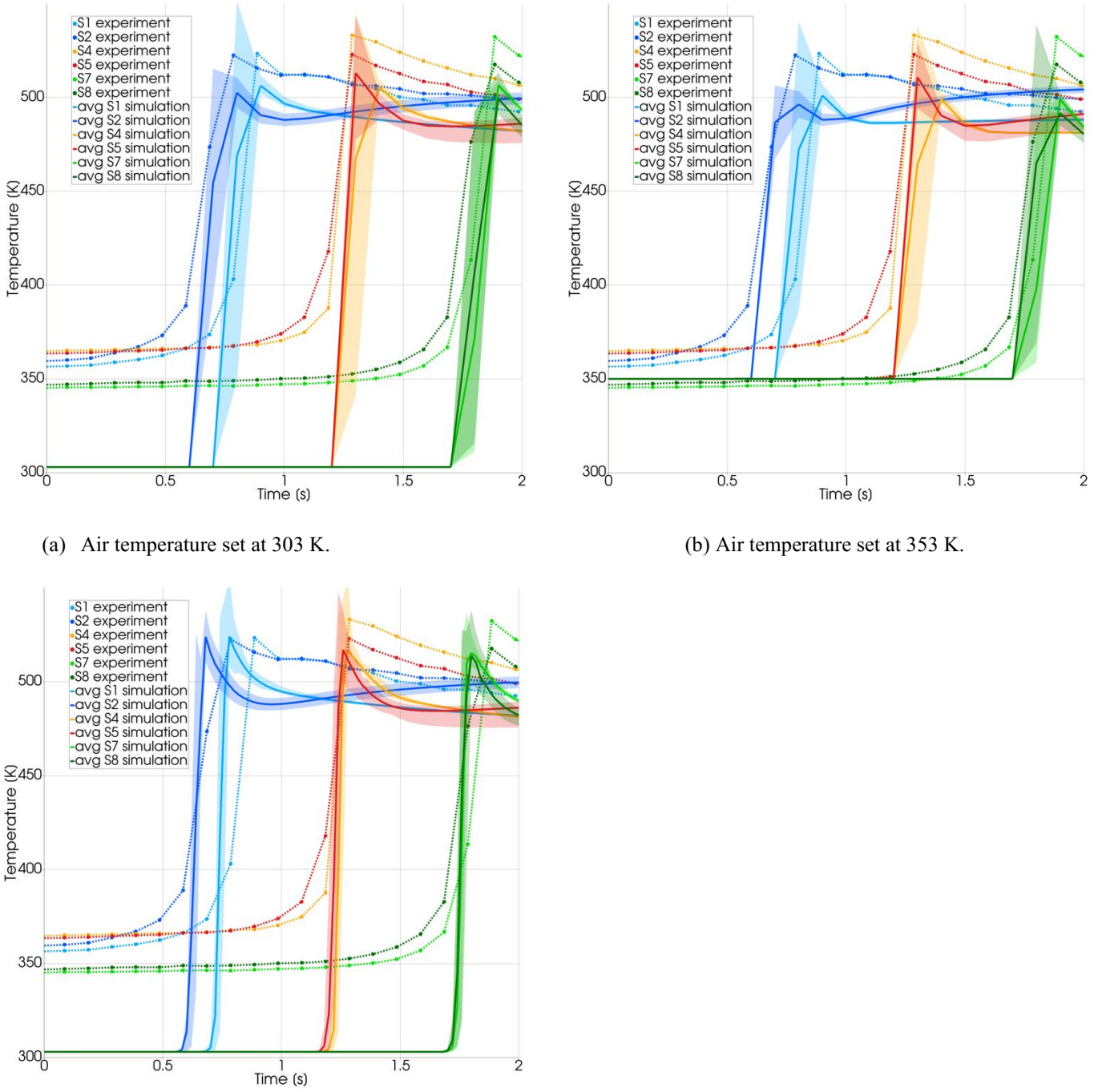

(a) Air temperature set at 303 K.

(b) Air temperature set at 353 K.

(c) Air temperature set at 303 K. Simulation sampling every 0.02 seconds.

Figure 2: Temperature at sensors S1, S2, S4, S5, S7, and S8 during cavity filling experiments and simulation, at a depth of ~0.53 mm. For the simulation results, the shaded areas represent the temperature range within the sensor area, and the continuous line represents the average. Simulation sampling every 0.1 seconds for (a) and (b).

4.2. Efficient solver with time refinement

4.2.1 Two-phase flow simulations

To provide a useful tool for the industry, it is essential to achieve not only precise simulations but also reasonable computational times. Efficient numerical methods are necessary to obtain accurate simulations while minimizing computational resource usage. Two-phase flow simulations using the level-set method face challenges due to the discontinuity of material properties at the interface.

Smoothing techniques can help alleviate this discontinuity and prevent divergence; however, they often result in a loss of accuracy. Another approach is to decrease the time step size and refine the mesh, which increases computational demands. Since very fine meshes and small time steps are primarily required near the interface, several researchers have adopted adaptive refinement techniques that adjust mesh size and refinement only in areas with discontinuities, significantly enhancing solver efficiency. Most authors and commercial software typically focus solely on spatial refinement while applying a uniform global time-stepping adaptation across the entire domain.

To address these limitations, we propose a novel method that incorporates local refinement in time, made possible through the use of simplex space-time finite elements. The mathematical formulation of this method is detailed in [6] and has been tested against various two-phase flow benchmark cases, including rising bubbles in both 2D and 3D, as well as step cavities. Additionally, this formulation has been adapted for axisymmetric cases and successfully validated with test scenarios such as static bubbles, rising bubbles, and dripping droplets [10]. This approach has proven effective for industrial applications; notably, droplet formation and detachment during gas metal arc welding (GMAW) were simulated and analyzed in [11].

4.2.2. Cavity filling simulations

The application presented in this work, the cavity filling simulation for polymer injection molding processes, benefits greatly from the adaptive time refinement technique. In [12], we previously investigated the mesh requirements necessary to achieve accurate results for the simulation of polymer injection into a thin channel. Due to significant shear-thinning effects, our findings indicated that a very fine mesh is required throughout the entire channel, rendering spatial refinement ineffective for this specific geometry and filling material. However, the potential of time refinement around the moving interface showed promising in this context.

Several studies in our group have been presented in this regard. In [13], we presented 2D and 3D cavity filling benchmark cases that account for shear-thinning and non-isothermal effects on polymer viscosity. The results qualitatively align with reference literature.

In [14], we simulated a 3D plate-shaped geometry, as depicted in Figure 1, where the filling pace qualitatively matched experimental results and the outcomes obtained using commercial software Moldflow. Similarly, in [15], we compared results from the same geometry with those from Moldflow, achieving comparable outcomes and quantitatively matching the pressure profile. In both studies, we assumed the polymer behaves as a Newtonian fluid; however, it was noted that cavity filling times appeared slower when employing the time refinement technique. Overall, in all cases examined, the use of adaptive time refinement significantly improved computational efficiency, resulting in reductions of up to 75% in the total time for the system solution.

5 Summary

The use of adaptive grids in time, utilizing a finite element space-time discretization, has proven to be a highly efficient method for cavity filling simulations in injection molding. Our findings indicate that grid refinement in time significantly reduces the computational time without compromising the accuracy of the results. This approach can yield both qualitatively and quantitatively robust results when compared to commercial numerical solvers and experimental data.

However, further advancements are necessary, particularly in the treatment of boundary conditions and the integration of multi-scale rheological models to enhance the simulation's precision. Regarding efficiency, our group continues to work in this direction by focusing on the simultaneous combination of space and time refinement, as well as exploring more complex error indicators for refinement.

Acknowledgements

The authors gratefully acknowledge the contributions to this work of Dr. Violeta Karyofylli, Darren Lam Ming Hui, José Fernández, Efstratios Moskofidis, Denis Kalmykov, Liubov Kamaldinova, Jegor Kravchenko, and Dr. Linda Gesenhues.

This work was funded by the German Research Foundation (DFG) under the program SFB 1120 "Precision Melt Engineering" – 236616214. The authors acknowledge the computing time provided to them at the NHR Center NHR4CES at TU Darmstadt (project number P0024828) and at RWTH Aachen University (project number p0020502). This is funded by the Federal Ministry of Research, Technology and Space, and the state governments participating on the basis of the resolutions of the GWK for national high performance computing at universities (www.nhr-verein.de/unsere-partner).

Conflict of Interest

The author declares no conflict of interest.

Data Availability Statement

The input and output files of the numerical simulation presented in this publication are available on request at the following link: http://hdl.handle.net/21.11102/a064ac05-b651-4d42-a822-c567b0cff115.

References

[1] S. Elgeti and H. Sauerland, "Deforming fluid domains within the finite element method : Five mesh-based tracking methods in comparison," *Archives ofComputational Methods in Engineering,* pp. 323-361, 2016.

[2] B. Ferrer Fabón, C. Kahve, J. Alms, M. Behr and C. Hopmann, "Two-phase flows simulations in a space-time framework for injection molding applications : Comparison with experimental results," *Proceedings in Applied Mathematics and Mechanics,* 2024.

[3] J. Donea and A. Huerta, Finite element methods for flow problems, New York City: John Wiley & Sons, 2003.

[4] M. Behr, "Simplex space-time meshes in finite element simulations.," *International Journal for Numerical Methods in Fluids,* vol. 57, pp. 1421-1434, 2008.

[5] N. Hosters, B. Ferrer Fabón, M. Billen and M. Behr, " Addressing a Major Bottleneck in Computational Mechanics with Simplex Space-Time Finite Elements: Application to Free-Surface Flows," in *Advances and Challenges in Computational Mechanics* , Cham, Springer, 2026, p. 161–172.

[6] V. Karyofylli, M. Frings, S. Elgeti and M. Behr, "Simplex space-time meshes in two-phase flow simulations," *International Journal for Numerical Methods in Fluids,* pp. 218-230, 2018.

[7] M. L. Williams, R. F. Landel and J. D. Ferry, "The temperature dependence of relaxation mechanisms in amorphous polymers and other glass-forming liquids.," *Journal ofthe American Chemical Society,* vol. 77, pp. 3701-3707, 1955.

[8] B. Ferrer Fabón, J. Alms, M. Behr and C. Hopmann, "Injection molding of semi-crystalline polymers in a space-time framework," *Proceedings in Applied Mathematics and Mechanics,* vol. 22, 2022.

[9] B. Ferrer Fabón, J. Alms, M. Behr and C. Hopmann, "Two-Phase Flow Simulations for Injection Molding Applications: Comparison between COMSOL Multiphysics and XNS in-House Solver," *Proceedings in Applied Mathematics and Mechanics,* vol. 25, 2026. In review.

[10] V. Karyofylli, L. Kamaldinova, M. Simon, O. Mokrov, U. Riesgen and M. Behr, "Axisymmetric two-phase flow simulations on space-time meshes," *Proceedings in Applied Mathematics and Mechanics,* vol. 19, 2019.

[11] V. Karyofylli, "Space-Time Finite Element Methods for Production Engineering Applications," Ph. D. dissertation, RWTH Aachen University, Aachen, Germany, 2021.

[12] B. Ferrer Fabón, J. Alms, M. Behr and C. Hopmann, "High-resolution numerical simulations of polymer injection molding: Analysis of mesh size and refinement," *Proceedings in Applied Mathematics and Mechanics,* vol. 23, 2023.

[13] V. Karyofylli, L. Wendling, M. Make, N. Hosters and M. Behr, "Simplex space-time meshes in thermally coupled two-phase flow simulations of mold filling," *Computers and Fluids,* vol. 192, 2019.

[14] V. Karyofylli, M. Behr, M. Schmitz and C. Hopmann, "Novel discretization methods for improved simulation precision in injection molding," *Materialwissenschaft undWerkstofftechnik,* vol. 48, pp. 1264-1269, 2017.

[15] V. Karyofylli, M. Schmitz, C. Hopmann and M. Behr, "Adaptive temporal refinement in injection molding," in *AIP Conference Proceedings*, 2018.

Date: 31.03.2026

Unified simulation of melt flow and solidification processes using a Smoothed Particle Hydrodynamics based method with a thermoplastic-viscous-elastic material model

Author: Lukas Westhofen

Authors: Lukas Westhofen[1*], Jan Bender[1], Oleg Mokrov[2], Sergej Warkentin[2], Rahul Sharma[2], Uwe Reisgen[2]

[1]RWTH Aachen University, Visual Computing Institute, Ahornstr. 55, 52074, AACHEN, GERMANY

[2]RWTH Aachen University, Welding and Joining Institute, Pontstr. 49, 52062, AACHEN, GERMANY

*Corresponding author: E-mail: l.westhofen@cs.rwth-aachen.de, ORCID: 0000-0003-4427-2377

Abstract

The numerical simulation of manufacturing processes involving molten materials requires an accurate description of melt flow, phase transitions, and the resulting geometry during solidification and cooling. The Smoothed Particle Hydrodynamics (SPH) method has proven to be a promising approach for such problems, particularly when strong deformations and topological changes of the melt occur. As a mesh-free Lagrangian method, SPH allows a natural representation of free surfaces and evolving geometries.

However, the accurate modeling of density changes during solidification remains a major challenge, since these changes strongly influence the final geometry and the thermomechanical stresses developing during cooling.

To address this problem, we propose an extension of the SPH approach by integrating a thermoplastic-viscous-elastic material model. This unified formulation enables the consistent description of both liquid metal behavior and temperature-dependent thermomechanical properties, allowing the simulation of melt flow and solidification processes within a single framework.

Keywords

process simulation, smoothed particle hydrodynamics, welding, solidification, volume contraction

1 Introduction

Welding and casting processes are heavily influenced by the thermal effects at play. For reliably assuring the quality of the process products, it is essential to understand and being able to control the complex thermomechanical phenomena. During the process, the material undergoes several phase changes, from solidified to half-solidified to liquid and back. Thus, the whole process

encompasses a multi-physics problem in which every part influences the others. One approach for the process simulation is to use dedicated methods for every state of matter and transfer the information from one method to the next. While this approach ensures, that every phase is simulated with a well-suited method, the mapping between these methods may introduce errors into the simulation chain. Additionally, capturing the interaction between different phases may require the use of surrogate models. Thus, it is advantageous to capture the whole simulation process with a single model. This approach eliminates the need for mapping and surrogate models as long as the unified simulation method is able to capture all simulation effects.

For welding and casting applications, the accurate depiction of several different phenomena is required. These include the phase change during melting and solidification, the free-surface flow of the molten material and the mechanical stresses arising during solidification and cooling. Additionally, all processes are governed by the heat transfer and its accompanying effects on the materials. The goal of this publication is to outline a unified simulation framework for the whole process of welding and casting.

The simulation framework is based on the Smoothed Particle Hydrodynamics (SPH) method. Traditionally, grid-based or mesh-based approaches have been employed [1-3]. For the whole process simulation chain, the requirements for handling strongly deforming melt pools, droplet impact and fragmentation as well as strongly deforming volumes, these methods require additional effort for the accurate depiction. SPH as a meshless, Lagrangian method natively handles strongly changing topologies and thus is well-suited.

This work proposes a unified, SPH-based framework for welding and casting processes. This includes the simulation of the melt-pool dynamics consisting of the interplay between pressure, viscosity, surface tension and temperature flow. First results capturing gas metal arc welding and thermal spraying processes will be shown and discussed. This method will be extended by the volume contraction happening in fluid and solid phases alike through the temperature dependent material density. Finally, further developments will be shown towards a unified SPH model for fluid and solid states.

2 Aim of the Investigation

The goal of this work is to present a unified, SPH-based framework for welding and casting processes. In the following the advantages of this Lagrangian, mesh-less method will be outlined and discussed. Further, the newly created method will be thoroughly analyzed in theoretical and practical use cases. The authors envision a full process simulation method using SPH as the main discretization method, that is able to capture melting, melt pool dynamics, solidification, internal stresses and deformation during cooling.

3 Materials and Experimental Details

3.1 Smoothed Particle Hydrodynamics

Smoothed Particle Hydrodynamics (SPH) [4, 5] is a meshless, Lagrangian simulation method. In detail, the SPH discretization works by sampling the simulation domain with mass points called particles. These points aggregate the surrounding mass, represent the local volume, and carry additional quantities like the density or temperature. As a Lagrangian method, the particles are advected with the fluid flow.

These properties allow SPH as a method to be well suited for the natural treatment of free surface flows. As a meshless method, large deformations and topological changes as in the droplet formation of the melting welding wire are natively supported. Furthermore, SPH allows for a unified and flexible treatment of the underlying multi-physics problem.

The core idea of SPH is that, in theory, given infinitely many sampling points, the particle discretization represents the continuum. With a finite number of particles, any field quantity A at position $\mathbf{x}$ can be calculated using the SPH interpolation using the surrounding particles j:

$$A(\mathbf{x}) \approx \sum_j \frac{m_j}{\rho_j} A(\mathbf{x}_j) W(\mathbf{x} - \mathbf{x}_j, \hbar),$$

where m is the particle's mass, ρ_j the density and $W(\mathbf{x} - \mathbf{x}_j, \hbar)$ the kernel function. The latter is a compactly supported, Gaussian-like scalar function which weighs the contribution of a particle dependent on their distance. The second argument $\hbar$, the smoothing length, influences the steepness of the Gaussian-like shape of the kernel function. A common assumption is to couple the smoothing length to the compact support radius $\tilde{h}$ and the particle radius R. In the following, properties are computed on the particles themselves. There, the abbreviations $A_i = A(\mathbf{x}_i)$, $W_{ij} = W(\mathbf{x} - \mathbf{x}_j, h)$ will be used for example for the computation on particle i. Further, all neighboring particles which have a non-zero contribution will be denoted as the neighborhood $\mathcal{N}_i$. For further details, the reader is referred to the works of Koschier et al. [6, 7] and Price [8].

SPH is commonly used to solve the momentum equation, that is:

$$\rho \frac{D\mathbf{v}}{Dt} = \nabla \cdot \sigma + \mathbf{f}_{\text{ext}},$$

where $\mathbf{v}$ denotes the velocity, $\mathbf{f}_{\text{ext}}$ external forces and σ the stress tensor. For the simulation of incompressible fluids, the suitable stress tensor leads to the well-known Navier Stokes equations:

$$\frac{D\rho}{Dt} + \rho \nabla \cdot \mathbf{v} = 0$$
$$\rho \frac{D\mathbf{v}}{Dt} = -\nabla p + \mu \nabla^2 \mathbf{v} + \mathbf{f}_{\text{st}} + \mathbf{f}_{\text{ext}},$$

where p denotes the pressure, μ the dynamic viscosity and $\mathbf{f}_{\mathrm{st}}$ the surface tension force. A common strategy for solving the momentum equation with SPH is operator splitting [7]. With it, non-pressure forces are solved with their own system before the pressure is being solved to comply with the incompressibility condition of the continuity equation. This allows each contributing force to have its own dedicated solver, improving the flexibility of the framework.

3.2 Simulation Framework

For the full process simulation, the framework must support the simulation of solids, liquids and temperature propagation. Concerning the depiction of the melt pool dynamics, the authors rely on the works of Bender et al. [9, 10] for solving pressure forces, Weiler et al. [11] for viscosity and Jeske et al. [12] for surface tension. These methods have been altered to fit the needs of the process simulation, most notably by the inclusion of temperature dependent parameters. That is, both the viscosity and surface tension method have been modified to accommodate spatially and time varying parameters, $\mu\big(T(x,t)\big)$ and $\sigma\big(T(x,t)\big)$ respectively. These are read from temperature dependent tables during the simulation.

The temperature is being calculated by solving Fourier's equation:

$$\frac{D\left(\rho c_p T\right)}{Dt} = \nabla \cdot (\lambda \nabla T) + \dot{q}''',$$

where T denotes the temperature, c_p the specific heat capacity, λ the thermal conductivity and $\dot{q}'''$ the contribution from volumetric heat sources. This equation is solved based on the work of Jeske et al. [13] by discretizing the left hand side of the equation in time and the right hand side with SPH while changing the parameter of interest from temperature to the specific enthalpy. Following the authors derivation, the next specific enthalpy is being calculated by:

$$h(t + \Delta t) = h(t) + \frac{\Delta t}{\rho}(\nabla \cdot (\lambda \nabla T) + \dot{q}''')$$

Following their work, both explicitly and implicitly solving Fourier's equation have been investigated. However, during most applications time step constraints for the fluid solver dominated the convergence requirements of all systems, that is, the thermal solver oftentimes already converged with the maximum time step sizes from the fluid solver.

For interaction with solids, a surrogate model of freezing particles in space and time has been used.

During development of the method, the option has been added to change the rest density of the material in dependence of the temperature, that is $\rho = const. \rightarrow \rho(T)$. This change breaks with several assumptions of classical SPH-based algorithms. Most importantly, SPH strives for having enough neighbors around the current position to ensure a good interpolation accuracy. Thus, with constant mass per particle, the volume which a particle represents changes with changing rest density. This must be accounted for in the compact support radius, which leads to a relation between density and smoothing length [8]. For this volume contraction, a new method is proposed which

relates a unit volume which the particle initially represents against the compact support radius. That is,

$$\tilde{h} \stackrel{!}{=} 4R, \quad V_0 \stackrel{!}{=} 8R^3 \rightarrow \tilde{h}(T) = 2\sqrt[3]{\frac{m}{\rho(T)}}$$

Here, the initial volume V_0 is assumed to be a cube with edge length $2R$, that is two times the particle radius. Additionally, a common heuristic in SPH is to set the compact support radius to be four times the particle radius. From that, the according smoothing length $\hbar$ can be determined.

4 Results

The aforementioned simulation framework has been implemented into the open source software SPlisHSPlasH [14]. The extension of the framework includes the thermal solver, an implicit and stable surface tension model, the coupling of viscosity and surface tension with temperature, a new and stable volume contraction method as well as a method for simulating elasticity catered to the needs of the welding process. In the following, key results during the development of the simulation method will be presented.

4.1 Surface Tension

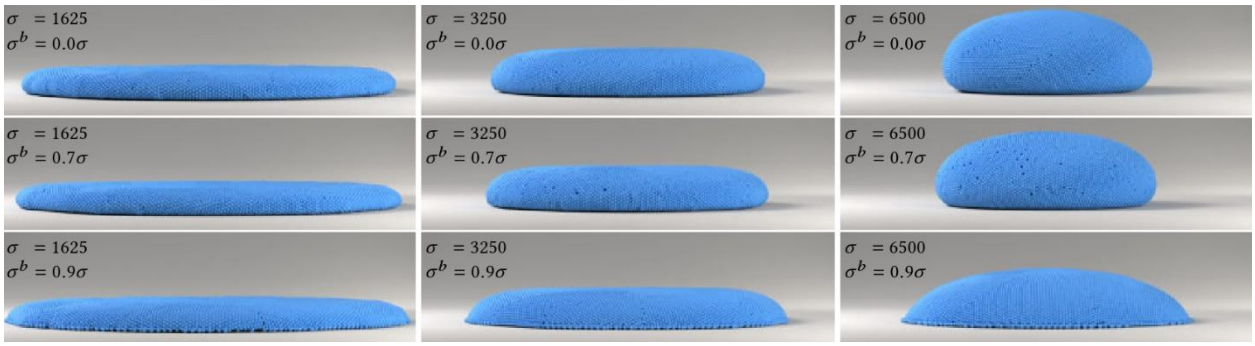

Figure 1: Simulation of a droplet on a flat plane with varying surface tension parameters. From left to right, the cohesion is increasing and from top to bottom, the adhesion is increasing. The simulation results depict the influence of these parameters on the droplet shape as well as the versatility of the method. Reproduced with permission [12].

A crucial aspect for the accurate depiction of the melt pool dynamics is the interplay between pressure, viscosity and surface tension. The latter is important for different effects like the droplet formation of the molten welding wire to the general melt pool dynamics. An important requirement here is that the simulation method remains stable and versatile under various geometric conditions and large surface tension forces. To that goal, Jeske et al. [12] developed a novel surface tension method. They derive the surface tension force from the imbalance of interior and exterior particles. This force is solved using a linearized implicit system which improves the stability of the method with large surface tension forces. This allows for capturing a wide range of surface tension effects for example depicted in Figure 1. As shown by the authors, their method outperforms other state-of-the-art methods [15-18] in for example the formation of droplets, an important requirement for

the process simulations. Thus, for different applications from welding to thermal spraying, their method has been proven to be indispensable [19-21].

4.2 TIG Spot Welding

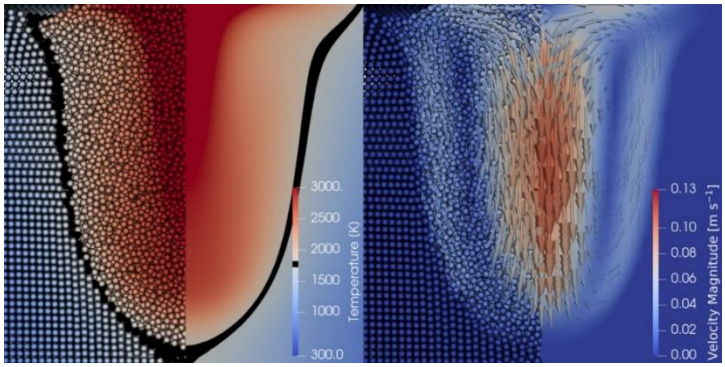

Figure 2: Comparison of SPH (left, particle view) and FEM (right, rendered view) simulation of the temperature distribution and velocity profile of the melt pool of a TIG welding scenario. SPH produces comparable results to the well-established FEM solution. Reproduced with permission [13].

To investigate the applicability of SPH for welding process simulations, Jeske et al. [13] conducted a quantitative analysis using the example of tungsten inert gas (TIG) spot welding. The authors compared their novel SPH-based method against Wolfram Mathematica® and COMSOL FEM® simulations. While this example is more suited to be simulated with an Eulerian simulation method due the continuous melt pool geometry, the authors conclude that their method is comparable to the other well-established methods in terms of simulation accuracy for the temperature flow and melt pool dynamics. The results can be seen in Figure 2. Additionally, they argue that while their method offers comparable results, the SPH-based method will be advantageous for the further depiction of real-world processes with topology changes and strong discontinuities in for example droplets or metal splatter. To conclude, the authors have proven with their study that the Smoothed Particle Hydrodynamics method is able to produce quantitatively similar results to well-established methods in the field.

4.3 Thermal Spraying

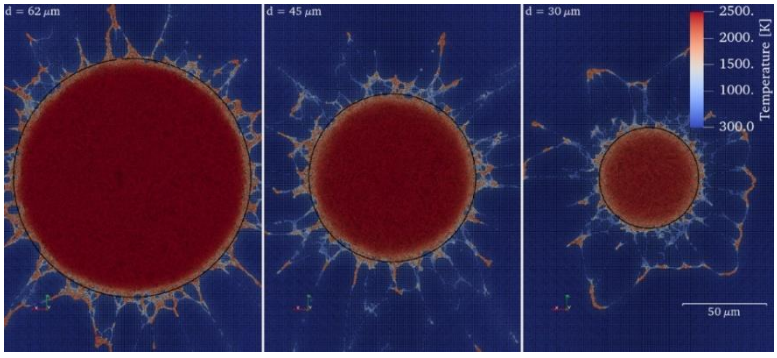

Figure 3: Splats of differently sized initial droplets simulated with SPH for thermal spraying. Reproduced with permission [20].

Another field of application to which the Smoothed Particle Hydrodynamics method was applied to is thermal spraying. In the work of Jeske et al. [20], the authors showcase the capabilities of SPH

and compare their method against the ANSYS Fluent® solver using the finite volume method (FVM) with the volume of fluent (VOF) method. There, the authors demonstrate the advantages of using SPH as a discretization method. The thermal spraying process involves large deformations of the droplet during impact with the substrate leading to geometry and topology changes during splat formation, see Figure 3. Additionally, the thermal spraying is a multi-physics process, requiring the correct interaction of temperature, pressure, surface tension and viscosity. The authors demonstrate the applicability of an SPH-based method by quantitatively comparing against the VOF method. They conclude a good agreement between the methods and provide explanations for the differences arising from both simulation methods. Furthermore, the authors point out the increased computational efficiency of their method. They report for a comparable simulation parameter that their method is able to use a 22 times higher discretization density while only needing a quarter of the simulation time while comparing against ANSYS Fluent®.

The method of Jeske et al. [20] has been further extended by Bobzin et al. [19]. They demonstrate the droplet impact on a realistic, irregularly shaped surface for which the splat fills in the crevices of the work piece. Additionally, they investigate the influence of the temperature of the substrate in regards to the splat diameter. Finally, and most remarkably, the method is able to simulate void regions that occur in the buildup of multiple splats in the spraying process. Thus, the authors have demonstrated that the method lays an important foundation for further research in that area.

4.4 Volume Contraction

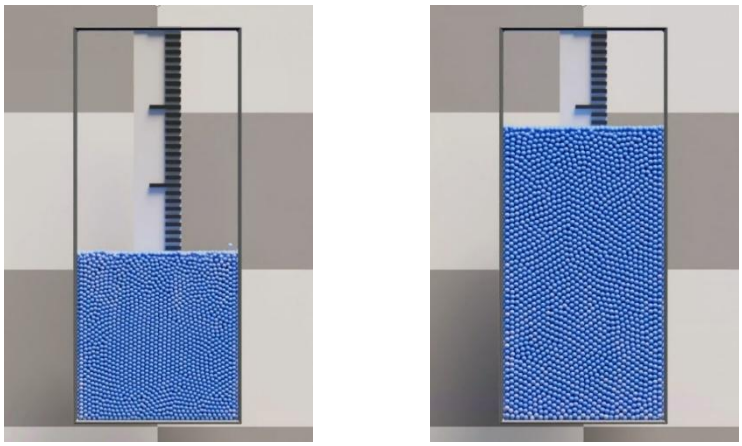

Figure 4: Simulation snapshots of a fluid column expanding and afterwards shrinking again through halving and doubling the rest density of the fluid.

For evaluating the stability and capabilities of the volume contraction method, the following synthetic test case has been devised. Here, the density of a fluid column is being altered over time to check for the stability of the simulation with changing rest densities and support radii, see Figure 4. As the simulation method, a modified version of divergence-free SPH [9, 10] has been chosen to support the material changes. The newly created volume contraction method has been compared against the version of Li et al. [22] and Winchenbach et al. [23] for incorporating different particle sizes and support radii.

In this example, the density of the fluid has been halved over time and afterwards doubled again. Both methods of Li et al. [22] and Winchenbach et al. [23] failed this scenario while with the geometrically-based method the scene could be successfully simulated. While the volume contraction processes happening in real material are usually much smaller, the results of the synthetic scenario demonstrated the following fundamental issues with the previous methods.

While the methods of Li et al. [22] and Winchenbach et al. [23] depend on the particle distribution, the here presented method is purely dependent on geometrical properties. The advantage is, that particle distributions with too few particles like single droplets or at the free surface must not be accounted for separately. Both previous methods need to define a maximum neighborhood search radius for not unnecessarily increasing the radius for isolated droplets. Without, the ill-distributed particles will increase their neighborhood radius to an unphysical degree which lead to an inability to resolve the demonstrated scene.

4.5 Blind Weld

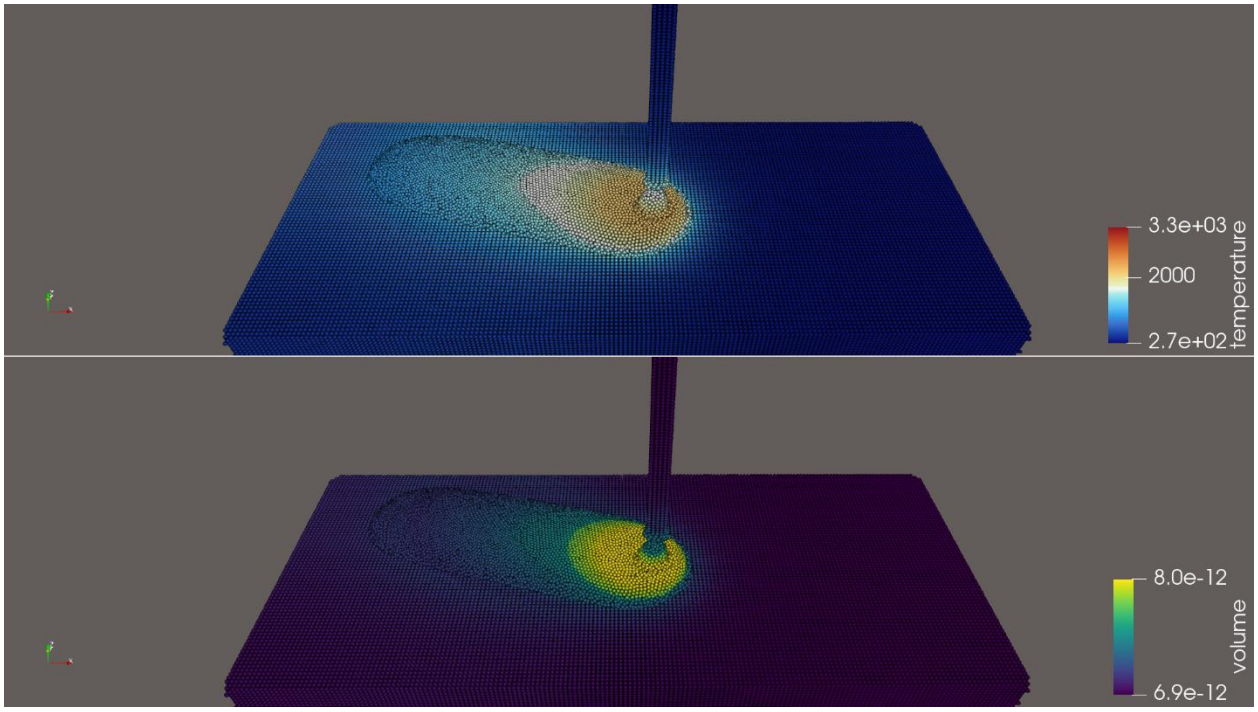

Figure 5: Temperature and volume distribution during a blind weld simulation as a demonstrator of a full process simulation. The simulation entails a full multi-physics process of the melt pool dynamics.

To demonstrate the applicability of the volume contraction method, a simulation of a blind weld using the cold metal transfer (CMT) variant of gas metal arc welding (GMAW) has been devised. This example showcases a complex scenario with several physical systems interacting with each other. The included effects and surrogate models apart from the temperature dependent volume have been described by Mokrov et al. [21]. The latter has been newly added. While the effects currently are only affecting the liquid melt pool, the results (Figure 5) show the applicability of the volume contraction method to the process simulation.

4.6 Discussion and Towards a Unified SPH Model for Fluid and Solid States

The results demonstrate the capability of SPH for melt-based processes. Especially for processes with large deformations and topological changes as in thermal spraying or CMT based welding, SPH has been shown indispensable for its native handling due to its Lagrangian, meshless nature. The first results show a promising direction for a unified SPH model for a full process simulation.

A remaining task for this framework is the handling of fluid-solid transitions and the mechanical behavior. First experiments have been conducted with a linear elasto-plastic model. Here, the elasto-dynamic behavior is handled – as in the works of Zerbe [24] and Yang et al. [25] – by updating the stress tensor over time. The plastic behavior is modeled using the von Mises yield criterion. This model has the advantage that it must not refer back to a reference configuration. Since new material will solidify over time, updating the internal stress seem to be a more natural depiction, since otherwise a constantly evolving reference configuration must be established.

5 Summary

Conclusively, the presented framework has shown the potential of SPH-based process simulations, both in qualitative and quantitative scenarios. SPH offers a unique suite of properties like its ability to depict large deformations, topological changes and the ability to capture a wide range of physical effects in a stable manner. Thus, SPH as a method thrives in processes which specify exactly these requirements as for example the CMT process, thermal spraying, but also other ones like WAAM (Wire and Arc Additive Manufacturing) [26] or LDNA (Laser-assisted double-wire welding with non-transferred arc) [27]. With further development of the solidification behavior, one can foresee a wide range of applications for SPH-based process simulations.

Acknowledgements

The authors gratefully acknowledge the work of Stefan Rhys Jeske on the development of the prototype version of the adapted version of SPlisHSPlasH.

The presented investigations were carried out at RWTH Aachen University within the framework of the Collaborative Research Centre SFB1120-236616214 “Bauteilpräzision durch Beherrschung von Schmelze und Erstarrung in Produktionsprozessen” and funded by the Deutsche Forschungsgemeinschaft e.V. (DFG, German Research Foundation). The sponsorship and support is gratefully acknowledged.

Conflict of Interest

The author declares no conflict of interest.

Data Availability Statement

The data that support the findings of this study are available at http://hdl.handle.net/21.11102/94ac8b57-c163-4854-842a-698831b4f027 upon request.

References

[1] O. Mokrov, M. Simon, A. Schiebahn, U. Reisgen *Mathematical modelling of weld phenomena*. **2019**, *12*.
[2] L. Liang, R. Hu, J. Wang, M. Luo, A. Huang, B. Wu, S. Pang *Metallurgical and Materials Transactions A*. **2019**, *50*.
[3] F. Chen, W. Yan *Materials & Design*. **2020**, *196*.
[4] R. A. Gingold, J. J. Monaghan *Monthly notices of the royal astronomical society*. **1977**.
[5] L. B. Lucy *Astronomical Journal*. **1977**, *82*.
[6] D. Koschier, J. Bender, B. Solenthaler, M. Teschner in Smoothed Particle Hydrodynamics for Physically-Based Simulation of Fluids and Solids, Vol. (Ed.^Eds.: Editor), City, **2019**.
[7] D. Koschier, J. Bender, B. Solenthaler, M. Teschner *Computer Graphics Forum*. **2022**, *41*.
[8] D. J. Price *Journal of Computational Physics*. **2012**, *231*.
[9] J. Bender, D. Koschier in Divergence-Free Smoothed Particle Hydrodynamics, Vol. (Ed.^Eds.: Editor), City, **2015**.
[10] J. Bender, D. Koschier *IEEE Transactions on Visualization and Computer Graphics*. **2017**, *23*.
[11] M. Weiler, D. Koschier, M. Brand, J. Bender *Computer Graphics Forum*. **2018**.
[12] S. R. Jeske, L. Westhofen, F. Löschner, J. A. Fernández-Fernández, J. Bender *ACM Transactions on Graphics*. **2023**, *43*.
[13] S. R. Jeske, M. S. Simon, O. Semenov, J. Kruska, O. Mokrov, R. Sharma, U. Reisgen, J. Bender *Computational Particle Mechanics*. **2022**.
[14] J. Bender, others in SPlisHSPlasH, Vol. (Ed.^Eds.: Editor), City, **2026**.
[15] N. Akinci, G. Akinci, M. Teschner *ACM Transactions on Graphics*. **2013**, *32*.
[16] M. Becker, M. Teschner in Weakly compressible SPH for free surface flows, Vol. 1 (Ed.^Eds.: Editor), Eurographics Association, City, **2007**, pp.209–217.
[17] F. Zorilla, M. Ritter, J. Sappl, W. Rauch, M. Harders *Computers*. **2020**, *9*.
[18] X. He, H. Wang, F. Zhang, H. Wang, G. Wang, K. Zhou *ACM Transactions on Graphics*. **2014**, *34*.
[19] K. Bobzin, H. Heinemann, K. Jasutyn, S. R. Jeske, J. Bender, S. Warkentin, O. Mokrov, R. Sharma, U. Reisgen *Journal of Thermal Spray Technology*. **2023**.
[20] S. R. Jeske, J. Bender, K. Bobzin, H. Heinemann, K. Jasutyn, M. Simon, O. Mokrov, R. Sharma, U. Reisgen *Computational Particle Mechanics*. **2022**.
[21] O. Mokrov, S. Warkentin, L. Westhofen, S. R. Jeske, J. Bender, R. Sharma, U. Reisgen *Materialwissenschaft und Werkstofftechnik*. **2024**, *55*.
[22] M. Li, H. Li, W. Meng, J. Zhu, G. Zhang *Visual Computing for Industry, Biomedicine, and Art*. **2023**, *6*.
[23] R. Winchenbach, H. Hochstetter, A. Kolb in Constrained neighbor lists for SPH-based fluid simulations, Vol. (Ed.^Eds.: Editor), City, **2016**.
[24] H. Zerbe, Modeling of laser welding with the smoothed particle hydrodynamics method, Shaker, **2020**.
[25] T. Yang, M. C. Lin, R. R. Martin, J. Chang, S.-M. Hu in Versatile interactions at interfaces for SPH-based simulations, Vol. (Ed.^Eds.: Editor), City, **2016**.
[26] S. Cadiou, M. Courtois, M. Carin, W. Berckmans, P. L. masson *Additive Manufacturing*. **2020**, *36*.
[27] U. Reisgen, R. Sharma, O. Mokrov, S. Emadmostoufi, J. Kruska, J. Hermsdorf, M. Lammers, T. Bokelmann *MATHEMATICAL MODELLING OF WELD PHENOMENA 13*. **2022**.

Date: 31.03.2026

New Material and Process Strategies to Reduce Intermetallic Phases in Brazed Joints

Author: Marvin Erck

Authors: K. Bobzin, M. Erck*,

RWTH Aachen University, Surface Engineering Institute, Kackertstr. 15, 52072, AACHEN, GERMANY

*Corresponding author: E-mail: erck@iot.rwth-aachen.de, ORCID: 0009-0004-8998-2895

Abstract

Brazing is commonly used to join hot work steels in injection mould manufacturing, typically with Ni-based filler alloys. Metalloids such as B are added to lower the melting temperature, yet they can promote intermetallic phase bands that weaken the joint. Limiting their formation is therefore essential to maintain mechanical reliability. Two strategies were examined. The first involved modifying the filler alloy with refractory metals that act as nucleation sites to influence solidification. The second involved supplementing vacuum brazing with a pulsed electric current to stimulate diffusion processes that support the dissolution of intermetallic phases. Samples produced by both methods were evaluated through microstructural analysis and mechanical testing. Alloy modification altered microstructure and yielded partial mechanical improvements. Pulsed electric current application produced direction dependent microstructural effects and further strengthened joint properties. Both approaches show clear potential to reduce brittle intermetallic phases in brazed joints.

Keywords: Vacuum Brazing, Ni-based filler metal, electric current assistance, hot work steel

1 Introduction and aim of the Investigation

Ni-based brazing alloys have been an integral part of joining technology for several decades and are valued for their excellent suitability for service under high thermal and cyclic loading [Tuc13]. These characteristics make them particularly attractive for tooling applications such as injection moulding dies. In this field, hot work tool steels like X37CrMoV5-1 are commonly employed due to their high strength, thermal fatigue resistance and good hardenability. Modern injection moulds often feature complex geometries and integrated cooling systems, which frequently necessitate manufacturing the cavities from multiple segments. These segments must then be joined in a manner that ensures dimensional accuracy, pressure tightness and minimal distortion. Vacuum

brazing with Ni 620 has proven to be well suited for this purpose, since the brazing temperature range coincides with the heat treatment of the steel, typically between T = 1,000 °C and T = 1,050 °C. This overlap allows joining and heat treatment to be combined in a single process.

From a metallurgical perspective, the use of Ni-based brazing alloys requires the deliberate addition of melting point depressing elements. While pure Ni melts at approximately T = 1,455 °C, alloying with B and Si significantly lowers the melting temperature and improves the wetting and flow behaviour of the molten filler metal. These effects are essential for achieving reliable gap filling. At the same time B and Si strongly influence the solidification behaviour of the brazed seam. During cooling, Ni-rich phases solidify first at the interfaces to the base material, whereas the remaining liquid becomes progressively enriched with B and Si. This enrichment promotes the formation of brittle intermetallic phases with Ni, Cr and Fe, which frequently accumulate in the centre of the joint. The resulting continuous brittle phase band represents a critical weak point, as cracks initiated under mechanical loading can easily propagate along this band and cause premature joint failure [SS19].

To avoid intermetallic phase bands in brazed joints, several countermeasures are applied in industrial practice. One widely used method is the restriction of the brazing gap width to values typically not exceeding $d \leq 35$ µm [LP83]. Alternatively, diffusion can be intensified by increasing the brazing temperature [PIS+21] or by applying extended holding times, sometimes lasting several hours [LP83]. Although these approaches are effective in decreasing the concentration of melting point lowering elements in the brazed seam, they are accompanied by significant drawbacks. Extremely narrow gaps demand precise surface preparation and complex fixturing, particularly for large components. Elevated temperatures and long dwell times increase energy consumption and may induce adverse effects such as grain coarsening in the base material. This creates a strong incentive to develop alternative strategies that suppress the formation of intermetallic phase bands under moderate process conditions and with gap widths that are feasible for industrial manufacturing.

Recent research has therefore focused on two different approaches. The first is a metallurgical strategy based on the targeted modification of Ni-based brazing alloys through the addition of small quantities of refractory metals, including Ti [BWH21], Mo [BHA+24], Nb [BHE23], V [BHE24] or W [BHE25]. This concept, described as inoculation, aims to alter the solidification sequence of the brazing alloy. During brazing, refractory metals form phases with B or Si, thereby reducing the effective concentration of these elements in the melt. Simultaneously, these phases act as heterogeneous nucleation sites for the Ni-rich matrix. As a result, solidification proceeds more uniformly and the intermetallic phases are distributed in a discontinuous manner, embedded within a Ni-based matrix. This microstructural refinement interrupts intermetallic phase bands and has been shown to improve the mechanical strength of brazed joints.

In parallel to the alloy design, a second, process-oriented approach has been developed in the form of current assisted vacuum brazing. In this method, an electric current is applied directly to the

molten brazing alloy during the joining process. Previous studies have demonstrated that the presence and direction of the current can significantly influence microstructural development in Ni-based brazed joints [BHH+21]. The applied current is assumed to affect mass transport and solidification phenomena within the molten filler, thereby modifying the distribution and morphology of the intermetallic phases. A key advantage of this technique is that it enables a reduction in intermetallic phase formation without the need for increased brazing temperatures, prolonged holding times or small gap widths.

Based on these considerations, the present work investigates the effects of refractory metal inoculation and current-assisted vacuum brazing on the Ni 620 filler metal. Special attention is given to, microstructural evolution and the resulting mechanical properties of the brazed joints. By systematically analysing both approaches, this work aims to provide new insights into the development of efficient and high-performance brazing processes for tool steel applications.

2 Materials and Experimental Details

2.1 Preparation of Samples for the Analysis of Alloy Modification

For the investigation of the influence of alloy modification with refractory metals, the Ni 620 brazing alloy was used as the base alloy. To investigate the effect on the microstructure and shear strength, the base alloy was modified with Mo, Nb, V and W. The chemical compositions of the investigated alloys are listed in Table 1.

Table 1: Chemical composition of filler metal in wt.%

	Ni	Cr	Fe	B	Si	X
Ni 620	Bal.	7.00	3.00	3.10	4.50	-
Ni 620 1.5X	Bal.	6.90	2.96	3.05	4.43	1.50
Ni 620 3.0X	Bal.	6.79	2.91	3.01	4.37	3.00

X = Mo, Nb, V or W

For alloy production, elemental granulates of the base elements as well as NiB and the respective refractory metals were weighed according to the target compositions and combined accordingly. Each alloy batch had a total mass of m = 10 g. Melting was performed in an Al_2O_3 crucible using a PVA MOV 553 high-temperature furnace manufactured by PVA TePla AG, Wettenberg, Germany. The alloys were processed under high-vacuum conditions of $p \leq 10^{-5}$ mbar at a temperature of T = 1,250 °C and held for t = 2 h to ensure complete melting and homogenization. Following, the modified Ni 620 alloys were converted into thin amorphous foils by melt spinning. This step was carried out using a Melt Spinner SC system supplied by Edmund Bühler GmbH, Bodelshausen, Germany. A detailed description of the manufacturing process can be found in [BHA+24]. Samples for microstructural characterization and shear strength testing were carried out in the high-vacuum furnace of type PVA MOV 553. The brazed specimens were designed as

butt joints consisting of two square rods with a length of L = 30 mm and a cross-sectional area of A = 5 × 5 = 25 mm². The hot work tool steel X37CrMoV5-1 was used as the base material for the investigations. The brazing foil was placed between the mating surfaces. During the brazing process, a constant load of F = 5 N was applied to ensure intimate contact between the components. Figure 1 illustrates the temperature-time profile applied during the brazing process and the sample configuration.

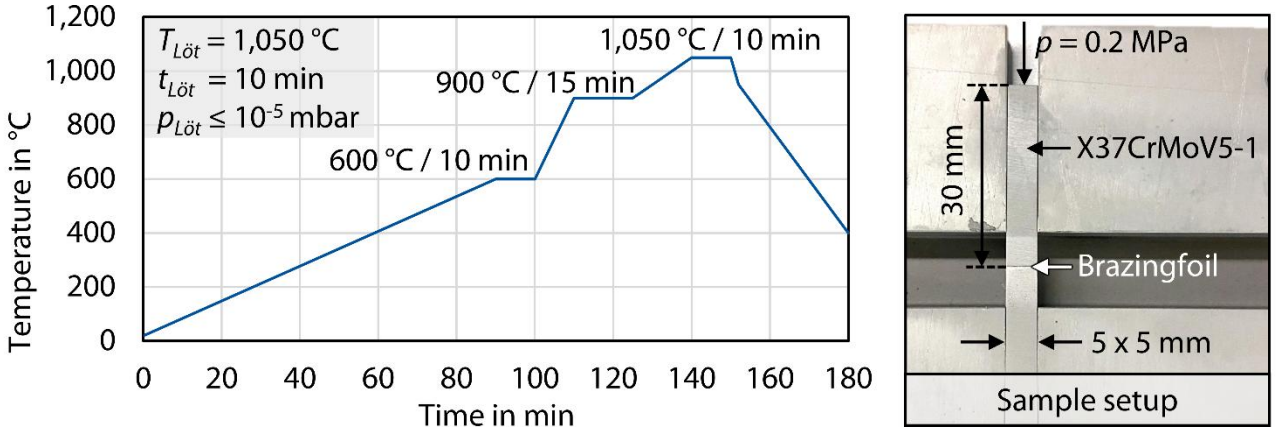

Figure 1: Temperature-time regime of the joining process and sample setup for vacuum brazing with modified Ni 620 brazing alloys

2.2 Preparation of Samples for the Analysis of Pulsed Current Assisted Vacuum Brazing

For the investigations regarding pulsed current assisted vacuum brazing, the brazing alloy Ni 620 and the hot work tool steel X37CrMoV5-1 were used as well. The brazing experiments were conducted using the vacuum furnace PVA MOV 553 T. For the current assisted vacuum brazing experiments, the furnace was modified by integrating an external current supply that enabled direct electrical loading of the samples during the brazing cycle. To this end, a high-frequency inverter spot welding system of type IS-Q3000A from Amada Weld Tech GmbH, Puchheim, Germany was connected to the sample holder located inside the furnace chamber. A schematic illustration of the test rig setup is shown in Figure 2 (left).

Electrical feedthroughs that are vacuum-tight and electrically insulated by ceramic components were employed to safely introduce the pulsed current into the furnace. The sample holder is designed in two electrically separated sections which are mechanically connected by two ceramic insulating rods. This configuration ensured that the electrical current is forced to pass directly through the brazed specimen. A detailed view of the sample holder is provided in Figure 2 (right).

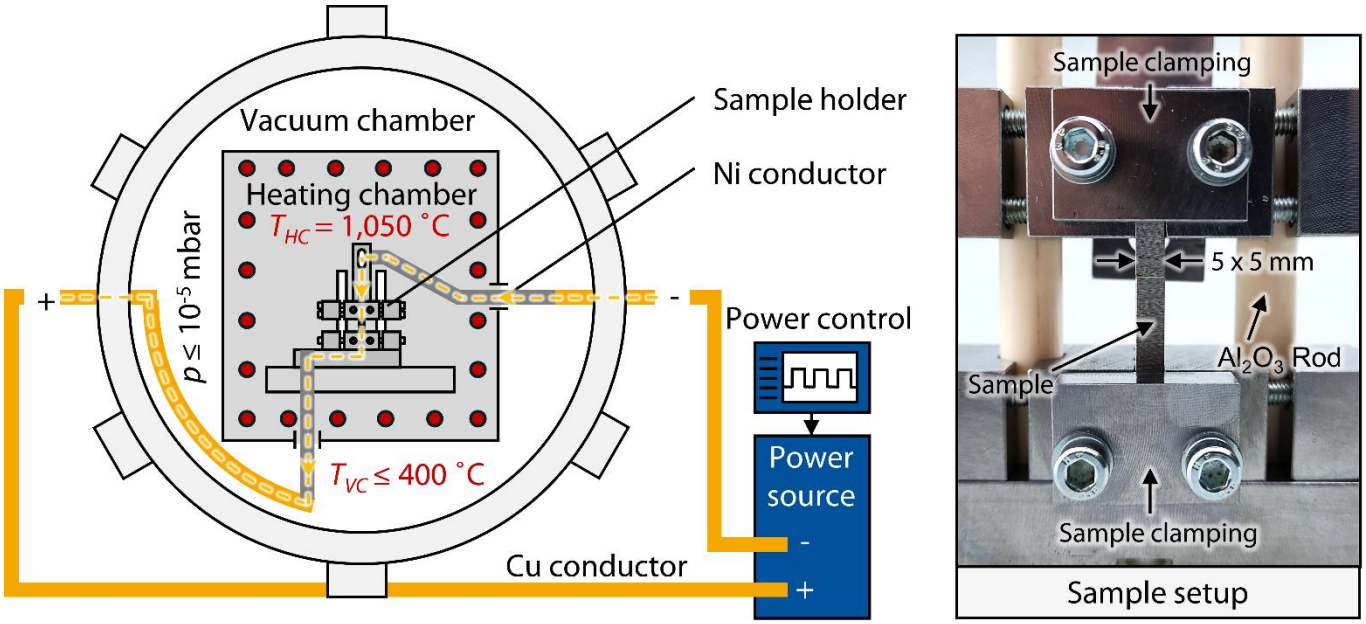

Figure 2: Schematic representation of the experimental setup for pulsed current assisted brazing in vacuum (left). Sample holder for pulsed current assisted vacuum brazing (right)

In the present study, a pulse duration of t_{puls} = 1 s, followed by a pause duration of t_{pause} = 1 s was selected. The temperature-time profile of the brazing process as well as the current-time profile of the electrical current flow are shown in Figure 3. Throughout the entire process, a vacuum level of $p \leq 10^{-5}$ mbar was maintained.

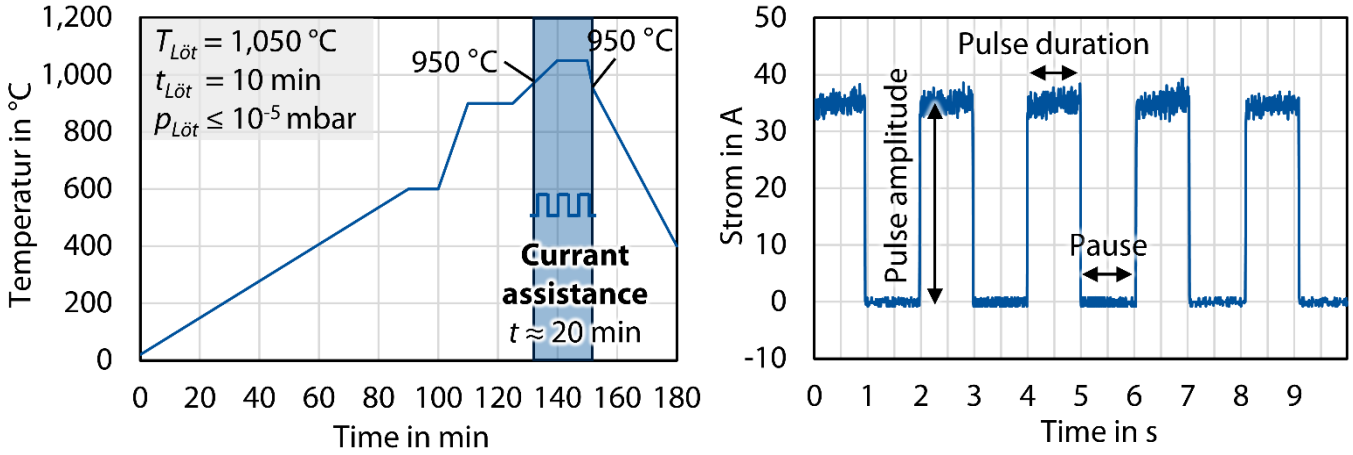

Figure 3: Temperature-time regime of the brazing process (left). Measurement of the current curve over time in the brazing process

The pulsed electrical current assistance was activated once the temperature reached T = 950 °C and remained active until the temperature decreased to the same level during cooling. For the experiments presented here, electrical currents of J = 200 A/cm^2, J = 400 A/cm^2 and J = 800 A/cm^2 were applied.

2.3 Analysis of the Produced Samples

The manufactured specimens underwent further metallographic preparation. The samples were embedded in epoxy resin and subsequently ground to enable detailed examination of the brazed joint region. Microstructural characterization was carried out using a Phenom XL scanning electron microscope (SEM) operated by Thermo Fisher Scientific in Waltham, USA.

Shear strength testing was carried out using an Instron 420 universal testing machine provided by Instron GmbH in Darmstadt, Germany. During the test, the force F required to cause failure of the brazed joint was recorded. Based on the measured force and the known joint area, the corresponding shear strength τ was calculated.

3 Results and Discussion

Microstructural analysis of the brazed joints, shown in Figure 4, reveals several characteristic solidification zones within the brazing gap of the Ni 620 alloy. Adjacent to the base material, a diffusion affected zone is observed, where B diffuses into the substrate and promotes the formation of Cr borides along grain boundaries. Next to this region, an isothermal solidification zone develops as a result of B depletion in the molten filler metal, leading to the formation of a Ni-rich γ solid solution at constant temperature. In the center of the brazing gap, the intermetallic phase band is present, which forms during cooling of the remaining liquid. Here, the dark phases can be assumed to be CrB, while the light gray phases are attributed to Ni-rich borides. The final solidification occurs as a two-phase structure composed of B and Si enriched phases with a lamellar morphology. A detailed description of the Ni 620 microstructure can be found in [BHE23].

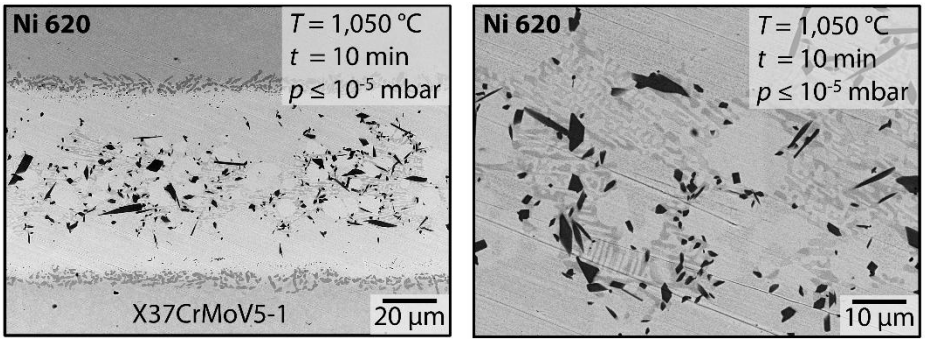

Figure 4: SEM cross-section of Ni 620 / X37CrMoV5-1 joint

Figure 5 presents microstructural images of the brazed joints produced using the modified Ni 620 filler alloys. Depending on the type and concentration of the added refractory metal, distinct variations in the morphology of the intermetallic phase band can be observed. For the alloys Ni 620 1,5Mo, Ni 620 1,5V, Ni 620 3,0V and Ni 620 3,0W, a clear separation of the intermetallic phase band is evident. In these cases, isolated islands of a Ni-based solid solution are visible between individual intermetallic phases. This observation indicates that the addition of the

refractory metals promotes a splitting of the otherwise continuous intermetallic phase band. In the case of the Ni 620 1,5W alloy, a partial breakdown of the intermetallic phase band is observed. In contrast, no such splitting is detected for the alloys Ni 620 3,0Mo, Ni 620 1,5Nb, and Ni 620 3,0Nb. However, the intermetallic phases present in these joints incorporate constituents of the respective refractory metals and exhibit morphologies that differ from those of the reference alloy Ni 620. A detailed discussion of these specific phase characteristics has been provided by the authors regarding Mo [BHA+24], Nb [BHE23], V [BHE24] and W [BHE25].

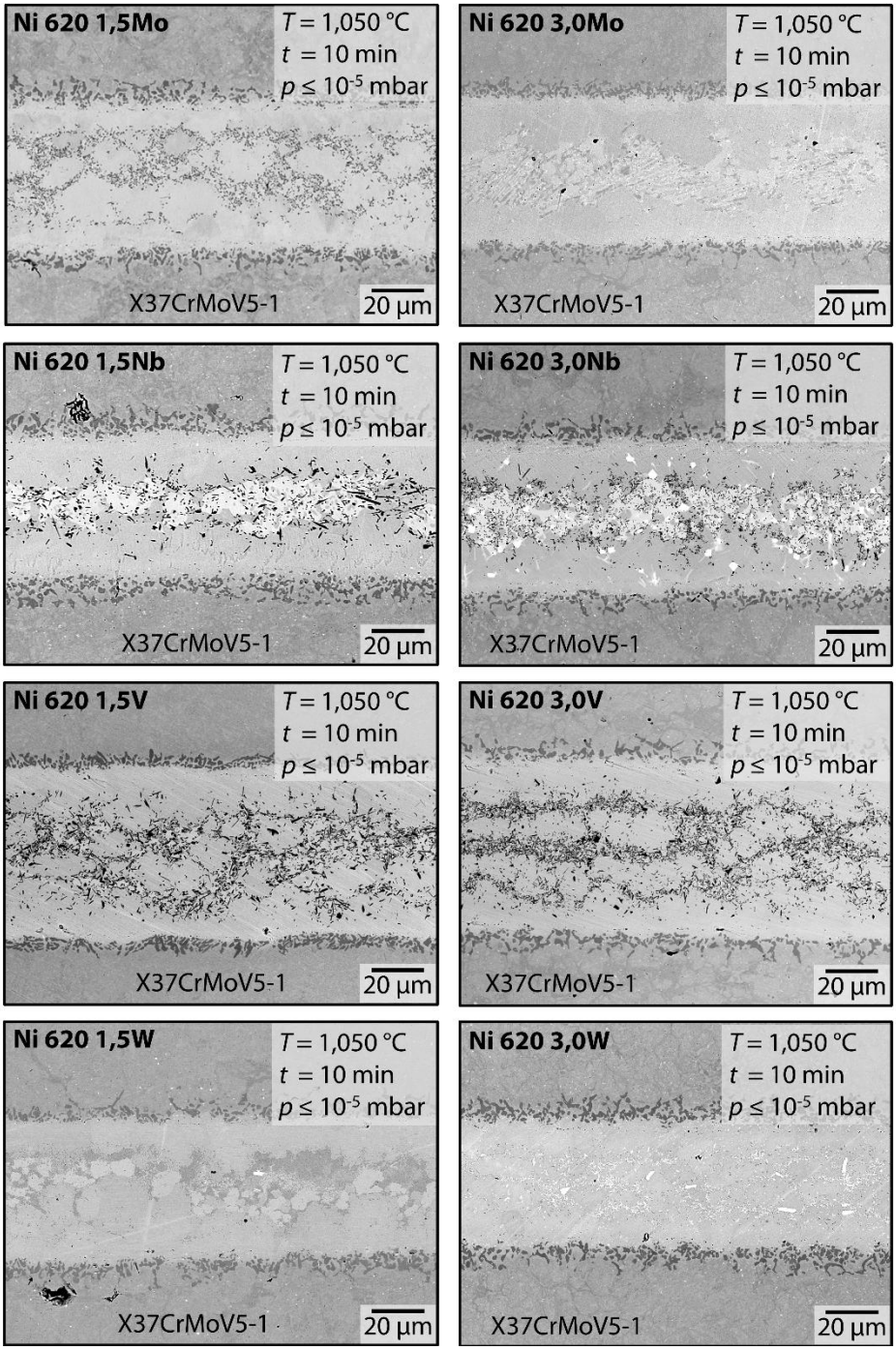

Figure 5: SEM cross-section of X37CrMoV5-1 joint manufactured with modified Ni 620 alloys

An examination of the microstructural images of the vacuum-brazed samples processed with pulsed current assistance, shown in Figure 6, reveals a progressive displacement of the intermetallic phase band toward the cathode with increasing current density. In addition, the overall fraction of intermetallic phases appears to decrease as the current density increases, resulting in a pronounced rise in the proportion of a Ni-based solid solution within the brazed joint. At current densities of J = 800 A/cm², the brazing seam itself can no longer be clearly distinguished, and distinct interfaces between the filler metal and the base material are no longer evident. These observations indicate that the application of pulsed electrical current promotes diffusion processes during brazing and introduces a current induced directional dependence in the microstructure of the joint. Possible mechanisms contributing to these effects include Joule heating, current-induced convective flow within the molten filler metal, or an electrically driven, direction dependent mass transport.

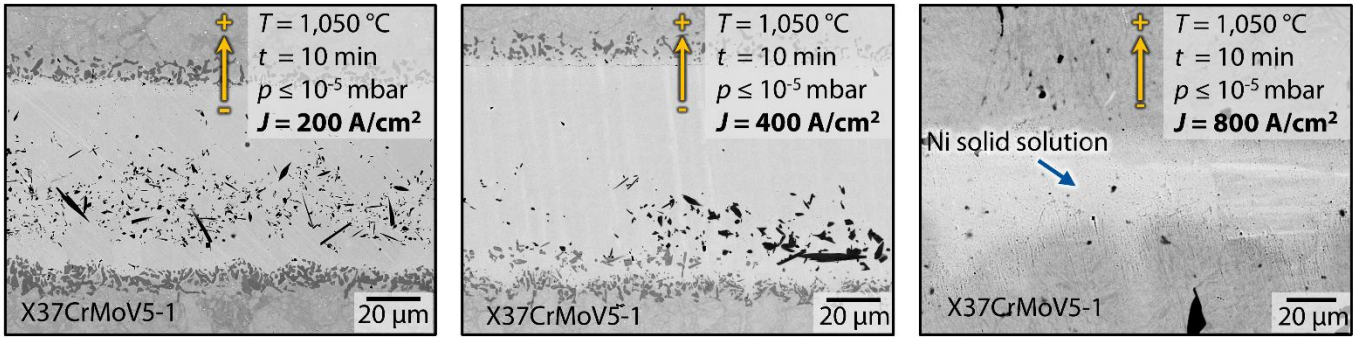

Figure 6: SEM cross-section of Ni 620 / X37CrMoV5-1 joint manufactured with different current densities

Figure 7 summarizes the shear strength results for specimens produced using modified filler alloys as well as for those fabricated with additional pulsed current assistance. Compared with the reference alloy, an increase in shear strength is observed for the modified alloys Ni 620 1.5Mo, Ni 620 1.5Nb, Ni 620 1.5W and Ni 620 3.0W. Among these compositions, the highest shear strength values are achieved with Ni 620 1.5W. In all cases, alloys containing lower additions of refractory metals exhibit higher shear strength than their counterparts with higher refractory metal content. The splitting of the intermetallic phase band observed for Ni 620 1.5Mo, Ni 620 1.5W, and Ni 620 3.0W therefore results in a direct improvement in shear strength. In contrast, for the alloys Ni 620 1.5V and Ni 620 3.0V, the separation of the intermetallic phase band does not translate into a measurable increase in mechanical strength.

For specimens produced with pulsed current assistance, an enhancement in shear strength is observed in all cases. The maximum shear strength is obtained at a current density of J = 200 A/cm². The acceleration of diffusion processes and the associated dissolution of the intermetallic phase band thus also lead to a direct improvement in shear strength under current assisted brazing conditions. The subsequent decrease in shear strength at higher current densities may be attributed to additional degradation of the base material by excessive Joule heating.

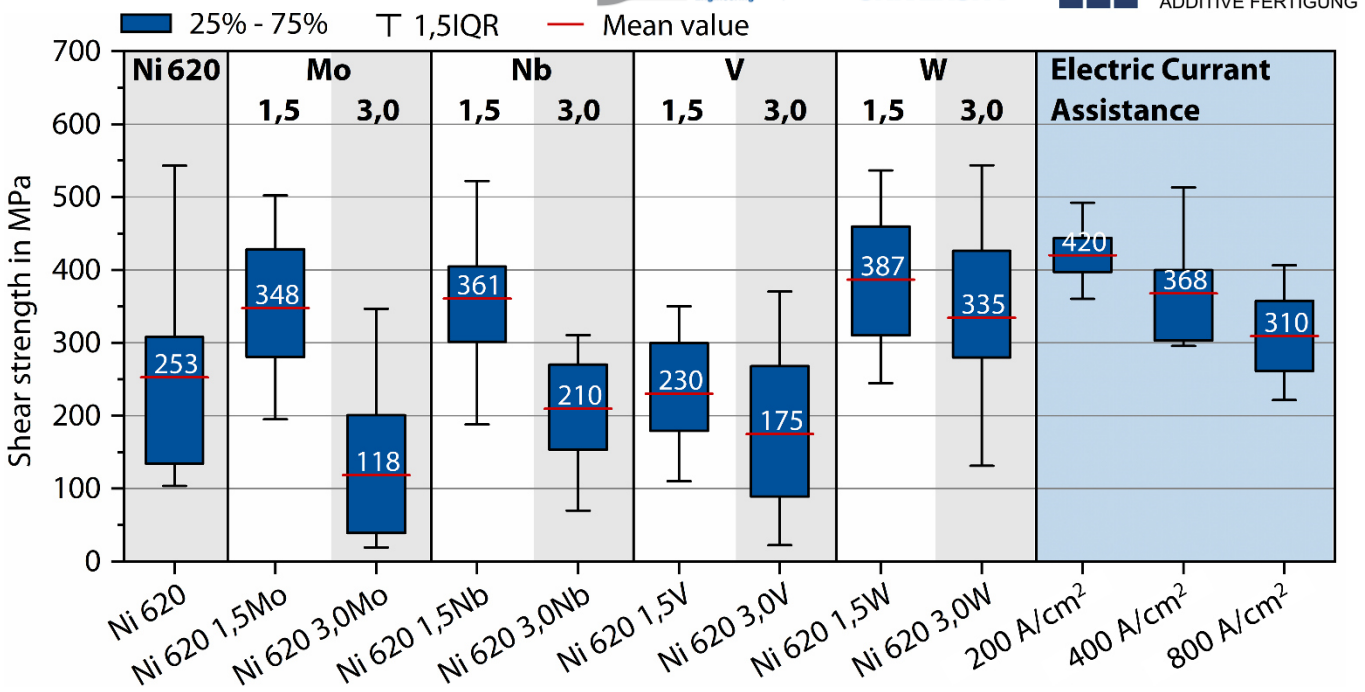

Figure 7: Box plot representation of shear strength in MPa

4 Summary

- Targeted modification of Ni 620 with small additions of refractory metals significantly alters solidification behavior and joint microstructure.
- Additions of Mo and W, particularly Ni 620 1.5W, promote splitting of the intermetallic phase band and lead to increased shear strength.
- Higher refractory metal contents generally result in lower strength improvements.
- Pulsed current assisted vacuum brazing reduces the fraction of brittle intermetallic phases and increases the Ni-based solid solution content.
- Maximum shear strength under current assistance is achieved at J = 200 A/cm².
- Excessively high current densities reduce joint strength, likely due to Joule heating effects on the base material.
- Both refractory metal inoculation and pulsed current assistance are effective strategies for improving the performance of Ni-based brazed joints under industrially relevant conditions.

Acknowledgements

The presented investigations were carried out at RWTH Aachen University within the framework of the Collaborative Research Centre SFB1120-236616214 “Bauteilpräzision durch Beherrschung von Schmelze und Erstarrung in Produktionsprozessen” and funded by the Deutsche Forschungsgemeinschaft e.V. (DFG, German Research Foundation). The sponsorship and support is gratefully acknowledged.

Conflict of Interest

The author declares no conflict of interest.

Data Availability Statement

The data that support the findings of this study are available from the corresponding author upon reasonable request on http://hdl.handle.net/ using the persistent identifier (PID): 21.11102/0a0c3f07-8e98-4ea4-8f29-7764ac7a4fb3

References

[BHA+24] K. Bobzin, H. Heinemann, M. Apel, B. Zhou, M. Erck, Use of molybdenum in Ni 620 filler metal to influence the microstructure of brazed hot work steel, Materialwissenschaft und Werkstofftechnik 55 **4** (2024), 544–554

[BHE23] K. Bobzin, H. Heinemann, M. Erck, Microstructural Modification by Redesigning the Chemical Composition of Ni 620 Filler Metal, Advanced Engineering Materials 25 **19** (2023)

[BHE24] K. Bobzin, H. Heinemann, M. Erck, Improving the microstructural properties of Ni-based filler metals by inoculating Vanadium, in: Proceedings of the 9th International Brazing and Soldering Conference, Charleston, South Carolina, USA: American welding society, 2024, 27–33, ISBN 978-1-64322-341-4

[BHE25] K. Bobzin, H. Heinemann, M. Erck, Dissolving brittle phases in Ni-based filler metals by adding W, Welding in the World 69 **6** (2025), 1697–1704

[BHH+21] K. Bobzin, H. Heinemann, J. Hebing, D. Machado, Current-assisted diffusion brazing of Ni-based filler metals to hot work steel, in: American Welding Society Proceedings of the 8th International Brazing and Soldering Conference, Miami, USA:, 2021, 87–93, ISBN 978-0-87171-939-3

[BWH21] K. Bobzin, W. Wietheger, J. Hebing, Influence of the Titanium Inoculation on the Melting Behavior and Microstructure of Ni 620/X38CrMoV5‐1 Brazing Joints, Advanced Engineering Materials 23 **12** (2021)

[LP83] E. Lugscheider, K. D. Partz, High Temperature Brazing of Stainless Steel with Nickel-Base Filler Metals BNi-2 BNi-5 BNi-7, Welding Journal 1983 **62** (1983), 160–164

[PIS+21] M. A. Penyaz, A. A. Ivannikov, O. N. Sevryukov, B. A. Kalin, Overview of nickel-based filler metals for brazing of austenitic stainless steels, Non-ferrous Metals (2021), 41–56

[SS19] M. Salmaliyan, M. Shamanian, Microstructure and Mechanical Characterization Study in the IN718/BNi-2/316L Joint by Transient Liquid Phase Bonding Process, Advanced Materials Letters 10 **9** (2019), 663–670

[Tuc13] Tucker, R. C., ASM handbook, Materials Park, Ohio: ASM International, 2013, ISBN 978-1-61503-996-8

Date: 24.03.2026

Additive manufacturing of an extrusion die using a multi-material DED-Arc plasma process

Author: Johannes Kellerwessel

Authors: J. Kellerwessel*[1], K. Mäde[1], M. Mierzwa[1], S. Kapil[2], R. Sarma[2], R. Sharma[1]

[1]RWTH Aachen University, Welding and Joining Institute, Pontstr. 49, 52062, AACHEN, GERMANY

[2]IIT Guwahati, 781309 Guwahati, Assam, India

*Corresponding author: E-mail: kel@isf.rwth-aachen.de, ORCID: 0009-0008-9433-8876

Abstract

This paper discusses a method for manufacturing an extrusion die using a multi-material strategy. To this end, the use of a wire-fed DED arc and a multi-wire plasma torch is investigated. The focus of this thesis is on the multi-material strategy, in which the processing of a component with a base body made of low-alloy steel and a nickel-based wire is examined. Furthermore, the path adjustments made are explained, and geometric deviations are presented.

Keywords

Functionally Graded Material (FGM)

Directed Energy Deposition (DED-Arc)

Multi-Wire-Process

1 Introduction

Additive manufacturing (AM) of metallic components is becoming increasingly important. This is due in particular to the high degree of design freedom and the high efficiency of modern manufacturing processes. Furthermore, this manufacturing process is characterized by high buy-to-fly ratios and automated production conditions [1]. The process class of directed energy deposition (DED) plays an important role in this context. It is known for high deposition rates and enables the fabrication of functional graded materials (FGM) [2,3, 4].

Additive manufacturing processes offer the possibility of producing FGMs in a single process step [4]. In conventional manufacturing processes, hardfacing or cladding is typically applied by

welding to optimize material properties at different locations on the component [5]. Hardfacing is defined as the application of weld metal, typically hard layers, with the aim of increasing the component's resistance to abrasive wear. In the case of cladding, weld metal is applied to protect a component against corrosion.

In conventional manufacturing, components are therefore first machined to bring them to a rough contour. In the subsequent process step, material is welded onto the component, followed by machining. FGM strategies in additive manufacturing enable the production of components with near-final contours, requiring only a single machining step in a subsequent process. This shortens the process chain, as fewer steps are required to produce a multi-material component.

DED processes are based on the principle that materials are melted by a heat source and, after cooling, are joined to a substrate with a material bond [6]. The most common application of DED-Arc welding involves wire-fed material supply and the GMAW welding process, which is also referred to as WAAM (Wire Arc Additive Manufacturing). A key advantage of the wire-fed DED-Arc process using GMAW is that it is an established and widely used joining method. Since the arc in the GMAW process is generated by a melting wire, the possibilities for varying the alloy composition are limited. A certain proportion of the melting wire always remains in the molten pool, so the material composition cannot be flexibly adjusted between two wires.

In DED-Arc processes based on non-consumable electrodes, the arc is generated independently of the consumable wires. This allows for a complete variation in material composition, such as when transitioning from alloy A to alloy B [8]. Plasma processes involve a large number of process parameters and typically lack control mechanisms in conjunction with wire feed rates, meaning that height deviations cannot be automatically compensated for. Therefore, precise adjustment of the process parameters is of particular importance for plasma processes. There are also powder-based processes, which are more cost-intensive compared to wire-based methods and are potentially hazardous to health.

2 Aim of the Investigation

In a wide range of applications, FGMs offer a significant advantage; however, their conventional manufacturing is extremely complex. As part of the study, which aims to achieve a complete transition from 100% Material A to 100% Material B using a compact system, the question arises as to whether the DED-Arc plasma process is capable of efficiently manufacturing multi-material components.

3 Materials and Experimental Details

The fabrication of a FGM component using DED-Arc Plasma first requires the definition of a component. A material concept must be developed for the component in question, which must then be implemented using a welding configuration and path planning.

The demonstrator component (Figure 1) is based on the shape of an extrusion die. The extrusion die consists of a base tube with an internal step that tapers the base tube. At the same height, the tube is divided into two semicircles by a central web. The base tube has an outer diameter of 362 mm, an inner diameter of 274 mm, and a height of 146 mm. The step results in a taper of the base tube with an inner diameter of 234 mm and a height of 59 mm. The center web has a width of 25 mm. The component therefore has a volume of 7659 cm^3 and thus a weight of 60.12 kg when produced at full scale. Due to the limited deposition rates in DED-Arc plasma welding, a scaling factor of 3 was applied to enable the component to be manufactured within an eight-hour timeframe.

The semicircles serve as shaping elements for the extruded material. During the extrusion process, the material primarily comes into contact with the step and the central web. It was found that increased tribological wear occurs in these areas. The direction of the material flow is shown in figure 1 as well as the area of highest wear (black rectangle). Until now, the component has been manufactured by machining a low-alloy material, followed by cladding. As part of the standard manufacturing process, cladding has been applied using manual metal arc (MMA) welding. A cobalt-based alloy of the *Stellite 6* type from *Kennametal* was used as the cladding material.

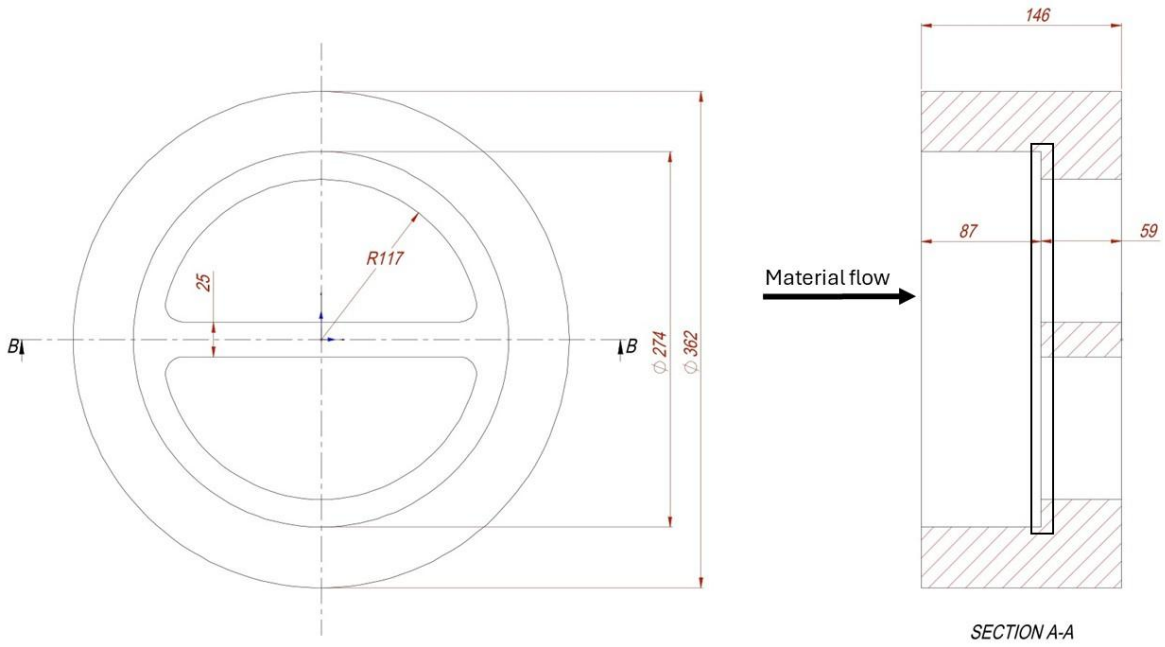

Figure 1: Demonstration component: top view (left), cross-section (right)

A DIN EN ISO 14341 G 3Si1 wire electrode was used as the base material. The transition zone between the low-alloy steel and the cladding was identified as a critical area. As part of the FGM strategy, a buffer layer was therefore considered instead of direct cladding, and cladding was omitted. A nickel-based wire in accordance with DIN EN ISO 18274 S Ni 6082 was used as the buffer wire. According to the specifications in the data sheet, the material provides an adequate buffer layer, particularly between low-alloy steels and nickel-based wires.

An *OTC Daihen FD-V8L* welding robot is used to process the wires. The robot consists of a 6-axis robotic arm and a two-axis swivel-tilt positioner. An *EWM Tetrix 352 Synergetic Plasma CW* is used as the welding power source, which is connected to a *PMC PMW 350-S180* welding torch. The wires are fed into the process zone using two *EWM Tetrix 352 AC/DC Hotwire* power sources, which are combined with two *EWM T-Drive 4 Rob 3* feed units. The two wires are fed into the process zone as cold wires. The speed of the wire feeders are controlled by a computer via an *NI* analog output module with a voltage range of 0 to 10 V. The wire-carrying hose bundles were routed to have the largest possible radii in order to minimize friction within the hose bundles.

Figure 2: Multi-material welding torch with a fixture for two wires on the left and a plasma torch on the right

In preliminary tests, a fixture was developed for two wires (see Figure 2) that converge concentrically toward the plasma torch. With this holder, the angle between the two cold wires and their angle relative to the welding torch can be adjusted using adjustment screws. In addition, it is possible to adjust the height, an offset from the center by a certain distance, and an angle. This holder is characterized by a specific arrangement of two wires positioned one above the other. This arrangement results in optimized droplet transfer and a compact design of the holder, which prevents restrictions on movement.

Paths are programmed using the Python programming language. First, individual path points are defined and then stored in a database. The welding parameters are stored along with the path points. In a subsequent step, the path points are converted into a syntax that can be interpreted and executed by the FD 19 robot controller.

4 Results and Discussion

Based on the combined adjustments to the welding parameters and path planning, two components were successfully manufactured. First, the workability of the two wires was tested using linear welds. It was determined that the following parameters proved to be suitable for the low-alloy wire: As part of the experiment, linear seams with a length of just under 100 mm were applied to plates made of structural steel DIN EN 10025-2 S235JR. Based on the available findings, the nozzle

spacing was 8 mm. The shielding gas nozzle and electrode were positioned at the same height. The electrode had a diameter of 4 mm and a bevel angle of 30°.

A plasma gas of type DIN EN ISO 14175 I1 with a flow rate of 2 l/min and a shielding gas of type M12 with 8 % CO_2 with a flow rate of 17 l/min were used. This led to the best results regarding porosity. The current was 140 A. During the experiment, the plasma torch was moved at a speed of 11 cm/min, and the low-alloy wire was fed into the process zone at 14 mm/s. The combination of these three parameters resulted in optimal weld outcomes. An increase in the energy input per unit length resulted in the occurrence of unstable weld pools. An increase in wire feed rate resulted in unstable wire melting behaviour. The lower connection of the fixture was determined to be the optimal position for the wire, as it demonstrated effective droplet transfer.

The following lists the parameters that were modified when nickel-based wire was used. The current was increased to 160 A, the plasma gas flow was set to 2.2 l/min, and DIN EN ISO 14175 M12 (2% CO2, 98% Ar) was used as the shielding gas. The nickel-based wire was fed into the process zone at a speed of 17.3 mm/s to ensure the best possible droplet transfer. The nickel-based wire was mounted in the higher holder with the aim of achieving a steeper entry into the molten pool and ensuring improved droplet transfer. This objective was achieved by minimizing droplet growth.

The available data suggest the use of an inert gas, such as argon at a concentration of 100% by volume, for processing the nickel-based wire. However, the wire exhibited excessively coarse droplet formation during the plasma process, so a switch was made to an active gas containing CO_2 (DIN EN ISO 14175 M12, 2% CO_2, 98% Ar).

To minimize the incorporation of carbon into the melt and the material, the shielding gas for the low-alloy wire was adjusted. According to the specifications in the welding wire data sheet, welding is performed using an active gas (18% CO_2, 82% Ar) of class M21 in accordance with DIN EN ISO 14175. Since a shielding gas with a higher carbon content had already been used for the nickel-based wire, the low-alloy wire was processed using a M20 shielding gas in accordance with DIN EN ISO 14175, to keep the carbon content introduced via the shielding gas as low as possible.

As part of the analysis of the welding parameters for the nickel-based wire, a wall 10.4 mm high and consisting of 12 layers was constructed (Figure 3). For the purposes of this study, the specimen was cut in half and tested for hardness. In addition, a macroscopic examination was conducted to identify any defects. It was determined that the hardness is divided into three levels. In the lower region of the weld, which has a width of up to 2.5 mm, an increased hardness of approximately 187 HV10 was observed. A decrease in hardness was observed in the range between 3 and 7.5 mm (approximately 170 HV10) as well as between 8 and 10.4 mm (approximately 150 HV10). The decrease in hardness may indicate different cooling conditions. In the lower layers, heat dissipation into the cold substrate sheet is still relatively high, which is also evident from the finer grain

structure in the lower region up to 2.5 mm. Based on the increased thermal properties observed in the demonstrator geometry while the deposition of the nickel-based wire was initiated, it can be assumed that the material properties will correspond to those in the uppermost layers.

No macroscopic defects, such as pores or bonding defects, were observed in the cross-section (Figure 2), so production continued using the determined parameters.

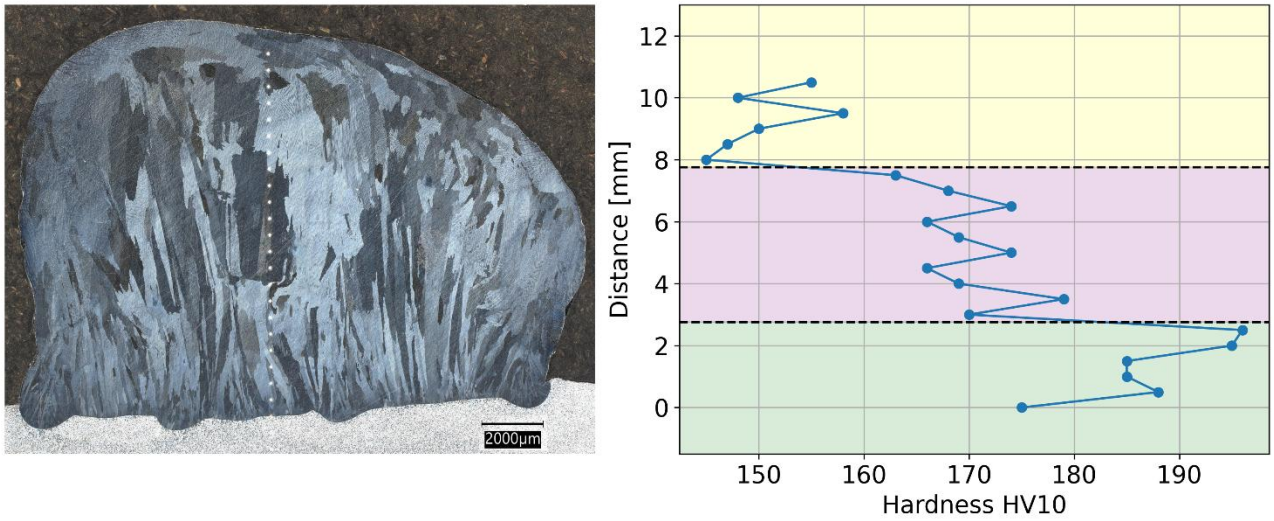

Figure 3: Macroscopic image of a nickel wall following etching and polishing (left), Hardness measurement of nickel wall (right)

During preliminary tests, it was observed that the wire was fed into the process zone from the side towards which the process was moving. This ensures a more uniform weld bead profile. This procedure is shown in Figure 4. The index indicates the order in which the points are welded. Index 0 is the first point to be welded, whereas a point with an index of 140 is near the end of the layer. At point 0, the wire is slightly above points 16–20. If points 16–20 were welded before point 0, there would be a risk of deflection, meaning the wire would not reach the process zone.

Furthermore this process order has the benefit that, a droplet which detached outside the weld pool is remelted and fed back into the molten pool, which prevents material depletion. Furthermore, it must be noted that a droplet detached outside the molten pool can lead to an increase in material. This can cause the wire to become dislodged from its position in a subsequent pass or impair the process. The plasma process is generally highly sensitive to height deviations exceeding one millimeter. These typically manifest as porosity or uneven scaling. Height deviations must therefore be strictly avoided in DED-Arc plasma welding.

Because the component can be broken down relatively easily into circles and lines, and because there is no transition zone requiring a mixture of materials beyond the blending ratio, the paths can be divided into four categories. This classification results from the combination of two materials and two path variations (circular path or line).

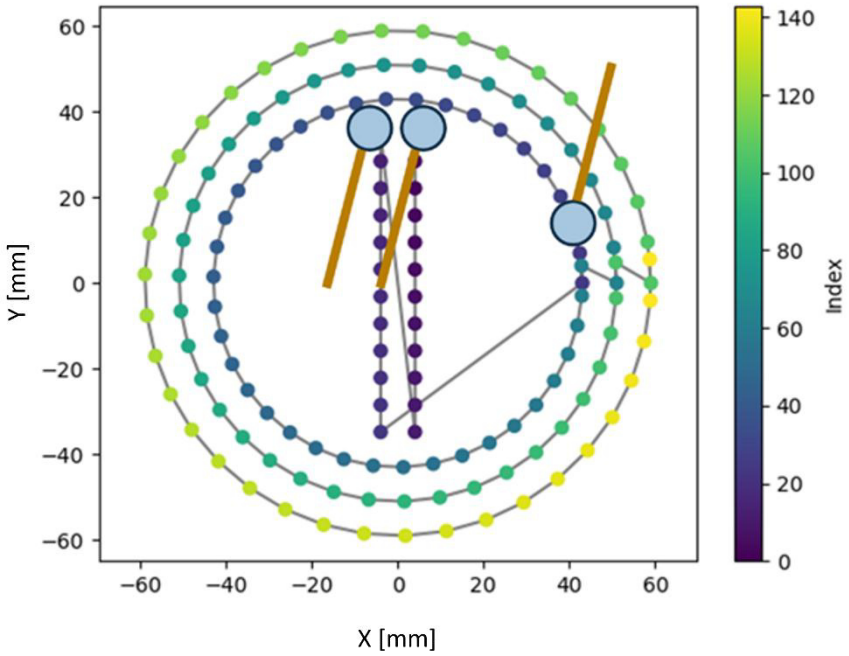

Figure 4: Path planning strategy of the demonstrator. Wire feed deflection shown by brown line.

The wire path of the forward-feeding system had to be deflected outward by 15° to close the circles. This measure was intended to ensure the smoothest possible seam transition and to prevent the cold wires from being deflected by previously deposited material, while simultaneously ensuring optimal droplet transfer. An overlap of 1.5% of the total circumference was deemed adequate (see Figure 4) to overlap the start and end craters and create a uniform height profile. The torch remained at a specific radius for each circular motion while the table rotated 365.4° (360° × 101.5°). To avoid repetitive positioning of the start and end points, the circular motion was shifted by 36°.

The wire feed was offset by 15°, as shown by the brown lines in Figure 4. Furthermore, the order in which the centre seams were welded is significant. To enable these to be welded, the process always proceeded from the centre seams towards the wire holder. The index in Figure 3 indicates the order in which the points are welded. Points with a low index are welded first. In this context, the seams in the centre were successively welded in a different direction in each pass to vary the start and end points. Furthermore, the line length was adjusted to the offset from the centre of the circle, ensuring a coordinated overlap between the circle and the central web.

In order to limit the warping of the base plate, a change in the substrate plates was necessary. Due to the significant warping of the 8 mm thick substrate plates by several millimetres, these were replaced with 30 mm thick substrate plates. The combination of adjustments made it possible to initially manufacture the demonstrator from low-alloy material and subsequently from a multi-material combination. As a result of the heat energy introduced, a slight reduction in layer height was observed, which meant that two layers had to be repeated in order to remain in a stable droplet transfer mode. Following the manufacture of the two demonstrators, the FGM demonstrator was

machined to size. Analysis of Figure 5 reveals that the component exhibits high dimensional accuracy. A defect is visible on the outer surface; however, this does not result in any loss of function for the application at the location in question.

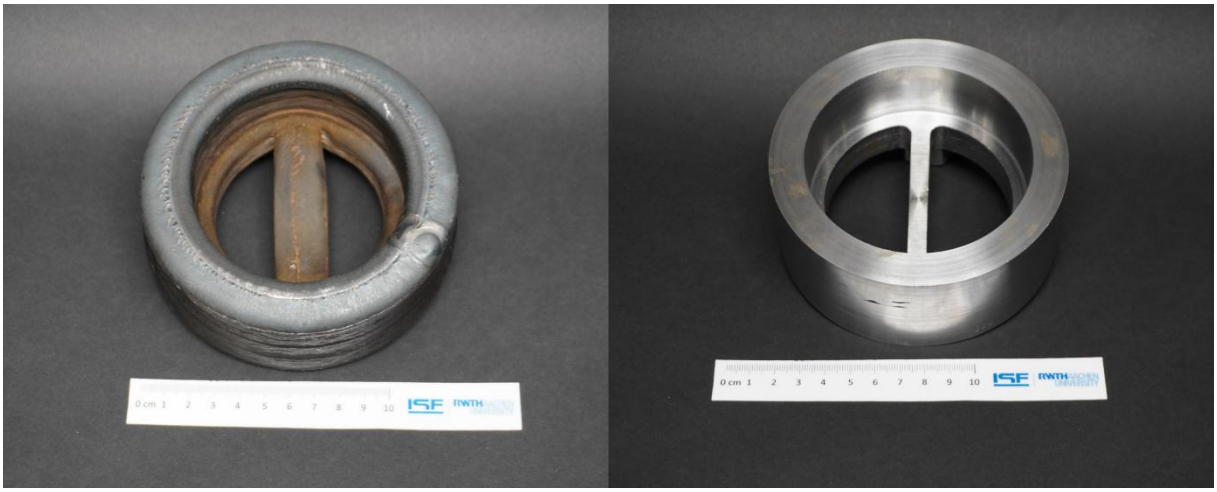

Figure 5: Demonstrators: low-alloy steel on the left, multi-material strategy on the right

5 Summary

It has been demonstrated that the use of multi-wire plasma torches enables the production of FGM components that would otherwise only be achievable conventionally through extensive process expertise.

Within the framework of the process, stable process parameters can be identified that enable autonomous production. Human interaction with the system is not required for this.

At present, the deposited mass is still limited. Higher welding speeds with a higher wire feed rate led to porosity. During the experiment, it was demonstrated that material can be applied at a rate of 0.28 kg/h. The production of the scaled-down demonstrators took eight hours. The actual demonstrator is 27 times larger, which would result in a nearly equivalent increase in production time if the parameters were maintained.

Furthermore, warpage monitoring is of crucial importance for components manufactured using DED-Arc, as the DED-Arc plasma process is highly sensitive to height deviations greater than 1 mm, and warpage of a similar magnitude can make the difference between success and failure in production.

Acknowledgements

Funded by the Federal Ministry of Education and Research (BMBF, Germany)

Project ID: 01DQ22007A

Conflict of Interest

'The author declares no conflict of interest.

Data Availability Statement

Upon request

References

[1] S. W. Williams, F. Martina*, A. C. Addison, J. Ding, G. Pardal and P. Colegrove, Wire + Arc Additive Manufacturing, 2015, Materials Science and Technology, https://doi.org/10.1179/1743284715Y.0000000073

[2] IvánTabernero, Amagoia Paskual, Pedro Álvarez, Alfredo Suárez, Study on Arc Welding Processes for High Deposition Rate Additive Manufacturing, 2018, Procedia CIRP, Volume 68, Pages 358-362, https://doi.org/10.1016/j.procir.2017.12.095

[3] Chong Wang, Wojciech Suder, Jialuo Ding, Stewart Williams, The effect of wire size on high deposition rate wire and plasma arc additive manufacture of Ti-6Al-4V, 2021, Journal of Materials Processing Tech. 288, https://doi.org/10.1016/j.jmatprotec.2020.116842

[4] Sainand Jadhav, Sambhaji Kusekar, Akash Belure, Satyavan Digole, Abhijeet Mali, Muralimohan Cheepu, Manoj Mugale, Suhas Alkunte, Duckbong Kim, Recent Progress and Scientific Challenges in Wire-Arc Additive Manufacturing of Metallic Multi-Material Structures, 2025, Journal of Manufacturing and Materials Processing, https://doi.org/10.3390/jmmp9080284

[5] DVS Media GmbH, Durchführung und Prüfungen von Auftragschweißungen im Anlagen-, Behälter- und Rohrleitungsbau, Merkblatt DVS 3010, Juli 2020

[6] DIN EN ISO/ASTM 52900, 2022

[7] Uwe Reisgen, Rahul Sharma, Lukas Oster, Samuel Mann, Effizienzsteigerung von Wire and Arc Additive Manufacturing durch Aerosolkühlung und Mehrdrahttechnologie, 2019, 1. Fachtagung "Additive Manufacturing" (Vortragsband), DVS Düsseldorf

[8] Uwe Reisgen, Rahul Sharma, Lukas Oster, Plasma Multiwire Technology with Alternating Wire Feed for Tailor-Made Material Properties in Wire and Arc Additive Manufacturing, 2019, Metals, https://doi.org/10.3390/met9070745

Date: 26.03.2026

A Multiscale Solidification Simulation Framework for Mushy Zone Permeability Prediction and Hot Tearing Susceptibility in Al-Mould Casting

Author: Bei Zhou,

Authors: B. Zhou, M. Apel

[1]Access e. V., Intzestraße. 5, 52062, AACHEN, GERMANY

*Corresponding author: E-mail: b.zhou@access-techology.de, ORCID: 0000-0002 -3061-1107

Abstract

Predicting defect formation in Al-alloy castings requires an accurate description of the solidification process and effective material properties in the mushy zone. In this work, a multiscale simulation framework is developed to account for the complex interactions across macro- and microscale. The two scales are iteratively coupled based on a common enthalpy-temperature relationship. The macroscopic model provides heat fluxes and temperature gradients that serve as boundary conditions for microstructure simulations resolving the solidification morphology. The resulting solidification path, effective heat capacity and the latent heat release are fed back to the macroscale. Based on the simulated solidification morphology, interdendritic permeability is calculated to quantify the feeding capability of the mushy zone. Hot-tearing susceptibility is then assessed using criteria combining mechanical strain, solid fraction, and permeability evolution. This integrated approach enables an improved assessment of hot-tearing risk by linking casting-scale conditions with microstructure-dependent feeding behavior.

Keywords

phase field simulation, hot tearing, permeability, Al-alloy

1 Introduction

Defect formation in castings with Aluminum (Al) alloys, such as component deformation and hot tearing, remains a major challenge in industry practice. Their occurrence is strongly influenced by the evolution of solidification morphology in the mushy zone. Accurate prediction of such defects requires a comprehensive understanding of the solidification process, including fraction solid-temperature relationship, microstructure evolution, and the associated material properties.

Traditional macroscopic casting simulations often rely on simplified phase transformation models, such as the Scheil-Gulliver approximation, which tend to underestimate solidification dynamic. For

prediction of hot tearing, Rappaz-Drezet-Gremaud (RDG) model incorporating with Carman-Kozeny expression is commonly applied [1]. However, the Carman-Kozeny expression has limitations in describing permeability evolution at the later stage of solidification, where hot tearing initiation normally occurs.

By contrast, temporally and spatially resolved microstructure simulations based on the multicomponent multiphase-field method (MMPF) can provide detailed insights into microstructure evolution and its dependence on thermal conditions, such as cooling rate and temperature gradient. Based on the simulated morphology, improved temperature dependent material properties, such as solidification path $f_S(\mathrm{T})$, effective thermomechanical properties or permeability, can be derived, offering the potential to enhance the accuracy of macroscopic simulations.

2 Aim

The objective of this work is to develop a micro–macro coupling framework for Al-alloy casting process, linking macroscopic process simulation with microstructure evolution based material properties. To ensure consistent thermodynamic behavior, a self-consistent iterative micro-macro coupling is developed based on homoenthalpic approach proposed by Böttger et. al. [2]. This coupling aims to improve the prediction of temperature prediction in macroscopic simulation and, consequently, temperature-dependent material property evolution. For study of hot tearing, special attention is given to the later stage of solidification with fraction solid $f_S > 0.8$, which is critical for a reliable assessment of hot tearing susceptibility. For this purpose, morphology-based permeability values and an improved analytic expression of permeability evolution is incorporated to refine the RDG hot-tearing criterion.

3 Methods

3.1 Micro-macro coupled simulation

At macroscale, the thermomechanical casting simulation is performed by using the finite element (FE) software Abaqus. At microscale, spatially resolved microstructure simulations are performed using a Calpha-based multicomponent multiphase-field (MMPF) approach [3]. The thermodynamic coupling between micro- and macroscopic simulation is established through the common enthalpy-temperature relationship.

In the process simulation, the casting alloys are treated as a liquid-solid coexistence system characterized by fraction solid f_s. The temperature is locally resolved based on energy balance:

$$\frac{\partial \langle \rho h \rangle}{\partial t} + \boldsymbol{\nabla} \cdot \langle \rho h \mathbf{v} \rangle = -\boldsymbol{\nabla} \cdot \mathbf{q} + \langle \rho \, \dot{r}_q \rangle \,, \tag{1}$$

where ρ denote the density, h is the specific enthalpy, and $\mathbf{q}$ and r_q represent heat flux vector and volumetric heat source, respectively. The operator $\langle \cdot \rangle$ denotes the volume average of a quantity

over the liquid-solid system. By decomposing average enthalpy into a temperature dependent contribution, characterized by $c_p(T)$ and a phase-transformation contribution associated the latent heat L_f, the time derivative of the averaged enthalpy can be written as

$$\frac{\partial\langle\rho h\rangle}{\partial t} = \langle\rho c_p^{\text{eff}}(T)\rangle\,\frac{\partial T}{\partial t} = \left(\langle\rho c_p(T)\rangle - \langle\rho\rangle L_f\,\frac{\partial f_s}{\partial T}\right)\frac{\partial T}{\partial t}\,. \tag{2}$$

Substituting this express into Eq. (1) yields the macroscopic energy equation:

$$\langle\rho c_p^{\text{eff}}(T)\rangle\frac{\partial T}{\partial t} + \boldsymbol{\nabla}\cdot\langle\rho h\mathbf{v}\rangle = -\boldsymbol{\nabla}\cdot\mathbf{q} + \langle\rho\dot{r}_q\rangle\,. \tag{3}$$

At microscale, the domain-averaged temperature is evaluated using a simplified model, as the characteristic microstructural length is typically much smaller than thermal diffusion length, particularly in the case of equiaxed solidification. For directional solidification, the temperature field is approximated by temperature gradient G_T in conjunction with a mean cooling rate. According to the energy balance law, there is

$$\frac{d}{dt}\left(\sum_\alpha h_\alpha\phi_\alpha\right) = -\dot{q}\,, \tag{4}$$

where $\dot{q}$ is the heat extraction rate per unit volume, and ϕ_α and h_α are the phase fraction and phase-specific enthalpy, respectively. Since the phase-specific enthalpy h_α is a function of temperature T and composition $\{c_k\}$, the differential form of the microscale energy balance can be rewritten as:

$$\sum_\alpha \phi_\alpha\left(c_{p,\alpha}dT + \sum_k \frac{\partial h_\alpha}{\partial c_k}\,dc_k\right) + \sum_\alpha h_\alpha d\phi_\alpha = -\dot{q}dt\,. \tag{5}$$

This leads to the evolution equation for the domain-averaged temperature:

$$d\bar{T} = \frac{1}{\bar{c}_p}\left(-\dot{q}dt - \sum_\alpha\sum_k \phi_\alpha\,\frac{\partial h_\alpha}{\partial c_k}dc_k + \sum_\alpha h_\alpha\,d\phi_\alpha\right) = \frac{1}{\bar{c}_p}(-\dot{q}dt - dl\,) \tag{6}$$

with an average specific heat capacity $\bar{c}_p = \sum_\alpha \phi_\alpha c_{p,\alpha}$ and the phase-specific heat capacity $c_{p,\alpha}$ as well as enthalpy $h_{p,\alpha}$ being read from the thermodynamic database via the Fortran TQ interface. Then the latent heat contribution dl caused by the temperature change dT can be estimated by

$$dl = dh - \bar{c}_p dT \quad \text{with} \quad h = \sum_\alpha \phi_\alpha\, h_\alpha \tag{7}$$

The bidirectional micro-macro coupling is realized through a consistent exchange of thermal quantities between both scales. In macroscale simulation, the local heat extraction rate per unit volume, $\dot{q}$, and temperature gradient G_T are read and applied as process conditions in MMPF

microstructure simulation. In Abaqus, $\dot{q}$ is calculated at integration points through the user-defined subroutine HETVAL based on Eq. (3). The microstructure simulation, in turn, provides the solidification path $f_s(T)$, the averaged specific heat capacity $\bar{c}_p(T)$ and the latent heat of fusion, $L_f = \int dl$, to macroscopic simulation. The coupled simulations are performed iteratively until a consistent temperature evolution achieved across both scales.

3.2 Morphology based permeability and hot tearing susceptibility

Permeability at selected states during the solidification is determined by performing computational fluid dynamics (CFD) simulations on the microstructures simulated by MMPF simulations. Here, superficial velocity vectors $\mathbf{v}_f$ of the flow driven by applied pressure gradient $\mathbf{g}_p$ is calculated by solving the Stokes equation in x-, y- and z-, respectively. This leads to the evaluation of the Darcy permeability tensor

$$\mathbf{K} = \frac{\tilde{\mu}}{|\mathbf{g}_p|}\left[\mathbf{v}_{fx}, \mathbf{v}_{fy}, \mathbf{v}_{fz}\right] \tag{8}$$

with $\tilde{\mu}$ denoting the viscosity. The permeability tensor can be converted to diagonal by evaluation of eigenvalues and eigenvectors. For equiaxial dendritic microstructures, it is expected to be isotropic.

By fitting the calculated permeability values along the solidification path using analytic expressions, the evolution of permeability as f function of temperature can be obtained. A commonly used expression is the Carman-Kozeny (CK) model,

$$K(T) = \frac{\lambda_2^2}{180}\frac{\left(1 - f_s(T)\right)^3}{f_s^2(T)}\ , \tag{9}$$

where λ_2 is the secondary arm spacing. For improved accuracy at high solid fractions, modified CK formulations proposed by Berger et al. [4] are employed to account for the progressive interdendritic bridging and its impact on permeability reduction. A subsequent study [5] demonstrated that the following modified Carman–Kozeny (MCK) model is capable of describing the permeability evolution with sufficient accuracy, i.e.,

$$K(T) = c_0\frac{\left(f_c - f_s(T)\right)^3}{S_V^2}\ . \tag{10}$$

Here, c_0 is a morphology constant. A critical fraction of solid f_c is introduced to characterize the transition at which the interdendritic liquid channels become fully disconnected, causing the permeability to approach zero. The interfacial area density S_V is defined as the area of solid-liquid interface per unit volume, and is evaluated through post-processing of the simulated morphology.

An accurate description of the permeability evolution along the solidification path enables the RDG hot-cracking model to account for the evolving microstructural morphology. In the RDG model, the onset of hot tearing is assumed to be associated with hydrostatic depression in the mushy zone, which arises primarily from the shrinkage and deformation of the solid skeleton. By assuming a homogeneous strain rate $\dot{\varepsilon}_p$ over the region spanning from massive feeding to coalescence, the pressure drop Δp can be calculated based on mass balance and Darcy's law for fluid flow as

$$\begin{aligned}\Delta p &= \Delta p_{\varepsilon} + \Delta p_{sh} \\ &= \frac{(1+\beta)\mu\dot{\varepsilon}_p}{G_T^2}\int_{T_{end}}^{T_{mf}} \frac{\tilde{E}(T)}{K(T)}\, dT + \frac{\dot{T}\beta\mu}{G_T^2}\int_{T_{end}}^{T_{mf}} \frac{1-f_s(T)}{K(T)}\, dT \quad . \end{aligned} \tag{11}$$

with the term $\tilde{E}(T) = \int_{T_{end}}^{T} f(\tilde{T})d\tilde{T}$. Here, β is the shrinkage factor, G_T is the temperature gradient, $\dot{T}$ is the cooling rate and μ is the dynamic viscosity of the liquid phase. When the pressure drop reaches the cavitation pressure Δp_c, a void can be nucleated and leads to a crack. A hot-cracking susceptibility (HCS) is then defined as the inverse of the maximal allowed local deformation rate,

$$HCS = \frac{1}{\dot{\varepsilon}_{p,max}} = \frac{\int_{T_{end}}^{T_{mf}} \frac{\tilde{E}(T)}{K(T)} dT}{\frac{G_T^2}{(1+\beta)\mu}\Delta p_c - \frac{\dot{T}\beta}{1+\beta}\int_{T_{end}}^{T_{mf}} \frac{1-f_s(T)}{K(T)}\, dT} \quad . \tag{12}$$

In this work, the RDG model is integrated with the permeability evolution obtained from microstructure simulations, and represented using the Carman-Kozeny type models expressed in Eq. (9) and Eq. (10).

4 Results and Discussion

4.1 Micro-macro coupled simulation of Sr-modified Al-Si-Mg in die casting

In commercial applications, Strontium (Sr) are usually added to the Al-Si alloys to modify the Al-Si eutectic to improve mechanical properties. Sr impacts both growth and nucleation of the eutectic Si phase in solidification of Al-Si alloy. The iterative micro–macro coupling framework was applied to the die-casting of a bowl-like component using a Sr-modified commercial Al–Si alloy (A356) [6, 7], to capture the effect of Sr-modification.

The procedure began with a thermomechanical FE simulation, in which phase transformation was initially approximated using the Scheil calculation. This is followed by MMPF microstructure simulations by taking the local heat extraction rate at selected bowl locations as process condition. Within the microstructure simulations, the effect of Sr on eutectic Si nucleation was accounted for by adjusting the number of initial nuclei, while its influence on eutectic growth is captured through calibration of the characteristic length scale of the eutectic morphology. In the subsequent iteration, the updated solidification path $f_s(T)$ and latent heat release by MMPF simulation were fed back

into FE casting simulation. In study [7], it was demonstrated that, despite variations in heat extraction rates on different locations, the solidification path $f_S(T)$ and enthalpy-temperature relationship obtained from MMPF simulations were quite similar. Therefore, uniform solidification path and latent heat release were applied for the entire bowl component in the present casting simulation.

As a result, Figure 1 presents the temperature evolution at two selected locations on the bowl component, namely BM (bottom middle) and BS (bottom surface) with relatively high cooling rates. For regions with lower cooling rates, as shown in previous studies [6,7], the temperature prediction based on the Scheil approximation already achieved good agreement with experimental measurements. As shown in Figure 1, the FE simulation with the Scheil approximation were significantly higher than the experimental measurements. After two iterative loops, the temperature prediction is significantly improved. Both 2D and 3D MMPF simulations improve the predictions, with the 3D approach yielding slightly higher accuracy. To quantitatively assess the agreement, the normalized L^1 error in percent

$$E = \frac{\int_{t_1}^{t_2} |T_{sim}(t) - T_{exp}(t)| dt}{\int_{t_1}^{t_2} |T_{exp}(t)| dt} \cdot 100\%$$

was evaluated over the solidification interval and summarized in *Table 1*.

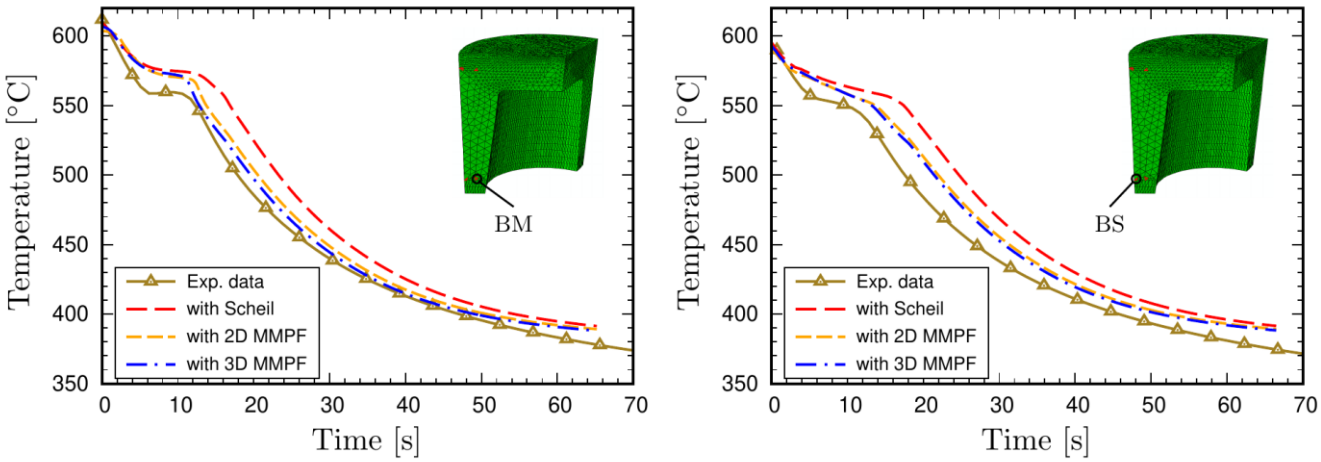

Figure 1: Temperature evolutions obtained by FE casting simulations in comparison with experimental measurements at selected locations on the bowl component, labelled as BM (bottom middle) and BS (bottom surface).

Table 1: Normalized L^1 errors of temperature predictions at BM and BS locations.

Location	Normalized L^1 error		
	with Scheil	with 2D MMPF	with 3D MMPF
BM	4.0 %	2.16 %	1.76 %
BS	5.08%	3.2%	2.81%

4.2 Morphology based permeability and hot cracking in Al-Cu alloys

In this section, hot-tearing-sensitive Al–Cu alloys are investigated. In a previous work [5], MMPF simulations were performed for an Al–Cu–Fe–Mg–Si alloy under different cooling rates to assess their influence on permeability evolution and the RDG hot-tearing index. Here, additional simulations are carried out for an Al–5 wt.% Cu alloy at cooling rates of −4 °C/s, −2 °C/s, and −1 °C/s, and the results are compared with experimental observations reported in [8]. The microstructure simulations were conducted within a representative volume of 300µm × 300µm × 600µm with a cell spacing of 1.5µm. The corresponding heat extraction rates were calibrated using simplified two-dimensional simulations. The initial number of fcc-Al grains is determined based on the experimentally measured average grain size in [8]. The calibrated heat extraction rates and the corresponding initial grain numbers are summarized in *Table 2*. Based on the simulated morphology, the permeability values were evaluated and subsequently used for the assessment of RDG hot-cracking index. Other constants required for the calculation of the RDG hot-cracking index were taken from [1].

Table 2: Cooling rates, corresponding calibrated heat extraction rates, and initial number of fcc-Al grains used in the MMPF simulations for the Al–5 wt% Cu alloy.

Cooling rate [°C/s]	Heat extraction rate [J/s*cm^3]	Number of fcc-Al grains
-4	-47	16
-2	-24	12
-1	-13	9

To ensure consistency between the simulated solidification morphology and experimental radiographs, as well as SDAS values, the diffusion coefficient of Cu in the liquid phase was scaled by a factor of 0.1. With the diffusion modification, a significantly finer microstructure was obtained under identical simulation settings, as shown in Figure 2a. It leads to reduced permeability values along the solidification process and consequently increased RDG hot-cracking index, see Figure 2b and 2c. The extracted morphology parameters for assessment of RDG index are summarized in *Table 3*.

Table 3: Morphological parameters extracted from MMPF simulations Al-5wt%Cu under -4°C with and without diffusion modification.

	CK	MCK	
	SDAS λ_2 [µm]	c_0	f_c
Unmodified	110,351	0,822	0,986
Modified	61,67	0,652	0,982

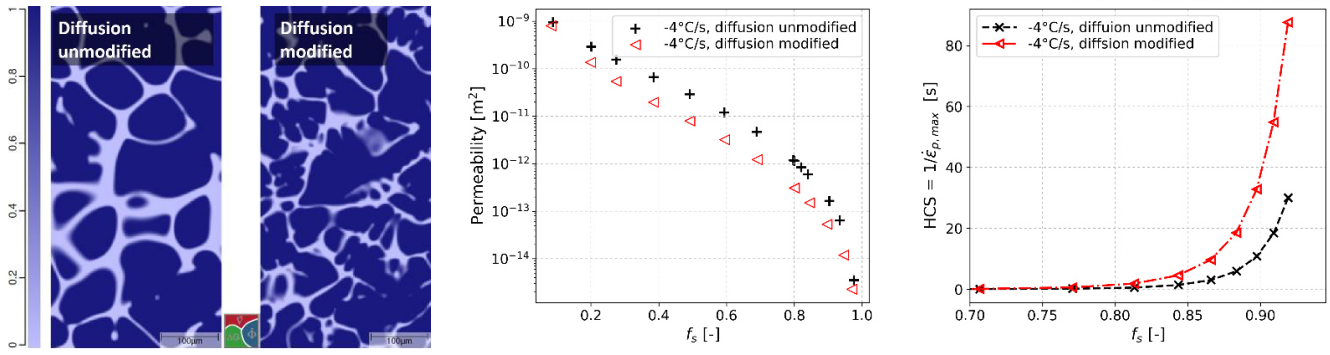

(a) (b) (c)

Figure 2: Comparison of results without and with diffusion modification (factor=0.1). (a) Simulated microstructure of the Al–5 wt.% Cu alloy under a cooling rate of −4 °C/s, shown at f_s=0.8; (b) calculated permeability based on the simulated microstructures; (c) Hot cracking susceptibility (HCS) as a function of solid fraction f_s, evaluated using the RDG criterion with the MCK model.

After calibrating the simulation setup, the solidification morphologies under different cooling rates are shown in Figure 3, showing good agreement with the radiographs reported in [8]. The microstructure becomes progressively finer with increasing cooling rate. Correspondingly, the calculated permeability decreases as the cooling rate increases (Figure 4a), and the extracted morphology parameters are summarized in *Table 4*. The RDG hot-tearing index was subsequently evaluated along the solidification path for all three cases using the CK1 model (Figure 4b). The results indicate that higher cooling rates significantly increase the hot-tearing susceptibility, and the onset of hot tearing occurs at lower solid fractions, in agreement with the experimental observations reported in [8].

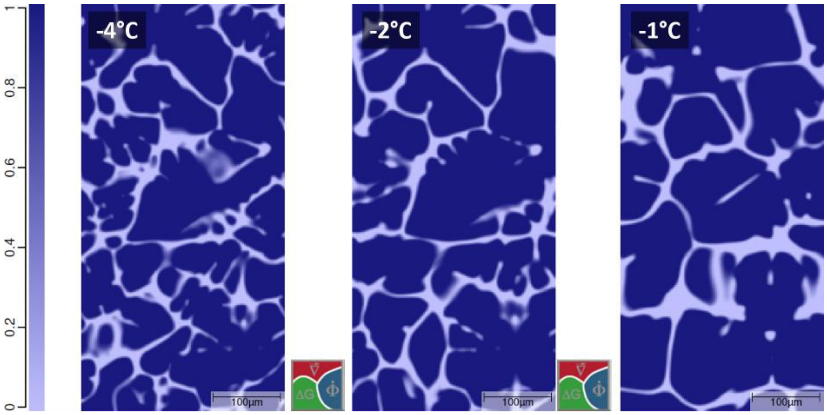

Figure 3: Simulated microstructure of the Al–5 wt% Cu alloy at different cooling rates, selected at a solid fraction of f_s=0.8. Left: −4 °C/s with 15 fcc-Al grains; middle: −2 °C/s with 9 fcc-Al grains; and right: −1 °C/s with 6 fcc-Al grains.

Table 4: Morphological parameters extracted from MMPF simulations Al-5wt%Cu under different cooling rates.

	CK	MCK	
Cooling rate [°C/s]	SDAS λ_2 [µm]	c_0	f_c
-4°C/s	61,676	0,652	0,982
-2°C/s	74,651	0,663	0,986
-1°C/s	70,472	0,674	0,983

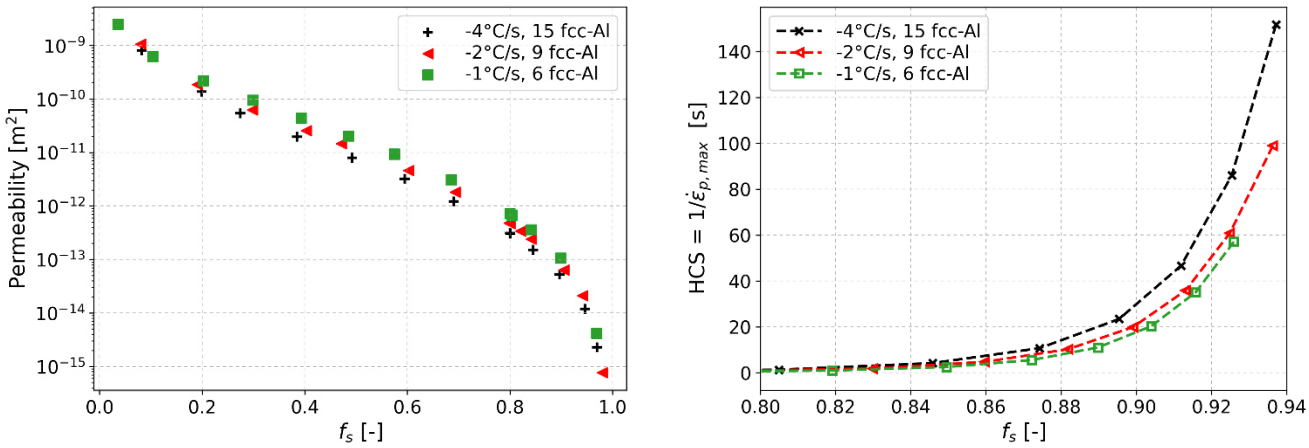

(a) (b)

Figure 4: (a) Calculated permeability based on the simulated microstructures under different cooling rates; (b) Hot cracking susceptibility (HCS) as a function of solid fraction f_s, evaluated using the RDG criterion with the MCK model.

5 Summary

The iterative micro–macro coupling framework provides a significant improvement in predicting temperature evolution in die-cast components, particularly in regions with high cooling rates, where the Scheil approximation alone could underestimate solidification dynamics. For purely thermodynamic coupling, both 2D and 3D MMPF simulations yield similar solidification paths, indicating that 2D MMPF can be appropriately used to reduce computational cost.

However, for reliable prediction of hot-tearing susceptibility, 3D microstructure simulations are essential, as they more accurately capture the evolution of permeability along the solidification path. For that purpose, experimental morphology parameters, such as average grain size and secondary dendrite arm spacing (SDAS), are crucial to refine and validate the simulated microstructures. Overall, for practical engineering applications, a detailed understanding of solidification thermodynamic and microstructural evolution at the microscale can substantially enhance the predictive accuracy of process simulations at the macroscale.

Acknowledgements

The presented work was carried out within the framework of the Collaborative Research Centre SFB1120-236616214 “Bauteilpräzision durch Beherrschung von Schmelze und Erstarrung in Produktionsprozessen” and funded by Deutsche Forschungsgemeinschaft e.V. (DFG, German Research Foundation). The sponsorship and support is gratefully acknowledged.

Conflict of Interest

The author declares no conflict of interest.

Data Availability Statement

The data and codes supporting the findings of this study are available in the following repository:

https://git.gi.rwth-aachen.de/bz_publications/emporia2026.git

The repository includes input files for the microstructure simulations, the pipeline code for the micro–macro coupling framework, and scripts for the evaluation of the RDG hot-cracking index.

References

[1] M. Rappaz, J. M. Drezet, and M. Gremaud, *Metall Mater Trans A Phys Metall Mater Sci*, vol. 30, no. 2, **1999**.

[2] B. Böttger, J. Eiken, and M. Apel, *J Comput Phys*, vol. 228, **2009**.

[3] J. Eiken, B. Böttger, and I. Steinbach, *Phys Rev E Stat Nonlin Soft Matter Phys*, vol. 73, **2006**.

[4] R. Berger, M. Apel, and G. Laschet, *Materialia (Oxf)*, vol. 15, **2021**.

[5] B. Zhou, M. Apel, J. Eiken, R. Berger, S. Gor, and N. Wolff, *Materwiss Werksttech*, vol. 55, **2024**.

[6] B. Zhou, G. Laschet, J. Eiken, H. Behnken, and M. Apel, *IOP Conf Ser Mater Sci Eng*, Institute of Physics Publishing, **2020**.

[7] B. Zhou, H. Behnken, J. Eiken, M. Apel, G. Laschet and N. Wolff, *EMPOrIA-International Joint Conference*. Springer International Publishing, **2021**.

[8] I. Han, S. Feng, F. Wilde, P. S. Grant, and E. Liotti, *Acta Mater*, vol. 262, **2024**.

Date: 13.03.2026

Narrowband aeroacoustic gas modulation for improved cut-edge quality in laser fusion cutting of austenitic stainless steels

Author: Marcelo de Oliveira Lopes[1]

Authors: Frank Schneider[2], Arnold Gillner[1], Constantin Häfner[3]

[1]RWTH Aachen University, Chair for Laser Technology, Steinbachstr. 15, 52074, AACHEN, GERMANY

[2]Fraunhofer Institute for Laser Technology, Steinbachstr. 15, 52074, AACHEN, GERMANY

[3]RWTH Aachen University, Templergraben 55, 52062 AACHEN, GERMANY

*Corresponding author: E-mail: marcelo.lopes@llt.rwth-aachen.de, ORCID: 0000-0003-0991-9016

Abstract

This paper summarizes fundamental studies of subproject A08 within SFB 1120 and addresses a limitation in laser fusion cutting of austenitic stainless steels: pronounced cut-edge roughness and burr formation, thereby constraining the process window. The presented approach introduces a resonator-equipped modulating nozzle (“cutting whistle”) that imposes a targeted narrowband aeroacoustic gas modulation to stabilize melt-film transport without increasing overall gas consumption. A reduced thin-film framework links gas-side interfacial shear and streamwise pressure gradients to blocking behavior and a film-side cutoff frequency, guiding frequency-band selection. The actuator provides a geometrically determined fundamental mode; modulation amplitude increases with stagnation pressure. High-speed imaging confirms a depth-dependent low-pass melt response, with lower and mid bands coupling more effectively into the exit region. Under matched throughput, narrowband modulation increases mean interfacial shear, stabilizes the melt transport, reduces roughness and burr in paired comparisons, and moderately increases the maximum cutting speed.

Keywords

laser fusion cutting, aeroacoustic modulation, melt-film stability, cut-edge roughness, austenitic stainless steel.

1 Introduction

Laser fusion cutting is widely used for manufacturing austenitic stainless steel components, offering high geometric flexibility and oxidation-free cut edges [1]. A persistent limitation, however, is pronounced cut-edge roughness and adherent burr, which constrain the usable process window in terms of feed rate, focus position, and gas pressure [2,3]. This becomes particularly

critical for sheet thicknesses above ~6 mm, where defects typically intensify toward the lower front region [4]. At the beginning of Collaborative Research Centre (SFB) 1120, roughness values of $R_z \approx 60–70$ µm with adherent burr were common for 6 mm stainless steel under industrial conditions. The long-term target is $R_z < 10$ µm with essentially burr-free edges.

Within SFB 1120, subproject A08 addresses this challenge through in-situ diagnosis and control of melt and solidification dynamics during laser fusion cutting, based on the hypothesis that the dominant quality limitations arise from insufficiently understood melt-front instabilities and their coupling to compressible gas flow. Accordingly, A08 follows an evolutionary approach: Phase 1 established a transparent trimming-cut test rig with high-speed imaging to directly observe melt-film motion and solidification, enabling experimental assessment of kerf multiple reflections [5,6] and demonstrating that controlled beam divergence can calm the melt stream and reduce instability-driven fluctuations [7]. In Phase 2, the diagnostic platform was expanded by schlieren imaging and acoustic measurements of the gas jet, revealing thickness-dependent resonances of the coupled gas–film system and motivating resonance-based actuation concepts [8]. Phase 3 consolidates these insights into process-compensation strategies using passive actuator-based modulation designed for compatibility with industrial cutting heads [9]. In this context, the present paper highlights a representative, industrially viable outcome: a resonator-equipped modulating nozzle ("cutting whistle") that superimposes a geometrically defined, narrowband aeroacoustic tone on the gas [10]. Building on a reduced thin-film framework, we relate this actuation to a depth-resolved melt response measured by high-speed imaging and to paired quality metrics (roughness, burr, maximum cutting speed) under matched gas throughput, thereby demonstrating how diagnostics-driven understanding and targeted actuation can increase cut-edge precision relative to the initial state at the start of SFB 1120.

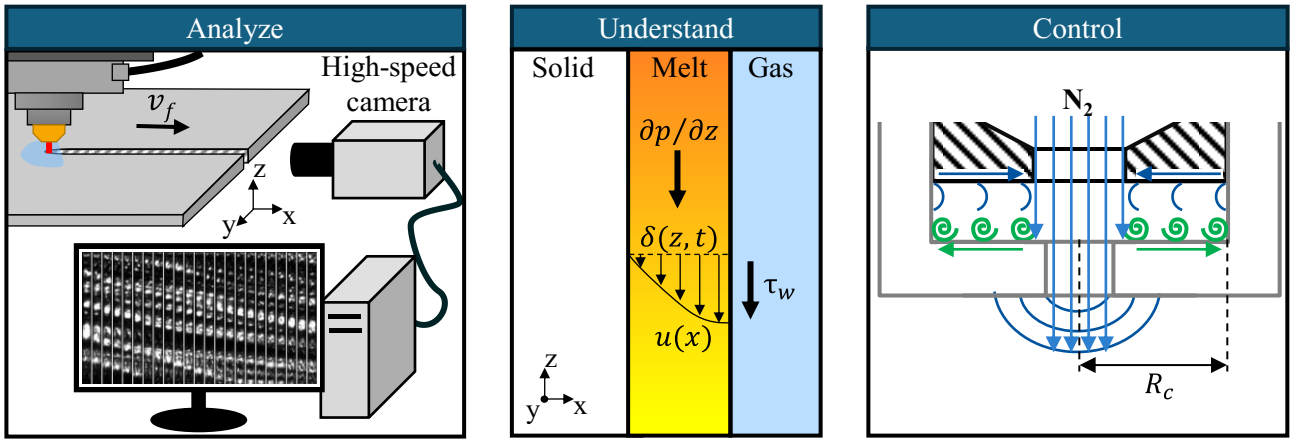

Figure 1: Methodological approach in SFB 1120: analyze–understand–control. In-situ process diagnostics quantify melt-film motion and gas–front interaction (Analyze). A reduced melt-flow framework interprets the dominant mechanisms and yields design-relevant guidance (Understand). Based on this, a resonator-equipped nozzle ("cutting whistle") is developed and applied to impose narrowband gas modulation that targets melt-film instabilities (Control).

2 Aim of the Investigation

The aim is to assess whether a resonator-equipped nozzle can stabilize melt evacuation near the lower front by imposing a depth-effective narrowband gas modulation without increasing gas

throughput. Specifically, we test whether band selection guided by a thin-film cutoff concept yields measurable reductions in lower-zone R_z and burr height H_{burr} in paired comparisons against a standard nozzle.

3 Materials and Experimental Details

Experiments were conducted on austenitic stainless steel (1.4301) sheets with thicknesses of 6 mm and 10 mm. Cutting was performed with a 1030 nm CW disk laser ($P_L = 6$ kW) using a Precitec HPSSL cutting head. The beam was delivered via a 100 µm fiber and shaped by 100 mm collimation and 200 mm focusing optics, resulting in an approximately 200 µm focus diameter. Focus position z_f and feed rate v_f were varied to span a representative process window, while comparisons between nozzle concepts were conducted under otherwise identical conditions. Nitrogen gas was supplied at stagnation pressures $p_0 = 12$–24 bar for cutting trials; additional 0–20 bar pressure ramps were used for actuator characterization. The gas was delivered coaxially through nozzles with 3 mm outlet diameter, comparing a standard conical nozzle against a resonator-equipped cutting whistle (variants A/B/C covering low-, mid-, and high-frequency bands). The nozzle stand-off N_z was adjustable and verified mechanically; the norm-volume flow Q_N was measured to enforce matched throughput in paired comparisons.

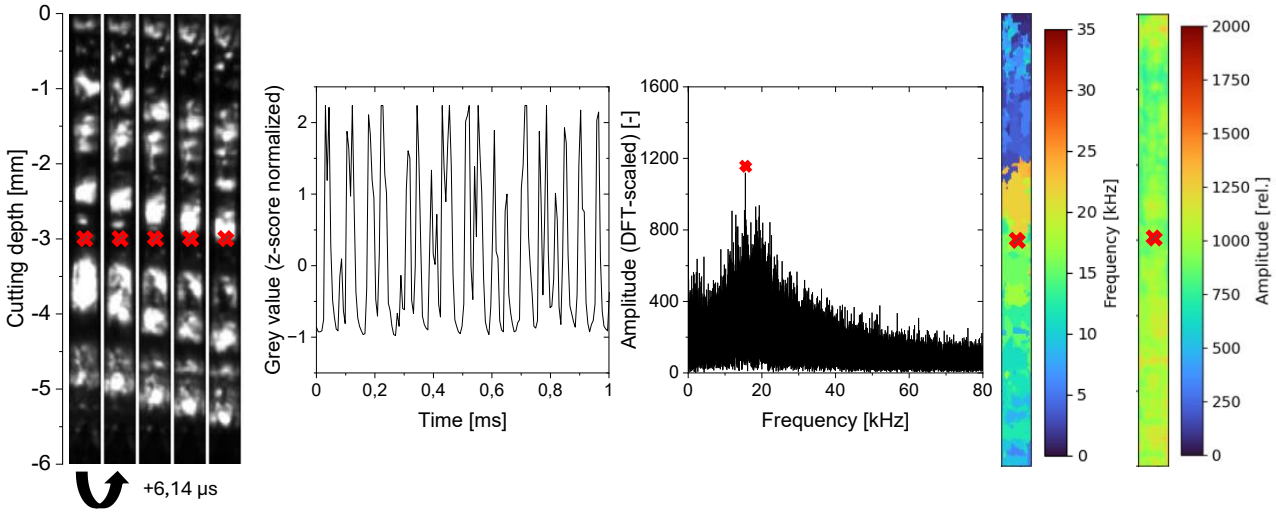

Figure 2: Pixel FFT pipeline for obtaining frequency-selective metrics. Left: z-normalized sample time series of a front pixel with dominant modulation. Right: corresponding amplitude spectrum with peak at and schematic derivation of frequency heatmaps and amplitude heatmaps.

Actuator behavior was quantified by microphone spectroscopy (STFT-based spectrograms/spectra for f_0, tonality, and pressure trends) and schlieren imaging of the gas jet in free jet and a transparent kerf model (coupling studies). Melt-front dynamics were captured by frontal high-speed imaging at approximately 1.6×10^5 fps, covering the full front depth from the top surface to the kerf exit. Pixelwise spectral analysis yielded dominant-frequency maps $f_{\mathrm{dom}}(y, z)$ and frequency-selective amplitude maps $A(y, z \mid f_0 \pm \Delta f)$ around the actuator fundamental; phase organization was evaluated using bandpass filtering around f_0, Hilbert-phase extraction, and phase-locking value (PLV) maps. Cut-edge quality was assessed under matched throughput by lower-zone roughness R_z (ISO 9013; optical profilometry at 1 mm above the lower edge), burr height H_{burr} (tactile

profilometry), and the maximum cutting speed $v_{f,\max}$ determined by feed-rate ramping to the last fully separating cut. Unless stated otherwise, results are reported from paired experiments (identical material, optics, p_0, N_z, and v_f), ensuring that differences in melt dynamics and quality are attributable to narrowband modulation rather than changes in average gas delivery.

4 Results and Discussion

4.1 Cutting whistle: schlieren- and acoustics-based results

The standard nozzle exhibits predominantly broadband acoustic emission with intermittently pressure-dependent bands appearing. Across the investigated pressure range, no single narrowband line can be tracked as a phase-stable fundamental mode. In contrast, all cutting-whistle variants (A/B/C) produce a pronounced narrowband fundamental mode with harmonic overtones. In pressure-ramp spectrograms this appears as a nearly vertical line whose amplitude increases with stagnation pressure, while its frequency remains essentially constant within the lock-in operating window. Any residual frequency variations are in the order of the spectral resolution and peak-fit uncertainty, i.e., no systematic pressure-induced frequency shift is observed in lock-in. For the representative mid-band configuration (Design B), the fundamental remains near $f_0 \approx 15$ kHz over the full investigated range (0–20 bar) (Fig. 3 (a)).

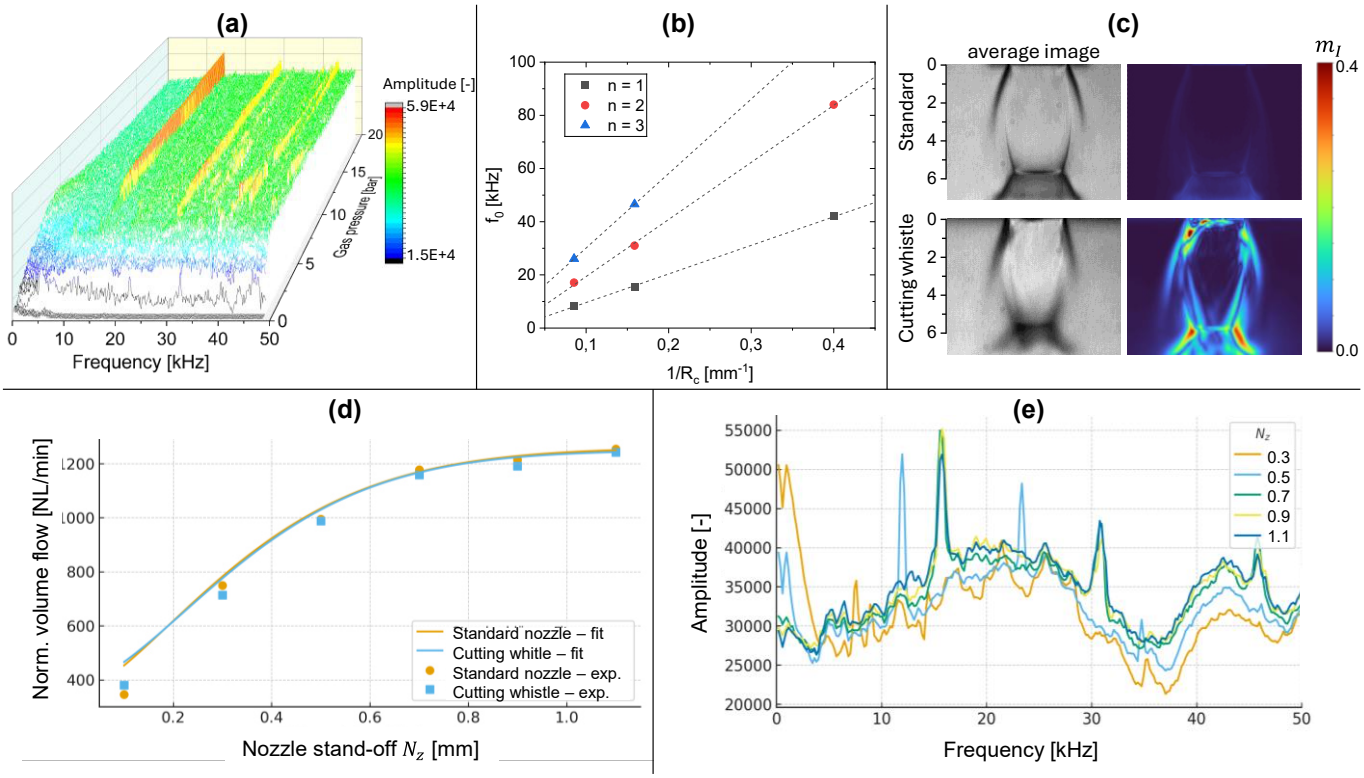

Figure 3: Cutting-whistle actuator characterization. (a) Pressure-ramp spectrogram showing a narrowband lock-in fundamental f_0 with amplitude increasing with p_0; (b) geometry scaling of f_0 versus $1/R_c$ (variants A–C); (c) time-averaged schlieren images and modulation-index maps m_I demonstrating coherent jet modulation for the cutting whistle (design B) compared to the standard nozzle; (d) norm-volume flow Q_N versus stand-off N_z indicating a hydraulic plateau near $N_z \approx 0.7$ mm; (e) microphone spectra for different nozzle stand-offs N_z(design B), illustrating lock-in near $f_0 \approx 15$ kHz for $N_z \geq 0.7$mm and detuning to lower bands at smaller N_z.

Across variants A–C, the fundamental frequency f_0 shifts systematically with cavity geometry and spans distinct excitation bands: A (low band, ≈ 8–17 kHz), B (mid band, ≈ 15–30 kHz), and C (high band, e.g., ≈ 40–80 kHz). When the lock-in-stable mean values of f_0 are plotted versus the inverse effective cavity radius $1/R_c$, the data follow a linear relationship (Fig. 3 (b)). This confirms the intended Rossiter/Strouhal-type geometry scaling [11]: larger cavity radii yield lower eigenfrequencies, smaller radii yield higher eigenfrequencies. Practically, this establishes a clear separation of roles: frequency selection is primarily geometric (A/B/C).

Schlieren imaging further demonstrates that the cutting whistle introduces a coherent narrowband modulation into the free jet that is absent for the standard nozzle (Fig. 3c). For the standard nozzle, schlieren sequences are dominated by broadband structures without a persistent narrowband corridor. For the cutting whistle (Design B), bandpass evaluation around f_0 yields a spatially connected modulation corridor in the near-field jet core. We quantify this effect by a schlieren-based modulation index $m_I = \hat{I}_{\mathrm{RMS}}/\bar{I}$, computed from the band-limited schlieren intensity fluctuations around f_0 and normalized by the local mean intensity. Although schlieren signals are not a direct velocity measurement, the band-limited intensity variations in the jet core scale with the strength of the coherent density-gradient structures associated with the imposed shear-layer mode; therefore m_I provides a conservative, dimensionless proxy of the relative modulation depth. Assuming $\hat{U}/\bar{U} \gtrsim m_I$ (lower-bound mapping), the quadratic dependence of wall shear on velocity implies a mean-shear increase $\Delta\bar{\tau}_w/\bar{\tau}_w \approx \frac{1}{2}(\hat{U}/\bar{U})^2 \gtrsim \frac{1}{2}m_I^2$. With $m_I \approx 0.2$–0.3 this yields $\Delta\bar{\tau}_w/\bar{\tau}_w \approx 2$–$4.5\%$ even under throughput parity, providing a mechanistic lever for stabilizing melt-film transport.

The nozzle stand-off N_z is shown to be the dominant coupling parameter between the modulated jet and the kerf entrance. Flow measurements at $p_0 = 20$ bar reveal a steep increase of $Q_N(N_z)$ at small stand-off and a clear approach to a plateau at larger N_z for both nozzle types (Fig. 3 (d)). Already at $N_z = 0.7$ mm both nozzles reach roughly 94 % of the plateau. Thus, increasing N_z beyond ~0.7 mm yields only marginal throughput gains out of the nozzle. Acoustically, N_z controls whether the cutting whistle operates in its intended lock-in band or becomes detuned (Fig. 3e). For $N_z \geq 0.7$ mm the dominant mode remains in the expected lock-in region around $f_0 \approx 15$ kHz and stays essentially constant, consistent with stable geometric resonance under hydraulically open conditions. At smaller distances, the system remains tonal but the dominant frequency shifts downward (≈12 kHz at $N_z = 0.5$ mm and ≈7 kHz at $N_z = 0.3$ mm), indicating detuned regimes linked to altered entrance impedance and inlet throttling. The Prominence Ratio PR is used here as a tonality metric, defined as the peak level at f_0 relative to a local broadband "mask" level around the peak (i.e., $PR = L_{\mathrm{peak}} - L_{\mathrm{mask}}$, where L_{mask} is obtained from locally smoothed spectral background). While PR can peak slightly near $N_z \approx 0.5$ mm, this primarily reflects a reduced broadband background; in the hydraulically open regime ($N_z \approx 0.7$ mm) the absolute tonal line amplitude is higher, but the broadband level is also higher, which reduces PR despite stronger

modulation. Overall, $N_z \approx 0.7$ mm provides the most robust operating point, combining near-full throughput with stable lock-in at the intended f_0 and strong tonal forcing.

4.2 Melt dynamics and reduced model: depth-resolved response to narrowband forcing

To interpret how a narrowband gas excitation translates into cut-edge quality, we employ a reduced thin-film framework in which the melt layer on the inclined cutting front is driven by two gas-side pathways: interfacial shear stress (Couette-type forcing) and a streamwise pressure gradient along the front (Poiseuille-type forcing) [12]. In this picture, stable evacuation requires that shear-driven transport remains sufficiently strong relative to locally adverse pressure forcing that would otherwise thicken the film and promote intermittent accumulation ("blocking-prone" behavior). Such adverse pressure forcing can arise locally when kerf coupling weakens or becomes non-uniform—for example due to jet spreading/leakage, or shock/boundary-layer interactions that impose spatially localized back-pressure regions along the front [13]. In the lower kerf, where the melt film is typically thicker and shear levels tend to decay, even modest local increases in streamwise pressure forcing or transient drops in interfacial shear can shift the film into a buildup/emptying regime rather than a global standstill. Linearizing the forced thin-film response yields a film-side cutoff frequency that separates effectively transmitted perturbations from strongly damped ones. In scaling form,

$$f_c \sim \frac{\bar{\tau}_w}{\eta_m \bar{\delta}},$$

where $\bar{\tau}_w$ denotes a representative mean shear stress, η_m an effective melt viscosity, and $\bar{\delta}$ an effective film thickness. Since $\bar{\tau}_w$ typically decreases and $\bar{\delta}$ tends to increase towards the kerf exit, the model predicts a depth-dependent low-pass behavior: higher-frequency forcing is increasingly filtered with depth, while lower-frequency forcing can penetrate further—provided the excitation remains at or below the local f_c of the target depth region.

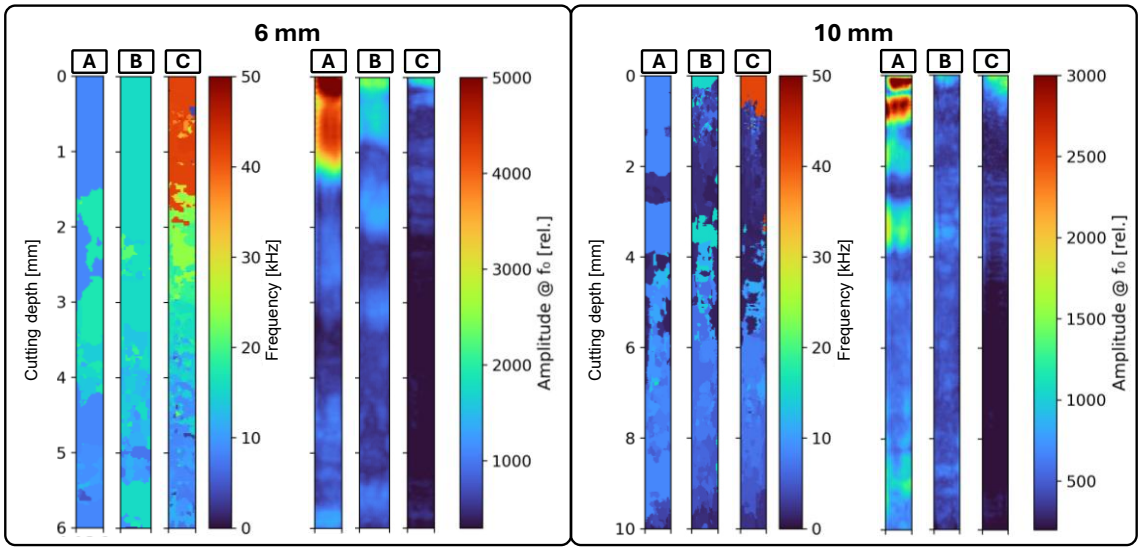

Figure 4: Depth-resolved melt response to cutting-whistle variants A/B/C at $p_0 = 20$ bar and $N_z = 0.7$ mm. $f_{\mathrm{dom}}(y,z)$ and $A(y,z \mid f_0 \pm \Delta f)$ show strong near-top response for all bands; low/mid bands penetrate deeper than the high band. Representative 10 mm cases indicate a downward shift of the depth-effective band.

The depth-resolved high-speed imaging results support these predictions (Fig. 4–5). For 6 mm stainless steel under representative conditions, the imposed fundamental is clearly visible in the upper front region for all cutting-whistle variants, including high-band excitation. With increasing depth, however, the response becomes strongly frequency selective: low and mid bands maintain a measurable signature deeper into the kerf, whereas the high band decays rapidly and remains largely confined to the upper portion. This trend is consistent with the depth-dependent low-pass filtering implied by $f_c(z)$. 10 mm datasets show the same hierarchy shifted toward lower effective bands: the deeply effective band moves to lower frequencies as thickness increases, in line with the expectation that $\bar{\delta}$ and/or η_m increase and thus reduce f_c.

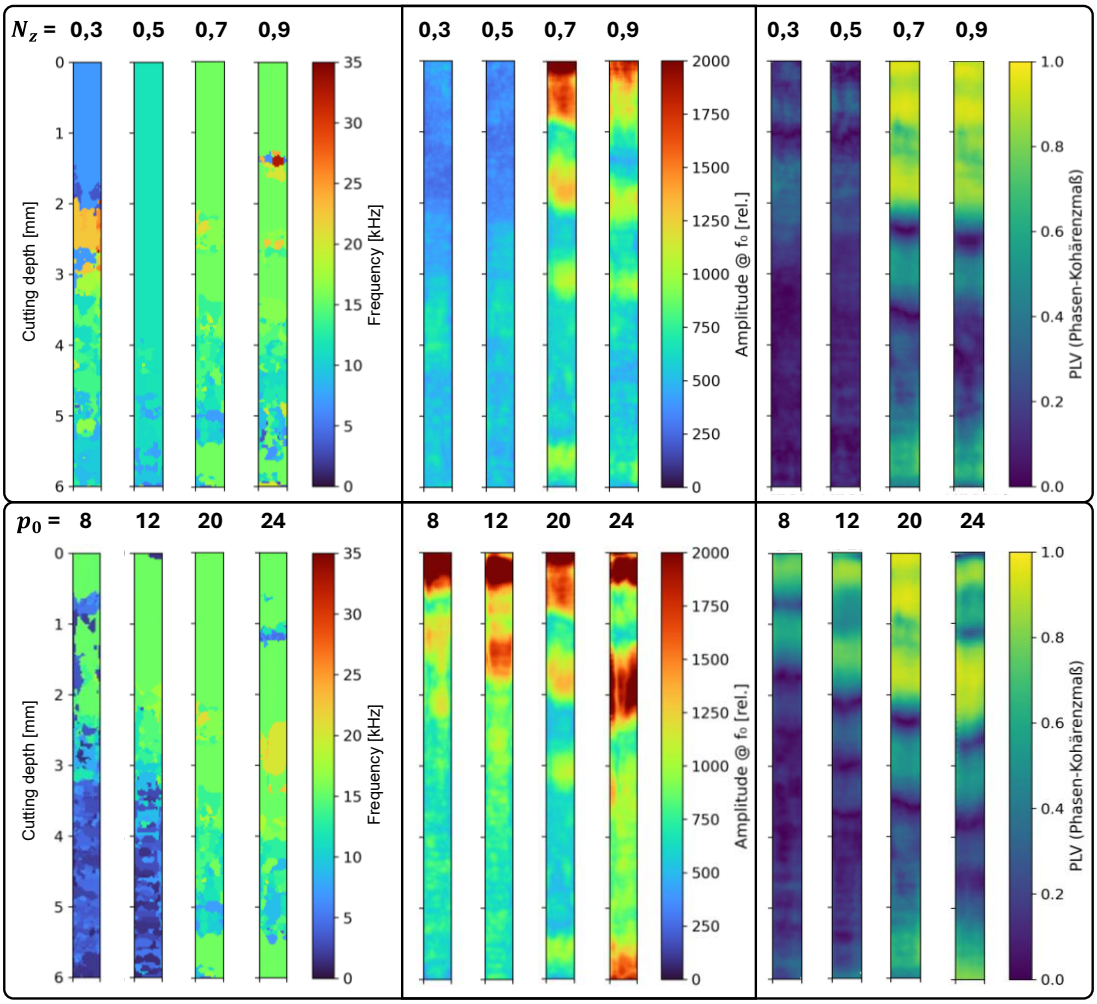

Figure 5: Lock-in and coupling trends for design B (6 mm): f_{dom}, $A(y,z \mid f_0)$, and PLV versus p_0 and N_z. Higher p_0 strengthens response and coherence; coupling is maximal near $N_z \approx 0.7$ mm, with detuning at small N_z.

Beyond amplitude trends, the measurements also confirm the model's operating-point dependence via pressure and stand-off. Increasing stagnation pressure strengthens the imposed modulation and, through the quadratic dependence of shear on velocity [14], increases the mean shear stress $\bar{\tau}_w$ [15], thereby widening the dynamic bandwidth and improving depth effectiveness. Correspondingly, coherence metrics (PLV) exhibit broader plateaus at higher pressures in the lock-in regime, indicating that the forced oscillation is not only detectable but remains phase-organized over a larger fraction of the front depth. The nozzle stand-off N_z acts as a coupling selector: at too

small N_z, the system detunes toward lower modes and the nominal excitation band couples less effectively; at too large N_z, jet spreading and leakage weaken the effective forcing. In the intermediate coupling window around $N_z \approx 0.7$ mm, both mode fidelity and coherence are maximized, which is consistent with the framework's requirement that a sufficiently strong and well-coupled shear forcing must be maintained to keep the melt film away from blocking-prone regimes near the exit.

Overall, the experiments corroborate the reduced framework in three key, design-relevant trends: (i) the cutting front behaves as a depth-dependent low-pass to narrowband forcing, (ii) frequency-band selection must target the exit region (i.e., $f_0 \lesssim f_c$ at the lower front), with the effective band shifting downward for larger thickness, and (iii) the depth effectiveness is controlled by operating point—notably stagnation pressure and stand-off—through their impact on mean shear and coupling efficiency.

4.3 Precision gains and process window

Across the full dataset of 70 paired parameter combinations (6 mm), the cutting whistle reduces lower-zone roughness R_z and burr height H_{burr} in the majority of operating points. In median, R_z decreases by ~18%, and in about four out of five paired cases the roughness with the cutting whistle is lower than with the standard nozzle. Burr height shows an even stronger improvement: the median reduction is ~33%, and approximately seven out of ten paired cases exhibit lower burr with the cutting whistle. These global trends indicate that the imposed narrowband modulation is not a marginal effect confined to isolated parameter points, but a reproducible process lever.

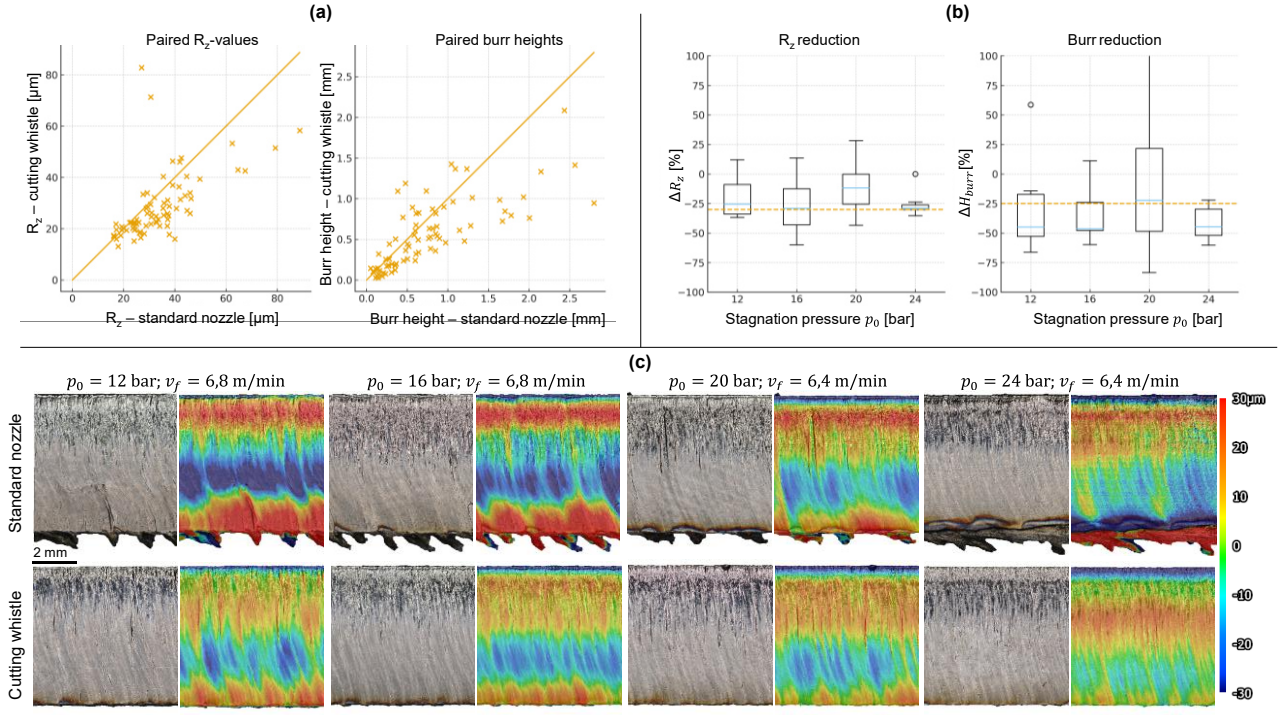

Figure 6: Quality impact under matched throughput (6 mm, $N_z = 0.7$ mm): (a) paired scatter of R_z and H_{burr} (cutting whistle vs. standard), (b) boxplots of relative changes versus p_0, and (c) representative edge images illustrating delayed burr onset with the cutting whistle.

The improvements become most pronounced within the coupling window identified earlier (sufficiently high stagnation pressure and a stand-off around $N_z \approx 0.7$ mm) and for focus settings that favor stable melt evacuation near the exit. In this regime, the cutting whistle produces an expanded "quality plateau" in terms of simultaneously low roughness and reduced burr, while moderately increasing the achievable cutting speed up to 10 %. This is consistent with the reduced framework introduced in Section 4.2: when the excitation band is depth-effective and the coupling is strong, the melt film is less prone to blocking-prone accumulation cycles near the lower front and can be evacuated more continuously. Conversely, outside this operating window—e.g., at insufficient pressure or at stand-off settings that reduce effective coupling—the quality gain becomes smaller and more variable.

Overall, the quality results support the central conclusion of this paper: temporal structuring of the gas forcing, implemented by a resonator-equipped nozzle at constant gas throughput, provides a robust pathway to reduce roughness and burr and to extend the usable process window in laser fusion cutting of austenitic stainless steels.

5 Summary

The work presented in this paper summarizes the main steps taken in subproject A08 of SFB 1120 to improve cut-edge precision in laser fusion cutting of austenitic stainless steels. Starting from industrial reference conditions with roughness values Rz of about 60–70 µm and pronounced burr at 6 mm thickness, the combination of in-situ diagnostics and targeted actuation has enabled a stepwise reduction of melt-film instabilities. In Phase 1, access to the cutting front via a transparent trimming-cut rig and high-speed imaging revealed the dominant instability mechanisms and showed that an appropriate use of beam divergence can already reduce roughness by roughly a factor of three.

In Phase 2, extending the diagnostic chain towards schlieren imaging and acoustic measurements exposed thickness-dependent resonances of the coupled gas–film system. This led to the development of a resonator-equipped nozzle that generates a geometrically fixed, narrowband aeroacoustic mode with pressure-dependent amplitude. A reduced thin-film framework links gas-side interfacial shear and streamwise pressure forcing to a film-side cut-off frequency and blocking logic and thereby guides the choice of effective modulation bands. High-speed imaging confirms a depth-dependent low-pass response of the melt film: lower and medium frequency bands couple more efficiently into the lower front, increase the time-averaged interfacial shear and suppress large-scale, low-frequency accumulation events.

Under matched gas throughput, this narrowband gas modulation leads to a robust reduction of cut-edge roughness and burr height and to a moderate increase of the maximum cutting speed. In favorable parameter windows, the achievable roughness is in the 10–20 µm range, thus approaching an order-of-magnitude improvement in surface precision, while simultaneously mitigating burr

formation. These results underline that the temporal structure of the gas field is a powerful additional design variable, complementary to beam and nozzle geometry.

Acknowledgements

The presented investigations were carried out at the Chair of Laser Technology LLT of RWTH Aachen University and Fraunhofer Institute for Laser Technology ILT within the framework of the collaborative Research Centre SFB1120-236616214 “Bauteilpräzision durch Beherrschung von Schmelze und Erstarrung in Produktionsprozessen” and funded by the Deutsche Forschungsgemeinschaft e.V. (DFG, German Research Foundation). The sponsorship and support are gratefully acknowledged.

Conflict of Interest

The author declares no conflict of interest.

Data Availability Statement

The data supporting the findings of this study are available at http://hdl.handle.net/21.11102/60822e64-6a99-4e54-9910-2bba1b0240f6.

References

[1] Petring, D.; Abels, P.; Beyer, E.; Herziger, G. (1988): Werkstoffbearbeitung mit Laserstrahlung. Teil 10: Schneiden von metallischen Werkstoffen mit CO2-Hochleistungslasern. In: Feinwerktechnik & Messtechnik 96, S. 364–372.

[2] Mahrle, Achim; Borkmann, Madlen; Pfohl, Peer (2021): Factorial Analysis of Fiber Laser Fusion Cutting of AISI 304 Stainless Steel: Evaluation of Effects on Process Performance, Kerf Geometry and Cut Edge Roughness. In: Materials (Basel, Switzerland) 14 (10). DOI: 10.3390/ma14102669.

[3] Stoyanov, S.; Petring, D.; Piedboeuf, F.; Lopes, M.; Schneider, F. (2023): Numerical and experimental investigation of the melt removal mechanism and burr formation during laser cutting of metals. In: Journal of Laser Applications 35 (4), Artikel 042028. DOI: 10.2351/7.0001182.

[4] Goppold, Cindy; Zenger, Karsten; Herwig, Patrick; Wetzig, Andreas; Mahrle, Achim; Beyer, Eckhard (2014): Experimental Analysis for Improvements of Process Efficiency and Cut Edge Quality of Fusion Cutting with 1µm Laser Radiation. In: Physics Procedia 56, S. 892–900. DOI: 10.1016/j.phpro.2014.08.108.

[5] Petring, Dirk; Molitor, Thomas; Schneider, Frank; Wolf, Norbert (2012): Diagnostics, Modeling and Simulation: Three Keys Towards Mastering the Cutting Process with Fiber, Disk and Diode Lasers. In: Physics Procedia 39, S. 186–196. DOI: 10.1016/j.phpro.2012.10.029.

[6] Arntz, D.; Petring, D.; Stoyanov, S.; Jansen, U.; Schneider, F.; Poprawe, R. (2018): In situ visualization of multiple reflections on the cut flank during laser cutting with 1 µ m wavelength. In: Journal of Laser Applications 30 (3), Artikel 032206. DOI: 10.2351/1.5040614.

[7] Arntz, D.; Petring, D.; Schneider, F.; Poprawe, R. (2019): In situ high speed diagnosis—A quantitative analysis of melt flow dynamics inside cutting kerfs during laser fusion cutting with 1 µ m wavelength. In: Journal of Laser Applications 31 (2), Artikel 022206. DOI: 10.2351/1.5096091.

[8] Arntz‐Schroeder, Dennis; Petring, Dirk (2020): Analyzing the Dynamics of the Laser Beam Cutting Process. In: PhotonicsViews 17 (2), S. 43‐47. DOI: 10.1002/phvs.202000015.

[9] Oliveira Lopes, M. de; Petring, D.; Stoyanov, S.; Gillner, A. (2023): Control of melt dynamics in laser cutting based on a resonant nozzle cavity. In: Journal of Manufacturing Processes 105, S. 399–406. DOI: 10.1016/j.jmapro.2023.09.051.

[10] Oliveira Lopes, M. de; Schneider, F.; Gillner, A.; Häfner, C. (2024): Suppression of melt flow instabilities by amplifying high-frequency melt waves in laser fusion cutting. In: Journal of Manufacturing Processes 131, S. 2255–2262. DOI: 10.1016/j.jmapro.2024.10.040.

[11] Rossiter, J. E. (1964): Wind tunnel experiments on the flow over rectangular cavities at subsonic and transonic speeds. In: *London: Aeronautical Research Council, Reports and Memoranda, Rept. 3488*. Online verfügbar unter https://reports.aerade.cranfield.ac.uk/handle/1826.2/4020.

[12] Vicanek, M.; Simon, G.; Urbassek, H. M.; Decker, I. (1987): Hydrodynamical instability of melt flow in laser cutting. In: J. Phys. D: Appl. Phys. 20 (1), S. 140–145. DOI: 10.1088/0022-3727/20/1/021.

[13] Borkmann, Madlen; Mahrle, Achim; Wetzig, Andreas (2023): Laser fusion cutting: The missing link between gas dynamics and cut edge topography. In: Journal of Laser Applications 35 (4), Artikel 042017. DOI: 10.2351/7.0001103.

[14] Schlichting, Hermann; Gersten, Klaus (2017): Fundamentals of Boundary–Layer Theory. In: Hermann Schlichting und Klaus Gersten (Hg.): Boundary-Layer Theory. Berlin, Heidelberg: Springer Berlin Heidelberg, S. 29–49. DOI: 10.1007/978-3-662-52919-5_2.

[15] Tennekes, H. and Lumley, J.L. (1972): A First Course in Turbulence. Cambridge, Massa-chusetts, and London, England: The MIT Press.

Date: 31.03.2026

Adaptive Process Control Strategies For Variable Wall Thickness In Laser Metal Deposition: A Framwork Utilizing Articifical Neural Networks

H. Kruse*, A. Kulkarni, G. Menezes de Souza Melo, M. Sudmanns, J.-H. Schleifenbaum

RWTH Aachen University, Chair for Digital Additive Production, Campus-Boulevard 73, 52074, AACHEN, GERMANY

*Corresponding author: E-mail: henrik.kruse@dap.rwth-aachen.de ORCID: 0000-0001-5674-2634

Abstract

Laser Metal Deposition (LMD) offers significant potential for optimizing local component properties through local reinforcement or coating, enabling enhanced performance and functionality. It is widely applied in repair and remanufacturing, where precise control of material deposition is essential for restoring component geometry. However, achieving high geometric accuracy requires robust process control strategies and a systematic link between target geometry and process parameters.

In this context, this paper presents a data-driven approach to realize variable wall thickness in LMD based on an artificial neural network (ANN). A multilayer feed-forward network is trained on a combined dataset of experimental measurements and FEM-based simulations to capture the relationship between process parameters and meltpool geometry. The model is embedded in an inverse optimization framework to determine process parameters for predefined target geometries. Experimental validation on a demonstrator confirms controlled variation of track width at approximately constant height, demonstrating improved dimensional controllability and process efficiency.

Keywords

Additive Manufacturing (AM), Laser Metal Deposition (LMD), Machine Learning (ML), Remanufacturing

1 Introduction

Laser Metal Deposition (LMD) has become an established additive manufacturing process for the fabrication, repair, and functional enhancement of metallic components, particularly in tooling and turbomachinery applications [1,2]. Its capability to locally add material makes it especially suitable for applications requiring tailored material distribution or geometry adaptation.

However, the reliable manufacturing of geometrically accurate structures remains a major challenge in LMD [3]. Due to the layer-wise deposition of overlapping melt tracks, local deviations in material accumulation frequently occur. Excess material deposition leads to surface irregularities and dimensional inaccuracies, while insufficient deposition in regions with complex geometries

can result in pores or incomplete filling of the target geometry. These effects limit the achievable dimensional accuracy and reproducibility of the process.

A key challenge lies in the lack of a direct relationship between desired track geometry and the corresponding process parameters. In conventional approaches, parameter selection is largely based on empirical knowledge or simplified assumptions, requiring extensive experimental effort.

Toolpath planning strategies are commonly used to improve process quality and can be divided into offline and online approaches [4,5]. While online approaches enable real-time adaptation based on sensor feedback and are therefore considered highly promising, their industrial application remains challenging due to sensor limitations, process complexity, and restricted controllability of certain parameters. In particular, the powder mass flow rate cannot be adjusted with sufficient temporal resolution during deposition. As a result, effective process control is primarily achieved through laser power and scanning speed.

Consequently, offline process planning remains widely used in industrial practice. Enhancing these approaches with predictive models enables a systematic adaptation of process parameters along the toolpath without requiring real-time feedback [6].

Machine learning approaches have been investigated to capture complex and nonlinear relationships in LMD processes [7–9]. However, most existing studies focus on monitoring or defect detection, while the direct prediction of process parameters for a predefined geometry, particularly in an inverse formulation, remains insufficiently explored [10,11].

2 Aim of the Investigation

Achieving high geometric accuracy in LMD requires a systematic link between target geometry and process parameters. Building on previous work of the authors, in which a finite element model (FEM) was developed to predict melt pool geometry, this study extends the approach toward geometry-driven process control [12–14].

The objective of this work is to enable the prediction of process parameters for a predefined single-track geometry using a data-driven surrogate model. For this purpose, an artificial neural network is trained on a combined dataset of simulation and experimental data, capturing both physically consistent trends and real-process variability.

The trained model is coupled with an inverse optimization strategy to determine suitable process parameters for a given target geometry, establishing a continuous pipeline from geometry definition to parameter selection.

The capability of the proposed approach is demonstrated by the realization of a variable wall thickness with predicted process parameters in single-track deposition. The results highlight the potential of machine-learning-assisted process parameter prediction to improve geometric accuracy

and process stability and underline its relevance as a building block for future geometry-aware toolpath planning strategies in LMD.

3 Materials and Experimental Details

3.1 Data Generation via FEM and Experiments

To establish a data-driven relationship between process parameters and resulting track geometry, a sufficiently large and consistent dataset is required. In this work, this requirement is addressed by combining experimental measurements with simulation-based data generation.

The simulation data are obtained from a finite element model of the LMD process which was developed and continuously refined in previous work of the authors [12–19]. The model describes track formation as a coupled thermo-physical problem, accounting for heat conduction, mass addition, and free surface evolution based on the Young–Laplace equation with mass conservation. Powder particles are treated as a volumetric heat source or sink depending on their thermal state and interaction with the melt pool. A detailed mathematical description can be found in previous publications [12]. Due to the high computational cost of fully transient simulations, a quasi-stationary approach is applied, enabling efficient evaluation of large parameter spaces while maintaining sufficient accuracy.

Figure 1 shows a comparison between the simulated temperature distribution of a representative single track and the corresponding experimental cross section in the YZ plane. Deviations between simulated and experimentally measured melt pool width, depth, and height remain below 10 %, confirming the validity of the model for data generation [13].

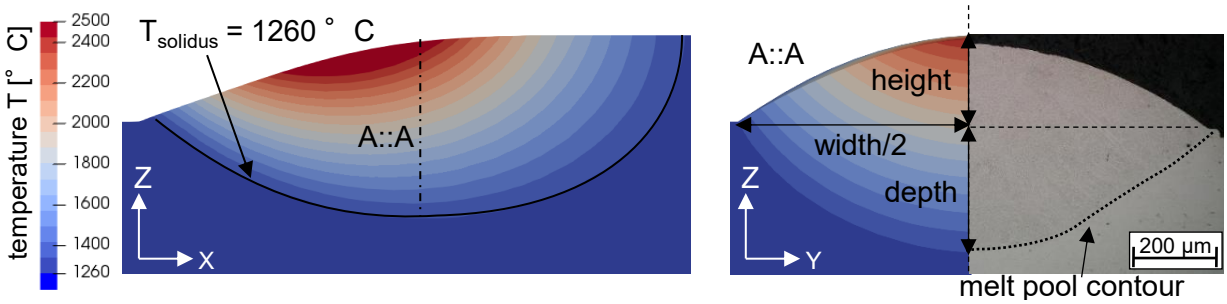

Figure 1: left: side view of the temperature distribution of an exemplary single track simulation, right: YZ cross section perpendicular to the scan velocity along A::A and overlay with optical microscopy [12,13]

An important model extension is the incorporation of powder shielding effects. The attenuation of the laser beam by the powder jet is considered by adapting the local energy input based on empirical particle distributions [20,21].

To enable high-throughput data generation, a fully automated simulation workflow is implemented. The workflow includes parameter generation based on a design of experiments (DoE), simulation execution, and automated extraction of melt pool geometries. Although the FEM solver itself operates sequentially, multiple simulations are executed in parallel at the process level. Using this approach, a total of 2,160 steady-state simulation cases are evaluated within a structured parameter

sweep. In this study, Inconel (IN625) was used as the deposited material and stainless steel as the substrate, with temperature-dependent thermophysical properties obtained from manufacturer datasheets (Special Metals), ASM Handbooks, and the NIST database [22].

The investigated DoE spans laser power in the range of 1000 W and 3000 W, scanning speed between 6.7 mm/s and 36.7 mm/s, and powder feed rates between 15 g/min and 30 g/min, covering the relevant process window for stable single-track deposition reported in literature for laser-based deposition of IN625 [23–25].

In addition to simulation data, experimental measurements from single-track depositions are incorporated. The experiments are carried out on an Okuma MU-6300V LASER EX machine equipped with a Trumpf Yb:YAG disk laser operating at a wavelength of 1030 nm and a maximum laser power of 4000 W. A Gaussian beam profile with a laser spot diameter of 3 mm is used. The deposition is performed using a ring-gap nozzle with argon as shielding gas, processing IN625 powder on steel. The experimental parameter space covers scanning speeds between 6.7 mm/s and 33.3 mm/s, laser power between 800 W and 2200 W, and powder mass flow rates between 12 g/min and 18 g/min. In total, 151 cross-sectional samples are generated and prepared metallographically. The resulting melt pool geometries are evaluated using optical microscopy to determine track width, depth, and height.

3.2 Data Processing

Data cleaning is performed to ensure physical consistency and robustness of the dataset. Non-physical simulation results, such as unstable melt pool formations or numerical artifacts, are removed. Additionally, statistical outliers are filtered using an interquartile range (IQR) method to eliminate extreme values that are not representative of stable process conditions. Only samples with complete geometric information are retained. After data cleaning, the final dataset consists of 1,869 valid samples, including 1,805 simulation-based data points and 64 experimental samples.

3.3 ANN Surrogate Model and Optimization Framework

To approximate the nonlinear relationship between process parameters and melt pool geometry, data-driven regression models are investigated. Different model configurations and preprocessing strategies are evaluated to identify a suitable representation of the process behavior. A systematic comparison of several regression algorithms further confirmed that the multilayer perceptron combined with standard z-score scaling provides the most reliable representation of the process behaviour, whereas linear models were unable to capture the strong nonlinear coupling between parameters and meltpool geometry, in agreement with thermo-physical analyses of DED track formation reported by Perani et al [8].

Based on this analysis, a multilayer perceptron (MLP) is selected as the most reliable surrogate model. The network consists of four hidden layers with a 256–128–64–32 neuron topology. Rectified linear unit (ReLU) activation functions are used in the hidden layers, while the output layer remains linear to enable regression of continuous geometric variables. The model is trained

using supervised learning on the combined dataset. To improve generalization, L2 regularization is applied, and the dataset is split into training and validation subsets using an 80/20 ratio with a fixed random seed. Different data scaling approaches are evaluated, and standardized normalization is selected to ensure stable training behavior.

The input vector of the forward ANN model consists of the relevant process parameters, including laser power, scanning speed, absorptivity, spot diameter, powder feed rate, and powder efficiency. The output vector represents the resulting melt pool geometry in terms of width, depth, and height. All input and output variables are normalized using a z-score transformation to ensure balanced learning across different feature scales. To represent systematic differences between simulation derived and experimental data, a binary indicator $IS_{exp} \in \{0,1\}$ is included, where $IS_{exp} = 0$ denotes simulation data and $IS_{exp} = 1$ experimental data, enabling the model to account for domain-specific deviations.

Model performance is evaluated using the coefficient of determination (R^2) and the mean absolute error (MAE). Once trained, the ANN serves as a computationally efficient surrogate model. This significantly reduces the need for computationally expensive FEM simulations during process design.

To enable geometry-driven process parameter selection, the trained forward ANN is embedded into an inverse optimization framework, where the surrogate model is iteratively queried to identify parameter sets that reproduce a desired target geometry, as illustrated in Figure 2.

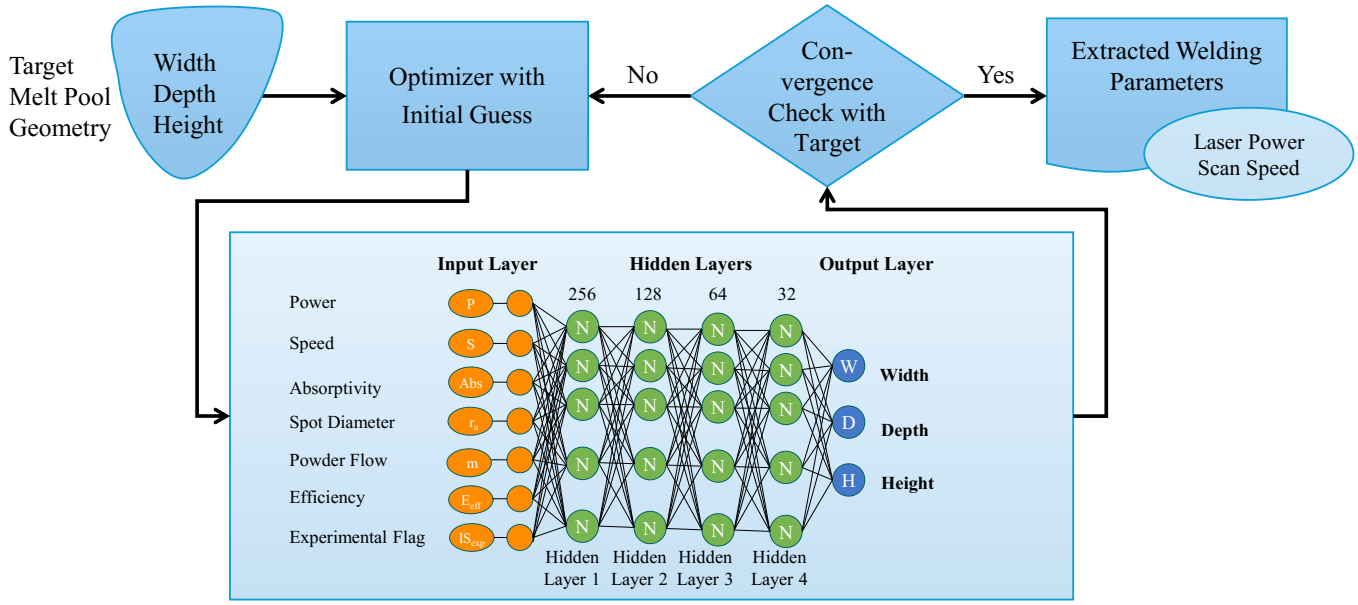

Figure 2: Schematic representation of the optimization framework developed for geometry-driven process parameter selection

The optimization starts from an initial guess within a predefined process window, where parameter bounds are set based on physically feasible ranges from the calibration study. An initial population of candidate parameter sets is generated via stochastic sampling and iteratively evolved by the optimizer. The resulting melt pool geometry is evaluated using the ANN surrogate model and

compared to the target geometry, with the population updated until the deviation is minimized. The final solution represents a physically consistent set of process parameters to achieve the desired melt pool geometry.

4 Results and Discussion

The following sections present the main results of this study with respect to the proposed framework for geometry-driven process parameter selection. The evaluation focuses on four key aspects: the acceleration of FEM-based data generation, the predictive accuracy of the surrogate model, the capability of the inverse optimization for geometry-based parameter prediction, and the experimental validation of the predicted parameters, including the realization of variable wall thickness.

4.1 Acceleration of FEM-Based Data Generation

A central contribution of this work is the significant improvement in computational efficiency of the FEM model of the melt pool formation through workflow automation and process-level parallelization. Through parallel execution of multiple simulation instances and optimization of the numerical workflow, the total runtime for approximately 50 parameter sets was reduced to approximately 8–10 h from around 150h.

This corresponds to an overall speedup factor of approximately 20–25, while maintaining the physical fidelity of the model. The improved efficiency enabled the systematic evaluation of more than 2,000 parameter combinations within a feasible time frame, which would not have been practical using the initial simulation setup. In addition, the integration of extended physical effects, such as powder shielding, further improved the consistency of the simulation results without increasing computational costs significantly.

4.2 Surrogate Model Accuracy for Melt Pool Geometry Prediction

Based on the dataset generated, a surrogate modeling framework was established to approximate the relationship between process parameters and melt pool geometry. The predictive performance of the trained ANN is evaluated on an unseen test dataset.

Figure 3a shows the training history of the selected model, where the loss decreases rapidly during the initial epochs and converges towards a stable plateau after approximately 200 epochs without divergence, indicating stable training behavior and effective regularization.

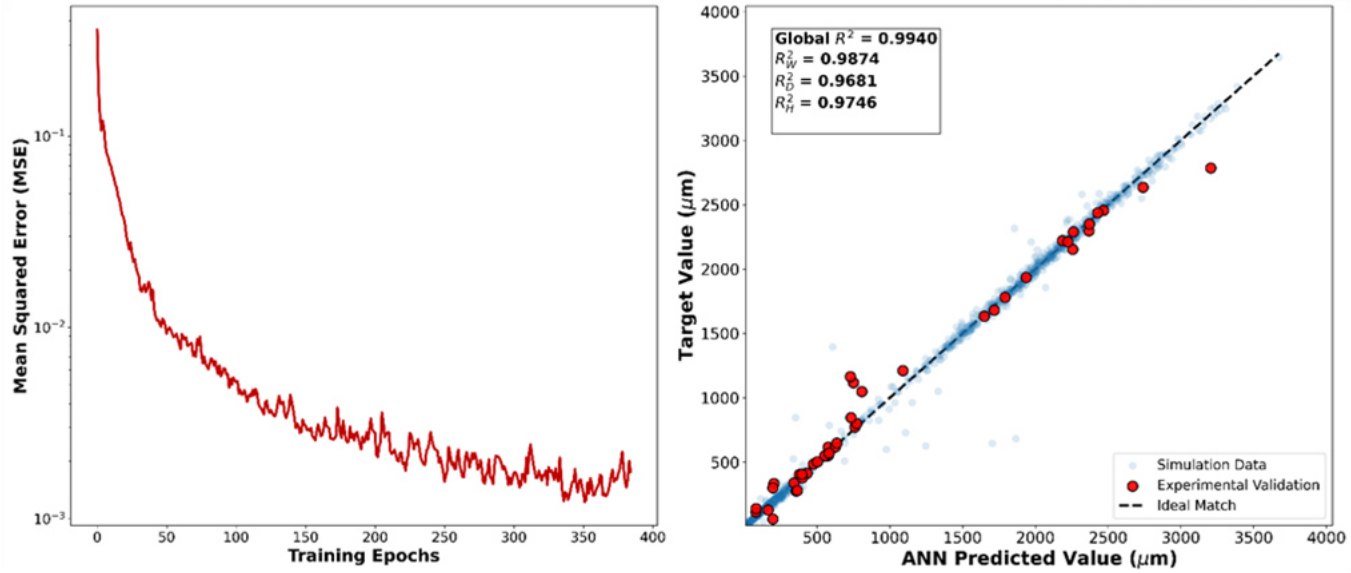

Figure 3: (a) Loss curve during training of the retained MLP (b) Combined parity plot showing predicted vs reference values

The predictive performance is illustrated in the combined parity plot in Figure 3b, showing the agreement between predicted and reference values for the summarized collection of melt pool geometries (width, depth, and height). The model achieves an overall coefficient of determination of $R^2 = 0.994$, demonstrating that the surrogate captures the dominant process relationships across the investigated parameter range. This behavior suggests that the applied normalization and regularization strategy effectively limits overfitting, which has been identified as a frequent challenge in deep-learning-based DED models [10].

A more detailed evaluation of the single melt pool predictions is summarized in Table 1. The model achieves R^2 values of 0.9681 for depth, 0.9874 for width, and 0.9746 for height, with corresponding mean absolute errors of 10.4 µm, 27.9 µm, and 48.7 µm. Over 93 % of all predictions lie within the ±100 µm tolerance band defined by the experimental measurement uncertainty. These values are comparable to, and slightly higher than, the maximum $R^2 = 0.975$ reported by Sarparast for a combined FEM–ANN morphology prediction framework et al. (2025) [27].

Table 1: The prediction metrics for each melt pool dimension.

Target	R^2	MAE(µm)	% ±100	Max |Resid| (µm)
Depth	0.9681	10.4	**98.9 %**	195
Width	0.9874	27.9	**96.5 %**	756
Height	0.9746	48.7	**93.3 %**	1 202

In summary the highest prediction accuracy is observed for melt pool depth. Melt pool width is also predicted reliably, while larger deviations are observed for melt pool height. This difference arises from the underlying formation mechanisms. Depth and width are mainly governed by thermal input and therefore show a more stable dependency on the process parameters. In contrast, track height is strongly influenced by the effective mass input into the melt pool, which introduces additional variability and makes accurate prediction more challenging. This includes not only the nominal powder mass flow rate but also the interaction between powder particles, melt pool

dynamics, and gas flow conditions. These effects introduce additional variability, which is only partially captured in the available training of FEM data. As a result, the relationship between process parameters and track height exhibits increased complexity and variability, leading to reduced prediction accuracy compared to depth and width.

Residual analysis confirms that the prediction errors are centred around zero with no systematic bias, indicating good generalization across the investigated geometry range. Overall, the achieved accuracy demonstrates that the surrogate model provides a reliable forward approximation of the process and is sufficiently accurate for use in inverse parameter optimization.

4.3 Inverse Optimization Results

The capability of the proposed framework to determine process parameters for predefined target geometries is evaluated using the inverse optimization approach.

Representative results for low, medium, and high-power conditions are summarized in Table 2. For each predefined target geometry, the inverse optimization determines a corresponding set of process parameters using the inverse ANN surrogate model. The resulting parameter sets are subsequently used to predict the melt pool geometry, and these predictions are compared with FEM simulations and experimental measurements.

Across all investigated cases, the predicted melt pool width shows small deviations, typically within +1–2 % compared to experimental results. This accuracy is comparable to the AIDED framework proposed by Shang et al. (2025) [26], who reported relative errors of 1.75 % for track width and 12.04 % for height during parameter recovery. The melt pool depth exhibits moderate deviations, particularly in the low-power regime, where small variations in energy input have a strong influence on penetration behavior. The largest deviations are observed for melt pool height, with errors up to approximately 30–40 %, reflecting the known sensitivity of reinforcement to powder-related effects.

Despite these deviations, the predicted geometries follow the expected trends across the parameter range investigated. Furthermore, all optimized parameter sets remain within the physically consistent operating window defined by the calibration study, indicating that the inverse optimization produces feasible and stable solutions.

Table 2: Inverse Optimization Results

Parameter	Case 1 (Low power)	Case 2 (Mid power)	Case 3 (High power)
Target (W/D/H)	1800/150/600	2000/300/800	2500/450/800
Power (W)	1000	1587.6	2074
Speed (mm/s)	23.83	33.33	26.67
Absorptivity (%)	50	50	50
Powder efficiency (%)	60	60	70
Predicted (W/D/H)	1698/126/818.2	2075/289.6/980	2444.8/490/819.2

Experimental Power (W)	1000	1600	2000
Experimental Speed (mm/s)	23.23	33.33	26.67
Experimental (W/D/H)	1673/150/733	2051/252/537	2393/498/636
Error Width (%)	+1.5	+1.2	+2.2
Error Depth (%)	-16.0	+14.9	-1.6
Error Height (%)	+11.6	+42.5	+28.8

4.4 Experimental Validation and Demonstration of Variable Wall Thickness

To validate the practical applicability of the proposed framework, the predicted process parameters are transferred to single-track deposition experiments. Figure 4 shows a representative single-track experiment, where the track width is continuously varied over a length of 36 mm while maintaining an approximately constant track height of about 200 µm. The profilometry data demonstrates a deviation of approximately 26 µm, corresponding to a relative error below 13%, while the track width is adjusted over a wide range. Within this configuration, a controllable width range from 0.9 mm to 1.95 mm is achieved, corresponding to an adjustment factor of 2.2. This confirms that width and height can be decoupled to a significant extent by appropriate parameter selection.

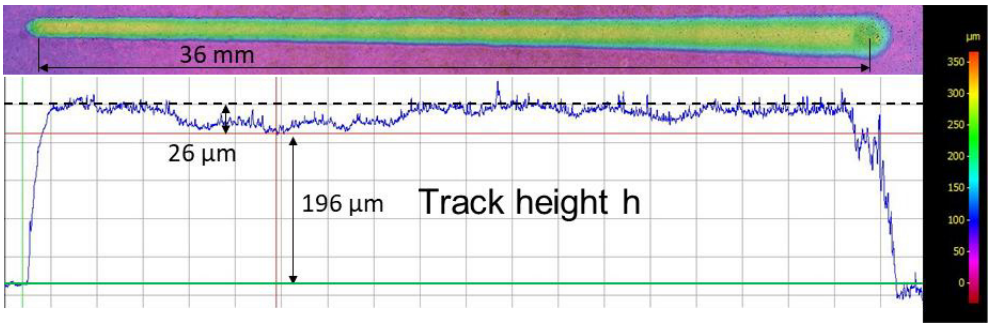

Figure 4: Profilometry of a melt track with variable width (between 1mm to 3mm) and constant track height (error <13%)

Beyond this representative example, additional validation experiments were conducted at different height levels and process conditions. For a second parameter set, a width range from 1914 µm to 2500 µm is obtained at approximately 500 µm track height, corresponding to a factor of 1.31. At a higher track height of approximately 900 µm, the adjustable width range increases to 1696 µm to 2772 µm, corresponding to a factor of 1.63.

These results demonstrate that, in contrast to conventional parameter selection, where the resulting geometry is largely determined by a fixed process equilibrium, the proposed framework enables a targeted and reproducible adjustment of track width at approximately constant track height. Across all investigated configurations, the achievable degree of geometric controllability is significantly increased, with an improvement factor of up to 2.2 in terms of targeted dimensional adjustment.

Although deviations remain, particularly for melt pool height due to variations in powder delivery and local process conditions, the overall geometric trends are reproduced reliably. These findings confirm that the proposed framework provides a viable basis for geometry-driven process control

and represents a key step towards adaptive toolpath strategies for variable wall thickness manufacturing in LMD.

5 Summary

This work presents a data-driven framework for geometry-based process parameter selection in Laser Metal Deposition (LMD), enabling the controlled variation of track geometry and the realization of variable wall thickness. By combining an improved FEM-based simulation workflow with process-level parallelization, a large and consistent dataset was generated with a computational speedup of approximately 20–25. Based on this dataset, an artificial neural network was trained to predict melt pool geometry from process parameters with high accuracy, achieving R^2 values up to 0.99 and predictions largely within the experimental tolerance of ±100 µm.

The trained model was further integrated into an inverse optimization framework, allowing the determination of process parameters for predefined target geometries. The results show good agreement between predicted, simulated, and experimental geometries, particularly for melt pool width. Experimental validation confirms that the predicted parameters can be transferred to real process conditions, enabling controlled variation of track width at approximately constant track height. This results in a significant improvement in dimensional controllability, with an adjustable width range corresponding to a factor of up to 2.2.

Despite these results, limitations remain, particularly regarding the reduced prediction accuracy for melt pool height due to the influence of powder-related effects and local process variations, as well as the restriction to single-track validation. Future work will focus on extending the experimental dataset, improving the representation of material deposition effects, and transferring the approach to multi-layer and geometry-dependent process control. For application to more complex geometries, layer-to-layer interactions, heat accumulation, and geometry-dependent process variations must be considered, along with integration into toolpath planning strategies. In addition, automated acquisition of track geometry is required to further reduce the effort for data generation and increase model versatility.

Acknowledgements

All presented investigations were conducted in the context of the Collaborative Research Centre SFB1120 "Precision Melt Engineering" at RWTH Aachen University and funded by the German Research Foundation (DFG). For the sponsorship and the support, we wish to express our sincere gratitude.

Conflict of Interest

The author declares no conflict of interest.

Data Availability Statement

The data that support the findings of this study are available at http://hdl.handle.net/21.11102/56ea1ed7-9bca-4912-930c-fcd08b86c671 upon request.

References

[1] A. Gasser, G. Backes, I. Kelbassa, A. Weisheit, K. Wissenbach, Laser Metal Deposition (LMD) and Selective Laser Melting (SLM) in Turbo-Engine Applications, LTJ 7 (2010) 58–63. doi:10.1002/latj.201090029.

[2] D.-G. Ahn, Directed Energy Deposition (DED) Process: State of the Art, Int. J. of Precis. Eng. and Manuf.-Green Tech. 8 (2021) 703–742. doi:10.1007/s40684-020-00302-7.

[3] A. Dass, A. Moridi, State of the Art in Directed Energy Deposition: From Additive Manufacturing to Materials Design, Coatings 9 (2019) 418. doi:10.3390/coatings9070418.

[4] Y.-Y. Chang, J.-R. Qiu, Y.-X. Chen, S.-J. Hwang, Research on deposition toolpath planning and laser head Z-axis rising height setting for directed energy deposition, Optics & Laser Technology 161 (2023) 109198. doi:10.1016/j.optlastec.2023.109198.

[5] J. Jiang, Y. Ma, Path Planning Strategies to Optimize Accuracy, Quality, Build Time and Material Use in AM: A Review, Micromachines (Basel) 11 (2020). doi:10.3390/mi11070633.

[6] M.-N. Bold, N. Pirch, S. Ziegler, J.H. Schleifenbaum, Evaluation of Offline Path Planning for Laser Metal Deposition on Freeform Surfaces, in: Lasers in Manufacturing, München, 2019.

[7] M. Gihr, A. Rashid, S.N. Melkote, Bead geometry prediction and optimization for corner structures in directed energy deposition using machine learning, Additive Manufacturing 84 (2024) 104080. doi:10.1016/j.addma.2024.104080.

[8] M. Perani, S. Baraldo, M. Decker, A. Vandone, A. Valente, B. Paoli, Track geometry prediction for Laser Metal Deposition based on on-line artificial vision and deep neural networks, Robotics and Computer-Integrated Manufacturing 79 (2023) 102445. doi:10.1016/j.rcim.2022.102445.

[9] D. Knüttel, S. Baraldo, A. Valente, F. Bleicher, K. Wegener, E. Carpanzano, Machine learning based track height prediction for complex tool paths in direct metal deposition, CIRP Annals 71 (2022) 193–196. doi:10.1016/j.cirp.2022.03.032.

[10] D.W. Rosen, X. Liu, Selected applications of artificial intelligence and machine learning in metal additive manufacturing, Weld World (2026). doi:10.1007/s40194-026-02335-z.

[11] F. Hermann, B. Chen, G. Ghasemi, V. Stegmaier, T. Ackermann, P. Reimann, S. Vogt, T. Graf, M. Weyrich, A Digital Twin Approach for the Prediction of the Geometry of Single Tracks Produced by Laser Metal Deposition, Procedia CIRP 107 (2022) 83–88. doi:10.1016/j.procir.2022.04.014.

[12] J. Zielinski, A holistic approach to understand laser additive manufacturing from melt pool to microstructure. Dissertation, 2022.

[13] J. Zielinski, H. Kruse, M.-N. Bold, G. Boussinot, M. Apel, J.H. Schleifenbaum, Melt Pool Formation and Out-of-Equilibrium Solidification During the Laser Metal Deposition Process (2021) 113–122. doi:10.1007/978-3-030-70332-5_11.

[14] N. Pirch, S. Linnenbrink, A. Gasser, K. Wissenbach, R. Poprawe, 2017. Analysis of track formation during laser metal deposition. Journal of Laser Applications 29, 022506. doi:10.2351/1.4983231.

[15] N. Pirch, M. Niessen, S. Linnenbrink, T. Schopphoven, A. Gasser, R. Poprawe, C. Schöler, D. Arntz, W. Schulz, 2018. Temperature field and residual stress distribution for laser metal deposition. Journal of Laser Applications 30, 032503. doi:10.2351/1.5040634.

[16] N. Pirch, H. Schleifenbaum, S. Linnenbrink, A. Gasser, R. Poprawe, M. Niessen, Influence of process strategy on distortion and residual stresses for the powder based laser metal deposition process, Materialwissenschaft Werkst 48 (2017) 1304–1313. doi:10.1002/mawe.201700169.

[17] M.-N. Bold, S. Linnenbrink, N. Pirch, A. Gasser, J. Mund, J.H. Schleifenbaum, Powder based laser material deposition on edges, Journal of Laser Applications 32 (2020) 32001. doi:10.2351/7.0000095.

[18] N. Pirch, S. Linnenbrink, A. Gasser, H. Schleifenbaum, Laser-aided directed energy deposition of metal powder along edges, International Journal of Heat and Mass Transfer 143 (2019) 118464. doi:10.1016/j.ijheatmasstransfer.2019.118464.

[19] M.-N. Bold, S. Ziegler, J. Zielinski, J.H. Schleifenbaum, Study Of Laser Metal Deposition Of In718 On Inclined Planes: Influence Of Inclination On Height And Width Of Deposited Material, in: Metal Additive Manufacturing Conference 2019, Wien, Austria, 2019.

[20] S. Ye, S. Benito, A. Berger, S. Weber, Development of a 3D multi-scale PBF-LB/M temperature history FEM simulation model, Int J Adv Manuf Technol (2025). doi:10.1007/s00170-025-16895-9.

[21] H. Qi, J. Mazumder, H. Ki, 2006. Numerical simulation of heat transfer and fluid flow in coaxial laser cladding process for direct metal deposition. Journal of Applied Physics 100, 024903. doi:10.1063/1.2209807.

[22] S. Saha, O.L. Kafka, Y. Lu, C. Yu, W.K. Liu, Microscale Structure to Property Prediction for Additively Manufactured IN625 through Advanced Material Model Parameter Identification, Integr. Mater. Manuf. Innov. 10 (2021). doi:10.1007/s40192-021-00208-5.
[23] D.R. Feenstra, A. Molotnikov, N. Birbilis, Utilisation of artificial neural networks to rationalise processing windows in directed energy deposition applications, Materials & Design 198 (2021) 109342. doi:10.1016/j.matdes.2020.109342.
[24] F. Zafar, O. Emadinia, J. Conceição, M. Vieira, A. Reis, A Review on Direct Laser Deposition of Inconel 625 and Inconel 625-Based Composites—Challenges and Prospects, Metals 13 (2023) 787. doi:10.3390/met13040787.
[25] J.P. Rodrigues, R.S. Thanumoorthy, S.K. Manjhi, P. Sekar, D.A. Perumal, S. Bontha, A. Balan, Hybrid additive manufacturing of ER70S6 steel and Inconel 625, Materials Today Communications 37 (2023) 106977. doi:10.1016/j.mtcomm.2023.106977.
[26] X. Shang, A. Talbot, E. Li, H. Wen, T. Lyu, J. Zhang, Y. Zou, Accurate inverse process optimization framework in laser directed energy deposition, Additive Manufacturing 102 (2025) 104736. doi:10.1016/j.addma.2025.104736.

Date: 31.03.2026

Title: Use of low transformation temperature alloys to reduce distortion in austenitic CrNi steels and insight into corrosive behavior

Author: Maximilian Gamerdinger[1]

Authors: Karthik Ravi Krishna Murthy[1], Simon Olschok[1], Uwe Reisgen[1]

[1]RWTH Aachen University, Welding and Joining Institute, Pontstr. 49, 52062, AACHEN, GERMANY

Corresponding author: E-mail: max.gamerdinger@isf.rwth-aachen.de, ORCID: 0000-0003-3992-6559

Abstract

Austenitic CrNi steels are increasingly being used in modern rail vehicle construction due to their high specific strength and good corrosion resistance. However, significant distortion of the welds can occur, particularly in long or flat sections of the outer shell of the railcar. It has already been demonstrated on several occasions that welding distortion can be effectively reduced by introducing a low transformation temperature (LTT) effect. Nevertheless, a decrease in the alloy content of the weld may lead to diminished corrosion resistance. To evaluate the corrosion behavior, various LTT alloys were welded with a laser beam using an in-situ alloying process and then tested for intergranular corrosion and in a salt spray test. Finally, corrosive behavior is compared with the resulting welding distortion, and the highest distortion reduction and the lowest corrosive attack were achieved with alloys with a Cr content between 15.7 % and 16.4 %.

Keywords

Laser beam welding, low transformation temperature (LTT) effect, corrosive behavior

1 Introduction

Modern rail cars are increasingly being built using austenitic, corrosion-resistant chromium-nickel steels. Steel grades such as 1.4318/AISI 301LN are favoured for their excellent mechanical properties and corrosion resistance. Due to the low carbon content (<0.03 wt.%) and increased nitrogen content (~0.15 wt.%), this material exhibits no significant signs of intergranular corrosion (IGC), even following sensitization [1]. However, a disadvantage of welding austenitic steels compared to mild steels is that they have a higher coefficient of thermal expansion ($\alpha_{austenite} \sim 2\alpha_{ferrite}$) and lower thermal conductivity ($\lambda_{ferrite} \sim 3.3\lambda_{austenite}$) [2]. Consequently, higher shrinkage stresses build up during welding, which are relieved through plastic deformation once the temperature-dependent yield strength is exceeded. After cooling, this results in increased welding distortion [3]. The low-transformation-temperature (LTT) effect can be used to control residual stress and welding distortion. In this approach, adjusting the chemical composition induces

a martensitic phase transformation at a low transformation temperature within the weld seam. The shrinkage stresses (tensile stresses) that build up during cooling are superimposed by transformation stresses (compressive stresses), which result from the restricted volume expansion of the austenite-martensite phase transformation [4]. Thus, both the resulting residual stresses and the weld distortion are effectively reduced [5, 6]. To enable an LTT effect in austenitic steel, the alloy content must be reduced using low-alloy filler wires. This is accompanied by an increase in C and Mn content, as well as a reduction in Cr, Ni and N, which alters corrosion resistance. In addition to being susceptible to intergranular corrosion (IGC), corrosion-resistant steels in chloride-containing environments may also develop pitting or crevice corrosion due to the local destruction of the passive layer [7]. Since the LTT effect is usually studied in combination with mild steel, there are no studies on the corrosion behavior of the alloys, but these are essential for industrial applications involving the LTT effect in austenitic CrNi steels.

2 Aim of the Investigation

The aim of the investigations presented here is to provide an initial insight into the corrosion behaviour of LTT alloys in 1.4318, and to compare this with their distortion reduction. For this purpose, various LTT alloys were produced using three different unalloyed and low-alloyed filler wires, as well as reference alloys using a matching filler wire. The distortion reduction of these alloys is compared, while their corrosion behavior regarding pitting corrosion, crevice corrosion and intergranular corrosion is investigated.

3 Materials and Experimental Details

In the welding trials, T-joints made of austenitic CrNi steel 1.4318 (X2CrNiN18 7/ ASTM 301LN), were welded, **Table 1**. The welded joints were executed as double-sided full-penetration welds both for the distortion and corrosion trails. The welding filler designated G19 9 (EN ISO 14343-A: G 19 9 L Si) is utilized as the standard welding filler for the base material, and the reference joints are welded from this. To produce alloys with an LTT effect, it is necessary to reduce the alloy content in the weld seam. For this purpose, three filler wires are used, an unalloyed G4Si1 (EN ISO 14341-A: G 4Si1) and two wire with low alloy content ER90S-B3 (DIN EN ISO 21952-B W 2C1M) as well as ER80S-B8 (DIN EN ISO 21952-A G CrMo9).
A Trumpf TruDisk 16002 with a wavelength of 1030 nm, an fiber diameter of 300 µm and optics from Kugler with an aspect ratio of 1:3 was utilized, resulting in a focus diameter of 900 µm. Since the filler wires had different diameters, the wire feed was adjusted based on the filling volume $FV = v_w * \pi d^2/4$ instead of the wire feed speed v_w. Six parameter variations for each filler wire were welded for the distortion trails and three for the corrosion trails, **Table 2**. Apart from the varying filling volumes, only the laser power was varied between the distortion trails and corrosion trails, while all other parameters were kept constant. The T-joints consist of a 2 mm flange plate and a 3 mm web plate, for the distortion trails each with a length of 250 mm and a width of 150 mm. The plates were connected with three tack welds on each side before welding, **Figure 1** a), c) and d).

Table 1: Chemical composition of base material and welding consumables measured by optical emission spectrometry (OES).

Materials	Diameter d [mm]	Chemical composition [wt.%]							
		Cr	Ni	Mo	Mn	Si	Fe	N	C
1.4318	-	17.70	6.39	0.073	1.19	0.42	73.6	0.155	0.034
G19 9	1.0	19.70	10.18	0.16	1.72	0.73	67.0	0.052	0.025
G4Si1	1.0	0.047	0.021	0.006	1.69	0.93	97.0	0.004	0.081
ER90S-B3	0.9	2.44	0.029	1.00	0.54	0.53	95.0	0.006	0.109
ER80S-B8	0.9	8.76	0.13	1.02	0.50	0.54	88.4	0.003	0.070

During the welding process, the development of welding distortion was measured in situ using two linear variable differential transformer (LVDT) sensors. Both LVDT sensors, LVDT1 and LVDT2, are located in the center of the sheets in the direction of welding and at a distance of ± 50 mm from the center of the sheet, perpendicular to the weld, **Figure 1** a) and c). After welding, the samples were unclamped and the resulting welding distortion was determined. Cross sections were then taken from the seams, which were used to measure the seam geometry, chemical composition and hardness.

Table 2: Welding parameter for distortion and corrosion trails

Trail	Wire feed speed 1.0 mm v_W [mm/min]	Wire feed speed 0.9 mm v_W [mm/min]	Filling volume [mm² x m/min] $FV = \frac{\pi d^2}{4} * v_F$	Laser power [W]	Welding angle (lateral) [°]	Welding speed [m/min]
Distortion	1.32	1.63	1.04	2240	30	1.5
	1.50	1.85	1.18			
	1.68	2.07	1.32			
	1.86	2.30	1.46			
	2.04	2.52	1.60			
	2.22	2.74	1.74			
Corro-sion	1.32	1.63	1.04	2560		
	1.68	2.07	1.32			
	2.22	2.74	1.74			

Further welding parameters:

Shielding gas flow Ar 4.6	[l/min]	20	Collimation length	[mm]	200
Fiber diameter	[µm]	300	Focus diameter	[µm]	900
Focus length	[mm]	600	Focus position	[mm]	0

For the corrosion tests, a 50 mm × 50 mm × 500 mm specimen was welded for each alloy and then cut into 70 mm long sections using a precision cutting machine. Two tests were conducted to evaluate corrosion behavior. The first was a salt spray test (NSS) in accordance with

DIN EN ISO 9227 [8], which was used to assess susceptibility to pitting corrosion. The second test, conducted in accordance with EN ISO 3651-2 [9], assessed susceptibility to intergranular corrosion using Method A (Strauss test). For the salt spray test, three typical surface conditions – as welded, brushed, and pickled – were examined. Brushing was performed using an austenitic steel brush until all heat tint was removed. Acid pickling was performed by immersion in a solution of 15 % nitric acid (HNO_3), 5 % hydrofluoric acid (HF), and water for 60 min [10]. The surface was then cleaned by rinsing with water. The salt spray test runs for 790 h in a corrosion test chamber. At a constant temperature of 35 °C, a 5 % NaCl solution with a pH between 6.5 and 7.2 is continuously sprayed. The volume of spray is defined by an average collection rate of 1.5 ml/h on a horizontal collection surface area of 80 cm². [8] In the Strauss test for intergranular corrosion, the welded specimens are examined without any further post-treatment. The standard specifies testing butt joints on sheet metal or pipes as test specimens, which are bent over a mandrel after the corrosion tests. For the alloys examined here, however, the test is performed on T-joints, eliminating the subsequent bending stress. For the test solution, 100 g of copper (II) sulfate pentahydrate ($CuSO_4 \cdot 5H_2O$) is dissolved in 700 ml of distilled water. Then 184 g (100 ml) of sulfuric acid (p20 = 1.84 g/ml) is added, and the volume is made up to 1,000 ml with distilled water. The samples are embedded in electrolytic copper in the form of chips at the bottom of the flask and boiled in the test solution for 24 h. Subsequently, the samples were examined for intergranular corrosion using scanning electron microscope (SEM). [9]

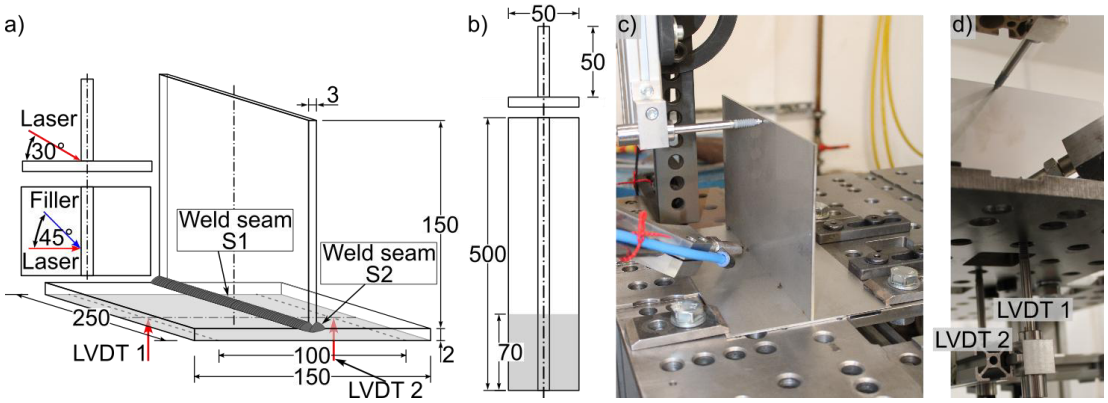

Figure 1: Component geometry of the distortion samples (a), sample geometry for corrosion testing (b), setup with clamping fixtures and LVDT positions (c and d).

4 Results and Discussion

Initially, cross-sections were used to examine the weld quality, hardness values and alloy content. Cross-sections of the distortion trails show that, as the filling volume increases, the weld head area increases and the penetration depth decreases, **Figure 2** a) to f). With the laser power of 2240 W used, a constant weld cross-sectional area of 6.96 ± 0.21 mm² is achieved. However, increasing the filling volume alters the ratio of molten filler wires to base material, represented by the seam ratio parameter, equation (1) and **Figure 2** j). Consequently, the seam ratio increases with an increase in filling volume, resulting in a higher proportion of filler wires in the weld and a weld with a more pronounced seam head. Furthermore, when the filling volume FV exceeds 1.46 mm² x m/min, the seam transition angle between the flange plate and the weld becomes very small (less than 90 °)

and there is almost no overlap between the two welds, **Figure 2** d) to f). To achieve a flatter transition angle and greater protection against an unwelded root gap, the laser power was increased to 2560 W for the corrosion tests, **Figure 2** g) to i). Increased laser power results in an increase in the seam cross-sectional area to 7.52 ± 0.5 mm², and with the same filling volume this leads to a reduced seam ratio compared to the distortion trails.

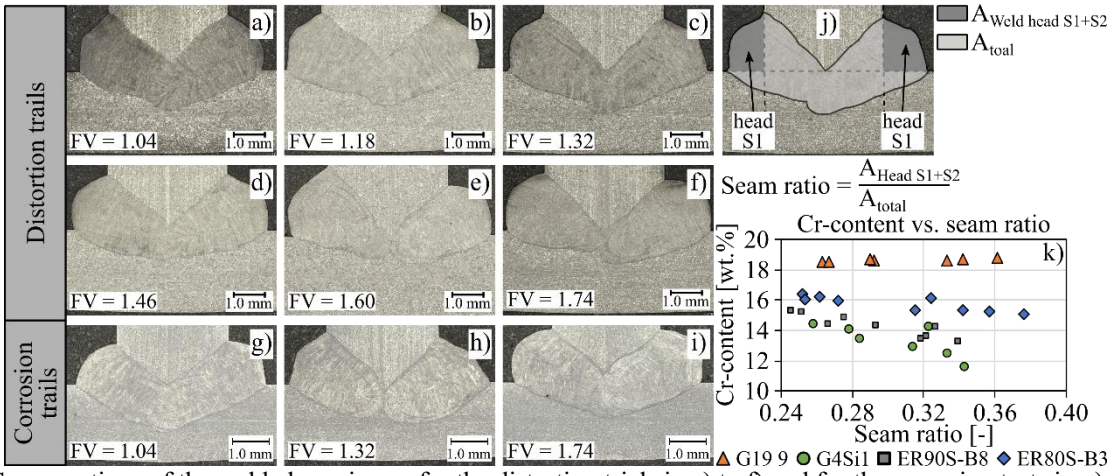

Figure 2: Cross-sections of the welded specimens for the distortion trials in a) to f) and for the corrosion tests in g) to i). Definition of the seam ratio in j), the relationship between alloy content and seam ratio, using chromium as an example in k).

The alloy content of the seams was determined using energy-dispersive X-ray spectroscopy (EDS), **Figure 2** k) and **Table 3**. For the reference series using G19 9 as the filler wire, the alloy content increases as the seam ratio increases, since the wire has a higher alloy content than the base material. For the three wires intended to generate the LTT effect in the weld, however, an increase in the seam ratio leads to a reduction in the alloy content. The Cr content ranged from 11.63 ± 1.21 wt.% (G4Si1, FV 1.74, seam ratio 0.34) to 16.24 ± 0.57 wt.% (ER80S-B8, FV 1.04, seam ratio 0.262).

$$Seam\ ratio\ [-] = \frac{A_{Weld\ head\ S1} + A_{Weld\ head\ S2}}{A_{total\ weld\ seam}} \quad (1)$$

$$Ms\ [°C] = 561 - 474 * \%C - 33 * \%Mn - 17 * (\%Ni + \%Cr) - 21 * \%Mo \quad (2)$$

$$PREN = \%Cr + 3.3 * \%Mo + 16 * \%N \quad (3)$$

The LTT effect is enabled by an increase in the martensite start temperature (Ms), which is caused by a reduced alloy content. To account for the effects of other important alloying elements on the LTT effect, such as C, Mo and Mn, the Ms temperature can be calculated using the empirical equation (2) from [11]. A comparison of the hardness values shows that the reference series with G19 9 is not hardened, regardless of the filling volume used and the resulting alloy content. In the welds, hardness is slightly reduced to 217 ± 11 HV1, while the base material has a hardness of 239 ± 13 HV1. For welds exhibiting the LTT effect, hardness values range from 337 HV1 to 414 HV1, **Figure 3** a). The highest hardness values occur at an Ms temperature of approximately 180 °C, decreasing as the Ms temperature drops. Based on the achieved hardness values, an LTT effect can be expected in all alloys containing G4Si1, ER90S-B3 and ER80S-B8.

Table 3: Chemical composition of the alloys measured using EDS

Trail	Wire	Filling volume [mm² x m/min]	Chemical composition [wt.%]						
			Cr	Ni	Mo	Mn	Si	C*	N*
Distortion	G19 9	1.04	18.49 ± 0.37	7.12 ± 0.38	0.44 ± 0.21	1.34 ± 0.25	0.54 ± 0.1	0.032*	0.128*
	G19 9	1.18	18.49 ± 0.8	7.1 ± 0.8	0.43 ± 0.39	1.32 ± 0.51	0.54 ± 0.21	0.032*	0.127*
	G19 9	1.32	18.58 ± 0.56	7.21 ± 0.62	0.34 ± 0.26	1.35 ± 0.36	0.55 ± 0.15	0.031*	0.125*
	G19 9	1.46	18.6 ± 0.8	7.24 ± 0.86	0.43 ± 0.39	1.39 ± 0.52	0.54 ± 0.21	0.031*	0.121*
	G19 9	1.60	18.7 ± 0.77	7.41 ± 0.81	0.47 ± 0.38	1.38 ± 0.47	0.55 ± 0.2	0.031*	0.12*
	G19 9	1.74	18.78 ± 0.72	7.45 ± 0.7	0.43 ± 0.33	1.39 ± 0.44	0.56 ± 0.19	0.031*	0.118*
	G4Si1	1.04	14.41 ± 0.77	4.99 ± 0.81	0.43 ± 0.38	1.19 ± 0.52	0.55 ± 0.23	0.051*	0.12*
	G4Si1	1.18	14.06 ± 1.13	4.97 ± 0.79	0.45 ± 0.4	1.22 ± 0.5	0.57 ± 0.23	0.055*	0.112*
	G4Si1	1.32	13.42 ± 0.96	5.03 ± 0.81	0.43 ± 0.38	1.23 ± 0.51	0.54 ± 0.22	0.055*	0.112*
	G4Si1	1.46	12.89 ± 1.11	4.78 ± 0.81	0.44 ± 0.4	1.25 ± 0.5	0.6 ± 0.24	0.056*	0.109*
	G4Si1	1.60	12.52 ± 1.19	4.18 ± 0.89	0.43 ± 0.37	1.2 ± 0.45	0.62 ± 0.22	0.06*	0.102*
	G4Si1	1.74	11.63 ± 1.21	4.05 ± 0.5	0.45 ± 0.25	1.21 ± 0.29	0.62 ± 0.12	0.059*	0.104*
	ER90S-B3	1.04	15.19 ± 1.02	5.05 ± 0.68	0.43 ± 0.3	1.25 ± 0.41	0.57 ± 0.18	0.046*	0.116*
	ER90S-B3	1.18	14.77 ± 0.8	4.95 ± 0.76	0.42 ± 0.38	1.26 ± 0.5	0.56 ± 0.21	0.047*	0.113*
	ER90S-B3	1.32	14.24 ± 1.15	4.76 ± 0.57	0.34 ± 0.27	1.27 ± 0.33	0.57 ± 0.14	0.047*	0.112*
	ER90S-B3	1.46	14.21 ± 1.17	4.56 ± 0.75	0.42 ± 0.38	1.29 ± 0.44	0.6 ± 0.21	0.049*	0.108*
	ER90S-B3	1.60	13.36 ± 0.93	4.38 ± 0.54	0.44 ± 0.25	1.28 ± 0.28	0.61 ± 0.12	0.05*	0.105*
	ER90S-B3	1.74	13.18 ± 0.94	4.09 ± 0.81	0.44 ± 0.4	1.34 ± 0.5	0.64 ± 0.22	0.05*	0.103*
	ER80S-B8	1.04	16.24 ± 0.65	5.05 ± 0.68	0.43 ± 0.3	1.25 ± 0.41	0.57 ± 0.18	0.046*	0.116*
	ER80S-B8	1.18	15.9 ± 0.83	4.95 ± 0.76	0.42 ± 0.38	1.26 ± 0.5	0.56 ± 0.21	0.047*	0.113*
	ER80S-B8	1.32	16.08 ± 0.96	4.76 ± 0.57	0.34 ± 0.27	1.27 ± 0.33	0.57 ± 0.14	0.047*	0.112*
	ER80S-B8	1.46	15.34 ± 0.79	4.56 ± 0.75	0.42 ± 0.38	1.29 ± 0.44	0.6 ± 0.21	0.049*	0.108*
	ER80S-B8	1.60	15.21 ± 1	4.38 ± 0.54	0.44 ± 0.25	1.28 ± 0.28	0.61 ± 0.12	0.05*	0.105*
	ER80S-B8	1.74	15.02 ± 0.91	4.09 ± 0.81	0.44 ± 0.4	1.34 ± 0.5	0.64 ± 0.22	0.05*	0.103*
Corrosion	G19 9	1.32	18.7 ± 0.54	5.19 ± 0.81	0.51 ± 0.43	1.08 ± 0.49	0.48 ± 0.22	0.052*	0.118*
	G4Si1	1.04	15.05 ± 0.88	5 ± 0.7	0.53 ± 0.34	1.07 ± 0.42	0.49 ± 0.18	0.055*	0.114*
	G4Si1	1.32	14.27 ± 0.79	4.81 ± 0.8	0.58 ± 0.43	1.04 ± 0.47	0.5 ± 0.19	0.056*	0.111*
	ER90S-B3	1.04	15.18 ± 0.95	4.8 ± 0.84	0.58 ± 0.42	1.02 ± 0.48	0.51 ± 0.21	0.058*	0.106*
	ER90S-B3	1.32	14.37 ± 0.84	4.52 ± 0.78	0.62 ± 0.47	0.99 ± 0.49	0.51 ± 0.21	0.058*	0.107*
	ER90S-B3	1.74	13.54 ± 0.54	4.38 ± 0.71	0.58 ± 0.44	0.99 ± 0.42	0.5 ± 0.2	0.059*	0.104*
	ER80S-B8	1.04	16.38 ± 0.81	4.8 ± 0.84	0.58 ± 0.42	1.02 ± 0.48	0.51 ± 0.21	0.058*	0.106*
	ER80S-B8	1.32	16.03 ± 0.6	4.52 ± 0.78	0.62 ± 0.47	0.99 ± 0.49	0.51 ± 0.21	0.058*	0.107*
	ER80S-B8	1.74	15.3 ± 0.94	4.38 ± 0.71	0.58 ± 0.44	0.99 ± 0.42	0.5 ± 0.2	0.059*	0.104*

$$*C\ (N)\ content\ [wt.\%] = m_{Filler} * C_{Filler} + m_{Base} * C_{Base}$$

$$m_{Filler} = \frac{A_{Head,S1} + A_{Head,S2}}{A_{total}}$$

$$m_{Base} = 1 - m_{Filler}$$

In the reference series with G19 9, the resulting weld distortion rises from 2.2 ° to 2.82 ° as the seam ratio rises, **Figure 2** b). This is due to the increasing volume of the weld heads, since the shrinking volume acts with maximum leverage in this case. Alloys exhibiting the LTT effect generally display the same behaviour. For G4Si1, distortion increases from a minimum of 1.02 ° to a maximum of 1.90 °, while for ER80S-B8 it increases from a minimum of 0.57 ° to a maximum of 1.40 °. However, compared to G19 9, there is a reduction in distortion depending on the alloy content respectively the Ms temperature. Thus, the smallest reduction in distortion is achieved with G4Si1 at the highest Ms temperature and the largest with ER80S-B8 at the lowest. Alloys containing ER90S-B3 fall between G4Si1 and ER80S-B8 in terms of distortion and alloy content. On average, distortion reduction is 36 % for G4Si1 and 54 % for ER80S-B8 compared to the reference with G19 9.

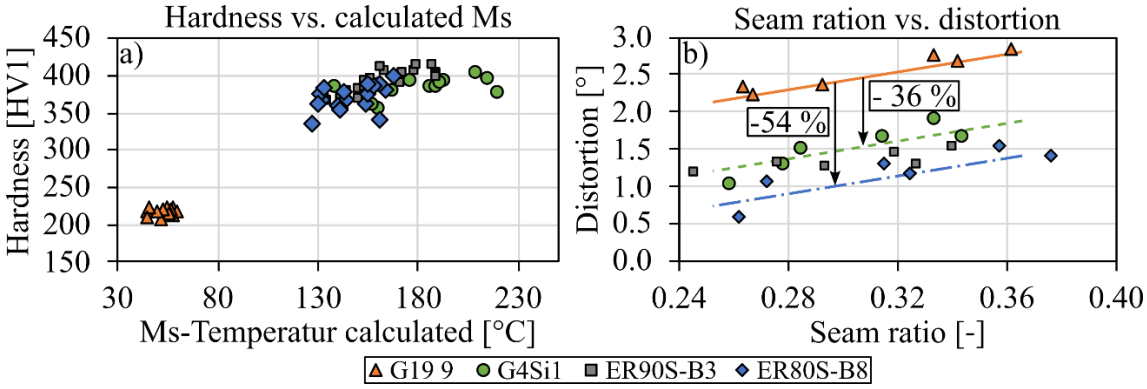

Figure 3: Effect of the achieved Ms-temperature on the hardness of the seams (a), effect of seam ratio on the resulting distortion angle (b).

Both pitting and crevice corrosion are localised forms of corrosion that occur particularly in chloride-containing environments [12]. While their initiation mechanisms differ – pitting corrosion typically results from a local breakdown of the passive film [13], whereas crevice corrosion is driven by restricted mass transport and oxygen depletion within confined geometries [14] – both processes share a common propagation mechanism.

Following the local destruction of the passive layer, a small anodic area forms within the pit or crevice, while the surrounding, still-passivated surface acts as a large cathode, leading to high local current densities and rapid metal dissolution [12]. The process is further accelerated by the accumulation of metal ions, local acidification, and chloride enrichment within the occluded region, which inhibit repassivation and promote continued corrosion [15]. The weld seams are subject to a salt spray test to determine their susceptibility to pitting and crevice corrosion. However, due to the similarity of these two corrosion phenomena, it is not always possible to distinguish between them.

After exposure in the salt spray test, the resulting corrosion attack is evaluated on cross-sections of the specimens. As-welded specimens exhibit the greatest number and depth of cavities, reaching up to 2.2 mm, **Figure 4** a). Post-treatment of the surface by brushing or pickling reduces the depth and number of cavities. In addition to the deep cavities, uniform corrosion also occurs at the weld seams, as represented by the median. The respective results are 15 µm for as-welded, 13 µm for

brushed and 17 µm for pickled specimens. After 790 h in the salt spray chamber, hardly any corrosion products were visible on the pickled welds compared to the other variants. Therefore, the increased roughness of the pickled surface is likely due to excessive pickling, **Figure 4** b) to g).

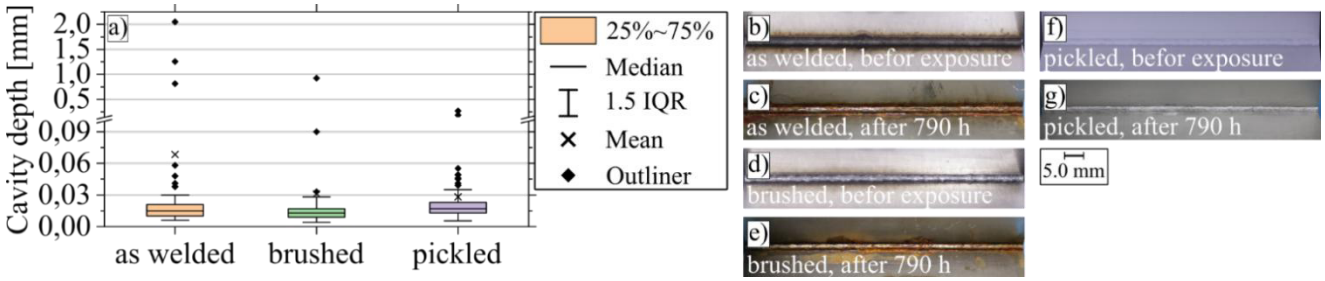

Figure 4: Effect of surface post-treatment on the depth of the resulting cavities in a). Examples of the three surface conditions before and after exposure in the salt spray chamber using the ER90S-B3 alloy with FV 1.04 mm² x m/min in b) to g).

The Pitting Resistance Equivalent Number (PREN), calculated using equation (3), is frequently used as a benchmark for a material's resistance to pitting and crevice corrosion [16]. At PREN values of up to 18.27, severe corrosion is observed, with cavity depths of up to 2.2 mm, **Figure 5** e). The maximum cavity depth of 2.2 mm was measured on the as-welded specimen with ER90S-B3 and FV1.04, with almost the entire weld being destroyed. As PREN increases, the maximum cavity depth decreases to 0.09 mm for PREN >18.27, **Figure 5** c), d) and f). Additionally, the appearance of the corrosion attack changes. While distinct cavities form at low PREN values, high PREN values tend to result in general surface roughening, with no local, deep corrosion pits present.

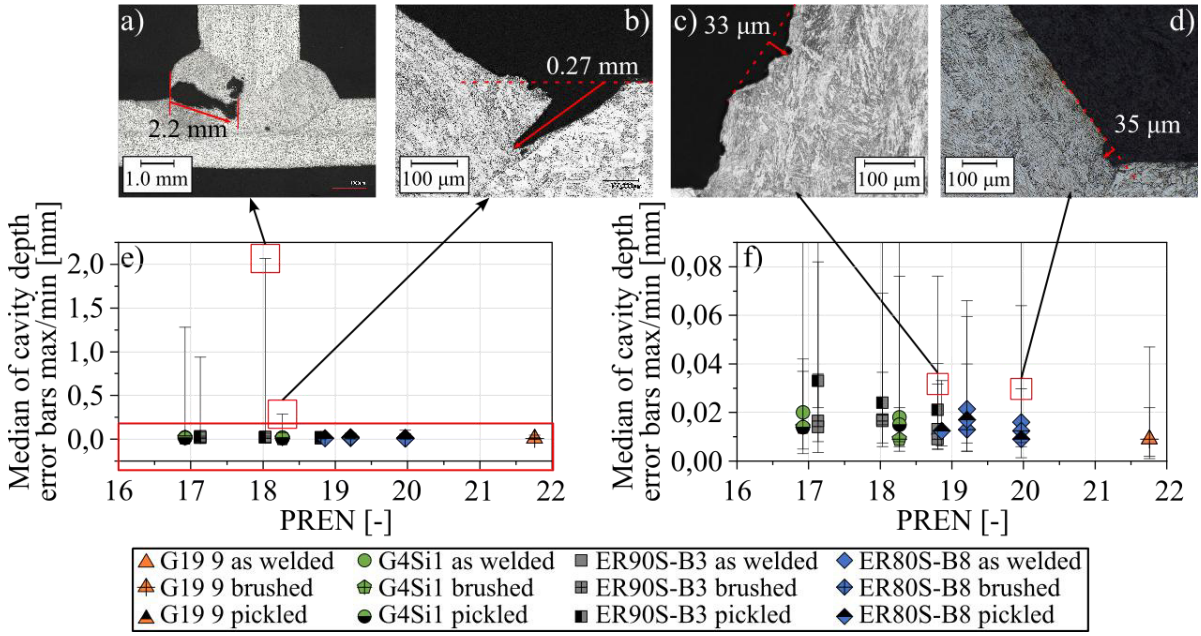

Figure 5: Results after 790 hours of exposure in the salt spray chamber. Cross-sections showing the extent of corrosion in a) through d). Summary of the results based on the median cavity depth, with the maximum and minimum cavity depths used as error bars in e) and f).

In addition to the salt spray test, susceptibility to intergranular corrosion was investigated using the Strauss test. With the exception of three specimens, the resulting IGC crack length is less than

60 µm, **Figure 6** c), d) and g). As with the salt spray test, the crack length decreases with increasing chromium content. At a chromium content of over 16 wt.%, the maximum crack length is 20 µm, **Figure 6** d) and g). No IGC cracks were detected in the reference sample with 18.7 wt.% Cr. For the three outliers, crack lengths of up to 650 µm were observed, with all cracks occurring at the fusion line, **Figure 6** a), b) and f). These cracks occur in the specimen with higher filling volumes: ER80S-B8-FV1.74 (650 µm), G4Si1-FV1.32 (260 µm) and ER90S-B3-FV1.74 (150 µm). Inhomogeneities in the alloy composition can particularly occur at high filling volumes, which is especially evident at the fusion line where partially molten and solid phases coexist, **Figure 6** e) and h). Consequently, the Cr content can vary significantly in these areas, potentially serving as an initiation point for IGC.

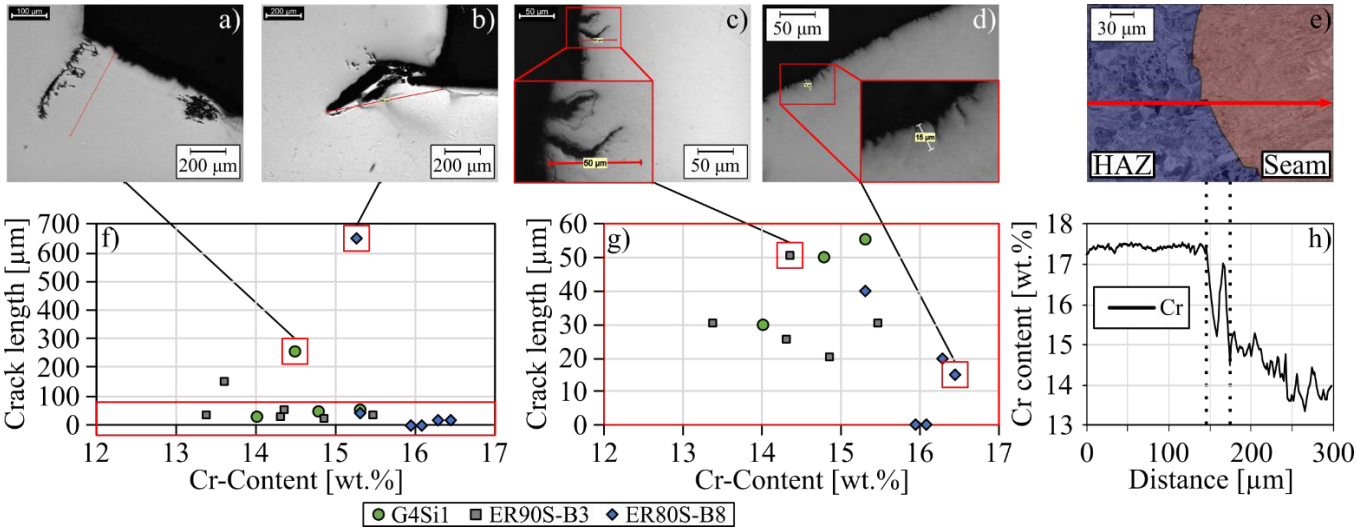

Figure 6: IGC crack length and SEM images in a)–d) and f)–g). Cr content at the fusion line in e) and h)

5 Summary

Both corrosion tests revealed that susceptibility to corrosion decreases as the alloy content (PREN and/or Cr) increases. However, corrosion was still observed in the alloys with the highest alloy content in both the salt spray and Strauss tests. No cavities were detected in the salt spray test starting at a PREN value of 18.27; only general surface roughening with a maximum depth of 90 µm was observed. In the Strauss test, deep intergranular corrosion (IGC) cracks were only found at the weld transition, which is attributable to inhomogeneity in the chemical composition. All other samples exhibited IGC cracks with a depth of less than 60 µm, with the depth of the cracks decreasing as the Cr content increased. Regarding component distortion, it was found that a small filling volume leads to lower distortion values. If an LTT effect is induced in the weld by reducing the alloy content, distortion is always reduced compared to the reference alloy with the same seam ratio. For alloys with the highest alloy content due to a small filling volume (Ms ~130 °C, Cr ~16.4 wt.%), an average distortion reduction of 54 % is achieved. Therefore, it is evident that a high alloy content with a small filling volume is advantageous in terms of corrosion and distortion. Ultimately, a decision must be made on a case-by-case basis as to whether the corrosion phenomena, which still occur even at high alloy contents, outweigh the advantage of reduced distortion. When combined with additional corrosion protection measures, which are frequently

used for finished parts, the reduction in distortion could be more beneficial than slightly lower corrosion resistance.

Acknowledgements

The presented investigations were carried out at RWTH Aachen University within the framework of the Collaborative Research Centre SFB1120-236616214 “Bauteilpräzision durch Beherrschung von Schmelze und Erstarrung in Produktionsprozessen” and funded by the Deutsche Forschungsgemeinschaft e.V. (DFG, German Research Foundation). The sponsorship and support is gratefully acknowledged.

Conflict of Interest

The author declares no conflict of interest.

Data Availability Statement

The data that support the findings of this study are available at http://hdl.handle.net/21.11102/042ce519-24d5-47d5-94c4-4acf1385d14f upon request.

References

[1] S. Ningshen and U. Kamachi Mudali, "Pitting and Intergranular Corrosion Resistance of AISI Type 301LN Stainless Steels," *J. of Materi Eng and Perform*, vol. 19, no. 2, pp. 274–281, 2010.
[2] G. Schulze, *Die Metallurgie des Schweissens: Eisenwerkstoffe - nichteisenmetallische Werkstoffe,* 4th ed. Heidelberg, New York: Springer, 2010.
[3] T. Nitschke-Pagel and H. Wohlfahrt, "Residual Stresses in Welded Joints – Sources and Consequences," *MSF*, 404-407, pp. 215–226, 2002.
[4] A. Kromm, J. Dixneit, and T. Kannengiesser, "Residual stress engineering by low transformation temperature alloys—state of the art and recent developments," *Weld World*, vol. 58, no. 5, pp. 729–741, 2014.
[5] M. Gamerdinger, S. Olschok, and U. Reisgen, "Reduction of distortion during laser beam welding by applying an in situ alloyed LTT effect and considering influencing factors," *Procedia CIRP*, vol. 124, pp. 409–412, 2024.
[6] F. Akyel, M. Gamerdinger, S. Olschok, U. Reisgen, A. Schwedt, and J. Mayer, "Adjustment of chemical composition with dissimilar filler wire in 1.4301 austenitic stainless steel to influence residual stress in laser beam welds," *Journal of Advanced Joining Processes*, vol. 5, p. 100081, 2022.
[7] J. C. Lippold, *Welding Metallurgy and Weldability*. Hoboken, New Jersey: John Wiley & Sons, Inc., 2015.
[8] *Corrosion tests in artificial atmospheres - Salt spray tests (ISO 9227:2022 + Amd 1:2024);*, DIN EN ISO 9227, DIN Deutsches Institut für Normung e. V, Berlin, Oct. 2024.
[9] *Determination of resistance to intergranular corrosion of stainless steels - Part 2: Ferritic, austenitic and ferritic-austenitic (duplex) stainless steels - Corrosion test in media containing sulfuric acid: ISO 3651-2*, EN ISO 3651-2, European Committee for Standardization, Brüssel, Mar. 1998.
[10] *Standard Practice for Cleaning, Descaling, Pickling, and Passivation of Stainless Steel Parts, Equipment, and Systems (A380/A380M − 25)*, A380/A380M − 25, ASTM International, West Conshohocken, Jan. 2025.
[11] W. Steven and A. G. Haynes, "The temperature of formation of martensite and bainite in low-alloy steels. Some effects of chemical composition," *Journal of the Iron and Steel Institute*, no. 183, pp. 349–359, 1956.
[12] G. S. Frankel, "Pitting Corrosion of Metals: A Review of the Critical Factors," *J. Electrochem. Soc.*, vol. 145, no. 6, pp. 2186–2198, 1998.
[13] T. G. Gooch, "Corrosion behavior of welded stainless steel," *Welding Journal-Including Welding Research Supplement*, vol. 75, no. 5, pp. 135–154, 1996.
[14] N. J. Laycock, J. Stewart, and R. C. Newman, "The initiation of crevice corrosion in stainless steels," *Corrosion Science*, vol. 39, 10-11, pp. 1791–1809, 1997.
[15] E. M. Costa *et al.,* "Crevice corrosion on stainless steels in oil and gas industry: A review of techniques for evaluation, critical environmental factors and dissolved oxygen," *Engineering Failure Analysis*, vol. 144, p. 106955, 2023.
[16] Outokumpu Oyj, Ed., *Handbook of Stainless Steel*. Espoo, 2013.

Date 31.03.2026

Welding Simulation with Damage Prediction

Authors: *T. Loose[1], M. Brodt[2], Ch. Schröder[2]

[1]Dr. Loose GmbH, Herdweg 13, 75045, WALZBACHTAL, GERMANY

[2]Technologie-Institut für Metall & Engineering GmbH (TIME), Koblenzer Str. 43, 57537, WISSEN (SIEG), GERMANY

*Corresponding author: E-mail: loose@dr-loose-gmbh.de, ORCID: 0000-0002-1756-0392

Abstract

To accurately simulate the strength and potential damage of welded joints in structural steel, a multi-phase welding simulation is required. This is because phase transformations in the heat-affected zone (HAZ) change the local mechanical properties significantly. The main microstructural phases of steel (ferrite/pearlite, bainite, and martensite) exhibit distinct mechanical properties such as tensile strength and fracture elongation. For the prediction of damage in welding seams, these properties play a critical role and must be considered.

Welding seams can be simulated with computational welding mechanics (CWM) by calculating stresses, strains, distortions, and microstructural transformations in the HAZ. For the microstructure transformations, the effects on structural properties are considered using multi-phase material models [1], [2]. Such a multi-phase material is developed and implemented in the commercial software LS-DYNA by [3], which is available as keyword *MAT_GENERALIZED_PHASE_CHANGE (*MAT_254). The model was specifically developed for process chain simulations using a consistent material description [4] [5].

The presented work focuses on the numerical simulation of damage evolution in welded joints, under consideration of local phase changes and their underlying properties. The aim was to keep the same material model from welding to loading while considering the effects of local phase transformations for the prediction of damage. To do so, the damage model *MAT_ADD_GENERALIZED_DAMAGE, which is a generalized form of *MAT_ADD_DAMAGE_GISSMO developed by [6], was adopted. Three optimized sets of parameters of GISSMO, one for each of the three main phases, were identified based on numerical simulations and experimental results using LS-OPT. The approach proposed in [7] reassigns elements to parts characterized by the same mechanical properties after welding. This technique of creating local material clusters was adopted to perform the damage simulation based on the respective present phase of the steel. The three unique sets of parameters were then combined into

a multi-phase damage model, which uses a mixing rule to calculate the material properties for arbitrary phase combinations.

For the final damage calculation to verify the correct damage prediction of a welded segment in a three-point bending test, it was realized that the damage model does not work properly in combination with *MAT_254. The predicted cracks occurred in an unrealistic manner. Further research must be carried out to determine the exact cause and to fix this problem.

Keywords

GISSMO, MAT_254, multi-phase damage model, welding, Steel C45, phase transformation.

1 Methodology for multi-phase welding simulation

To capture the influence of microstructural phase transformations on damage evolution in the HAZ of structural steel welds, a systematic workflow was established comprising specimen preparation, experimental characterization, material model calibration, and data-field generation for LS-DYNA's generalized phase-change material (MAT_GENERALIZED_PHASE_CHANGE, MAT 254).

Four distinct specimen geometries were manufactured from the same base steel, which was used for the welding task. These geometries were selected to impose varying stress triaxialities during fracture testing. The manufactured specimens were heat treated to create the different phases which are present in the HAZ of the selected base steel.

This results in a suite of specimens representing pure ferrite/pearlite, bainite, and martensite microstructures obtained by special heat treatment [8]. Each condition was verified via optical microscopy and image analysis to confirm the expected phases.

The uniaxial stress–strain curves for ferrite/pearlite, bainite, and martensite were each fitted to the piecewise linear plasticity Model (MAT 24). Key parameters (effective plastic strain/yield stress values) were optimized via least-squares matching in LS-OPT.

Using the damage model including triaxialities, the GISSMO parameters – triaxial break elongation curve and triaxial material instability curve were calibrated for each phase. The resulting three sets of GISSMO parameters encapsulate the distinct ductile fracture behaviour of each microstructure.

In MAT 254, local phase fractions are provided as state variables at each element. To account for arbitrary mixtures in the HAZ, the single-phase material models must be combined into a continuous material data field. The plastic and fracture responses for the pure phases are tabulated as functions of equivalent plastic strain and stress triaxiality. For any combination of φF, φB, φM (Ferrite, Bainite, Martensite) the resulting effective plastic strain rate as a function of yield stress is already calculated in MAT 254. For the fracture response, the arbitrary combination of the phases needs to be computed by linear equations into a multi-dimensional material map, which returns the material parameters in relation to the triaxiality.

2 Material phases after welding

To establish the multi-phase welding simulation, the different material properties for the different phases must be tested. Several phases can form during the welding process, such as upper bainite, lower bainite, martensite or tempered martensite. To keep the simulation complexity manageable, the three main phases ferrite-perlite, bainite and martensite are selected. The material chosen was the normalized structural steel C45 and C60, as it is prone to harden after welding due to its higher carbon content. The different main phases of this steel after hardening and bainitisation, which can occur in the heat affected zone are shown in the figure below (figure 1).

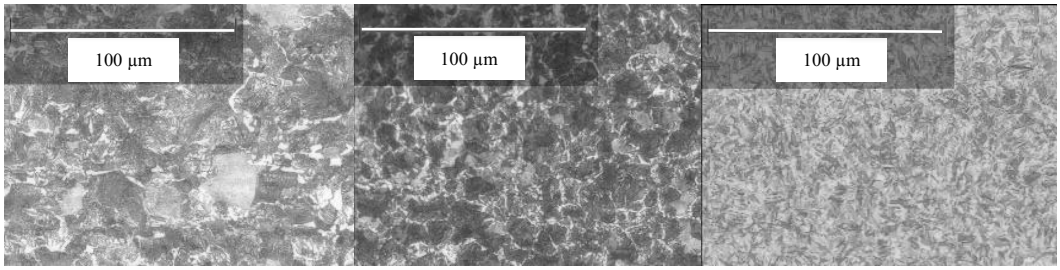

Figure 1: Different phases of C45 steel of the tensile test specimens. Left: Ferrite-Pearlite, mid: Bainite, right: Martensite

3 Plastic material properties

F. X. C. Andrade developed in [9] special triaxial tensile test specimens, which are also used in this study. The geometry of the tensile test specimens and the mount for the tensile testing machine are shown in figure 2. The simulation time of the implicit simulation was chosen to be 10 s to ensure no dynamics effects are present. To account for large deformations and stretching of the elements during the simulation, element formulation -2 was used, which corresponds to an 8-point hexahedron element whose algorithm is especially suitable for elements with poor aspect ratio. A mesh size of 0.5 mm was used in the critical area around

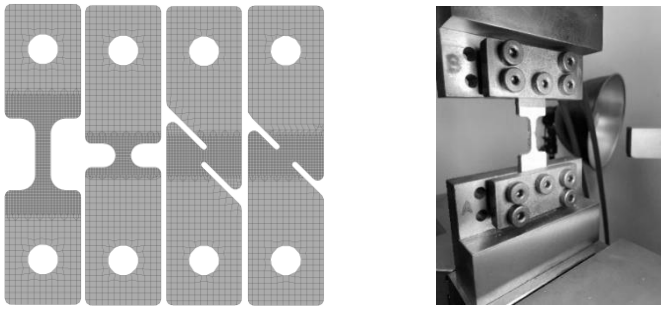

Figure 2: Different tensile test specimens for different stress triaxialities. Starting from left to right: short specimen, notched specimen, shear 0° specimen and shear 45° specimen. 1

The plastic material behaviour, which is necessary for the material card in LS-DYNA, was identified based on the experimental median curve of the tensile test with the short specimen (see figure 2 on the left). The identification of the parameters was done by least-squares matching in LS-OPT. To do so, the post-critical part of the curves was removed. The tensile tests were carried out for each phase and the results for the normalized experiments are shown in figure 3. The nominal cross-section area is 25 mm²

the crack for each simulation. The meshes are shown below for each specimen.

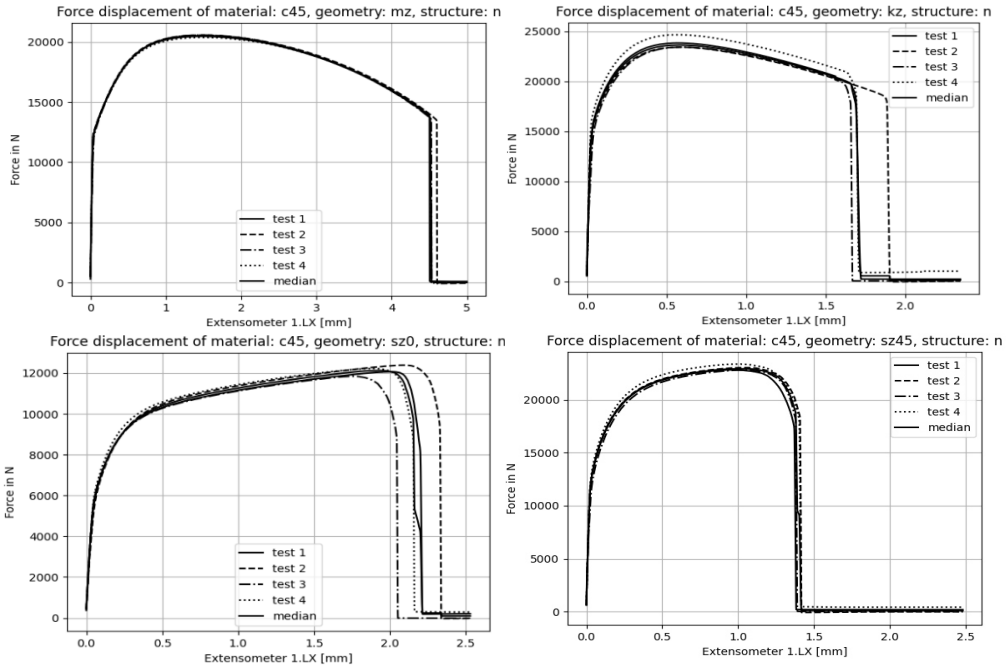

Figure 3: Force displacement curves for the normalized specimens: short (MZ), notched (KZ), shear 0° (SZ0) and shear 45° (SZ45). For each specimen, four tests were carried out.

For the martensitic phase, the novel multiphase fracture model development for single layer welding needs especially the plastic behaviour of the material and Martensite has nearly no plastic elongation anymore, so an approximated value for the tensile strength can be used.

4 GISSMO damage model material properties

The GISSMO Model developed by F. Neukamm [6] was primarily conceptualized for sheet metal forming processes. The advantage of this model is that it defines the failure strain curve and the instability curve as a function of triaxiality, which makes implementation into the simulation easy, if tensile tests of different geometries are available. It is parameterized by the two curves mentioned above as well as by its exponents FADEXP and DMGEXP, where the first one controls the post-critical fadeout of the material and the later one controls the type of damage accumulation e.g. linear or non-linear. The parameters of GISSMO were identified by a multi-objective optimization using LS-OPT. The median experimental curve, including post-critical failure, was matched against the resulting curve of the simulation by using the Genetic Algorithm (GA) in combination with the Leapfrog optimizer (LFOP) to speed up the optimization after a global optimum was found by GA. As an error measure, the mean squared error and curve mapping are available within LS-OPT. The authors of [10], showed that the mean squared error is the superior error measure for this optimization problem and, therefore, it was chosen. The identified fracture and critical strain curves are shown below (figure 4). For the normalized material, the FADEXP and DMGEXP were identified as 2.0 and 1.6 respectively and for the bainitized material they were identified as 2.0 and 2.5 respectively. For the martenized material, the fracture curve was chosen such that the material is allowed to strain up to 0.5 % plastically. This small amount of plastic strain helped with

numerical stability and the location of the crack happened reasonable in the middle of the part. Both damage and fade exponent were taken as 1.0.

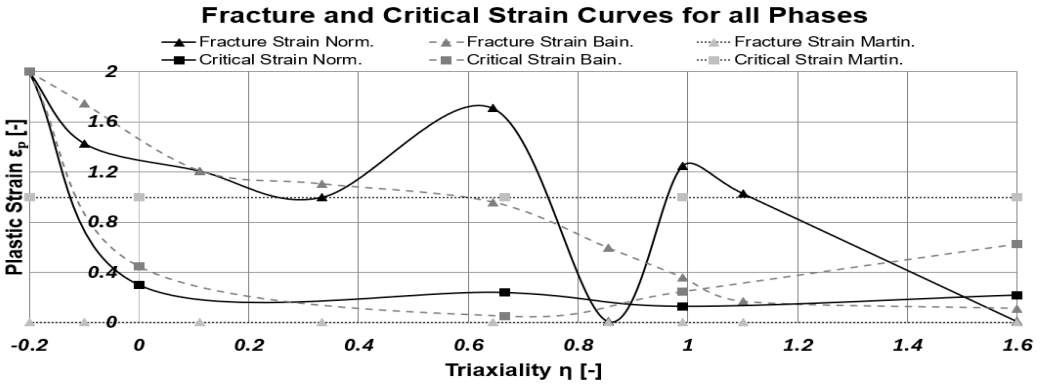

Figure 4: Different phases of C45 steel of the tensile test specimens. Left: Ferrite-Pearlite, mid: Bainite, right: Martensite

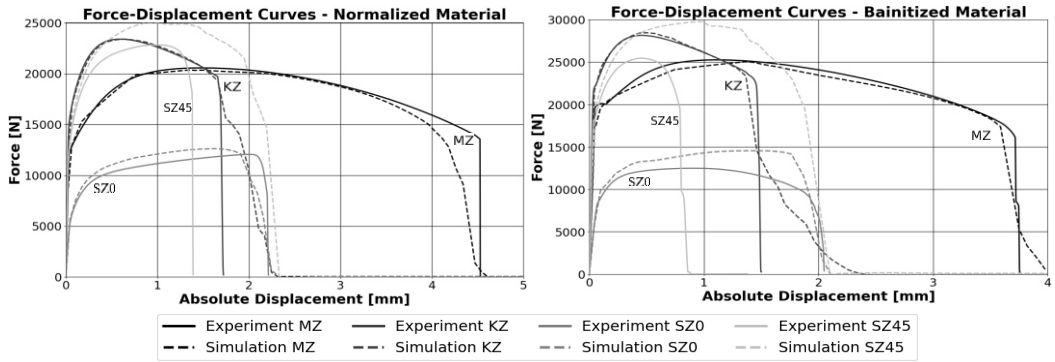

Figure 5: Force vs. displacement curves for the GISSMO optimization

Figure 5 compares experimental curves with simulations, showing good agreement for MZ, KZ, and SZ0 within the experimental scatter (see figure 3).

However, for the SZ45, both the plastic material behavior and the predicted material failure deviate noticeably from the experimental results. The calculated force exceeds the experimentally measured force, which is a phenomenon reported by the authors of [9] as well. The plastic material model *MAT_024 makes use of the J2-based plasticity model which assumes that yielding of the material happens only due to shear stresses. It neglects the influence of hydrostatic stress states. In reality, however, the material is in a complex combination of stresses and the growth of micro defects, due to hydrostatic stresses, might be a reason for the misprediction of the plastic straining. Further research is required to fully understand the underlying process.

A visual comparison of the fracture surfaces from the normalized experimental samples and the simulations is presented below (figure 6). The fracture surfaces for the MZ and KZ specimens were reproduced well by the simulation. For both cases, a smooth crack can be seen.

For the shear specimens, the experimental fracture surfaces appear macroscopically smooth. In contrast, the simulated fracture shows torn elements, leading to an artificially rough surface. This can be attributed to the relatively large mesh size, which is insufficient to resolve microscale

fracture mechanisms. A microscopic examination of the experimental surface would likely reveal features more consistent with those observed in the simulation.

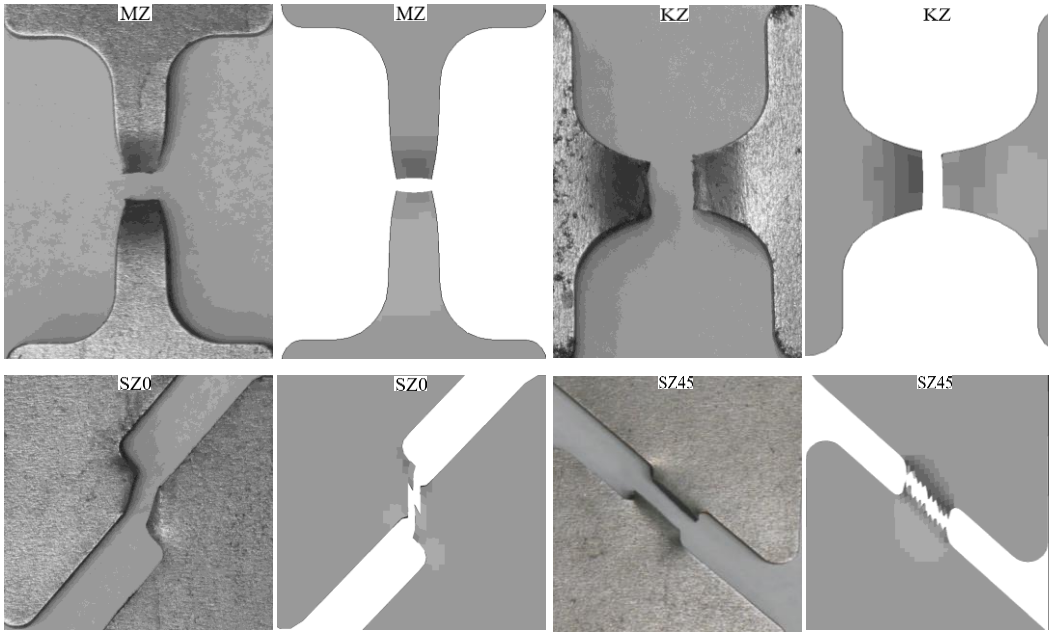

Figure 6: Comparison of fracture surfaces of experiments vs. simulation

5 Interpolation of material properties with linear equations

To build the multiphase GISSMO damage model, mainly two curves are necessary to define, the material instability curve ECRIT and the failure curve LCSDG. To calculate the two material curves for every phase combination, a linear system of equations is used to find an explicit description for this problem and the described function ϵ_η solves both curves. These equations are working in two curve definitions in LS-Dyna and calculate the material failure properties for every node as a function of stress triaxiality η. To get the solution parameters a-d for every phase composition, the following linear system of equations must be solved, in which φ_F, φ_B and φ_M are the phase rations of ferrite/perlite, bainite and martensite. The first equation

$$\epsilon_\eta \begin{pmatrix} \varphi_F \\ \varphi_B \\ \varphi_M \end{pmatrix} = a * \varphi_F + b * \varphi_B + c * \varphi_M + d$$

describes a straight line in the $\mathbb{R}^4$ and the second equation

$$\varphi_F + \varphi_B + \varphi_M = 1$$

a plane in the $\mathbb{R}^3$ as a boundary condition, because the phases added up cannot be more than 100%. Only three points are necessary to solve this problem with four unknown variables because of the boundary condition, which cuts the solution plane into a solution line. The three points are already calculated in the GISSMO analysis of the three material simulations with the three different material phases ferrite/perlite, bainite, and martensite. The described solutions

$$\epsilon_\eta \begin{pmatrix} 1 \\ 0 \\ 0 \end{pmatrix} = LCSDG_{\eta,\varphi_F}, \qquad \epsilon_\eta \begin{pmatrix} 0 \\ 1 \\ 0 \end{pmatrix} = LCSDG_{\eta,\varphi_B}, \qquad \epsilon_\eta \begin{pmatrix} 0 \\ 0 \\ 1 \end{pmatrix} = LCSDG_{\eta,\varphi_M}$$

solve the equation ϵ_η for every triaxiality point η of the curves ECRIT and LCSDG and the solutions must be entered into the associated material card.

6 Microstructure simulation and source data

The LS-DYNA Material Model *MAT_GENERALIZED_PHASE_CHANGE (*MAT_254) supports different models to calculate the phase transformation. For this investigation the Koistinen-Marburger Law is applied for the diffusion-free Austenite-Martensite transformation. The decomposition from Austenite to Bainite and Ferrite-Pearlite is calculated with the generalized Johnson-Mehl-Avrami-Kolmogorov model (JMAK). In welding tasks, the cooling is continuous and does not contain any hold times. The transformation is described by Constant-Cooling-Time (CCT) diagrams. The phase proportion at complete cooling is defined by cooling time needed for the temperature-interval between 800 °C and 500 °C. The value for PEQ TAU and N of the JMAK model are kept constant and the Leblond parameter F which describes the transformation velocity depending on the cooling rate is used to adjust the phase transformation. For this work the source data for the phase transformation is taken from WeldWare® [11] [12]. The data based on many physical experiments known as physical welding simulation performed by Seyffarth, Groß and Scharff and published in [13]. WeldWare® provides the data for phase transformation from Austenitisation at 1350 °C down to complete cooling according the cooling time between 850 °C and 500 °C. The chemical composition for the Steel C45 used in this work is given in Table 1

Table 1: Chemical Composition C45 in wt%

Material	C [m%]	Si [m%]	Mn [m%]	P [m%]	S [m%]	Cr [m%]	Ni [m%]	Mo [m%]	Cu [m%]	Al [m%]
C45	0,47	0,24	0,68	0,01	0,001	0,22	0,02	0,004	0,01	0,22

A simple model of single independent cube is used to check phase transformation. At each cube a thermal cycle with constant cooling rate is applied. figure 7 shows the phase – cooling time – transformation diagram with source data from WeldWare® and the result from simulation check.

In addition, the yield stress, tensile stress, elongation at break and hardness for uniaxial tensile test are provided by Weldware® according the cooling time. *MAT_GENERALIZED_PHASE_CHANGE (*MAT_254) provides eight history variables, which can be defined by user defined functions. This enables the output of the mechanical properties after change of microstructure. Figure 8 shows the elongation at break over cooling time. Both diagrams point out that the source data is hit exactly by the simulation approach.

The use of WeldWare® data enables engineering in advance without any physical material testing. In this work, tensile test of the material was performed for base material (normalized), bainitic

microstructure and martensitic microstructure. As a result, a difference between tensile tests of the chosen material and WeldWare® data can be seen. The mechanical properties and flow curve data from tensile tests are applied in the material model used for the simulations.

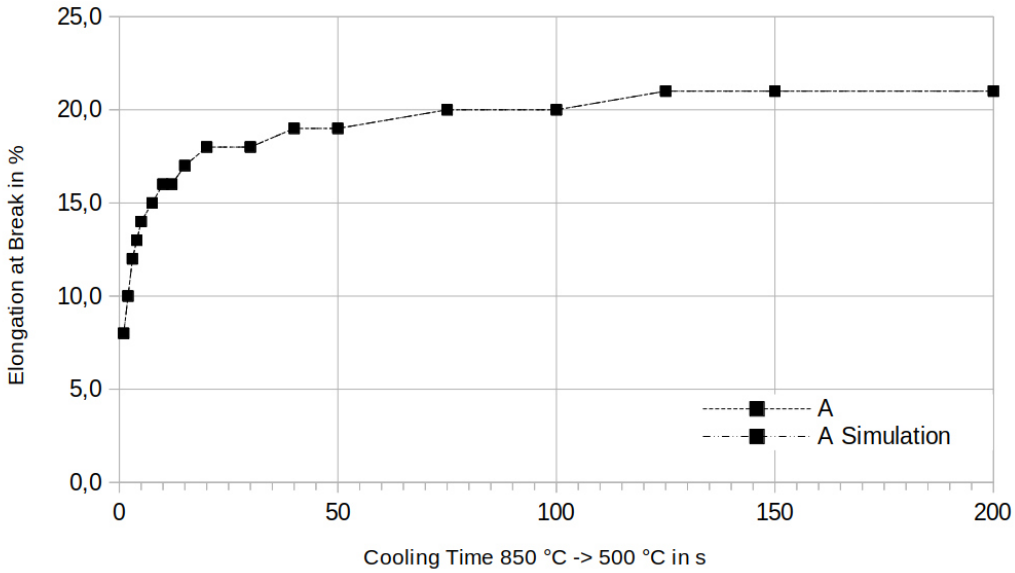

Figure 8: Elongation at break over cooling time

7 Experimental validations of the damage model – first results

In order to validate the predictive capability of the proposed damage model for simulated weld seam strength and fracture behaviour, a series of TIG (Tungsten Inert Gas) welding specimens were produced and mechanically tested with a three-point bending experiment. This chapter details the welding parameters, specimen geometry, testing procedure, and observed results for both top-side and bottom-side bending tests.

All specimens were produced as blind butt welds in 5 mm thick plates of the selected structural steel. An argon-shielded TIG process was employed with the following nominal parameters: Current: 300 A; Voltage: 13 V; Welding Speed: 5 mm/s Shielding gas: Argon; flow: 15 L/min Joint type: Blind weld (no full penetration)

Prior to welding, joint faces were prepared by manual grinding to a clean surface. The root side remained unwelded to simulate a common partial-penetration condition. Each weld pass was executed with no filler material added in the root region to ensure consistent lack of penetration and no material mixing.

After welding, specimens were allowed to cool to ambient temperature under still-air conditions. The resulting macro section of weld experiment, compared with the peak temperature of the simulation are shown in figure 12 and show a good accordance. The temperature over time at bottom side in the centerline measured by thermocouple is also in good accordance with the result of the simulation (figure 12).

After welding the plate is cut to the size of specimen for the bending test. The cutting is also considered in the simulation by erasing all elements outside the test specimen.

Figure 9 displays the e stress computed by evaluating the cooling time according to the data provided by WeldWare®.

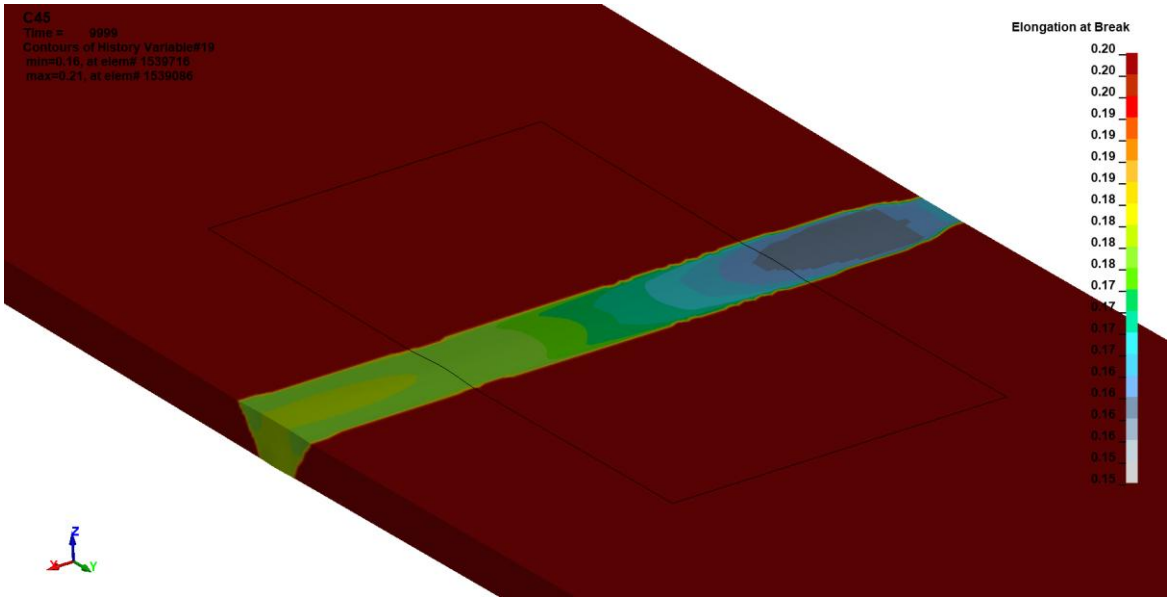

Figure 9: Calculated elongation at break after welding displayed over whole specimen.

with the weld crown facing upward (top-side bending) and four with the weld root facing upward (bottom-side bending). During each test, load–deflection curves were recorded continuously. Mechanical validation was performed according to DIN EN ISO 5173 (“Bend Test”) in an universal testing machine. Specimens were machined into rectangular cross-sectional bars (dimensions: 95 mm × 40 mm × 5 mm), with the weld seam running longitudinally at mid-span. Four specimens were tested with the weld crown facing upward (top-side bending) and four with the weld root facing upward (bottom-side bending) (figure 10). During each test, load–deflection curves were recorded continuously.

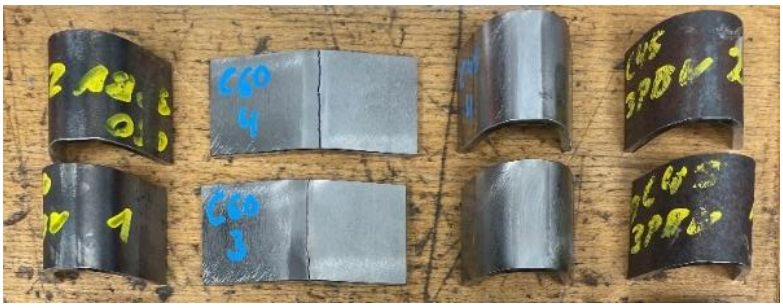

Figure 10: Left side: C60, right side: C45. Fracture pattern of the top-side specimens with martensitic brittle fracture pattern of C60. C45 shows no fracture pattern.

Mechanical validation was performed according to DIN EN ISO 5173 (“Bend Test”) in an universal testing machine. Specimens were machined into rectangular cross-sectional bars (dimensions: 95 mm × 40 mm × 5 mm), with the weld seam running longitudinally at mid-span. Four specimens were tested

This was also proven by testing the hardness of the welding seam. C45E has a maximum hardness of 369 HV10 and C60E 654 HV10. The described behaviour of the two different tests is shown in the force displacement curves in figure 11. The ductile behaviour of the bottom-side of the welding seam confirms that the absence of full penetration allows stress redistribution, preventing critical damage accumulation as described by the model.

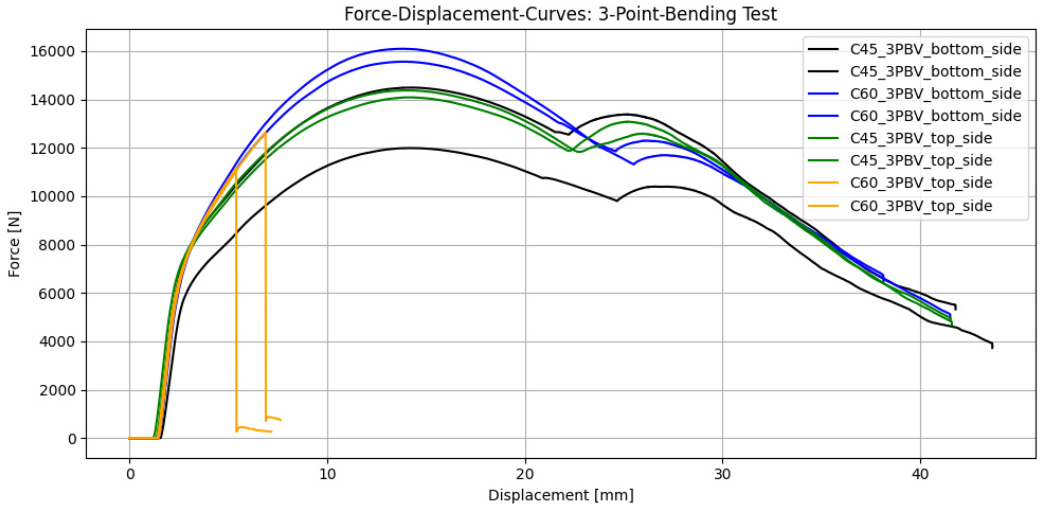

Figure 11: Force displacement curves of the bending test.

4 Results and Discussion

In this study, a methodology for mixing rules for the mechanical properties of different phases in steel was successfully demonstrated. The approach considers both, elastic–plastic behaviour and damage properties. This was made possible through single-phase, standardized tensile specimens that represent the distinct mechanical characteristics of the steel microstructures. Based on the proposed linearized mixing rule, the mechanical properties of phase mixtures present in the heat-affected zone of welded joints were subsequently determined. Experimental three-point bending tests provided a basis for validating the developed simulation model. A final validation has not yet been completed at the time of publication, as errors occur in the applied GISSMO implementation in LS-DYNA in combination with the multiphase material model MAT254.

Acknowledgements

This project is supported by Federal Ministry for Economic Affairs and Climate Action (BMWK) on the basis of a decision by the German Bundestag.

Conflict of Interest

The author declares no conflict of interest.

References

[1] T. Loose, *Einfluß des transienten Schweißvorganges auf Verzug, Eigenspannungen und Stabilitätsverhalten axial gedrückter Kreiszylinderschalen aus Stahl*, Diss., Karlsruhe, **2007**.

[2] J. Hildebrand, Numerische Schweißsimulation Bestimmung von Temperatur, Gefüge und Eigenspannung an Schweißverbindungen aus Stahl- und Glaswerkstoffen, Diss., Weimar, **2008**.

[3] T. Loose, T. Klöppel, *An LS-DYNA material model for the consistent simulation of welding, forming and heat treatment*, 11th International Seminar Numerical Analysis of Weldability, 27. - 30. September **2015,** Seggau, Austria

[4] T. Klöppel, A. Erhart, A. Haufe, T. Loose, *Recent developments in L-DYN to close the virtual process chain for forming, press hardening and welding*, 18th international ESAFORM conference on metal forming, 15.-17. April **2015**, Graz, Austria

[5] T. Loose, J. Rohbrecht, J. Prehm, U. Diekmann, *Simulation chain of material simulation heat treatment simulation and welding simulation for industrial application,* 15th. LS-DYNA Forum Bamberg 2018 15.-17.10.**2018** Bamberg, Germany

[6] F. Neukamm, *Lokalisierung und Versagen von Blechstrukturen*, Diss., Stuttgart **2018**

[7] J. Prehm, T. Loose, *Determination of weld joint strength by welding simulation,* Simulationsforum Schweißen und Wärmebehandlung, 05. - 07.11.2**019**, Weimar, Germany

[8] E. Roos, K. Maile, *Werkstoffkunde für Ingenieure*, Springer, **2015**

[9] C. Aandrade, M. Feucht, A. Haufe, F. Neukamm, *An incremental stress state dependend damage model for ductile failure prediction*, CrossMark, **2016**

[10] J. Effelsberg, M. Feucht, *Identifikation von Materialparameern mit LS-OPT – GISSMO und andere Anwendungen*, **2014**

[11] A. Scharff, C. Köthe, *Ermittlung der mechanischen Kennwerte von MAG-Schweißgut mit Hilfe des Schweißtechnlogischen Beratungssystems WeldWare®*," DVS-Berichte, vol. 156, pp. 102-156, **1993**.

[12] A. Scharff, WeldWare® - *The weldability of steel-based materials, Computer in Welding Education & Engineering,* Stockholm, **1995**.

[13] P. Seyfarth, B. Meyer, A. Scharff, *Großer Atlas Schweiß-ZTU-Schaubilder*, Düsseldorf, DVS-Verlag, **1992**

Date: 30.03.2026

The road to multi-directional Directed Energy Deposition with Plasma Arc Welding

Author: Max Mierzwa

Authors: Max Mierzwa[1]*, Konrad Mäde[1], Rahul Sharma[1], Jan Wiartalla[2], Mark Witte[2], Markus Schmitz[2], Mathias Hüsing[2], Burkhard Corves[2]

[1]Welding and Joining Institute, RWTH Aachen University, Aachen, Germany

[2]Institute of Mechanism Theory, Machine Dynamics and Robotics, RWTH Aachen University, Aachen, Germany

*Corresponding author: E-mail: max.mierzwa@isf.rwth-aachen.de,
ORCID: 0009-0000-0330-0314

Abstract

Directed Energy Deposition (DED) of mild steel with Plasma arc welding (PAW) is applied using an industrial 6 axis robot. Pure object manipulation enables multi-directional, support-free deposition. A unified monitoring and control framework in the Robot Operating System (ROS) iteratively adapts path planning and welding parameters based on sensor feedback. High-speed imaging and arc voltage measurements reveal distinct metal transfer modes as a function of wire feed speed and stand-off distance. For thin-walled closed-contour parts, a weld-end parameter set ensures continuous deposition and uniform overlap, demonstrated by a 100-layer hollow cylinder. Laser profile scans show an approximately circular bead cross-section which define the rotation center for multi-directional DED. Tilting between layers enables fabrication of a nozzle-shaped geometry with increasing inclination. Stable tilted deposition is achieved by reducing current and nozzle-to-work distance, which promotes a transition from intermittent to continuous metal transfer. The bead-surface-based path planning may be transferable to other DED applications.

Keywords

DED, plasma arc welding, pure object manipulation, ROS, multi-directional

1 Introduction

DED offers the potential to reduce part costs by improving material utilisation and minimising the necessary machining effort [1]. TIG and PAW are often used for welding of titanium alloys because of their stable arc characteristic and good shielding of the melt pool [1]. Efficient resource utilisation is key to reducing the carbon footprint of welding applications [2]. DED-PAW is usually

limited to unidirectional layer build-up due to high arc pressure and a large melt pool [3–5]. The production of more topologically optimised parts presents a significant economic and environmental opportunity that is currently unrealised. This work presents a method for achieving multi-directional DED-PAW, an important step towards DED-PAW for more complex designs.

Closed-contour paths have distinct areas of overlap where the path meets the start of the layer again. These areas are prone to defects due to arc striking and arc extinguishing events. In gas metal arc welding (GMAW), increasing the welding speed at the arc striking point or adjusting the overlap position has produced promising results [6]. In contrast to GMAW, heat input and material deposition can be controlled independently with PAW. This advantage is used in this study to achieve a smooth overlap area.

The term “multi-directional” refers to the flexible build direction enabled by DED with industrial 6-axis robots. Different build directions may be used for part segments [7], each layer of a part [8] or even within a layer. Through multi-directional AM the necessity for support structures is mitigated, unlocking higher resource efficiency as well as shorter printing times. One method suitable to layer-wise multi-directional path planning is Continuous three-dimensional path planning (CTPP) [8]. In this study, the concept of skeletonisation, whereby weld beads are modelled as circles, was adapted from CTPP [8] for DED-PAW with pure object manipulation [9]. However, depending on the welding parameters, other approximations of the weld bead may provide a better fit [10]. By using real surface data decisive steps were taken towards a more universal 3D path planning approach.

Even with suitable path planning, large overhangs still exhibit irregular surfaces, demonstrating the need for further optimisation of welding parameters [8]. Stable deposition for horizontal (2G) and overhead (4G) with GMAW is only possible at low wire feed speeds [11]. The melt pool of PAW is larger than that of GMAW [3,12]. Additionally, stable deposition largely depends on the metal transfer mode, which in turn depends on the nozzle-to-work distance and the wire feeding setup [4]. Therefore, the manufacturing of overhangs with DED-PAW is very challenging.

2 Aim of the Investigation

The main hypothesis of this study is that, when combined with pure object manipulation, a path planning algorithm ensuring a build direction perpendicular to the surface will enable DED-PAW with flexible roll angles between layers.

3 Materials and Experimental Details

Figure 1 illustrates the components of the experimental setup. The weld torch (2), wire supply (3), camera (6) and laser profile scanner (7) are mounted on a fixed aluminium extrusion rig (1). An industrial 6-axis robot Kuka KR6 R900 sixx (5) is used to manipulate the build plate (4). The employed welding power source Castolin GAP 2501, weld torch Castolin GAP E52 and plasma

nozzle are originally intended for plasma powder cladding applications. The wide nozzle provides a low arc pressure which is advantageous for DED-PAW [13].

Previous publications [9,14] have focused on the control system of the experimental setup developed within the Robot Operating System (ROS). A wide range of sensors are used to comprehensively monitor the welding process. The system saves sensor and robot data for each layer as a .bag file. Arc current and arc voltage are converted to a measurable range of 0–10 V by a Hall sensor and an isolation amplifier. The part geometry is measured by the laser profile scanner microEpsilon 2910-100 in conjunction with the robot providing up to 1 µm precision. As the laser scanner is synchronised with the robot's motion the point cloud is automatically transformed into world coordinates. Combining multiple scans avoids line-of-sight issues. The Basler acA1440-73gm camera provides continuous monitoring of the welding process at 73 fps. A Navitar MVL50M23 lens with a focal length of 50 mm produces the desired narrow field of view. With a distance of 200 mm between the camera and the welding process, the camera system is protected from excessive heat and spatter. Despite the very bright plasma arc, a 1000 nm bandpass filter and a neutral density filter with an optical density of 1.0 enable acceptable visibility of the melt pool.

In this project, mild steel is used instead of titanium, as the goal of multi-directional additive manufacturing is not material-specific. The build plates made of S235 JR have a size of 150x150x4 mm. The feedstock wire has the specification G 42 3 M21 3Si1 according to EN ISO 14341-A and has a diameter of 1.2 mm. The plasma gas is argon (Ar ≥ 99,996 %). A flow rate of 0.8 l/min is used, which ensures low arc pressure while providing sufficient cooling to the electrode. A shielding gas mixture of argon and CO2 (82% argon, 18% CO2) at a flow rate of 10 l/min was chosen due to its good wetting behaviour and sufficient shielding properties. The main welding parameters are based on previous experience [14]: welding speed v = 5 mm/s, wire feed speed wfs = 3 m/min. The current is adjusted layer by layer due to changing heat dissipation conditions. The individual current settings for the first four layers were set to: I = 180 A, 160 A, 140 A, 140 A. After the fourth layer, a current of I = 120 A is used in all subsequent layers. The exact movement and timing of the wire feed, as well as the current settings, are included in the results. Compressed air is used to cool the component down to an interlayer temperature of 100 °C.

Figure 2 illustrates the steps involved in this study:

1) The overlap parameters are investigated.

1.1) The quality of the overlap parameters is evaluated based on process stability using a cylindrical demonstrator, see Figure 4.

2) Multi-directional path planning based on bead shape fitting is implemented.

3) The welding parameters for the multi-directional layer build-up are set.

3.1) The interplay of overlap parameters (1), multi-directional path planning (2) and welding parameters (3) for multi-directional layer build-up is investigated using a nozzle shaped demonstrator, see Figure 8.

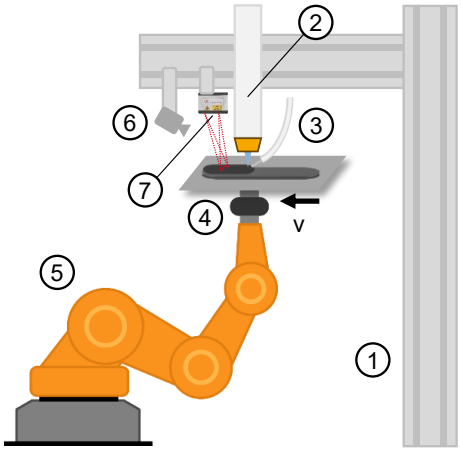

Figure 1: Components of the DED system

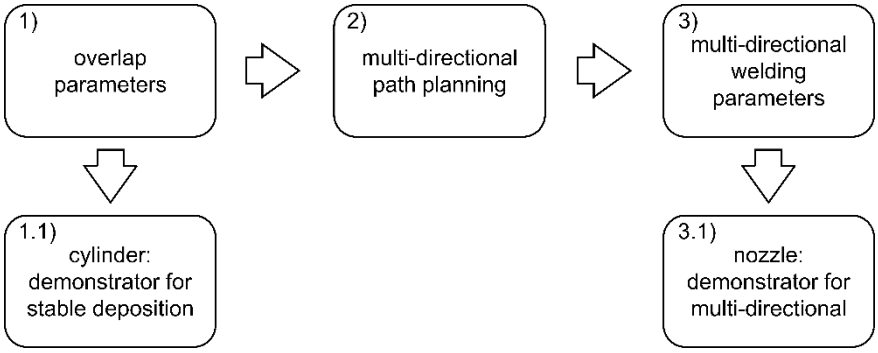

Figure 2: Steps of the conducted experimental work

4 Results and Discussion

4.1 Overlap parameters

Preliminary tests showed that no closed contour circle is produced with a calculated circular path of 360°. According to observations, the reason for this is twofold. Firstly, the ignition of the transferred arc marks the start of the welding process at $t = 0$ s, and the movement begins simultaneously with the arc to prevent defects caused by arc ignition. However, the heat transfer to the substrate and wire is not instantaneous. Therefore, some time is required for the melt pool to form. Since the movement starts before the actual material deposition a delay in time and position occurs. This delay is the first reason why the circle does not close. The second reason is the shifted deposition which has been explained in the authors' previous work [14]. Due to the arc pressure, the melt pool forms a keyhole. The molten wire then flows around the keyhole and is deposited behind it, forming the weld bead. The shift between the melting and deposition positions can be compensated for through overlap.

The overlap movement was set to 30°, resulting in total circular path of 390°. Three parameters were introduced to control the welding process, with the aim of achieving a smooth overlap. The first of these, tadvance, is used to advance the wire feed stop and the start of the current end ramp. Stopping the wire feed before the arc prevents the wire from sticking within the melt pool. The second parameter, tramp, sets the duration of the end slope. During the end slope, the current decreases linearly between the main current setting and the third parameter, the end current Iramp. The steepness of the end slope is defined by tramp and Iramp, which can be used to prevent sloshing of the melt pool and control the total heat input during the end slope. Since no material is added during the end slope, the main effect of the heat input is to smoothen the overlap area. The

parameters tramp and Iramp were tuned to avoid sloshing and insufficient or excessive heat input. Figure 3 visualises the overlap angle (s), the current (I) and the wire feed speed (wfs).

Five values for tadvance were tested: 2.0 s, 2.3 s, 2.4 s, 2.5 s and 3.0 s. With a setting of tadvance = 2.4 s, a circular path was achieved with no visible excess material deposition. The final droplets formed the connection between the start and the end of the layer. Additionally, three values for tramp were tested: 0.7 s, 1.0 s and 1.4 s. At tramp = 0.7 s the weld bead displayed an excessive height after ten layers. At tramp = 1.4 s, however, the opposite occurred. Excessive heat caused a dip in the overlap area. The final setting of tramp = 1.0 s provided a smooth overlap without any change in layer height at the overlap. Next, four values for Iramp were investigated: 50 A, 75 A, 85 A and 100 A. At Iramp = 85 A and Iramp = 100 A, a pointed elevation formed at the overlap. In contrast, Iramp = 50 A caused a longitudinal melt pool overflow. The setting of Iramp = 75 A provided an overlap without any discernible changes to the weld bead geometry.

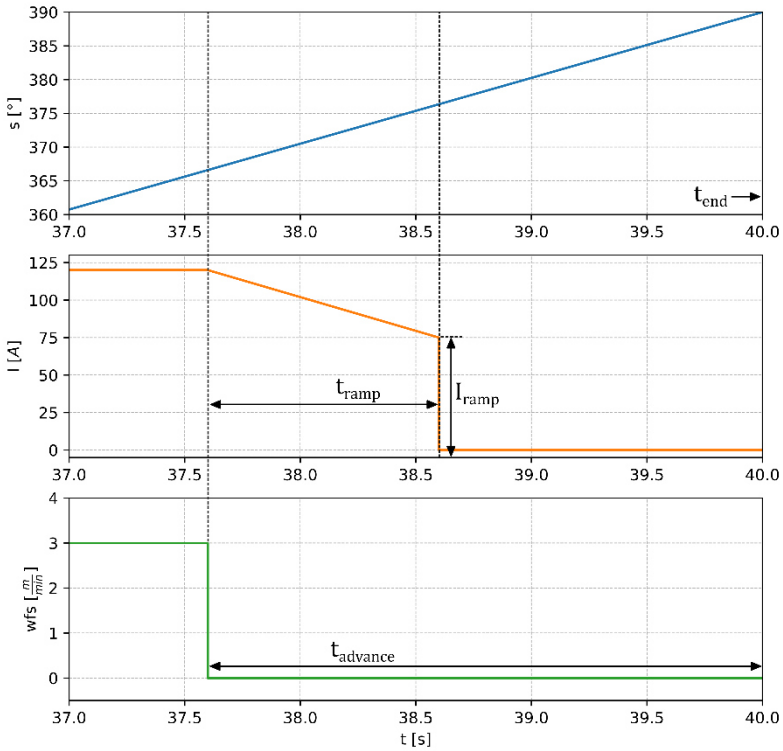

Figure 3: Movement, current and wire feed speed in the overlap area, $t_{advance}$ = 2.4 s, t_{ramp} = 1.0 s, I_{ramp} = 75 A

Figure 4: Photo of the cylindrical demonstrator

A 100-layer cylindrical demonstrator with a radius of 30 mm, visualised in Figure 4, was additively manufactured in order to test the robustness of the determined overlap welding parameters. Figure 5 shows the corresponding current, voltage and droplet frequency along each layer. The data of the 44th, 53th, 62nd and 66th layer are missing in this plot because their data was corrupted. The current and voltage are averaged over intervals of 0.1 s. The droplet frequency can be determined from the voltage signal [4]. Using the periodogram function from the python library scipy the dominating frequency of the voltage signal (see Figure 5b) was calculated which corresponds to the droplet frequency (see Figure 5c). Based on the experience gained when determining the

overlap parameters, the layer height of the first layer was set to 1.21 mm. A height of 0.97 mm is used for all subsequent layers.

In Figure 5, the overlap area is clearly visible. This overlap area caused no problems during the printing process. Between the 50th and 70th layer some pores formed during the welding process, but they were located far away from the overlap area. After finishing the 70th layer the manufacturing was interrupted in order to clean the nozzle and to sharpen the tungsten electrode. No visible marks were left on the part were by the interruption. Afterwards, the formation of pores stopped. This observation demonstrates the importance of a clean nozzle for proper shielding of the melt pool. A significant decrease in the average voltage was also measured, from U = 24 V to U = 21 V. However, this did not affect the welding process visibly. Increased arc voltage could be used as an indicator for nozzle cleaning.

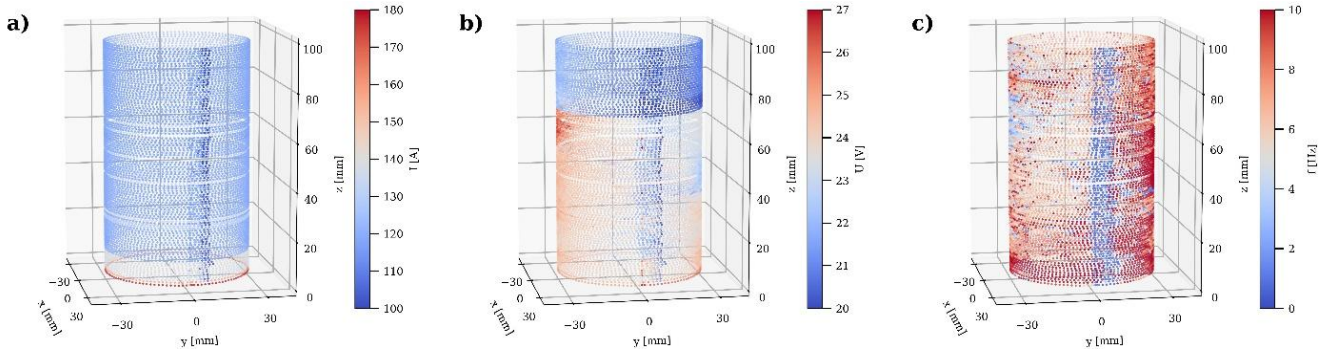

Figure 5: Cylindrical demonstrator, a) current, b) voltage, c) droplet frequency

4.2 Multi-directional path planning based on bead shape fits

In this work a path planning approach using circular bead shape fits is presented, as illustrated in Figure 6a. Compared to other bead shape modelling approaches [10], the circular bead shape fit is a simple solution requiring only radius and layer height for multi-directional path planning. The idea is to use actual surface data to ensure that the weld torch is perpendicular to the component, regardless of the intended build direction. Circular bead shape fitting is a simplification of this concept. The implementation of a universally applicable algorithm for complex 3D surfaces, as sketched in Figure 6b, is planned for future work.

The workflow consisted of the following steps: First, the geometry of a test part was measured. Figure 6a shows the overlay of a cross-section and the surface profile as measured by the laser line scanner. The selected welding parameters produced a weld bead surface corresponding to a partial circle. Least squares optimisation of the laser scan data determines the centre of the circle and its radius. In this case, the main current of I = 120 A produces a weld bead with an average radius of r = 3.15 mm. The pivot points along the path are then determined using the circular weld bead model. Figure 7a illustrates the layer built-up based on a given spline. Rotation around the centre of the circle ensures a constant distance, regardless of the roll angle, which is essential for a stable PAW process. Finally, the robot trajectory for pure object manipulation is generated.

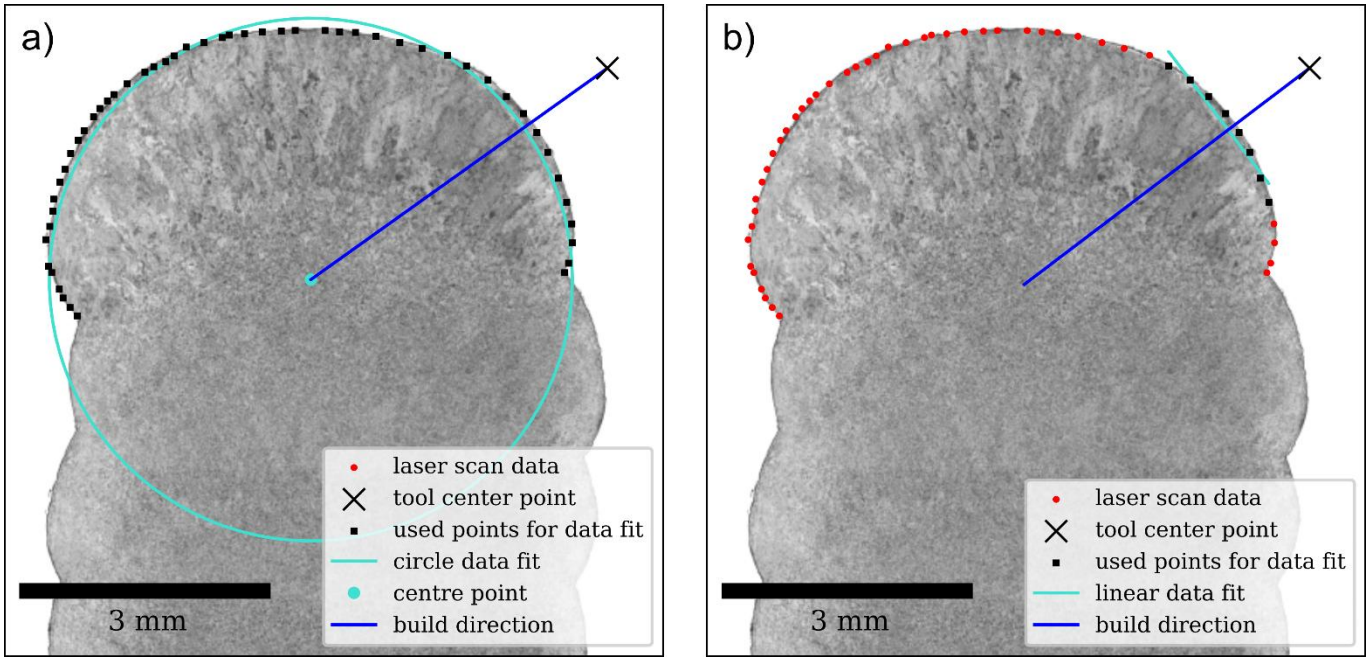

Figure 6: overlay of cross-section and surface measurement, a) circular bead shape fit, b) possible universal approach

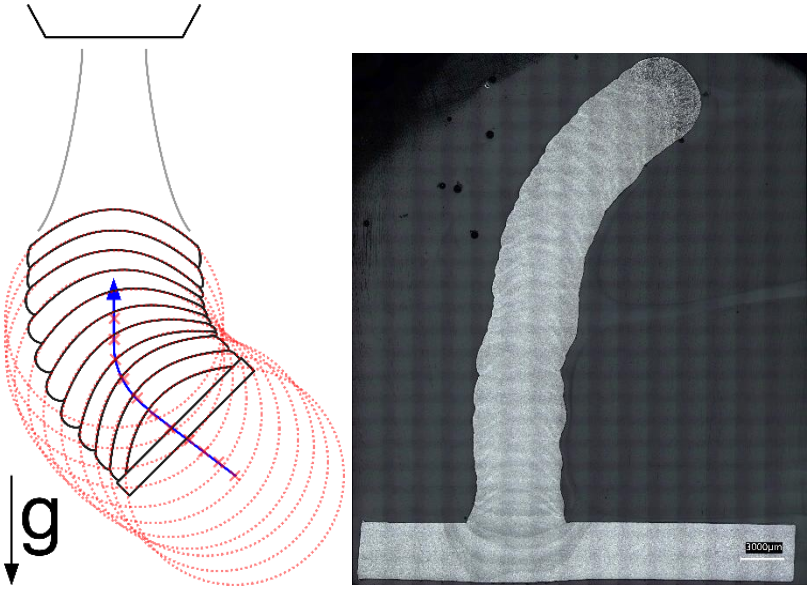

Figure 7: a) Illustration of layer build-up based on a given blue spline, b) Resulting cross-section of nozzle part (right)

4.3 Welding parameters for changing build-up direction

The idea behind pure object manipulation is that the welding parameters don't need to be changed because the flat welding position (1G) is maintained. Therefore, no reduction in current or wire feed is applied. The same parameters used for the cylinder are also used for the nozzle; the only difference is the changing build direction.

A nozzle component, see Figure 8 a), was manufactured to test multi-directional path planning combining the two approaches of overlap parameter adjustment and weld bead modelling described above. The welding direction in Figure 8 is counterclockwise. The nozzle itself consists of 25

layers. In order to avoid collision ten additional vertical layers were added below the actual nozzle geometry, see Figure 8 b). The 34th layer, shown during manufacturing in Figure 8 c), was manufactured at a roll angle of 65°. The final, 35th layer was printed at a roll angle of 70°. The manufactured nozzle exhibits a homogeneous surface over three quarters of its circumference. The stable deposition demonstrates the fundamental effectiveness of the bead-shape-based path planning approach.

Figure 8: a) CAD model of the nozzle, b) manufactured nozzle, c) manufacturing process of the 34th layer

However, the last quarter of the circumference is irregular. During the welding of the 22nd layer, there was a brief lack of deposition. A short gap remained in the layer. In the subsequent layers the increased distance of the wire tip to the melt pool changed the metal transfer mode from intermittent transfer to free droplet transfer. The falling droplets caused sloshing in the melt pool, resulting in a weld bead with an inhomogeneous surface and reduced height. This defect propagated and expanded through the layers. The expansion is visible in the recorded data of Figure 9. By the 30th layer the erratic welding process reached the overlap area. From the 31st layer onwards, the increased distance caused the wire to collide with the existing weld bead from the start of the layer. The collision caused the wire to slide down the side of weld bead, throughout which the material deposition was interrupted in the overlap area. Despite the problems that arose, the surface quality in the overhang area was significantly improved compared to tool manipulation [8].

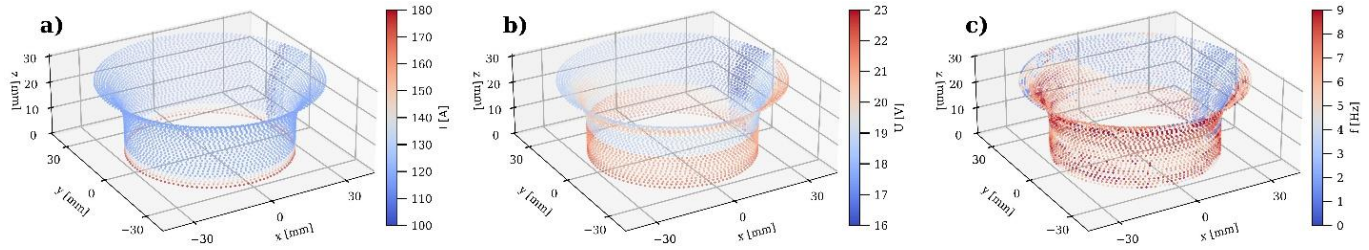

Figure 9: nozzle demonstrator – a) current, b) voltage, c) droplet frequency

It is interesting to note that the irregularity mainly propagated in the direction of the weld. This suggests that the welding process has a “self-healing” property. During continuous metal transfer, we observed the capillary effect between the wire and the melt pool. This pulling force, illustrated in Figure 10, strongly stabilised the melt pool. No sloshing was observed during continuous

transfer. The region with the most regular surface, where the individual layers are clearly distinguishable, correlates strongly with the droplet frequency shown in Figure 9 c). Additionally, the data shows the propagation of the continuous metal transfer in the welding direction, which explains the observed “self-healing” effect. Implementing a control loop to stabilise the continuous transfer would help to consistently achieve stable deposition and high surface quality.

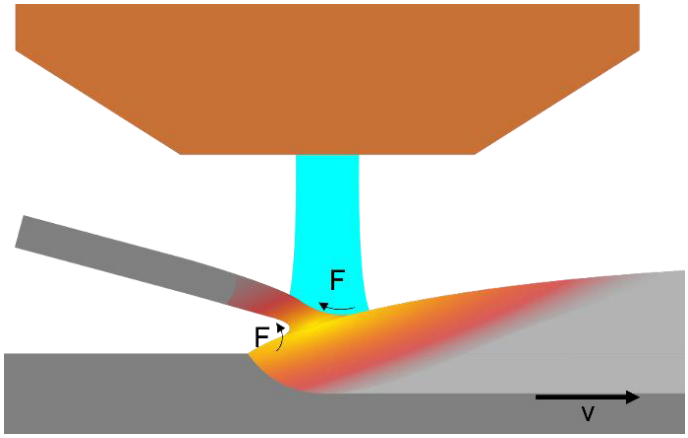

Figure 10: Capillary pull effect during continuous metal transfer

5 Summary

The main hypothesis was proven. A path planning algorithm based on circular bead shape fits ensured a build direction perpendicular to the surface. In conjunction with pure object manipulation the multi-directional layer build-up with DED-PAW was successfully demonstrated.

- The process monitoring using ROS facilitates rapid data-driven optimisation of the welding process. The parameters enabling a smooth overlap area were determined quickly in this way.
- The fabrication of a cylinder with 100 layers was accomplished using DED-PAW. The cylindrical component offered a tangible illustration of the determined overlap parameters' reliability. The height deviation at the overlap was < 0.9 mm in the final layer.
- We demonstrate that a circular bead-shape model is sufficient for multi-directional DED-PAW path planning, requiring only two user-defined parameters (radius r and layer height h).
- Pure object manipulation allows unrestricted, unsupported overhangs without sacrificing deposition rate. For small- to medium-size parts (1-16 kg), that can be handled by an industrial robot, this result means that shorter manufacturing times and greater ressource efficiency.
- Plasma arc welding remains highly sensitive to changes in distance. Defects in one layer can propagate and expand, eventually causing critical problems. Voltage-based control algorithms could be used to regulate the distance as well as nozzle cleaning.
- Areas with continuous metal transfer exhibited the best surface quality. Due to its inherent process stability, it was even possible to weld over previous, irregular layers with continuous metal transfer. A control loop for continuous transfer would facilitate DED-PAW.

Acknowledgements

Funded by the Deutsche Forschungsgemeinschaft (DFG, German Research Foundation) – Project ID 442454814. We would like to thank the Deutsche Forschungsgemeinschaft for their support.

Conflict of Interest

The authors declare no conflict of interest.

Data Availability Statement

Data provided upon request.

References

[1] Williams, S. W., Martina, F., Addison, A. C., Ding, J., Pardal, G., and Colegrove, P., 2016, "Wire + Arc Additive Manufacturing," Materials Science and Technology, **32**(7), pp. 641–647. https://doi.org/10.1179/1743284715Y.0000000073.
[2] 2025, *DVS-Studie "Nachhaltigkeit in der schweißtechnischen Produktion": DVS-Berichte, Band: 396 ; Studie im Auftrag der Forschungsvereinigung Schweißen und verwandte Verfahren des DVS e.V*, DVS Media GmbH, Düsseldorf.
[3] Ríos, S., Colegrove, P. A., Martina, F., and Williams, S. W., 2018, "Analytical Process Model for Wire + arc Additive Manufacturing," Additive Manufacturing, **21**, pp. 651–657. https://doi.org/10.1016/j.addma.2018.04.003.
[4] Ríos, S., Colegrove, P. A., and Williams, S. W., 2019, "Metal Transfer Modes in Plasma Wire + Arc Additive Manufacture," Journal of Materials Processing Technology, **264**, pp. 45–54. https://doi.org/10.1016/j.jmatprotec.2018.08.043.
[5] Wang, Y., Ding, J., Williams, S., and Cong, B., 2025, "Effect of Plasma Gas Composition on Deposition Characteristics in Plasma Arc Directed Energy Deposition of Ti-6Al-4 V," Weld World, **69**(4), pp. 883–895. https://doi.org/10.1007/s40194-024-01843-0.
[6] Xiong, J., Yin, Z., and Zhang, W., 2016, "Forming Appearance Control of Arc Striking and Extinguishing Area in Multi-Layer Single-Pass GMAW-Based Additive Manufacturing," Int J Adv Manuf Technol, **87**(1–4), pp. 579–586. https://doi.org/10.1007/s00170-016-8543-2.
[7] Ding, D., Pan, Z., Cuiuri, D., Li, H., Larkin, N., and van Duin, S., 2016, "Automatic Multi-Direction Slicing Algorithms for Wire Based Additive Manufacturing," Robotics and Computer-Integrated Manufacturing, **37**, pp. 139–150. https://doi.org/10.1016/j.rcim.2015.09.002.
[8] Diourté, A., Bugarin, F., Bordreuil, C., and Segonds, S., 2021, "Continuous Three-Dimensional Path Planning (CTPP) for Complex Thin Parts with Wire Arc Additive Manufacturing," Additive Manufacturing, **37**, p. 101622. https://doi.org/10.1016/j.addma.2020.101622.
[9] Schmitz, M., Wiartalla, J. T., Corves, B., Mann, S. M., Hüsing, M., and Gelfgren, M., 2021, *A Robot-Centered Path-Planning Algorithm for Multidirectional Additive Manufacturing for WAAM Processes and Pure Object Manipulation*, RWTH-2021-07625, MDPI. https://doi.org/10.18154/RWTH-2021-07625.
[10] Lambiase, F., Scipioni, S. I., and Paoletti, A., 2022, "Accurate Prediction of the Bead Geometry in Wire Arc Additive Manufacturing Process," Int J Adv Manuf Technol, **119**(11), pp. 7629–7639. https://doi.org/10.1007/s00170-021-08588-w.
[11] Kerber, E., Knitt, H., Fahrendholz-Heiermann, J. L., Ergin, E., Brell-Cokcan, S., Dewald, P., Sharma, R., and Reisgen, U., 2024, "Variable Layer Heights in Wire Arc Additive Manufacturing and WAAM Information Models," Machines, **12**(7), p. 432. https://doi.org/10.3390/machines12070432.
[12] Richter, A., Gehling, T., Treutler, K., Wesling, V., and Rembe, C., 2021, "Real-Time Measurement of Temperature and Volume of the Weld Pool in Wire-Arc Additive Manufacturing," Measurement: Sensors, **17**, p. 100060. https://doi.org/10.1016/j.measen.2021.100060.
[13] Wang, C., Suder, W., Ding, J., and Williams, S., 2021, "The Effect of Wire Size on High Deposition Rate Wire and Plasma Arc Additive Manufacture of Ti-6Al-4V," Journal of Materials Processing Technology, **288**, p. 116842. https://doi.org/10.1016/j.jmatprotec.2020.116842.
[14] Mierzwa, M., Mäde, K., Sharma, R., Reisgen, U., Wiartalla, J., Schmitz, M., Hüsing, M., and Corves, B., 2024, "Monitoring and Control of Additive Manufacturing with the Robot Operating System," *2024 International Conference on Control, Automation and Diagnosis (ICCAD)*, pp. 1–6. https://doi.org/10.1109/ICCAD60883.2024.10553877.

Date: 27.03.2026

Title: An analysis of welding fume generation during GMAW: A comparison with previous research results

Author: Mirco Olesch[1], K. Mäde, R. Sharma

[1]RWTH Aachen University, Welding and Joining Institute, Pontstr. 49, 52062, AACHEN, GERMANY

*Corresponding author: E-mail: mirco.olesch@isf.rwth-aachen.de, ORCID: 0009-0006-0372-0953

Abstract

The formation of welding fumes during gas metal arc welding (GMAW) has been extensively researched, particularly since Germany classified them as hazardous substances in 2005 under the Hazardous Substances Ordinance. This classification has increased focus on measures to reduce welding fumes. Correctly interpreting the processes within the arc is essential for selecting effective measures, as fume emissions result from complex interactions influenced by factors such as electrical power, wire feed speed, and the synergy characteristic curve stored in the welding power source based on shielding gas and filler material. These parameters affect both arc characteristics and material transfer, with alloy component evaporation contributing to fume formation. Various explanations for this phenomenon have emerged, often derived from simulations. This study aims to compile these explanations and evaluate their consistency with existing findings, focusing on fundamental similarities between theoretical approaches and experimental results while critically assessing simplified simulation models.

Keywords

Gas Metal Arc Welding, Welding Parameters, Welding Fume Generation, Comparison

1 Introduction

Gas metal arc welding (GMAW) is an arc welding process using a consumable electrode. The use of the arc as a heat source causes components from the wire electrode to overheat and vaporize. The oxidation of these components outside the shielding gas produces fine particles which agglomerate and are carried into the surrounding air by convection. This is perceived as welding fumes escaping from the process [Pires06, Deam00]. Since 2005, welding fumes have been classified as a hazardous substance, as the fine particles can penetrate deep into the lungs when inhaled [Rose11, Keane14]. In addition, various alloy components are carcinogenic or are suspected of leading to Parkinson's-like sickness [Keane14]. To protect staff, it is therefore

essential to keep exposure to a minimum and to reduce welding fume emissions as much as possible. To achieve this, various explanatory approaches have been pursued in the past, describing the formation of welding fumes depending on the material interface. To this end, both experimental and simulation-based approaches have been employed [Pires06, Deam00, Rose11, Boselli13, Tashiro18].

2 Aim of the Investigation

This paper aims to discuss and contextualize theoretical models of various material transitions relating to welding fume emissions in the light of current research findings. To this end, high-speed footage of different process variants will be analyzed on the basis of these theoretical approaches and compared with findings on welding fume emissions. The current findings will be used to review existing assumptions and, where necessary, to supplement them.

3 Materials and Experimental Details

The high-speed images were recorded using a camera manufactured by Photron. The backlighting for the images was generated using a mercury vapor lamp, and the images were illuminated using a laser light source manufactured by Cavilux. The welding fume emission rates were determined in accordance with DIN EN ISO 15011. To this end, the welding fumes are collected on a glass fiber filter and measured gravimetrically. Relative to the welding time, this yields the fume emission rate (FER), which can subsequently be evaluated together with calculated parameters. The parameters are calculated on the basis of current and voltage waveforms, which are measured and recorded at high resolution during welding. Table 1 shows general materials, which are identical for all tests, whilst Table 2 contains the specific process parameters for the different process variants.

Table 1: General used materials for weldments

Filler wire (diameter)	ISO 14341-A-G 3Si1 (1.2 mm)
Shielding gas (flow rate)	ISO 14175-M21-ArC-18 (15 l/min)
Base metal	EN 10277-S235JR, mild steel

Table 2: Welding parameters for investigated process variations

	Spray transfer mode (STM)	Pulsed arc (PA)	Short circuit mode (SCM)
Wire feed speed (wfs) [m/min]	12	10	4
Welding speed (ws) [cm/min]	45	40	20
Contact tip to weldpiece distance (CTWD) [mm]	17	16	12
Mean Power [kW]	Low FER: 8.2 High FER: 13.5	Low FER: 9.2 High FER: 7.0	Low FER: 2.2 High FER: 2.2

4 Results and Discussion

Scientific papers published to date on the physical mechanisms of welding fume formation have focused on different aspects. Furthermore, various approaches have been used to arrive at the results. In addition to experimental methods, semi-empirical, analytical and numerical approaches have been employed. However, when describing the origin of welding fumes, all authors describe similar mechanisms. The studies distinguish between material transfer in short-circuit welding, material transfer in pulsed arc welding and material transfer in spray arc welding [Pires06, Rose11, Chae06]. Apart from this, the same physical conditions apply to all process variants, meaning that welding fumes are primarily generated by the evaporation of metal. When the vapor pressure is exceeded, nucleation and growth of metal vapor droplets occur. This process is described in more detail by Tashiro et al. [Tashiro18]. Oxidation by CO2 or O2 in the shielding gas or atmospheric oxygen leads to the formation of fumes, which are emitted into the environment. Furthermore, according to Pires et al., the active gas content increases the arc temperature and accelerates the evaporation of the droplet [Pires06]. The three main sources of metal vapor are the melting wire end, the free-falling droplet in the arc and the molten pool. However, evaporation from the molten pool is the lowest and, according to Pires et al., amounts to approximately 10 % [Pires06, Pires10]. Consequently, the same particle formation chain applies to the formation of welding fumes for all material interfaces, comprising the following steps:

Evaporation → Supersaturation → Nucleation → Condensation → Coagulation → Oxidation

In addition to the formation of welding fumes from the arc as a direct source, welding spatter has been identified as a further secondary source [Jenkins05]. This is particularly important to note when processes are unstable, and the amount of spatter consequently increases.

Short-arc processes are characterized by the fact that material transfer takes place under short-circuit conditions. The transition occurs periodically and is initiated by the constriction of the melting wire end caused by the rising current after immersion in the molten pool. The arc ignites

when the free end of the wire is severed from the molten pool. This keeps the molten pool liquid and melts the free end of the wire. The wire feed ensures that the molten wire end dips into the melt and the cycle repeats. Consequently, at no point is a single free droplet exposed to the high temperature of the arc. Nevertheless, there are specific mechanisms that can lead to increased smoke emission. Deam et al. describe the breakdown of the short circuit caused by a rapid rise in current. [Deam00] In this process, the molten bridge between the wire end and the molten pool bursts, leading to spatter and turbulence in the process. Scotti describes that an increase in FER can also be observed when the short-circuit current, arc length or droplet diameter is increased [Meneses14]. Accordingly, the conclusion drawn from the literature sources considered is that the material transfer during a short circuit generally yields low FER results, as this process condition is achieved at low current [Pires06]. Furthermore, however, the FER can be reduced further if the current is reduced during short-circuit resolution in order to suppress the bursting of the molten bridge.

Pulsed arc processes are characterized by the fact that the current is specifically modulated over time. In conventional pulsed arc processes, there is a periodic alternation between a pulse phase and a base current phase. The material transfer occurs through the detachment of a droplet from the free end of the wire during the pulse phase. The driving force for the constriction above the droplet is the Lorentz force, which is particularly strong during the pulse phase. Gravity[MO1] ensures transfer into the melt. According to Boselli et al., a 2D model specifically for the pulsed metal-shielding-gas process has shown that the metal vapor emanates mainly from the wire tip during the pulse phase. Smoke formation subsequently occurs at the edge of the arc, where the oxygen partial pressure is higher [Boselli13]. Individual large droplets, which are detached in each period, result in a higher volumetric heat capacity. Consequently, metal evaporation is lower during the pulse phase despite a higher peak current [Rose12, Nemchinsky97]. Nevertheless, there is a risk that, if the current rise rate is too low and the pulse frequency too high, the free-flying droplet will re-enter the pulse phase, causing significant metal evaporation [Rose 2012; Nemchinsky 1997].

Spray arc processes are characterized by high power and a quasi-steady state. These processes are operated at high wire feed rates and thus at high current. Due to the high power and the continuous melting of the wire, a comparatively long arc forms, in which small droplets detach from the end of the wire and fall into the molten pool. As the droplets have a higher surface-to-volume ratio and lower heat capacity, they heat up faster than larger droplets and metal can evaporate more rapidly [Bosworth00, Deam00]. Added to this is the greater distance the droplets must travel within the arc and the high average current at which the process is operated [Rose12]. In this process, the arc length and process power are the parameters that significantly influence the FER. Due to these conditions, the spray arc process is classified as a high-emission process.

In recent studies, the three material transitions described were examined in relation to welding fume emissions under various parameter variations. To this end, high-speed footage of the processes was captured, and current and voltage waveforms were recorded. The data were analyzed synchronously in order to interpret all aspects of the process behavior.

For the material transition during short-circuit welding, various sources have identified the current flow during short-circuit resolution as the primary source of welding fumes. In the experimental investigations, two SCM processes were compared with regard to FER. Figure 1 shows four process phases for a conventional process. The waveform plot shows a triangular current curve. The voltage responds to the different process states. The short-circuit resolution, which was identified as the main source, occurs at high current and a brief voltage rise. This releases spatter, which in turn releases welding fumes (b). This process, using the settings from Tables 1 and 2, shows an FER of 1.9 mg/s.

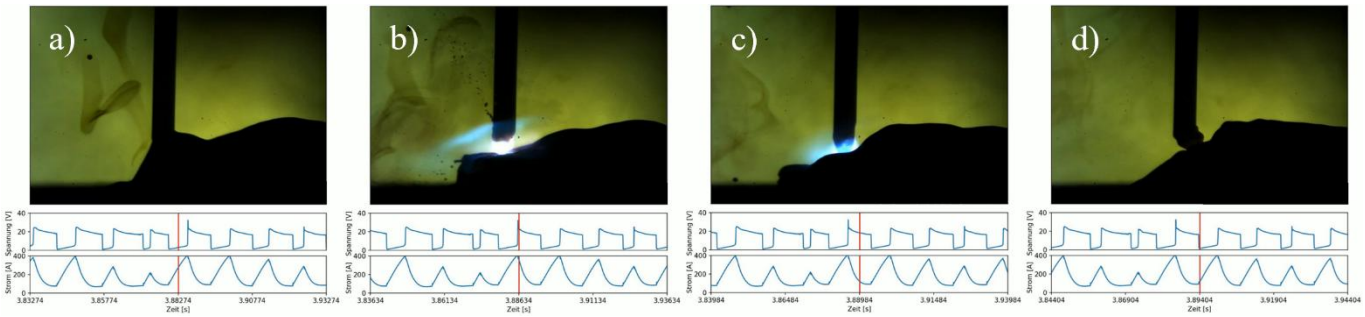

Figure 1: High-speed recording of a conventional SCM process. a) Short-circuit phase, b) Short-circuit resolution, c) Arc burning phase, d) Begin of short circuit

In comparison, short-circuit resolution can be precisely controlled by reducing the current. Various process variants from different manufacturers have already incorporated this control mechanism. Figure 2 also shows four process phases, with the difference that short-circuit resolution occurs at a lower current and the current profile has otherwise been adjusted (b). To enable a comparison between the processes, both were carried out at the same wire feed rate and power. The FER for this process was measured at 0.4 mg/s, which is around 80 % lower than that of a comparable conventional process. Accordingly, the results of the previous studies can be confirmed here.

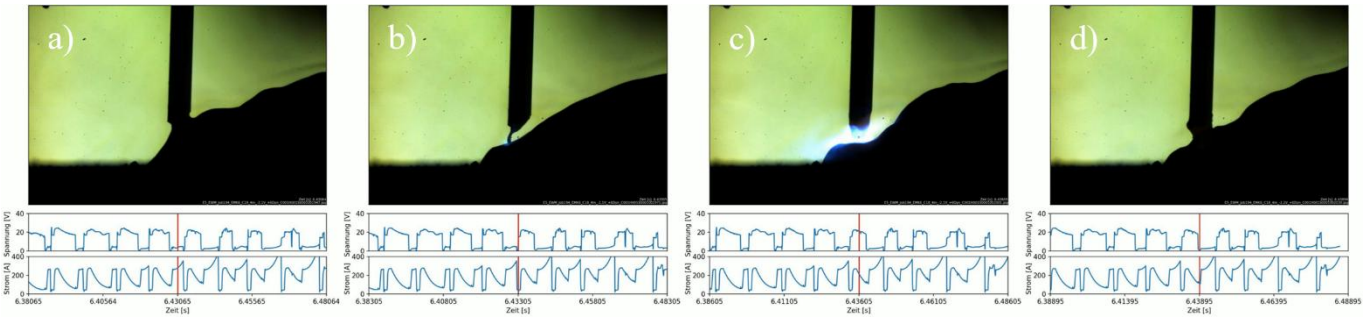

Figure 2: High-speed recording of a energy-reduced SCM process. a) Short-circuit phase, b) Short-circuit resolution, c) Arc burning phase, d) Onset of short circuit

When set appropriately, the pulsed process emits little welding fume, even though very high pulse currents are achieved. Nevertheless, some process conditions were identified as critical in the studies mentioned. If droplet detachment is not fully complete or the droplet is still in free fall, the high pulse current can lead to excessive evaporation. Figure 3 illustrates such a process condition. Process adjustments reduced the pulse current and slightly reduced the pulse frequency. Consequently, the current-induced Lorentz force is insufficient to detach the droplet. The result is an uneven process, which repeatedly exhibits disturbances in the material transfer. This results in

a FER of 4.4 mg/s for this process. In the event of more severe disturbances, the FER may rise even further.

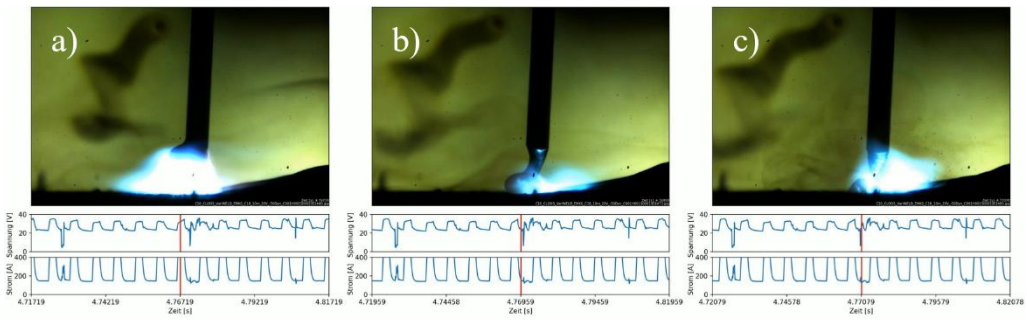

Figure 3: High-speed recording of a conventional PA process with reduced pulse-current. a) Pulse phase, b) Droplet constriction, c) Droplet detachment

The images in Figure 4 show the same process with a higher pulse current and a slightly increased frequency. The result is that droplet detachment occurs at the end of the pulse phase and the droplet flight is completed during the base current phase. The droplet is therefore not exposed to the high energy of the pulse phase. In this process, a FER of 1.5 mg/s was achieved. Consequently, welding fume emissions have been positively influenced by the trouble-free process behavior.

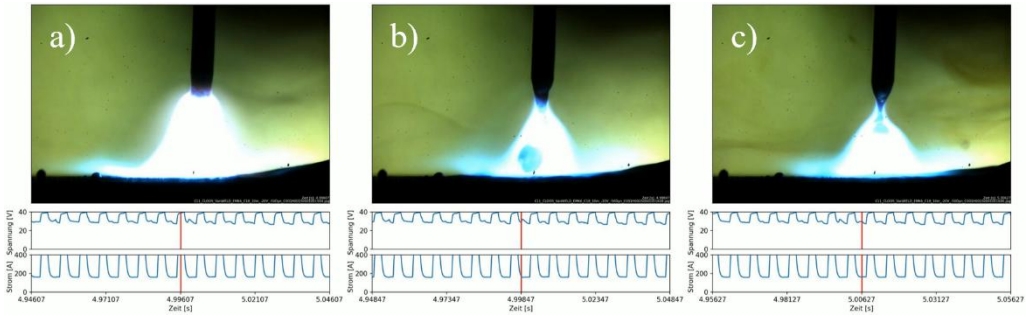

Figure 4: High-speed recording of a conventional PA process with standard parameters. a) Pulse phase, b) Droplet constriction, c) Droplet detachment

Due to the consistently high-power output in the spray arc process, the main factors influencing welding fume emissions are the arc length and droplet size. Figure 5 illustrates two process conditions. In (a), the process was carried out at a reduced voltage. A FER of 2.7 mg/s was measured. On the right-hand side (b), the process is shown with a slightly increased voltage compared to the zero point of the characteristic curve. Here, a FER of 6.6 mg/s was measured. The findings from the studies therefore correspond with the results. However, the investigations reveal further peculiarities that were not taken into account in the reviewed studies. Firstly, in process a) with a low FER, an increased number of micro-short circuits can be observed, which are an indicator of a short arc. When setting up the process, care can be taken to keep the arc length for the droplet as short as possible. Accordingly, it is possible in SCM to significantly reduce the FER at high melting rates, which makes the SCM process particularly stand out.

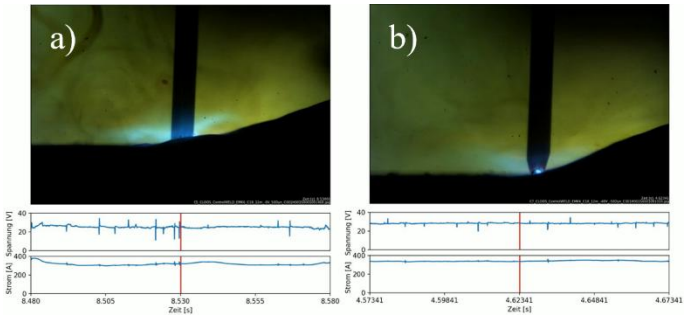

Figure 5: High-speed recording of a conventional STM process. a) reduced voltage, b) increased voltage

Another point is that reducing the voltage results in a particularly narrow and deep penetration. This effect is shown more clearly in Figure 6. This could provide a further explanation for the low FER. The high arc pressure at reduced arc voltage pushes the molten metal to the side and forms a cavity. The altered surface conditions of the melt can have a positive effect on the condensation of the metal vapor during the process. Thus, the metal vapor is not forced out of the process zone, but is absorbed by the molten pool.

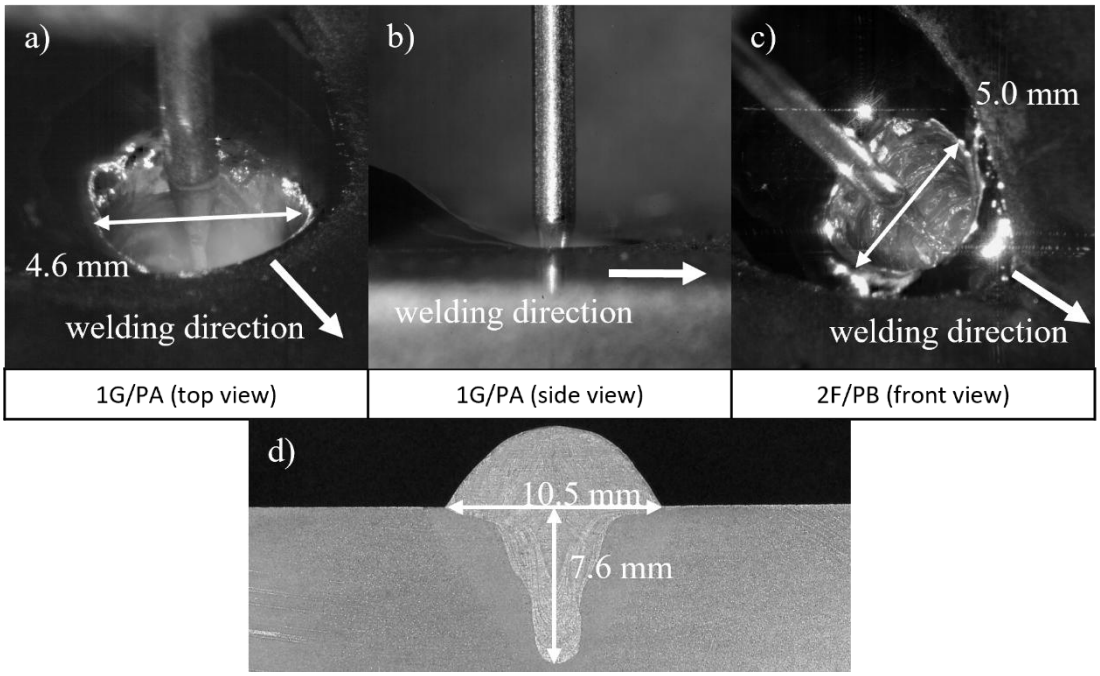

Figure 6: High-speed recording of a conventional STM process. a) Top view, b) Side view, c) Front view, d) Cross-section

5 Summary

This study investigated fume generation mechanisms during gas metal arc welding (GMAW) for three metal transfer modes: short circuit mode (SCM), pulsed arc (PA), and spray transfer mode (STM). Theoretical explanations from previous research were reviewed and compared with experimental high-speed camera recordings and fume emission rate (FER) measurements conducted in accordance with DIN EN ISO 15011. For all transfer modes, metal evaporation from the wire tip, the free droplet, and the weld pool were identified as the common primary source of fume formation, following the particle formation chain. Weld spatter was confirmed as a secondary fume source, particularly under unstable process conditions. For the SCM, the current level during short circuit dissolution was identified as the dominant driver of fume emission. A conventional

SCM process yielded a FER of 1.9 mg/s, while an energy-reduced variant achieved a FER of only 0.4 mg/s, representing a reduction of approximately 80 %. These results are in good agreement with findings from earlier investigations. For the PA process, stable operation with complete droplet detachment prior to the subsequent pulse phase yielded a FER of 1.5 mg/s. An unstable variant with insufficient pulse current, which prevented regular droplet detachment, resulted in a FER of 4.4 mg/s. This confirms that the timing of droplet transfer relative to the pulse phase is critical for minimizing fume emissions. For the STM, arc length and droplet size were confirmed as the dominant parameters governing fume emission. A reduced arc voltage setting yielded a FER of 2.7 mg/s, while an elevated voltage resulted in 6.6 mg/s. Additionally, a previously unreported mechanism was observed: low arc voltage produced a narrow, deep penetration cavity under high arc pressure. This geometry may promote re-absorption of metal vapor into the weld pool, thereby further reducing fume emissions.

Acknowledgements

Supported by:

Federal Ministry for Economic Affairs and Climate Action

on the basis of a decision by the German Bundestag

INDUSTRIELLE GEMEINSCHAFTSFORSCHUNG

The project is funded by the German Federal Ministry for Economic Affairs and Climate Action on the basis of a resolution of the German Bundestag.

Reference number: 01|F22017N

Conflict of Interest

The author declares no conflict of interest.

Data Availability Statement

Data available on request.

References

[Tashiro18] Tashiro, S.; Murphy, A.B.; Tanaka, M.: Numerical simulation of fume formation process in GMA welding. Welding in the World, Vol. 62, 2018, pp. 1331–1339. DOI: 10.1007/s40194-018-0656-9.

[Pires06] Pires, I.; Quintino, L.; Miranda, R.M.; Gomes, J.F.P.: Fume emissions during gas metal arc welding. Toxicological & Environmental Chemistry, Vol. 88, No. 3, 2006, pp. 385–394. DOI: 10.1080/02772240600720472.

[Deam00] Deam, R.T.; Simpson, S.W.; Haidar, J.: A semi-empirical model of the fume formation from gas metal arc welding. Journal of Physics D: Applied Physics, Vol. 33, 2000, pp. 1393–1402. DOI: 10.1088/0022-3727/33/11/318.

[Rose11] Rose, S.: Entstehung und Reduzierung der Schweißrauchemissionen beim MSG-Schweißen – Ergebnisse des 1. EWM-Awards. DVS-Berichte, Vol. 275, DVS Media GmbH, Düsseldorf, 2011, pp. 599–606.

[Chae06] Chae, H.; Kim, C.; Kim, J.; Rhee, S.: Fume Generation Behaviors in Short Circuit Mode during Gas Metal Arc Welding and Flux Cored Arc Welding. Materials Transactions (Japan Institute of Metals), Vol. 47, No. 7, 2006, pp. 1859–1863. DOI: 10.2320/matertrans.47.1859.

[Boselli13] Boselli, M.; Colombo, V.; Ghedini, E.; Gherardi, M.; Sanibondi, P.: Two-dimensional time-dependent modelling of fume formation in a pulsed gas metal arc welding process. Journal of Physics D: Applied Physics, Vol. 46, No. 22, 2013, Art. 224006. DOI: 10.1088/0022-3727/46/22/224006.

[Bosworth00] Bosworth, M.R.; Deam, R.T.: Influence of GMAW droplet size on fume formation rate. Journal of Physics D: Applied Physics, Vol. 33, 2000, pp. 2605–2610. DOI: 10.1088/0022-3727/33/20/316.

[Rose12] Rose, S.: Ansätze zur Entstehung und Reduzierung von Schweißrauchemissionen beim MSG-Schweißen unter Berücksichtigung neuer Verfahrensvarianten. Schweißen und Schneiden, Vol. 64, No. 4, DVS Media GmbH, 2012, pp. 188–193.

[Meneses14] Meneses, V.A. de; Gomes, J.F.P.; Scotti, A.: The effect of metal transfer stability (spattering) on fume generation, morphology and composition in short-circuit MAG welding. Journal of Materials Processing Technology, Vol. 214, 2014, pp. 1388–1397. DOI: 10.1016/j.jmatprotec.2014.02.011.

[Jenkins05] Jenkins, N.T.; Eagar, T.W.: Fume formation from spatter oxidation during arc welding. Science and Technology of Welding and Joining, Vol. 10, No. 5, 2005, pp. 537–543. DOI: 10.1179/174329305X48310.

[Pires10] Pires, I.; Quintino, L.; Amaral, V.; Rosado, T.: Reduction of fume and gas emissions using innovative gas metal arc welding variants. International Journal of Advanced Manufacturing Technology, Vol. 50, 2010, pp. 557–567. DOI: 10.1007/s00170-010-2551-4.

[Nemchinsky97] Nemchinsky, V.A.: Electrode evaporation in an arc with pulsing current. Journal of Physics D: Applied Physics, Vol. 30, 1997, pp. 2895–2899. DOI: 10.1088/0022-3727/30/20/021.

[Keane14] Keane, M.J.; Siert, A.; Chen, B.T.; Stone, S.G.: Profiling Mild Steel Welding Processes to Reduce Fume Emissions and Costs in the Workplace. Annals of Occupational Hygiene, Vol. 58, No. 4, 2014, pp. 403–412. DOI: 10.1093/annhyg/meu007.

Date: 31.03.2026

Electron Microscopic Analysis of Melting Processes and Solidification Structures via *in situ* LC-SEM: Microstructural Transformations during Joining and Thermal Processing

Author: Shohreh Khatami

Authors: Sh.Khatami[1*], J.Mayer[1], A.Aretz[1]

[1]RWTH Aachen University, Central Facility for Electron Microscopy (GFE) 52074 Aachen, Germany
*Corresponding author: E-mail: khatami@gfe.rwth-aachen.de, ORCID: 0009-0004-6622-0708

Abstract

Performing in situ experiments within large-chamber scanning electron microscopes (LC-SEM) enables the direct observation of metallurgical transformations under realistic thermal and mechanical processing conditions. As case studies, this manuscript presents four investigations covering welding, brazing, and the local thermodynamic behavior of aluminum- and steel-based systems. Laser micro-welding of aluminium alloy 6082 reveals distinct keyhole behavior and the influence of local conduction modes, with grain growth, porosity, and elemental redistribution governed by feed rate and alloy chemistry. In situ brazing of Sn–Cu on Al–Si substrates demonstrates the effect of filler composition on wetting and intermetallic formation. Ni-620 solder on a steel base exhibits limited interfacial reactions due to Cr and Si diffusion barriers. Al–Si fillers are further evaluated for joining aluminum alloys. Overall, LC-SEM provides direct, real-time insight into microstructural evolution crucial for optimizing joining processes.

Keywords

LC-SEM, in situ microscopy, brazing and welding, intermetallic compounds, microstructural evolution

1 Introduction

Joining processes such as welding, brazing, and soldering are essential in modern manufacturing technologies, particularly for lightweight materials like aluminum alloys or high-strength steels. The performance of the formed joints is governed by complex thermodynamic phenomena, including melting, wetting, diffusion, and interfacial reactions, which are difficult to study using conventional ex situ characterization approaches that only provide post-process information [1, 2]. In situ scanning electron microscopy (SEM), enables direct observation of these processes in real time, offering deeper insight into microstructural evolution and dynamic processes [3, 4]. However, conventional SEM systems are limited by their small chamber sizes and sample constraints with respect to size and weight [5]. To address this, large-chamber SEM (LC-SEM) has been developed,

allowing the study of larger specimens under more realistic conditions and enabling the integration of experimental devices for real-time observation of thermal processes such as heating, welding, and brazing [4,6]. In technological processes, brazing and soldering of aluminum alloys presents additional challenges due to the presence of the stable native alumina layer. Al–Si filler metals are commonly used because of their low melting temperature, good fluidity, and favorable wetting behavior. These fillers, particularly those containing 10–12 wt.% Si, are widely applied in industrial processes such as automotive heat exchanger production. During brazing, interactions between filler and substrate lead to diffusion zones and intermetallic phase formation, which strongly affect joint properties [7, 8]. In addition, Sn–Cu solder alloys have gained attention as environmentally friendly, lead-free alternatives. Their wetting behavior and interfacial reactions are strongly influenced by the substrate composition, as alloying elements such as Mg, Si, and Mn affect oxide stability, diffusion, and intermetallic phase formation [9]. For steel systems, nickel-based brazing alloys such as Ni-620 are widely used due to their high-temperature strength and corrosion resistance. However, their interaction with steel can lead to the formation of complex phases such as borides and silicides, while elemental diffusion (e.g., Cr and Si) may influence interfacial structures and final joint performance [10, 11].

2 Aim of the Investigation

This study investigates metallurgical transformations and interfacial reactions during joining processes using in situ large-chamber scanning electron microscopy (LC-SEM). Unlike conventional ex situ methods, LC-SEM enables real-time observation of dynamic phenomena such as melting, wetting, diffusion, and intermetallic formation. The research focuses on aluminum alloys and steels in various joining processes, including welding, brazing, and soldering, using different filler materials. By combining the in situ observations with SEM and EDX analyses, the study aims to improve understanding of microstructural evolution and support the optimization of advanced joining technologies.

3 Materials and Experimental Details

The joining experiments were performed using a custom-built heating module integrated into a large-scale scanning electron microscope (LC-SEM). Figure 1a shows the heating module beneath the electron column. The chamber temperature was monitored with three thermometers to ensure stable conditions and protect the electron column. All experiments were conducted under high vacuum at $(2.9 \pm 0.6) \times 10^{-6}$ mbar. The Base material were cut to size of 10×10 mm², grounded, polished, ultrasonically cleaned in ethanol, and air-dried, achieving a surface roughness of Ra = 60 ± 5 nm. Filler pieces (~2×2 mm², 0.2 mm thick) were placed on the substrate without fixation or flux. The assemblies were heated at a rate of 30 °C min^{-1}, and the brazing process was observed in situ using the SE detector under flux-free vacuum. After reaching the target temperature, samples were held for varying durations and cooled naturally. This setup enabled real-time observation of wetting and spreading during filler–substrate interaction. The chemical compositions (in wt.%) of the utilized base and filler materials are presented in Table 1.

For the laser welding experiments, the laser source (λ =1024 nm, P=120 W) was installed outside the vacuum chamber and the laser beam enters through a coupling window, where it is guided via a beam expander and a system of flanges into the chamber. Inside, four adjustable mirrors redirect the beam in the Y and Z directions to align it with the electron beam position and focus it on the sample. The mirror system is height-adjustable for precise alignment. At the end of the setup, a sample holder inclined at 30° was mounted on a movable stage, allowing positioning of the sample and adjustment of the laser target during the experiment (Fig. 1b).

Table 1: Chemical composition of utilized base and materials in weight-%

Material	C	Si	Mn	Cr	Mo	V	Al	Cu	Mg	Fe	Ni	B	Others
Steel	0.38	1.1	0.4	5.0	1.3	0.4	–	–	–	–	–	–	–
EN-AC42100	–	6.5–7.5	–	–	–	–	Bal.	≤0.2	0.25–0.45	≤0.55	–	–	Ti, others
EN-AW6082	–	0.7–1.3	0.4–1.0	≤0.25	≤0.1	≤0.05	Bal.	≤0.1	0.6–1.2	≤0.5	–	–	Zn, Ti
Ni 620	0.06	4.5	–	7.0	–	–	0.05	–	–	3.0	Bal.	3.1	Co, S, Se, Ti, Zr, P

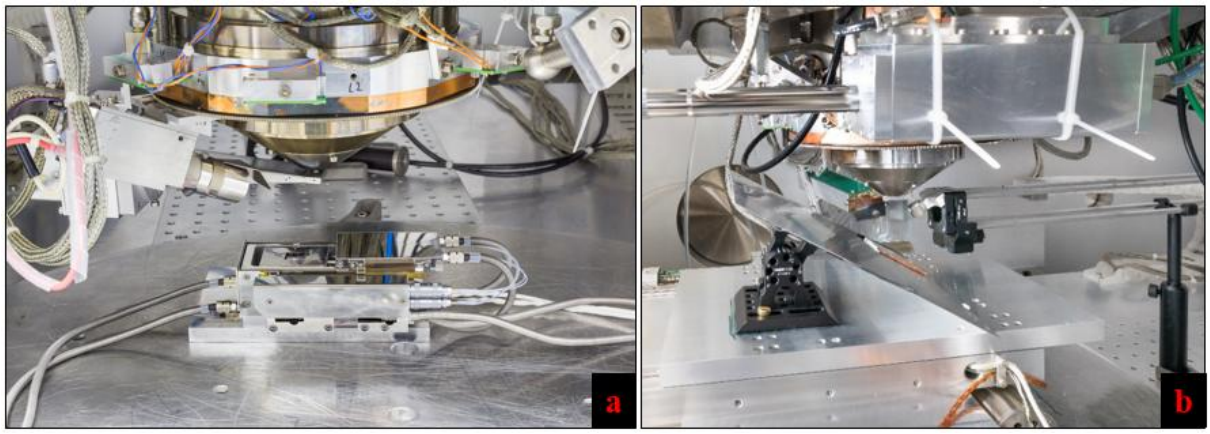

Figure 1: The experimental setup of (a) heating experiment, and (b) laser welding experiment

4 Results and Discussion

4-1 The *in situ* brazing results of applying Ni620 on Steel

The outcomes of a heating experiment of a Ni-620 filler on steel are presented in Figure 2. The system was rapidly heated up to reach a temperature of approximately 1080°C. The initial signs of melting were observed after 7.5 min, then the sample was held at 1080°C for an additional 2.5 min, followed by a rapid cooling process which took 7 min.

The high-magnification SEM results, combined with EDX analysis, were conducted in the region where the fillers melted on the substrate. The initial images revealed that the morphology of the filler changed in the melting region, appearing larger than in the unmelted area (Fig. 3c). The top-view EDX results showed no detectable Fe or Ni penetration. Furthermore, Si, a component of the filler, remained confined to the filler region.

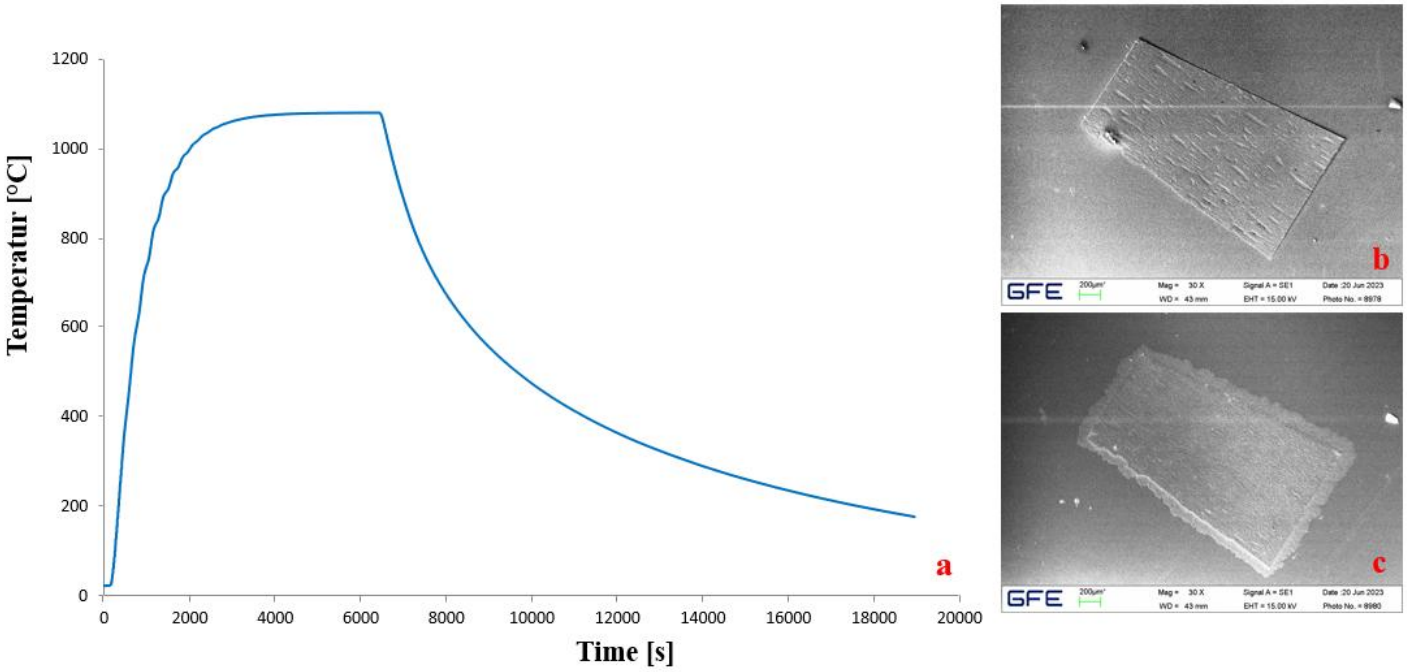

Figure 2: The brazing results of Nickel 620 on steel (a) the heating diagram, (b) The SEM image before heat treatment, and (c) The SEM image after heat treatment

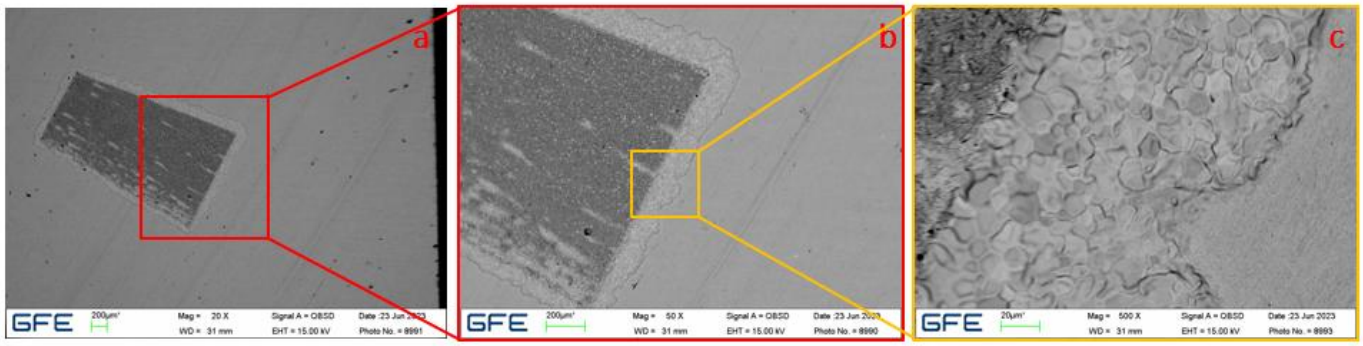

Figure 3: The top view SEM images of Ni620 on Steel. (a) 20x BSE image after finishing the brazing,(b) x50 BSE image ,and (c) x500 BSE image

The EBSD analysis of the cross-sectioned solder/substrate region (Fig. 4) shows that grain size at the interface is significantly smaller than in the bulk solder. The microstructure is heterogeneous due to rapid thermal processing and diffusion-controlled reactions.At the interface, Cr_2B forms from boron in the Ni620 filler and chromium from the steel substrate. The Z-IPF map indicates random orientation, suggesting nucleation-dominated growth without preferred texture. High KAM values in this region indicate elevated local strain and dislocation density, caused by lattice mismatch and the brittle nature of the boride phase.In the filler region, CrB and Fe_3C phases are observed. CrB forms under lower chromium availability and also shows random orientation, consistent with rapid solidification. Fe_3C appears in higher fraction and exhibits slight orientation clustering, likely due to partial inheritance from the ferritic parent structure. The KAM values here are moderate, reflecting phase transformation strain, thermal stresses, and limited recrystallisation. The Ni-rich region shows uniform grain structure and low KAM values, indicating reduced dislocation density due to stress relaxation following complete melting and re-solidification of the filler.

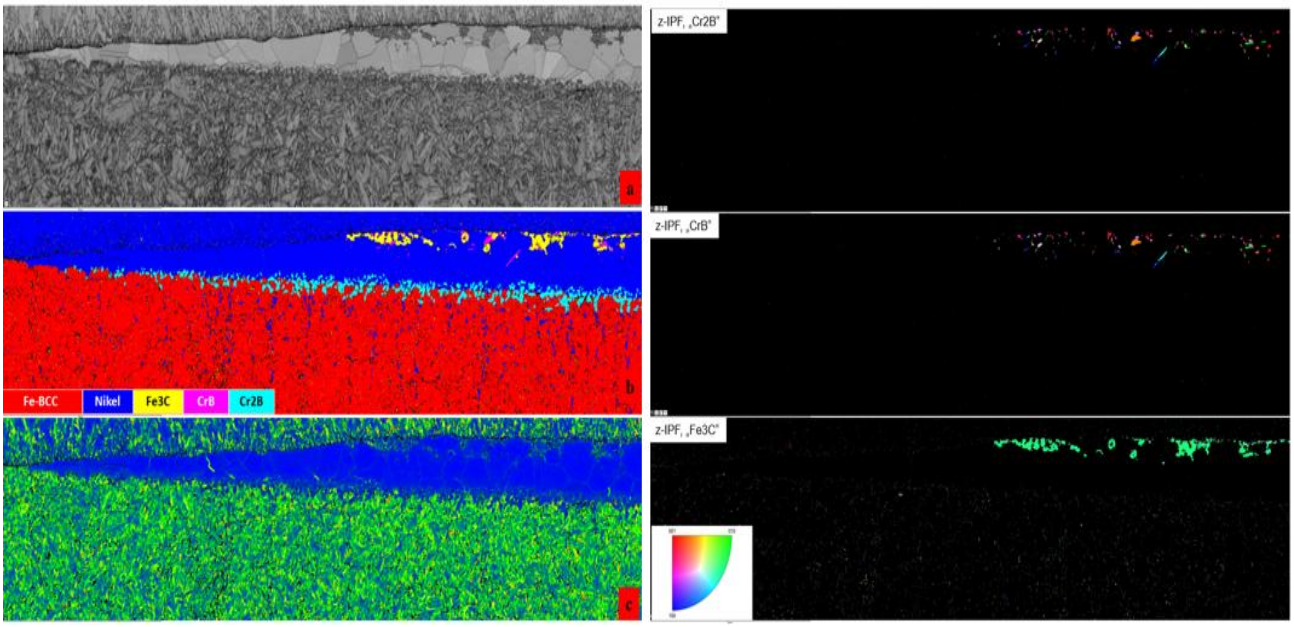

Figure 4: The EBSD result of brazing of Ni620 on Steel. (a) Band contrast, (b) phase distribution pattern, (c) KAM pattern , and (right) z-IPF map for Cr2B,CrB,and Fe3C

4-2 Brazing of Sn50Cu50 filler on En-Ac42100

In previous work, Sn78Cu22 was used as a filler on various Al alloys [12]. In the present study, SnCu50 was used to investigate the effect of filler composition on brazing behavior. The in situ brazing process involved heating to 560 °C, holding for approximately 6.5 min, and cooling to room temperature. Initial wetting appeared at the filler edge 24 s after reaching 560 °C, followed by faint wetting in the outer regions approximately 30 s later. After 42 s, the solder edges swelled, and about 1 min later the filler reached a semi-liquid state, began to spread across the substrate shortly after. Wetting was completed after ~2 min. Around 2.2 min later, changes in surface morphology were observed, followed by pore formation in the central region after 10 s. No further changes occurred until cooling under vacuum. The heating profile and SE images are shown in Figure 5.

Top-view BSE micrographs from different regions (Fig. 6) show significant spatial variation in solder density and morphology. In the initial wetting stage, low solder coverage is observed, with discontinuous, island-like spreading over the aluminum substrate. EDX analysis indicates that Sn from the filler spreads widely across the surface, with a broader distribution than Cu. Then, the solder density increases and more defined structures form, suggesting the onset of metallurgical reactions rather than simple liquid spreading (Fig. 6b). EDX analysis in this region shows ~47 wt. % Al and 51 wt. % Cu with only trace Sn, corresponding to ~68 at.% Al and 32 at.% Cu. This closely matches the stoichiometry of θ-Al_2Cu, confirming it as the dominant phase. This phase forms through diffusion-controlled reactions during brazing. Molten Sn acts as a transport medium, dissolving Cu and enabling its diffusion toward the Al substrate. Due to the stronger Al–Cu affinity, Cu reacts with Al to form θ-Al_2Cu, while Sn is rejected and remains in the surrounding liquid. Toward the outer wetting edge, the microstructure changes gradually as the liquid film thins,

reducing Cu availability, diffusion time, and slowing intermetallic formation. The continuous Al_2Cu network becomes discontinuous and eventually disappears. In these regions, Sn-rich phases dominate along grain boundaries, often with Si segregation. At the extreme edge, only a thin Sn layer remains before transitioning to the nearly pure Al substrate. This transition is driven by reduced liquid thickness, lower Cu concentration, limited diffusion, and capillary thinning (Fig.6c).

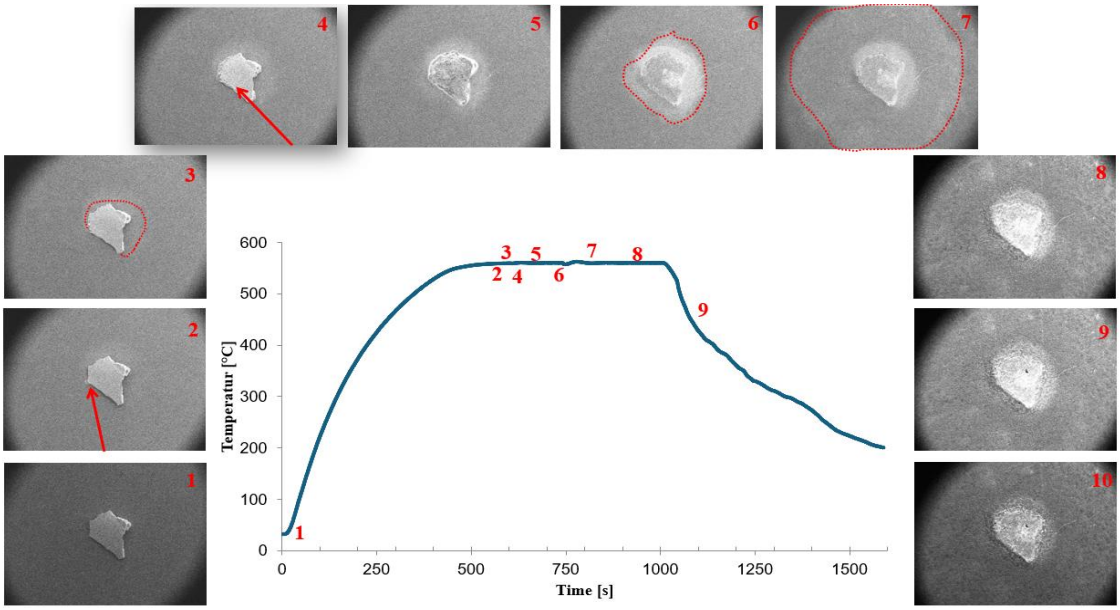

Figure 5: Thermal curve for brazing process: SnCu50/EN-AC 42100 at T=560°C

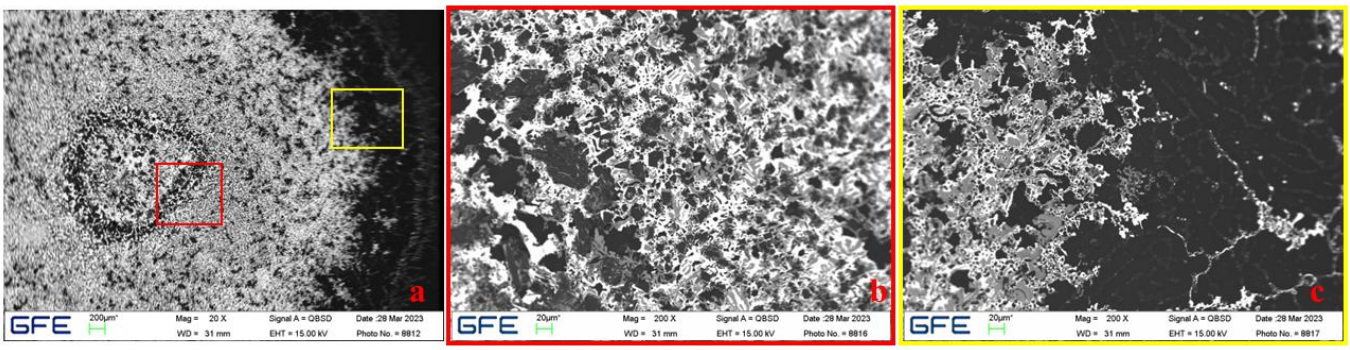

Figure 6: The top view BSE image of brazing of SnCu50 on En-Ac42100. (a) x20 red selected area in image(a), (b)x200, and (c)x200 of yellow selected area in image (a)

4-3 Sandwich joining of EN-AW 3003 and EN-AW 6060 with AlSi9Cu and Sn78Cu22

The cross-sectional BSE image of the sandwich brazing system composed of EN-AW 6060 / Sn78Cu22 / EN-AW 3003, processed at 600 °C with a holding time of 720 s in the LC-SEM, is shown in Figure 7. At this elevated temperature, complete melting of the Sn78Cu22 filler occurred, accompanied by pronounced wetting on both aluminum substrates. Clear interfacial reactions were observed. Microstructural analysis using BSE imaging and EDX mapping confirmed the formation

of the Al_2Cu intermetallic compound (IMC) at the aluminum–filler interfaces. The higher temperature significantly enhanced copper diffusion into the aluminum substrates, leading to the development of a continuous reaction layer. While the formation of this IMC improves metallurgical bonding, it also alters the wetting dynamics of the molten filler. In addition to IMC formation, cavities were detected within the filler zone. These void-like features are attributed to the growth of the Al_2Cu reaction layer, which locally consumes aluminum and copper and restricts further spreading of the molten filler metal. The formation of a rigid intermetallic layer at the interface limits wetting and hinders homogeneous filler flow, resulting in localized shrinkage effects and the development of cavities during solidification. Such defects can negatively influence joint integrity by acting as stress concentrators.

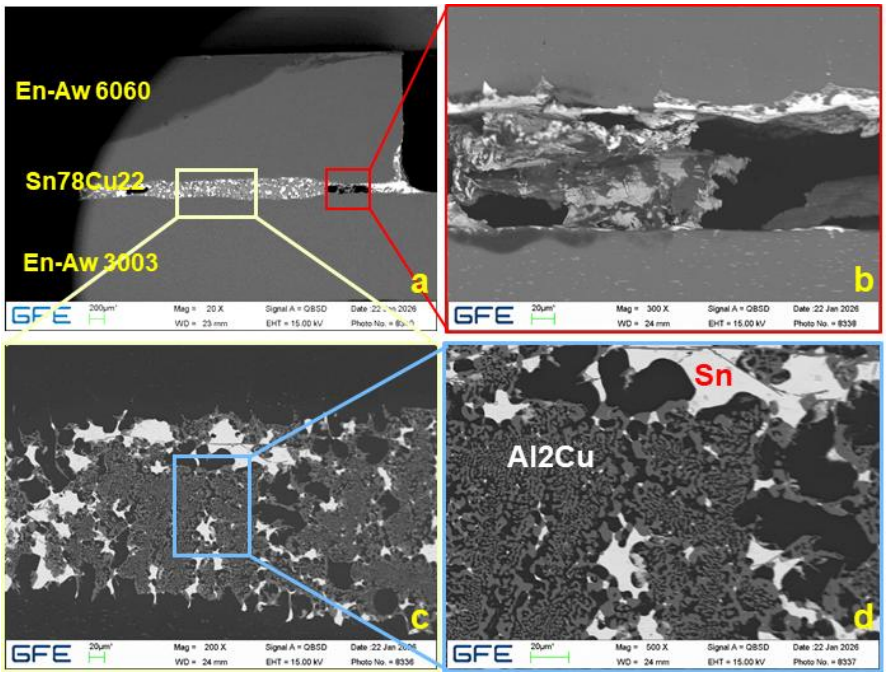

Figure 7: Cross-sectional BSE images of the 6060 / Sn78Cu22 / 3003 sandwich joint at 600 °C (720 s) at (a)×20, (b) ×300,(c)×200, and (d)×500 magnification, illustrating Al_2Cu IMC formation and cavity development in the filler

As a second model system, the sandwich brazing configuration EN-AW 3003 / AlSiCu / EN-AW 6060, processed at 630 °C for 1200 s, exhibits pronounced interfacial reactions and extensive elemental redistribution. Cross-sectional BSE images and EDX maps are shown in Figure 8. Due to the higher temperature and prolonged holding time, strong interdiffusion occurs between the filler and both aluminum substrates, resulting in thick reaction zones and multiphase regions. EDX analysis clearly reveals silicon concentrated in the middle region of the joint, corresponding to the original AlSiCu filler. The Si-rich phase is distinctly visible because silicon is not present in comparable concentrations in the EN-AW 3003 and EN-AW 6060 base materials, making its localization in the bonding zone easily distinguishable. This confirms the redistribution of filler-derived silicon within the joint center and its role in microstructural modification during solidification. In contrast, the distributions of copper and aluminum is less distinct. Although small amounts of copper are detected within the reaction zones, their contrast in the EDX maps is relatively weak. This is partly due to the low copper concentration and partly due to enhanced

diffusion at 630 °C, which leads to a more homogeneous elemental distribution. Furthermore, aluminum is difficult to distinguish clearly because it is the primary constituent of both substrates as well as the AlSiCu filler. As a result, aluminum appears continuously across the entire joint region, making precise interface delineation based solely on Al mapping challenging.

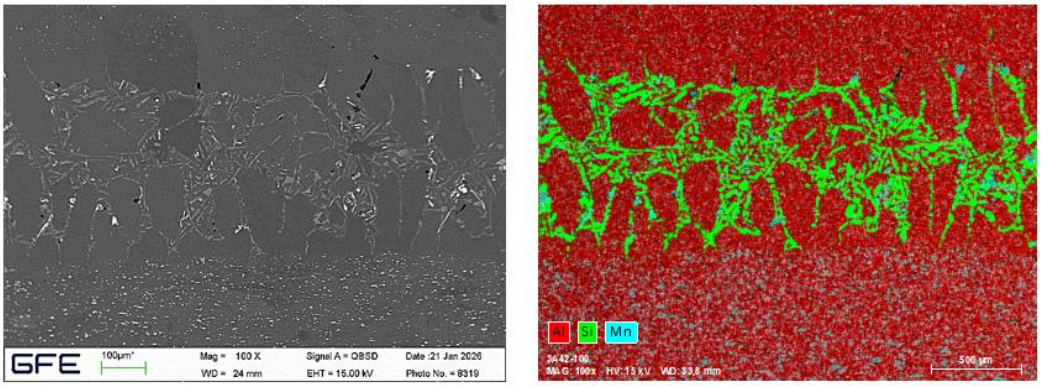

Figure 8: Cross-sectional BSE images and EDX maps of the 3003 / AlSiCu / 6060 sandwich joint after heating to 630 °C and holding for 1200 s. (left) the x100 BSE image, and (right) the EDX map

4-4 Laser welding of En-Aw6082 under vacuum conditions

Figure 9 presents SEM images of laser-welded EN AW-6082 aluminum alloy under vacuum conditions at a constant laser power of 40 W in deep-penetration mode. The welds were produced using two different feed rates, 1 mm/s and 0.5 mm/s, representing deep-penetration (keyhole) and heat conduction modes. At a feed rate of 1 mm/s (Figure 9a,c), the weld surface exhibits a highly irregular and porous morphology. At lower magnification (a), the weld seam appears rough, with non-uniform solidification patterns and scattered surface discontinuities. At higher magnification (c), a significant number of micro-pores and voids are clearly visible. These pores vary in size and distribution, indicating instabilities in the keyhole during welding. Such instabilities are typically associated with insufficient energy input per unit length, leading to rapid fluctuations in vapor pressure within the keyhole. Additionally, the high feed rate reduces the interaction time between the laser beam and the material, limiting the melt pool lifetime.In contrast, at a feed rate of 0.5 mm/s (Figure 9b,d), the welds show a markedly improved surface morphology. At lower magnification (b), the weld seam appears more uniform and continuous, with a smoother surface profile compared to the higher feed rate condition. The characteristic wave-like (ripple) patterns observed along the weld indicate a stable melt pool and a consistent solidification front. At higher magnification (d), the surface reveals significantly fewer pores, which are smaller and more uniformly distributed. This improvement can be attributed to the increased energy input per unit length at the lower feed rate, enhancing melt pool stability and prolonging its lifetime.

Figure 10 depicts SEM images of laser-treated samples in heat conduction mode. The bright, fine-structured band observed adjacent to the weld zone corresponds to the heat-affected zone (HAZ), where the material experiences temperatures below the melting point but high enough to induce microstructural transformations (Figure 10a). At a feed rate of 1 mm/s, the lower heat input results

in steep thermal gradients and rapid cooling, promoting localized grain refinement through partial recrystallization. This leads to the formation of a narrow band of fine equiaxed grains along the fusion boundary. In contrast, at a lower feed rate (0.5 mm/s), the increased heat input prolongs thermal exposure, allowing grain growth and reducing the visibility of this refined structure (Figure 10b).

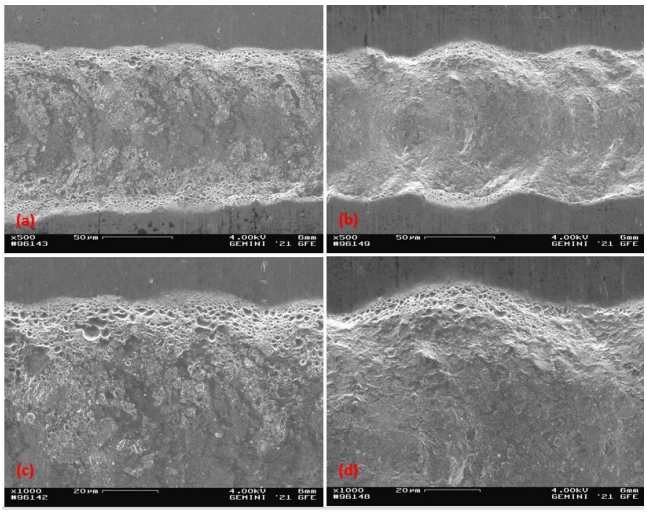

Figure 9: SEM images of sample EN-AW 6082. (a&c) deep penetration mode with 1mm/s feed rate, and (b&d) deep penetration mode with 0.5 mm/s feed rate

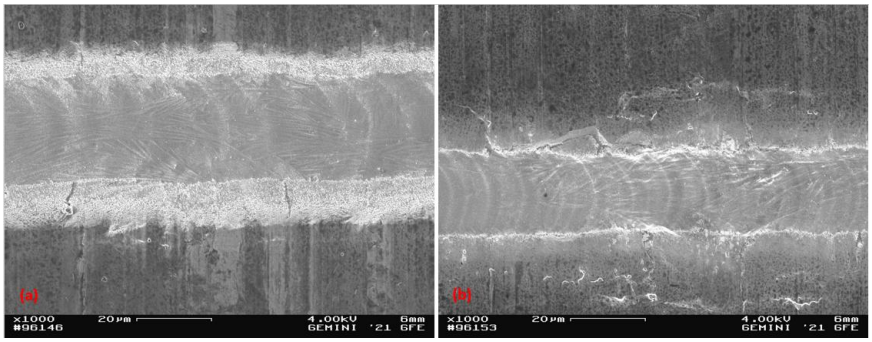

Figure 10: SEM images of sample EN-AW 6082. (a) heat conduction mode with 1mm/s feed rate, and (b) heat conduction mode with 0.5 mm/s feed rate

The quantitative measurements of surface roughness, penetration depth, and weld width are summarized in Table 2. The results demonstrate a clear distinction between deep-penetration and heat conduction welding modes in terms of weld geometry and surface quality. In deep penetration mode, significantly greater penetration depths and widths are achieved, with depths of approximately 20 µm (1 mm/s) and 30 µm (0.5 mm/s), and widths ranging from 112–125 µm and 111–114 µm, respectively. In contrast, heat conduction mode produces much shallower welds, with depths of 3.6 µm (1 mm/s) and 6 µm (0.5 mm/s), and narrower widths of 25–54 µm. These differences are attributed to the underlying welding mechanisms: keyhole formation in deep penetration mode enables efficient energy transfer and deeper welds, whereas conduction mode relies on surface heating and thermal diffusion. Reducing the feed rate from 1 mm/s to 0.5 mm/s increases the energy input per unit length, resulting in greater penetration depth in both modes,

with a more pronounced effect in deep penetration mode (approximately 50% increase). Surface roughness further highlights the contrast between the two modes. Deep penetration mode exhibits significantly higher roughness, increasing from 6.2 µm to 11.79 µm as the feed rate decreases, due to intensified melt pool dynamics and keyhole instability. In comparison, heat conduction mode produces smoother surfaces, with roughness values of 1.65 µm (1 mm/s) and 1.33 µm (0.5 mm/s), reflecting the stability of the conduction-driven process.

Table.2: The measured parameters

	Feed rate (mm/s)	**Roughness (µm)**	**Depth (µm)**	**Average width (µm)**
Keyhole mode	1	6.2	20	112-125
Heat conduction	1	1.65	3.6	30-52
Keyhole mode	0.5	11.79	30	111-114
Heat conduction	0.5	1.33	6	25-54

The cross-sectional analysis demonstrates that feed rate significantly affects not only weld geometry but also microstructural evolution (Figure 11). A higher feed rate (1 mm/s) results in a more homogeneous, laterally solidified dendritic structure, whereas a lower feed rate (0.5 mm/s) promotes directional solidification with columnar dendrites aligned along the weld depth. These findings highlight the strong dependence of weld microstructure on thermal conditions and energy input during laser welding.

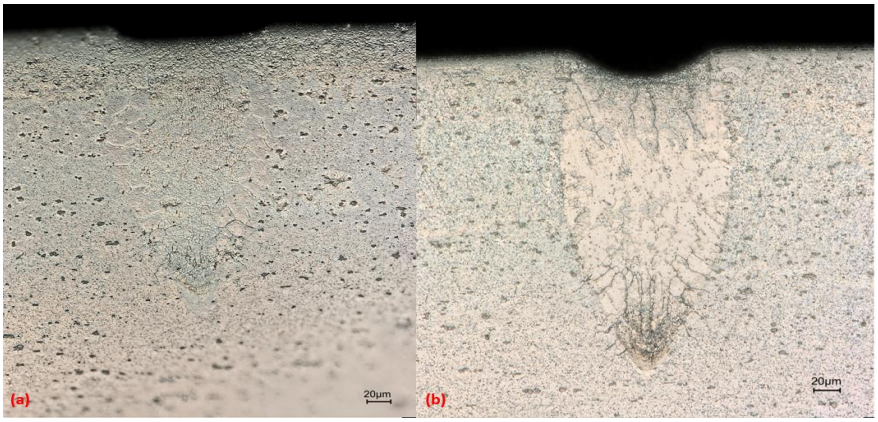

Figure 11: The cross section images of EN-AW 6082. (a) Deep penetration with 1mm/s, (b) deep penetration with 0.5mm/s feed rate

5 Summary

The study demonstrates that in situ LC-SEM is a powerful tool for understanding dynamic metallurgical processes, providing insights that cannot be obtained from conventional post-process analysis. Real-time observation reveals that joining processes are not only governed by material composition but also strongly by kinetic effects such as temperature, diffusion rates, and thermal cycling. For the Ni-620/steel system, limited interfacial interaction was observed despite complete melting of the filler. Elemental interdiffusion between Ni and Fe was negligible, indicating the presence of diffusion barriers. However, localized formation of boride phases (Cr_2B and CrB) occurred at the interface due to reactions between boron from the filler and chromium from the

substrate, resulting in fine, randomly oriented microstructures with high local strain. In Sn–Cu brazing of aluminum alloys, molten Sn acts as a transport medium for Cu, promoting diffusion-driven formation of θ-Al_2Cu intermetallic compounds. A pronounced radial microstructural gradient develops, with continuous intermetallic networks in the central region and Sn-rich phases toward the edges. This behavior is governed by variations in liquid film thickness, Cu availability, and diffusion kinetics.

For sandwich brazing systems, increased temperature and holding time enhance interdiffusion and reaction layer growth. In the Sn78Cu22 system, continuous Al_2Cu layers improve metallurgical bonding but also lead to cavity formation due to restricted filler flow and solidification shrinkage. In the AlSiCu system, strong elemental redistribution occurs, with silicon acting as a clear tracer of the original filler location, while aluminum and copper exhibit more homogeneous distributions due to enhanced diffusion. Laser welding of EN AW-6082 reveals a strong dependence of weld quality and microstructure on feed rate. Higher feed rates result in unstable keyhole behavior, increased porosity, and rough surface morphology, whereas lower feed rates improve melt pool stability, reduce defects, and produce smoother welds. Deep penetration mode achieves significantly greater weld depth and width compared to heat conduction mode, while also exhibiting higher surface roughness. Microstructural evolution transitions from fine equiaxed dendrites at higher feed rates to columnar dendrites at lower feed rates due to directional solidification. The results highlight that joining performance is controlled by the interaction of thermodynamic and kinetic factors, including diffusion, temperature, and process parameters. Real-time LC-SEM observations provide a powerful approach for correlating process conditions with microstructural evolution, enabling improved control and optimization of advanced joining technologies.

Conflict of Interest

The authors declare no conflict of interest.

Data Availability Statement

The data that supports the findings in this study are available upon reasonable request. Selected data are available after authorization in Coscine with the persistent identifier (PID) http://hdl.handle.net/21.11102/64572c1f-b45b-48fe-8ddc-a2e638b343e5

References

1. Kou, S. (2003). Welding metallurgy. *New Jersey, USA*, *431*(446), 223-225.
2. Messler Jr, R. W. (2024). *Principles of welding: processes, physics, chemistry, and metallurgy*. John Wiley & Sons.
3. Goldstein, J. I., Newbury, D. E., Michael, J. R., Ritchie, N. W., Scott, J. H. J., & Joy, D. C. (2017). *Scanning electron microscopy and X-ray microanalysis*. springer.
4. Pekin, T. C. (2018). *in situ Deformation Studies with Scanning Nanobeam Electron Diffraction*. University of California, Berkeley.

5. Reimer, L. (2000). Scanning electron microscopy: physics of image formation and microanalysis. *Measurement Science and Technology*, *11*(12), 1826-1826.
6. Podor, R., Ravaux, J., & Brau, H. P. (2012). In situ experiments in the scanning electron microscope chamber. *Scanning electron microscopy*, 32-54.
7. Xia, C., Li, Y., Puchkov, U. A., Gerasimov, S. A., & Wang, J. (2008). Microstructure and phase constitution near the interface of Cu/Al vacuum brazing using Al–Si filler metal. *Vacuum*, *82*(8), 799-804.
8. HUANG, J. H. (2016). Effects of germanium additions on microstructures and properties of Al–Si filler metals for brazing aluminum. *Transactions of Nonferrous Metals Society of China*, *26*(3), 775-782.
9. Laurila, T., Vuorinen, V., & Kivilahti, J. K. (2005). Interfacial reactions between lead-free solders and common base materials. *Materials Science and Engineering: R: Reports*, *49*(1-2), 1-60.
10. Penyaz, M. A., Ivannikov, A. A., Sevryukov, O. N., & Kalin, B. A. (2021). Overview of nickel-based filler metals for brazing of austenitic stainless steels. *Chin J Nonferrous Met*, *1*, 41-56.
11. Liu, S., Luan, Y., & Shohji, I. (2025). Brazing of Thin-Walled Stainless Steel Using Environmentally Friendly Ni-Cr-P Electrodeposition: Degradation Mechanism of Brazed Joint and Corresponding Improvement Strategy. *Materials*, *18*(10), 2406.
12. Khatami, S., Mayer, J., Aretz, A., Zhou, B., & Apel, M. (2026). Brazing of Sn78Cu22 on aluminum substrates observed via in-situ experiments in a large-chamber SEM. *Discover Mechanical Engineering*, *5*(1), 39.